SUPERCONDUCTING CIRCUITS WITH π-SHIFT ELEMENTS

Aleksandar Andreski

SUPERCONDUCTING CIRCUITS WITH π-SHIFT ELEMENTS

Aleksandar Andreski

Ph.D. Committee

Chairman
Prof.dr.ir. H. Zandvliet (Universty of Twente)

Secretary
Prof.dr. G. van der Steenhoven (University of Twente)

Promotor
Prof.dr.ir. H. Hilgenkamp (University of Twente)

Members
Prof.dr.ir. H. Rogalla (University of Twente)
Prof.dr.ir. A. Brinkman (University of Twente)
Prof.dr. J.E. Mooij (Delft University of Technology)
Prof.dr. J. Clarke (University of California at Berkeley)
Prof.dr.ir. G. Rijnders (University of Twente)

Back cover: A wordcloud consisting of the 70 most frequent words found throughout this thesis, including mathematical symbols. The size of each member in the wordcloud is proportional to the relative frequency with which it occurs in the text.

The research described in this thesis was carried out in the Faculty of Science and Technology as well as the MESA+ Instituite of Nanotechnology at the University of Twente, in collaboration with the Technische Universität Ilmenau (Germany). This work was financially supported by the NanoNed programme of the Dutch Technology Foundation (STW).

Superconducting Circuits with π-shift Elements
Ph.D. Thesis, University of Twente
Printed by Wöhrmann Print Service
ISBN 978-90-8570-853-7

SUPERCONDUCTING CIRCUITS WITH π-SHIFT ELEMENTS

PROEFSCHRIFT

ter verkrijging van
de graad van doctor aan de Universiteit Twente,
op gezag van de rector magnificus,
prof. dr. H. Brinksma,
volgens besluit van het College voor Promoties,
in het openbaar te verdedigen
op donderdag 15 September 2011 om 14.45

door

Aleksandar Andreski

geboren op 28 Juni 1978
te Ohrid, Macedonië

Dit proefschrift is goedgekeurd door:

prof.dr.ir. H. Hilgenkamp (promotor)

Table of contents

Chapter 1
Introduction

In the 25 years since the surprising discovery of high temperature superconductors, a wealth of knowledge about these materials, both in the academic and technological areas, has been accumulated. There are still many questions left as to the exact nature of superconductivity in high-T_c materials but nevertheless, research and development brought continuous progress, even leading to commercial exploitation of some advanced areas. The most evident benefit of high-T_c superconductors is that their transition temperatures are typically higher than 77K, the boiling point of nitrogen, thus simplifying the cryogenic aspects of a superconductive system since liquid nitrogen is widely available as an industrial coolant. This makes it possible to deploy superconductors in large-scale applications such as energy transport or high-field magnets without excessive infrastructural and safety costs. At the same time, higher transition temperatures opened up new application areas, for instance passive superconducting microwave components in telecommunication backbone networks. Other superconducting devices, among which magnetic field sensors, radiation/photon detectors and superconducting digital circuits, also stand to benefit from high-T_c materials although in this area the fabrication of complex high-T_c devices is challenging.

Looking from the point of view of solid-state material science, the charge transport mechanism in high-T_c materials is of a different nature than in the traditional metallic superconductor. Besides typically high transition temperatures, high-T_c superconductors exhibit a rich set of other interesting and unique phenomena, some of which may also have a technological potential. It is the purpose of this work to explore one such property of high-T_c superconductors, the *unconventional order parameter symmetry*, for use in superconducting electronic circuits. The next paragraphs will introduce the various aspects of the idea as structured in the rest of the thesis.

The most common representative of high-T_c materials, and among the first to be discovered, is the rare-earth perovskite oxide $YBa_2Cu_3O_{7\text{-}\delta}$ (in short YBCO). The transition temperature depends on the oxygen content δ that is fixed during the manufacturing of a particular YBCO crystal. The maximum value of the transition temperature is $T_c = 93\text{K}$, achieved for $\delta \approx 0.05$. This was much higher than the T_c of the conventional superconducting substances at the time of its discovery. To better illustrate the point, the measured difference in the supercon-

ducting transitions of a high-T_c and an "ordinary", low-T_c metallic superconductor, respectively YBCO and Niobium in this case, is plotted in Figure 1.1. Two lengths of superconducting thin films made from YBCO and Nb are connected in series and the combined resistance of the structure is measured vs. the temperature.

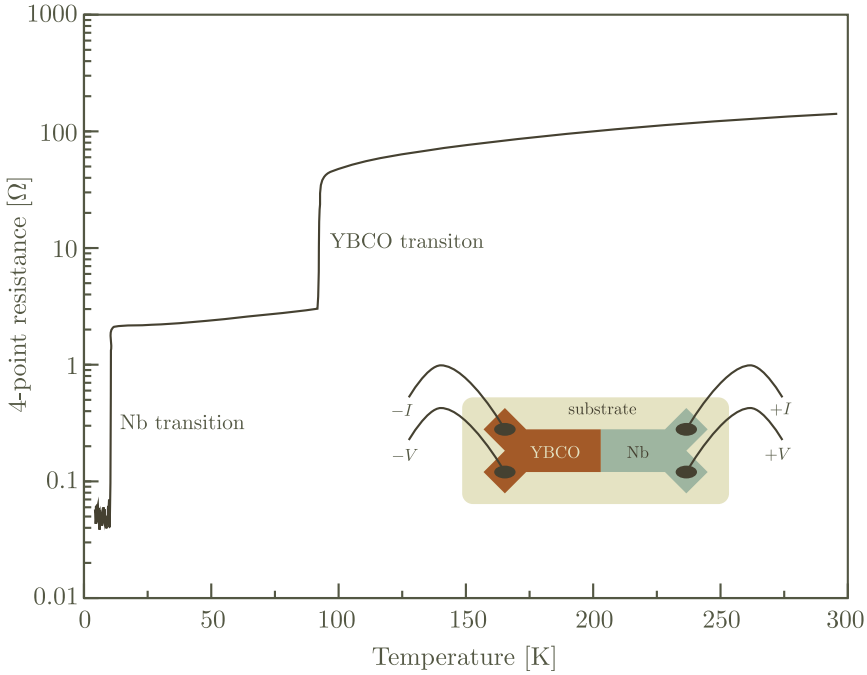

Figure 1.1. Electrical resistance vs. temperature of a series connection between a high-T_c and a low-T_c material measured in a 4-point configuration. The remaining resistance of about 50mΩ reflects the limitation of the equipment in this particular measurement.

Although the two superconducting *phase transitions* manifest in the same manner, just one aspect of which is the abrupt disappearance of DC electrical resistance shown in Figure 1.1, scientists speculated they are probably a result of unlike physical processes. This claim is nowadays well accepted in the scientific community, there being much evidence about the different nature of the superconducting phase of high-T_c and low-T_c materials (even in the absence of an exact microscopic model for the former). Indeed, a few key characteristics differentiate the two groups of superconductors, the most prominent being the already mentioned unconventional order parameter symmetry. It is a feature superficially similar to anisotropy in crystals and results in a number of interesting effects distinctive to high-T_c superconductors. The aspects of the unconventional order parameter symmetry relevant to superconducting circuits, which is the main focus of this thesis, are presented in Chapter 2.

The idea of making superconducting circuits utilizing the unconventional order parameter symmetry is connected to experiments observing *fractional flux quantization* in heterogeneous low-T_c/high-T_c rings [1]. These ring devices were formed by joining two semicircular segments, one made of a thin YBCO film and the other of a thin Nb film, in a superconducting planar loop where the contact between the materials is electrically conductive. The magnetic flux threading the loop after it was brought below the T_c of the two materials was investigated. It was found that in these rings the magnetic flux is quantized as $n + \frac{1}{2}$ times a quantization constant (n is integer). These fractionally quantized flux states are symmetrically distributed around the zero-flux origin but do not include it. As a result, the lowest energy configuration is a *pair* of $\pm\frac{1}{2}$ symmetric states and the loop is thus exhibiting a *symmetric bistable regime*. Further, the effect is a direct consequence of the unconventional order parameter of the YBCO component. Since the last is a material property, the bistability is *intrinsic* to the loop. Opposed to this is a homogeneous loop made from a single material where a similar symmetric two-state regime does not appear spontaneously and must be externally induced, for the flux states are distributed as n times the quantization constant where the lowest energy configuration is a single, zero-flux state (for $n = 0$). These homogeneous loops typically made from Nb are used as basic building blocks in ultra-fast state-machine superconducting circuits [2] operating in the magnetic flux domain. The circuits would benefit from reduced complexity and greater isolation from the noisy external environment were they to utilize the intrinsically bistable heterogeneous YBCO-Nb loops instead [3] [4].

In the next Chapter, after the principles behind superconducting (or Josephson) electrical networks and circuits are first presented, the details of the application of such YBCO-Nb loops, also known as π-*loops*, as bistable elements in digital gates are given.

Early exploration of the hybrid YBCO/Nb planar fabrication technology [5] [6] [7] in basic devices revealed the key obstacles and set the direction that further research should take. In the following step, an experiment with simple digital circuits of the SFQ (Single Flux Quantum) family, fabricated with π-loops for the first time, was performed [8]. The results showed correct operation, albeit only in a very narrow range of environmental variables (temperature, electrical bias). Those and follow-up experiments however did not allow to test the predicted advantages of using π-loops in digital SFQ circuits. The reasons were found to be twofold. Foremost is the low reliability in the manufacturing of π-loop SFQ designs that implement larger functional blocks for the purposes of realistic comparison with conventional SFQ circuits. Here, the circuits suffered from excessive spread in the parameters obtained during the experimental fabrication process, as well as frequent mistakes forced by the complexity of the processing steps. The other obstacle is the lack of sufficient shielding against stray magnetic fields that is essential for experiments with superconducting circuits of any kind. At present, building

measurement set-ups for high-T_c superconducting electronic devices is technically intricate and specialized components are not readily available, requiring much effort to be separately developed. Illustrating these problems are the results from many samples of the two integrated circuit (IC) designs containing SFQ circuits, the πChip2.1 and πChip2.2 series, both described in detail in Chapter 3. A micro-photograph of an SFQ device on one of these IC's is given in Figure 1.2 for illustrative purposes.

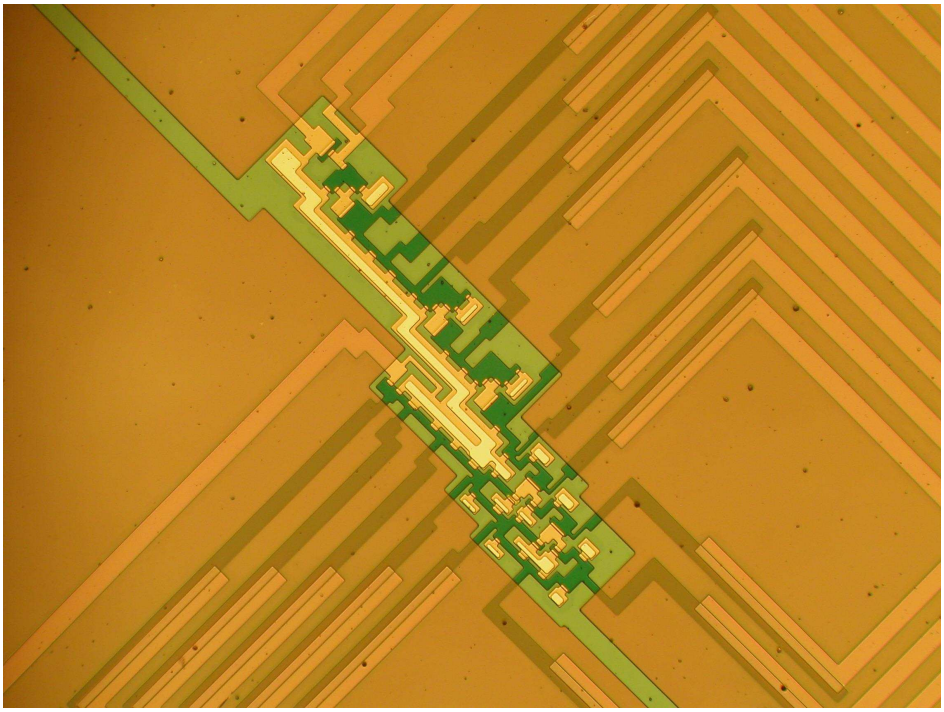

Figure 1.2. A circuit from the RSFQ family on a sample from the πChip2.2 series fabricated using the hybrid YBCO-Nb superconducting thin film process. The smallest structures seen at the photo are about 5μm in size. Detailed description of the manufactured circuits is given in Chapter 3.

Chapter 4 describes the improvements to the hybrid YBCO-Nb fabrication process and discusses the results of the implemented changes that, together with the knowledge gained about particular procedures, show a positive trend in process robustness. Also presented are electromagnetic simulation techniques modelling electrical parameters of the superconducting thin films as well as comparison with experimentally obtained values. Subsequently, the same Chapter briefly addresses the experimental difficulties with magnetic shielding, where measurements were

found vulnerable to systematic spread between cooling cycles. This especially affected complex SFQ designs and prohibited further experimentation with such circuits.

In parallel to developing the experimental aspects of the YBCO/Nb hybrid technology, a new application of π-loops was discovered, inspired by current research on superconducting quantum computers built with flux qubits [9] [10]. Calculations show that when a π-loop structure is connected to an inductive load and has a magnetic modulation terminal, it exhibits signal gain in the magnetic flux domain, in analogy to the voltage gain of semiconducting transistors. The behaviour of this novel structure is explored in Chapter 5, while subsequent measurements performed in order to confirm the models, as well as details about the design of the test structures, are presented in Chapter 6.

Whenever the discovery of an interesting phenomenon motivates the inception of an applied research effort, there is usually a good understanding of the starting hypotheses and constraints but rarely can the end results be clearly defined. This lies in the nature of scientific research, one never knows what lies behind the boundaries of the known nor is there any way to know whether said boundaries can be pushed in the anticipated direction. In many research endeavours that are skirting the limits of existing technology, it is experimentation that often sets those limits and deflects one away from the initial intention. Fortunately, experience shows that interesting, unanticipated results sometimes follow initially unsuccessful experiments. Such are the results of the work presented in this thesis as well. Experimental difficulties with SFQ circuits inspired the search for other, more simple, π-loop structures and eventually resulted with the devices described in Chapters 5 and 6 that are novel in the superconducting electronics field.

Chapter 2

Superconducting (Josephson) Networks

The literature about superconducting electronics focuses both on the physical processes within individual devices [11] [12] [13] as well as the engineering aspects [14] [15] [16] of the electrical systems built with them. In this Chapter, the concepts from the latter are placed within general circuit theory, enabling the analysis of superconducting circuits from a network perspective. Although advanced applications are not included, for instance quantum circuits (qubits) or vortex devices, the basics presented in this Chapter can be extended to encompass such structures as well.

Circuit theory is used as a basic tool in electrical engineering for visualization and algorithmic analysis (simulation) of the relevant processes in a given electromagnetic system by representing it with a network model. On the other side, abstracting physical processes with a network model is also necessary in order to design and build functional electromagnetic systems. The frame of a network model for systems that include interconnected superconducting parts, as Section 2.1 illustrates on a simple example, should preferably differ from the one used for ordinary electrical circuits. Section 2.2 describes this Josephson network model in detail, using examples and gradually introducing the various elements contained in such a network. It begins by first describing the nature of electrical current flow in superconductors and then suggests a new state variable for the system that better suits phenomena connected to superconducting planar circuits. Using this new network representation, the practical aspects of superconducting network modeling are given in Section 2.3, together with examples of superconducting circuits.

2.1 Classical electrical networks containing superconductors

An electrical network, as an abstract equivalent of a physical electromagnetic system, is completely described by a nodal diagram together with the constitutive equations (laws) of the elements inserted as branches between the nodes of the

diagram. Each of those equations connects the nodal quantity, or voltage V, and the flow quantity, or current I, across a branch. In addition, one has to also apply the Kirchhoff law of flow conservation at every node. Each element in the network corresponds to a distinct part of the system, its constitutive equation reflecting the physics taking place within it. These are usually integral versions of Maxwell's laws and/or specific charge transport aspects in the materials of which the element is made. For instance, Ohms law $V = I \cdot R$ is the constitutive equation defining a resistor element, while a relation associated to Faraday's induction law, $V = L \cdot \frac{\mathrm{dI}}{\mathrm{dt}}$, defines an inductor. Other elements that have more terminals and thus spread across more than one branch, such as transformers and transistors, are defined as a set of equations on more than one (I, V) pair.

A typical wire or a piece of conductor in the physical system will, in the network equivalent, be represented by two branches connected in series: one containing an inductor and the other a resistor element (the inductor is often neglected). Since an electrical current will flow through a superconducting wire without requiring a voltage difference between the wire's terminals, its equivalent element will contain only a series inductance as the resistor $R \equiv 0$. A simple example of a network containing both superconductors and conventional elements is illustrated in Figure 2.1.

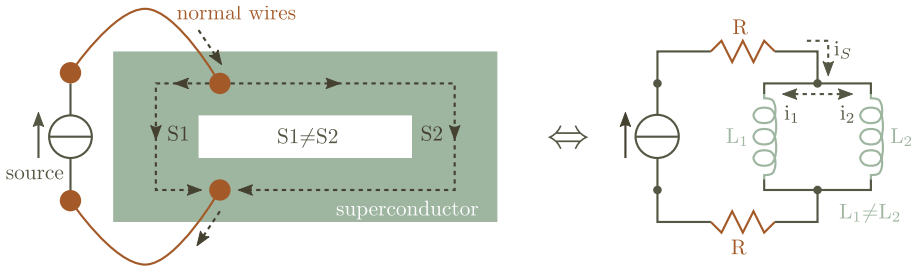

Figure 2.1. A simple electrical system consisting of a DC current source and (super)conducting parts on the left and its equivalent electrical network model on the right. The inductance of the normal wires has been neglected.

The question about how currents distribute between the branches in an electrical network is usually answered by solving the circuit differential equations, arrived at by combining the constitutive laws, the nodal architecture, Kirchhoff's law and eventually initial conditions. In the above example, if one starts by assuming the system is in a steady state where the time derivatives of all network variables are zero, i.e. the DC state as suggested by the sole source in the network, then the circuit equations acquire a trivial form that is not sufficient to solve for the distribution of current between the two superconducting branches.

In situations when steady-state solutions are not definite, one must resort to solving the system of differential equations including the history of the circuit by assuming a set of initial conditions and a turn-on transient for each source. Following the above method, one obtains

$$\begin{cases} L_1 \dfrac{\mathrm{d}i_1(t)}{\mathrm{d}t} = L_2 \dfrac{\mathrm{d}i_2(t)}{\mathrm{dt}} \\ i_1(t) + i_2(t) = i_S(t) \end{cases}$$

for the currents from Figure 2.1. Combining and integrating the above gives the solution

$$\begin{aligned} i_1(t) &= \frac{L_2}{L_1 + L_2} \cdot (i_S(t) - I_{S,0}) + I_1 \\ i_2(t) &= \frac{L_1}{L_1 + L_2} \cdot (i_S(t) + \frac{L_2}{L_1} I_{S,0}) - I_1 \end{aligned} \tag{2.1}$$

with the initial condition

$$i_1(0) = I_1 \tag{2.2}$$

and where $I_{S,0} = i_S(0)$. Choosing a value for the initial condition 2.2, one can now obtain $i_1(t)$ and $i_2(t)$ as functions of time, provided the excitation $i_S(t)$ is also known. A common method to explicitly include the initial condition for an inductor in the circuit is to add an independent constant current source in parallel, while the inductor is considered to have zero current at $t = 0$. The sum of the current through the inductor and the extra current source will be then equal to the current through the physical inductor element. In the circuit from Figure 2.1, it will amount to adding a second DC current source across L_1 with a value of I_1 and solving the circuit equations with zero initial conditions.

From 2.1, it is seen that the currents in the superconducting branches at any time t depend not only on the excitation source $i_S(t)$, but also on the initial current through the inductor at $t = 0$. In a network where each branch has some resistive losses, no matter how small, the initial conditions "decay away" after a finite time τ and are not necessary to be known for a steady state solution for every $t \gg \tau$. According to 2.1 however, the steady state of a network with at least one superconducting loop is always influenced by the initial conditions, thus they must be taken into account. This is a consequence of the fact that a current can indefinitely circulate around a closed superconducting path.

It can be concluded that in order to analyse a network containing superconductors and especially those including superconducting loops, one needs to solve the complete set of differential network equations even when a static solution is sought after, as well as keep track of initial conditions that can, in general, propagate infinitely forward in time.

However, superconductivity is a *macroscopic quantum phenomenon* and exhibits features other than just perfect electrical conductivity $R=0$. An example of one such effect is *flux quantization*, described in detail in Section 2.2, which states that the magnetic flux threading a superconducting loop must always be an integer multiple of a flux constant at any moment in time. For the circuit in Figure 2.1, this means that one more circuit equation must be added:

$$L_1\, i_1(t) - L_2\, i_2(t) = n \cdot C \tag{2.3}$$

where n is an integer and C is a constant. Taking flux quantization into account in the network of Figure 2.1, the solutions are still given by relations 2.1 but the initial condition in 2.2 will have to be modified:

$$I_1 = \frac{L_2}{L_1 + L_2}\, I_{S,0} + n \cdot C\, \frac{1}{L_1 + L_2} \tag{2.4}$$

where again $I_{S,0} = i_S(0)$. Explicitly including this initial condition in the circuit as an independent DC current source across L_1 is now no longer possible since I_1 is a function of the source i_S and the quantization integer n. Taking account for the initial condition now typically needs 2.3 to be added in the standard circuit equations, requiring modifications to the network analysis algorithm.

Generally, the flux quantization principle must be applied to each superconducting loop in a circuit. In other words, every time when two superconducting branches are placed in parallel, thus forming an uninterrupted superconducting loop, an additional circuit equation similar to 2.3 must be added. As a consequence, not only does the number of circuit equations rapidly grow in multi-loop superconducting circuits, one must also keep track of an integer n per each superconducting loop. The quantization integers act like extra degrees of freedom in the circuit, requiring even further modifications to the standard network analysis methods.

As a conclusion of the above discussion, it can be stated that the classical network model is impractical for systems where superconducting loops are present, especially for large networks with many components where flux quantization is important.

It is however possible to construct a network model suitable for superconducting circuits while remaining compatible with the methodology developed for classical networks, avoiding the above disadvantages. The key is the introduction of the *phase of the superconducting condensate* which will replace voltage as a nodal quantity while keeping all other determinants of the network the same. Fur-

thermore, the newly introduced nodal variable is closely connected to the charge transport mechanisms in the various superconducting devices. In Section 2.2, the *Macroscopic Quantum Model* (MQM) [14] of superconductors is used to introduce this new network variable.

2.2 Network aspects of current flow in superconductors

In a superconductor, a part of the mobile charge carriers exist in a single macroscopic quantum state. The condensation of the charge in the single state is a phase transition taking place when certain conditions are satisfied, for instance when the temperature becomes lower than the transition temperature T_c. An interesting fact is that, in general, good room-temperature conductors do not become superconducting. It is the nature of the processes leading to superconductivity that determine this counter-intuitive behaviour. The description of superconductivity given below uses the contrast between good conductors and superconductors to qualitatively explain those processes.

In good conductors, the mobile charge-carriers (electrons or holes) interact weakly between themselves and with the crystal lattice, forming a "charge gas" of almost uncorrelated entities that experience scattering from collisions, albeit little, as they move through the material. The lower the temperature becomes, the less collisions will happen and the easier the carriers move through the crystal lattice, but scattering and hence resistance never stops completely at any $T > 0$. Conversely, materials exist where the charge carriers experience strong interactions with the crystal lattice other than scattering collisions. In superconductors at temperatures below T_c, such complex interactions result in two particles being paired together in a bound state of net *integer* electronic spin, each particle contributing a spin of $+\frac{1}{2}$ or $-\frac{1}{2}$ to the pair. In many metallic superconductors for instance, the pairing mechanism couples electrons of opposite spin, resulting in a total electronic spin of zero and charge of $-2e$ for the pair.

A second process taking place in such a material is finally responsible for superconductivity. Since each of the paired states is bosonic, i.e. carrying an integer electronic spin, wavefunction interference between the paired entities forms a superfluid (Bose-Einstein) condensate, resulting in a single macroscopic quantum state described by a collective wavefunction $\Psi(\boldsymbol{r}, t)$ throughout the whole of the superconductor. The motion of the condensed pairs of charge carriers within the superconductor is thus collective on a macroscopic scale. Scattering, on the crystal lattice scale, does not hamper the motion of charge any more. Hence, the appearance of zero DC resistance in superconductors.

The temperature at which the phase transition happens is called the transition temperature T_c, while the macroscopic quantum wavefunction Ψ is also known as the *order parameter* due to its dual interpretation as a phenomenological quantity indicating the order *gained* in the material when the phase transition happens.

In metallic low-Tc superconductors, for instance in Niobium, individual electrons interact with each other through atomic-scale vibrations in the crystal lattice, called phonons, that result in a small attractive force between nearby electrons. As the temperature drops, the phonon-mediated electron interaction grows stronger in relative terms and the "free electron gas" becomes correlated over an increasing length scale. At $T \approx T_C$, it becomes energetically favourable for some of the electrons to condense in pairs bound by a phonon interaction, where the electron spins are necessarily opposite. The bound state, called a *Cooper pair*, has a total charge $-2e$ and zero electronic spin - it is thus bosonic. Since the effective diameter of a Cooper pair is larger than the average distance between them, they overlap and interfere in a coherent manner, hence forming a single charged entity described by a macroscopic quantum function as given above.

The phonon-mediated superconductivity found in Niobium and other low-T_c materials is different than the pairing mechanisms leading to the forming of a charged condensate in high-T_c superconductors, including YBCO. The exact details of the latter are still under debate but nevertheless, in all superconducting materials a condensate of bosonic charge carrier-pairs exists that, although exhibiting specific properties in specific materials, is phenomenologically similar.

It is further important to note that not all mobile charge in the superconductor will belong to the superfluid condensate. Unpaired electrons or holes will still exist at $T > 0$ and thus, in the case when electric fields are present in the material, also contribute to conduction. Fortunately, this "normal channel" of conduction in a superconductor needs to be considered only at frequencies much higher than what will be used in this text, so it will be disregarded. One exception is the current across a contact between two superconductors, the Josephson Junction, where normal electrons (or holes) contribute significantly to the transport of charge when there is voltage across it.

The behaviour of the charged condensate in a superconductor is described by the macroscopic quantum wavefunction

$$\Psi(\boldsymbol{r}, t) = \sqrt{n(\boldsymbol{r}, t)} \cdot e^{i \cdot \theta(\vec{r}, t)}. \tag{2.5}$$

that is a coherent sum of the individual wavefunctions of the paired carriers over the space that the superconductor occupies. This embodies the process of interference between the Cooper pairs as explained above but in a compact quantitative form.

The square of the wavefunction's amplitude, $n(\boldsymbol{r}, t)$, is associated with the number density of the charge-pairs in the condensate at a given coordinate $\boldsymbol{r}$ and time t, while one finds information about the interaction of the condensate with electromagnetic fields in the phase θ.

The *supercurrent density* $\boldsymbol{J}_S$ is a charge flux locally defined through a quantum mechanical "probability flow" of the coherent condensate. The classical view of current flow as originating from charge density changes:

$$-\nabla \boldsymbol{J} = q \cdot \frac{\partial \rho}{\partial t} \tag{2.6}$$

can be used in this context, except that the charge density ρ is now taken as the absolute value of the wavefunction squared $|\Psi \cdot \Psi^*|$. Applying the Schrödinger equation for the motion of a single charged quantum particle-wave in a electromagnetic field to the "collective" wavefunction from 2.5 and using the definition for current from 2.6, where $\rho = |\Psi \cdot \Psi^*|$, the supercurrent is calculated to be [14]:

$$\boldsymbol{J}_S(\boldsymbol{r}, t) = -\frac{2e \cdot n}{2m} \cdot (-\hbar \cdot \nabla\theta(\boldsymbol{r}, t) + 2e \cdot \boldsymbol{A}(\boldsymbol{r}, t)) \tag{2.7}$$

where $\boldsymbol{J}_S$ is the supercurrent density, θ is the phase of the macroscopic wavefunction while $\boldsymbol{A}$ is the magnetic vector potential. It is assumed that the individual particles of the charged superfluid are Cooper pairs carrying twice the charge $-2e$ and having twice the mass $2m$ of an electron. Further, it is assumed that the material is homogeneous and that the charged superfluid density is constant (equilibrium) i.e. $n(\boldsymbol{r}, t) = n$. The *supercurrent equation* 2.7 is central in the MQM and is used extensively in this text.

On a first look, it seems that an inconsistency appears: neither the magnetic vector potential $\boldsymbol{A}$ nor the wavefunction phase θ can be directly determined from experiment but yet, 2.7 relates them to the measurable quantity $\boldsymbol{J}_S$. Namely, the vector potential $\boldsymbol{A}$, given by

$$\boldsymbol{B} = \nabla \times \boldsymbol{A}$$

as a derivate of Gauss's law $\nabla \boldsymbol{B} = 0$, is just a mathematical convenience easing calculations in electromagnetic systems. As a matter of fact, since $\nabla \times (\nabla \chi) = 0$ for any scalar function χ, all members of the ensemble $\boldsymbol{A}' = \boldsymbol{A} + \nabla \chi$ across χ would produce the same flux density $\boldsymbol{B}$. Hence, $\boldsymbol{A}$ is not uniquely determined. On the other hand, θ is the absolute phase of a quantum wavefunction and can have no direct physical meaning. Yet, both $\boldsymbol{A}$ and θ are directly related through 2.7 to a macroscopically measurable quantity $\boldsymbol{J}_S$.

If one chooses a particular $\boldsymbol{A}'$ from the ensemble above, it is said that the system's *gauge* has been chosen. Inherently, Maxwell's equations are *gauge-invariant*, meaning that the measurable quantities, such as $\boldsymbol{E}$ and $\boldsymbol{B}$ for example, remain the same in any gauge. A consequence of the gauge invariance of Maxwell's equations is that the electric scalar potential ϕ of the system, also a gauge-dependent conceptual construct, is then fixed in relation to $\boldsymbol{A}'$ when a particular gauge is chosen.

It is important to note that advanced theories of electromagnetic phenomena treat the electromagnetic potentials $\boldsymbol{A}$ and ϕ as a more fundamental field than either $\boldsymbol{B}$ or $\boldsymbol{E}$, not just as a mathematical convenience. However, that does not change the principle of gauge invariance described above and all calculations henceforth are still true.

It can be shown [14] that gauge invariance also holds for 2.7, where now $\boldsymbol{A}$ and θ are connected such that the macroscopic variable $\boldsymbol{J}_S$ is independent on the particular choice of gauge. Namely, when a gauge transform of the system is performed by selecting another vector potential from the ensemble of functions, i.e. the transformation

$$\boldsymbol{A}' \rightarrow \boldsymbol{A} + \nabla\chi \tag{2.8}$$

is made, then also the macroscopic quantum phase θ and the electric scalar potential ϕ must be transformed accordingly

$$\begin{aligned} \theta' &\rightarrow \theta - \frac{2e}{\hbar}\chi \\ \phi' &\rightarrow \phi - \frac{\partial\chi}{\partial t} \end{aligned} \tag{2.9}$$

where the latter equation holds for all EM systems while the former pertains only to the superconducting parts in them. Obviously, the use of the quantum phase θ as a nodal variable in a network model should be no different than the use of electric potential ϕ from the point of view of gauge invariance.

The rest of this Chapter introduces the Josephson Network model, defining the basic elements as well as giving examples of functional circuits. Section 2.2.1 begins by looking at the specifics of current flow through a superconducting wire while section 2.2.2 introduces the phenomenon of flux quantization in superconducting rings. After a discussion on the correct nature of the nodal variable in a general electromagnetic network and the introduction of the concept of partial inductances in section 2.2.3, the superconducting network model is presented in section 2.2.4 followed with the circuit definitions of the most common elements in Section 2.2.5. At the end, in Section 2.2.6, an analysis procedure based on the free (Gibbs) energy of the network is presented, after which examples of simple circuits and basic digital blocks are given.

2.2.1 Current flow in a superconducting cylindrical wire

In superconductors, the flow of current and the distribution of the magnetic field are qualitatively different than in a normal conductor. For the purposes of illustrating the most general properties of current flow in superconducting segments, the simple system shown in Figure 2.2 will be analysed in this section. A constant axial current I_{app} flows through an infinitely long superconducting wire of circular cross section and radius a, creating the magnetic flux density $\boldsymbol{B}$. The distribution of the current density and the field within the wire should be determined.

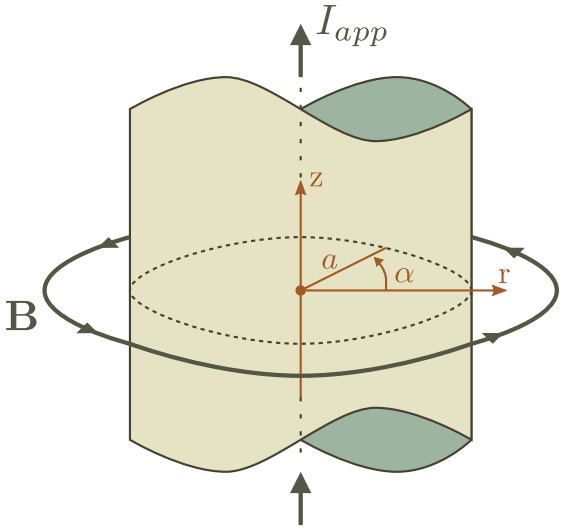

Figure 2.2. A section of a superconducting wire of circular cross section and the cylindrical coordinate system used in the text.

To accomplish this, two relations are used that are valid inside a superconductor, derived from 2.7 using vector identities and Maxwell's equations. These are the First and Second London equations, respectively:

$$\frac{\partial}{\partial t}(\Lambda \boldsymbol{J}_S) = \boldsymbol{E} + \frac{1}{n \cdot 2e}\nabla\left(\frac{1}{2}\Lambda \boldsymbol{J}_S^2\right) \tag{2.10}$$

$$\nabla \times (\Lambda \boldsymbol{J}_S) = -\boldsymbol{B} \tag{2.11}$$

where the parameter $\Lambda = \frac{2m}{n \cdot (2e)^2}$ is called the London coefficient. The factor containing the gradient of the square of the current in the First London equation arises from the Lorentz force $\boldsymbol{v} \times \boldsymbol{B}$ on the charged condensate moving with velocity $\boldsymbol{v}$ relative to the field $\boldsymbol{B}$. Its effect is small compared to the acceleration provided by the electric field $\boldsymbol{E}$ on the charges and hence the second part on the right of 2.10 is very often neglected.

From the symmetry of the problem and using the cylindrical coordinate system (r, α, z) as given in Figure 2.2, it is concluded that the current will have just a z component that can depend on the radius r only, i.e. $\boldsymbol{J}_S = J_z(r) \cdot \boldsymbol{i}_z$. Through 2.11, it is found that the magnetic field inside the wire will then be tangential and depend solely on the radius r:

$$\boldsymbol{B} = B_\alpha(r) \cdot \boldsymbol{i}_\alpha = \Lambda \cdot \frac{\partial J_z(r)}{\partial r} \cdot \boldsymbol{i}_\alpha \tag{2.12}$$

Outside the superconductor, the magnetic field will obey Maxwell's equations in free space for the given geometry. This again results in only an α component but with a fixed dependence $\sim\frac{1}{r}$ away from the wire.

To find the field and current distribution, the system is considered to be in *magneto-quasistatic* (MQS) conditions. Under MQS, the magnetic fields dominate the system, meaning that the electric fields are secondary and that none are externally applied. Another way to define MQS is to claim that the electric fields in the system are generated only by magnetic induction and not by free charges. The electric fields being secondary, they are calculated from Faraday's induction law *after* the magnetic fields are found with the assumption $\boldsymbol{E} = \boldsymbol{0}$. Mathematically, MQS is manifested in taking a form of Ampere's law that neglects the displacement part:

$$\nabla \times \boldsymbol{H} = \boldsymbol{J} + \frac{\partial \boldsymbol{D}}{\partial t} \cong \boldsymbol{J}$$

The MQS approximation in practical superconductors is valid for almost all frequencies provided that they are lower than the "pair frequency" ω_{pair} [14], when the energy associated with driving the paired charge carriers becomes greater than $\hbar\,\omega_{\text{pair}}$, the energy binding the pair together. They would then break into their individual constituents.

A second assumption is necessary for a general quasistatic regime to be valid: the lengthscale of the system l is much smaller than the typical wavelength λ of the EM fields developed. This is actually the same limit that allows a single, or in other words a *lumped*, element to be used for modelling a specific device in EM networks. Since every device can be divided in increasingly smaller parts until it satisfies $l \ll \lambda$, it is usual in electrical networks to always assume quasistatics and use a *distributed* model for those devices considered electromagnetically large at the frequencies of interest. The distributed model is simply a series connection

of repeating lumped elements that represent the pieces of the broken-up "large" device. Since a time-constant current is assumed in the example from 2.2, this condition is obviously satisfied.

Using the second London equation 2.11 together with Ampere's law in the MQS limit, the Helmholtz equation is found for the magnetic flux inside the superconductor:

$$\left(\frac{\mu_0}{\Lambda} - \nabla^2\right) \cdot \boldsymbol{B} = 0 \tag{2.13}$$

which, in cylindrical coordinates with the given system symmetry, transforms into:

$$\frac{\mathrm{d}^2 B_\alpha(r)}{\mathrm{dr}^2} + \frac{1}{r} \cdot \frac{\mathrm{dB}_\alpha(r)}{\mathrm{dr}} - \left(\frac{\mu_0}{\Lambda} + \frac{1}{r^2}\right) \cdot B_\alpha(r) = 0$$

The only physical solution is a modified Bessel function of the first kind and first order $I_1(x)$:

$$B_\alpha(r) = B_0 \cdot \frac{I_1(\frac{r}{\lambda_L})}{I_1(\frac{a}{\lambda_L})}, \quad r \leqslant a \tag{2.14}$$

where a characteristic length, the *London penetration depth* $\lambda_L = \sqrt{\frac{\Lambda}{\mu_0}}$ is introduced while the constant B_0 is the field at the surface of the superconducting wire.

The penetration depth is a material constant and indicates how much does a magnetic field penetrate inside a superconductor. The values of λ_L for typical superconductors are in the 10s to 100s of nanometers. A superconducting structure with its smallest dimension much greater than the penetration depth would have no magnetic field inside the bulk, except for a surface region with approximate thickness equal to λ_L. This is the *Meissner effect* where a superconductor expels all magnetic flux from its bulk save for a thin surface sheet. The effect is seen in 2.14 if one takes the wire's diameter $a \gg \lambda_L$ (see also Figure 2.3).

After the constant B_0 is calculated from the integral form of Ampere's law at the boundary $r = a$ as $B_0 = \frac{\mu_0 \cdot I_{\mathrm{app}}}{2\pi \cdot a}$, the end result for the magnetic flux density becomes:

$$B_\alpha(r) = \begin{cases} \dfrac{\mu_0 \cdot I_{\mathrm{app}}}{2\pi \cdot a \cdot I_1(\frac{a}{\lambda_L})} \cdot I_1(\dfrac{r}{\lambda_L}) & r \leqslant a \\ \dfrac{\mu_0 \cdot I_{\mathrm{app}}}{2\pi \cdot r} & r \geqslant a \end{cases} \tag{2.15}$$

where it was used that the tangential component of the magnetic field at the boundary $r = a$ does not change. From 2.12 and 2.15, one calculates the current distribution to be:

$$J_z(r) = \frac{I_{\mathrm{app}}}{\lambda_L \cdot 2\pi \cdot a \cdot I_1(\frac{a}{\lambda_L})} \cdot I_0(\frac{r}{\lambda_L}) \tag{2.16}$$

where now the modified Bessel function $I_0(x)$ is of the first kind and zeroth order. Both the magnetic flux and current density are plotted in Figure 2.3 for three values of the penetration depth λ_L compared to the radius a of the wire. One can clearly see the Meissner effect in the plots of Figure 2.3 for $a \gg \lambda_L$ (solid line): the quick exponential-like decrease of the magnetic flux density away from the surface justifies taking $\boldsymbol{B} = \boldsymbol{0}$ inside the superconductor, save for a thin surface sheet a few λ_L thick.

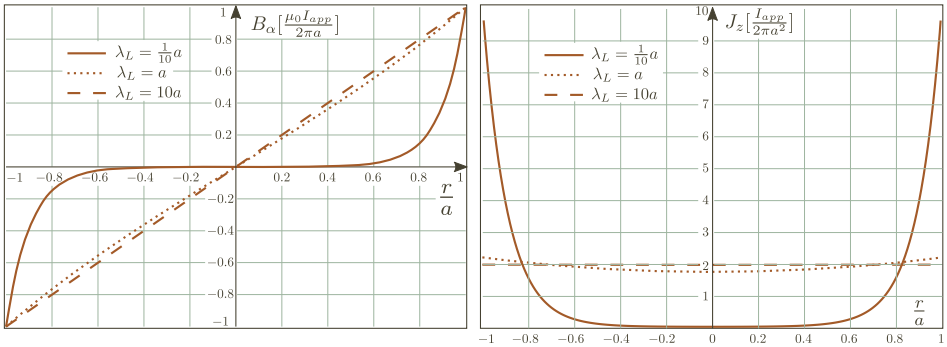

Figure 2.3. Calculated profiles of the magnetic field B_α and current density J_z inside the long cylindrical superconducting wire of radius a for a few values of the London penetration depth λ_L. There is little change in the profiles for λ_L equal and less than a.

If the analysed superconductor had a rectangular shape, the profile of the magnetic field when calculated in the same way as above would be a strictly exponential decay, save for edge effects. To see this, recall that the Helmholtz equation 2.13 for $\boldsymbol{B}$, in Cartesian coordinates aligned with the rectangular geometry of the superconductor, will have a solution that is

$$B_y(x) = B_0 \cdot e^{-(x/\lambda_L)}$$

The x coordinate is normal to the superconductor's boundary and is pointing towards the bulk while y is in a direction tangential to the boundary but normal to the current flow.

According to the supercurrent equation 2.7, the current density $\boldsymbol{J}_S$ is proportional to the vector sum of the phase gradient $\nabla\theta$ and the magnetic potential $\boldsymbol{A}$. An argument often made is that the gradient of the phase is responsible for "driving" a current through a superconductor. Indeed, choosing a gauge where $\nabla\theta(\boldsymbol{r}, t) = C(\boldsymbol{r}) \cdot \boldsymbol{J}_S(\boldsymbol{r}, t)$ satisfies the London and supercurrent equations for any scalar function $C(\boldsymbol{r})$, including the ones that are constant in space. Although

the phase is then not connected to the material properties of the system due to C being an arbitrary scalar constant, it is a function of the geometry and thus a helpful tool to visualize current flow in a superconductor.

If one allows for the small restriction of the gauge freedom as indicated above with C constant, it follows that for any circle lying on a normal cross-section within the cylindrical superconductor from Figure 2.2, the phase gradient around the circle will be constant since $\boldsymbol{J}_S$ is constant around it. This will also include the circular superconductor circumference line. Moreover, such paths that roughly follow the superconductor's cross-sectional symmetry can always be found inside it even for an arbitrary geometry. A continuum of paths along which the current density is constant can be visualized as cylinder-like surfaces symmetrical with the system's geometry, see Figure 2.4. These "sheets" are characterized by a constant phase gradient proportional to the current that is tangential to the sheet's surface. Deeper in the superconductor the absolute values of both quantities on such equi-phase-gradient sheets will exponentially decrease per the Meissner effect.

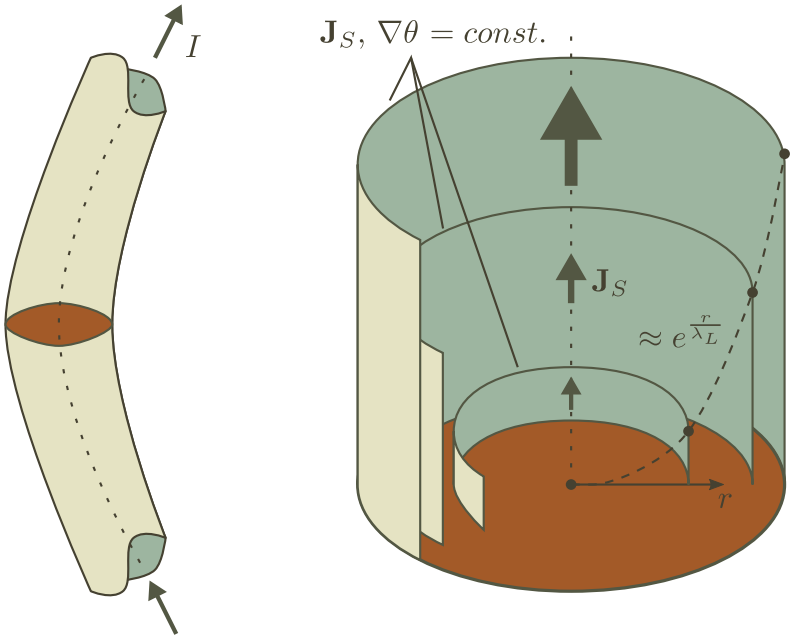

Figure 2.4. A section of a superconducting wire and a visualization of the "sheets" of constant current and phase gradient in the vicinity of the marked cross-section. The height of each sheet corresponds to the value of the current density and phase gradient along its circumference.

In a superconductor with a cross-section much smaller than the penetration depth, the current distribution, the magnetic field and the phase gradient will be cross-sectionally homogeneous and constant along the length, as the plots from Figure 2.3 illustrate. It is therefore possible to visualize the thin superconductor as a normal conductor carrying current, except that voltage differences should be thought of as phase differences along its length.

2.2.2 Flux(oid) quantization in a superconducting ring

When a length of superconductor forms an uninterrupted superconducting loop, the quantum-mechanical nature of the charge flow within it manifests macroscopically through the effect of *flux quantization*. This result is similar to the quantization of the orbital momentum of electrons in an atom. To illustrate flux quantization, the geometry in Figure 2.5 will be used.

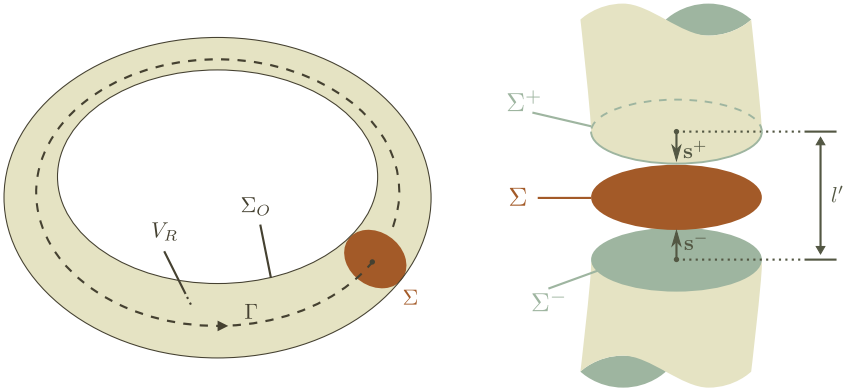

Figure 2.5. A superconducting ring and the definition of the surfaces used in the text.

The supercurrent equation can be written as

$$\boldsymbol{A} + \Lambda \boldsymbol{J}_S = \frac{\Phi_0}{2\pi} \cdot \nabla\theta \tag{2.17}$$

where the constant

$$\Phi_0 = \frac{h}{2e} \cong 2.07 \times 10^{-15}\, T \cdot m^2$$

is named the *magnetic flux quantum*. Integrating both sides along the closed contour Γ, it is obtained

$$\frac{2\pi}{\Phi_0}\left(\oint_\Gamma \boldsymbol{A} \cdot \mathrm{d}\boldsymbol{l} + \Lambda \oint_\Gamma \boldsymbol{J}_S \cdot \mathrm{d}\boldsymbol{l} \right) = \oint_\Gamma \nabla\theta \cdot \mathrm{d}\boldsymbol{l}$$

The order parameter $\Psi = |\Psi| \cdot e^{i\theta}$ must have a single value at each point within the superconductor. This allows the phase to have multiple values at the same point but of only $2\pi \cdot n$ difference between them as $e^{i2\pi \cdot n} = 1$. Thus, the integral of the gradient of the phase along a closed path, yielding the difference of the phase at the same arbitrary point along Γ, also has a value of $2\pi \cdot n$:

$$\oint_{\Gamma} \nabla\theta \cdot \mathrm{d}\boldsymbol{l} = 2\pi \cdot n$$

where n is an integer. If the contour Γ is chosen deep inside the bulk of the ring where $\boldsymbol{J}_S = 0$ due to the Meissner effect, then it is obtained

$$\Phi = n \cdot \Phi_0 \tag{2.18}$$

where from Gauss' law

$$\Phi = \int_{S_\Gamma} \boldsymbol{B} \cdot \mathrm{d}\boldsymbol{s} = \oint_{\Gamma} \boldsymbol{A} \cdot \mathrm{d}\boldsymbol{l}$$

is the magnetic flux through the surface S_Γ enclosed by the contour Γ. The flux quantization condition 2.18 implies that the magnetic flux threading the loop is always equal to an integer multiple of the magnetic flux quantum Φ_0. This is true even when external magnetic fields are applied, inducing a current through the loop which will create an equal and opposite flux such that the total flux stays an integer multiple of Φ_0.

When a closed path along which $\boldsymbol{J}_S = 0$ cannot be found, the middle part of the equation

$$2\pi \cdot n = \frac{2\pi}{\Phi_0} \left(\oint_{\Gamma} \boldsymbol{A} \cdot \mathrm{d}\boldsymbol{l} + \Lambda \oint_{\Gamma} \boldsymbol{J}_S \cdot \mathrm{d}\boldsymbol{l} \right) = \frac{2\pi}{\Phi_0} \cdot \Phi_l \tag{2.19}$$

within the brackets is called the *fluxoid* Φ_l. Therefore, in the most general case, one speaks of *fluxoid quantization* $\Phi_l = n \cdot \Phi_0$ in superconducting loops.

Note that the fluxoid is a quantity that is not dependent on the path of integration Γ, as long as it is made within the superconductor. It is hence a property of the superconducting ring and not of any particular path around it. Secondly, the fluxoid is linearly dependent on the current I through the ring: it can always be written as a product of I and a constant of proportionality L, the last depending on the geometry and the properties of the material and medium around it (in the case that no other currents are present in the system):

$$\Phi_l = \oint_{\Gamma} \boldsymbol{A} \cdot \mathrm{d}\boldsymbol{l} + \Lambda \oint_{\Gamma} \boldsymbol{J}_S \cdot \mathrm{d}\boldsymbol{l} = L \cdot I \tag{2.20}$$

This is a consequence of the linearity of Maxwell's laws and the London equations when the media and materials are linear as well. For instance, scaling $\boldsymbol{J}_S$ with a scalar constant α everywhere will result in $\boldsymbol{B}$, and hence the flux, also being everywhere scaled by the same constant. Hence, there exists a constant of proportionality L that relates the two in a linear way. More on this property of superconductors is found in later sections.

The quantity L is referred to as the ring's *self-inductance*. From 2.20, it can be seen that it has two contributions:

$$L = \frac{\oint_\Gamma \boldsymbol{A} \cdot \mathrm{d}\boldsymbol{l}}{I} + \frac{\Lambda \oint_\Gamma \boldsymbol{J}_S \cdot \mathrm{d}\boldsymbol{l}}{I} = L_m + L_k$$

The first part is the geometric inductance L_m while the second part is the kinetic inductance L_k. The former is related to the magnetic field created by the current flow in the ring, while the latter is a measure of the kinetic motion of the charges in the same. Both are present in every conductor, but only for superconductors is the kinetic inductance significant, in normal metals it is usually very small compared to L_m.

As given above, the two components of the self-inductance of the rings are expressed as

$$\begin{aligned} L_m &= \frac{\oint_\Gamma \boldsymbol{A} \cdot \mathrm{d}\boldsymbol{l}}{I} = \frac{\oint_\Gamma \boldsymbol{A} \cdot \mathrm{d}\boldsymbol{l}}{\int_S \boldsymbol{J}_S \cdot \mathrm{d}\boldsymbol{s}} \\ L_k &= \frac{\oint_\Gamma \Lambda \boldsymbol{J}_S \cdot \mathrm{d}\boldsymbol{l}}{I} = \frac{\oint_\Gamma \Lambda \boldsymbol{J}_S \cdot \mathrm{d}\boldsymbol{l}}{\int_S \boldsymbol{J}_S \cdot \mathrm{d}\boldsymbol{s}} \end{aligned} \tag{2.21}$$

where S is any cross-section of the superconductor and Γ is any internal closed contour going around its length. It is important to stress that if the self-inductance L is calculated partially from the two relations in 2.21, care must be taken to use the same contour Γ since, in general, the integrals in the nominators of 2.21 are not Γ-independent (although their sum is).

It is worth noting that although an inductance is usually considered as an element of the circuit that interacts with and creates magnetic fields, the kinetic inductance L_k does not have that property.

Combining the relations 2.19 and 2.20, the fluxoid quantization now yields:

$$2\pi \cdot n = \frac{2\pi}{\Phi_0} \cdot L\, I = \varphi \tag{2.22}$$

where a new variable φ, named *the (generalized) flux angle* [17] [18], is introduced. The flux angle, in this case given by

$$\varphi = \frac{2\pi L}{\Phi_0} \cdot I \tag{2.23}$$

is later defined in section 2.2.4 in a broader sense. Suffice it to state at this point that if L is the self-inductance of a closed superconducting loop, then the normalized flux angle is proportional to the normalized fluxoid in that loop: $\frac{\varphi}{2\pi} = \frac{L \cdot I}{\Phi_0} = \frac{\Phi_l}{\Phi_0}$.

2.2.2.1 Free energy of a superconducting ring

The total free energy W of the isolated superconducting ring can be written as a sum of the magnetic field energy W^m in the whole volume of space V_∞ and the kinetic energy $W^{m,k}$ of the moving charges in the volume of the ring V_R [19] ($n \cdot \frac{2m \cdot \boldsymbol{v}^2}{2} = \frac{1}{2} \Lambda \boldsymbol{J}_S^2$):

$$W = W_0 + W^m + W^{m,k} = W_0 + \frac{1}{2} \int_{V_\infty} \boldsymbol{B}\boldsymbol{H} \cdot \mathrm{dV} + \frac{1}{2} \int_{V_R} \Lambda \boldsymbol{J}_S^2 \cdot \mathrm{dV}$$

where W_0 is the energy associated with the existence of the superfluid condensate (the long-range order) in the ring. In weak fields W_0 can be considered constant and will be left out from any further calculations. Using Maxwell's equations, the supercurrent equation and vector algebra, the above relation is reduced to

$$W = \frac{1}{2} \frac{\Phi_0}{2\pi} \cdot \int_{V_R} \boldsymbol{J}_S \cdot \nabla\theta \cdot \mathrm{d}V = \frac{1}{2} \frac{\Phi_0}{2\pi} \cdot \int_{V_R} \nabla(\theta \cdot \boldsymbol{J}_S) \cdot \mathrm{d}V$$

since for the divergence of the product between a scalar and vector it holds

$$\nabla(\theta \cdot \boldsymbol{J}_S) = \boldsymbol{J}_S \cdot \nabla\theta - \theta \cdot \nabla \boldsymbol{J}_S$$

and $\nabla \boldsymbol{J}_S = 0$ in V_R due to law of charge conservation. The function $\theta \cdot \boldsymbol{J}_S$ is discontinuous due to θ that may experience $2\pi \cdot n$ phase jumps - this was indeed the basis for the fluxoid quantization. Without any loss of generality, it can be assumed that all discontinuities in the phase θ are brought together to lie on the surface Σ, as shown in the diagram of Figure 2.5. This would imply that the phase is taken to be continuous everywhere, except for the points on Σ where it may experience a phase jump:

$$\{\theta^+(\boldsymbol{r}) - \theta^-(\boldsymbol{r})\}_{\boldsymbol{r} \in \Sigma} = 2\pi \cdot n = 2\pi \frac{\Phi_l}{\Phi_0}$$

where Φ_l is the fluxoid defined in 2.19 and θ^+, θ^- symbolize the superconducting phases taken on each side of the surface Σ. Lets surround Σ by a small cylinder of volume V', length l' and two base surfaces Σ^+ and Σ^- with normals as given in Figure 2.5. The goal is to calculate the free energy W of the ring when the volume V' shrinks to zero, i.e. in the limit of $l' \to 0$.

The Gauss divergence theorem

$$\int \nabla \boldsymbol{X} \cdot \mathrm{d}V = \oint \boldsymbol{X} \cdot \mathrm{d}\boldsymbol{S}$$

can be applied to the volume integral of the function $\nabla(\theta \cdot \boldsymbol{J}_S)$ on $V_R - V'$:

$$\frac{4\pi}{\Phi_0} W = \int_{V_R - V'} \nabla(\theta \cdot \boldsymbol{J}_S) \cdot \mathrm{d}V + W(V') =$$

$$= \Big\{ \int_{\Sigma_O} \theta\, \boldsymbol{J}_S \cdot \mathrm{d}\boldsymbol{s} + \int_{\Sigma^+} \theta\, \boldsymbol{J}_S \cdot \mathrm{d}\boldsymbol{s}^+ + \int_{\Sigma^-} \theta\, \boldsymbol{J}_S \cdot \mathrm{d}\boldsymbol{s}^- \} + W(V')$$

where Σ_O is the exterior surface of the ring. The first integral is identical to zero because $\boldsymbol{J}_S$ is normal to $\mathrm{d}\boldsymbol{s}$ along the whole outer surface Σ_O, i.e. no current is flowing out of the ring. In the limit of $l \to 0$, the volume V' and hence the energy $W(V')$ is zero while the remaining terms give ($\mathrm{d}\boldsymbol{s}^+ = -\mathrm{d}\boldsymbol{s}^- = \mathrm{d}\boldsymbol{\sigma}$)

$$\lim_{l' \to 0} \Big(\int_{\Sigma^+} \theta\, \boldsymbol{J}_S \cdot \mathrm{d}\boldsymbol{s}^+ + \int_{\Sigma^-} \theta\, \boldsymbol{J}_S \cdot \mathrm{d}\boldsymbol{s}^- \Big) = \int_{\Sigma} \{\theta^+(\boldsymbol{r}) - \theta^-(\boldsymbol{r})\} \cdot \boldsymbol{J}_S \cdot \mathrm{d}\boldsymbol{\sigma} =$$

$$= \int_{\Sigma} 2\pi \cdot \frac{\Phi_l}{\Phi_0} \cdot \boldsymbol{J}_S \cdot \mathrm{d}\boldsymbol{\sigma} = 2\pi \frac{\Phi_l}{\Phi_0} \int_{\Sigma} \boldsymbol{J}_S \cdot \mathrm{d}\boldsymbol{\sigma} = 2\pi \frac{\Phi_l}{\Phi_0} \cdot I$$

where $I = \int_{\Sigma} \boldsymbol{J}_S \cdot \mathrm{d}\boldsymbol{\sigma}$ is the total current through the ring and $\mathrm{d}\boldsymbol{\sigma}$ is an infinitesimal part of Σ. Combining the last two relations, the total free energy of the ring structure calculates to:

$$W = \frac{1}{2} \Phi_l \cdot I = \frac{1}{2} \cdot L\, I^2 = \left(\frac{\Phi_0}{2\pi} \right)^2 \frac{\varphi^2}{2 \cdot L}$$

with φ the flux angle of the ring given by 2.23. This expression will be later important when the free energy of a superconducting network is calculated.

2.2.2.2 Mutual inductance (coupling) between rings

If the medium is linear, and if another current I_{ext} in a nearby structure was present creating a magnetic field reaching the ring under investigation, the fluxoid through the ring will be given by:

$$\Phi_l = \oint_{\Gamma} (\boldsymbol{A}_{\mathrm{self}} + \boldsymbol{A}_{\mathrm{ext}}) \cdot \mathrm{d}\boldsymbol{l} + \Lambda \oint_{\Gamma} \boldsymbol{J}_S \cdot \mathrm{d}\boldsymbol{l} = \Phi_{\mathrm{self}} + \Phi_{\mathrm{ext}}$$

where

$$\Phi_{\mathrm{self}} = \oint_{\Gamma} \boldsymbol{A}_{\mathrm{self}} \cdot \mathrm{d}\boldsymbol{l} + \Lambda \oint_{\Gamma} \boldsymbol{J}_S \cdot \mathrm{d}\boldsymbol{l} = L \cdot I$$

is the flux(oid) created from the current I in the ring when $I_{\mathrm{ext}} = 0$, while

$$\Phi_{\mathrm{ext}} = \oint_{\Gamma} \boldsymbol{A}_{\mathrm{ext}} \cdot \mathrm{d}\boldsymbol{l}$$

is the flux in the ring created by the current I_{ext} when $I = 0$. Again, from the linearity of the Maxwell/London laws, $\Phi_{\text{ext}} = M \cdot I_{\text{ext}}$, where M is a constant of proportionality that is referred to as the mutual inductance. Same as the self inductance, the mutual inductance depends only on the material/medium properties and the geometry of the system, as well as the reference orientations for the currents I and I_{ext}.

Thus, when a current I_{ext} flows through a remote structure magnetically coupled to the ring, the flux quantization condition is

$$2\pi \cdot n = \frac{2\pi}{\Phi_0}(\Phi_{\text{self}} + \Phi_{\text{ext}}) = \frac{2\pi \cdot L}{\Phi_0} \cdot I + \frac{2\pi M}{\Phi_0} I_{\text{ext}} = \varphi_{\text{self}} + \varphi_{\text{ext}} \tag{2.24}$$

where $\varphi_{\text{self}} = \frac{2\pi \cdot L}{\Phi_0} \cdot I$ and $\varphi_{\text{ext}} = \frac{2\pi M}{\Phi_0} I_{\text{ext}}$ are the self- and external flux angles. It is seen that the presence of a coupled structure adds an extra "induced" flux angle φ_{ext} in the loop.

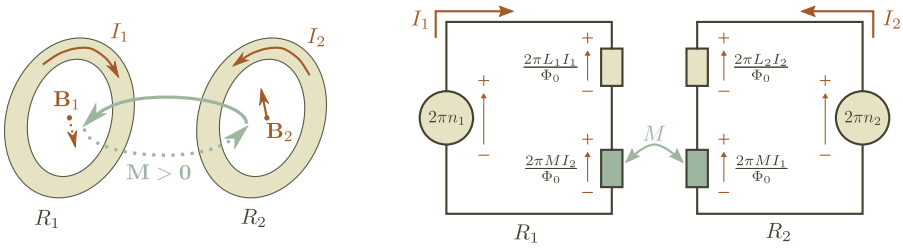

Figure 2.6. Two inductively coupled superconducting rings R_1 and R_2, as well as a network structure implementing equation 2.24

The drawing in Figure 2.6 attempts to illustrate 2.24 in a graphical way. Depicted are two loops of superconductors that are magnetically coupled through M as well as a schematic implementation of 2.24 that will be the basis for the superconducting network model given later. Here, the nodal variables can be identified as the flux angles φ and the flow variables as the currents I. The constitutive laws of the circuit elements stem from linear flux-current relationships

$$\varphi = \frac{2\pi}{\Phi_0}(L, M) \cdot I$$

Equation 2.24 can then be seen as a *circuital summation law for the flux angles*, similar to the circuital summation law of voltages in standard electromagnetic networks (II Kirchhoff law).

It should be noted that the mutual inductance is the same whether one looks at the external flux in the ring 1 created by a current flowing in ring 2 or at the external flux in ring 2 created by the current in ring 1. The mutual inductance is always reciprocal.

The following expression is given for the coupling energy between the two loops [19]:

$$W^{m12} = \int_{V_\infty} \boldsymbol{B}_1 \boldsymbol{H}_2 \cdot \mathrm{d}V = \int_{V_\infty} \boldsymbol{B}_2 \boldsymbol{H}_1 \cdot \mathrm{d}V = M I_1 I_2$$

that is valid in linear media. Above, M is the mutual inductance, I_1, I_2 are the currents through the magnetically coupled structures and $\boldsymbol{B}_i$, $\boldsymbol{H}_i$ are created by the current I_i when the other current is zero. The total free energy of the coupled two-loop system is then:

$$W = \frac{1}{2} L_1 \cdot I_1^2 + \frac{1}{2} L_2 \cdot I_2^2 + M \cdot I_1 I_2$$

It is instructive to use the total flux angle $\varphi_i = \varphi_{\mathrm{ext},i} + \varphi_{\mathrm{self},i}$ of the fluxoid for the ring i (which is equal to $2\pi \cdot n_i$). This gives for the total free energy of the coupled system the following expression:

$$W = \left(\frac{\Phi_0}{2\pi}\right)^2 \cdot \frac{1}{2} \cdot \frac{1}{L_1 L_2 - M^2} \cdot (L_2 \varphi_1^2 + L_1 \cdot \varphi_2^2 - 2\, M \cdot \varphi_1 \cdot \varphi_2)$$

where φ_i is the flux angle of the fluxoid of the ring i. The mutual inductance M is usually written as $M = \pm\kappa \cdot \sqrt{L_1 L_2}$ where the (positive) coupling coefficient κ is always $\kappa < 1$ due to inevitable flux loss between two loops in a realistic system ($\kappa = 1$ when all the magnetic flux created by the loop L_1 is threading the loop L_2). Interestingly, even if the flux was ideally shared between the loops, in superconductors κ is still smaller than 1 due to the kinetic inductance that does not participate in the magnetic coupling between the loops.

The sign of M depends on the chosen reference orientations of the two currents I_1 and I_2. If the magnetic fields they create add inside the rings, then M is positive. If the fields are opposite, then M is negative. This is used in the drawing in Figure 2.6, where the reference directions are chosen such that $M > 0$.

Using the above relation for W and the fact that $\varphi_i = 2\pi \cdot n_i$, plus assuming that the loops are identical with $L_1 = L_2 = L$, it is obtained:

$$\frac{2W \cdot L}{\Phi_0^2} = \frac{n_1^2 + n_2^2 \mp 2\kappa \cdot n_1 \cdot n_2}{(1 - \kappa^2)} \tag{2.25}$$

where n_i are integer and $0 < \kappa < 1$. In Fig 2.7, the normalized free energy $\frac{2W \cdot L}{\Phi_0^2}$ is plotted on the landscape of the integers n_i for various values of the coupling coefficient and for positive M.

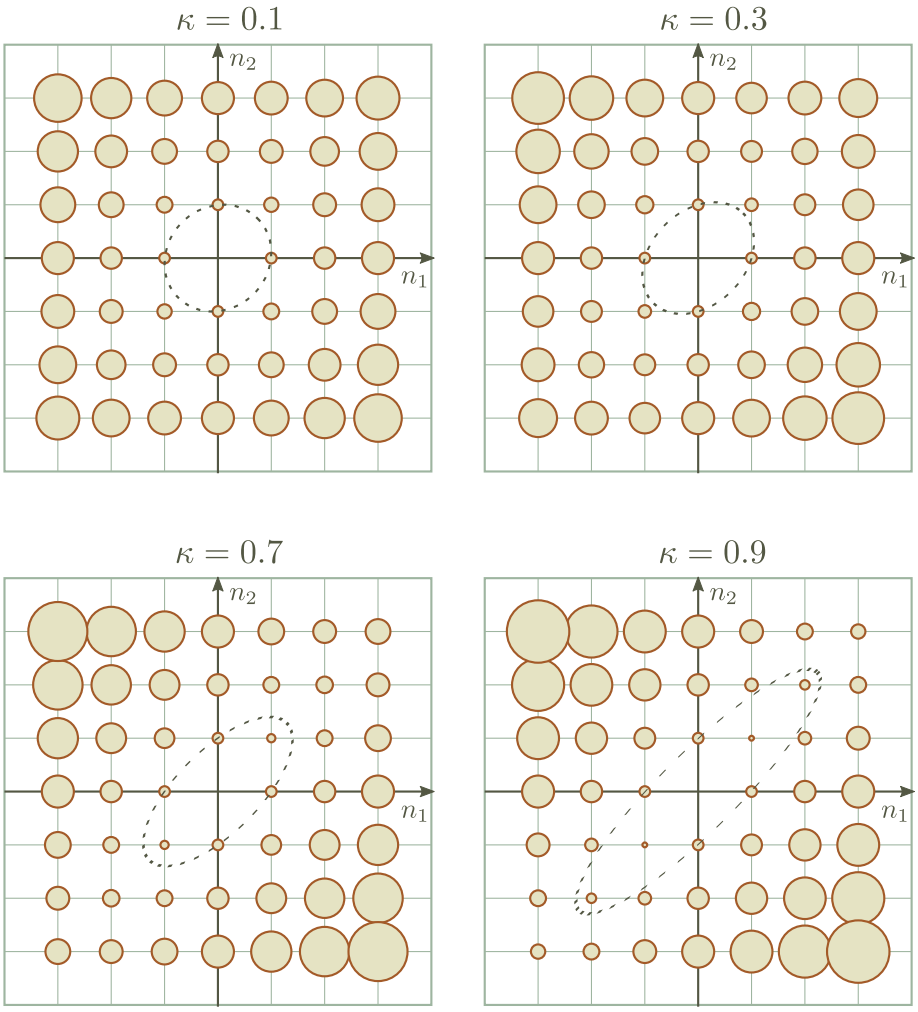

Figure 2.7. The free energy of the coupled two-ring system from Figure 2.6 plotted on the landscape of integers (n_1, n_2) for a few values of the coupling coefficient κ. The value of the energy is proportional to the area of the circles at each point, with the free energy for (n_1, n_2) equal to $(0, 1)$ or $(1, 0)$ taken as a reference for each plot. The dotted line is a contour of constant (unit) free energy if the quantization integers are treated as continuous variables in equation 2.25.

For weak coupling, the energy landscape is rotationally symmetric, while for strong coupling the magnetic interaction between the loops results in a lower energy for the states where the n_i has the same sign in the two loops. This means that the preferred arrangements are those where the flux through the loops is

antiferromagnetically ordered if the conventions for the directions in 2.6 are taken into account. However, the trivial zero energy state for $(n_1, n_2) = (0, 0)$ is dominant for the system $(W = 0)$ and flux ordering is rarely observed for these loops without any external action. The π-loops on the other hand, that are introduced later, have no zero-energy ground state and antiferromagnetic ordering is spontaneous for coupled systems of such loops [20] [21].

2.2.3 Nodal network variables and partial inductances

In the previous section, the circuital summation law of flux angles was derived for a superconducting system comprising of two coupled loops and was graphically represented by a network model. However, before expanding it further for more complex geometries, it is necessary to elucidate some general properties of electrical network modeling.

A network representation of the electromagnetic phenomena for a given system is an abstraction of the physical processes taking part in it. The network model visualises the system by equivalenting it with point-to-point connections of various elements where the nodal and branch quantities are related to each other in ways mimicking natural laws. It is however not required to exactly match measurable physical quantities and network variables. Sometimes it is not even possible to do so.

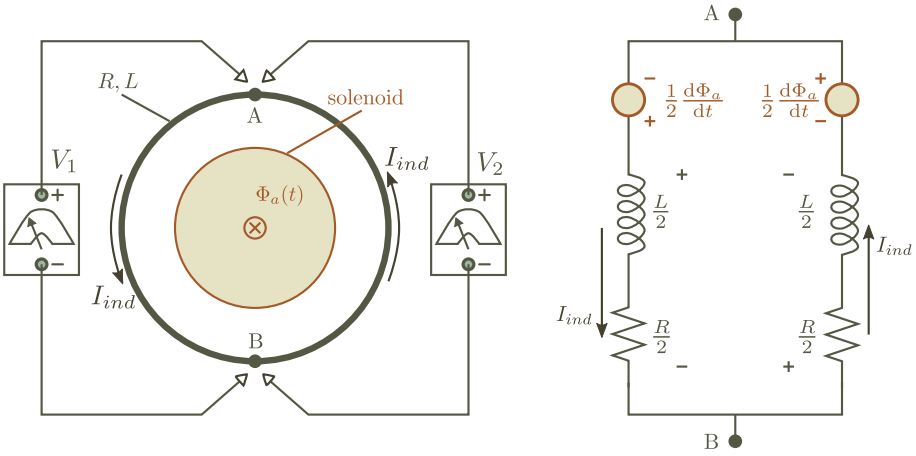

Figure 2.8. A conductive loop placed concentric with a solenoid, enclosing it completely. The solenoid has a time-dependent drive and produces the magnetic flux $\Phi_a(t)$. This, in turn, induces a current I_{ind} in the conductive loop. The equivalent electrical schematic of the loop-solenoid system is given on the right. The voltmeters are identical and have large internal impedance.

An example of where the nodal variables of a network do not correspond with the ones measured from its physical counterpart is given in Figure 2.8. Two identical voltmeters are connected symmetrically to a normal conductive loop. The loop encloses a region of space with a changing external magnetic field so that the flux Φ_a threading the loop is time dependent. As a consequence, an electromotive force $\epsilon = -\frac{\partial \Phi_a}{\partial t}$ is felt around the ring and a current I_{ind} is induced. No magnetic field is present in the loops comprising the voltmeter leads.

The voltages that the two voltmeters report will be, if the loop is symmetrically divided, non-zero and equal but *inverted* in sign, a fact that is experimentally confirmed [22] [23] ! But how can one reconcile this with the network model of the system, also given in Figure 2.8, where the voltage between the two nodes A and B does not depend on the side from which one looks at the schematic? Moreover, the solution of the network equations for the circuit yields $V_A - V_B = 0$ while the voltmeters report a significant non-zero value [24].

The resolution can be found by pointing out a property of network modeling of electromagnetic phenomena that is rarely discussed in the literature but nevertheless, it leads to the strange effect presented above. The next subsections will examine the nature of the nodal variables in a general network and, in connection with it, the basis upon which the circuit elements are defined. The presented discussion is relevant for EM networks that model physical structures where magnetic fields are predominant, like for instance superconducting circuits. The conclusions reached at the end will be essential in building the superconducting network model in section 2.2.4.

2.2.3.1 Scalar potentials as nodal variables

Voltmeters are instruments measuring the effects that a (small) internal current, excited by the electric field at the ends of their probes, will have on their sensor of choice. Effectively, the value that they report is a measure of $\int \boldsymbol{E}\, \mathrm{d}\boldsymbol{l}$ along their (conductive) probe leads and interior, with the direction of integration fixed in relation to the polarity marked on their terminals [25]. The integration path circulates in the opposite direction for the two voltmeters in Figure 2.8 (clockwise and anti-clockwise). That is why the voltmeters read values with an opposite sign.

Secondly, and more importantly, the nodal variable used in electrical networks (i.e. circuit schematics) is not voltage in time-dependent cases. This stems from the definition of voltage as the line integral of the electric field between two points. In a static situation, when the time derivatives of the fields are zero, the voltage ΔV_{AB} between some points A and B is

$$\Delta V_{\mathrm{AB}} = V_A - V_B = -\int_B^A \boldsymbol{E} \cdot \mathrm{d}\boldsymbol{l} = \int_B^A \nabla U \cdot d\boldsymbol{l} = U_A - U_B$$

The scalar function $U(\boldsymbol{r})$ is usually called the "electrostatic potential" or "Coulomb potential" in EM circuit literature [26]. If the fields do not alter with time, a voltmeter probe between two points will report the difference in their electrostatic potential which is a unique property of those points. This value is the same as the difference in the nodal variables attached to the two points in the equivalent circuit schematic.

In a situation when there is a changing electromagnetic field, the electric field is given by

$$-\boldsymbol{E} = \nabla\phi + \frac{\partial \boldsymbol{A}}{\partial t} \tag{2.26}$$

where ϕ is the scalar potential and $\boldsymbol{A}$ is the magnetic vector potential. It follows that the voltage between two points is path dependent in this case:

$$\Delta V_{\mathrm{AB}} = -\int_A^B \boldsymbol{E}\cdot \mathrm{d}\boldsymbol{l} = \int_A^B \left(\nabla\phi + \frac{\partial \boldsymbol{A}}{\partial t}\right)\cdot \mathrm{d}\boldsymbol{l} = \phi_B - \phi_A + \int_A^B \frac{\partial \boldsymbol{A}}{\partial t}\cdot \mathrm{d}\boldsymbol{l}$$

Changing the path of integration between A and B also changes ΔV_{AB} by the amount of magnetic flux enclosed by the closed contour consisting of the old and new path connected together. The voltage is no longer a property of only the coordinates of the two physical points, but also of the choice of path between them. However, the scalar potential difference $\Delta\phi = \phi_B - \phi_A$ is, by definition, path independent.

The Second Kirchhoff law, or the circuital law of voltage summation, states that the sum of voltages on the elements around a closed loop in the circuit is zero. But, as can be seen from the relation above by choosing a closed path, i.e. letting the end-points $A = B$, the sum of voltages (the closed line integral of $\boldsymbol{E}$) around the loop equals the circuital integral of $\frac{\partial \boldsymbol{A}}{\partial t}$:

$$\sum_{\mathrm{loop}} \Delta V = -\oint \boldsymbol{E}\cdot \mathrm{d}\boldsymbol{l} = \oint \left(\nabla\phi + \frac{\partial \boldsymbol{A}}{\partial t}\right)\cdot \mathrm{d}\boldsymbol{l} = 0 + \oint \frac{\partial \boldsymbol{A}}{\partial t}\cdot \mathrm{d}\boldsymbol{l} \neq 0$$

which is not zero in a general case. What is *always* zero around a closed loop is the integral of the scalar potential's gradient, a trivial identity from vector algebra:

$$\begin{aligned} &\oint \nabla\phi\cdot \mathrm{d}\boldsymbol{l} \equiv 0 \quad \leftarrow \qquad \mathbb{I}\,\text{Kirchhoff Law} \\ &\oint \boldsymbol{E}\cdot \mathrm{d}\boldsymbol{l} \neq 0 \quad \text{when} \quad \oint \frac{\partial \boldsymbol{A}}{\partial t}\cdot \mathrm{d}\boldsymbol{l} = \frac{\partial \Phi}{\partial t} \neq 0 \end{aligned} \tag{2.27}$$

where Φ is the magnetic flux enclosed by the integration path around the closed loop.

In circuit theory, the above is implicitly addressed: the changing magnetic field in a loop is said to create an *electromotive force* $\epsilon = -\oint \frac{\partial \boldsymbol{A}}{\partial t} \cdot \mathrm{d}\boldsymbol{l} = -\frac{\partial \Phi}{\partial t}$ in the loop's conductors and the Second Kirchhoff law is made to pertain to the sum of the voltages *and* of the electromotive forces around the loop. The consequence of the above formulation is however rarely mentioned explicitly: the nodal variables between two points in a circuit are voltages $-\int \boldsymbol{E} \cdot \mathrm{d}\boldsymbol{l}$ *plus* electromotive forces $-\int \frac{\partial \boldsymbol{A}}{\partial t} \cdot \mathrm{d}\boldsymbol{l}$, i.e. *the nodal variables are the scalar potentials* ϕ per equation 2.26.

2.2.3.2 Gauge invariance in electromagnetic networks

If the nodal quantities in a network are scalar potential differences $\Delta\phi = \int \nabla\phi \cdot \mathrm{d}\boldsymbol{l}$ and not voltages $\Delta V = \int \boldsymbol{E} \cdot \mathrm{d}\boldsymbol{l}$, then the question of gauge invariance in the constitutive laws of the network elements arises. Any gauge transformation

$$\boldsymbol{A}' \to \boldsymbol{A} + \nabla\chi \;\; ; \;\; \phi' \to \phi - \frac{\partial \chi}{\partial t}$$

will change the scalar potential difference $\Delta\phi$ across all elements in the circuit

$$\Delta\phi' \to \Delta\phi - \frac{\partial(\Delta\chi)}{\partial t}$$

where $\Delta\chi$ is the difference of the arbitrary scalar function $\chi(\boldsymbol{r}, t)$ between the nodes of the affected circuit element. On the other hand, the current I flowing through the elements does not change under a gauge transform. Hence, the constitutive laws of the elements that connect the nodal variable $\Delta\phi$ and the current I are not gauge invariant.

However, it is only when the individual elements are taken separately from each other that gauge dependence is observed. For any closed circuit, the solutions of the network equations for the currents remain independent from the choice of gauge since the Second Kirchhoff law 2.27 is gauge invariant. In other words, when the Second Kirchhoff law is written for any given loop in a circuit using the element's constitutive laws, all the extra contributions $-\frac{\mathrm{d}(\Delta\chi)}{\mathrm{d}t}$ will cancel each other out. The network equations, when written with currents as the unknown quantity, are then gauge invariant. Still, the nodal variables $\Delta\phi'$ across the individual elements in the network remain gauge-dependent. Moreover, one may even claim that they lack a physical meaning due to the gauge dependence.

This apparent problem is resolved by realizing that when the magnetic field does not change, then the difference in the nodal variable between two network nodes should be equal to the Coulomb (electrostatic) potential difference ΔU between the corresponding two points in the physical system. The latter is defined

through the work required to move a unit test charge between the two points [26], and is clearly gauge-invariant. Hence, if the nodal variable differences $\Delta\phi$ are written in such a gauge that they are equal to ΔU when the magnetic field does not alter, they would have a physical meaning. For the dynamic case, when the fields alter with time, it is necessary to simply have continuity in the values of the nodal variables. In other words, it is not allowed to write the scalar and vector potentials in a gauge where $\Delta\phi \neq \Delta U$ when the time derivative of the magnetic field becomes zero at a certain point in time.

The above requirement amounts to restricting the gauge freedom to a subset. It is here postulated that this subset must satisfy either

$$\frac{\partial \boldsymbol{B}}{\partial t} = \boldsymbol{0} \;\Rightarrow\; \nabla\phi = -\boldsymbol{E} = \nabla U \tag{2.28}$$

or

$$\frac{\partial \boldsymbol{B}}{\partial t} = \boldsymbol{0} \;\Rightarrow\; \frac{\partial \boldsymbol{A}}{\partial t} = \boldsymbol{0}$$

which are equivalent using 2.26. The above simply states that the gauge must be chosen such that the vector potential's time derivative is zero when the magnetic field's time derivative is zero.

Note that the gauge subset relations in 2.28 are not trivial. From

$$\nabla \times \boldsymbol{A} = \boldsymbol{B}$$

it follows that when

$$\frac{\partial \boldsymbol{B}}{\partial t} = \boldsymbol{0}$$

the gauge freedom to choose the vector potential is given by

$$\frac{\partial \boldsymbol{A}}{\partial t} = \nabla\zeta$$

where $\zeta(\boldsymbol{r}, t)$ is an arbitrary scalar function. The gauge subset 2.28 requires that $\nabla\zeta = 0$ and in fact restricts gauge freedom.

When the gauge subset 2.28 is used in this thesis, the symbol ΔU will denote the nodal variable difference in a network.

The gauge subset 2.28 can also be expressed in circuit terms. The condition $\frac{\partial \boldsymbol{B}}{\partial t} = 0$ is equivalent to one of the following two possible situations: a) zero time derivatives in the currents and b) either the fields created by the currents cancel or the currents themselves are zero. Thus, when the currents in the system have a zero time derivative or are zero themselves, then 2.28 requires that the nodal variable difference equals the Coulomb potential difference.

The element that models the physics of changing magnetic fields (induction) is an inductor. If there are no inductors in a network, meaning that the magnetic fields can be neglected, then the nodal variables will always, even when the currents change with time, be the voltages a voltmeter would record between the corresponding points of the system that the network models. However, *the presence of inductors transforms the nodal variables in a network from voltages to scalar potentials*. They are then expressed in a particular gauge chosen such that if the currents in the network are constant in time, those nodal variables would be the electrostatic potentials ΔU.

Lastly, only when using the circuit gauge subset 2.28 is the product of the nodal and flow network variables across an inductor element equal to the power stored in/extracted from that element. Using U to denote the nodal variable in the gauge subset 2.28, the constitutive law for an inductor can be shown to be $\Delta U = L \cdot \frac{\mathrm{d}I}{\mathrm{d}t}$ (see next subsection) and the energy stored per unit time, or the power delivered/extracted from it, is equal to $\Delta U \cdot I$:

$$P = \frac{\mathrm{d}W}{\mathrm{d}t} = \frac{\mathrm{d}}{\mathrm{d}t}\left(\frac{1}{2} L \cdot I^2\right) = L \cdot \frac{\mathrm{d}I}{\mathrm{d}t} \cdot I = \Delta U \cdot I$$

where $W = \frac{1}{2}\ L \cdot I^2$ is the gauge-invariant expression for the energy stored in the inductor. In a gauge that does not belong to the subset 2.28, the inductor's constitutive law would have an additional arbitrary component $-\Delta\zeta(t)$ added to the nodal variable and the nodal-flow product would not be equal to the power delivered/extracted from the inductor. The same is valid for the rest of the circuit elements. Although the network equations will produce correct solutions for the branch currents regardless of the gauge, as shown at the beginning of this subsection, the network will be unable to represent the thermodynamics of the system using the nodal quantities as free variables, unless the circuit gauge subset 2.28 is used.

2.2.3.3 Partial inductances

The self inductance L of a closed conductive path is defined through the magnetic flux $\Phi = L\, I$ threading the path. The constitutive law of a closed-loop inductor is based on electromagnetic induction, more precisely on the electromotive force felt around the loop per unit flux change in the absence of external fields:

$$\epsilon = -\frac{\mathrm{d}\Phi}{\mathrm{d}t} = -L \cdot \frac{\mathrm{d}I}{\mathrm{d}t}$$

Magnetic flux can not be defined for open-ended conductive paths since there is no unique surface through which to measure it. Still, electromagnetic induction does have an effect on the current flowing in such an open path when it is a part

of a larger, closed circuit, structure. In practical situations however, knowledge about the "rest of the circuit" is rarely precise and often there is only a generic description available. Hence, it is necessary to define a stand-alone model for the effects of electromagnetic induction on open-ended conductors where magnetic flux can not be trivially defined due to lack of knowledge for the rest of the loop.

From a network-theoretic perspective, the appearance of these open-ended inductor elements, called *partial inductances*, is actually connected to the process of segmentation of the physical system in the node-branch graphical architecture of an electrical network. The basic premise in using partial inductances is that the electromotive force ε, strictly defined only for closed paths, can also be segmented along the branches constituting that path. Partial inductances were introduced by E. Rosa in 1908 [27] along with examples on how to calculate them for several conductor geometries. Closed formulae were then derived [28] for many specific cases and under certain assumptions. The concept of partial inductances as network elements for electronic circuits was summarized by Ruehli [29] and was later expanded [30] to also include partial capacitances and resistances. In the following few paragraphs, the partial inductance concept of [29] is presented for a system of interconnected perfect conductors that is later, in subsection 2.2.4.1, adapted for superconducting circuits.

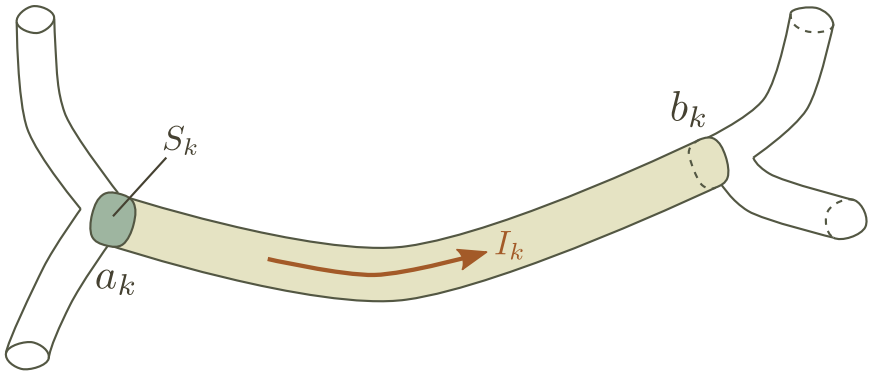

Figure 2.9. A conductive segment as a part of a larger circuit.

A physical system made from a plurality of conductive paths is partitioned in a total of N segments, each segment k identified with a current I_k and two nodes a_k and b_k where the other segments are attached. The current I_k is chosen to flow from the node a_k towards the node b_k. The cross sectional area S_k of each segment is taken to be constant along its length.

The partial electromotive force between the ends of segment k is given through the magnetic vector "potential drop" along the segment's length and averaged across S_k [29]:

$$-\epsilon_k = \frac{\mathrm{d}}{\mathrm{d}t}\left(\frac{1}{S_k} \cdot \int_{S_k} \int_{a_k}^{b_k} \boldsymbol{A} \cdot \mathrm{d}\boldsymbol{l}_k \, \mathrm{d}s_k \right)$$

where $\boldsymbol{A}$ is the magnetic vector potential (chosen within the gauge subset 2.28) and $\mathrm{d}\boldsymbol{l}_k$ is an infinitesimal length vector in the direction of the current flow in the segment k. This cross-sectionally averaged partial electromotive force is then equated to the potential difference between the nodes a_k and b_k:

$$-\epsilon_k = -[U(b_k) - U(a_k)] = \Delta U_k = \frac{\mathrm{d}}{\mathrm{d}t}\left(\frac{1}{S_k} \cdot \int_{S_k} \int_{a_k}^{b_k} \boldsymbol{A} \cdot \mathrm{d}\boldsymbol{l}_k \, \mathrm{d}s_k \right) \tag{2.29}$$

where it is important to notice that the polarity of $\Delta U_k = U(a_k) - U(b_k)$ is such that a_k is the positive and b_k the negative node.

Note that for perfect conductors, the conductivity $\sigma = \infty$ and one obtains that the electric field $\boldsymbol{E} = \frac{1}{\sigma}\boldsymbol{J} = \boldsymbol{0}$. The relation 2.29 can now be seen to originate from

$$-\boldsymbol{E} = \nabla\phi + \frac{\partial \boldsymbol{A}}{\partial t}$$

by integrating both sides of the equation with $\boldsymbol{E} = \boldsymbol{0}$:

$$\frac{\partial}{\partial t}\left(\int_A^B \boldsymbol{A} \cdot \mathrm{d}\boldsymbol{l} \right) = -\int_A^B \nabla\phi \cdot \mathrm{d}\boldsymbol{l} = -\int_A^B \nabla U \cdot \mathrm{d}\boldsymbol{l} = U_A - U_B = \Delta U_{\mathrm{AB}}$$

along a filamentary perfect conductor path of zero cross-sectional area between some points A and B. Since the segments in the system of Figure 2.9 have a non-zero cross-section S_k, [29] suggests to average the potentials U_A and U_B across S_k which leads directly to 2.29.

Were the path of integration of the line integral in 2.29 closed, i.e. was the segment k forming a closed loop, then the term within the brackets would have been a measure of the magnetic flux $\Phi = \int \boldsymbol{B} \cdot \mathrm{d}\boldsymbol{s} = \oint \boldsymbol{A} \cdot \mathrm{d}\boldsymbol{l}$ through the surface bound by the closed segment. For the open segment in the example from Figure 2.9, a *partial flux variable* γ_k can be defined such that, for the segment k of the multiloop system, it equals:

$$\gamma_k = \frac{1}{S_k} \cdot \int_{S_k} \int_{a_k}^{b_k} \boldsymbol{A} \cdot \mathrm{d}\boldsymbol{l}_k \, \mathrm{d}s_k$$

and then

$$\Delta U_k = -\epsilon_k = \frac{\mathrm{d}\gamma_k}{\mathrm{d}t}$$

The sum of the partial fluxes γ_i of each segment around a closed loop would now be a measure for the flux Φ in the loop. The partial flux variable is not a part of the concept in [29] but will used later for superconducting networks where it can be more precisely constructed.

Assuming the medium is linear, the magnetic vector potential at a point is written as a sum

$$\boldsymbol{A}(\boldsymbol{r}) = \sum_{i=1}^{N} \boldsymbol{A}_i(\boldsymbol{r}) \tag{2.30}$$

of contributions $\boldsymbol{A}_i$ from each of the N segments separately. Further, choosing the Coulomb gauge (which belongs to the subset 2.28)

$$\nabla \boldsymbol{A} = 0$$

$$\boldsymbol{A} \cdot \boldsymbol{n} = 0$$

where $\boldsymbol{n}$ is the normal of the segment surfaces, and using Maxwell's equations, the vector potential $\boldsymbol{A}_i$ created by the current I_i in the ith segment at the coordinate $\boldsymbol{r}$ is given by the Biot-Savart law:

$$\boldsymbol{A}_i(\boldsymbol{r}) = \frac{\mu}{4\pi} \cdot \frac{I_i}{S_i} \cdot \int_{S_i} \int_{a_i}^{b_i} \frac{\mathrm{d}\boldsymbol{l}_i \cdot \mathrm{d}s_i}{|\boldsymbol{r} - \boldsymbol{r}_i|} \tag{2.31}$$

where $\boldsymbol{r}_i$ is the coordinate of the infinitesimal vector $\mathrm{d}\boldsymbol{l}_i$, the last within the segment i and in the direction of the current flow I_i, while S_i is the cross-section of the segment i. The permeability of the homogeneous and linear medium is μ.

In addition to assuming a constant cross-sectional area, equation 2.31 also assumes that the current I_i flows homogeneously in the segment i. This is a reasonable approximation for low frequencies and negligible kinetic inductance of the conductive materials. Further, when inhomogeneities appear at higher f, they can be taken into account by weighing the integrand of 2.31 with a fixed scalar function modeling the cross-sectional distribution of I_i. For cross-sections considerably smaller than the physical separation between the segments, a situation typically found in actual systems, the weighing distribution is universal for each segment, geometrically scalable and depends only on the frequency through the skin effect.

Combining 2.29, 2.30, 2.31, it can be written for the segment k:

$$\Delta U_k = \frac{\mathrm{d}\gamma_k}{\mathrm{d}t} = \frac{\mathrm{d}}{\mathrm{d}t}\left(\sum_{i=1}^{N} L_{ik} \cdot I_i \right) = \sum_{i=1}^{N} L_{ik} \cdot \frac{\mathrm{d}I_i}{\mathrm{d}t}$$

where

$$L_{ik} = L_{ki} = \frac{\mu}{4\pi} \cdot \frac{1}{S_i \cdot S_k} \cdot \int_{S_i} \int_{S_k} \int_{a_k}^{b_k} \int_{a_i}^{b_i} \frac{\mathrm{d}\boldsymbol{l}_i \cdot \mathrm{d}\boldsymbol{l}_k}{|\boldsymbol{r}_i - \boldsymbol{r}_k|} \mathrm{d}s_i \, \mathrm{d}s_k \tag{2.32}$$

is the partial inductance between the ith and kth segment. When $i = k$, then the partial self inductance is obtained while for $i \neq k$, the partial mutual inductances are obtained. For the partial self-inductances, although the integrand diverges when $\mathrm{d}\boldsymbol{l}_i$ and $\mathrm{d}\boldsymbol{l}_k$ coincide, the integral itself can be solved.

The sign of the partial inductance L_{ik} is determined by the orientation of the currents in the segments i and k. This is seen from 2.32, where the sign of L_{ik} is given by the polarity of the line integral of the scalar product of the vectors $\mathrm{d}\boldsymbol{l}_k \cdot \mathrm{d}\boldsymbol{l}_i$ that are each coincident with the currents I_k and I_i (note that $\frac{1}{|\boldsymbol{r}_k - \boldsymbol{r}_i|}$ is always positive).

The orientations of the currents on the other hand, which were at the beginning defined to flow from node a towards node b in each segment, are, by the same convention, fixed in relation to the polarity of the potential difference $\Delta U = U(a) - U(b)$ across the segment. Hence, even if one is free to choose which node will be a and which b, once the choice is made then the relation of the polarity between the potential difference and the current is fixed: the current flows in through the positive node and leaves through the negative node. This is the reference orientation of the nodal and flow variables for the constitutive laws of all circuit elements for electromagnetic networks (except for voltage sources).

From 2.32, the partial self-inductances L_{kk} will always be positive while the partial mutual inductances L_{ik} will have a negative sign if the geometry of the system and the choice for the polarity of the nodes in segments i and k is such that the currents I_i and I_k flow predominantly in opposite directions. Conversely, if I_i and I_k flow predominantly in the same direction, the mutual inductance L_{ik} will be positive. Interestingly, if the segments are perpendicular to each other, the partial mutual inductance will be zero.

For the $N \times N$ matrix $\boldsymbol{L}$ consisting of elements L_{ik}, the following can be written

$$\Delta \boldsymbol{U} = \frac{\mathrm{d}}{\mathrm{d}t}(\boldsymbol{L} \cdot \boldsymbol{I}) \tag{2.33}$$

where $\Delta \boldsymbol{U}$ and $\boldsymbol{I}$ are vectors of size N containing at position j the nodal and flow variables for the segment j respectively. The relation 2.33 is useful when the network equations are written in a matrix form, a method readily used in circuit simulators. Another useful relation is

$$W^m = \frac{1}{2} \boldsymbol{I}^T \cdot \boldsymbol{L} \cdot \boldsymbol{I}$$

which equals the total magnetic energy stored in the system. Note that since the energy $W^m > 0$, the partial inductance matrix $\boldsymbol{L}$ must be positive definite. This fact is used in simplifying the analysis of systems with a large N, where leaving out low-value elements in $\boldsymbol{L}$ must be done such that the matrix remains positive definite and network instability is avoided. Another feature of $\boldsymbol{L}$ is that it is diagonally symmetric since from 2.32 it is obvious that $L_{ik} = L_{ki}$.

In section 2.2.4, the concept presented above will be adapted for the case of interconnected superconducting loops. In addition to including the kinetic inductance, also the validity of the assumptions for the current flow homogeneity and, related to it, the method of cross-sectional averaging will be evaluated for the specific case of superconducting structures.

In this section it was shown that for a network that models the electromagnetics of a given system, the nodal variables are the *scalar potential differences* which, in time dependent cases, do not equate the measurable quantity *voltage*. The scalar potentials are given in the circuit gauge 2.28 that requires them to have no time dependence when the fields do not change. In that case, they will equal the Coulomb potentials U.

Further, it was concluded that the above property of the nodal variables can be observed only in a circuit where inductances are present and where magnetic field changes are thus important. This is typically the case for superconducting systems and therefore care must be taken to choose the correct nodal quantities when defining the circuit elements for a superconducting network.

At the end, it was found that the segmentation of the physical system in the node-branch architecture of a network necessitates inserting open-ended inductor elements, called partial inductances, in the branches. They model the partial electromotive force felt between the terminals of the branch the element belongs to. Since a superconductor is, within reasonable approximations, a pure inductance, multi-loop arrangements of superconducting paths will need to be treated as networks of purely partial inductances.

2.2.4 Network model of a superconducting multi-loop circuit

In this section, the superconducting network model will be created for a circuit of superconducting segments connected in a multiple loop arrangement, in a similar way as in the previous section. First, the partial inductance concept for a single superconducting segment is applied and then the inductive coupling with other segments is included. As a new feature of a superconducting network, the model for the phenomenon of flux quantization is then discussed. After that, a new element, the Josephson Junction, is introduced in the network model. At the end, the rest of the elements typically found in a superconducting network will be presented. Expressions for the free energy of the elements are also provided in each section.

2.2.4.1 Partial inductance of a superconducting segment

Lets take a length of a superconductor with a constant cross-sectional area S, as given in Figure 2.10. The cross-section and length profile can be of arbitrary shape. There is a current I flowing through the superconducting segment along its length, entering at the interface Σ_a and exiting at Σ_b. The goal is to derive an expression for the partial self-inductance according to the concept that was discussed in the previous section.

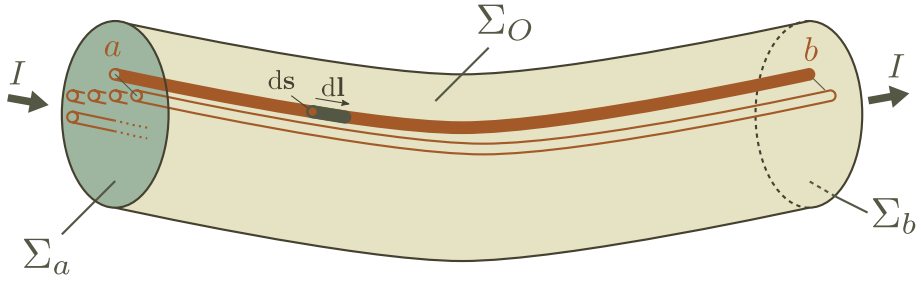

Figure 2.10. A superconducting segment of constant, albeit arbitrary, cross section carrying a current I. The interior of the segment is divided into infinitesimal tubes that follow the length profile and are parallel to the current flow at each point.

The partial flux variable was, for normal conductors and homogeneous current flow, given previously by:

$$\gamma = \frac{1}{S} \int_S \int_a^b \boldsymbol{A} \cdot \mathrm{d}\boldsymbol{l} \cdot \mathrm{d}s \tag{2.34}$$

where the surface integral serves the purpose of cross-sectional averaging of the magnetic vector "potential drop" between the ends of the segments. The end-points a and b are chosen to be at the same position on the end cross-sections Σ_a and Σ_b, see Figure 2.10 for exact detail. The path of the line integral is, at each point, in the direction of the current I and unique for every configuration of the end points. Since the position of both end points changes with each iteration of the surface averaging, the whole volume V_S of the conductor is "covered" by the above double integration.

In superconductors, the cross-sectional current distribution is not homogeneous even at zero frequency. The expression for the partial flux 2.34, although suitable for the majority of normal conducting segments, where inhomogeneities must be taken into account only at high f (skin effect), can not be directly applied to superconducting network segments. One has to take into account the non-homogeneous current distribution in a superconductor.

Lets normalize the current distribution $\boldsymbol{J}_S$ with the total current I through the segment

$$\boldsymbol{j}_S(\boldsymbol{r}) = \frac{\boldsymbol{J}_S(\boldsymbol{r})}{I}\,, \quad \int_S \boldsymbol{j}_S(\boldsymbol{r}) \cdot \mathrm{d}\boldsymbol{s} = 1 \tag{2.35}$$

and construct an expression for the partial flux γ by using the normalized distribution $\boldsymbol{j}_S$ to "weigh" the integrand:

$$\gamma = \int_S \int_a^b \boldsymbol{j}_S \cdot \boldsymbol{A} \cdot \mathrm{d}l \cdot \mathrm{d}s = \int_{V_S} \boldsymbol{j}_S \cdot \boldsymbol{A} \cdot \mathrm{d}V$$

with $\mathrm{d}V = \mathrm{d}l \cdot \mathrm{d}s$ and where V_S is the volume of the segment. The term $\frac{1}{S}$ is removed so that the dimension of γ remains the same ($\boldsymbol{j}_S$ is in units of m^{-2}). The requirement of constant cross-section can now be removed since S does not appear anymore in the expression for the partial flux, neither explicitly through $\frac{1}{S}$ nor implicitly through a surface integral. Finally, to complete the expression for γ, the kinetic inductance component $\Lambda \cdot \boldsymbol{J}_S$ must be added to $\boldsymbol{A}$:

$$\gamma = \int_{V_S} \boldsymbol{j}_S \cdot (\boldsymbol{A} + \Lambda \cdot \boldsymbol{J}_S) \cdot \mathrm{d}V = \frac{\Phi_0}{2\pi} \int_{V_S} \boldsymbol{j}_S \cdot \nabla\theta \cdot \mathrm{d}V \tag{2.36}$$

where the supercurrent equation

$$\frac{\Phi_0}{2\pi} \nabla\theta = \boldsymbol{A} + \Lambda \cdot \boldsymbol{J}_S$$

was used. From the vector algebra identity

$$\nabla(\theta \cdot \boldsymbol{j}_S) = \boldsymbol{j}_S \cdot \nabla\theta + \theta \cdot \nabla \boldsymbol{j}_S$$

and

$$\nabla \boldsymbol{j}_S = \frac{1}{I} \cdot \nabla \boldsymbol{J}_S = \frac{1}{I} \cdot 0 = 0$$

the following expression for the partial flux is now obtained:

$$\gamma = \frac{\Phi_0}{2\pi} \cdot \oint_{\Sigma_S} \boldsymbol{j}_S \cdot \theta \cdot \mathrm{d}\boldsymbol{\sigma} \tag{2.37}$$

where the divergence theorem was applied to the volume integral of $\nabla(\theta \cdot \boldsymbol{j}_S)$ and $\Sigma_S = \Sigma_a + \Sigma_b + \Sigma_O$ is the closed surface bounding the volume V_S of the segment. The surface element vector $\mathrm{d}\boldsymbol{\sigma}$ is oriented normal to Σ_S and pointing out of the superconductor's bulk. At the outer boundary Σ_O of the superconductor $\boldsymbol{j}_S \cdot \mathrm{d}\boldsymbol{\sigma}_O = 0$ since there is no current exiting through it. Then,

$$\gamma = \frac{\Phi_0}{2\pi} \cdot \left(\int_{\Sigma_a} \boldsymbol{j}_S \cdot \theta \cdot \mathrm{d}\boldsymbol{\sigma}_a + \int_{\Sigma_b} \boldsymbol{j}_S \cdot \theta \cdot \mathrm{d}\boldsymbol{\sigma}_b \right)$$

Choosing the interface surfaces Σ_a and Σ_b normal to the current flow, then it follows $\boldsymbol{j}_S \cdot \mathrm{d}\boldsymbol{\sigma}_a = -|\boldsymbol{j}_S| \cdot \mathrm{d}\sigma_a$ and $\boldsymbol{j}_S \cdot \mathrm{d}\boldsymbol{\sigma}_b = |\boldsymbol{j}_S| \cdot \mathrm{d}\sigma_b$:

$$\gamma = \frac{\Phi_0}{2\pi} \cdot \left(\int_{\Sigma_b} |\boldsymbol{j}_S| \cdot \theta \cdot \mathrm{d}\sigma_b - \int_{\Sigma_a} |\boldsymbol{j}_S| \cdot \theta \cdot \mathrm{d}\sigma_a \right) = \frac{\Phi_0}{2\pi} (\bar{\theta}_b - \bar{\theta}_a) = \frac{\Phi_0}{2\pi} \cdot \bar{\theta}_{ba} \tag{2.38}$$

where $\bar{\theta}_{ba} = \bar{\theta}_b - \bar{\theta}_a$ is the difference between the *current-weighted cross-sectional average phases* $\bar{\theta}_b$ and $\bar{\theta}_a$ at the segment's interfaces Σ_a and Σ_b respectively.

Combining the Second London equation and the definition of the vector potential

$$\nabla \times \boldsymbol{A} = \boldsymbol{B} = -\nabla \times (\Lambda \, \boldsymbol{J}_S)$$

the linear relationship between the magnetic vector potential and the current density can be easily seen (I is a constant scalar):

$$-\nabla \times (\Lambda \, \boldsymbol{j}_S) = -\nabla \times (\Lambda \frac{\boldsymbol{J}_S}{I}) = -\frac{1}{I} \nabla \times (\Lambda \, \boldsymbol{J}_S) = \frac{1}{I} \nabla \times \boldsymbol{A} = \nabla \times (\frac{1}{I} \boldsymbol{A}) = \nabla \times \boldsymbol{a}$$

where $\boldsymbol{a} = \frac{1}{I} \boldsymbol{A}$ is the normalized magnetic vector potential, i.e. the vector potential when the current density flowing through the superconductor is $\boldsymbol{j}_S$. Therefore, scaling the current density by $\frac{1}{I}$ at every point will result in the magnetic vector potential also being scaled by the same amount. Then, from 2.36, the partial flux is

$$\gamma = \int_{V_S} \boldsymbol{j}_S \cdot (\Lambda \cdot \boldsymbol{J}_S + \boldsymbol{A}) \cdot \mathrm{d}V = I \cdot \int_{V_S} \boldsymbol{j}_S \cdot (\Lambda \cdot \boldsymbol{j}_S + \boldsymbol{a}) \cdot \mathrm{d}V = I \cdot L \tag{2.39}$$

where

$$L = \int_{V_S} \boldsymbol{j}_S \cdot (\Lambda \cdot \boldsymbol{j}_S + \boldsymbol{a}) \cdot \mathrm{d}V \tag{2.40}$$

is the partial self-inductance of the segment of volume V_S. Note that the partial inductance is a function of only the geometry and material properties as neither $\boldsymbol{j}_S$ nor the normalized vector potential $\boldsymbol{a}$ depend on the intensity I of the current. The normalized current density distribution $\boldsymbol{j}_S(\boldsymbol{r})$ can always be found for the particular geometry of the segment by using the Maxwell/London equations. An example was the cylindrical wire from section 2.2.1. In general, the differential equation that governs the normalized current distribution inside a superconducting segment is obtained by combining Ampere's law and the First London equation:

$$\nabla^2 (\Lambda \, \boldsymbol{j}_S(\boldsymbol{r})) = -\mu \, \boldsymbol{j}_S(\boldsymbol{r}), \; \int_S \boldsymbol{j}_S(\boldsymbol{r}) \cdot \mathrm{d}\boldsymbol{s} = 1$$

where S is any cross-section of the segment. After solving the above for $\boldsymbol{j}_S(\boldsymbol{r})$, using a numerical method for instance, the normalized magnetic vector potential $\boldsymbol{a}(\boldsymbol{r})$ can be found from Maxwell equations. In the Coulomb gauge $\nabla\boldsymbol{a}=0$ for instance, the solution is given by the Biot-Savart law

$$\boldsymbol{a}(\boldsymbol{r})=\frac{\mu}{4\pi}\int_{V_S}\frac{\boldsymbol{j}_S(\boldsymbol{r}')}{|\boldsymbol{r}-\boldsymbol{r}'|}\cdot\mathrm{d}V'$$

Then, once $\boldsymbol{j}_S$ and $\boldsymbol{a}$ are known, the partial inductance can be calculated by evaluating the integral 2.40.

Combining 2.38 and 2.39, it is finally obtained

$$\bar{\theta}_{ba}=\frac{2\pi\cdot L}{\Phi_0}\cdot I$$

The form of this expression suggests that the flux angle variable φ, introduced previously as the normalized magnetic flux threading a closed superconducting loop, can also be defined for a partial superconducting inductor as well. In the latter case, the flux angle is simply the difference between the superconducting phases, current-weighted and cross-sectionally averaged, on the end surfaces of the partial inductor segment:

$$\varphi_{ab}=\bar{\theta}_{ba}=\frac{2\pi}{\Phi_0}\cdot\gamma=\frac{2\pi\cdot L}{\Phi_0}\cdot I \tag{2.41}$$

Note that the flux angle's $\varphi_{ab}=\varphi_a-\varphi_b=\bar{\theta}_b-\bar{\theta}_a$ positive side is taken to be the one where current enters, node a, so that it is compatible with network conventions. This is opposite to the polarity of the average phase difference $\bar{\theta}_{ba}$ where the positive node is b.

From the First London equation $\boldsymbol{E}=\frac{\partial(\Lambda\cdot\boldsymbol{J}_S)}{\partial t}$ and the supercurrent equation, it can be written that

$$\nabla U=-(\boldsymbol{E}+\frac{\partial\boldsymbol{A}}{\partial t})=-\frac{\partial}{\partial t}(\Lambda\cdot\boldsymbol{J}_S+\boldsymbol{A})=-\frac{\Phi_0}{2\pi}\cdot\frac{\partial(\nabla\theta)}{\partial t}$$

Differentiating 2.36 w.r.t. time and combining the result with the above, it is obtained

$$-\frac{\partial\gamma}{\partial t}=\int_{V_S}\boldsymbol{j}_S\cdot\nabla U\cdot\mathrm{d}V \tag{2.42}$$

assuming $\frac{\partial\boldsymbol{j}_S}{\partial t}=0$ which is true as long as the normalized current distribution does not change with frequency. This holds up to frequencies where conduction from the normal charge carriers in the superconductor becomes important. As mentioned before, in this text the frequencies of interest are always below this limit and the assumption $\frac{\partial\boldsymbol{j}_S}{\partial t}=0$ holds.

Applying to 2.42 the same process that was used to develop 2.36, the following is true

$$\frac{\partial \gamma}{\partial t} = \bar{U}_a - \bar{U}_b = \bar{U}_{ab}$$

where $\bar{U}_a$ and $\bar{U}_b$ are the current-weighed cross-sectionally averaged Coulomb potentials at the segment's interfaces Σ_a and Σ_b respectively. From 2.38 and 2.41, it can be written that

$$\bar{U}_{ab} = \frac{\partial \gamma}{\partial t} = \frac{\Phi_0}{2\pi} \cdot \frac{\partial \bar{\theta}_{ba}}{\partial t} = \frac{\Phi_0}{2\pi} \cdot \frac{\partial \varphi_{ab}}{\partial t} \tag{2.43}$$

This relation makes it possible to create an equivalence between the conventional $(U-I)$ and the superconducting $(\varphi - I)$ networks. One can take a network where the nodal variables are the Coulomb potentials U and replace them with their time-integrals through the new variable φ_{ab} according to 2.43. This would also give physical meaning to the nodal difference φ_{ab} across superconducting segments as the time antiderivative of the (weighted and averaged) Coulomb potential. The relation 2.43 together with the flux quantization relations are actually the cornerstone of the superconducting network model.

In a similar way as with the superconducting closed ring from section 2.2.2, one can write the (partial) free energy of the segment

$$W = \frac{1}{2} \int_{V_\infty} \boldsymbol{B} \cdot \boldsymbol{H} \cdot \mathrm{d}V + \frac{1}{2} \int_{V_S} \Lambda \, \boldsymbol{J}_S^2 \cdot \mathrm{d}V = \frac{1}{2} \cdot \int_{V_S} \boldsymbol{J}_S \cdot (\boldsymbol{A} + \Lambda \, \boldsymbol{J}_S) \cdot \mathrm{d}V$$

where it was used

$$\boldsymbol{B} \cdot \boldsymbol{H} = (\nabla \times \boldsymbol{A}) \cdot \boldsymbol{H} = \nabla \, (\boldsymbol{A} \times \boldsymbol{H}) + \boldsymbol{A} \cdot (\nabla \times \boldsymbol{H}) = \nabla \, (\boldsymbol{A} \times \boldsymbol{H}) + \boldsymbol{A} \cdot \boldsymbol{J}_S \tag{2.44}$$

and

$$\int_{V_\infty} \nabla \, (\boldsymbol{A} \times \boldsymbol{H}) \cdot \mathrm{d}V = \oint_{S_\infty} (\boldsymbol{A} \times \boldsymbol{H}) \cdot \mathrm{d}\boldsymbol{S} = 0 \tag{2.45}$$

since $\boldsymbol{H}$ will vanish at infinity in any realistic system. Further, substituting $\boldsymbol{A} = I \cdot \boldsymbol{a}$ and $\boldsymbol{J}_S = I \cdot \boldsymbol{j}_S$ while keeping in mind the definition of the partial self-inductance 2.40, it is easy to see that

$$W = \frac{1}{2} \cdot I^2 \cdot \int_{V_S} \boldsymbol{j}_S \cdot (\boldsymbol{a} + \Lambda \, \boldsymbol{j}_S) \cdot \mathrm{d}V = \frac{1}{2} \cdot L \, I^2 = \frac{1}{2} \, \frac{\Phi_0^2}{(2\pi)^2} \cdot \frac{\varphi_{ab}^2}{L} = \frac{1}{2} \, \frac{\Phi_0}{2\pi} \cdot \varphi_{ab} \cdot I \tag{2.46}$$

just as it was the case for a superconducting ring.

For the superconducting network model it is important that the energy, aside from the "universal" expression $\frac{L \cdot I^2}{2}$, can also be written in terms of the nodal variable φ_{ab} by using the constitutive law 2.41. This makes the pair (I, φ) a suitable state-variable for superconducting segments since the energy can be calculated as a function of the pair.

2.2.4.2 Inductive coupling

Continuing with the analogy from the section on normal conducting segments, and using the same derivation method ($\boldsymbol{A} = \sum A_k$), one gets for the segment i

$$\varphi_{ab,i} = \frac{2\pi}{\Phi_0} \cdot \sum_{k=1}^{N} L_{ik} \cdot I_k \tag{2.47}$$

for a multi-loop superconducting system with N segments. The coefficients L_{ik} are the partial inductances between the segments i and k. In the Coulomb gauge, they can be calculated as:

$$\begin{aligned} L_{ii} &= \int_{V_{S,i}} \boldsymbol{j}_{S,i}(\boldsymbol{r}) \cdot \left(\Lambda \cdot \boldsymbol{j}_{S,i}(\boldsymbol{r}) + \frac{\mu}{4\pi} \int_{V_{S,i}} \frac{\boldsymbol{j}_{S,i}(\boldsymbol{r}')}{|\boldsymbol{r} - \boldsymbol{r}'|} \cdot \mathrm{d}V' \right) \cdot \mathrm{d}V \\ L_{ik} = L_{ik} &= \frac{\mu}{4\pi} \int_{V_{S,i}} \boldsymbol{j}_{S,i}(\boldsymbol{r}) \cdot \left(\int_{V_{S,k}} \frac{\boldsymbol{j}_{S,k}(\boldsymbol{r}')}{|\boldsymbol{r} - \boldsymbol{r}'|} \cdot \mathrm{d}V' \right) \cdot \mathrm{d}V = \\ &= \frac{\mu}{4\pi} \int_{V_{S,k}} \boldsymbol{j}_{S,k}(\boldsymbol{r}) \cdot \left(\int_{V_{S,i}} \frac{\boldsymbol{j}_{S,i}(\boldsymbol{r}')}{|\boldsymbol{r} - \boldsymbol{r}'|} \cdot \mathrm{d}V' \right) \cdot \mathrm{d}V \end{aligned} \tag{2.48}$$

where $\boldsymbol{j}_{S,n}(\boldsymbol{r})$ is the normalized current density through the segment n and $\boldsymbol{r}'$ is the (help) coordinate of the volume element $\mathrm{d}V'$ of the inner volume integral.

The coefficients L_{ik} are symmetrical due to the property of reciprocity of the fields created by currents flowing in different parts of the system:

$$\int_{V_1} \boldsymbol{J}_1 \cdot \boldsymbol{A}_2 \cdot \mathrm{d}V = \int_{V_2} \boldsymbol{J}_2 \cdot \boldsymbol{A}_1 \cdot \mathrm{d}V$$

where the current $\boldsymbol{J}_1$ flowing in the volume V_1 creates the field $\boldsymbol{A}_1$ while $\boldsymbol{J}_2$ flowing in V_2 creates $\boldsymbol{A}_2$. The above can be proved with the identities 2.44 and 2.45. Replacing the currents and vector potentials with their normalized values, the relation $L_{ik} = L_{ki}$ is obtained.

Just like in the case of a normal-conducting multiloop circuit, 2.47 allows one to create a partial inductance matrix and write:

$$\boldsymbol{\varphi} = \frac{2\pi}{\Phi_0} \boldsymbol{L} \cdot \boldsymbol{I} \tag{2.49}$$

where $\boldsymbol{L}$ is a matrix of elements L_{ik} and $\boldsymbol{\varphi}$, $\boldsymbol{I}$ are vectors whose elements contain the current and flux angle of each segment.

The total free energy for a superconductor network of N segments will yield:

$$W_{\mathrm{tot}} = \sum_{i=1}^{N} \left[\frac{1}{2} \cdot \int_{V_S} \boldsymbol{J}_{S,i} \cdot \left(\sum_{k=1}^{N} \boldsymbol{A}_k + \Lambda \, \boldsymbol{J}_{S,i} \right) \cdot \mathrm{d}V \right] = \frac{1}{2} \sum_{i=1}^{N} \sum_{k=1}^{N} L_{ik} \cdot I_i \cdot I_k$$

The case where only two segments are coupled in the circuit will be very important in this text. The free energy of the two segments will be ($L_{12} = L_{21}$):

$$W_{\mathrm{tot},M} = \frac{L_{11} \cdot I_1^2}{2} + \frac{L_{22} \cdot I_2^2}{2} + L_{12} \cdot I_1 \cdot I_2$$

which, using 2.49 in the case of two segments $N = 2$, transforms in

$$\left(\frac{2\pi}{\Phi_0} \right)^2 \cdot W_{\mathrm{tot},M} = \frac{1}{2} \cdot \frac{1}{L_{11} \cdot L_{22} - L_{12}^2} \cdot (L_{22} \cdot \varphi_1^2 + L_{11} \cdot \varphi_2^2 - 2 \cdot L_{12} \cdot \varphi_1 \cdot \varphi_2)$$

which is very similar to the case of two coupled superconducting rings, except that the partial flux angles are now used.

In the last two subsections, it was shown that the energetic state of a physical system of superconductors can be modeled with a lumped (filamentary) superconducting network in (φ, I) space and with constitutive laws 2.41. Usually, if the electromagnetic variables of a system are spatially not homogeneous, as is the case for the current at high f in normal conductors for instance, then a distributed network is required to model the system and correctly represent its energetic state. Such a distributed model is based on a finite-element subdivision of the segments and the number of nodal/flow variables in its network model is as large as the accuracy wished to be to achieved. For superconductors, this is not necessary: one can represent a superconducting segment with just three scalar quantities φ, I, L even though the electromagnetic variables are spatially non-homogeneous.

2.2.4.3 Calculation of the partial inductances

To find the partial inductances from 2.48, one must know the (normalized) current densities in each segment. To calculate the current densities in each segment on the other hand, it is often necessary to employ a numerical algorithm or a field solver. There are some general properties of current flow and magnetic coupling between segments that may simplify this process.

If the segments are far apart relative to their cross-sectional size, then one can use the current distribution calculated as if the segments were isolated. This is so because the vector potential created by the current $\boldsymbol{j}_{S,i}$ flowing in the segment i,

$$\boldsymbol{a}_i(\boldsymbol{r}) = \int_{V_i} \frac{\boldsymbol{j}_{S,i}(\boldsymbol{r}')}{|\boldsymbol{r}-\boldsymbol{r}'|}\,\mathrm{d}V'$$

hardly changes with $\boldsymbol{r}$ within the cross-section of any other segment k that is far away from the segment i due to the term $\frac{1}{|\boldsymbol{r}-\boldsymbol{r}'|}$. Then, the magnetic field associated with such a homogeneous $\boldsymbol{a}_i$ will be small and not induce any changes in the spatial distribution of the current in the segment k. The vector potential $\boldsymbol{a}_i$ however does create a flux angle difference between the ends of the segment k, even if the magnetic field associated with $\boldsymbol{a}_i$ is negligible, giving a non-zero value for L_{ik}.

If the segments are close to each other, then the current distributions are different than in the isolated case. In this situation, one must solve the full electromagnetic problem, including screening currents in adjacent regions of the segments involved in the coupling. Both the definitions of the current distributions $\boldsymbol{j}_{S,i}$ and $\boldsymbol{j}_{S,k}$ as well as the process of calculating the partial inductance must be correctly applied. To obtain $\boldsymbol{j}_{S,i}$, the normalized current distribution of the segment i, one would set its current to I_i and the current through the *interfaces* of all other segments to zero, $I_k = 0,\ \forall k \neq i$, but allow screening currents to locally exist in them. These screening currents on the other hand influence the current distribution in the segment i and solving for $\boldsymbol{j}_{S,i}$ must take that into account. After performing the same for segment k and obtaining $\boldsymbol{j}_{S,k}$, the partial inductance is calculated according to the integral expression from 2.48. The important point is that the calculation of the current distribution in a given segment must include screening effects from other nearby segments.

When the current distribution of a given structure needs to be calculated, regardless of the method employed, one must assume or "force" the boundary conditions at the structure's interfaces with the external world (save for some very symmetrical geometries). For a single isolated superconducting segment for instance, this entails fixing either the current or the phase distribution across the end interfaces. Any results of the analysis will then apply only to such a "forced" situation and will not be general enough. One can reduce the inaccuracies by the method of continuation if the segment is relatively straight (length-wise) at the ends. First, the segment is extended by a length of approximately few λ_L on each side and a cross-sectionally constant current is fixed at the ends. After finding the current distribution inside the segment with those boundary conditions, one calculates the inductance from 2.48 using an integration volume excluding the extensions.

For large circuits with many segments, obtaining the partial inductances is a momentous numerical task (complexity $\sim N^2$). Fortunately, in superconducting thin-film circuits there is always a common "groundplane" superconducting film in close proximity to each segment. The coupling with the superconducting groundplane dominates the partial inductances, implying that the mutual inductances between the segments are negligible. To illustrate this, lets take a look at the thin-film system from Figure 2.11 that is realistically dimensioned.

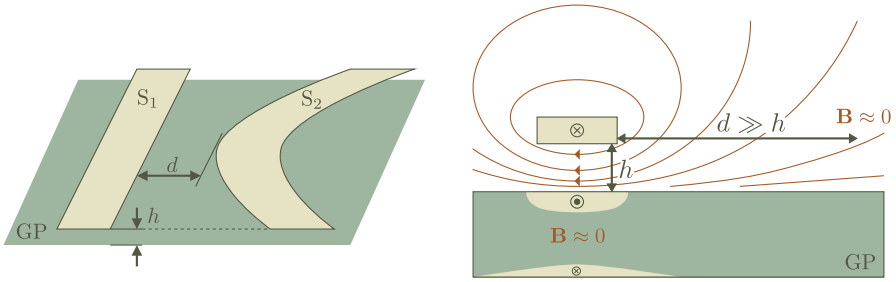

Figure 2.11. Two segments above a groundplane in a thin-film technology (left) and a sketch of the magnetic field lines showing the concentration of the field in the area between the superconductor and groundplane (right). After just a few lengths of h in the horizontal direction, $\boldsymbol{B}$ effectively reduces to zero (as well as $\boldsymbol{A}$). Typically, d is never less than a couple of μm, while the thickness of the isolation layer between the segments h measures 100s of nm. At the bottom of the groundplane, the "sandbelt" current is flowing as a return path of the screening current on the top of the groundplane.

The segments S_1 and S_2 are coupled only to the groundplane GP but not between themselves. That is so because the superconducting groundplane effectively shields the two segments by confining the magnetic field of each segment to the thin region between the plates, and is thus unable to horizontally reach the other segment. The great benefit in this case is that the segments can be analysed in isolation from each other other: in the example from 2.11 this will mean that the geometry to analyse for L_{11} will be GP + S_1 and for L_{22} it will be GP + S_2. The partial inductance $L_{12} = L_{21} = 0$. More complex thin-film geometries will be analysed in detail in Section 2.3 using a field solver.

It is not often necessary to compute the integrals 2.48 in order to obtain the partial inductances in the circuit. Once $\boldsymbol{j}_S$ and $\boldsymbol{a}$ are known, one can also find the (current-normalized) superconducting phase at the interfaces only and hence calculate the flux angle across each segment. Dividing it with the appropriate constants, the partial inductance is directly obtained. This is the process used later in Section 2.3 when a commercial EM software package is used to obtain the inductance parameters of thin-film superconducting circuits.

If one disregards edge effects, possible when the width w and length l of a rectangular segment are far greater then the separation between the groundplane and the wiring thin-films, as well as greater than the λ_L's of the used superconducting materials, then one can use the following approximation for the self-inductance of the segment:

$$L = L_{\square} \cdot \frac{l}{w} \tag{2.50}$$

where $L_{\square}$ is called the *sheet inductance* of the superconducting electrode [15]. The sheet inductance is a function of the material properties, the thickness of the electrode and groundplane as well as the separation d between them. Note that for superconducting, as well as for normal conducting, segments not placed in the vicinity of a groundplane or any other conductors, the inductance will depend roughly logarithmically on the dimensions of the segment due to the mutual coupling between adjacent parts of it. For segments closely separated from a groundplane, a system also called a microstrip line, there is little of such coupling taking place and the inductance will obey a different dependence on the segment's dimensions.

The formula 2.50 is most accurate for relatively straight thin-film segments with a groundplane. It is evident that its form is analogous to the capacitance formula of a parallel-plate capacitor and the resistance formula of a thin-film resistor. The reason for the simplicity of 2.50 is that for a straight, wide and long superconducting segment, covered by a superconducting groundplane from which it is closely separated, the magnetic field will be largely homogeneous across it surface. Also, there will be no coupling between adjacent parts of the segment. Therefore, increasing the length l of the segment, there will be a longer path travelled by the charge carriers in the same normalized field and the "vector potential drop", defined as the partial inductance of a segment, will be linearly higher, $L \sim l$. If the segment width w is larger, then the normalized field on the surface will be proportionally weaker due to the lower normalized current density, resulting in an inverse-proportional effect on the inductance $L \sim \frac{1}{w}$. The constant of proportionality in front of $\frac{l}{w}$ is the sheet inductance.

2.2.4.4 Joining segments in a node

When two segments are connected, one of each of the interface surfaces are joined together and it is obvious that the nodal variables of those interfaces are the same. One would then build the network representation of the two connected segments by connecting the two individual elements in series (including the mutual inductance terms) at the common node. However, this is not as simple when more than two segments meet at a node. The question is illustrated in Figure 2.12, where

4 segments meet, and the task is to investigate whether it is correct to build an equivalent network by connecting the circuit elements together at a common node.

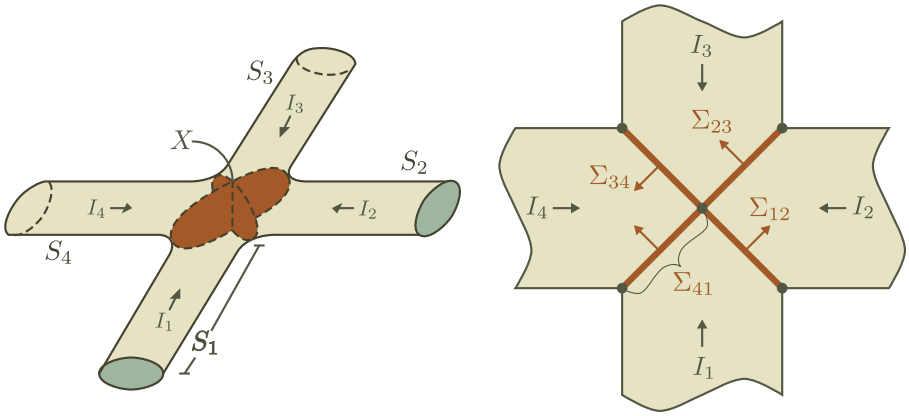

Figure 2.12. Four segments are joined together at one of their interfaces. Parts of the interface surfaces in the common area are shared between the segments.

Let's first establish the interface surfaces of all segments at the connection area X. One choice is depicted in Figure 2.12 and indicated as $\Sigma = \Sigma_{12} + \Sigma_{23} + \Sigma_{34} + \Sigma_{41}$. Combinations of these components of Σ yield whole cross-sections of each segment. For simplicity, it is chosen that the interface surfaces are not necessarily normal to the current density at each point.

From the definition of the interface variables in 2.38, for the segment labeled with 1, the following can be written:

$$\bar{\theta}_1 = \int_{\Sigma 12} \boldsymbol{j}_{S1} \cdot \theta \cdot \mathrm{d}\sigma_{12} + \int_{\Sigma 41} \boldsymbol{j}_{S1} \cdot \theta \cdot \mathrm{d}\sigma_{41} =$$
$$= \frac{1}{I_1} \cdot \left(\int_{\Sigma 12} \boldsymbol{J}_S \cdot \theta \cdot \mathrm{d}\sigma_{12} + \int_{\Sigma 41} \boldsymbol{J}_S \cdot \theta \cdot \mathrm{d}\sigma_{41} \right)$$

since $\boldsymbol{J}_S = \boldsymbol{j}_{S1} \cdot I_1$. Likewise, for the rest of the segments

$$\bar{\theta}_2 = \frac{1}{I_2} \cdot \left(- \int_{\Sigma 12} \boldsymbol{J}_S \cdot \theta \cdot \mathrm{d}\sigma_{12} + \int_{\Sigma 23} \boldsymbol{J}_S \cdot \theta \cdot \mathrm{d}\sigma_{23} \right)$$
$$\bar{\theta}_3 = \frac{1}{I_3} \cdot \left(- \int_{\Sigma 23} \boldsymbol{J}_S \cdot \theta \cdot \mathrm{d}\sigma_{23} + \int_{\Sigma 34} \boldsymbol{J}_S \cdot \theta \cdot \mathrm{d}\sigma_{34} \right)$$
$$\bar{\theta}_4 = \frac{1}{I_4} \cdot \left(- \int_{\Sigma 34} \boldsymbol{J}_S \cdot \theta \cdot \mathrm{d}\sigma_{34} - \int_{\Sigma 41} \boldsymbol{J}_S \cdot \theta \cdot \mathrm{d}\sigma_{41} \right)$$

where the "−" signs are used where the normals of the surface elements are opposite than those used in the definition of the nodal phases from 2.38. From the above equations, it is obtained

$$I_1 \cdot \bar{\theta}_1 + I_2 \cdot \bar{\theta}_2 + I_3 \cdot \bar{\theta}_3 + I_4 \cdot \bar{\theta}_4 = 0 \tag{2.51}$$

The law of charge conservation for the structure is:

$$I_1 + I_2 + I_3 + I_4 = 0 \tag{2.52}$$

It can be seen that there is a degree of arbitrariness in the choice of the nodal variables $\bar{\theta}_i$ such that both 2.51 and 2.52 are satisfied. If it is allowed for the value of a nodal variable to change when the current passing through it changes, one would have to specify a whole new set of constitutive relations in the network (note that the constitutive law arrived at so far connects the *differences* in the nodal variable and the currents, not the nodal variables themselves with the current passing through them). In order to avoid extra equations and additional complexity, lets set an additional requirement that the nodal variables and currents are *linearly independent* at connection nodes. Then, 2.51 and 2.52 are both satisfied only when

$$\bar{\theta}_1 = \bar{\theta}_2 = \bar{\theta}_3 = \bar{\theta}_4 = \bar{\theta}_X \tag{2.53}$$

where the common value is labelled $\bar{\theta}_X$ and declared as the nodal phase variable. It is now clear that the current-weighed and cross-sectionally averaged phases $\bar{\theta}_i$ of the segments must be equal when they are joined together in the connection area.

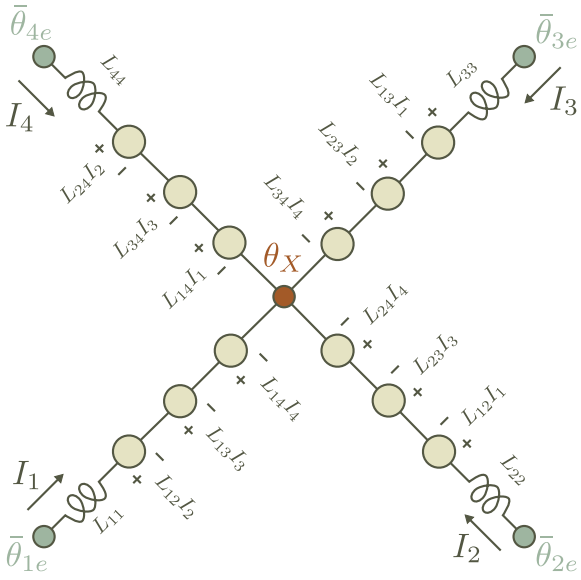

Figure 2.13. An equivalent schematic of the 4-segment network from Figure 2.12.

The resulting circuit schematic is now given by Figure 2.13. The extraction of the 9 unknown elements of the partial inductance matrix can now be performed by using the external interfaces, labeled with the (sub)index e in Figure 2.13, of the segments in pairs of two. The total number of unknowns is however less than 9 due to the extra equation of charge conservation 2.52. In Section 2.3, a number of examples of this process are given.

2.2.4.5 Flux quantization in multiloop superconducting networks

In section 2.2.2, it was postulated that the superconducting phase can experience $2\pi n$ jumps at any point inside a superconductor, which led to the flux quantization phenomenon in a superconducting ring. It is however not clear if such discontinuities are compatible with certain relations of the MQM. Also, methods on how to deal with flux quantization in a multiloop geometry need to be precisely developed. Trying to discuss these questions, this subsection expands the flux quantization principle for circuits beyond just galvanically isolated superconducting rings.

Before implementing flux quantization in networks of superconducting segments, it is necessary to first discuss some properties of the superconducting phase $\theta(\boldsymbol{r}, t)$ in a superconductor.

Let's again use the geometry of the superconducting ring from Figure 2.5 in section 2.2.2. The exterior surface of the ring is labeled with Σ_O while its volume is V_S. There is no external field present.

The Coulomb gauge condition $\nabla \boldsymbol{A} = \boldsymbol{0}$ is, for a superconductor, equivalent to

$$\nabla^2 \theta(\boldsymbol{r}) = 0, \ \boldsymbol{r} \in V_S \tag{2.54}$$

by substitution of $\boldsymbol{A}$ from the supercurrent equation. The above Laplace equation can be solved given boundary conditions: either $\theta(\boldsymbol{r})$ or $\boldsymbol{n} \cdot \nabla\theta$ should be known at Σ_O with $\boldsymbol{n}$ being the normal of the exterior surface. From the supercurrent equation, one can write

$$\boldsymbol{n} \cdot \nabla\theta = \frac{2\pi}{\Phi_0} \cdot (\Lambda \, \boldsymbol{n} \cdot \boldsymbol{J}_S + \boldsymbol{n} \cdot \boldsymbol{A})$$

It is known that the current does not flow out of the surface Σ_O, so therefore it has no normal component along it: $\boldsymbol{n} \cdot \boldsymbol{J}_S = 0$. Using the second requirement of the Coulomb gauge, $\boldsymbol{A} \cdot \boldsymbol{n} = 0$, the boundary condition for the phase's gradient at Σ_O is obtained:

$$\boldsymbol{n} \cdot \nabla\theta = 0, \ \boldsymbol{r} \in \Sigma_O \tag{2.55}$$

The only solution to a Laplace equation with zero boundary conditions is

$$\theta(\boldsymbol{r}) = \text{const.}$$

However, it was already shown that when the superconductor is multiply-connected, like for instance the ring from section 2.2.2, the phenomenon of flux quantization appears as a consequence of phase jumps of $2\pi \cdot n$ within the superconductor. This leads to a contradiction: it is not possible to have both $n \neq 0$ (trapped flux) and $\theta = \text{const.}$ at the same time!

The resolution of this problem is found in the fact that, rigorously, the phase is defined only modulo 2π or, in other words, $\theta(\boldsymbol{r}, t)$ is a *multiple valued* scalar function. Many of the standard identities and theorems in vector algebra do not apply for such functions, including the integral(s) above. In fact, the lack of proper inclusion of this property of θ makes most of the calculations performed so far in danger of being invalid! To obtain rigorously valid expressions, the fact that the phase $\theta(\boldsymbol{r}, t)$ can have multiple values at the same point must be somehow taken into account in the fundamental equations of the MQM.

It is convenient to "capture" the multi-valuedness of the superconducting phase without deviating from conventional algebra tools. One such *ad-hoc* procedure was already used in section 2.2.2 when the phase in the superconducting ring was allowed to be $2\pi \cdot n$ step-wise discontinuous only on a cross-sectional surface, leaving the rest of the ring with a single-valued θ. This method is formalized in [31], where the description of the dynamics of superconductors using a multivalued θ and the description where θ is an ordinary, single-valued, scalar but with step-wise jumps in its value have been found to be equivalent. However, if one uses a step-wise discontinuous single-valued phase instead of a multivalued function for θ, it is required to modify the supercurrent equation:

$$\boldsymbol{A} + \Lambda \cdot \boldsymbol{J}_S = \frac{\Phi_0}{2\pi} \cdot (\nabla\theta - \boldsymbol{\theta}^{\upsilon}) \tag{2.56}$$

where θ is now a single-valued function and

$$\boldsymbol{\theta}^{\upsilon}(\boldsymbol{r}; \Sigma_J) = 2\pi \cdot n \cdot \boldsymbol{\delta}(\boldsymbol{r}; \Sigma_J)$$

is the *vortex (gauge) field* where

$$\boldsymbol{\delta}(\boldsymbol{r}, \Sigma_J) = \int_{\Sigma_J} \delta^{(3)}(\boldsymbol{r} - \boldsymbol{r}') \cdot \mathrm{d}\boldsymbol{\sigma}'_J$$

Further, $\delta^{(3)}(\boldsymbol{r}) = \delta(x) \cdot \delta(y) \cdot \delta(z)$ is the 3D Dirac delta function at the position vector $\boldsymbol{r} = (x,\ y,\ z)$ and $\mathrm{d}\boldsymbol{\sigma}'_J$ is the normal element vector of an open surface Σ_J within the superconductor. The 2π n step-wise discontinuity of the phase is confined on the "jump" surface Σ_J in the above equations; the phase's gradient there being a vector delta function - hence the appearance of $\boldsymbol{\theta}^{\upsilon}(\boldsymbol{r};\ \Sigma_J)$. The direction of the surface's normal $\mathrm{d}\boldsymbol{\sigma}'_J$ is arbitrary since the integer n can absorb its sign. When there are multiple jump surfaces $\Sigma_{J,i}$, the vortex field is the sum of the individual vortex fields $2\pi \cdot n_i \cdot \boldsymbol{\delta}(\boldsymbol{r}; \Sigma_{J,i})$.

Note that if the points where the phase has a step-wise jump do not lie on a surface but are instead "peppered" all throughout the superconductor, the phase's gradient will contain derivatives of the Dirac delta function which is an unphysical result. Hence, the points of $2\pi n$ jumps in the phase must lie on a surface.

There are a few properties the surface Σ_J needs to have in order for the concept from [31] to apply for the network topology of a superconducting system. First, since *all* non-contractible closed paths within a multiply connected superconductor must pass through at least one point where a phase jump can happen, the surface Σ_J, if it exists, must have a boundary that lies on the surface of the superconductor, completely enclosing it. In other words, for multiloop superconducting circuits the jump surfaces Σ_J are always cross-sections. Secondly, there has to be *at least one* unique jump surface Σ_J with its own flux quantization number n for each *unique* loop (a collection of uncontractible closed paths) in the multiloop circuit. In the example from Figure 2.14, where two loops sharing a center path are shown, it is not possible to place a single jump surface only in the middle segment - the closed path circulating along the outside segments would then not pass through a phase-jump surface. It is thus necessary to have at least two surfaces, one in each of the outside arms for example, carrying its own flux quantization number. For a general configuration, this requires that there exists at least one phase-jump surface Σ_J and integer n per unique loop.

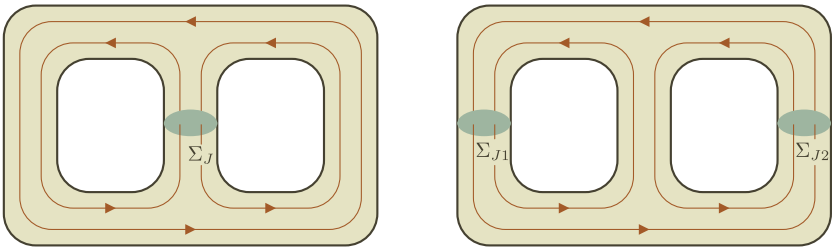

Figure 2.14. A network of two loops sharing a center conductor must contain two jump surfaces: in the drawing on the left, all closed paths that do not pass through the center conductor can not experience a phase jump. The drawing on the right is an example of a correct choice of the jump surfaces.

A simple algorithmic method to determine the jump surface sites can rely on iterating the following simple procedure for each closed loop: if the loop does not pass through an existing jump surface, add one at an arbitrary position in an arbitrary segment belonging to the loop. Each new jump surface has a unique integer number n attached to it.

Another property of the jump surface is the invariance of the system's observables under shape transformation of Σ_J. Choosing a different shape for Σ_J is shown in [31] to be a new form of gauge transformation: it does not affect the observable physics of the system. In this text, cross-sectional surfaces that are normal to the current are of interest, see for instance the derivation for partial inductance from the previous section. Therefore, also the jump surfaces Σ_J will be chosen such that they are normal to the current flowing through the superconductor.

In general, there are two ways to take into account the step-wise discontinuity of the phase in the description of the system. The first one is to modify the system equations, like in [31], to explicitly include the vortex field in the expressions for the fields and currents. The second is to exclude the jump surface from the region of validity of the system equations while simultaneously using it as a boundary condition. The former is more suitable for describing observable discrete features in the currents and fields distributed locally inside a single segment, like for instance Abrikosov vortices, while the latter is more suitable for the systems presented in this text where flux quantization is treated as a feature of circuit geometry.

Since it is desired not to make any further modifications in the MQM, like for instance including the vortex field in the London equations as in [31], the concept of the jump surface Σ_J will in this text be used only as a boundary condition and all equations will be left unchanged. This requires the jump surface to be excluded from the equations governing the superconducting phase, in a similar manner that the interior of voltage sources (example batteries) is excluded from the Maxwell equations governing conventional electronic circuits. While a voltage source is an ideal element forcing a potential difference between its terminals, a jump surface Σ_J forces a phase difference of $2\pi \cdot n$ across its sides. In the most general way, this boundary condition is expressed by

$$\lim_{|\boldsymbol{u}]\to 0} \left\{ \int_{\Sigma_J} [\boldsymbol{f}(\boldsymbol{r}-\boldsymbol{u}) \cdot \theta(\boldsymbol{r}-\boldsymbol{u}) - \boldsymbol{f}(\boldsymbol{r}) \cdot \theta(\boldsymbol{r})] \cdot \mathrm{d}\boldsymbol{\sigma} \right\} = 2\pi \cdot n \cdot \int_{\Sigma_J} \boldsymbol{f}(\boldsymbol{r}) \cdot \mathrm{d}\boldsymbol{\sigma} \qquad (2.57)$$

where Σ_J is the jumping surface, $f(\boldsymbol{r})$ is any continuous (vector) function and n is an integer.

Getting back to the example from the beginning of this subsection, the use of the extra boundary condition 2.57 when seeking the solutions of the differential Laplace equation 2.54 for the phase in the ring from Figure 2.5 (section 2.2.2) will now not result in the contradiction "$\theta = \text{const}$ while $n \neq 0$".

Let's take a superconducting loop consisting of M segments, each segment i having volume $V_{S,i}$ and surface $\Sigma_{O,i}$. There is a single jump surface Σ_J defined in one of the segments. Applying the boundary condition 2.57 with $f(\boldsymbol{r}) = \boldsymbol{j}_S(\boldsymbol{r})$ to

the definition of the partial flux variable from 2.37, the following can be written:

$$\frac{2\pi}{\Phi_0}\cdot\sum_{i=1}^{M}\gamma_i=\sum_{i=1}^{M}\left(\oint_{\Sigma_{O,i}}\boldsymbol{j}_S\cdot\theta\cdot\mathrm{d}\boldsymbol{\sigma}_i\right)=2\pi\cdot n\cdot\int_{\Sigma_J}\boldsymbol{j}_S\cdot\mathrm{d}\boldsymbol{\sigma}_J=2\pi\cdot n$$

since all the surface integrals are either zero (at the outer surfaces) or will cancel each other out except at Σ_J. Using the definition of the flux angle, $\frac{2\pi}{\Phi_0}\gamma_i=\varphi_i$, it is finally obtained

$$\sum_{i=1}^{M}\varphi_i=2\pi\cdot n \tag{2.58}$$

The relation 2.58 is similar to the Second Kirchhoff law in conventional networks, except that here: a) it pertains to the sum of the flux angles and b) it is not zero but equal to $2\pi\cdot n$. It is convenient to simply shift the $2\pi\cdot n$ term on the left side of the equation and add a "$2\pi\cdot n$ flux angle source" in the network at the place where a jumping surface was placed. This source has a magnitude of $2\pi\cdot n$ and zero electromagnetic length, just like ideal voltage sources/batteries in conventional networks. One can always change the sign of the source and it is often convenient to write $\pm 2\pi\cdot n$ in graphical symbols to make clear that its polarity is ambiguous.

Several conclusions can be made from the above presentation:

- A multi-valued scalar function can be alternatively treated as a single-valued but step-wise discontinuous function as shown in [31]
- Applying this method to the superconducting phase function, jumping surfaces Σ_J will need to be included in the description of any multiple-connected superconducting system
- For a multi-loop superconducting circuit, the jumping surfaces Σ_J have the following properties
  - they are always a cross-section of a superconducting segment
  - can be chosen using the "at least one Σ_J per unique loop" rule
  - have an arbitrary position along the length of the segment as well as an arbitrary shape. In this text all cross sectional surfaces of interest are normal to the current flow.

- The equations of the MQM need not be modified if the jumping surface is excluded from them and the boundary condition 2.64 is used instead
- As a consequence, the Second Kirchhoff law is shown to be valid for superconducting networks, but pertaining to the sum of the flux angles around a loop and an additional flux angle source of $\pm 2\pi \cdot n$

All necessary tools have now been developed to create a superconducting network model for concrete examples of multiloop circuits. One can identify nodes and segments in the circuit, draw the equivalent network schematic by choosing the interface surfaces and joining elements at connecting nodes, calculate the values of the (mutual and self) partial inductances of the segments, position the jump surfaces according to the algorithm above and finally write the network equations or calculate the free energy of the circuit as a function of the free variables. The small example from the next subsection will illustrate this process.

2.2.4.6 Multiloop network example

Let's use the thin-film example from Figure 2.15, where two loops sharing the same center conductor are given. There is a groundplane present which makes the partial inductance matrix diagonal since the mutual inductance terms are negligible. Two nodes and three segments can be identified, as well as two $\pm 2\pi \cdot n$ flux angle sources modeling the two jumping surfaces. Based on this information, an equivalent network schematic is drawn in Figure 2.15.

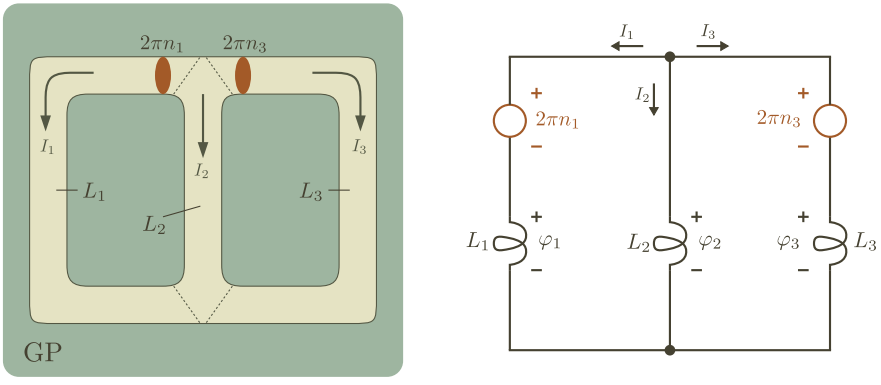

Figure 2.15. A structure consisting of two superconducting loops sharing a center conductor above a groundplane (left) and the structure's equivalent superconducting network model (right).

The network equations, with the reference directions as given, are:

$$\varphi_1 + 2\pi\, n_1 = \varphi_2$$

$$\varphi_3 + 2\pi\, n_3 = \varphi_2$$

$$\begin{pmatrix} \varphi_1 \\ \varphi_2 \\ \varphi_3 \end{pmatrix} = \frac{2\pi}{\Phi_0} \cdot \begin{pmatrix} L_1 & & 0 \\ & L_2 & \\ 0 & & L_3 \end{pmatrix} \cdot \begin{pmatrix} I_1 \\ I_2 \\ I_3 \end{pmatrix}$$

$$I_1 + I_2 + I_3 = 0$$

The solution of the above system of network equations is:

$$\varphi_1 = 2\pi \cdot (L_1 \| L_2 \| L_3) \cdot \left(n_3 \frac{1}{L_3} - n_1 \frac{1}{L_2 \| L_3} \right)$$

$$\varphi_2 = 2\pi \cdot (L_1 \| L_2 \| L_3) \cdot \left(n_3 \frac{1}{L_3} + n_1 \frac{1}{L_1} \right)$$

$$\varphi_3 = 2\pi \cdot (L_1 \| L_2 \| L_3) \cdot \left(n_1 \frac{1}{L_1} - n_3 \frac{1}{L_2 \| L_1} \right)$$

where the "in parallel" operation was used: $A \| B = \frac{A\,B}{A+B}$. It can be seen that the quantization numbers parametrize the network's solutions. To find the quantization integers, it is necessary to calculate the free energy and then pick the (n_1, n_3) combination yielding minimal energy.

To simplify the calculation, let's choose a symmetrical system $L_1 = L_3 = L$ and $L_2 = q \cdot L$ where q is an arbitrary positive number. Then, the free energy W is

$$W \cdot \frac{2L}{\Phi_0^2} = \left[2 \left(\frac{q}{2q+1} \right)^2 + 1 \right] \cdot \left[n_1^2 + n_3^2 - 2 \cdot \frac{q\,(q+2)}{2q^2 + (q+1)^2} \cdot n_1\, n_3 \right]$$

The part that depends on the quantization numbers can be written in the same form as equation 2.25 that was developed before for the system of two flux-coupled rings from section 2.2.2.2:

$$W \sim n_1^2 + n_3^2 - 2 \cdot \kappa \cdot n_1\, n_3$$

where now $\kappa = \frac{q\,(q+2)}{2q^2 + (q+1)^2}$ in this case. The potential landscape will also be the same as before, see Figure 2.7. It is interesting to observe that galvanic coupling, where two structures are coupled by sharing a common current path as in Figure 2.15, acquires similar potential landscape as the system of flux (inductive) coupled but otherwise isolated structures, save for the different meaning of the coupling constants and the scaling of the absolute energy levels.

Again, a stable minimum exists only for $n_1 = n_3 = 0$ making all quantities in the circuit equal to 0 at the lowest energy state, which is expected when no external sources are present. There is also the tendency to have the loop currents circulate in opposing rather than aligned directions (anti-ferromagnetic ordering is preferred) if the system is excited.

In the following section, the Josephson Junction element will be introduced (along with other elements). These devices add a periodic component to the free energy which, when combined with the parabolic components from the inductive elements, can result in multiple local minima other than the zero-state. Equally important, a Josephson Junction adds a mechanism which enables the circuit to undergo self-sustained transitions between stable states, these transitions triggered by suitable stimuli.

2.2.5 Circuit elements

In the previous sections, the superconducting network model for structures of interconnected segments was given. Therein the most basic network element, a (coupled) superconducting segment, was already defined. In this section, all other circuit elements typical to superconducting circuits will be presented, along with their most important properties and constitutive law. An expression for the free energy and, if needed, a discussion of their equivalent circuit will be also given.

2.2.5.1 Josephson Junction

A Josephson Junction is a device consisting of two superconducting electrodes brought in contact through a non-superconducting layer acting as a barrier to supercurrent flow. If the barrier is very thin, on the order of the size of a Cooper pair, a limited supercurrent will still be able to flow between the electrodes as a result of tunneling or other transport mechanisms preserving the condensate's coherence across the barrier. Although the class of Josephson Junction devices is rather wide, they share some common properties. These are: a periodic current-phase relationship and the existence of a current limit above which a voltage appears across the electrodes.

In Figure 2.16, the most instructive type of Josephson junction is illustrated. Two superconducting segments of rectangular and equal cross-sections are joined together through a thin barrier of isolating material. The superconducting charge carriers can tunnel through the barrier and a current can flow even without any voltage across it. This effect was predicted by B. D. Josephson in 1962 [32]. The device shown in Figure 2.16 is often called an S-I-S, a superconductor-insulator-superconductor junction. There are also S-N-S, S-N-I-S, etc, junctions stacks where the N stands for "normal metal". Although the charge transport mechanism is different between the various types of Josephson Junctions, there is not as large a difference in the junction element models used in superconducting networks.

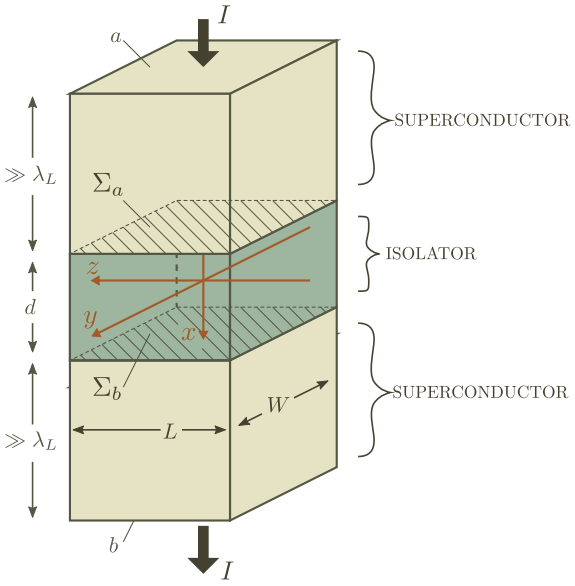

Figure 2.16. The most basic Josephson junction geometry together with the coordinate system used in the text. The barrier thickness d, not shown to scale in the drawing, is of the order of the size of the individual superconducting charge-pairs.

The barrier layer between the electrodes is typically not more than a few 10s of nanometers thick in order to allow for sufficiently strong coupling between the superconducting condensates in the two sides. The lateral dimensions W, L of the devices are usually application-dependent and range from 1 to 100s of μm. In this text, the lateral device dimensions are not greater than a few micrometers.

As drawn in Figure 2.16, the total current through the junction is I flowing from a towards b, while the surfaces of the junction terminals Σ_a, Σ_b are parallel to the $y-z$ plane. The junction width is W, its length is L and the thickness of the electrodes along the x direction is greater than the penetration depth λ_L of the superconductors.

From a simple one-dimensional tunneling analysis of the structure from Figure 2.16, see for instance [14], the First Josephson relation is obtained for the supercurrent through the junction $\boldsymbol{J}_{SJ}$:

$$\begin{aligned} \boldsymbol{J}_{SJ}(y,z,t) &= \boldsymbol{i}_x \cdot J_C(y,z) \cdot \sin\left[\phi(y,z,t)\right] \\ \phi(y,z,t) &= \theta_a(y,z,t) - \theta_b(y,z,t) + \frac{2\pi}{\Phi_0} \int_{x_a}^{x_b} \boldsymbol{A}(x,y,z,t) \cdot \mathrm{d}\boldsymbol{x} \end{aligned} \tag{2.59}$$

where $J_C(y,z)$, the *critical current density*, depends on the material properties of the isolation layer and superconducting electrodes as well as on the isolation layer's thickness d. Current transport within the barrier is only along $\boldsymbol{i}_x$, the unit vector

in the x direction, while within the superconductors the current can have rotational components so as to screen any applied or self-created magnetic field. The critical current density $J_C(y, z)$ is not a function of the coordinates in the vast majority of the cases and can be taken to be constant across the interface: $J_C(y, z) = J_C$.

The argument under the sine function in 2.59, $\phi(y, z, t)$, is called *the gauge invariant phase (difference)*. The superconducting phases θ_a and θ_b are indexed based on the segment interfaces on each side of the barrier:

$$\theta_a(y, z, t) = \theta(x_a, y, z, t)$$
$$\theta_b(y, z, t) = \theta(x_b, y, z, t)$$

where x_a and x_b are the x coordinates of the interfaces Σ_a and Σ_b. The integration of the vector potential in 2.59 is in the direction of the current flow inside the barrier, i.e. the x direction. Finally, since there is only an x component of the current inside the barrier, charge conservation $\nabla \boldsymbol{J}_S = 0$ requires that the Josephson supercurrent $\boldsymbol{J}_{SJ}(y, z, t)$ does not depend on the x coordinate.

The same one-dimensional tunneling analysis also yields the Second Josephson relation:

$$\frac{2\pi}{\Phi_0} \cdot \int_{x_a}^{x_b} \boldsymbol{E} \cdot \mathrm{d}\boldsymbol{x} = \frac{2\pi}{\Phi_0} \cdot V(y, z, t) = \frac{\partial \phi(y, z, t)}{\partial t} \tag{2.60}$$

where V is the voltage across the barrier. Due to the sine function in 2.59, $\boldsymbol{J}_{SJ}$ has a maximum that is limited by J_C. If a current greater than this maximum is forced through the junction, a voltage V will appear across the electrodes. Since the junction barrier also has a (large) normal resistance, which is electrically in parallel to the superconducting channel, the "extra" current will be carried by normally conducting electrons, called quasiparticles, through the barrier. Since from 2.60 a voltage produces a time-changing ϕ, which in turn produces a time-varying supercurrent according to 2.59, a dynamic situation will arise and hence the capacitance between the electrodes will have to be taken into account. A complete model of the junction will thus also need a resistor and capacitor in parallel to the superconducting transport channel. This model will be later presented in a concise form.

Combining 2.59 with the Maxwell/London equations for the barrier and superconductors respectively, see for instance [12], the following can be written

$$\begin{aligned} \frac{\partial \phi}{\partial z} &= \frac{2\pi}{\Phi_0} \cdot (2\lambda_L + d) \cdot B_y(x = x_a = x_b, y, z) \\ -\frac{\partial \phi}{\partial y} &= \frac{2\pi}{\Phi_0} \cdot (2\lambda_L + d) \cdot B_z(x = x_a = x_b, y, z) \end{aligned} \tag{2.61}$$

using the assumption that the y and z components of the magnetic field do not change with x inside the barrier, as well as that there is no B_x component present.

Differentiating the relations 2.61 one more time w.r.t. z and y respectively and subtracting them, while keeping in mind the x component of the Ampere law inside the barrier

$$\boldsymbol{J}_{SJ} = J_C \sin(\phi) \cdot \boldsymbol{i}_x = \frac{\partial B_z}{\partial y} - \frac{\partial B_y}{\partial z}$$

it follows that

$$\frac{\partial^2 \phi}{\partial z^2} + \frac{\partial^2 \phi}{\partial y^2} = \frac{\sin(\phi)}{\lambda_J^2} \tag{2.62}$$

where a new parameter is introduced:

$$\lambda_J = \sqrt{\frac{\Phi_0}{2\pi \cdot \mu_0 \cdot J_C \cdot (d + 2\,\lambda_L)}}$$

called the *Josephson penetration length*. For the junctions typically found in this text, with λ_L in in the 100s and d in the of 10s of nm range, together with a typical J_C of 10 $\frac{\mu A}{\mu m^2}$, the Josephson penetration length is of the order of 10s of micrometers.

If the dimensions W, L of the device are much smaller than λ_J, then the right-hand side of 2.62 can be approximated with zero and the two dimensional Laplace equation is obtained for the gauge invariant phase difference:

$$\frac{\partial^2 \phi}{\partial z^2} + \frac{\partial^2 \phi}{\partial y^2} = 0 \tag{2.63}$$

A solution for a Laplace equation is dependent on the boundary conditions and the geometry of the system. The relations 2.61 valued along the edges of the junction (for $y = \pm\frac{W}{2}$ or $z = \pm\frac{L}{2}$) can be used as the Neumann boundary conditions in, for example, a Green's function method. The magnetic field at the sides, B_y and B_z in the boundary conditions 2.61, is then a sum of an externally applied field (if any) and the self-field of the total current I. It is however possible to approximately find the phase distribution for small junctions where $W, L \ll \lambda_J$ without resorting to a full solution of the Laplace equation.

Let's first try to estimate the self-created magnetic field of the current I. That field will circulate around the device and be roughly tangential to the junction's sides in the $y - z$ plane. Disregarding edge effects, we can assume that $\boldsymbol{B}$ is constant along the sides. The highest theoretical values of the field are achieved when the total current through the junction is maximum $I = J_C \cdot W \cdot L$. From Ampere's integral law, $\oint \boldsymbol{B} \cdot \mathrm{d}\boldsymbol{l} = \mu_0 \cdot I = \mu_0 \cdot J_C \cdot W \cdot L$, the highest values that the right-hand sides of 2.61 can achieve at the sides are found to be

$$\begin{aligned} \left|\frac{\partial \phi}{\partial z}\right|_{z=\pm\frac{L}{2}} &\cong \frac{W}{\lambda_J^2} \cong 0 \\ \left|\frac{\partial \phi}{\partial y}\right|_{y=\pm\frac{W}{2}} &\cong \frac{L}{\lambda_J^2} \cong 0 \end{aligned} \tag{2.64}$$

in the case where the dimensions W, L are much smaller than λ_J. The solution of a Laplace equation 2.63 with boundary conditions 2.64 is a constant: $\phi = \phi_0$. Consequently, from 2.59, the junction current will be also constant across the interface

$$\boldsymbol{J}_{SJ} = \boldsymbol{i}_x \cdot J_C \cdot \sin(\phi_0)$$

and the total current is:

$$I = \int_{-\frac{L}{2}}^{\frac{L}{2}} \int_{-\frac{W}{2}}^{\frac{W}{2}} J_C \cdot \sin(\phi_0) \cdot \mathrm{d}y \cdot \mathrm{d}z = I_C \cdot \sin(\phi_0)$$

where $I_C = J_C \cdot W \cdot L$ is the junction's *critical current*. In conclusion, the self field of a small junction can be neglected, resulting in a spatially homogeneous current across the interface surfaces.

When there is an externally applied constant field, for instance B_A in the y direction, then 2.61 transforms to

$$\frac{\partial \phi}{\partial z} = \frac{2\pi}{\Phi_0} \cdot (2\lambda_L + d) \cdot B_A$$
$$\frac{\partial \phi}{\partial y} = 0$$

which can be directly integrated to yield a linearly changing ϕ along z

$$\phi(y, z) = \phi_0 + \frac{2\pi}{\Phi_0} \cdot (2\lambda_L + d) \cdot B_A \cdot z \tag{2.65}$$

where $\phi_0 = \phi(y = 0,\ z = 0)$. The Josephson current will now be sinusoidally distributed in the z direction and constant in y:

$$J_{SJ}(y, z) = J_C \cdot \sin\left(\phi_0 + \frac{2\pi}{\Phi_0} \cdot (2\lambda_L + d) \cdot B_A \cdot z\right) \tag{2.66}$$

The total current through the junction then calculates to

$$I = \int_{-\frac{L}{2}}^{\frac{L}{2}} \int_{-\frac{W}{2}}^{\frac{W}{2}} J_{SJ}(y, z) \cdot \mathrm{d}y\, \mathrm{d}z = I_C \cdot \frac{\sin\left(\frac{\pi \Phi}{\Phi_0}\right)}{\frac{\pi \Phi}{\Phi_0}} \cdot \sin(\phi_0) = I_C(\Phi) \cdot \sin(\phi_0) \tag{2.67}$$

where $\Phi = (2\lambda_L + d)\, L \cdot B_A$ is the magnetic flux present in the junction's barrier, penetrating approximately λ_L on both sides into the superconductors after which it is screened. Hence, applying an external field modulates the critical current of the junction according to a Fraunhofer $\left(\frac{\sin x}{x}\right)$ pattern. Notable is the fact that ϕ_0 and

$I_C(\Phi)$, taken as parameters, are completely describing the junction's behaviour as far as the total current I is concerned.

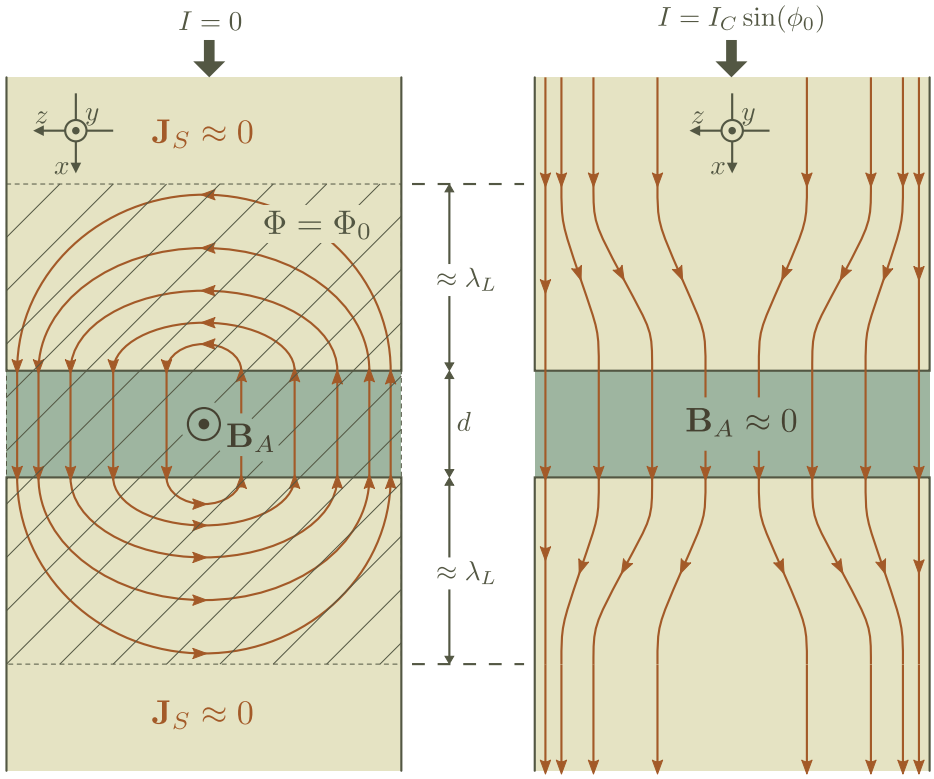

Figure 2.17. A sketch of the current distribution profile when an external flux $\Phi = \Phi_0$ is applied to the junction in the y direction (left) and when no field is applied $\Phi = 0$ (right). $\boldsymbol{J}_S$ is proportional to the density of the lines of current in the drawing. Note that d and λ_L are not drawn to scale as $d \ll \lambda_L$.

When there is external field, the current through the junction and the superconductors in the neighbourhood of the barrier will follow a (partially) circulating path. The situation is sketched in Figure 2.17 when a full flux quantum is present in the junction $\Phi = \Phi_0$. Since $I_C(\Phi_0) = 0$ in this case, the total I is zero while locally a current flows in a vortex structure, enveloping the barrier and extending a length $\sim\lambda_L$ within the superconductors in the x direction. When $\Phi = 0$, the current will flow homogeneously through the junction and relax to its "regular" distribution at a distance of $\sim\lambda_L$ within the superconductors, sketched in Figure 2.17 as well. For other values of the applied magnetic flux, the current distribution can be visualized as a linear combination of the two cases from Figure 2.17.

Large junctions ($W, L \gg \lambda_J$) can accommodate (multiple) vortices of average size λ_J within the barrier that interact and form complex current flow patterns. In dynamic conditions, the vortices move through the junction with speeds specific to material properties and physical constants. Such junctions are often used as oscillators, exhibiting accurate propagation speeds. Large junctions will not be used in this text and the analysis will focus exclusively at small (or short) junctions.

When there is no external flux in the junction, the gauge-invariant phase difference is spatially homogeneous and equal to ϕ_0. Hence, from 2.59,

$$\theta_a(y,z,t) - \theta_b(y,z,t) = -\frac{2\pi}{\Phi_0} \int_{x_a}^{x_b} \boldsymbol{A}(x,y,z,t) \cdot \mathrm{d}\boldsymbol{x} + \phi_0 \cong \phi_0$$

is also spatially constant across the interface surface if the integral of the vector potential is neglected due to the small distance $d = x_b - x_a$. Consequently, the nodal variable between the surfaces Σ_a and Σ_b calculates to:

$$\frac{2\pi}{\Phi_0}\gamma_J = \varphi_J = \int_{\Sigma_a} \boldsymbol{j}_S \cdot \theta_a \cdot \mathrm{d}\boldsymbol{\sigma}_a + \int_{\Sigma_b} \boldsymbol{j}_S \cdot \theta_b \cdot \mathrm{d}\boldsymbol{\sigma}_b = \theta_a - \theta_b = \phi_0$$

since the normals of the surface elements of Σ_a and Σ_b, $\mathrm{d}\boldsymbol{\sigma}_a$ and $\mathrm{d}\boldsymbol{\sigma}_b$ respectively, are oppositely oriented with respect to $\boldsymbol{j}_S = \frac{1}{W \cdot L} \cdot \boldsymbol{i}_x$. The constitutive law for the junction can then be written as

$$I = I_C \cdot \sin(\varphi_J) \tag{2.68}$$

where I is the flow variable (current) and φ_J is the nodal variable (flux angle) for the junction circuit element.

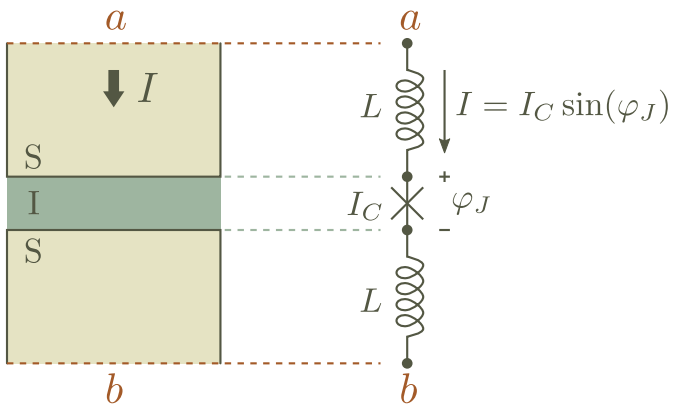

Figure 2.18. An equivalent circuit of the superconducting channel of an unmodulated Josephson junction, including the inductance of the electrode segments.

The equivalent circuit of the whole junction structure, shown in Figure 2.18, consists of the Josephson junction element, defined by the constitutive law 2.68, and two inductive elements in series with it representing the electrodes. Note that the inductance of the electrodes close to the junction will be slightly modified with respect to the case when the junction is removed and the electrodes attached together. This is due to the modified current distribution at the junction interfaces (homogeneous vs. $\sim e^{-z/\lambda_L}$; see also Figure 2.17). The difference is however small and is usually neglected. If necessary, one can take into account this effect by calculating the inductances of the segments attached to the junction using the boundary condition of constant current at the interfaces Σ_a and Σ_b.

In the case when external flux is present in the junction, building the equivalent circuit is not as simple. The applied field will penetrate the superconducting electrodes within a length of $\sim\lambda_L$ away from the barrier, thereby significantly modifying the current distribution in the region, as for instance shown on the left in Figure 2.17. Hence, the behaviour of the electrodes will be different compared to the no-field case and the equivalent circuit elements of the electrode segments should also reflect the change. The problem is difficult to solve exactly for a general junction geometry.

An intuitive solution can be found by moving the interface surfaces Σ_a and Σ_b at a distance of $\sim\lambda_L$ away from the barrier inside the superconducting electrodes. The external vector potential in the junction barrier, for a constant external magnetic field B_A in the y direction, can be written as

$$A_x = B_A \cdot z$$

and will penetrate until a depth of approximately λ_L inside the superconductors at each side, that is, until the newly translated interface surfaces. In the light of the discussion on coupled segments from the previous section, volume-integrating the external $\boldsymbol{A}$ between the interfaces of a segment in the direction of the (normalized) current will produce an extra term in the nodal variable that reflects the coupling between the segment and the external field. This additional term will, in the case of the flux-modulated junction, reflect the external's field coupling into the electrode segments of length λ_L attached to the junction. Hence, integrating $A_x = B_A \cdot z$ in that region and including the barrier, $\sim\frac{2\pi}{\Phi_0} B_A \cdot (2\lambda_L + d) \cdot z$ will be added to the phase difference at each point if a constant current profile is assumed to flow in the sub-segments. This cancels with the same term present in $\phi(y, z)$, see 2.65, leaving again only $\varphi_J = \phi_0$ as the nodal difference. Then, from 2.67,

$$I = I_C(\Phi) \cdot \sin(\phi_0) = I_C(\Phi) \cdot \sin(\varphi_J)$$

is the constitutive law of the junction when an external field is present.

Although this approximation is very rough, the expression above is consistent with experiments. A more accurate derivation of the constitutive law for a flux-modulated junction will need to use accurate expressions for both the current

and the vector potential inside the segments, after which the extra flux angle arising from the coupled field can be calculated. The crux is that the additional contribution will cancel with the spatially-dependent term in $\phi(y,\, z)$ after the surface averaging of the superconducting phase is performed, thereby resulting in $\varphi_J = \phi_0$ and the same equivalent schematic from Figure 2.18 as when no field was present, except that the critical current I_C is now flux-dependent $I_C(\Phi)$.

Flux-modulation of Josephson Junctions is usually an undesired effect in superconducting circuits. The reason is both the fact that the critical current is reduced ($|\frac{\sin x}{x}| < 1$) as well as the nonlinear nature of the coupling. The latter may result in unwanted feedback effects when currents from other parts of the circuit couple to a junction. One strives to eliminate the effects of junction flux modulation by careful design of the circuit structures and the use of groundplanes so that magnetic fields stay local and confined. There is however always coupling left from currents that flow in the electrodes nearby the junction but do not pass through it, for example when other structures are attached close to the sides of the junction. A good example of this effect is given in Chapter 4, Figure 3.20.

The energy stored in the Josephson junction depends periodically on the flux angle across its terminals [14]:

$$W_J = \frac{\Phi_0 \cdot I_C}{2\pi} \cdot \left(1 - \frac{I_C(\Phi)}{I_C} \cdot \cos\left(\varphi_J\right)\right)$$

For an unmodulated junction, where $I_C(\Phi) = I_C$, the simple expression

$$W_J = \frac{\Phi_0 \cdot I_C}{2\pi} \cdot \left(1 - \cos\left(\varphi_J\right)\right) \tag{2.69}$$

is obtained. The most interesting part of 2.69 is that, for an isolated junction, it gives the values of the flux angle $-\frac{\pi}{2} < \varphi_J < \frac{\pi}{2}$, i.e. in the first and fourth quadrant, a lower energy than when φ_J is in the second and third quadrant. As a result, if an isolated junction is biased with a current $I < I_C$, then the correct flux angle across it can be determined by the solution of the inverse trigonometric problem of $I = I_C \cdot \sin\left(\varphi_J\right)$:

$$\varphi_J = \arcsin\left(\frac{I}{I_C}\right)$$

where the $\arcsin(x)$ function is defined to return values in the output base interval $\left(-\frac{\pi}{2}, \frac{\pi}{2}\right)$. The solutions for φ_J where $\pm\pi$ is subtracted from the base value of the arcsin will yield a higher absolute energy and even more importantly, they will result in $\frac{\mathrm{d}^2 W_J}{\mathrm{d}\varphi^2} < 0$, making those solutions unstable (a local maximum is formed).

If the junction is not isolated, then the free energy of all other circuit components must be summed in order to obtain the total W. It then often happens that, after finding the local minima in W, a junction can have a flux angle outside of the

base interval. In any case, the periodic energy - flux angle relationship 2.69 creates interesting potential landscapes of Josephson junction circuits, where multiple stable states can be identified and transitions between them can be (conditionally) triggered by input signals. Indeed, therein lies the principle of operation of many digital superconducting architectures.

From the Second London equation, 2.60, a voltage

$$\frac{2\pi}{\Phi_0} \cdot V = \frac{\mathrm{d}\phi_0}{\mathrm{d}t} = \frac{\mathrm{d}\varphi_J}{\mathrm{d}t}$$

appears when the flux angle across the junction changes with time (and vice-versa). This voltage will make it possible for quasiparticles (normal conducting carriers) to travel across the thin barrier. There will thus be an additional current $\frac{V}{R_N} = \frac{\Phi_0}{2\pi \cdot R_N} \frac{\mathrm{d}\varphi_J}{\mathrm{d}t}$ flowing through the junction, where R_N is the "normal" resistance of the barrier. Additionally, a capacitance between the superconducting electrodes C will allow the displacement current $C \frac{\mathrm{d}V}{\mathrm{d}t}$ across the barrier. In total,

$$I = I_C \cdot \sin(\varphi_J) + \frac{\Phi_0}{2\pi \cdot R_N} \cdot \frac{\mathrm{d}\varphi_J}{\mathrm{d}t} + \frac{\Phi_0 \cdot C}{2\pi} \cdot \frac{\mathrm{d}^2\varphi_J}{\mathrm{d}t^2} \tag{2.70}$$

which corresponds to the equivalent circuit given in Figure 2.19. Extra terms for noise can be added if fluctuations are important. The normal resistance R_N is assumed to be independent on the voltage in 2.70, although that is far from true for the typical SIS tunnel junction as there can be considerable non-linearity in the quasiparticle tunneling current around zero voltage. However, as discussed below in more detail, it is a common practice in electronic circuits to externally shunt the junction with a (linear) resistor of a value much less than the intrinsic tunneling resistance of the junction, so that the latter is neglected in the equivalent circuit and there are only linear coefficients left in the differential equation 2.70.

When a current higher than I_C is forced through the junction, the junction is said to be in the voltage-state. The flux angle as well as its derivative, the voltage, will change with time according to the differential equation 2.70, usually in a form of a steady-state periodic oscillation. In Figure 2.19, the voltage and the flux angle across a current-biased junction is presented, using the typical values of I_C, R_N and C found in this text. Also interesting is the plot of the period-averaged voltage versus the current through the junction. This is exactly what one would obtain as an $I - V$ curve of the junction when the device is measured, since the measurement leads and instruments will filter (average-out) the high-frequency oscillating content of the voltage, leaving only the DC component. One such $I - V$ curve measurement of a junction manufactured with the YBCO/Nb hybrid π-shift technology is presented in Figure 2.19 as well.

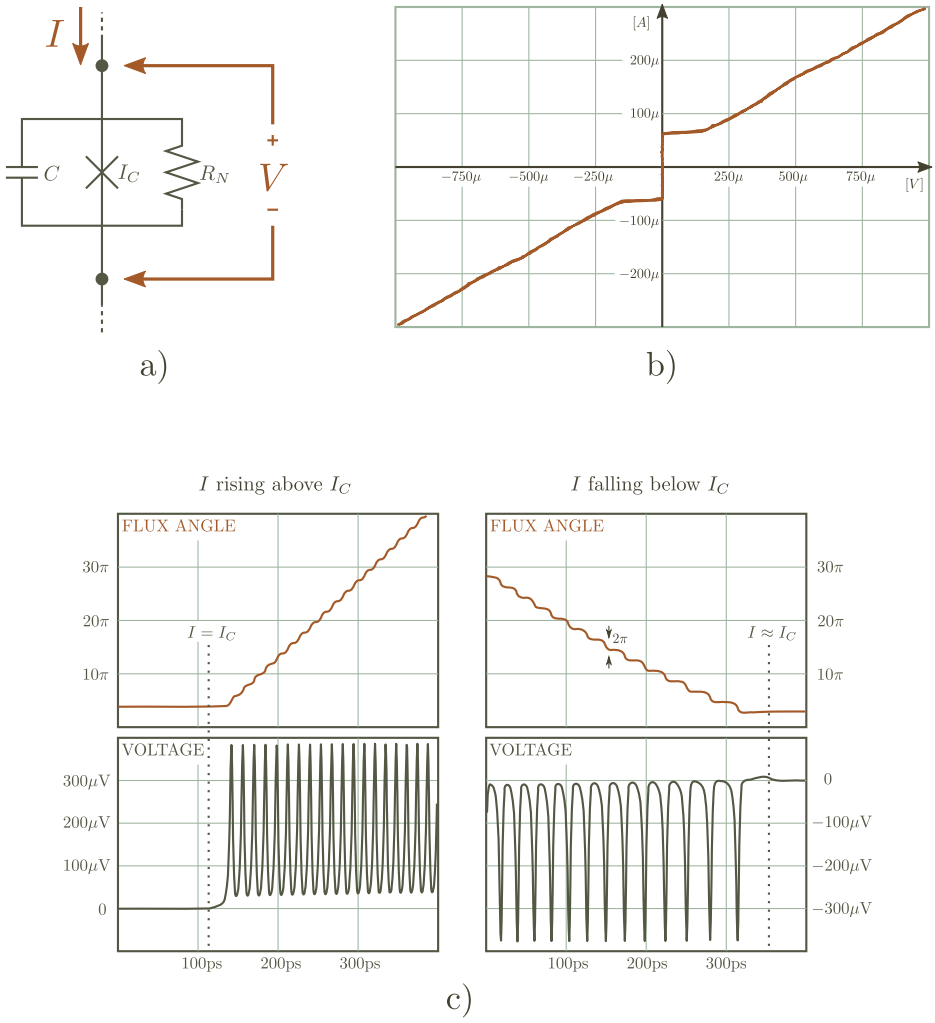

Figure 2.19. The equivalent circuit of a Josephson junction, usually referred to as the RCSJ (Resistively and Capacitively Shunted Junction) model, is given in a). Under b) one finds a measured $I - V$ curve of a typical junction fabricated in the YBCO-Nb technology introduced later. At the end, c) is a transient plot obtained from a circuit simulator implementing 2.70 with $R_N = 3\Omega$, $I_C = 72\mu A$, $C = 0.42$pF and linearly changing drive current. These junction parameters roughly correspond to the properties of the measured device from b). At $I > I_C$, each single oscillation of the voltage corresponds to a change of 2π in the flux angle across the junction. As a consequence, the time-integral of the voltage across the junction is exactly Φ_0 per each period.

Several time constants are evident from the differential equation 2.70. The first is obtained when a constant voltage is applied to the junction. The flux angle will then change linearly with time, while the junction current sinusoidally with the Josephson frequency $\omega_J = \frac{2\pi \cdot V}{\Phi_0}$. The value of $\frac{2\pi}{\Phi_0}$ is approximately $480\frac{\mathrm{GHz}}{V}$, a very large number. Alternatively, if the current carries a periodic component then there will be a constant (DC) component in the voltage. This effect is used in accurate frequency-voltage converters since the factor of proportionality, $\frac{2\pi}{\Phi_0} = \frac{2e}{\hbar}$, is a fundamental constant of nature.

Two more specific parameters can be found when one normalizes the current and time in 2.70:

$$i = \sin\varphi_J + \frac{\mathrm{d}\varphi_J}{\mathrm{d}\tau} + \beta_C \frac{\mathrm{d}^2\varphi_J}{\mathrm{d}\tau^2} \tag{2.71}$$

where $i = \frac{I}{I_C}$ and $\tau = \frac{t}{\tau_J}$ for

$$\tau_J = \frac{\Phi_0}{2\pi} \cdot \frac{1}{I_C R_N}$$

$$\beta_C = \frac{\tau_{\mathrm{RC}}}{\tau_J} = \frac{R_N \cdot C}{\tau_J}$$

The parameter β_C, called the *Stewart-McCumber parameter*, is a ratio of the capacitive time constant, $\tau_{\mathrm{RC}} = R_N \cdot C$ and the period τ_J of the Josephson frequency at the characteristic voltage $V = V_C = I_C \cdot R_N$. The relative importance of the capacitive element in the equivalent circuit is now clearly reflected in the value of β_C. For $\beta_C \ll 1$, that is for a small C, the capacitive term $\frac{\mathrm{d}^2}{\mathrm{d}t^2}$ can be neglected while for $\beta_C \gg 1$ the resistive term $\frac{\mathrm{d}}{\mathrm{d}t}$ can be neglected in 2.71. The current-voltage characteristic for those cases is shown in Figure 2.20, along with some of the important features.

The hysteresis in the characteristic for $\beta_C \gg 1$ makes such junctions unsuitable for those electronic applications where the devices either must repetitively switch between the voltage and superconducting state or operate in a current drive regime close to I_C. For instance in RSFQ circuits, where the swing in the junction drive current around I_C is limited in amplitude by the circuit architecture, it is necessary to use junctions with no return currents (i.e. a $\beta_C \leqslant 1$) in order to make sure they settle in the zero-voltage state after each operation cycle. Therefore, in many superconducting circuits, hysteretic junctions are shunted externally with a resistor, thus tuning the $\beta_C \approx 1$. In that case, the two time constants $\tau_{\mathrm{RC}} \approx \tau_J$ are approximately equal to the period of oscillation when the junction is biased just above I_C. It is worth noting that in some circuits, like for instance quantum bits or the devices in Chapter 5, hysteretic junctions can be used - they are even necessary in the case of qubits.

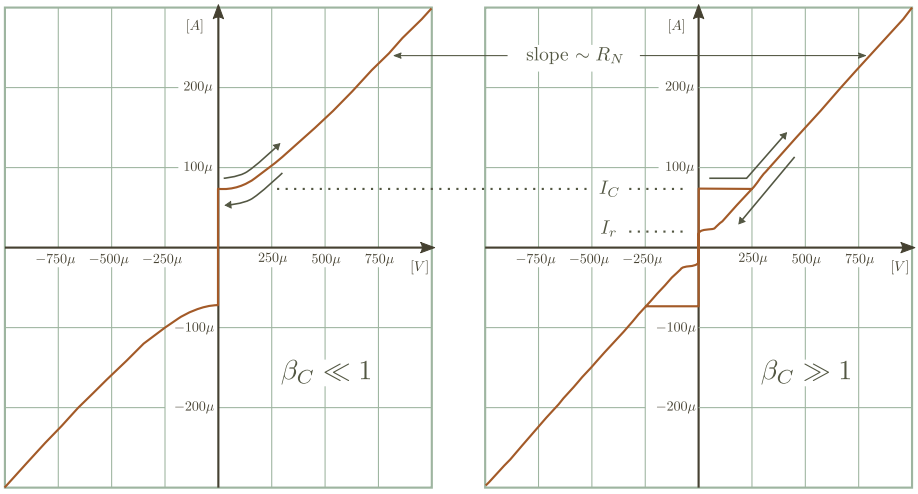

Figure 2.20. $I-V$ characteristics based on the results from a circuit simulation of two junctions with the same I_C ($72\mu A$) and R_N (3Ω) but different capacitances C. On the left plot, the capacitance $C \approx 0.1$pF and the McCumber parameter is $\beta_C \approx 0.2$, while at the right the capacitance is $C \approx 6.5$pF and $\beta_C \approx 12.5$. The junction with the large β_C exhibits a hysteretic $I-V$ curve: the voltage state begins at $I > I_C$ when the drive current rises, but the superconducting state is not reached back until the drive current becomes less than the return current $I_r < I_C$. Junctions with a $\beta_C \leqslant 1$ are not hysteretic.

The power dissipation and speed of many superconducting circuits depend on the parameters given in 2.71 since the Josephson junctions are the only active elements. In many applications, especially those where each single voltage oscillation from Figure 2.19 represents a data processing step, the characteristic voltage $I_C \cdot R_N$ is sought for to be maximized as it provides the highest transition speed (lowest τ_J). On one hand, $I_C \cdot R_N$ is limited by the maximum value of the resistive shunt R_N for which the junction is still non-hysteretic, $R_N \leqslant \sqrt{\frac{\Phi_0}{2\pi I_C C}}$. On the other hand, using a high I_C increases the dissipation in the junction. To see this, let's calculate the energy delivered per single oscillation (transition) to a junction with a constant current bias $I \approx I_C$:

$$\Delta E_T = \int_0^T I \cdot V \cdot \mathrm{d}t \approx I_C \cdot \int_0^T V \cdot \mathrm{d}t = \frac{\Phi_0 \cdot I_C}{2\pi} \cdot \int_0^{2\pi} \mathrm{d}\varphi = \Phi_0 \cdot I_C$$

Every cycle, this energy is dissipated at the resistor in the junction since the other two elements are conservative (non-dissipative). The energy delivered and dissipated at every cycle is thus directly proportional to I_C: one should avoid

excessively increasing the critical currents in a circuit in order to achieve a higher $I_C R_N$.

The value of ΔE_T is of the order of 10^{-19}J for a typical $I_C = 100\mu$A, indicating a much lower "energy per bit" for circuits using Josephson junctions than those utilizing semiconducting devices. For instance, a capacitor of 0.1pF holding a stable 1V state stores about 10^{-11}J of energy in a typical semiconducting IC. Superconducting circuits use just a fraction of the energy per bit used in conventional circuits.

On the other end of the spectrum, a low critical current reduces the energy required to transit between the states in a superconducting circuit, increasing the probability of noise-induced transitions and excessive error rates in digital circuits. Using ΔE_T as an energy scale of the states in the circuit and $k_B \cdot T$ as the typical noise energy at temperature T, preventing noise transitions then requires $\Delta E_T \gg k_B \cdot T$, which typically limits I_C to not less than $10\mu A$ at a 4K operation temperature, depending on the desired error rate. It has however been shown [33] that other factors, like for instance the clocking mechanism and specific circuit architecture, can introduce other types of errors in a digital device, thereby requiring even greater I_C. In practical circuits, for instance RSFQ, the values of the junction I_C's are about $100\mu A$ for a 4K operation temperature.

In SIS tunnel junctions, the $I_C \cdot R_N$ product is approximately equal to the "gap voltage" V_g, the potential difference between the electronic levels of the Cooper pairs and normal electrons [11] in the junction electrodes. This parameter strongly depends on the temperature and the material in question. V_g is usually on the order of mV for metallic superconducting materials, like for instance Nb where $V_g = 2.8$mV at liquid helium temperatures.

However, SIS junctions are usually hysteretic and an external shunt resistor is necessary to tune β_C close to unity. Typical values of $I_C R_N$ are then lower than V_g, ranging $0.3\text{mV} - 1\text{mV}$ for shunted SIS tunnel junctions of $\beta_C \approx 1$ in electronic applications [2], thus theoretically being capable of sub-picosecond transition times. Simple circuits using such junctions, for instance an RSFQ toggle flip-flop [34], can operate at frequencies in the order of 100s of GHz. In practice, larger systems are limited by signal integrity and local power dissipation issues (which are difficult to solve at cryogenic temperatures) to about 20-30GHz [35].

Other junctions technologies, like for instance the devices in the YBCO-Nb technology introduced later, have a metallic or otherwise highly conductive barrier, thereby already possessing a low intrinsic resistance. In these junctions, one can obtain a $\beta_C \leqslant 1$ without external shunts, simplifying the manufacturing process. It is however worth mentioning that, typically, non-SIS devices have significantly lower $I_C R_N$ products.

When $\beta_C \approx 1$ is achieved by using the optimal value for the shunt resistor, $R_N = \sqrt{\frac{\Phi_0}{2\pi I_C C}}$, the $I_C \cdot R_N$ product becomes

$$I_C \cdot R_N = \sqrt{\frac{\Phi_0 \cdot I_C}{2\pi \cdot C}} = \sqrt{\frac{\Phi_0 \cdot J_C}{2\pi \cdot C'}}$$

where C' is the capacitance per unit area of the junction. The critical current density increases exponentially with lower barrier thickness, while C' increases only linearly. Hence, the thinner the barrier - the higher the $I_C R_N$. Moreover, a junction process technology that provides thinner barriers will allow to implement the same circuit (same I_C) with a greater speed of operation while at the same time keeping the energy per operation ΔE_T the same. Conversely, if one keeps the same speed of operation, the energy can be decreased when using junctions with a thinner barrier. A second advantage of thin barriers is that the intrinsic normal tunneling resistance of the junction becomes lower, so that at a given thickness a junction may approach $\beta_C \approx 1$ without a shunt resistor.

As a rule of thumb and for all technologies, the more homogeneous a junction's barrier is, the thinner it can be manufactured without crystal defects and other sources of uncertainties. Most efforts in junction technology are thus directed towards tightly controlling the electrode/barrier growth process and obtaining clean, defect-free interfaces in order to achieve the most homogeneous material stack. The best junctions so far have shown to be the tunnel SIS devices with metallic electrodes and metal-oxide barriers, for example $Nb - Al_2O_3 - Nb$. Junctions with electrodes made of complex high-T_c materials require very thin barriers to obtain tunnel-like properties, in the order of just a few crystal lattice unit cells. This has shown to be virtually impossible to reliably achieve with heterogeneous barriers and only "intrinsic" devices, where the barrier is formed by purposefully damaging or otherwise manipulating the electrode crystal lattice on a short length scale locally, can produce high-quality high-T_c tunnel junctions.

In this subsection, the Josephson junction device was introduced as a length of superconductor interrupted by a non-superconducting thin barrier normal to the current direction. A junction has a periodic $I - \varphi_J$ constitutive law when the current through it is less than I_C, the critical current. An external field modulates the critical current according to a Fraunhofer pattern, creating circulating screening currents in the barrier and adjacent electrodes. The free energy of a Josephson junction also has a periodic relationship with φ_J. When the current through a junction $I > I_C$, a voltage appears across the electrodes and one must also take into account the capacitance and normal resistance across the barrier when building the junction's equivalent circuit model. In the following sections, after briefly completing the list of common superconducting circuit elements, example circuits containing junctions are given, as well as some basic logic cells using Josephson technology.

2.2.5.2 π-shift element

In all parts of the previous presentation, it was silently assumed that the properties of the superconducting material were isotropic. Although that is true for the majority of low-T_c superconductors, all high-T_c superconductors are anisotropic: their superconducting properties are direction-dependent. So, for example, an external magnetic field incident on a YBCO slab penetrates to a length that differs when the orientation of the crystal lattice of the material with respect to the field is changed. The penetration depth of YBCO is thus different along the three crystal axes of the material.

The macroscopic quantum model [14] takes the anisotropy of the superconducting material into account as a direction-dependent London coefficient: there is a different value of Λ for each of the vector components of the electromagnetic quantities. In other words, the two London equations are modified

$$\begin{aligned} \boldsymbol{E} &= \frac{\partial}{\partial t}(\bar{\Lambda}\,\boldsymbol{J}_S) \\ \nabla \times (\bar{\Lambda}\,\boldsymbol{J}_S) &= -\boldsymbol{B} \end{aligned} \tag{2.72}$$

where the scalar London coefficient Λ was replaced with the tensor

$$\bar{\Lambda} = \begin{pmatrix} \Lambda_a & 0 & 0 \\ 0 & \Lambda_b & 0 \\ 0 & 0 & \Lambda_c \end{pmatrix} \tag{2.73}$$

The London tensor has the diagonal form of 2.73 only when the (a, b, c) crystal axes of the superconducting material coincide with the (x, y, z) coordinates of the the electromagnetic quantities. In this thesis, such an alignment of the material principal axes with the coordinate system used to describe the superconducting structures will be assumed to always hold.

In YBCO, whose crystal structure is depicted in Figure 3.1 of Chapter 3, the values of Λ_a and Λ_b are approximately equal, while the value of Λ_c is much larger than the two. Typically, at 70K, the penetration depth of crystalline thin YBCO films in the a/b direction $\lambda_{a/b} = \sqrt{\frac{\Lambda_{a/b}}{\mu_0}}$ is in the order of $\sim$150nm while in the c direction it is about ten times larger. The exact values of the penetration depths differ for YBCO films and are especially sensitive to the oxygen content per unit cell but nevertheless, the large anisotropy between the a/b and c directions remains across all the various types of YBCO films.

It is thus convenient to regard the YBCO material as a planar a/b-isotropic superconductor (or stacked 2D sheets) where the current transport is predominantly in the a/b directions. In all further analysis, the thin-film YBCO segments used to build superconducting circuits will be assumed to be isotropic, $\lambda_L = \lambda_a = \lambda_b$, with the caution that the supercurrent must be flowing in the $a-b$ plane of the material. The presentation from the previous sections thus remains valid as long as the YBCO segments are oriented such that the current is parallel to the $a-b$ plane.

The origin of the anisotropy in high-T_c materials lies in the microscopic mechanism that is responsible for the existence of a superconducting phase at temperatures $T < T_c$. Although the exact nature of this mechanism is not yet known, it is well accepted that the amplitude of the order parameter $|\Psi|$ is not rotationally symmetric (isotropic) in the $a-b$ plane of the material, but changes as the direction of observation changes. The direction-dependent amplitude of Ψ then translates in anisotropic superconducting properties of the material. The shape of the dependence is believed in YBCO to follow a $d_{x^2-y^2}$ orbital structure (a planar cloverleaf), also called a *d-wave order parameter symmetry*.

Of very great importance is the fact that in a d-wave superconductor, not only the amplitude but also the phase of Ψ changes as a function of the direction. Namely, whenever the direction is changed by 90°, the phase of the superconducting order parameter must be changed by $\pm\pi$ as well. Hence, whenever the direction of current propagation inside a superconducting segment is orthogonally altered, the superconducting phase θ experiences a jump of $\pm\pi$.

More details about the symmetry of the order parameter in high-T_c materials, as well as various experimental methods to determine the same can be found in [36], [21] and the references therein.

The above 'π-phase-shift' phenomenon in high-T_c materials can be formally treated in the same way as the $2\pi n$ phase jumps along a closed superconducting path, discussed previously in Section 2.2.4.5. There, it was determined that in order to account for the multi-valuedness of the superconducting phase, every unique closed path in a circuit receives a cross-sectional $2\pi n$ jump surface in an arbitrary segment along the path. In the network representation of the circuit, this method was equivalent to adding a series flux angle source of amplitude $2\pi n$ at an arbitrary position along every unique circuit loop. Similarly, cross-sectional $\pm\pi$ jump surfaces can be defined every time the geometry of a YBCO segment is such that the current must make a 90° turn in direction. Equivalently, in the network schematic, a flux angle source of $\pm\pi$ is added in series with the YBCO segment. The segment is further treated as if it was made of an isotropic material.

In Figure 2.21, an example of adding a π-shift source is given. The constitutive law of a π-shift element is

$$\varphi = \pm\pi$$

where the sign must be carried in all network equations as undetermined. Fortunately however, the network equations for almost all circuits are invariant to the sign of the π-shift source.

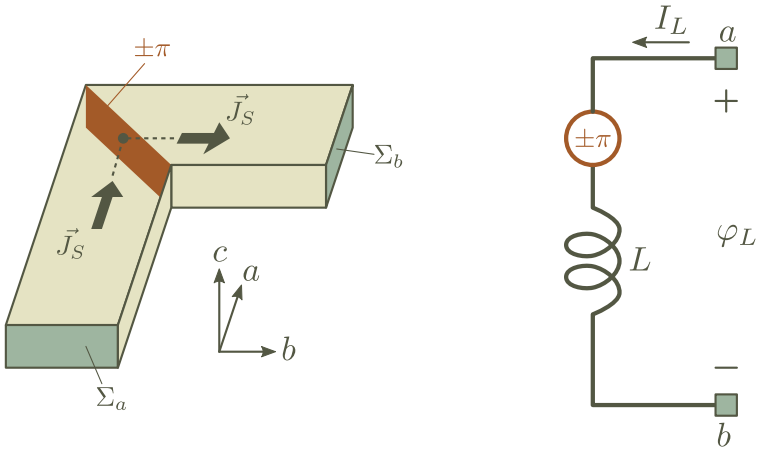

Figure 2.21. A YBCO segment with a right-angle corner and its equivalent circuit schematic. The inductance of the segment L is the same as if the material was isotropic while the π-shift source models the d-wave order parameter symmetry. Using the constitutive law of the π-shift element, the circuit equation of the segment will be written as $\varphi_L = \frac{2\pi}{\Phi_0} L\, I_L \pm \pi$.

Note that if the YBCO segment makes an even number of 90° turns, the total flux angle added in series will be of an amplitude equal to an even amount of $\pm\pi$. Since it will be always possible to place this source in series with the $2\pi n$ quantization source of the loop to which the segment belongs to, the integer n will absorb all even number of π-shifts in the YBCO segment. There will be thus no need to add separate $\pm\pi$ flux sources for each of the 90° turns if there is an even number of them. Conversely, if there is an odd number of orthogonal corners in the YBCO segment, just one $\pm\pi$ source will suffice. It is important to stress that a 90° turn in a segment of isotropic material, like Nb for instance, is not associated with such π-shifts.

The new element, the π-shift source, is a phenomenon local to a YBCO segment (a 90° turn), unlike the $2\pi n$ quantization source that is a property of a circuit loop and not of any particular segment in that loop or, indeed, the material of the segments. The physical localization of the π-shift element in a circuit leads to some interesting consequences. For instance, hybrid YBCO/Nb structures that are geometrically symmetrical across a given axis still have asymmetry in the (φ, I) network representation due to the presence of a π-shift in one of the symmetrical arms. More details are given in the discussion around Figure 5.5 from Chapter 5.

Note that there is no free energy term associated with the presence of π-shift element in a circuit. However, the network equations are different compared to a case where the π-shift element is removed.

Besides using d-wave superconducting segments, a π-shift source can also be implemented by a number of other methods, see for instance Section 5.1 or [37]. In any case, all π-shift structures are interpreted in the network equivalent of the system as a series flux angle source of amplitude $\pm\pi$.

2.2.5.3 Current source

This element is the same as the classical current source in (V, I) networks, except that an expression for the free energy should be attached to the constitutive law

$$I = I_B$$

where I_B is the current of the source. The free energy of a current source can be obtained by calculating the energy stored in the element

$$E_G = -\int_0^t U I \, \mathrm{d}\tau = -I_B \cdot \int_0^t \frac{\Phi_0}{2\pi} \cdot \frac{\partial \varphi}{\partial \tau} \cdot \mathrm{d}\tau = -\frac{\Phi_0 I_B}{2\pi} \cdot (\varphi - \varphi_0) = -\frac{\Phi_0 I_B}{2\pi} \cdot \varphi + \text{const.}$$

as the flux angle across its terminals is changed from $\varphi_0 = \varphi(0)$ to some $\varphi = \varphi(t)$. The constant term can be neglected and the free energy of the current source is then $-\frac{\Phi_0}{2\pi} I_B \varphi$.

The minus sign in front of the expression is a consequence of the choice for reference directions of the flux angle and the current for this element, see Figure 2.22. Namely, the power delivered to any electrical element is always equal to the product $U \cdot I$ across its terminals, but only if the reference directions of U and I are such that the current *enters* the positive voltage terminal. If, on the other hand, the reference directions are such that the current *exists* the positive node, then the delivered power is $-U \cdot I$. The latter is the case in Figure 2.22 and one thus obtains the above result.

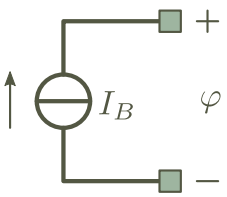

Figure 2.22. The symbol of a current source. Note that the reference directions for the current and the flux angle are opposite than for the other elements (ex. Figure 2.21 or Figure 2.19).

A realistic current source also has an internal impedance that in electrical networks is represented as a shunt across its terminals. Since these are typically in the kΩs range, they be safely neglected as they are always in parallel with the very small impedance of the superconducting elements comprising the rest of the circuit across the current source terminals.

2.2.5.4 Transformer (pair of coupled segments)

It is very often that the magnetic coupling between the segments in a superconducting circuit is kept very small on purpose so as not to complicate the circuit design. If however magnetic coupling is desired in a circuit, then usually it is allowed for only pairs of segments. Two segments, magnetically isolated from the rest of the circuit but not from each other constitute a transformer element. The circuit symbol together with a conceptual drawing of a transformer are given in Figure 2.23.

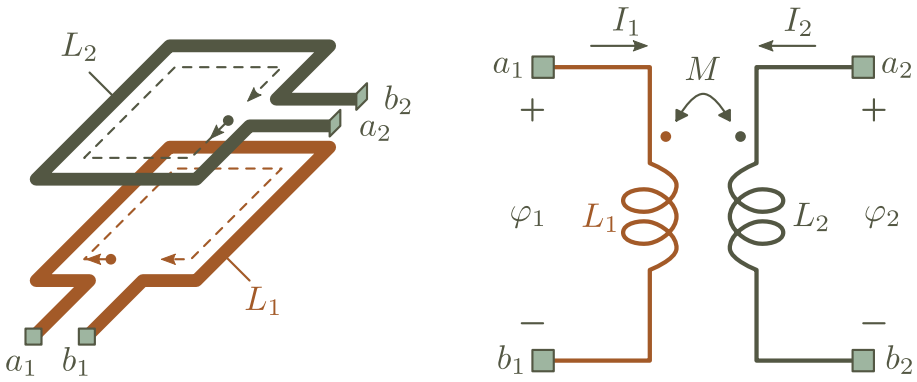

Figure 2.23. Two loop-shaped inductively coupled segments (left) and the circuit symbol of a transformer (right), together with the reference directions of the nodal and flow variables relative to the 'coupling dots'.

The constitutive circuit equations for a transformer in the superconducting network model are

$$\begin{cases} \varphi_1 = \dfrac{2\pi}{\Phi_0}\,(L_1\, I_1 + M\, I_2) \\ \varphi_2 = \dfrac{2\pi}{\Phi_0}\,(M\, I_1 + L_2\, I_2) \end{cases}$$

where $M = L_{12}$ is the mutual coupling inductance between the segments, while L_1 and L_2 are the self-inductances of the two segments.

A convention for the reference directions in a transformer is necessary when the symbol from Figure 2.23 is used: all the parameters L_1, L_2 and M have a positive value if the reference currents of the two segments are such that they both 'enter' the dots and the flux angles are defined with their positive terminal on a dot. As any network analysis is far more practical when all the inductive parameters are positive, the reference directions of the flux angles and the currents given above should be always followed.

Before the circuit symbol is drawn however, the physical structure that implements the transformer must be investigated in order to find the positions of the two dots on the terminals. As it was already established, the mutual coupling inductance between segments is positive if the current directions are predominantly in the same direction. Hence, given a transformer structure, it is enough to fix one of the currents and then choose the other one so that it flows in roughly the same direction. The dots are subsequently placed at the terminals where the two currents enter. An example is given in Figure 2.23 above.

The mutual coupling was previously understood to create a "vector potential drop" along the normalized current direction in a given segment, the source of this vector potential found in a current flowing in a different, remote, segment. Another very often used representation of 2-segment inductive coupling is via the "flux lines per unit current" frame. There, the mutual coupling is viewed as due to the flux lines created by a unit current flowing in one segment that are intersecting a second segment and vice-versa. It is here easy to imagine that the mutual inductance M is proportional to the self-inductances L_1 and L_2, i.e. the number of flux lines created by the first and intercepted by the second segment scale with both the source (first) and the receiver (second) geometries. Further, due to the geometric nature of the partial inductances, scaling the segment geometries will scale both the self and mutual inductance by the same factor. Hence, $M \sim \sqrt{L_1 L_2}$. Note that when the system is viewed from this perspective, it is evident that the segments can never be positioned such that all flux lines created by the segment with self-inductance L_1 will intersect the segment of self-inductance L_2, and vice-versa. The result is then

$$M = \kappa \cdot \sqrt{L_1 \cdot L_2}$$

where $0 < \kappa < 1$ is called the transformer coupling coefficient. At $\kappa = 1$, ideal coupling is achieved, meaning that the two segments share all lines of flux between them.

Due to the fact that the self-inductance of a superconducting segment has a significant kinetic inductance component, especially when it is a thin-film, the coupling factor can not be even close to unity (kinetic inductance does not take part in magnetic coupling). Typically, $\kappa < 0.7$ in large superconducting structures [38] while for the small devices found in this thesis (Chapter 5) the coupling coefficient is between 0.4 and 0.6.

2.2.6 Network analysis and circuit examples

In this section, a procedure is presented that allows one to calculate and analyse the Gibbs free energy of a superconducting circuit based only on its network representation. The analysis yields the network equations and also guides the creation of potential landscape diagrams, thus allowing one to investigate the behaviour of a given circuit in the static (DC) regime, as well as give a qualitative understanding of the transient (time-dependent) processes. At the end, such an analysis of a couple of simple example circuits is given, followed by a brief introduction to basic digital devices such as RSFQ cells.

2.2.6.1 Potential landscapes by a network analysis

The (Gibb's) free energy E_G for any superconducting circuit can be obtained from its equivalent schematic by following the procedure described below. The method is applicable for a network that has only 5 types of elements: inductors, transformers (coupled inductors), current sources, junctions and a π shift element. Resistors and capacitors are allowed to be present (typically across junctions) but do not influence the free energy. Rather, they take part in the (classical) equations of motion. Voltage sources must be replaced with their current source equivalent by a Norton transformation. Ideal voltage sources are not allowed. Also, all elements in series with a current source must be deleted.

It is necessary to draw the network schematic of the superconducting circuit beforehand. The analysis presented here is performed in the (φ, I) space where the branch variables are the currents I and the nodal variables are the flux angles (phases) φ. In Section 2.2.4, it was shown that the network's branch-node architecture is exactly the same with the classical (U, I) network representation of the same circuit, except for the existence of $2\pi n_k$ quantization sources in each unique loop of the circuit and eventually π-shift sources where necessary.

When a $2\pi n_k$ quantization source appears in series with a Josephson junction, it can be deleted as long as the flux angle across the junction is allowed to range between $(-\infty, \infty)$ instead of the basis interval $\left(-\frac{\pi}{2}, \frac{\pi}{2}\right)$. This follows from the fact that the junction can "absorb" the quantization source while keeping both the nodal and flow variables of the series junction-source subcircuit the same. In other words, the circuits with and without the quantization source are equivalent when the last appears in series with a junction.

The procedure for obtaining the Gibb's free energy of the circuit consists of a number of steps. These are summarized below.

Step 1 (flux quantization sources, externally applied flux):

- Follow a closed loop in the circuit and add a $2\pi n_k$ phase source in an arbitrary position along the loop's path if there is no such source already encountered while circling around the path. Iterate the above for each possible circular path in the circuit.

- Try to shift the $2\pi n_k$ sources through the nodes of the circuit in such a way as to place them in series with a junction (when shifting a source through a node, reproduce the source with the same direction and magnitude in each branch connected to the node, except in the originating branch of course). Delete those quantization sources that come in series with a junction. Also delete the quantization sources that end up in series with a current source. Note that the same source can, from multiple shifting steps through nodes, come to sit in the same branch with an opposite sign: cancel these sources. If, during the shifting procedure, two *different* quantization sources appear in the same branch, they can be replaced by a single quantization source.

- The quantization sources that can not be positioned in series with a junction will now always remain in the circuit in series with a (coupled) inductor element. The integer n_k of these sources then becomes a new degree of freedom in the circuit.

- π-shift sources seem to always appear in series with junctions, if also the parasitic ones are included

- An externally applied flux Φ_{ext} in a loop is accounted for in the circuit's schematic by flux angle sources $\varphi_{e,x}$ in series with the inductors comprising that loop. Each inductor receives one such source. The sum of these phase sources in the loop is $\Phi_{\text{ext}} \cdot \frac{2\pi}{\Phi_0}$ while their relative amplitudes are proportional to the relative value of the inductors in the loop. For example, if the left inductor in a divided loop is twice as big as the right inductor, $\varphi_{e,L} = 2 \cdot \varphi_{e,R}$ as well.

Step 2 (node numbering and initial expression for E_G):

- Number each node and assign it a nodal variable φ_j

- Write the free energy of each element in the circuit as a function of the difference in the nodal variables across its terminals. Use Figure 2.24 as a template.

- Treat each junction in series with a π-shift element as a single (composite) device, see Figure 2.24. The flux angle across the device thus *includes* the π-shift.

- The $2\pi n_k$ quantization sources that remained after "Step 1" must appear in series with a (coupled) inductor. Write the energy of the (coupled) inductor as a function of the flux angle across the series combination of the source

and inductor elements, as shown in Figure 2.24. The same holds for an externally applied flux source $\varphi_{e,x}$ in series with the inductor.

- Sum the free energy contributions from all elements in order to obtain an initial expression for E_G.

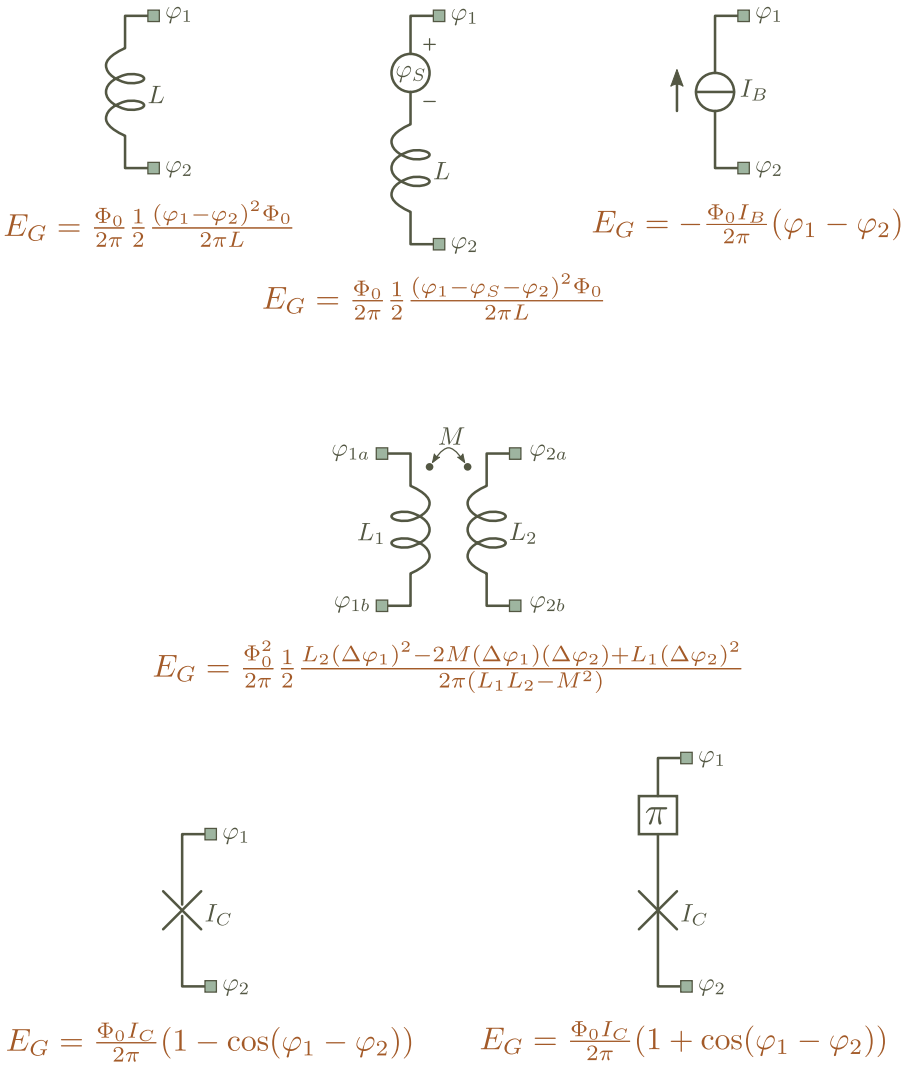

Figure 2.24. A template for the free energy of the elements in a superconducting circuit

Step 3 (simplification and analysis of the potential landscape):

- Try to rewrite the free energy as a function of only the flux angles across the junctions (or across loose R's and C's) and the external sources. This will always be possible by simple algebraic operations, unless there are nodes to which only (coupled) inductors and current sources are attached to. In this latter case, continue the procedure with the next substep below. If the free energy can be written exclusively as a function of the flux angles across junctions (or loose R's and C's) and across external sources, skip the next substep.

- Write $\frac{\partial E_G}{\partial \varphi_i} = 0$, where φ_i is the flux angle of any node except the ones to which only junctions (or only loose resistors/capacitors) are attached to. Obtain an expression for φ_i from $\frac{\partial E_G}{\partial \varphi_i} = 0$ and then replace the result back in the expression for E_G.

- Repeat the above until E_G is a function of the flux angles across junctions (or across loose R's and C's) or external sources. The former variables are the independent degrees of freedom in the circuit - the expression for E_G obtained at this moment is the sought after potential landscape.

- Writing $\frac{\partial E_G}{\partial(\Delta\varphi_{\text{junction}})} = 0$ will yield the Kirchhoff law of current conservation (sans the R_J and C_J contributions) for one of the nodes across which the junction having a flux angle $\Delta\varphi_{\text{junction}}$ is connected. The same expression also marks an extremum (max, min, saddle point) in E_G as a function of $\Delta\varphi_{\text{junction}}$.

- Identifying a maximum, a minimum or a saddle point in the potential landscape is done using the inequalities of a second partial derivative test on E_G.

- Unstable points, where a potential minimum becomes a saddle point or a maximum, mark the onset of either a continuous voltage state or the trigger moment of a single transition between stable states. Such points can be identified from the second partial derivative inequalities by solving them with an "=" sign. This is useful for obtaining threshold curves of SQUIDs and similar structures.

- The expression for E_G should also contain terms where the flux angle $\Delta\varphi_{\text{ter}}$ across the circuit's input and/or output terminals appears. When another superconducting circuit is attached to those terminals, the free energies are

summed and the phase difference across the common terminal is eliminated by seeking $\frac{\partial(\Sigma E_G)}{\partial(\Delta\varphi_{ter})} = 0$.

- The classical equations of motion are a set of of partial differential equations

$$\frac{\partial E_G}{\partial(\Delta\varphi_J)} + \frac{\Phi_0 \cdot C_J}{2\pi} \cdot \frac{\partial^2(\Delta\varphi_J)}{\partial t^2} + \frac{\Phi_0}{2\pi \cdot R} \cdot \frac{\partial(\Delta\varphi_J)}{\partial t} = 0$$

written for each phase difference $\Delta\varphi_J$ across a junction with capacitance C_J and resistance R_J. One such equation is added for the phase difference across each loose resistor and one for the phase difference across each loose capacitor, of course respectively leaving out the term for the capacitor and resistor from the equation above.

2.2.6.2 Example of an E_G analysis

The procedure for obtaining the E_G of a superconducting circuit is illustrated with a common example. Two superconducting loops, each interrupted by two junctions, are given below in Figure 2.25. The loops are identical except for the presence of a π-shift element in one of them.

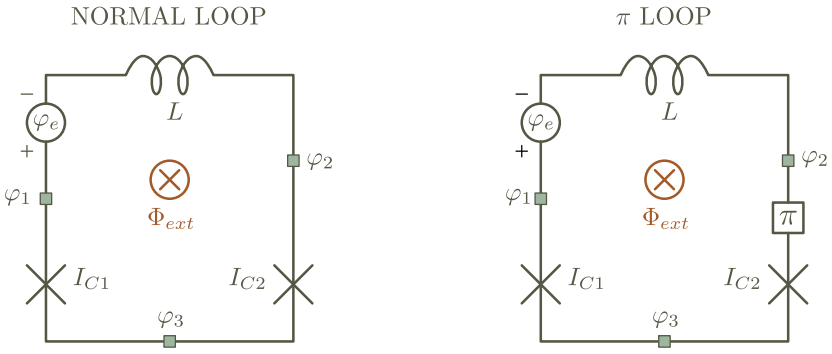

Figure 2.25. The schematic drawing of the two loops

The critical currents of the two junctions are

$$I_{C1} = (1 - \alpha) \cdot I_C$$

$$I_{C2} = (1 + \alpha) \cdot I_C$$

where $-1 < \alpha < 1$ is the junction asymmetry parameter and I_C is the average critical current of the junctions. One more parameter that is important in the analysis is the normalized loop inductance:

$$\beta_L = \frac{2\pi \cdot L \cdot I_C}{\Phi_o}$$

The flux angles across the two junctions are

$$\Delta\varphi_{J1} = \varphi_1 - \varphi_3$$

$$\Delta\varphi_{J2} = \varphi_2 - \varphi_3$$

hence including the π-shift for the π-loop's second junction as previously suggested. These two variables will be the degrees of freedom in the circuit. The externally applied flux Φ_{ext} is creating an equivalent flux angle source $\varphi_e = 2\pi \cdot \frac{\Phi_{\text{ext}}}{\Phi_0}$ in series with the inductor L. The flux angle across the inductor is then equal to $\varphi_1 - \varphi_2 - \varphi_e$.

There is one $2\pi \cdot n$ quantization source in each loop, inserted in an arbitrary position. Since they can be immediately placed to stand in series with a junction, the quantization sources are deleted.

Lets write the free energy for the normal loop $E_{G,N}$ and for the π-loop $E_{G,\pi}$ (consult Figure 2.24):

$$E_{G,N} = \frac{\Phi_0 \cdot I_C}{2\pi} \cdot \left(\frac{1}{2} \cdot \frac{\Phi_0}{2\pi\, L\, I_C} \cdot (\varphi_1 - \varphi_2 - \varphi_e)^2 - (1-\alpha) \cdot \cos(\varphi_1 - \varphi_3) - (1+\alpha) \cdot \cos(\varphi_2 - \varphi_3) \right)$$

$$E_{G,\pi} = \frac{\Phi_0 \cdot I_C}{2\pi} \cdot \left(\frac{1}{2} \cdot \frac{\Phi_0}{2\pi\, L\, I_C} \cdot (\varphi_1 - \varphi_2 - \varphi_e)^2 - (1-\alpha) \cdot \cos(\varphi_1 - \varphi_3) + (1+\alpha) \cdot \cos(\varphi_2 - \varphi_3) \right)$$

where the constant terms were removed. Following the procedure outlined before, in Step 3, the free energy should now be optimized w.r.t. φ_1 and φ_2 (not w.r.t. the node φ_3 since only junctions are attached to it). However, this substep is not necessary. The free energies can, for these simple circuits, be immediately written exclusively as a function of the flux angles across the junctions, $\Delta\varphi_{J1}$ and $\Delta\varphi_{J2}$, as well as the external source φ_e:

$$\frac{E_{G,N}}{\frac{\Phi_0 \cdot I_C}{2\pi}} = \frac{(\Delta\varphi_{J1} - \Delta\varphi_{J2} - \varphi_e)^2}{2\,\beta_L} - (1-\alpha) \cdot \cos(\Delta\varphi_{J1}) - (1+\alpha) \cdot \cos(\Delta\varphi_{J2})$$

$$\frac{E_{G,\pi}}{\frac{\Phi_0 \cdot I_C}{2\pi}} = \frac{(\Delta\varphi_{J1} - \Delta\varphi_{J2} - \varphi_e)^2}{2\,\beta_L} - (1-\alpha) \cdot \cos(\Delta\varphi_{J1}) + (1+\alpha) \cdot \cos(\Delta\varphi_{J2})$$

Minimizing the free energy with respect to either $\Delta\varphi_{J1}$ or $\Delta\varphi_{J2}$ will yield the current conservation law for the node φ_1 or φ_2. For example, making $\frac{\partial E_{G,N}}{\partial(\Delta\varphi_{J1})}=0$, the following is obtained

$$\frac{\Delta\varphi_{J1}-\Delta\varphi_{J2}-\varphi_e}{\beta_L}=-(1-\alpha)\cdot\sin\left(\Delta\varphi_{J1}\right)$$

which, taking into account that the currents through the left junction and the inductor are given by

$$I_{J1}=I_C\cdot(1-\alpha)\sin\left(\Delta\varphi_{J1}\right)$$

$$I_L=\frac{1}{L}\cdot\frac{\Phi_0}{2\pi}\cdot(\varphi_1-\varphi_2-\varphi_e)=\frac{1}{L}\cdot\frac{\Phi_0}{2\pi}\cdot(\Delta\varphi_{J1}-\Delta\varphi_{J2}-\varphi_e)$$

results in $I_L=-I_{J1}$, the current conservation law for the node marked by φ_1 if the currents across the junction's resistance and capacitance are neglected (in a static case thus).

The free energies can be re-written by the variable change

$$x=\frac{\Delta\varphi_{J1}-\Delta\varphi_{J2}}{2}\quad y=\frac{\Delta\varphi_{J1}+\Delta\varphi_{J2}}{2}$$

resulting in the following simple expressions:

$$\begin{aligned}\frac{E_{G,N}}{\frac{\Phi_0\cdot I_C}{2\pi}}&=\frac{(2\,x-\varphi_e)^2}{2\,\beta_L}-2\cos\left(x\right)\cos\left(y\right)-2\,\alpha\sin\left(x\right)\sin\left(y\right)\\ \frac{E_{G,\pi}}{\frac{\Phi_0\cdot I_C}{2\pi}}&=\frac{(2\,x-\varphi_e)^2}{2\,\beta_L}+2\sin\left(x\right)\sin\left(y\right)+2\,\alpha\cos\left(x\right)\cos\left(y\right)\end{aligned}\tag{2.74}$$

The free energies for both loops have a parabolic component along the x direction, given by the first term, and an $x-y$ symmetric periodic component given by the two other terms.

In the following pages, a number of contour plots are given, for different values of the parameter β_L, the external flux source φ_e and asymmetry coefficient α.

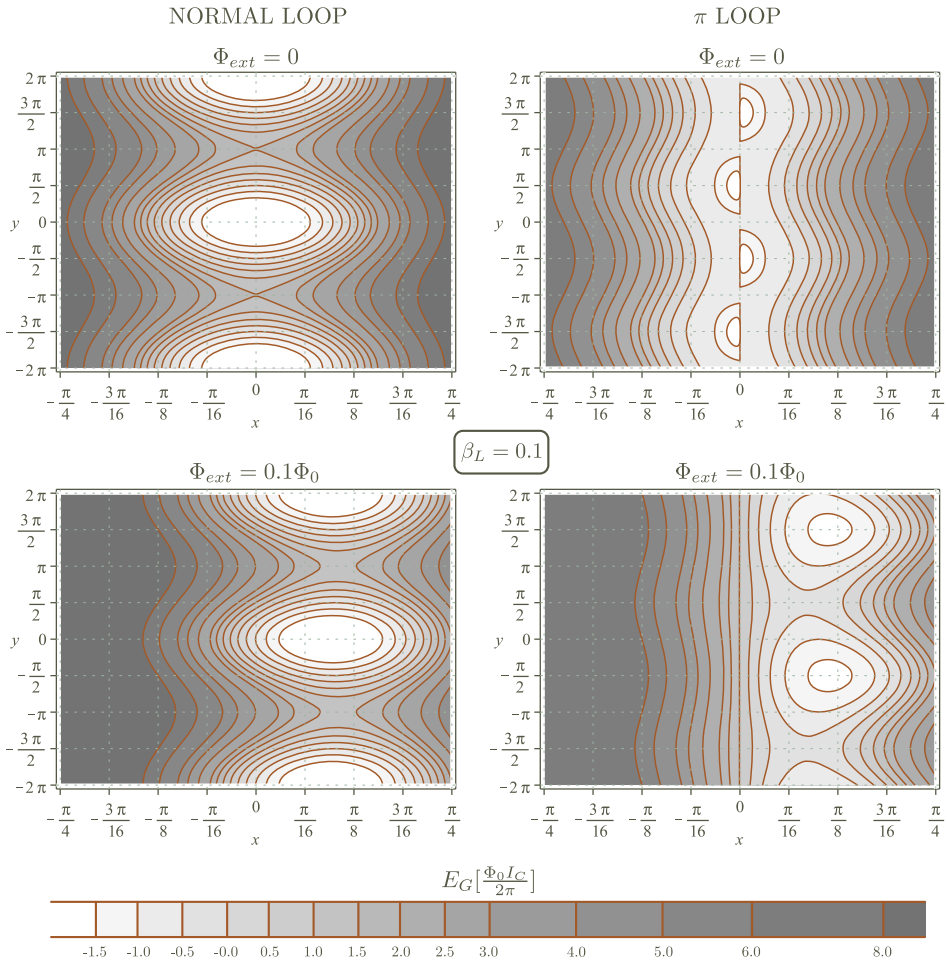

Figure 2.26. Potential landscapes at $\beta_L = 0.1$ and $\alpha = 0$.

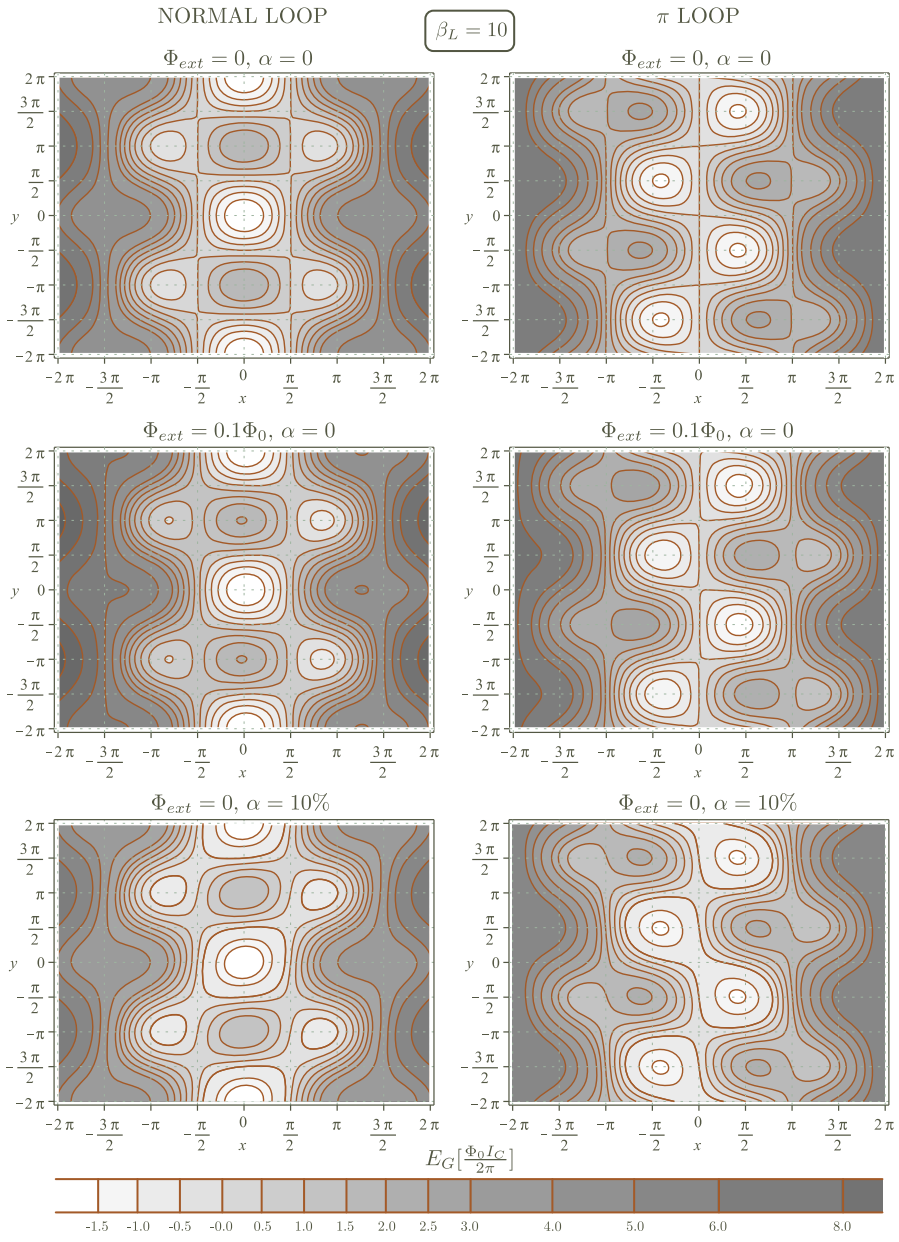

Figure 2.27. Potential landscapes at $\beta_L = 10$.

The potential landscapes of the Gibb's energy for the two loops from equations 2.74 posses a few interesting characteristics.

First, from Figure 2.26, it is concluded that for very small β_L's, when either I_C or L are small (or both), the parabolic component in the potential landscapes of both loops is dominant. The lower the β_L is, the less "room" there is along the x direction for the motion of the circuit in an excited state. In other words, during a transient state, the amplitude of the oscillations in the y direction will be dominant while motion around x will be very small. This implies that the two junctions will change their phases in approximately the same way across time since x, proportional to their difference, is restricted in amplitude.

In the case of small β_L, zero asymmetry and no external flux, in the normal loop all the potential minima are at $x=0$, manifesting physically as a *single* stable state of 0 total flux ($\Phi_{\text{tot}} = \frac{\varphi_1 - \varphi_2}{2\pi}\,\Phi_0 = \frac{x}{\pi}\,\Phi_0$). The π-loop on the other hand has *two*, symmetrically opposite, stable states of small x (small flux). To find the last, one can substitute $\sin(x) \approx x$ in the system 2.74 and, after looking for a 2D potential minimum, obtain the stable points $x \approx \pm\frac{\beta_L}{2}$, $y = \frac{2n+1}{2}\,\pi$. This, on the other hand, gives a flux of $\Phi_{\text{tot}} = \frac{x}{\pi}\,\Phi_0 \approx \pm L\,I_C$ in the π-loop for the two stable states. Were one to build a device with these two loops in the small β_L limit, a π-loop is a better choice as it has a more complex structure in its potential landscape, allowing a bistable mode of operation. In comparison, the normal loop is completely symmetrical in all respects and cant discriminate externally supplied information as it always ends up at the same state.

When $\beta_L = 0$, for instance if we take a very small loop of $L \approx 0$, then the motion across the x coordinate will not be allowed at all: x is fixed at $\frac{\varphi_e}{2}$. Then, $\varphi_e = 2x = \Delta\varphi_{J1} - \Delta\varphi_{J2}$ and the potential landscapes become 1D:

$$\begin{aligned}
\frac{E_{G,N}}{\frac{\Phi_0 \cdot I_C}{2\pi}} &= -2\cos\left(\frac{\varphi_e}{2}\right)\cos(y) - 2\,\alpha\sin\left(\frac{\varphi_e}{2}\right)\sin(y) \\
\frac{E_{G,\pi}}{\frac{\Phi_0 \cdot I_C}{2\pi}} &= 2\sin\left(\frac{\varphi_e}{2}\right)\sin(y) + 2\,\alpha\cos\left(\frac{\varphi_e}{2}\right)\cos(y)
\end{aligned} \tag{2.75}$$

Note that, in the case of $\beta_L \approx 0$ and $\alpha = 0$, the loop can be treated as a composite junction of critical current $2\,I_C\cos\left(\pi\,\frac{\Phi_{\text{ext}}}{\Phi_0}\right)$ for the normal and $2\,I_C\sin\left(\pi\,\frac{\Phi_{\text{ext}}}{\Phi_0}\right)$ for the π-shift loop. This is very convenient as a basic superconducting device since it offers a junction-like element of controllable critical current that can be incorporated in a larger structure. So, for example, in the classical flux qubit that uses three junctions, one of the junctions is usually replaced by an externally modulated normal loop of small L: this effectively offers a way to tune the barrier between the two persistent-current states of the qubit. A small modulated π-loop on the other hand can be used to drive an inductive load and perform the logical operation of static state inversion since the $\sin()$ is an odd function of its argument. In Chapter 5, circuits based on such small modulated π-loops are proposed.

A second observation is connected to the effect opposite from the one above: large β_L's. Since the parabolic component will then be less sharp, the features of the trigonometric functions - multiple peaks and valleys - will be more visible. So, for $\beta_L = 10$ in Figure 2.27, one can see that the normal loop exhibits secondary stable states at $x \approx \pm\pi$ in its potential landscape. These correspond to $\pm\Phi_0$ total flux in the loop and are hence called single-flux-quantum (SFQ) states. It can be shown that the SFQ states appear when $\beta_L > 2$. The normal loop however remains dominated by the $\Phi_{\text{tot}} \approx 0$ state for any β_L. Only if a large external bias Φ_{ext} is applied to the normal loop, Figure 2.27 indicates that the zero-flux and SFQ states could have potential minima of similar level - the two states are then symmetrised. This situation is important for RSFQ devices, as shown in the next subsection.

The π-loop on the other hand shows a symmetric two-state structure manifesting as a half-flux quantum ($\frac{\Phi_0}{2}$) through the loop in either direction. The symmetry persists both for small and large values of the externally applied flux. Imagining for a moment that the external flux is an unwanted external influence, like for instance a stray field, the information processing capability of the π-loop will not be affected very much by such disturbances. A similar conclusion can be made when the disturbance is in the junction inequality, i.e. when $\alpha \neq 0$. The π-loop is thus more robust than a normal loop when it serves as an information processing/memory unit.

The total flux in the loop is proportional to $\varphi_1 - \varphi_2$, which is equal to $2\,x$, and the coordinate x is thus the only one with a physical (measurable) manifestation. This is important to take into account when building devices, as the only quantity that is available for either measuring or coupling to other devices is proportional to the degree of freedom represented by x. Only if the loops are asymmetrical, for instance by adding other components or connecting other branches, does the other free variable, y, become available for processing.

2.2.6.3 RSFQ devices

The Rapid Single Flux Quantum devices [2] belong to a digital family of circuits where the computation is, in effect, implemented with conditional transitions between the stable states in the circuit's potential landscape. The conditionality is of a "if-then-else" type where a state transition will be performed only if the correct sequence of input signals is found. This conditional state transition mechanism is then used as a basic block for building more complex logic functions.

The most basic RSFQ cell, a sequential storage (memory) unit, is very similar to the normal loop from Figure 2.25 with a large β_L. The difference is that, instead of an external applied flux, the basic RSFQ cell uses a current source to bias the potential diagram by adding an E_G component linearly proportional to one of the state variables (see the E_G of a current source in Figure 2.24). The result is that the zero-flux and SFQ states in the potential landscape are symmetrised. In Figure 2.28, both the circuit schematic and the potential landscape of an RSFQ storage loop is shown.

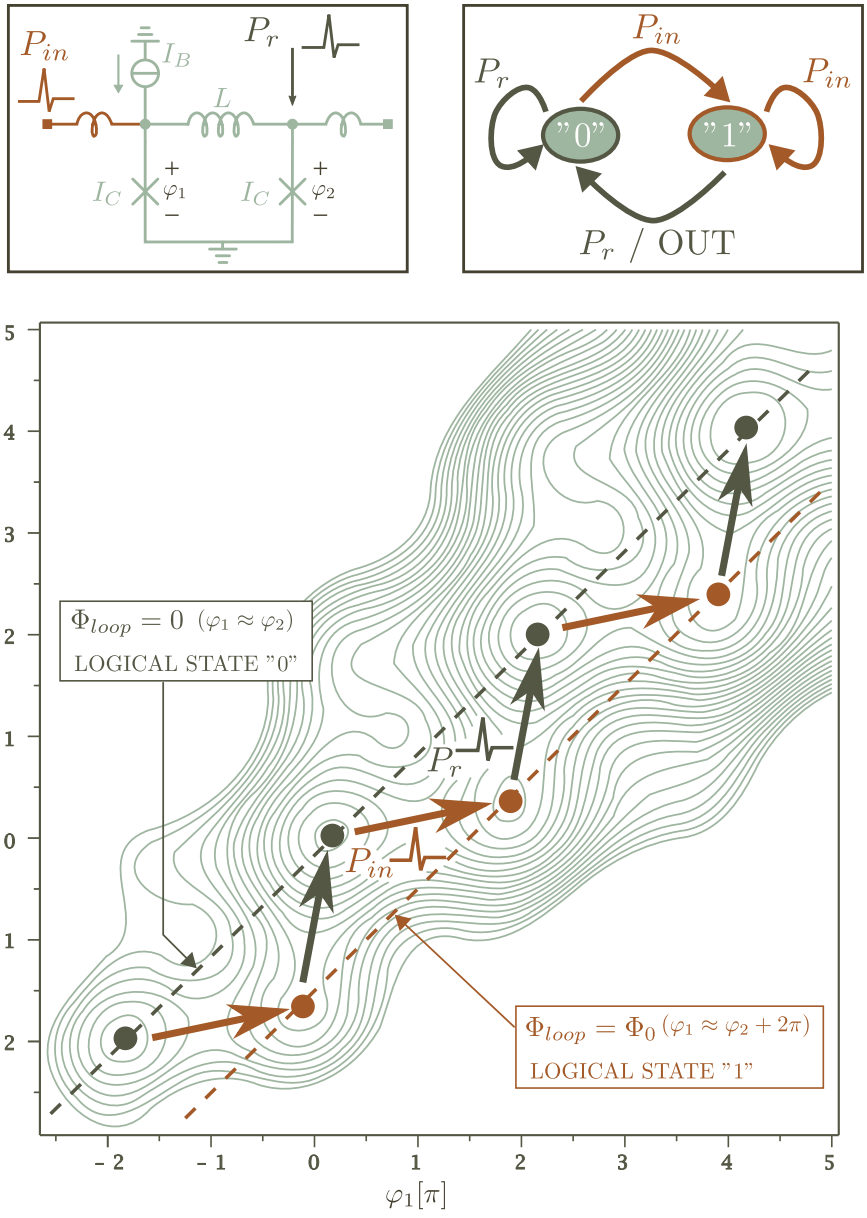

Figure 2.28. The circuit schematic, the state diagram and the potential landscape of a conventional RSFQ storage element. Above, $\beta_L = 5.5$ and $I_B = 0.75\, I_C$. The junctions are symmetric. The most likely trajectory between the stable states is indicated with arrows.

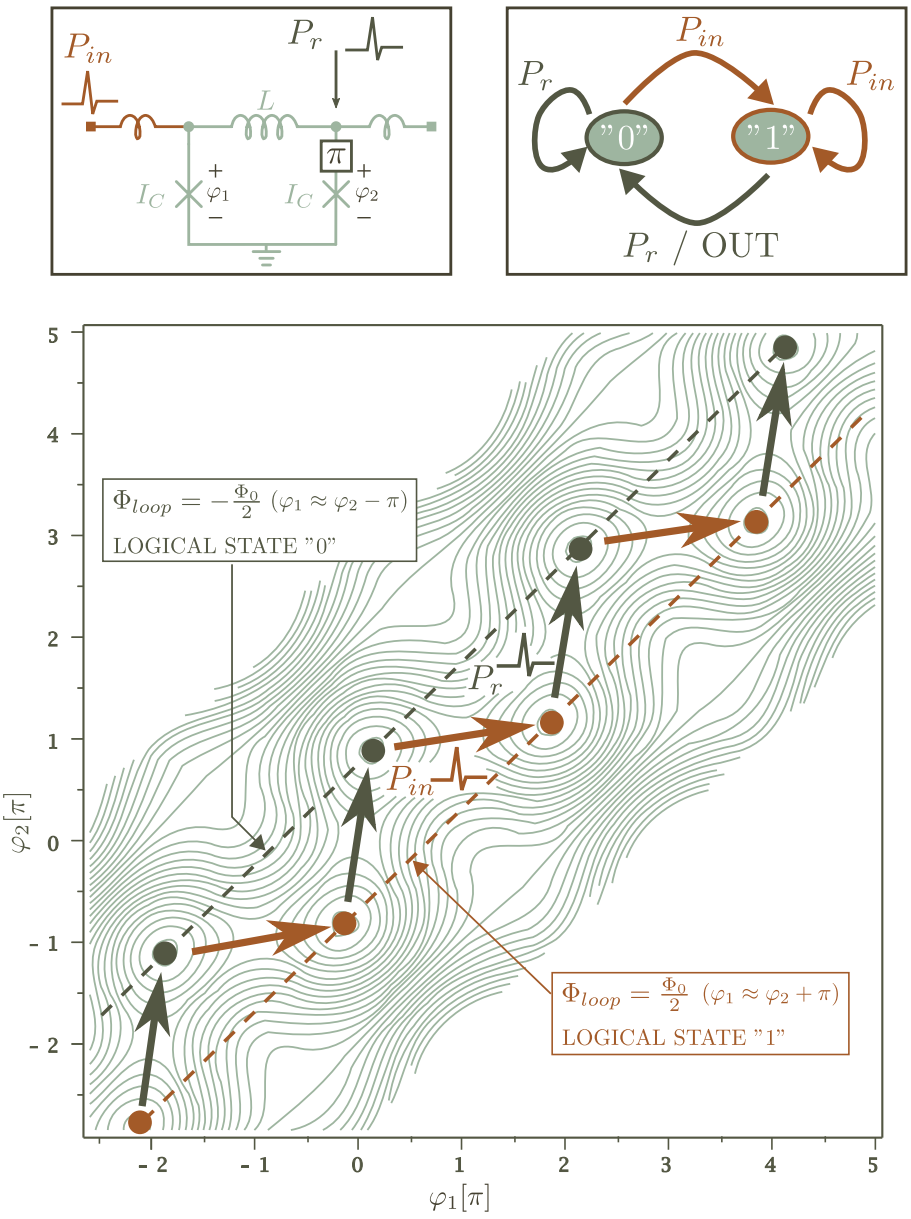

Figure 2.29. A circuit schematic, state diagram and the potential landscape of a RSFQ storage element using a π-shift loop. Above, $\beta_L = 5.5$ while the junctions are symmetric as well.

RSFQ circuits use short voltage pulses, usually called SFQ pulses, as input/output signals. The pulses trigger the state transitions in the circuits by adding a directional and momentary impulse to the state variables, overcoming the potential barrier between the states. Typically, there are just two states in each element, roughly corresponding to the zero-flux and SFQ states in a normal loop and to the $\pm\frac{\Phi_0}{2}$ states in a π-loop. These two states are indicated in the Figures above with the "0" and "1" states respectively.

Lets first focus on the normal loop, Figure 2.28. The operation of the RSFQ storage loop is guided by two input signals, P_{in} and P_r. The former is typically a data input while the latter a "reset" pulse. While a pulse at P_{in} mostly gives an impulse to the state variable φ_1 (the flux angle of the left junction), a pulse at P_r impacts the other state variable φ_2 (the flux angle across the right junction). As the potential landscape indicates, when the circuit is in the "0" state ($\Phi = 0$), a pulse at P_{in} gives an impulse in the positive φ_1 direction, almost directly across the lowest point in the potential barrier with the next ("1") state. A "0" to "1" transition will then be easily achieved. If, on the other hand, the pulse arrived at the P_r input while in the "0" state, the impulse would have been in the positive φ_2 direction where only an approximately parabolic potential wall is found. A second device, not shown in Figure 2.28, would then absorb the pulse energy and the storage loop remains in the "0" state. In other words, when the circuit is in the "0" state, only a pulse at P_{in} triggers a state change to "1" while a pulse at P_r does not trigger a state transition (or, more precisely, does that in a different subcircuit specially designed for that purpose alone). The situation is reversed when the circuit is in the "1" state: only a pulse at P_r triggers a transition from "1" back to "0". It is important to mention that the output signal, positioned at the far right of the circuit, is also a voltage pulse defined by the dynamics of the state variable φ_2 as the circuit state changes from "1" to "0".

The process is captured in the state-machine diagram at the top right. The output signal is released by a transition from "1" to "0" i.e. only when a single pulse at P_{in} is followed by a single pulse at P_r. The basic logical operation is then akin to "Out generated only if (P_r after P_{in})". In any case, the sequential diagram of the state machine implements a logic function on the two input signals and generates an output signal as well.

The same state-machine diagram is valid for the π-loop.

In practice, for every normal loop from Figure 2.28, a second identical loop is present, with flux states very strongly coupled to the ones of the first loop. The new loop however has an opposite tilt in the potential landscape (a negative I_B). Then, due to the strong coupling, as the common state transitions are sequentially triggered one of the loops "descends" while the other "ascends" its tilted potential landscape. Hence, contrary to what the plot in Figure 2.28 suggests, a normal storage device in a practical RSFQ circuit is designed as a double-loop

coupled symmetrical structure and exhibits no net potential energy loss during its sequential operation. Nevertheless, circuit asymmetry of intentional design is usually ecountered in RSFQ circuits as a consequence of the Monte-Carlo collective optimization of the elements, typically seeking the highest speed of operation or lowest process sensitivity. Then, there is indeed *a net tilt in the potential diagram* of the double-loop storage device.

Consequently, for every state transition, the circuit releases a portion of its potential energy equal to the net difference in the energy levels between the starting and end states. A part of the energy is used to compensate for the friction (resistance) during the motion (transient) between the states while a part is "absorbed" at the current source. The latter results in dissipation at the leads and other elements connected in series with the current source, as well as on its internal resistance. Since the current sources are most often implemented as resistors connected at the remote end to a voltage-biased rail, this net-tilt dissipation occurs locally on the RSFQ IC. As such, it is difficult to remove it in the cryogenic environment of the circuit.

Were RSFQ circuits optimized for power dissipation instead of speed or process robustness, the most likely outcome of such a Monte-Carlo simulation would have been a complete symmetry in the double-loop storage devices.

However, even when the double-loop device is physically symmetrical, an asymmetry is still found when considering the "0" to "1" and reverse state transitions. The circuit would, in principle, follow a different trajectory across the potential landscape: the barrier presented when going from "0" to "1" is different than when going from "1" to "0". This is seen at the plot in Figure 2.28 as a difference in the density of the potential contour lines across the most likely trajectory for the two types of transition.

In order to have approximately symmetrical "0" to "1" and "1" to "0" transitions, the potential level of a "0" state has to lie exactly half-way between the potential levels of two consecutive "1" levels and vice-versa. In this way, every transition from a "0" to a "1" state will transverse approximately the same potential barrier. The above can be achieved by tuning the I_B of the current source in relation to the β_L of the loop. Nevertheless, every deviation of the bias source away from the chosen value will result in asymmetric state transitions, producing data-dependent jitter in the circuit and decreasing the robustness of the same. Moreover, the current source as an external element introduces noise in the circuit as well.

In the π-loop on the other hand, all state transitions are symmetrical. Additionally, as mentioned before, the symmetry in the π-loop holds for any β_L while for the normal loop $\beta_L > 2$ in order for any SFQ states to appear. Taken together, the absence of the current source (no tilt in the potential landscape) and the much broader β_L range for which the π-loop can operate as a storage loop, makes it a better choice in implementing RSFQ circuits. In [8], [3], [4] and partially [21], [36] one can find more details about the π-shift based RSFQ logic circuits. In the

next Chapter, such circuits implemented with a hybrid YBCO/Nb process are presented, together with measurement results of the manufactured samples.

2.3 Superconducting network modelling in practice

Previously, in Section 2.2, the basics of the Josephson Network model were presented, with the most important result being the equivalence between the (φ, I) and (U, I) network representations of the superconducting system. This enables the use of standard network analysis methods in superconducting circuits. While they correctly model the system's thermodynamics, specific phenomena like flux quantization, non-homogeneous current distribution at zero frequency and devices like Josephson junctions are encompassed as well.

Nevertheless, a challenging component of electromagnetic network analysis remains present also in superconducting circuits: the calculation of the partial inductances of the segments in the equivalent circuit. This task is difficult because magnetic fields permeate all known materials, including superconductors (to a certain extent) as well. As a result, the fields created by currents in one device are usually felt over an area containing many other devices and thus remote magnetic interactions are necessary inclusions in accurate network models. When a circuit has many current-carrying devices and segments, the calculation of the partial inductance matrix becomes very cumbersome and the network schematic cluttered with coupled elements.

Fortunately, in thin-film (i.e. planar) superconducting circuits with a groundplane, the complexity of the inductance analysis is lowered because its shielding property decreases the range of magnetic interactions (see Section 2.2.4.3). Further, since the planar dimensions of the circuit structures are large compared to their thicknesses, a (nearly) homogeneous field exists in the dielectric between the various superconducting layers. Along with other methods of simplification, the electromagnetic analysis of superconducting circuits can then be applied in a practical manner and within acceptable accuracy limits, as illustrated in the following subsections.

First, in subsection 2.3.1, the geometry of a superconducting thin-film segment of given thickness is simplified by replacing it with a 2D superconducting sheet and defining the parameter of *surface inductance*. Afterwards, in subsection 2.3.2, the practice of correct positioning of the segment interfaces (or ports) is discussed, as a result of which, for instance, the awkward process of segmenting the groundplane in a node-branch network becomes not necessary. At the end, in subsection 2.3.3, the partial inductances of a circuit structure are calculated with an electromagnetic simulator as an example.

2.3.1 Surface inductance

The goal is to replace a 3-dimensional superconducting segment of thickness d, width W, length L and penetration depth λ_L with a 2-dimensional superconducting sheet with surface inductance L_S and of the same W, L planar dimensions.

This equivalence makes it possible for electromagnetic simulators to reduce the dimensionality of the conductive layers and hence simplify the field-solving process. The 2D sheet method [26] is, in general, applicable for any conductive structures that have a large W, H to d ratio. Figure 2.30 shows a common example containing superconducting thin films of planar geometry replaced with 2D sheets.

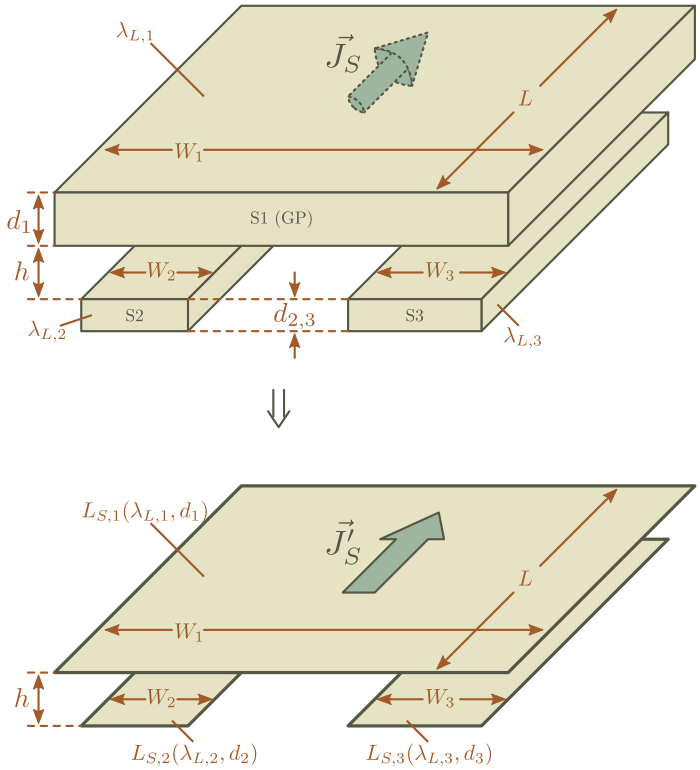

Figure 2.30. Three segments in a configuration that is often encountered in planar circuits (the top segment is usually the groundplane). The thin film segments of thickness d_i and penetration depth $\lambda_{L,i}$ are replaced with 2D sheets of surface inductance $L_{S,i}$ and the same planar dimensions. The surface inductance is a function of d_i and λ_i.

The (volumetric) supercurrent density $\boldsymbol{J}_S$ is replaced by a surface current density $\boldsymbol{J}'_S$ with the requirement that the magnetic field be equal at the corresponding surfaces of the segments in the two systems. This requirement is necessary for the magnetic field to be (approximately) the same everywhere since it defines the boundary conditions in the dielectric outside the segment. The equivalence is then, when looking at the magnetic field $\boldsymbol{B}$ outside the segments (and hence in the rest of the circuit), established. Additionally, it is also necessary for the stored

energy in the surface conducting sheet to be equal to the stored energy in the superconducting layer of thickness d in order for the dynamics of the two systems to be equivalent.

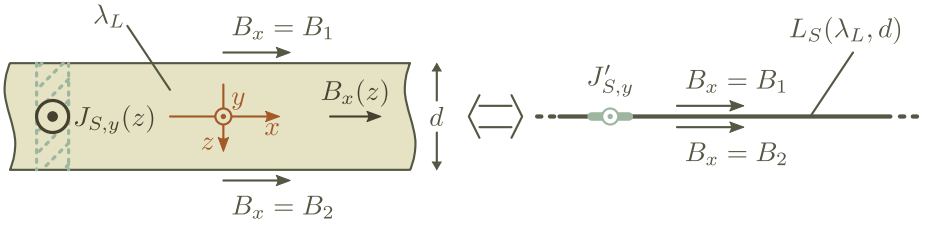

Figure 2.31. The different quantities and the coordinate system used during the calculation of the surface inductance.

Let's assume a planar-homogeneous magnetic field in the x direction and equal to B_1 and B_2 at the top and bottom surfaces respectively:

$$\begin{gathered} \boldsymbol{B} = B_x(z) \cdot \boldsymbol{i}_x \\ B_x\left(z = -\frac{d}{2}\right) = B_1 \\ B_x\left(z = \frac{d}{2}\right) = B_2 \end{gathered} \tag{2.76}$$

Inside the superconductor, the magnetic field is found as a solution to the Helmholtz equation $\lambda_L^2 \cdot \nabla^2 \boldsymbol{B} = \boldsymbol{B}$. Using the boundary conditions above, the magnetic field inside the superconducting film can then be solved:

$$B_x(z) = \frac{1}{\sinh\left(\frac{d}{\lambda_L}\right)} \cdot \left[B_1 \cdot \sinh\left(\frac{\frac{d}{2} - z}{\lambda_L}\right) + B_2 \cdot \sinh\left(\frac{\frac{d}{2} + z}{\lambda_L}\right) \right] \tag{2.77}$$

The supercurrent in the layer can be calculated from Ampere's law $\nabla \times \boldsymbol{H} = \boldsymbol{J}_S$, yielding only a y component that depends on z:

$$\begin{gathered} \boldsymbol{J}_S = J_{S,y}(z) \cdot \boldsymbol{i}_y \\ J_{S,y}(z) = \frac{1}{\mu \cdot \lambda_L \cdot \sinh\left(\frac{d}{\lambda_L}\right)} \cdot \left[-B_1 \cdot \cosh\left(\frac{\frac{d}{2} - z}{\lambda_L}\right) + B_2 \cdot \cosh\left(\frac{\frac{d}{2} + z}{\lambda_L}\right) \right] \end{gathered} \tag{2.78}$$

In order to satisfy the requirement of field equality between the two systems, it is necessary to set the magnetic field to B_1 and B_2 just above and just under the 2D sheet respectively. The surface current $\boldsymbol{J}'_S = J'_{S,y} \cdot \boldsymbol{i}_y$ flowing in the sheet can now be found from the integral form of Ampere's law $\oint \boldsymbol{H} \cdot \mathrm{d}\boldsymbol{l} = \int \boldsymbol{J}'_S \cdot \mathrm{d}\boldsymbol{x}$ as

$$J'_{S,y} = \frac{B_2 - B_1}{\mu} \tag{2.79}$$

If the surface current $J'_{S,y}$ given by 2.79 flows in the 2D sheet, the magnetic field in the space outside will be the same in the two systems (same boundary conditions).

When an electromagnetic field solver encounters a thin conductive sheet, it assigns the properties of surface inductance and surface resistance to the sheet. In the case of superconductors at frequencies below the "two-fluid" threshold, which is the case for the circuits from this text, only the surface inductance L_S (in units of H) will be non-zero. The energy density stored in the sheet (per unit width and unit length) will then be

$$w_S = \frac{(J'_{S,y})^2 \cdot L_S}{2} = L_S \cdot \frac{1}{2} \cdot \left(\frac{B_2 - B_1}{\mu} \right)^2 \tag{2.80}$$

by using equation 2.79 to substitute $J'_{S,y}$. Note that, for both the thin film and 2D sheet, the total energy stored in the whole structure will then be a sum of the internal energy w_S and the energy stored in the magnetic field outside the structures. Only w_S is important for establishing the equivalence since it was already taken care that the external field is the same in the two systems.

In the case of the system containing the superconducting film of thickness d, the energy density stored inside the layer is a sum of the magnetic field energy and of the kinetic energy of the moving condensate particles (see Chapter 2):

$$w_S = \frac{1}{2} \int_{-\frac{d}{2}}^{\frac{d}{2}} \left(\frac{1}{\mu} B_x^2 + \Lambda \, J_{S,y}^2 \right) \cdot \mathrm{d}z$$

Replacing $J_{S,y}$ and B_x from the expressions 2.78 and 2.77 respectively, the solution of the above integral is

$$w_S = \lambda_L \, \mu \cdot \coth\left(\frac{d}{\lambda_L} \right) \cdot \frac{1}{2} \cdot \frac{B_1^2 + B_2^2 - 2 \cdot B_1 \, B_2 \cdot \frac{1}{\cosh\left(\frac{d}{\lambda_L} \right)}}{\mu^2} \tag{2.81}$$

Since the energy density stored in the superconductor and the thin sheet should be the same in both cases, equating the right-hand sides of 2.80 and 2.81 yields:

$$L_S = \lambda_L \, \mu \cdot \coth\left(\frac{d}{\lambda_L} \right) \cdot \frac{B_1^2 + B_2^2 - 2 \cdot B_1 \, B_2 \cdot \frac{1}{\cosh\left(\frac{d}{\lambda_L} \right)}}{(B_2 - B_1)^2} \approx \lambda_L \cdot \mu \cdot \coth\left(\frac{d}{\lambda_L} \right) \tag{2.82}$$

if the term containing B_1 and B_2 is approximated to ≈ 1.

In Appendix B, an analysis of the accuracy of the above approximation is given. The conclusion states that, for the most practical segment-groundplane configurations, the surface inductance of the sheets given as $L_S = \lambda_L \cdot \mu \cdot \coth\left(\frac{d}{\lambda_L}\right)$ does not yield an error greater than $\sim 25\%$. This error on the other hand, does not result in more than 10% error in the *total* inductance of a given segment. The exceptions are:

- a thin film segment placed in an external magnetic field, excited from both sides, that is approximately equal in direction and magnitude at the top and bottom surfaces ($B_1 \approx B_2$)
- when a thin ($d_{\mathrm{GP}} < 2\ \lambda_L$) or narrow ($W_{\mathrm{GP}} \leqslant 10\ W_{\mathrm{SEG}}$) groundplane above/below a segment is connected at a single point, or not connected at all, to the circuit of which the segment is part of
- generally, any groundplane that is thinner than $\sim 2\,\lambda_L$
- an *isolated* segment thicker than $\sim \lambda_L$ (a different and exact expression for L_S is however available, see Appendix B)

The model of a single 2D sheet representing a thin film is not appropriate for the cases listed above (except the last): one must use two 2D sheets, one for each surface of the film. The two sheets, positioned at the top and bottom surfaces of the thin film, are connected together at the far ends of the segment (along its length and width thus). The derivation of the surface inductance of the two sheets, of equal value for both, can follow the same path as above, resulting in an expression that is more complex than 2.82. The two-sheet representation will however not be used as the accuracy of the single sheet model is acceptable for the geometries commonly found in the π-shift circuits from this text (also see Figure 2.32 below). Note that a two-sheet model doubles the number of conductive surfaces, resulting in a four-fold increase in the complexity of any subsequent EM field analysis. Often, the computation time saved with a single sheet representation justifies the modest accuracy degradation. More details about the two-sheet 2D representation of superconducting thin films can be found in [15] and [39].

In the (single) 2D sheet model given above, it was assumed that the magnetic fields at the surfaces of the film and at the sheet must be equal for the equivalence to hold. It was however not required for the electric field to be equal as well: this equivalence is nevertheless necessary when there are electromagnetic waves present in the system. Namely, the substitution of the superconducting film with a 2D sheet will lead to loss of information about the wave propagation in the superconductor's interior. In general, one then has to try and draw the equivalence between the thin film and the 2D sheet from the perspective of a planar wave incident to the structure and define equivalence criteria for both the electric and magnetic

fields. Fortunately, it can be shown [39] that if the characteristic impedance of the space on each side of the sheet, $Z_\eta = \sqrt{\frac{\mu}{\epsilon}}$ ($\approx 377\Omega$ in vacuum), is much larger than $2\pi f \cdot \mu \cdot \lambda_L$, where f is the frequency of analysis, then the 2D sheet model above will also be able to handle wave propagation phenomena well. Assuming vacuum and a $\lambda_L = 100$nm, the maximum frequency is about 5×10^{14}Hz - this is clearly much higher than the range that is commonly used in superconducting circuits.

The 2D sheet model is based on a homogeneous magnetic field that points only in the x direction. For a finite width and length of the superconducting structures, the field is not homogeneous and there will be an x (or y) dependence of the quantities as well as a small z component of the magnetic field (field lines have to close around the segment). Although for a large W, L to d ratio the segments can be considered to be infinite in the planar directions, at their edges one encounters a different situation. To address this, EM simulators divide the 2D sheet in a number of cells by creating a (typically) rectangular mesh on its surface. Every cell is then assigned the same surface inductance but is allowed to have a different surface current. In effect, each cell is treated as if the field and current were homogeneous in their vicinity. By taking care that the current conservation law holds during the field solving process, the interactions between the cells will yield planar (x, y) distributions in both the magnetic field and the surface current. These will become more accurate as the number of cells in this finite-element approximation is increased.

Besides errors due to the finite number of cells, there are other systematic errors made with the meshing method above:

- the z component of the field inside the thin film is not taken into account during the derivation of the surface inductance L_S
- the penetration depth of the material along the x and y directions is neglected

The former usually has a small contribution to the total errors due to the low magnitude of B_z relative to B_x in planar circuits (unless when externally applied). The latter is also negligible when $W, L \gg \lambda_{L,\mathrm{xy}}$, which is almost always the case for planar circuits.

To support the above estimations, the plot in Figure 2.32 is presented. The total (sheet) inductance of a YBCO segment above a Nb groundplane is shown as a function of the width of the line, in the case when the structure is treated as a microstrip transmission line (the segment and the groundplane are connected to the same source at the far terminals, see Appendix B). The plot compares three common methods of inductance calculation of thin superconducting films which are then benchmarked for accuracy against a 3D field solver (FastHenry [40] adapted for superconductors).

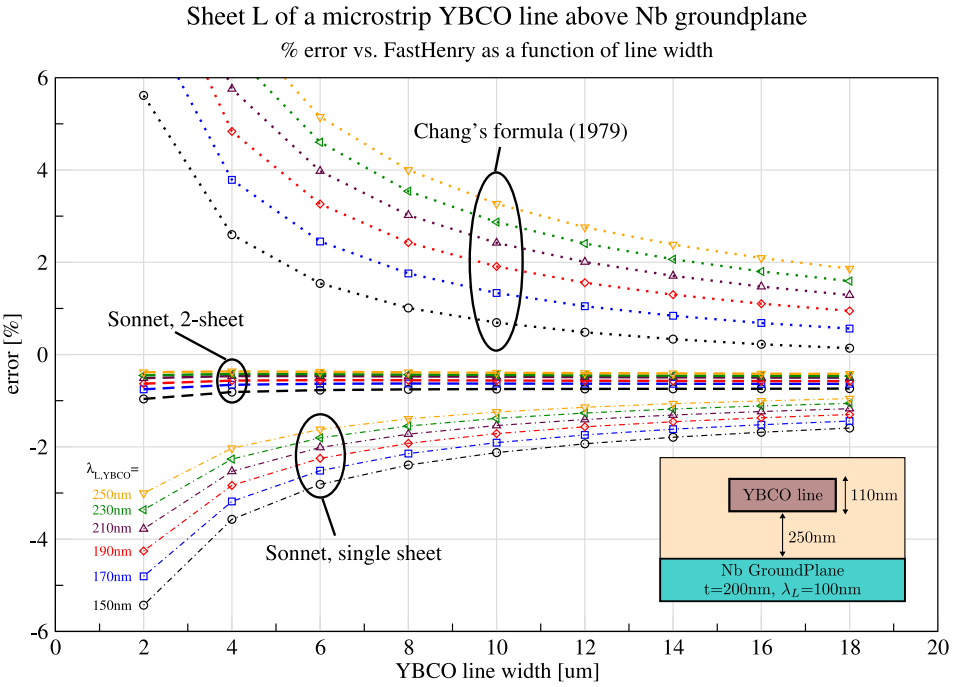

Figure 2.32. Comparison of the systematic errors for few common methods of inductance calculation. "Chang's formula" is an analytical expression approximating the inductance of superconducting segments with a rectangular cross-section [41] while the other two results are obtained with a 2D sheet representation of the thin films and subsequently applying a planar field solver (Sonnet em [42]). The reference is the 3D inductance extraction program FastHenry adapted for superconductors. The computer codes implementing FastHenry and Chang's formula are available at www.wrcad.com.

The plot demonstrates that the surface inductance method is well suited for inductance extraction of thin film planar circuits, especially the double sheet representation. The single sheet model is less accurate for decreasing W to d ratios (large edge effects), but the errors are still just a few percent for reasonable geometries. Using approximate analytical formulae on the other hand, generates greater errors but has the benefit of (virtually) zero computing time. The 2D sheet method is hence a good compromise between accuracy and computation speed.

2.3.2 Equivalent circuits of multi-port structures

Previously in this Chapter, a network model for a system of interconnected superconducting segments and other devices was developed. The basis for the model lies in the concept of partial inductance for conventional electrical networks, addended

by the equivalence between the (φ, I) and (U, I) network descriptions of the devices typically found in a superconducting system. In the course of the presentation of the model however, it was assumed that a superconducting segment can have only two interface terminals, or in other words, only a single port (port=pair of terminals). The equivalent electrical network of the system was then built exclusively out of two-terminal elements attached at their ends to other two-terminal elements. Such an assumption is not correct for some circuit structures. A typical example is the groundplane which can not be treated as a single segment since it often has multiple connections to the rest of the circuit. A groundplane is, in itself, a multiple-port network of a distributed kind that is coupled to all segments in the circuit. The segmentation of the physical structure of a groundplane in a branch-node architecture is thus not trivial. This type of problem is solved by creating equivalent circuits, finding circuit symmetries and using approximations when appropriate. In the next few subsections, a method is presented that guides the creation of a practical equivalent network for most types of structures made of superconducting segments. At the end, also the other types of elements are included.

2.3.2.1 Galvanically coupled segments

The joined 4-segment structure presented in section 2.2.4.4 is an example where representing a superconducting system with a network of two-terminal (or single-port) segments is not always practical. The structure and its "default" network model are reproduced below for clarity.

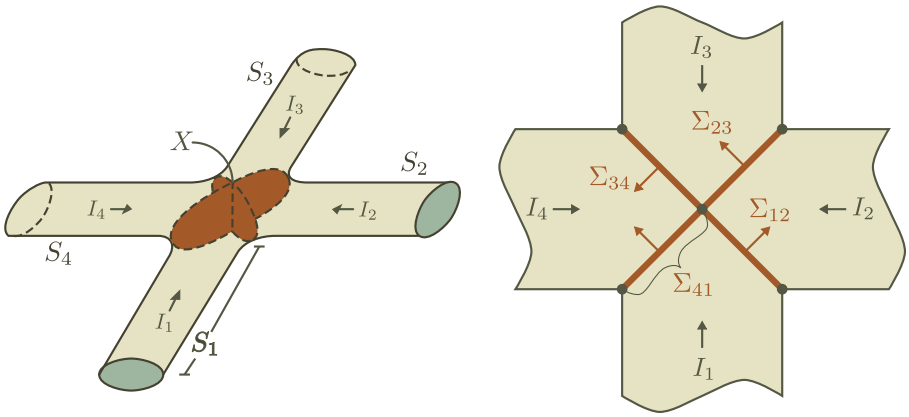

Figure 2.33. Four segments connected together at a joint node.

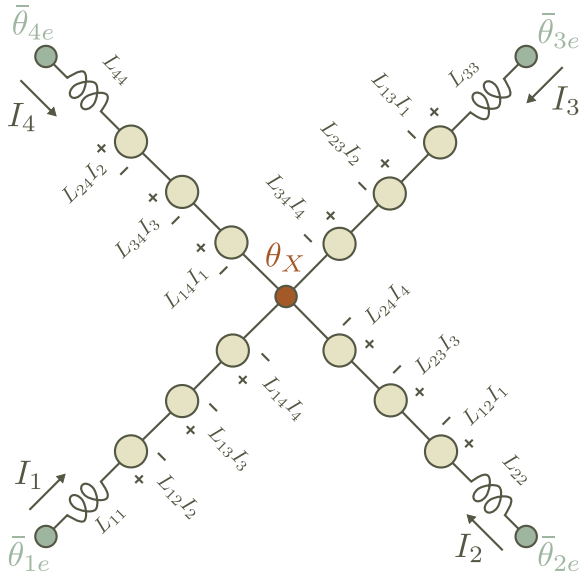

Figure 2.34. The single-segment network schematic of the structure from Figure 2.33.

The situation does not easily lend itself to a single-port segment analysis due to the galvanic coupling between the segments, resulting from them sharing common current paths in the joint area. To illustrate the problem, lets try to apply the superposition method of section 2.2.4.3. The goal of the procedure was to obtain the normalized currents $\boldsymbol{j}_{S,i}$ and vector potentials $\boldsymbol{a}_i$ for each segment i when the currents through the interfaces of the other segments are set to zero. The partial inductance elements present in the schematic of Figure 2.34 were then to be found with integral expressions of $\boldsymbol{a}_i$ and $\boldsymbol{j}_{S,i}$ over the volume of the segments. However, setting the currents through all but one of the segments to zero, in order to obtain the normalized current and vector potential for each, is not possible for Figure 2.33. For example, setting $I_2 = I_3 = I_4 = 0$ to find the first segment's field variables ($i = 1$), immediately leads to $I_1 = 0$ from current conservation. In other words, the inductance calculation method of section 2.2.4.3, based on a single-port approach, is not directly applicable for galvanically-coupled (sub)circuits with more than two interface terminals.

Actually, due to the current conservation law that adds one more relation to the circuit equations for a general multiple-port structure, not all of the elements of the partial inductance matrix shown in the equivalent network of Figure 2.34 are relevant, nor can they can be calculated individually. It is necessary to find a new description of the circuit equations where the amount of coefficients is reduced and they are independent.

Let's try to eliminate the ambiguity in the network description of the system. The network equations for the schematic from Figure 2.34 were given by an expression involving the partial inductance matrix $\boldsymbol{L}$:

$$\begin{pmatrix} \bar{\theta}_{1e}-\theta_X \\ \bar{\theta}_{2e}-\theta_X \\ \bar{\theta}_{3e}-\theta_X \\ \bar{\theta}_{4e}-\theta_X \end{pmatrix} = \frac{2\pi}{\Phi_0} \begin{pmatrix} L_{11} & L_{12} & L_{13} & L_{14} \\ L_{21} & L_{22} & L_{23} & L_{24} \\ L_{31} & L_{32} & L_{33} & L_{34} \\ L_{41} & L_{42} & L_{43} & L_{44} \end{pmatrix} \cdot \begin{pmatrix} I_1 \\ I_2 \\ I_3 \\ I_4 \end{pmatrix} \tag{2.83}$$

The current conservation law is also important

$$I_1 + I_2 + I_3 + I_4 = 0 \tag{2.84}$$

Additionally, the partial inductance matrix $\boldsymbol{L}$ is diagonal

$$L_{ij} = L_{ji} \tag{2.85}$$

having 10 unique elements. The relations 2.83 and 2.84 can be combined to yield a new system of node-branch equations:

$$\begin{pmatrix} \bar{\theta}_{1e}-\theta_X \\ \bar{\theta}_{2e}-\theta_X \\ \bar{\theta}_{3e}-\theta_X \\ \bar{\theta}_{4e}-\theta_X \end{pmatrix} = \frac{2\pi}{\Phi_0} \begin{pmatrix} L_{11}-L_{14} & L_{12}-L_{14} & L_{13}-L_{14} \\ L_{21}-L_{24} & L_{22}-L_{24} & L_{23}-L_{24} \\ L_{31}-L_{34} & L_{32}-L_{34} & L_{33}-L_{34} \\ L_{41}-L_{44} & L_{42}-L_{44} & L_{43}-L_{44} \end{pmatrix} \cdot \begin{pmatrix} I_1 \\ I_2 \\ I_3 \end{pmatrix} \tag{2.86}$$

Note that all twelve of the elements of the 3x4 matrix above can now be calculated by the superposition method of section 2.2.4.3, but excluding the step for the segment 4. So, for $I_2 = I_3 = 0$ and $I_1 = I$ which, implicitly, also requires $I_4 = -I$ to be set, the quantities $\boldsymbol{a}_1$ and $\boldsymbol{j}_{S,1}$ are calculated in the whole volume of the structure by an EM analysis. Then, for $I_1 = I_3 = 0$ and $I_2 = -I_4 = -I$, one finds $\boldsymbol{a}_2$ and $\boldsymbol{j}_{S,2}$. Similarly, $\boldsymbol{a}_3$ and $\boldsymbol{j}_{S,3}$ are calculated. The integral expressions for the partial inductances evaluated over the appropriate volume will then yield the elements of the matrix in 2.86. For example, integrating $\boldsymbol{j}_{S,1} \cdot (\Lambda\, \boldsymbol{j}_{S,1} + \boldsymbol{a}_1)$ over the volume bordered by the first segment (between the interface surfaces of $\bar{\theta}_{1e}$ and θ_X), will yield $L_{11} - L_{14}$, the element in the most upper left. The next element to the right, $L_{12} - L_{14}$, will be equal to the integral of $\frac{\mu}{4\pi}\, \boldsymbol{j}_{S,1} \cdot \boldsymbol{a}_2$ evaluated over the same volume. The element below on the other hand, $L_{21} - L_{24}$, will be equal to the integral of $\frac{\mu}{4\pi}\, \boldsymbol{j}_{S,2} \cdot \boldsymbol{a}_1$ over the volume between $\bar{\theta}_{2e}$ and θ_X.

Only nine of the elements in the matrix from 2.86 are independent, the remaining three can be written as a linear combination of them (this can be proved by a Gauss-Jordan elimination of the system of equations relating the

elements of the matrix in 2.86 and the elements of $\boldsymbol{L}$). For example

$$L_{23} - L_{24} = -(L_{42} - L_{44}) + (L_{32} - L_{34}) + (L_{43} - L_{44})$$

$$L_{13} - L_{14} = (L_{31} - L_{34}) - (L_{41} - L_{44}) + (L_{43} - L_{44})$$

$$L_{12} - L_{14} = -(L_{41} - L_{44}) + (L_{21} - L_{24}) + (L_{42} - L_{44})$$

when also relation 2.85 is taken into account. If one calculates the elements of the 3x4 matrix in 2.86 and wishes to map the results back to the elements of $\boldsymbol{L}$, there will be not enough information: there are 10 unique elements in $\boldsymbol{L}$ while only 9 equations will be available. Hence, the schematic in Figure 2.34 can never be used since all elements can not be calculated individually. They will always appear in pairs of which 9 are unique, as indicated by 2.86.

Note that the relation 2.86 is not a proper system of network equations. It lacks a schematic interpretation and the symmetries of a true partial inductance matrix. It is also not relevant to any circuits attached to the external terminals how exactly the internal coupling between the segments is realized: it is only the (φ, I) relationship at the external terminals that is important. To that end, lets try to eliminate the internal node X from the network equations:

$$\begin{pmatrix} \bar{\theta}_{1e} - \bar{\theta}_{4e} \\ \bar{\theta}_{2e} - \bar{\theta}_{4e} \\ \bar{\theta}_{3e} - \bar{\theta}_{4e} \end{pmatrix} = \frac{2\pi}{\Phi_0} \begin{pmatrix} L_{S11} & L_{S12} & L_{S13} \\ L_{S21} & L_{S22} & L_{S23} \\ L_{S31} & L_{S32} & L_{S33} \end{pmatrix} \cdot \begin{pmatrix} I_1 \\ I_2 \\ I_3 \end{pmatrix} \tag{2.87}$$

where the new partial inductance matrix $\boldsymbol{L}_S$ of size 3x3 is also diagonally symmetric

$$\begin{aligned} L_{S11} &= L_{11} - 2\,L_{14} + L_{44} \\ L_{S22} &= L_{22} - 2\,L_{24} + L_{44} \\ L_{S33} &= L_{33} - 2\,L_{34} + L_{44} \\ L_{S12} = L_{S21} &= L_{12} - L_{24} - L_{14} + L_{44} \\ L_{S13} = L_{S31} &= L_{13} - L_{34} - L_{14} + L_{44} \\ L_{S23} = L_{S32} &= L_{23} - L_{34} - L_{24} + L_{44} \end{aligned} \tag{2.88}$$

and consequently, has only 6 unique elements (hence, not all 9 of the unique elements in 2.86 are relevant to the outside world). The system 2.87 is equivalent to the network equations for a circuit of 3 segments that share a common interface

surface (at $\bar{\theta}_{4e}$) but are otherwise not galvanically coupled, Figure 2.35. One can now apply the procedure from 2.2.4.3 and calculate the elements of $\boldsymbol{L}_S$ (the calculated $\boldsymbol{a}_i$ and $\boldsymbol{j}_{S,i}$ are the same as for the elements of the matrix in the system 2.86, only the integration volumes now always include the segment 4). This matrix is the sought after reduced description of the structure of Figure 2.33, while the equivalent network is given by Figure 2.35.

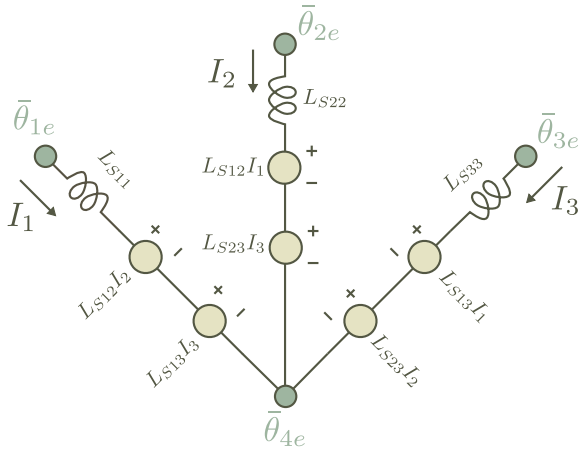

Figure 2.35. The reduced equivalent network for the structure of Figure 2.33

It is here important to mention that, very often, the mutual coupling inductances in multiple-segment joint structures such as the one in Figure 2.33 are neglected. It is then possible to use the "star" network architecture of Figure 2.34, without the mutual terms of course, since all four self inductance elements can be calculated. First, the elements of $\boldsymbol{L}_S$ are found and then the system 2.88 is solved for L_{11}, L_{22}, L_{33} and L_{44} by using that the other elements of $\boldsymbol{L}$ are zero. Sometimes, only some of the mutual coupling elements of $\boldsymbol{L}$ can be approximated to zero (by inspection) - in these cases it may also be possible to invert the system 2.88.

The method above can be applied to a general structure with n interface terminals ($n/2$ ports if n is even), where $n > 2$. One needs to declare one of the interfaces as a common one and then find the elements of the partial matrix $\boldsymbol{L}_S$ as if the segments were defined between the common and each of the other interface surfaces. A reduced equivalent network of the type as given in Figure 2.35 must be used in any further network analysis instead of the full "star" architecture with internal node from Figure 2.34. Sometimes however, a simple inspection of the structure can already lead to neglecting some of the elements of $\boldsymbol{L}$. In these cases, it may be possible to invert the system from relation 2.88 and arrive back at the original schematic, albeit always with less elements than shown in Figure 2.34.

2.3.2.2 Groundplane interfaces

The same analysis given by the previous subsection could have been done if, for example, one of the segments in Figure 2.33 was a groundplane placed below (or above) the other three segments and connected to them at a single or multiple points. A good practice is to then declare the interface of the groundplane as the common one (i.e. the "ground" terminal).

When there are no clear interface surfaces for the groundplane in the structure, that is often the case in practical circuits, they need to be added manually. For example, lets consider the structure in Figure 2.36. One of the arms of a T-shaped segment is connected to the groundplane with a via structure. For the T-segment alone, there are 2 interface surfaces to the outside world. The groundplane on the other hand, covers the entire structure with no interface surfaces that can be trivially defined. In this case, in order to cover the most general situation where other circuits can be attached to all 4 sides of the planar circuit (even through just a continuation of the groundplane on each side), one interface terminal must be defined for each side-edge of the groundplane. The circuit will then have $2+4=6$ interfaces in total. Declaring one of them as a common interface, the 5x5 matrix $\boldsymbol{L}_S$ can be defined as shown previously. Often however, other (sub)circuits do not appear in the vicinity of all 4 edges of the shown structure, and thus some of the groundplane terminals can be forgone.

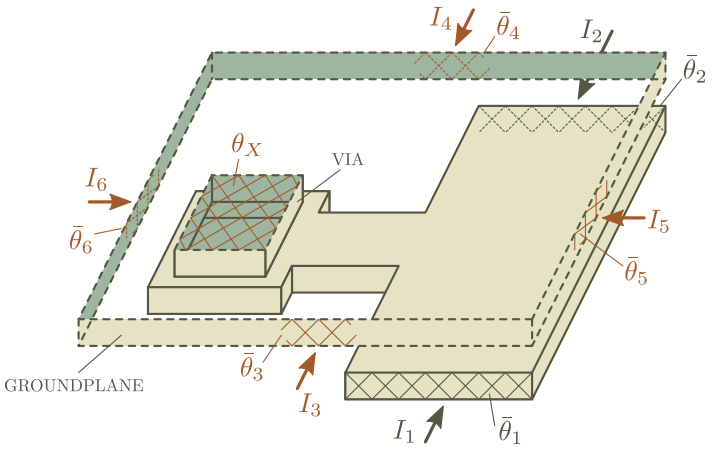

Figure 2.36. A groundplane (shown hollow) above a "T" segment structure, where one arm of the structure is connected to the groundplane with a via. There are two external interfaces of the T-shaped structure, denoted by nodes $\bar{\theta}_1$ and $\bar{\theta}_2$, and a maximum of four groundplane interfaces marked by nodes $\bar{\theta}_3$ through $\bar{\theta}_6$. The interface surfaces are indicated by a hatched pattern. The interface surfaces for the groundplane cover the whole edge (only small part is hatched for clarity). The interface surface for the internal node θ_X is also shown.

In circuits with a groundplane, the inductive mutual coupling between (parts of) segments is greatly reduced due to the groundplane's shielding effect. It is thus

important to first inspect the circuit and look for any symmetries or any elements that can be easily neglected.

Lets assume, for simplicity, that there are no circuits attached to the nodes marked with $\bar{\theta}_5$ and $\bar{\theta}_6$. There will be thus in total 4 external nodes for the whole structure, same as the example from the previous section. Hence, for the outside world, the network description of the structure:

$$\begin{pmatrix} \bar{\theta}_1 - \bar{\theta}_4 \\ \bar{\theta}_2 - \bar{\theta}_4 \\ \bar{\theta}_3 - \bar{\theta}_4 \end{pmatrix} = \frac{2\pi}{\Phi_0} \begin{pmatrix} L_{S11} & L_{S12} & L_{S13} \\ L_{S21} & L_{S22} & L_{S23} \\ L_{S31} & L_{S32} & L_{S33} \end{pmatrix} \cdot \begin{pmatrix} I_1 \\ I_2 \\ I_3 \end{pmatrix} \tag{2.89}$$

and the equivalent network, Figure 2.35, will be also the same as before. Both the schematic and its corresponding description are however not very intuitive for the structure from Figure 2.36: one cannot directly identify the elements that are tightly coupled from the ones that are very weakly coupled and hence negligible. To solve the problem, a more intuitive network schematic is first drawn, the weak elements are then neglected and at the end the network equations are brought in the form from relation 2.89.

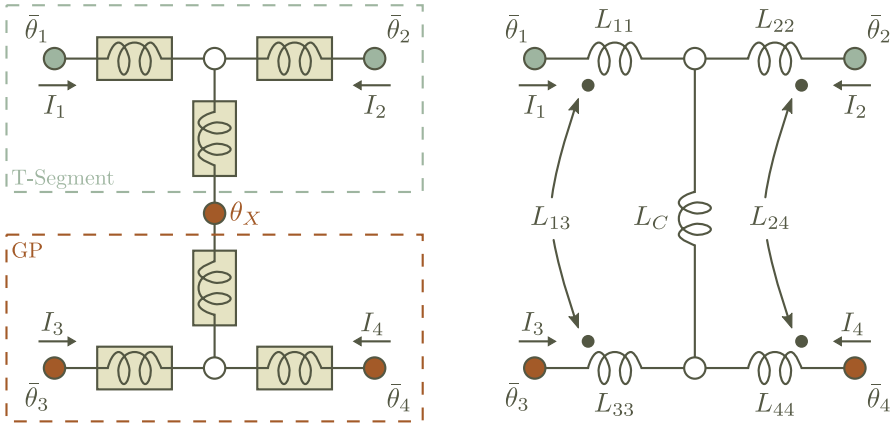

Figure 2.37. A "natural" equivalent network of the structure from Figure 2.36. The most generalized network, shown on the left, contains elements that can be in principle coupled to any other element (indicated by enclosing in a "coupling" rectangle). If one considers that only the current paths adjacent across the dielectric separating the two films are significantly coupled, the simplified schematic on the right appears. The elements appearing in series within the common branch are equivalented together in L_C.

The "natural" network for the T-segment alone would be a joint structure of 3 segments with an internal node. The node X will then connect it to the groundplane. Since the current paths in the groundplane will be, in general, mirror

images of those in the T-segment, it is reasonable to assume the same network architecture for the groundplane as well. The two networks will be attached at the node X while, in principle, all elements in the network can be coupled to each other. In Figure 2.37, on the left, such a schematic is given.

The presence of the groundplane will make most of the mutual coupling elements negligible, resulting in the simplified schematic given in Figure 2.37 on the right. The result is thus a very simple network of a few coupled elements that can be easily described by network equation. So, from circuit inspection, (note the definition of the coupled inductance element previously in this Chapter) it can be written

$$\bar{\theta}_1 - \bar{\theta}_2 = \frac{2\pi}{\Phi_0}\left(L_{11}\cdot I_1 - L_{22}\cdot I_2 + L_{13}\cdot I_3 - L_{24}\cdot I_4\right)$$

$$\bar{\theta}_1 - \bar{\theta}_3 = \frac{2\pi}{\Phi_0}\left(L_{11}\cdot I_1 + L_C\cdot(I_1+I_2) - L_{33}\cdot I_3 + L_{13}\cdot I_3 - L_{13}\cdot I_1\right)$$

$$\bar{\theta}_2 - \bar{\theta}_4 = \frac{2\pi}{\Phi_0}\left(L_{22}\cdot I_2 + L_C\cdot(I_1+I_2) - L_{44}\cdot I_4 + L_{24}\cdot I_4 - L_{24}\cdot I_2\right)$$

which, when using the law of current conservation, can be condensed in the form of equation 2.89

$$\begin{pmatrix} \bar{\theta}_1 - \bar{\theta}_4 \\ \bar{\theta}_2 - \bar{\theta}_4 \\ \bar{\theta}_3 - \bar{\theta}_4 \end{pmatrix} = \frac{2\pi}{\Phi_0}\begin{pmatrix} L_{11}+L_C+L_{44} & L_C - L_{24} + L_{44} & L_{13}+L_{44} \\ L_{44}+L_C-L_{24} & L_C + L_{22} + L_{44} - 2\,L_{24} & L_{44}-L_{24} \\ L_{13}+L_{44} & L_{44}-L_{24} & L_{33}+L_{44} \end{pmatrix}\cdot\begin{pmatrix} I_1 \\ I_2 \\ I_3 \end{pmatrix}$$

where the elements L_{Sij} can be identified as linear combinations of the elements L_{ij} and L_C from Figure 2.37.

The elements of $\boldsymbol{L}_S$ can now be calculated by a field analysis, as shown previously. However, if one then attempts to find the elements of Figure 2.37 from the elements of $\boldsymbol{L}_S$, a problem arises: there are six unique elements of $\boldsymbol{L}_S$ but seven elements in Figure 2.37 (interestingly, L_C *can* be obtained). It is again not possible to find all elements of the natural equivalent network in Figure 2.37 with an inductance analysis. In general, one must at this point make some symmetry assumptions and add one more equation (eq. $L_{33} = L_{44}$). Note that this type of assumption is only graphical, i.e., there is no consequence for the outside world: the description from equation 2.89 with its schematic from Figure 2.35 remains the same.

The most general assumption for the elements of the schematic in Figure 2.37 follows from the layer-thickness homogeneity of the structure in Figure 2.36. We can safely assume that the coupling between L_{22} and L_{44} is of the same strength

as between L_{11} and L_{33}. In other words, the coupling coefficients of the coupled inductor-pairs from Figure 2.37 are equal:

$$\frac{L_{11}\cdot L_{33}}{L_{13}^2}=\kappa_{13}=\kappa_{24}=\frac{L_{22}\cdot L_{44}}{L_{24}^2} \tag{2.90}$$

There is now enough information to solve for the elements L_{ij} knowing the elements L_{Sij}. One can then use the schematic in Figure 2.37 in further circuit analyses (eg. calculate the Gibb's free energy).

It is a common practice in circuits with a groundplane to make the approximation that the groundplane is an ideal short circuit: $L_{33}=L_{44}=0$ which also means that $L_{13}=0=L_{24}$. In this case, the two nodes $\bar{\theta}_3\equiv\bar{\theta}_4=\theta_X$ and the circuit schematic as well as its network equations are very simplified. The schematic is just the upper part of the circuit on the left of Figure 2.37 (labeled as "T-segment"), without any coupling between the elements, while the network equations are:

$$\begin{pmatrix}\bar{\theta}_1-\theta_X\\ \bar{\theta}_2-\theta_X\end{pmatrix}=\frac{2\pi}{\Phi_0}\begin{pmatrix}L_{11}+L_C & L_C\\ L_C & L_C+L_{22}\end{pmatrix}\cdot\begin{pmatrix}I_1\\ I_2\end{pmatrix}$$

The EM analysis for calculating the elements of the partial inductance matrix above is also much easier. First, there will be only 3 interface terminals $\bar{\theta}_1$, $\bar{\theta}_2$, θ_X and two independent currents I_1, I_2 with the current at the node X always equal to I_1+I_2 from current conservation. The groundplane is shorted at all 4 sides by placing an ideal superconducting "ring" (λ_L=0) around and in contact with it. The field variables $\boldsymbol{a}_1$ and $\boldsymbol{j}_{S,1}$ are found by taking $I_1=I$ and $I_2=0$. The variables $\boldsymbol{a}_2$ and $\boldsymbol{j}_{S,2}$ are found for $I_2=I$ and $I_1=0$. Note that the shielding currents in the groundplane must also be taken into account during the field-solving. Then, $L_{11}+L_C$ and $L_{22}+L_C$ are equal to the self-inductances of the segments $\bar{\theta}_1-\theta_X$ and $\bar{\theta}_2-\theta_X$ respectively. These are calculated by integrating $\boldsymbol{j}_{S,1}\cdot(\Lambda\,\boldsymbol{j}_{S,1}+\boldsymbol{a}_1)$ and $\boldsymbol{j}_{S,2}\cdot(\Lambda\,\boldsymbol{j}_{S,2}+\boldsymbol{a}_2)$ over the whole volume of the T-segment. The mutual coupling element L_C is an integral of either $\frac{\mu}{4\pi}\cdot\boldsymbol{j}_{S,1}\cdot\boldsymbol{a}_2$ or $\frac{\mu}{4\pi}\cdot\boldsymbol{j}_{S,2}\cdot\boldsymbol{a}_1$ over the same volume.

Note that, using this assumption, there will be one node X for every via structure in a general circuit. For example, the layout drawings of the RSFQ cells in Chapter 3 are given in this approximation, using the designation "G" for the via node. It is here also important to mention that were the EM analysis performed with the 2D sheet representation of the superconducting films, the interface surface for the via node degenerates in a line. Finally, this approximation is not only cosmetic as the one given by equation 2.90: the number of network variables are here reduced and there will be consequences for the accuracy of any subsequent network analysis.

In conclusion, it can be stated that the calculation of the partial inductances for a given multi-port superconducting structure with a groundplane is a process

where the drawing of equivalent circuits stands as a central task. First, it is necessary to add interface surfaces for the groundplane at its edges if these can not be trivially defined. Next, the network equations in a form where one of the interface nodes is declared as common, i.e. in the "$\boldsymbol{L}_S$" form, are written. The elements of the partial inductance matrix L_{Sij} can then always be found by a field analysis.

Nevertheless, the network equations in the "$\boldsymbol{L}_S$" form, together with the accompanying circuit schematic, are often not intuitive for the structure. It is then desirable to draw a new, more natural, equivalent network schematic with partial inductance elements L_{ij} and try to map them from the elements L_{Sij}. Often, all elements L_{ij} of the inductance matrix can then not be found. In that case, one needs to make assumptions either about the mutual coupling or the symmetry between the segments in the equivalent circuit in order to make the mapping possible. Usually, this involves the elimination of all mutual coupling except between current paths immediately across the dielectric separating the groundplane from the rest of the structure.

It is also common to disregard the groundplane segments by neglecting their self inductance (the groundplane is still included in the EM analysis). It then must be taken into account that the resulting network schematic is no longer accurate.

2.3.2.3 Differential interface pairs

The calculation of the network elements for a superconducting structure with multiple interfaces can sometimes be very simplified if the circuit is driven differentially, i.e. if there are interface-pairs that are symmetrically excited by the rest of the circuit attached to them. It is interesting to note that such an externally imposed symmetry does not always happen by intentional design. In fact, the most common occurrence of differential interface pairs (differential ports) is due to the lack of (other) connection between the circuits attached to them. This situation is shown in Figure 2.38, where a 2-port superconducting circuit, attached between two other (sub)circuits, is the only connection between them.

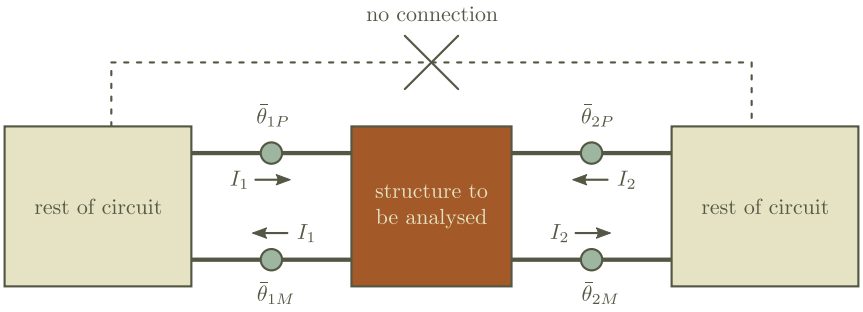

Figure 2.38. A superconducting subcircuit providing the only connection between different parts of the rest of the circuit.

Current conservation dictates that, in the case of Figure 2.38, the current going in the terminal $\bar{\theta}_{1P}$ must be equal to the current going out of the terminal $\bar{\theta}_{1M}$. The same is valid for the pair $\bar{\theta}_{2P}$ and $\bar{\theta}_{2M}$. Using this symmetry, the network equations for the structure in the middle of the diagram of Figure 2.38 condense to:

$$\begin{pmatrix} \varphi_1 \\ \varphi_2 \end{pmatrix} = \begin{pmatrix} \bar{\theta}_{1P} - \bar{\theta}_{1M} \\ \bar{\theta}_{2P} - \bar{\theta}_{2M} \end{pmatrix} = \frac{\Phi_0}{2\pi} \begin{pmatrix} L_{S11} & L_{S12} \\ L_{S12} & L_{S22} \end{pmatrix} \cdot \begin{pmatrix} I_1 \\ I_2 \end{pmatrix}$$

if the "standard" circuit notation with the flux angles φ as nodal variables is used. Note that the two-port circuit is described in a manner identical to a pair of coupled inductors (see Section 2.2.5.4). Similarly, for a structure that has n differential ports ($2n$ interface nodes, n unique pairs):

$$\begin{pmatrix} \varphi_1 \\ \varphi_2 \\ . \\ \varphi_n \end{pmatrix} = \begin{pmatrix} \bar{\theta}_{1P} - \bar{\theta}_{1M} \\ \bar{\theta}_{2P} - \bar{\theta}_{2M} \\ . \\ \bar{\theta}_{nP} - \bar{\theta}_{nM} \end{pmatrix} = \frac{\Phi_0}{2\pi} \begin{pmatrix} L_{S11} & L_{S12} & . & L_{S1n} \\ L_{S21} & L_{S22} & . & . \\ . & . & . & . \\ L_{Sn1} & L_{Sn2} & . & L_{Snn} \end{pmatrix} \cdot \begin{pmatrix} I_1 \\ I_2 \\ . \\ I_n \end{pmatrix}$$

The difference with the situation discussed previously is that in the case of a general network of $2n$ interfaces, the matrix $\boldsymbol{L}_S$ was of size $(2n-1)$x$(2n-1)$ with $\frac{(2n-1)^2+n}{2}$ independent elements ($\boldsymbol{L}_S$ is diagonally symmetric). If all the interfaces of the structure could be paired in differential ports, as given above, the size of $\boldsymbol{L}_S$ will be nxn with just $\frac{n(n+1)}{2}$ independent elements - this is a considerable reduction for most practical circuits where usually $n \geqslant 2$ (eg. for $n=2$ there is two times less unique elements).

Note that any structure with just two interfaces ($n=1$) automatically possesses nodal symmetry.

An instructive example of the use of differential symmetry is the T-segment with a groundplane from the previous section, Figure 2.36, if the other structures attached at each side between the adjacent segment and groundplane interfaces have no other connections. The pairs are then $\varphi_a = \bar{\theta}_1 - \bar{\theta}_3$ and $\varphi_b = \bar{\theta}_2 - \bar{\theta}_4$, while the currents are $I_1 = -I_3 = I_a$ and $I_2 = -I_4 = I_b$. Consequently,

$$\begin{pmatrix} \varphi_a \\ \varphi_b \end{pmatrix} = \frac{\Phi_0}{2\pi} \begin{pmatrix} L_{Saa} & L_{Sab} \\ L_{Sba} & L_{Sbb} \end{pmatrix} \cdot \begin{pmatrix} I_a \\ I_b \end{pmatrix} \tag{2.91}$$

where $L_{Sab} = L_{Sba}$. Again, the three elements of $\boldsymbol{L}_S$ above can be calculated from a field analysis by performing the usual superposition method of 2.2.4.3 and integrating the field variables over the whole volume of the structure. Comparing

with the equivalent network of Figure 2.37, it is seen that

$$L_{Saa} = L_{11} + L_{33} + L_C - 2 \cdot L_{13}$$

$$L_{Sbb} = L_{22} + L_{44} + L_C - 2 \cdot L_{24}$$

$$L_{Sab} = L_C$$

Declaring, arbitrarily, that

$$L_a = \frac{L_{11} + L_{33} - 2 \cdot L_{13}}{2} = \frac{L_{Saa} - L_C}{2}$$

$$L_b = \frac{L_{22} + L_{44} - 2 \cdot L_{24}}{2} = \frac{L_{Sbb} - L_C}{2}$$

the network schematic of Figure 2.39 is obtained. Note that all elements of the schematic of Figure 2.39 can be obtained from the elements of $\boldsymbol{L}_S$ appearing in equation 2.91. As there are just three parameters and no coupled inductors, any further network analysis is greatly simplified.

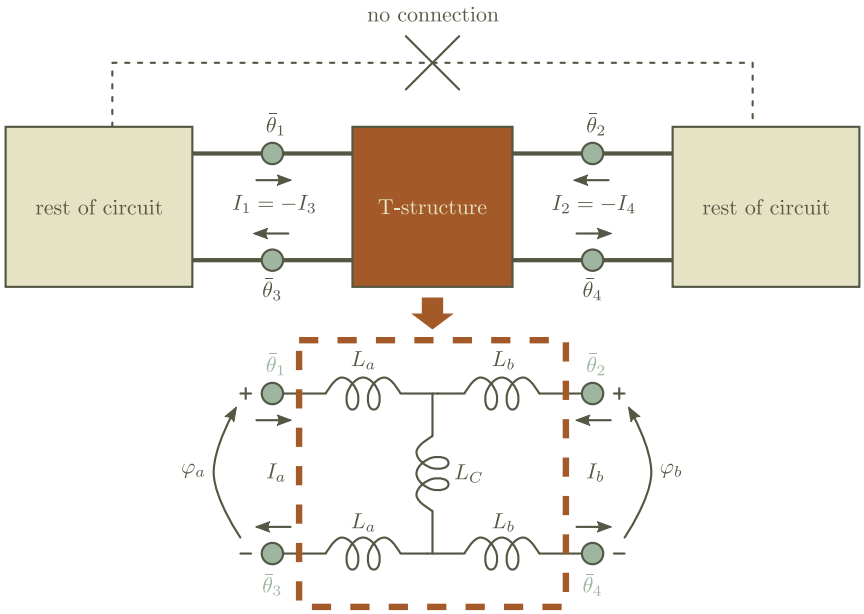

Figure 2.39. An equivalent network for the T-structure from Figure 2.36 in the case of differential port symmetry.

To make use of the differential nodal symmetry, it is also necessary that the EM field analysis program supports differential ports. Most of the automated field solvers can only work with common nodes however. The user chooses one of the interface surfaces of the structure to be the common node by declaring it as a "ground" node in the input data for the field solver. The circuit ports are then defined between each of the other interface nodes and the ground node. In a solver allowing the use of differential ports on the other hand, each port can be defined between arbitrary interface surfaces: a ground node is not necessary.

2.3.2.4 Structures with non-inductive elements

All the circuits in the previous subsections consisted of, basically, interconnected superconducting segments. Their equivalent networks were thus exclusively made of interconnected coupled inductor elements. Due to the linear properties of the Maxwell and London equations, mirrored in linear (φ, I) constitutive laws for the coupled inductive elements, the principle of superposition can be applied to such networks. It is thus possible to make equivalent network transformations by substitution of the base variables with linear combinations between them.

If a non-linear network element is present, for example a Josephson junction, making equivalent network transformations is difficult. Fortunately, the non-linear elements are all two-interface structures. They are thus nodal-symmetric and one can always define a differential port between the two interfaces. The correct procedure for a structure containing such elements is to define the two interface surfaces as an external differential port.

Often, the nonlinear single-port elements interrupt the current path along the length of a single segment: they are, effectively, in series with a (coupled) inductor in the equivalent schematic. It is then possible to simply remove the non-linear element from the structure and short the two interface terminals. The analysis of the structure and the calculation of the inductances in the equivalent network, including the one in series with the removed non-linear element, is next performed. At the end, the schematic is modified by returning the non-linear element back in series with the (coupled) inductor.

2.3.3 Example of inductance extraction

In this section, the calculation of the inductances for a moderately complex structure is given. All the methods of the previous sections: choosing the interfaces, drawing a "natural" equivalent network and finding the mapping of its elements to the ones of L_{Sij}, the use of a field solver with a 2D sheet approximation etc. are applied. First, it is necessary to briefly mention a few practical issues typically associated with EM field analysis.

2.3.3.1 $\boldsymbol{Y}$ and $\boldsymbol{Z}$ parameters

A typical field-solving algorithm does not directly provide the matrix $\boldsymbol{L}_S$ but instead gives the results of the field analysis in the (U, I) domain by providing the $\boldsymbol{Y}$ or the $\boldsymbol{Z}$ matrix, i.e. the Y or the Z parameters, at a given excitation frequency $\omega = 2\pi f$ (note that the solver usually needs a minimum frequency to be able to accurately model EM wave propagation). The two matrices are inverses of each other: $\boldsymbol{Y}^{-1} = \boldsymbol{Z}$. They relate the current and voltage vectors between the terminals of a network.

Were there no capacitances and resistances in the structure, then $\boldsymbol{Z} = j\omega \cdot \boldsymbol{L}_S$ where $j = \sqrt{-1}$ (remember that $U = \frac{\Phi_0}{2\pi} \cdot \frac{d\varphi}{\mathrm{dt}}$ which, in a frequency-harmonic network analysis typical for electrical networks, is equivalent to $U = \frac{\Phi_0}{2\pi} \cdot j\omega \cdot \varphi$). In the presence of capacitances (resistors are excluded in this thesis), which is always the case, the estimation of $\boldsymbol{L}_S$ from the Z or Y parameters needs more attention.

To see why, lets take a 2-port structure with differential symmetry and a partial inductance matrix $\boldsymbol{L}_S$. There will be capacitances present during the analysis, equivalently appearing across the ports, as shown in Figure 2.40.

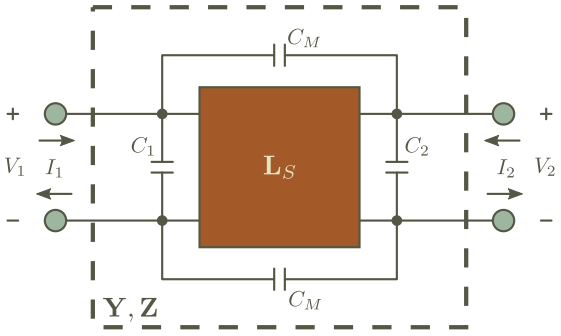

Figure 2.40. A symmetric two-port network with parasitic capacitances

The EM analysis is performed in the (U, I) domain while the choice of network equations is between the Z and Y version:

$$\begin{pmatrix} U_1 \\ U_2 \end{pmatrix} = \boldsymbol{Z} \cdot \begin{pmatrix} I_1 \\ I_2 \end{pmatrix}$$
$$\begin{pmatrix} I_1 \\ I_2 \end{pmatrix} = \boldsymbol{Y} \cdot \begin{pmatrix} U_1 \\ U_2 \end{pmatrix}$$

From an inspection of the schematic in Figure 2.40,

$$\begin{pmatrix} U_1 \\ U_2 \end{pmatrix} = j\,\omega \cdot \boldsymbol{L}_S \cdot \left[\begin{pmatrix} I_1 \\ I_2 \end{pmatrix} - j\,\omega \cdot \begin{pmatrix} C_1 + \frac{C_M}{2} & -\frac{C_M}{2} \\ -\frac{C_M}{2} & C_2 + \frac{C_M}{2} \end{pmatrix} \cdot \begin{pmatrix} U_1 \\ U_2 \end{pmatrix} \right]$$

which, writing the capacitance matrix above as $\boldsymbol{C}$, yields:

$$j\,\omega \cdot \boldsymbol{Y} = \boldsymbol{L}_S^{-1} - \omega^2 \cdot \boldsymbol{C}$$

Note that the elements of $\boldsymbol{L}_S^{-1}$ and $\boldsymbol{C}$ are both real and not a function of the frequency ω. This means that the Y parameters (the elements of $\boldsymbol{Y}$) should be imaginary, with their amplitudes depending on the frequency as $\frac{1}{\omega}(a - \omega^2)$ where a is some real constant. If the Y parameters have a significant real component, then the analysis has flaws since the real parts of the Y (or the Z) parameters are a result of resistive losses in the circuit. One should then, for example, look for errors in the material properties (lossy dielectrics). Small real components can exist at high frequencies where they represent EM radiation losses.

To obtain the elements of $\boldsymbol{L}_S$, the Y parameters should be calculated for a number of frequencies. Multiplying the Y parameters with $j\,\omega$ and looking at the "flat" part of the remaining ω dependence, the elements of $\boldsymbol{L}_S^{-1}$ are found. The part that, eventually, depends as ω^2 is due to the elements of $\boldsymbol{C}$. In practice, if the elements of $j\,\omega \cdot \boldsymbol{Y}$ change with frequency then the analysis is modified to include increasingly lower frequencies until the elements no longer depend on ω. Inverting the matrix $j\omega \cdot \boldsymbol{Y}$ calculated at those frequencies then directly yields $\boldsymbol{L}_S$. Since $\boldsymbol{Y}^{-1} = \boldsymbol{Z}$, one can also directly calculate $\boldsymbol{L}_S = \frac{1}{j \cdot \omega} \cdot \boldsymbol{Z}$ if the solver provides $\boldsymbol{Z}$ simultaneously. Note that the same frequency analysis can be performed on $\boldsymbol{Z}$: divide the Z parameters with $j\,\omega$ and look for the frequency span where they are constant with frequency.

The basic message of this method is that at lower frequencies the capacitance matrix can be neglected. It is however necessary to confirm that assumption by plotting the Y or Z parameters as a function of the frequency. The method has a more general use however. Every time the circuit elements of a linear equivalent

network are calculated and they depend on the frequency, then either the analysis is not valid or the equivalent network does not model all circuit phenomena correctly. Another source of frequency-dependent elements is wave dispersion when there are other modes of wave propagation alongside the TEM mode - this rarely occurs in standard superconducting electronics.

2.3.3.2 Circuit layout and interfaces

Both the physical structure as well as its equivalent network are given in Figure 2.41. Also all interfaces used in the analysis are indicated.

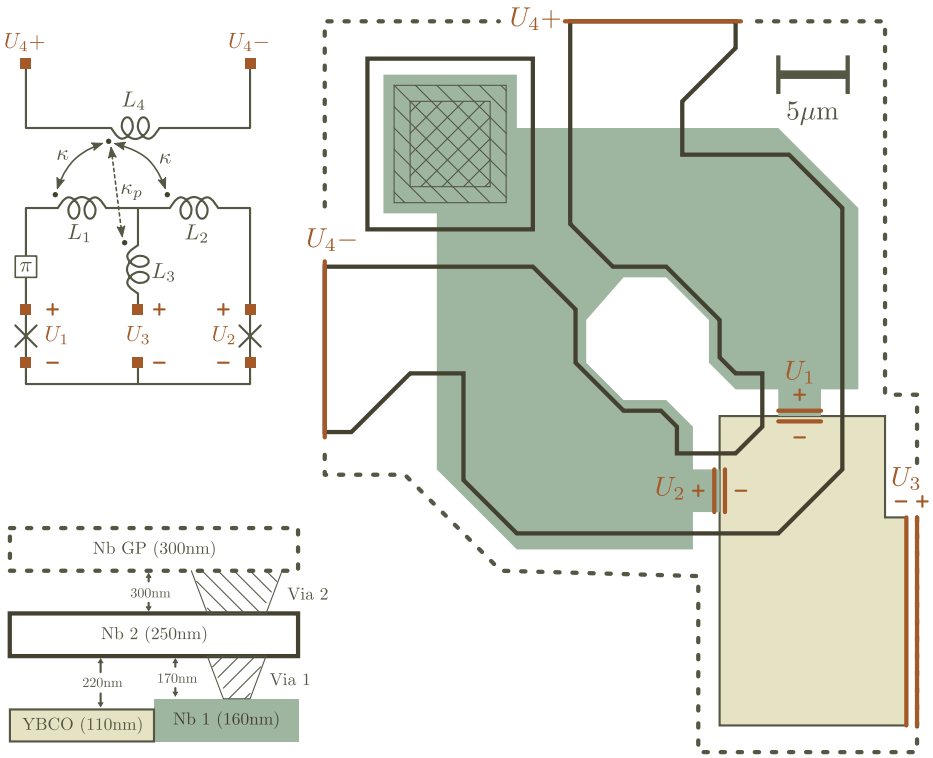

Figure 2.41. The physical layout of a inductively modulated π-loop, its equivalent schematic and the parameters of the used layers. The interface lines (2D sheet model used - hence surfaces become lines) as used later are also drawn. A ramp-type junction appears along every contact line between the YBCO and Nb1 layers. The overlap of the Nb1 on top of the YBCO layer is not shown. The groundplane layer continues on the top and left edges towards other circuits.

The drawing depicts an inductively modulated π-loop, the basic building block of the circuits later described in Chapter 5 and 6. The loop consists of two junctions positioned between the differential terminals U_1 and U_2, two inductive π-loop arms L_1 and L_2 coupled to the (single-turn) modulating coil L_4 and, at the end, a symmetrical output terminal denoted as U_3.

The output terminal has a small but significant series inductance L_3. It is defined as the inductance along the sum of two current paths: a) from the stacked vias to U_{3+} through the groundplane and b) the common path of the two junction currents to U_{3-} through the YBCO layer. Both these paths are bundled together in the element L_3. A high L_3 is detrimental for the properties of the modulated π-loop (Chapter 6) and one should therefore keep it as low as possible.

The coupling coefficient between the modulation coil and the loop's arms is κ. A parasitic modulation with a small coupling coefficient κ_p exists between the modulation coil and the output series inductor L_3. The presence of the groundplane makes the mutual coupling between the other elements negligible.

In the application of this circuit, the modulation coil L_4 is driven by a current source. Hence, its self-inductance value is not important: only the mutual coupling inductances $L_{14} = \kappa\sqrt{L_1 \cdot L_4}$, $L_{24} = \kappa\ \sqrt{L_2 \cdot L_4}$ and $L_{34} = \kappa_p\ \sqrt{L_3 \cdot L_4}$ are of significance for the circuit. This fact makes the positioning of the terminals $U_{4\pm}$ on the Nb2 layer largely arbitrary as long as they are on the outside of the Nb1 structure (the flux coupled from L_4 to the other elements stays the same).

For this structure, all terminals can be paired in differential ports, four in total: U_1, U_2, U_3 and U_4.

2.3.3.3 Equivalent schematics

After removing the junctions and the π-shift element, the schematic on the left in Figure 2.42 remains. Since the value of L_4 is not important for this analysis, the network can be split in two cases where the branch containing L_4 is removed: one case where the terminal U_4 is open ($I_4 = 0$) and one case where it is shorted ($U_4 = 0$). The equivalence is given in Figure 2.42 on the right.

The network when $I_4 = 0$ is trivial (nothing is coupled into the elements), while the network for $U_4 = 0$ is obtained after solving

$$\frac{U_4}{j\,\omega} = L_4\,I_4 - \kappa\,\sqrt{L_2\,L_4}\,I_2 + \kappa\,\sqrt{L_1\,L_4}\,I_1 - \kappa_p\,\sqrt{L_3\,L_4}\,I_3 = 0$$

for I_4 and replacing it in the remaining network equations for the loop. The two schematics on the right of Figure 2.42 have now only three differential terminals.

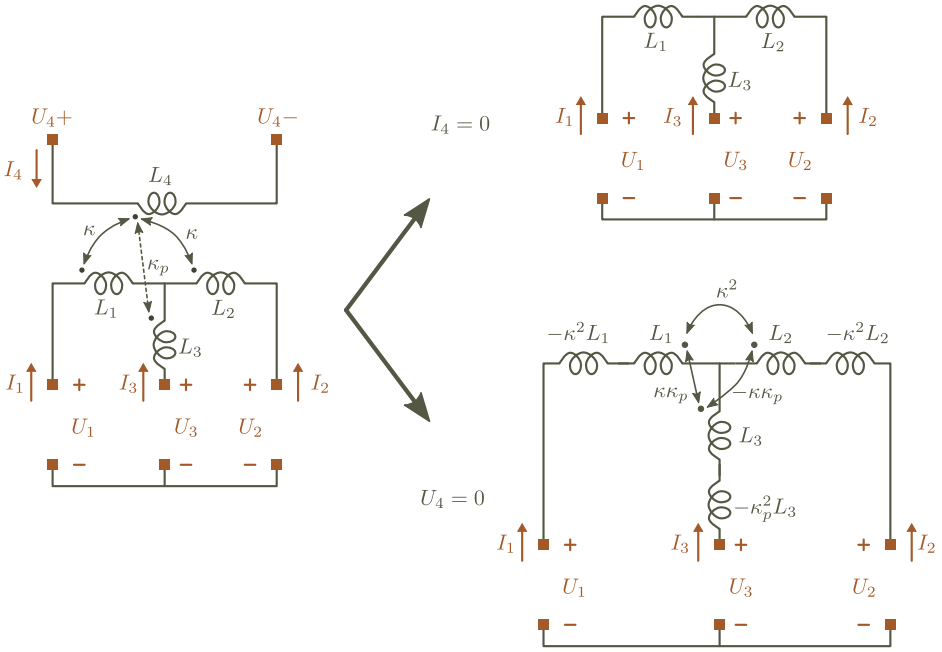

Figure 2.42. The equivalent schematic of the inductively modulated π-loop on the left and the equivalent schematics in the two cases where L_4 is left open (top) and short (bottom).

The EM wave analysis program will provide either the Y (or Z) parameters of the simulated structure, connecting the $\boldsymbol{U} = (U_1 U_2 U_3)^T$ and $\boldsymbol{I} = (I_1 I_2 I_3)^T$ vectors as $\boldsymbol{I} = \boldsymbol{Y} \cdot \boldsymbol{U}$ ($\boldsymbol{U} = \boldsymbol{Z} \cdot \boldsymbol{I}$). Indeed, they may also be calculated as a function of the frequency, although this may not be necessary as shown further below.

There will be two sets of these parameters, one set for the case $I_4 = 0$ and one set for the case $U_4 = 0$. These are obtained by manually changing the structure's layout and simulating the two cases separately. First, one of the terminals of port U_4 is deleted and left unconnected (floating), while the other is shorted to the general ground node (case $I_4 = 0$). The structure is then simulated, providing the $\boldsymbol{Y}$ and $\boldsymbol{Z}$ matrices. Next, the unconnected terminal of U_4 is also shorted to ground (case $U_4 = 0$) and the simulation is performed again, yielding the second set of $\boldsymbol{Y}$ and $\boldsymbol{Z}$.

Circuit analysis shows that, for the two cases separately, the following holds

- $I_4 = 0$

$$L_1 = -\frac{1}{j\omega}\cdot\left(\frac{Y_{23}}{Y_{13}Y_{12}+Y_{12}Y_{23}+Y_{13}Y_{23}}\right)$$

$$L_2 = -\frac{1}{j\omega}\cdot\left(\frac{Y_{13}}{Y_{13}Y_{12}+Y_{12}Y_{23}+Y_{13}Y_{23}}\right) \tag{2.92}$$

$$L_3 = -\frac{1}{j\omega}\cdot\left(\frac{Y_{12}}{Y_{13}Y_{12}+Y_{12}Y_{23}+Y_{13}Y_{23}}\right)$$

- $U_4 = 0$ and assuming $L_1 = L_2 = L$

$$(1-2\kappa^2)\,L - 2\,\kappa\,\kappa_p\sqrt{L\,L_3} = -\frac{1}{j\omega}\cdot\left(\frac{Y_{23}}{Y_{13}Y_{12}+Y_{12}Y_{23}+Y_{13}Y_{23}}\right)$$

$$(1-2\kappa^2)\,L + 2\,\kappa\,\kappa_p\sqrt{L\,L_3} = -\frac{1}{j\omega}\cdot\left(\frac{Y_{13}}{Y_{13}Y_{12}+Y_{12}Y_{23}+Y_{13}Y_{23}}\right) \tag{2.93}$$

$$(1-\kappa_p^2)L_3 + \kappa^2\,L = -\frac{1}{j\omega}\cdot\left(\frac{Y_{12}}{Y_{13}Y_{12}+Y_{12}Y_{23}+Y_{13}Y_{23}}\right)$$

Note that the assumption $L_1 = L_2 = L$ made in the latter case is not necessary for a solvable $L \longleftrightarrow Y$ mapping but it simplifies the equations considerably. This approximation is however very reasonable, looking at the symmetry of the circuit. Furthermore, since L_1 and L_2 were individually calculated in the former case, the approximation can be easily checked.

From the above equations, one can now calculate all unknown elements of the equivalent network in Figure 2.41 except for L_4. The calculation of this element will be performed in parallel with the estimation of the capacitive components in the next subsection.

2.3.3.4 EM simulation with sonnet em

The single 2D sheet approximation for the superconducting layers will be used in this EM simulation. A short analysis is performed in order to find whether the approximation is justified for the structure from Figure 2.41.

The groundplane is 300nm thick so that, taking $\lambda_{L,\mathrm{Nb}} \approx 100\mathrm{nm}$, it is well suitable for a single-sheet replacement ($\frac{d}{\lambda_L} = 3$). Further, the groundplane shielding current, when excited by a current in the Nb2 layer (element L_4), flows in a circular fashion on the groundplane bottom surface and closes outside the structure

beyond which the groundplane extends. If shielding currents in the groundplane are otherwise excited then the two connections of the groundplane to the rest of the circuit, through the vias and the terminal U_3, provide a symmetric return path. Hence, there will be no shielding-return currents on the top surface of the groundplane and, in the spirit of section 2.3.1 and Appendix B, the groundplane can be safely replaced with a single 2D sheet of surface inductance $L_S = \mu_0 \cdot \lambda_L \cdot \coth\left(\frac{d}{\lambda_L}\right)$.

From the rest of the presentation in the those sections, it can be concluded that since none of the rest of the segments are excited by sources of the same direction from both sides, the 2D approximation for them is also valid. Note that the segment in the Nb2 layer, element L_4, is sandwiched between two layers and one may imagine the possibility for the field at both surfaces of Nb2 to be of the same magnitude and direction. This is however not the case since the layers enclosing L_4 are, more or less, passive structures that will always try to respond by strengthening the antisymmetric field created by the current through Nb2 - a field of the same direction at the top and bottom surfaces of Nb2 is then unlikely.

The single 2D sheet surface inductances of the layers are given in Table 2.1 below.

	YBCO	Nb1	Nb2	GP
d [nm]	110	160	250	300
λ_L [nm]	200	100	100	100
L_S [pH]	0.502	0.136	0.127	0.126

Table 2.1. The single-2D-sheet surface inductance of the thin film layers implementing the modulated π-loop circuit.

To find whether the capacitive contribution to the Y and Z parameters is negligible and, if so, at which frequencies, the following procedure is performed. The ports U_1 and U_2 are removed and their terminals pairs are shorted ($U_1 = U_2 = 0$), while port U_3 is left open ($I_3 = 0$) by removing U_{3-} and connecting the interface line of the terminal U_{3+} to the general ground node (so that the whole circuit is not at a "floating" potential). Only the differential port U_4 remains, resulting in a schematic as given on the left in Figure 2.43. The circuit is, in essence, a thin-film transformer with a shorted secondary. A simple circuit analysis then results in

$$Y_{44} = j\,\omega \cdot C_4 + \frac{1}{j\,\omega \cdot L_4\,(1 - 2\kappa^2)}$$

where C_4 is the equivalent capacitance "seen" between the terminals of port U_4. Note that the Nb2 segment between the terminals of U_4 has the highest capacitance of all other segments since it is sandwiched between two layers and has a

rather big area. Consequently, if the capacitive contributions can be neglected for this worst-case port, the same is valid for the rest of the ports.

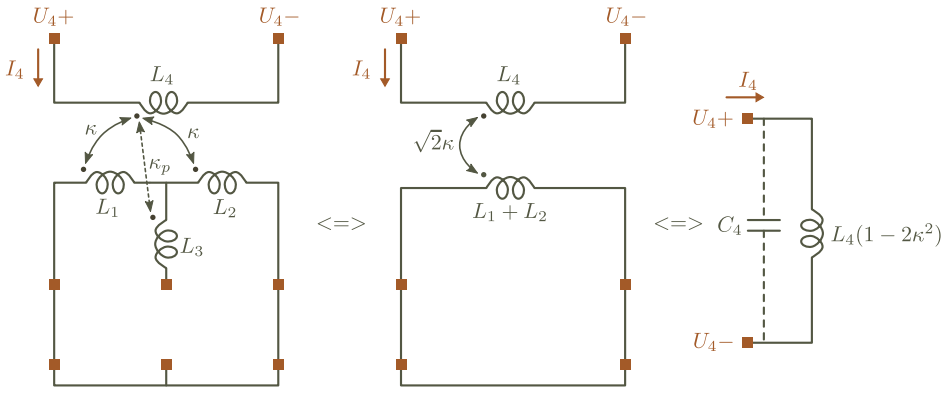

Figure 2.43. The equivalence steps when obtaining the schematic of the modulated π-loop for shorted junction ports $U_2 = U_1 = 0$ and open output port $I_3 = 0$.

Using Table 2.1, the material properties of the various metal layers are defined (sonnet allows to define a metal layer with a non-zero surface inductance parameter and zero resistivity - a superconductor thus) as well as the properties of the intervening dielectric (SiO_2). The relative permittivity of the dielectric is set to SiO_2, $\varepsilon_r \approx 5.4$, while the magnetic permeability is that of vacuum $\mu_r = 1$.

An EM analysis of this single port structure as a function of frequency yields a single Y_{44} parameter. The result is tabulated in Table 2.2.

frequency [GHz]	3	5	10	30	50	100	200	300	400	500
$\mathrm{Im}\left\{\frac{1}{\omega \cdot Y_{44}}\right\} \times 10^{12}$	2.61	2.61	2.61	2.61	2.62	2.69	2.9	4.5	7.8	10.3

Table 2.2. The imaginary component of $\frac{1}{\omega} \cdot \frac{1}{Y_{44}}$ against frequency. At low frequencies, it is equal to $L_4(1 - 2\kappa^2)$.

From the shown values and f-dependence, the analysis frequency can be fixed at 10GHz while the value of $L_4(1 - 2\kappa^2)$ is calculated to be 2.61pH.

The original structure is next set, returning the ports U_1, U_2 and U_3 and the two sets of Y parameters are obtained with two separate analyses at 10GHz: one for $U_4 = 0$ and one for $I_4 = 0$. Using the equations 2.92 and 2.93, all the elements can be found: L_1, L_2, L_3, κ and κ_p. Then the element L_4 can also calculated by using the values of κ and $L_4(1 - 2\kappa^2)$. The procedure is repeated for a few values of the YBCO penetration depth, resulting in the plot of Figure 2.44.

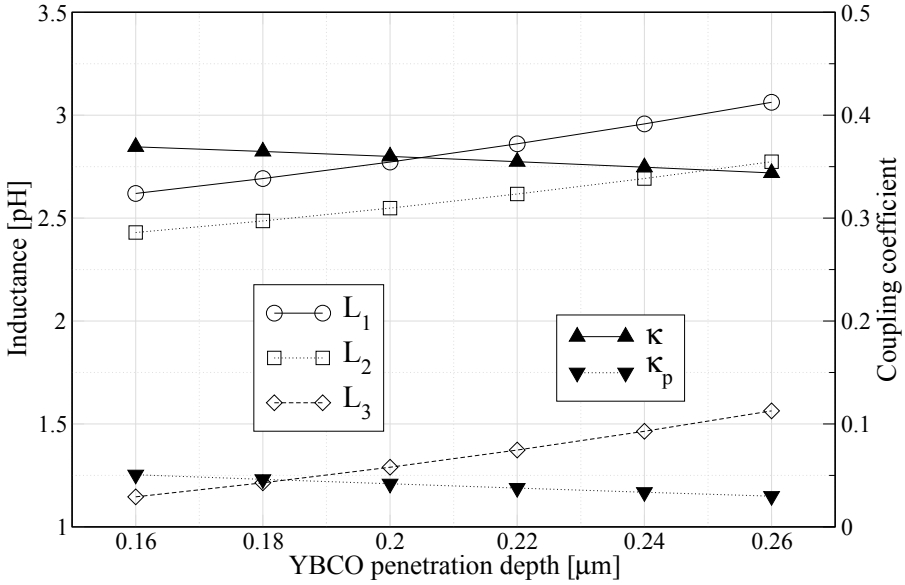

Figure 2.44. The results of the inductance calculation for the elements of the network from Figure 2.41. It was used that $\lambda_{L,\mathrm{Nb}} = 100\mathrm{nm}$.

The results let see that L_1 and L_2 are not the same but differ by about 10%. The difference is a result of the slight physical asymmetry in the structure from Figure 2.41. It is more pronounced for higher YBCO penetration depths. Extrapolating towards $\lambda_{L,\mathrm{YBCO}} = 0$, the difference between L_1 and L_2 shrinks to a few percent. As the penetration depth and the inductance are proportional, it can be concluded that the arms of the π-loop have a significant asymmetrical contribution in their inductance originating in the YBCO segment. To make L_1 and L_2 more equal, the structure should be altered in such a way as to influence the path between the junctions and the terminal U_{3-} that goes through the YBCO segment. For example, one can stretch the terminals of port U_3, together with the nearby corner in the YBCO segment, closer towards the first junction. L_1 and L_2 can be made almost identical in this way.

The element L_3, on the other hand, is even more dependent on the YBCO film. To reduce L_3, it is thus necessary to reduce the inductance of the YBCO segment. Note that the groundplane is vertically far removed for the YBCO segment: there is $d = 220\mathrm{nm} + 300\mathrm{nm} = 520\mathrm{nm}$ thick dielectric between the Nb3 groundplane and the area of the YBCO segment not already covered by the L_4 modulation coil. As

a consequence, the YBCO segment has a high self-inductance ($L \sim d$). To reduce it, one can cover the "free" area of the YBCO segment with a Nb2 structure as completely as possible. This new structure would also need to be locally connected to the groundplane with a via. It then acts as a new groundplane that is much closer to the YBCO segment, reducing its self-inductance. Adding such a structure reduces the value of L_3 by about a quarter.

Chapter 3
SFQ circuits with π-loops

While the previous Chapter introduced the basic operation principles behind superconducting digital circuits, analysed from the perspective of the Josephson Network model, the implementation of the same circuits with a focus on π-loop RSFQ devices is discussed in this part of the text. First, in section 3.1, the hybrid YBCO-Nb thin-film process technology that enables manufacturing of π-shift elements is described. The Josephson junction structures are initially presented, followed by a description of the whole process stack that includes the wiring and groundplane layers. The devices that were designed for the purpose of testing the assumed benefits of π-shift devices over traditional RSFQ are then shown in section 3.2, followed by the integrated circuits (ICs) implementing them. At the end, the results of the measurements are discussed.

3.1 Hybrid YBCO-Nb manufacturing technology

In order to implement a digital superconducting circuit as a thin-film IC, it is necessary that the manufacturing technology supports at least 3 dielectric-separated superconducting thin-film layers: one layer for the first junction electrode, another layer for the second electrode while the last is reserved for the groundplane. The junction electrode layers are also used to implement the superconducting segments (wiring) between junctions. Additionally, for the purpose of routing of the circuit connections, there must be the possibility to locally connect the superconducting layers through the isolation between them by using "via" structures etched in the dielectric.

Although it is possible to combine the groundplane with one of the electrode layers, such circuits can not reach a complexity of more than two junctions in a series connection and at the same time have a groundplane coverage over the whole current path.

As mentioned in the previous Chapter, a groundplane layer is necessary in order to prevent inductive coupling between *all* segments in the circuit, reducing the number of mutual-inductance elements in the equivalent network schematic to just the ones that are needed by design. At the same time, a groundplane layer provides a small degree of shielding from environmental magnetic fields, to which superconducting circuits are very sensitive.

Process technologies for implementation of VLSI (Very Large Scale of Integration) superconducting circuits based on metallic thin films, for instance RSFQ microprocessors [35], have many separate superconducting layers, up to nine for the most advanced process so far [43]. Other manufacturing processes on the other hand, focus on sub-μm structured junctions with large J_C, suitable for ultra high-speed applications [44].

In contrast to the implementation technologies for digital circuits with metallic superconductors, the area of high temperature thin-film devices shows only modest progress. Although the cryogenic requirements for high-T_c electronics are significantly reduced, making them attractive for digital circuits, the same feature would also place an upper bound on the thermally activated error events since $k_B\,T$ is higher. More significantly however, junctions of sufficiently high $I_C\,R_N$ product are very difficult to implement reliably, exhibiting spreads in the I_C's of the manufactured junctions that are too large for the requirements of complex digital designs. Nevertheless, analog sensors and other low junction-count applications draw relatively high benefit from high-T_c thin-film technologies.

There are several specific properties to the implementation of high-T_c thin-film circuits. The materials themselves, contrary to elemental metallic low-T_c superconductors, have complex crystal unit cells, see Figure 3.1. To grow thin high-T_c films, one must use an epitaxial technique: matching of the crystal lattice parameters with the substrate material, tight control of the environmental gas pressure and composition, high substrate temperatures (>650°C) as well as the need of precise stoichiometric transfer of the multi-element source material from the target to the substrate. Such growth methods require specialised apparatus, for instance dedicated PLD (Pulsed Laser Deposition), plasma sputter or other PVD (Physical Vapour Deposition) equipment to avoid cross-contamination with other materials while offering optimized superconducting and morphological properties of the grown films.

Further, the large number of elements in the composition of high temperature superconductors increases the probability of forming undesired phases and other substances during the film growth. These manifest as crystal defects and impurities embedded in the film, generally to the detriment of the superconducting properties. Also note that multi-layer high-T_c circuits require the alternate stacking of superconductor-isolator thin films, where the growth of each subsequent layer combination must also be performed epitaxially. A low density of surface defects is important in that regard.

Another problem is that many of the high-T_c materials have strongly anisotropic superconducting properties. Hence, the coupling through thin barriers with other superconductors, necessary to obtain Josephson junctions, has a preferable current direction with respect to the substrate crystal orientation. This direction unfortunately lies in parallel to the surface of the substrate when

the film is optimally grown, prohibiting the implementation of simple planar top-surface-contact junctions. One must then either use a non-optimal growth orientation of the high-T_c thin film or various edge-contact methods, decreasing process robustness. In this text for instance, the contact area is a ramped surface etched at the sides of a YBCO segment under an angle with the substrate normal, as shown in section 3.1.1, Figure 3.2.

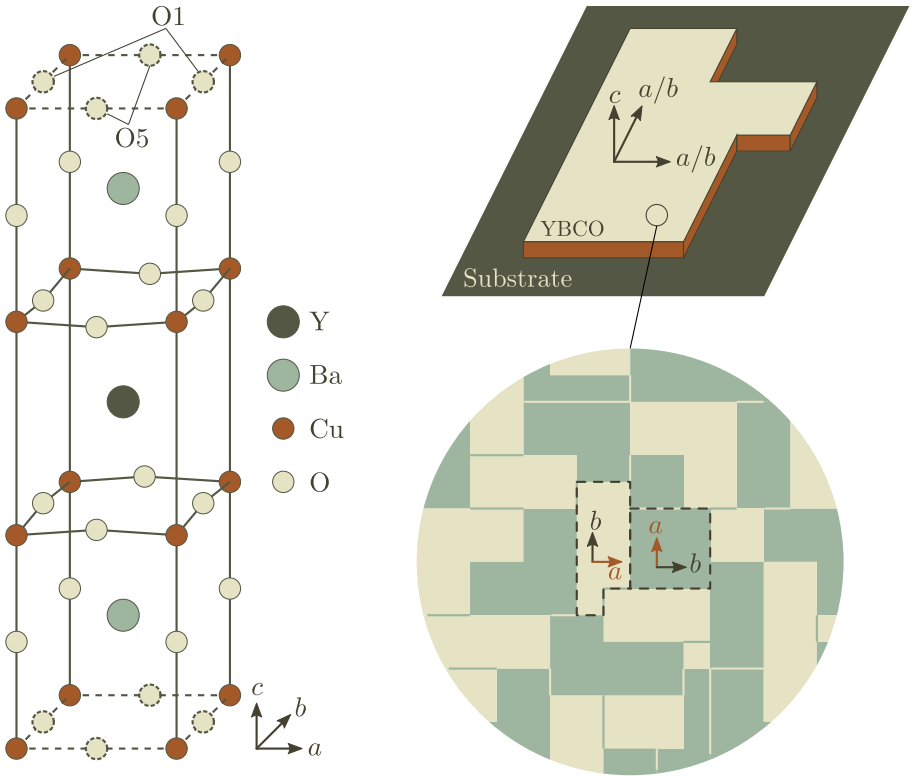

Figure 3.1. The crystal unit cell of $YBa_2Cu_3O_{7-\delta}$ is shown on the left, together with the two oxygen sites of variable occupancy O1 and O5. For optimally doped YBCO, about $\frac{9}{10}$ of the O1 sites are occupied while almost all O5 sites are vacant. This also creates the slight difference in the a and b axis of the unit cell. The diagram on the right depicts the phenomenon of "twinning": crystal domains, orthogonally orientated in the $a-b$ plane, are randomly alternating throughout the thin film. The domains are much smaller than the dimensions of the YBCO circuit structures on the sample, thus averaging-out the differences between the a and b axes on the macroscopic scale. All YBCO films used in this text are twinned. An "untwinned" film, where the domains are larger than the typical size of the YBCO structures on the sample, can be grown on specially prepared substrates [36].

At the end, the growth of the junction barrier and second electrode (usually called counter-electrode) must be performed in an epitaxial manner as well. The surface roughness and defect/impurity level of the first junction interface is of high importance. This step is the most challenging, severely limiting the advancement in the manufacturing technology of high-T_c circuits with high junction counts.

Today, there are few commercially available products that comprise of high-T_c electronic components, mostly magnetic sensors and RF/microwave passive devices. If necessary, Josephson junctions are implemented as grain boundary or step-edge devices that offer the best properties but at the cost of a restricted junction placement and number count.

The manufacturing technology presented in this text is a combination between the low-T_c and high-T_c methods: one of the junction electrodes is a metallic Nb thin film while the other electrode is YBCO. The barrier layer is metallic, consisting of a $\sim$20nm gold layer. The isolation between the superconducting layers is a sputtered SiO_2 film, while the substrate material is either $SrTiO_3$ (STO) or Al_2O_3 (sapphire), depending on the sample series. There is only one YBCO layer and two or three Nb layers used as counterelectrode, wiring and groundplane layer. Some of the circuits also have a second Au layer used to implement resistor elements. The use of the high-T_c material is exclusively for the purpose of exploiting its unconventional order parameter, as shown in the previous Chapter. The high T_c of YBCO is an undesired property in this case, increasing the measurement difficulties as shown later in Chapter 4.

In the following sections, the YBCO-Nb manufacturing technology is explained, beginning with the junction and π-shift structures and then proceeding to the whole multi-layer process stack.

3.1.1 Josephson junctions and π-shift elements

As mentioned above, the crystal orientation of an optimally grown YBCO film is such that the preferred coupling directions, labeled with a/b in Figure 3.1, lie in parallel to the substrate. The c crystal direction is, with optimal growth conditions, normal to the surface of the film and substrate. If one makes a junction in the c-axis direction, then the barrier layer would be required to be a couple of nm thick due to the low amplitude of the order parameter along that direction. If the barrier layer is thicker, coupling will be weak and consequently the J_C of the c-axis junctions will be very low. Even when a YBCO film is of high crystal regularity, the required c-axis barrier thickness is of a value similar to the typical roughness of the top YBCO surface, creating shorts and other inhomogeneities when the top junction electrode is deposited over the barrier. On the other hand, the order parameter has approximately 4 times greater amplitude in the other crystal directions, relaxing the requirements for the barrier thickness if a contact is to be made along the a/b axis [5].

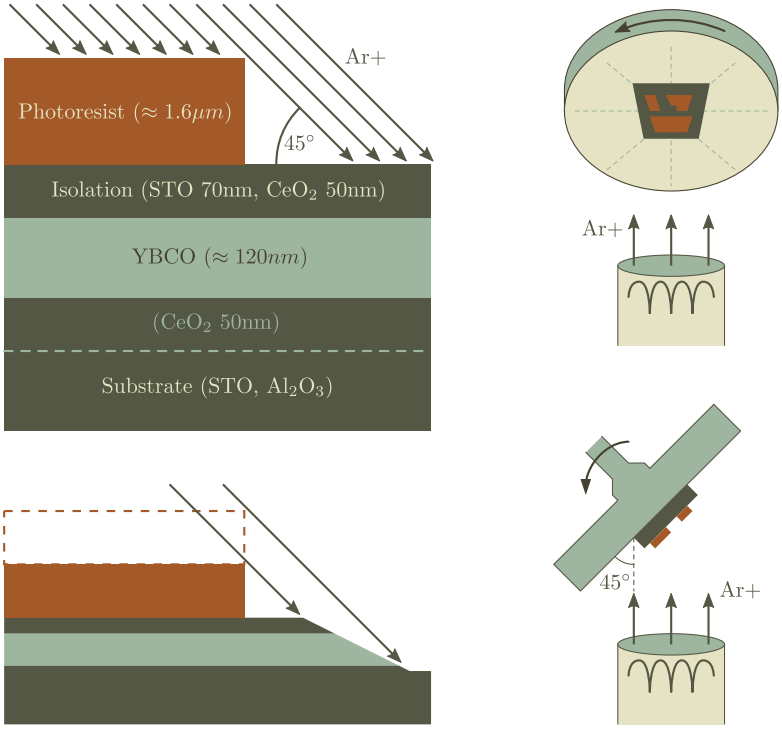

Figure 3.2. Preparation of the ramp-type edge surfaces with an Ar+ ion gun. A diagram of the etch process is shown on the left, together with the ramp profile obtained at a constant angle of incidence of the Ar+ ions. The drawings on the right depict the sample rotation method that creates a uniform ramp surface at each edge of the structured YBCO film. The slope profile is however more complex in the case of sample rotation, see Chapter 4.

Figure 3.2 depicts the process of creating the ramp-type side contact [45] used in the YBCO-Nb process technology. A ∼120nm thick YBCO layer is epitaxially grown on the substrate, together with a top isolation layer for protection. The latter is either STO or CeO_2, depending on the sample series, of 70nm and 50nm thickness respectively. A photoresist structure is lithographically patterned on the bilayer and the sample is placed in the path of a beam of Ar ions, accelerated to 500V. The ion beam etches both the unprotected superconductor-isolator bilayer as well as the top surface of the resist and is switched off after the exposed YBCO layer is completely removed. Since the ion beam and the surface normal are positioned under an angle, the profile of the edges of the YBCO structure, shown also in Figure 3.2, takes the form of a ramped surface. The final angle is $\arctan\left(\frac{\tan\beta}{1+x}\right)$

with β the ion beam angle of incidence and x the ratio between the resist and thin film etch rates [36]. With a standard photoresist and $\beta = 45°$, the resulting ramp surface angle is about 20°.

The effective angle is however lower since the sample is rotated for the purpose of creating ramped surfaces at every edge of the YBCO segment. The sample rotation effectively modulates the angle of incidence in the range $[\beta, -\beta]$ on the sample surface and partially exposes the "shadow" region, as well as the photoresist wall, creating a secondary ramp surface (not shown in Figure 3.2). More details about this method can be found in the next Chapter. Sample rotation provides a uniform ramp surface profile for each edge of the YBCO structures on the sample.

After dissolving the remaining photoresist, the sample is then exposed to a second Ar+ gun step, but under a 90° incidence of the beam. This has the purpose of removing the amorphous YBCO layer on the sloped surface resulting from ion impact damage, as well as any photoresist remains hardened with material redeposited during the initial ramp etch step. Without breaking the vacuum, i.e. *in-situ*, the sample is then prepared for the PLD deposition of a thin YBCO interlayer [5] that has the purpose of recovering the crystal structure at the ramp surface area lost during the previous process steps. At the end, after an anneal step in 1bar O_2 atmosphere, between 20nm and 30nm of gold is *in-situ* deposited as a barrier with PLD.

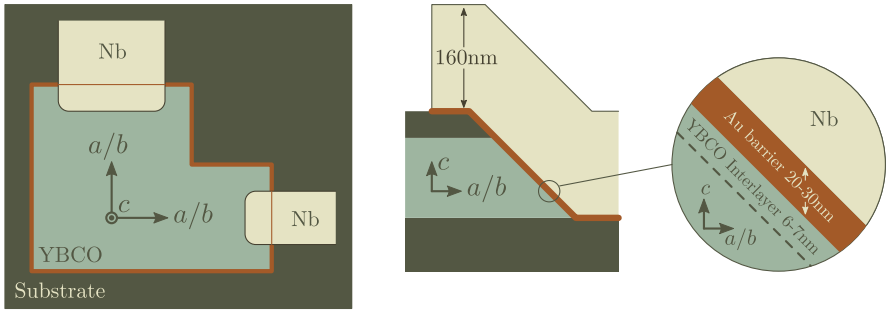

Figure 3.3. Top and side view of a YBCO structure with ramp-type junctions. Note that the YBCO interlayer thickness must be low (<7nm) so that it does not become superconducting on the substrate surface, as it will otherwise short any series-connected junctions through the current path underneath their common Nb electrode.

The Nb counterelectrode layer of 160nm thickness is then sputtered on the sample and patterned with either standard lift-off or a reactive SF_6 plasma etch, the latter used only for the sample series πChip2.2X (see Chapter 4 for more details on the SF_6 process step). The final step is the etching (with either Ar RF plasma or Ar ion gun) of the unnecessary interlayer/barrier film on the bare parts of the

substrate using the just deposited Nb as a hard mask. At the end, the final ramp-type junction structure, depicted in Figure 3.3, is obtained. The YBCO segments are in the beginning patterned such that their edges are length-wise aligned with the a/b crystal directions of the YBCO film along which the order parameter has a maximum amplitude. The J_C of the ramp-type junctions will then be the highest.

The above process results in an approximate critical current density of 10μA per micrometer of junction length. In Tables 3.1, 3.2 and 3.3, the technical parameters of the main processing steps are given. More details can be found in [8], [3], [37] [5], [21], [36] and [7].

	Base Layer*	Base Layer*	Interlayer	Barrier
material	YBCO	STO	YBCO	Au
deposition T	780 C	740 C	780 C	100 C
Background P Deposition P	$<10^{-6}$ mbar 0.25 mbar O_2	←*in-situ* 0.1 mbar O_2	$<10^{-6}$ mbar 0.25 mbar O_2	$<10^{-6}$ mbar 0.22 mbar Ar
Fluency Spot Size Preablation Pulse Rate d to substrate	$1.5\,\mathrm{J/cm^2}$ $5-6\,\mathrm{mm^2}$ 2min@10Hz 4Hz $55-60$ mm	$1.5\,\mathrm{J/cm^2}$ $\sim 6\,\mathrm{mm^2}$ 2min@10Hz 4Hz ~ 60 mm	$1.5\,\mathrm{J/cm^2}$ $5-6\,\mathrm{mm^2}$ 2min@10Hz 1Hz $55-60$ mm	$3.5-4\,\mathrm{J/cm^2}$ $2.5-3\,\mathrm{mm^2}$ 2min@10Hz 4Hz $40-45$ mm
Deposition rate Layer thickness	0.1 nm/pulse $110-130$ nm	0.09 nm/pulse 70 nm	0.1 nm/pulse $6-7$ nm	0.05 nm/pulse $20-30$ nm
Annealing 1 bar O_2	/	15min @600C 50min @450C	15min @600C 30min @450C	/

Table 3.1. PLD parameters for the thin films used to define the ramp-type Josephson junctions in the πChip samples.
* Base layers for the series πChip2.2X, grown by a thermal co-evaporation technique, are acquired from a commercial supplier.

Other remarks:
a) The substrate for the PLD-grown base layers is a 0.5×1cm polished STO sample.
b) The commercially acquired base layers are grown on a 1×1cm r-cut sapphire substrate with a 50nm CeO_2 buffer layer. The isolation layer is then 50nm CeO_2 instead of STO.
c) The laser spot is shaped as 7 equidistant 5:1 rectangles at the target.
d) Background pressure is read out at substrate T=200C.
e) T is slowly ramped up, first in vacuum to 450C and then in process P to 780C.
f) The YBCO/STO base layer is annealed in one step.
g) A KrF excimer laser is used, wavelength 248nm and pulse duration of ∼15ns

	YBCO ramp & SiO_2 via etch	Ramp clean (hard)	Ramp clean (soft)
Background P Etch P	$<2 \cdot 10^{-6}$ mbar $5 \cdot 10^{-3}$ mbar Ar	$<10^{-6}$ mbar $3 \cdot 10^{-3}$ mbar Ar	←*in-situ* $3 \cdot 10^{-3}$ mbar Ar
Beam voltage	500 V	500 V	50 V
Beam current	15 mA	10 mA	5 mA
Beam incidence	45°	90°	90°
Beam on/off	8: 12 sec	8: 12 sec	8: 12 sec
Sample rotation	∼11 rot./8 sec .	None	None
Material etched per pulse (8 sec .)	YBCO/STO ∼2nm CeO_2 >9nm SiO_2 ∼4nm	/	/
Number of pulses	different	4	10

Table 3.2. Parameters for the Ar ion gun etching steps, all done with a 3cm Kaufmann source. The discharge and acceleration voltages are 40V and 100V. The distance between the source and the sample is about 30cm. The hard and soft clean steps are sequentially applied, in that order, before the YBCO interlayer is deposited with PLD *in-situ*.

	Au barrier* (DC sputter)	Sample clean (RF sputter etch)	Niobium (DC Sputter)
Background P Process P	$2 \cdot 10^{-6}$ mbar Ar 20 mbar Ar	$\sim 10^{-7}$ mbar Ar $13 \cdot 10^{-3}$ mbar Ar	←*in-situ* $7.3 \cdot 10^{-3}$ mbar Ar
Temperature	100 C	Ambient	Ambient
Power	30 W	50 W	250 W
Voltage	480V	265 V	300 V
Target diameter	∼5cm	/	∼10cm
d target to sample	∼15cm	/	∼10cm
Deposition/etch rate	21 nm/min	6nm Au (1min)	80 nm/min

Table 3.3. Parameters of the sputtering process steps. Sample cleaning and Niobium deposition are done sequentially *in-situ*. Two pre-sputter steps (4 min) are performed before the sample is exposed to the Nb flux. The DC sputtering of gold, replacing the PLD Au barrier deposition, is also done *in-situ* after the PLD deposition and anneal of the YBCO interlayer. Both DC sputter steps are magnetron-assisted.

* The Au sputter source was not available for πChip samples.

As indicated in the previous Chapter, the anisotropic superconductivity of YBCO can be utilized to create a π-shift element by using a segment where the current path experiences a 90° turn in the $a-b$ crystal plane of YBCO film. The simplest structure that satisfies the requirement is a square YBCO segment with junctions contacting neighbouring sides. The structure is drawn to be aligned with the crystal lattice, additionally offering at the interfaces an a/b oriented ramped surface where junctions can be formed if necessary. Figure 3.4 depicts a π-shift SQUID loop manufactured using such a structure, together with two junctions and bias/sense terminals.

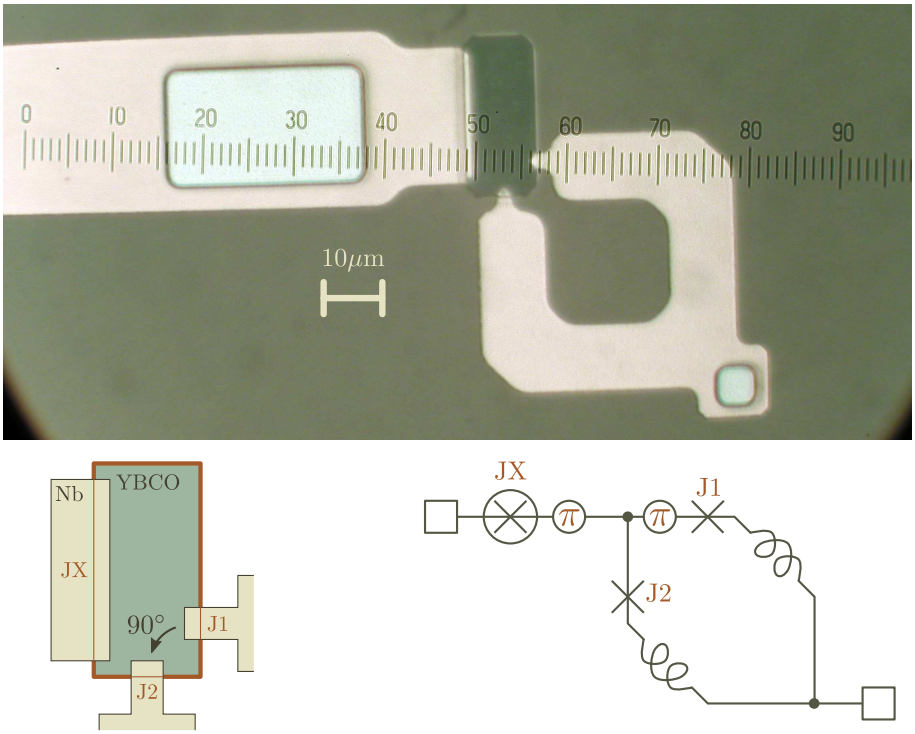

Figure 3.4. A microphoto of a πSQUID loop manufactured with the hybrid YBCO/Nb technology, taken just before the deposition of the second Nb layer (top); A drawing showing a detail of the π-shift structure from the photo with the nearby junctions (bottom left) and a schematic of the circuit (bottom right). In the middle a dark rectangle of YBCO is visible, the white-pink structures are Nb1 counterelectrode segments while the two bright rectangles are vias etched in the transparent SiO_2 isolation layer. The junction labeled with JX, necessary to connect the YBCO segment with the rest of the circuit, is much larger than the two SQUID junctions J1, J2 and can be considered to be just a short-circuit.

For circuits with a large number of junctions and many superconducting segments, the last implemented both in the YBCO and Nb1 layers, there is a need for a reference direction when determining the position of the π-shift elements in the schematic. The convention followed in this text is:

- when designing the schematic of a circuit, all π-shift elements must be placed in series with a junction either directly or through an equivalent circuit transformation
- when the layout (physical design) of a circuit is being drawn on the basis of a schematic, then a junction in series with a π-shift will be drawn such that its length is aligned with the vertical (y) axis of the substrate. Junctions without a series π-shift element will be drawn aligned with the horizontal (x) axis.

The essence of the second rule above is that a π-shift will always exist in a loop connecting one junction of vertical and one junction of horizontal orientation. This elegantly removes the need of manually checking each loop in the layout for eventual π-shifting structures. Note that rotating the whole physical design by 90° does not affect the circuit since only the relative orientation of the elements matters. Hence, one can also choose a convention where the roles of the axes are reversed. As long as the same convention is applied to the whole circuit, the choice which junction direction carries a π-shift element in series does not matter.

The above convention is very important to be well adhered to, as a missing π-element or a surprise appearance of one in a loop will cause a malfunction. Additionally, problems of both missing and unwanted π's are difficult to track down in a large circuit.

At the end, it is important to mention that this "geometric" convention is only necessary for circuits where the π-shift is implemented by using a material exhibiting anisotropic superconductivity, i.e. a d-wave order parameter symmetry. Other technologies implementing π-shifts do not need a geometric convention.

3.1.2 Process Stack

After the junction devices are defined on the IC sample, the manufacturing proceeds with the "back-end" part of the process: deposition and structuring of the SiO_2 and the second Nb layer (Nb2), the latter used for wiring/groundplane, while the former as an isolation dielectric. The isolation dielectric is deposited by a standard RF sputtering method. The via connections are structured with an argon ion gun and with the same parameters as for the YBCO etching of the ramped surface, see Table 3.2. The 45° angle of incidence as well as the rotation of the sample produces vias through the SiO_2 dielectric that have gently sloping edges, avoiding eventual step-coverage problems when the top Nb2 layer is deposited.

All structures are defined with a standard photolithographic process. The photoresist is used as an etch mask and as a (negative) lift-off stencil for structuring

the SiO_2 and Nb2 layers respectively. In Figure 3.5, the complete process stack is depicted, along with the thicknesses of the superconducting and isolation layers.

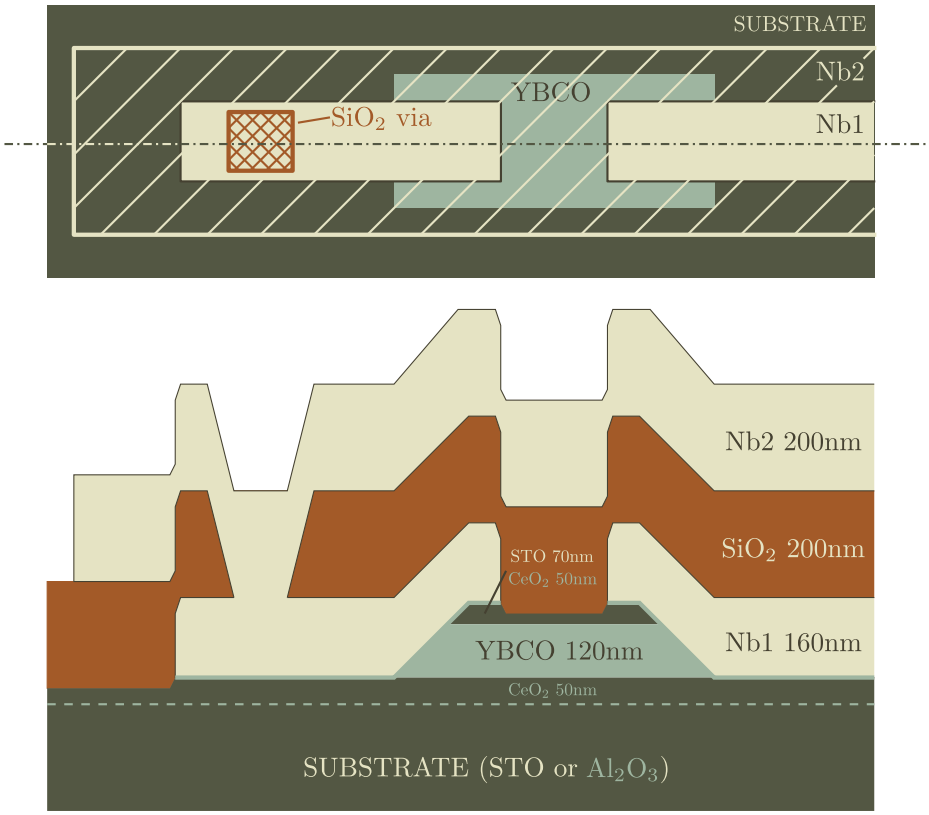

Figure 3.5. Cross-section of a simple structure with a groundplane (process stack).

3.2 πChip2: a π-shift RSFQ IC

The first RSFQ device using a π-shift loop, implementing a simple functional digital block (a toggle flip-flop), was built using the Nb-YBCO technology described in the previous section [8] [3]. After a successful measurement result of this initial πChip1 design, a second and more complex IC was created, the πChip2. Together with a number of circuits based on variations of the same simple digital block, the IC also comprises a special block with the purpose of more thoroughly testing the influence of the π-shift elements in RSFQ circuits. This section contains both the implementation details of the πCHIP2 IC as well as the obtained measurement results.

First, in the next section, the basic cells (building blocks) used to construct the π-shift RSFQ circuits are documented. After that, Section 3.2.2 describes the functional digital circuits as implemented on the πChip2, together with the layout of the IC. At the end, section 3.2.3 summarizes the results of the measurements of the manufactured πChip2 samples.

3.2.1 Basic π-shift RSFQ cells

In this section, the basic cells used in the πChip2 IC design are presented. The values of the circuit parameters in the schematic of each circuit are also given, as well as a drawing of the structure as it should appear on the IC (as a part of a larger circuit). In all drawings presented in this section, the groundplane layer Nb2 covers the whole structure and is hence omitted for clarity. All circuits have been designed by the RSFQ design group at the University of Ilmenau in Germany.

The I_C of each junction is calculated by multiplying its length L with the critical current density $J_{C,\mathrm{nominal}} = 12\,\frac{\mu\mathrm{A}}{\mu\mathrm{m}}$ that, on the other hand, was experimentally obtained from $I-V$ curves of test junctions previously fabricated. From the same measurements, the value of $I_C R_N \approx 250\mu\mathrm{V}$ at $T = 4.2\mathrm{K}$ was also found. The normal resistance R'_N of a junction per unit length can then be calculated to be $\approx \frac{I_C R_N}{J_C} = 20.8\,\Omega \cdot \mu\mathrm{m}$. In the absence of experimental data about the capacitance of the junctions, a guess based on a simple parallel-plate model was used, yielding $C \approx 0.253\,\frac{\mathrm{pF}}{\mu\mathrm{m}}$. The three values above fully determine the RCSJ model of each junction if its length L is known.

Values for the partial inductances in the πChip2 circuits were calculated by using a thin-film superconductor inductance calculation program (LMeter), accepting the geometry of the segment(s) and the properties of the superconducting films (e.g. the London penetration depths) as inputs while providing the partial inductances of the segments as output. In the description of each cell, the interfaces used to define the partial inductance segments are also drawn. The calibration of the calculation program was based on experimental data from the initial πChip1 design. The sheet inductances $L_{\square,\mathrm{YBCO}} = 2\,\frac{\mathrm{pH}}{\mathrm{sq.}}$ and $L_{\square,\mathrm{Nb1}} = 0.55\,\frac{\mathrm{pH}}{\mathrm{sq.}}$ were experimentally obtained from direct-injection SQUID measurements and then used as input parameters in the design of the circuits found on the πChip2.

For all parameters given above, a sample temperature of 4.2K is assumed.

3.2.1.1 Josephson Transmission Line (JTL)

Figure 3.6 depicts the schematic of the basic JTL cell as used in the functional circuits, indicating the values of the I_C of the junctions as well as the values of the inductances between them. Note that the junctions are positioned along the same direction, resulting in no π-shift element in the equivalent schematic.

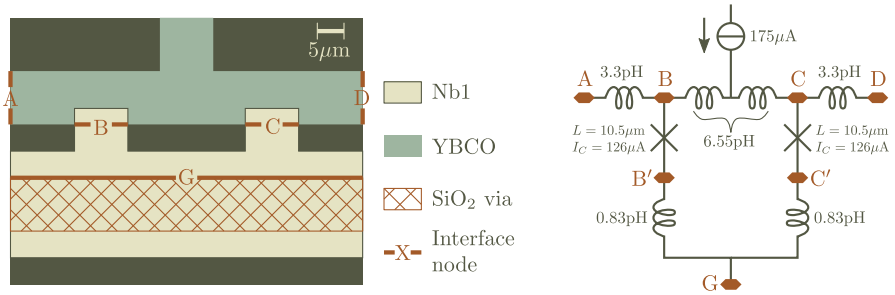

Figure 3.6. The layout and the equivalent schematic of the JTL cell, together with the nominal values of the circuit elements.

3.2.1.2 Confluence buffer

This circuit's output signal *out* is triggered whenever there is an SFQ pulse at any of the two inputs *in1* and *in2*. The bias current makes sure that there is at least one junction critically biased in each of the two branches forming the 4-junction loop at the bottom and available for triggering by a pulse incoming at the nearest input terminal. Consecutive pulses at just one of the input terminals will alternatively trigger the junctions closest to it, isolating the other input from any influence while always causing the output junction to switch and produce a pulse.

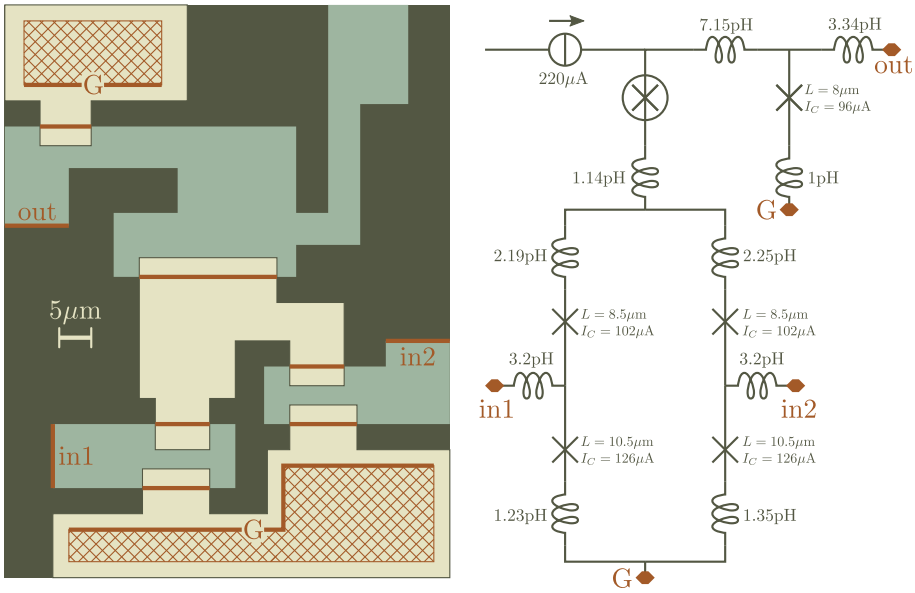

Figure 3.7. Layout and equivalent schematic of the confluence buffer. All interfaces are indicated in the layout, but only the in/out and ground terminals are labeled.

3.2.1.3 Pulse splitter

Performing the opposite function to the confluence buffer, the pulse splitter cell reproduces the pulses arriving at the input terminal *in* simultaneously at each of the output terminals *out1* and *out2*. This circuit is in essence a JTL but with a branched (double) output and optimized for simultaneous triggering of the output junctions.

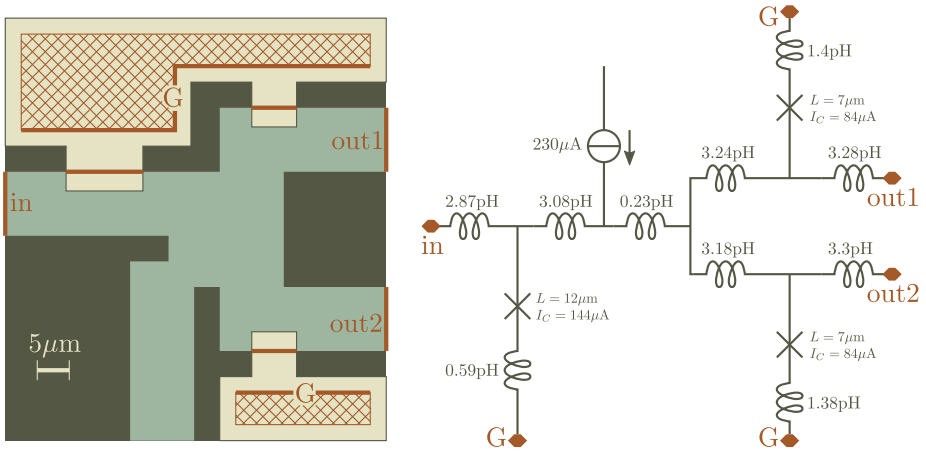

Figure 3.8. Layout and equivalent schematic of the pulse splitter cell.

3.2.1.4 π-shift T flip-flop

The memory of this flip-flop cell is based on the π-shift principle presented in Chapter 2, albeit with a modification in order to achieve a more practical circuit where the input and output terminals are not adjacent. The storage unit here is designed as two π-loops galvanically coupled by a shared inductive segment. The values of the elements are chosen such that only states carrying the opposite flux in the loops, i.e. approximately $(\frac{\Phi_0}{2}, -\frac{\Phi_0}{2})$ and $(-\frac{\Phi_0}{2}, \frac{\Phi_0}{2})$, are allowed while the other two states with aligned magnetic flux directions are energetically unfavourable.

Any pulses arriving at the input T will alter the state of the double π-loop between the two antiferromagnetically aligned flux configurations. The junctions then trigger in pairs, one from each π-loop, as the state of the TFF is changed back and forth with every input pulse (hence the name *flip-flop*). As a result, every second input pulse will be reproduced at the output Q. Note that the complementary output ($\bar{Q}$), positioned at the opposite side of the double π-loop, is not used in the circuit from Figure 3.9 and is instead terminated by a passive circuit in order to symmetrically load the flip-flop's output sections.

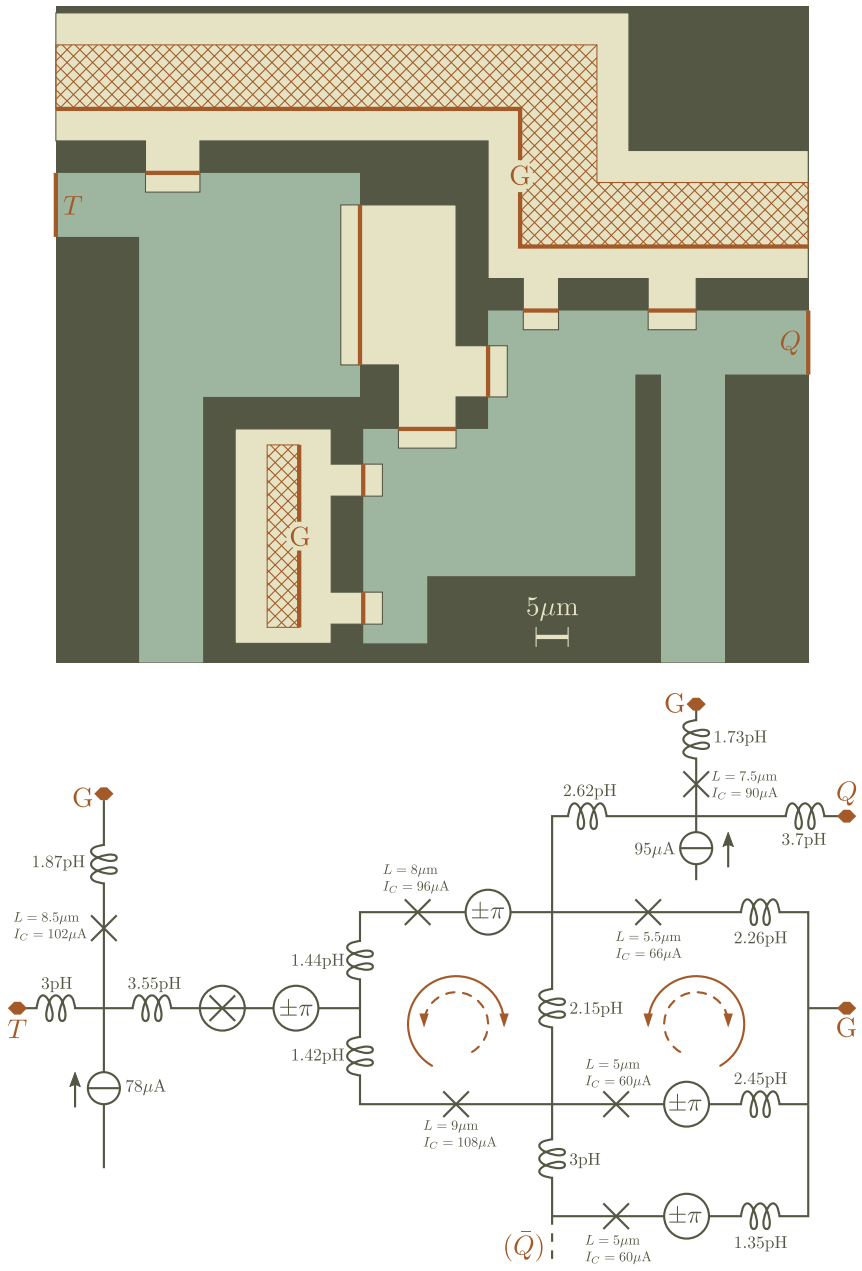

Figure 3.9. The layout and the equivalent schematic of the π-shift TFF used in the πChip2 integrated circuit design. The two coupled π-loops are indicated in the schematic.

3.2.1.5 DC-SFQ converter

This bistable cell is always placed at the input interface of any RSFQ circuit, converting a current with a triangular or sawtooth waveform at its input to a sequence of SFQ pulses at its output. When the input current reaches a value above a given threshold, the state of the loop indicated in the schematic becomes unstable (the curvature $\frac{\mathrm{d}^2 W}{\mathrm{d}\varphi_x^2} > 0$ in the potential landscape) and a transition is triggered towards the next stable state. Effectively, a flux quantum enters the loop through the switching action of the junction in the middle and an SFQ pulse is created that propagates towards the output terminal of the cell. When the input current then returns below another threshold (there is a hysteresis built in), a reverse transition is initiated where the series input junction switches this time. The circuit then goes back to the original state. A π-loop is not used in this cell.

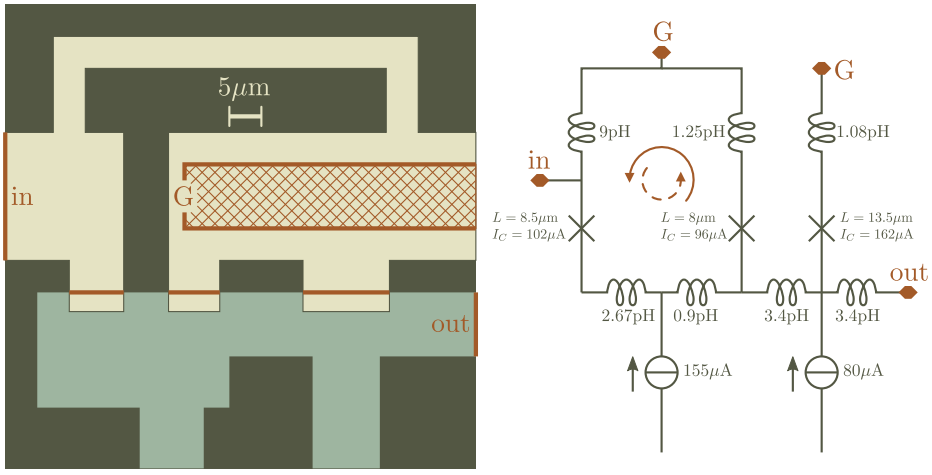

Figure 3.10. The layout and circuit schematic of a DC-SFQ converter.

3.2.1.6 SFQ-DC converter

The conversion of an SFQ pulse to an externally measurable signal is the function of an SFQ-DC converter cell. Opposite to its counterpart, this cell is always placed on the output interface of RSFQ circuits. The task that the SFQ-DC cell performs is however more difficult: converting a picosecond long pulse to a voltage level that can be accessed by room temperature measurement equipment.

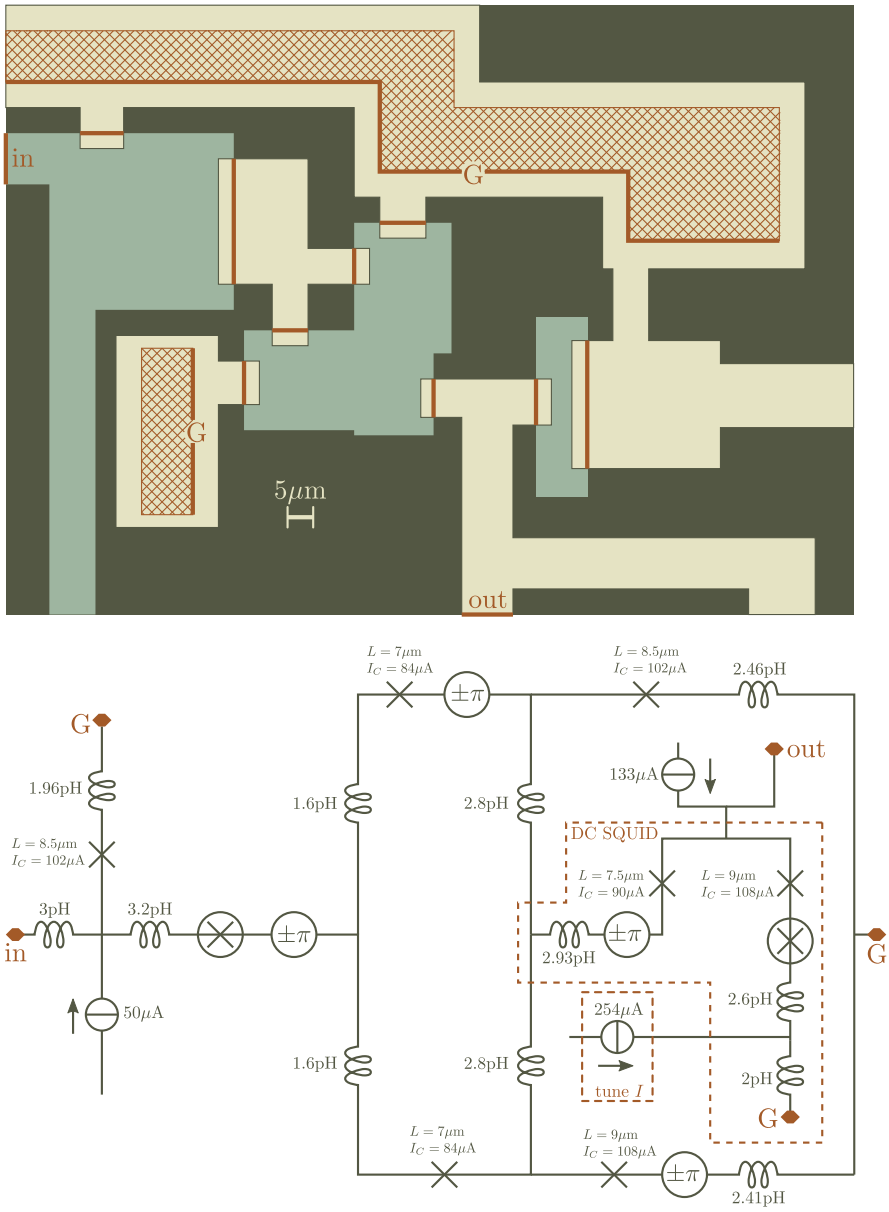

Figure 3.11. An SFQ-DC converter built using a π-loop based TFF. Although the right arm of the DC SQUID should contain two π-shift elements in series (has two vertical junctions), they are omitted since their sum is 2π. An extra current source is used to fine-tune the operating point of the DC SQUID during measurements.

Functionally, the cell is a bistable oscillator that can parametrically be controlled to switch between a static (DC) and an oscillatory state. During the former, no signal is produced while the latter results in an average DC voltage at the output, similar to a Josephson junction's voltage state. The oscillatory circuit in this case is a DC SQUID, its position indicated in the drawing. Every SFQ pulse at the input switches the output DC SQUID circuit between the two states. After filtering the high-frequency Josephson oscillations at the cell output, there remains a square-wave voltage signal with transitions controlled by the input SFQ pulses .

The implementation of the above concept is based on the double loop π-shift TFF, Figure 3.9, where the shared inductor is centrally "tapped" by one arm of the DC SQUID circuit. As the states of the TFF change, so does the equivalent flux angle between the center-tap and the ground terminal (from approximately $+\frac{\pi}{2}$ to $-\frac{\pi}{2}$) across which the DC SQUID is connected. The values of the bias current(s) and circuit parameters are chosen such that this change triggers the DC SQUID to transition between the static and the oscillatory state. As the incoming SFQ pulses at the terminal *in* change the TFF state back and forth, so does the voltage state of the DC SQUID, sensed at the terminal *out*, alternate between on and off. Hence, every level transition in the measured (and filtered) output voltage of the SFQ-DC cell corresponds to a single SFQ pulse that arrived at its input.

3.2.2 πChip2 circuits and IC layout

The πChip2 contains various circuits in multiple variants as well as other test structures. These are summarized in Table 3.4. Each of the circuits and structures will be presented with a brief description, followed by the layout of the IC and the placement of each block on the sample.

Circuit type	# of copies on chip	Purpose
DC/JTL/DC	4	RSFQ DC testing
DC/JTL/TFF/JTL/DC	1	RSFQ DC testing
Pattern generator	1	RSFQ bit-error rate test
Direct injection DC SQUID	2	measurement of $L_\square$ for Nb1 and YBCO layers
YBCO bridge structure	1	measurement of YBCO T_c
Josephson junctions	4 (10 πChip2.2X)	measurement of I/V curves

Table 3.4. A summary of the contents of the πChip2 samples

3.2.2.1 RSFQ test circuits

These blocks are designed with two objectives in mind

- check the basic functionality of simple π-shift based RSFQ circuits by low-speed testing (i.e. "DC" tests)

- test the hypothesis that a π-shift loop used as a storage unit offers better immunity against noise and external influence by measuring the bit-error rate of a circuit at a high speed

In Figure 3.12, the general block diagram of the first group of circuits is given. The sequence of SFQ-driven events is also depicted for the purpose of illustrating the functionality of the circuit.

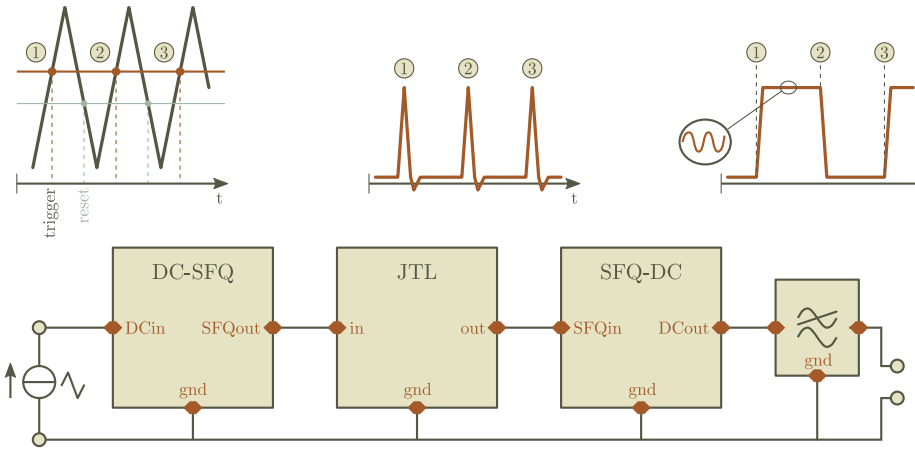

Figure 3.12. A block diagram of a DC/JTL/DC circuit, together with a summary of the relevant signal processing steps. SFQ pulses are created at every rising slope of the input current after crossing a threshold and are then transported via the JTL to a SFQ-DC cell that changes the level of the output voltage for each incoming pulse. At the end, the frequency of the output signal is two times lower than the input signal. Note that the filter element at the end of the signal chain does not need to be explicitly present as the measurement leads and other parasitics act as a low-pass filters at Josephson frequencies.

The block diagram of a DC-JTL-TFF-JTL-DC cell is similar to the one depicted in Figure 3.12. The difference is that a T flip-flop cell is inserted in the middle, additionally dividing the SFQ pulse rate by two. The operation of the other cells being the same, the end result is that the frequency of the output signal is 4 times lower than the input signal.

A "pattern generator" circuit for the purposes of testing the bit-error rates has also been designed. The block diagram is shown in Figure 3.13 and a timing diagram in Figure 3.14.

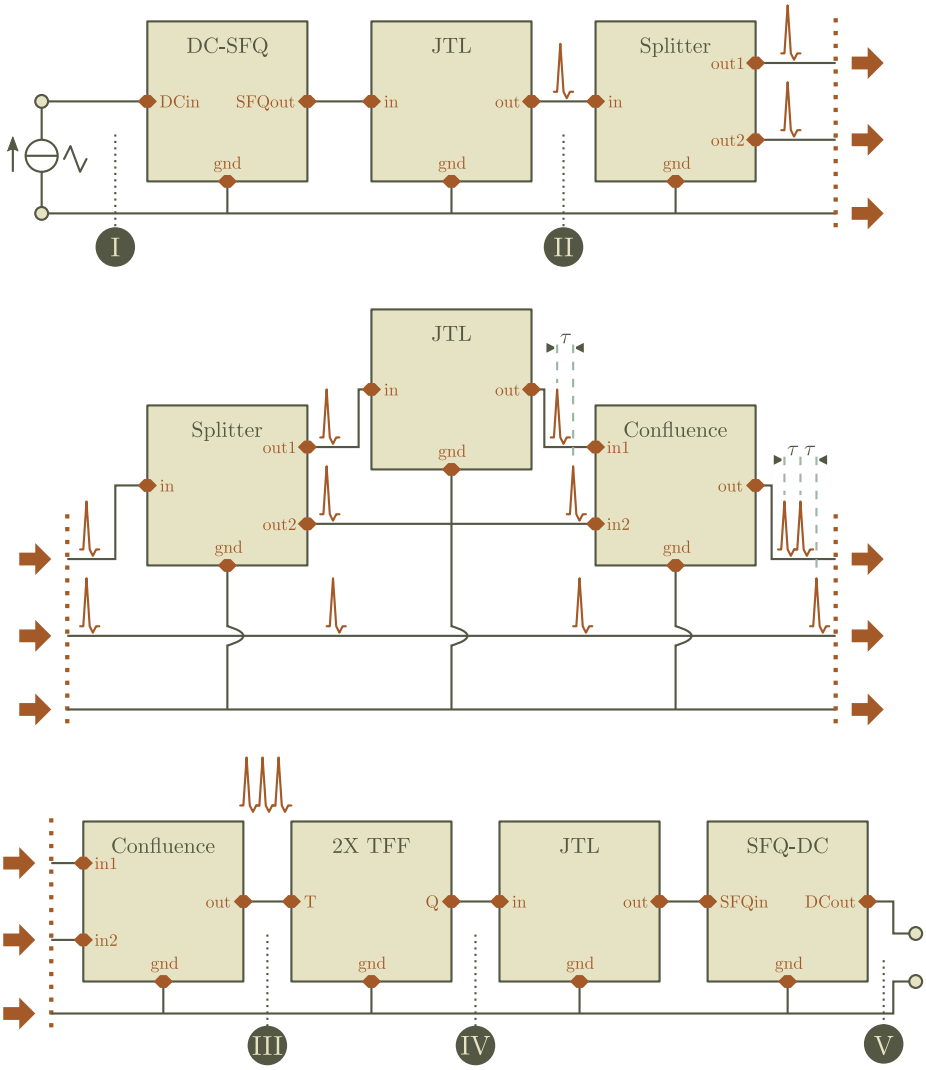

Figure 3.13. The block diagram of the "pattern generator" circuit. The series-parallel connection of the splitter and the confluence buffer circuits has the purpose to create three closely spaced SFQ pulses for each input pulse, as depicted in the drawing. The propagation delays τ of the cells, in the 10s of picoseconds, are used to define the pulse-to-pulse distance. The cell named "2X TFF" is a series connection of two TFF cells.

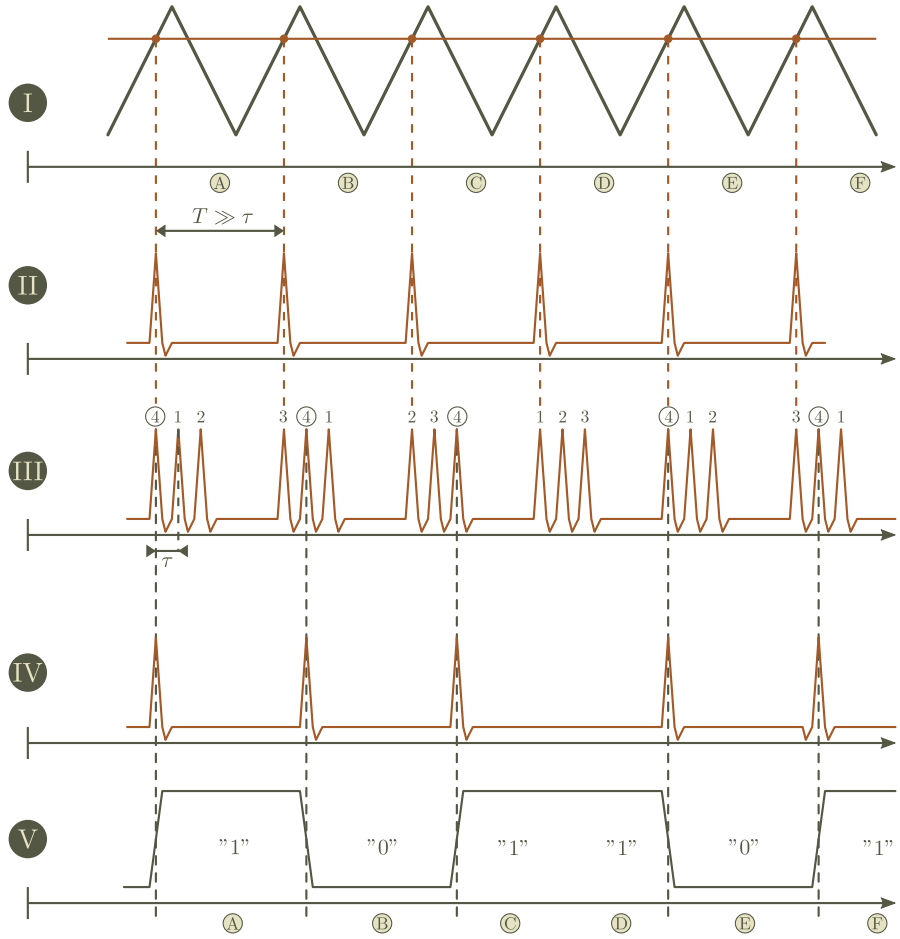

Figure 3.14. A timing diagram of the block from Figure 3.13. Each input pulse is first transformed in a sequence of 3 closely spaced pulses. The two series connected TFF cells (2X TFF) then divide the pulse frequency by 4, effectively letting every fourth pulse pass. The net non-integer (3/4) pulse count then results in a pattern of "zeros" and "ones" generated at the SFQ-DC output, as shown in the diagram. Only a part of the full pattern sequence is shown. The full pattern is 8 bits long: 10110100 and keeps repeating as long as the input signal is present. Since the rate of the 3-pulse train is in the 10s of GHz, the two T flip-flops in the block operate close to the "full RSFQ" frequency even though the input signal is typically a waveform of just a few kHz.

The repeating 8-bit binary pattern that this cell produces can be fed to a logic analyser continuously monitoring for errors in the bit pattern. The error events are then recorded and one can make a statistical analysis of the error rate per bit as a

function of, for instance, the level of the supply (bias) currents or even artificially injected noise at the supply terminals. It is expected that a RSFQ circuit using a π-shift loop will have a substantially lower sensitivity to these external influences compared to the same circuit implemented with a normal loop.

3.2.2.2 Device test structures

The two direct-injection SQUID circuits are shown in Figure 3.15, together with their equivalent circuit schematic. A network analysis of the circuit, given in Appendix A, shows that the maximum current that can be passed through the bias terminal without generating a voltage, i.e. the SQUID critical current, depends periodically on the modulation current I_{mod} with a period:

$$\Delta I_{\mathrm{mod}} = \frac{\Phi_0}{L_{\mathrm{DI}}}$$

where L_{DI} is the self inductance of the direct-injection segment. The relation is valid when the modulation current source is "floating", that is, when it is weakly (or not at all) connected to the ground terminal of the rest of the circuit. This removes any stray modulation originating from the "common-mode" current I_{cm}. Therefore, during the measurement of ΔI_{mod}, it is common practice for either the modulation source or the bias source to be battery-powered (or both). In any case, the resistance R_{cm} between any terminal of the the modulation source and the biasing/measurement circuitry must be very large.

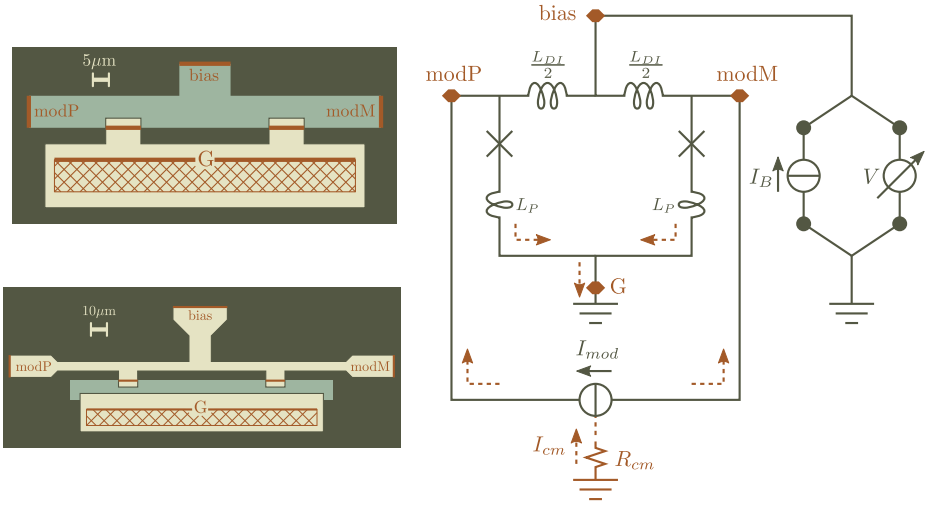

Figure 3.15. The layout drawing and (application) schematic of the direct-injection SQUID structures. In the upper drawing L_{DI} is created by a YBCO while in the lower drawing by an Nb1 segment. Note the difference in scale of the drawings. The path of the common-mode current through the device is depicted on the schematic with a broken line.

By measuring the modulation period ΔI_{mod} of the direct-injection SQUID, the inductance L_{DI} is indirectly found. From the geometry of the segment one can then determine the parameters of the layers, for instance the sheet inductance.

In Figure 3.16, the four Josephson junctions and the YBCO bridge are depicted. The junctions are placed in pairs, each junction in the pair has a different orientation ("V" vertical and "H" horizontal) while the difference between the pairs is the lengths of the junctions ("L" large 25μm and "S" small 10μm). The YBCO bridge structure is intended for a 4-terminal resistance measurement of an YBCO segment in order to determine the T_c of the film.

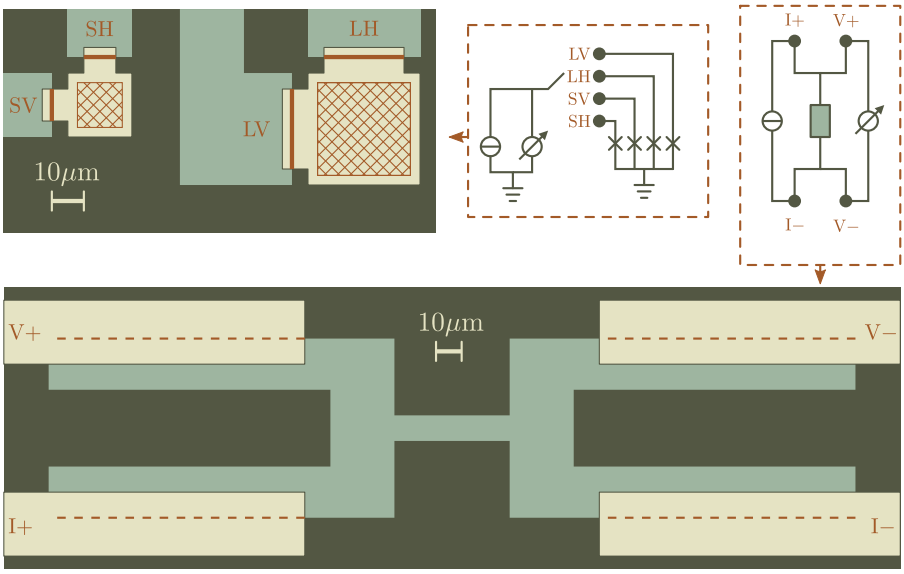

Figure 3.16. Layout drawings with application schematics of the Josephson junction and YBCO bridge test structures. The large junctions connecting the bridge with the measurement leads are treated as short circuits.

For the sample series πChip2.2X, six more test junctions are added with a similar layout. They are of 10μm length and also divided in two groups: one with and one without a groundplane coverage in order to check whether the groundplane has any influence on the characteristics of the Josephson junctions.

3.2.2.3 IC layout

The placement of the blocks discussed in the previous subsections on the IC, as well as microphotographs of the same can be found in Figure 3.17. The chip has 91 bondpads, staggered in two rows, circling around the perimeter. Each bondpad can be either a ground connection, bias/sense lines or an RSFQ input/output terminal.

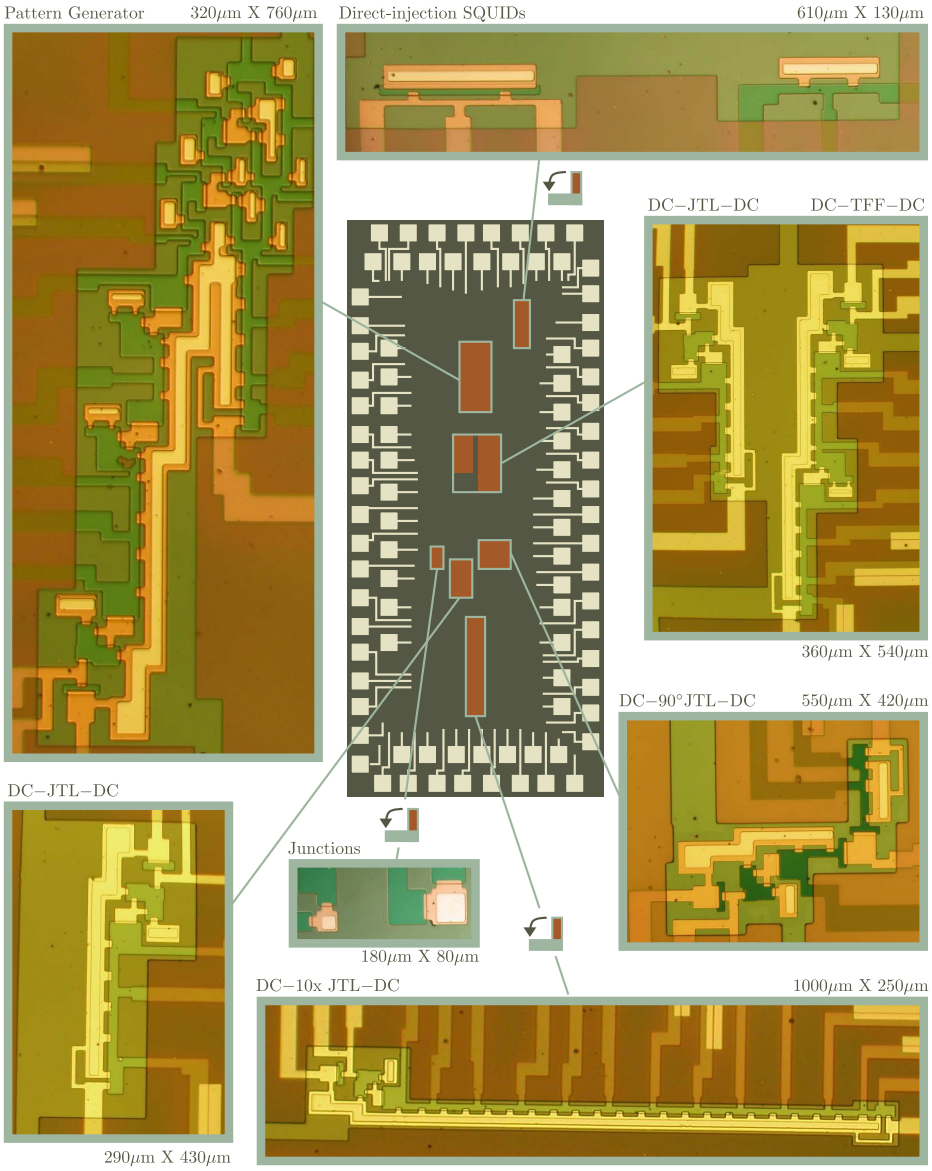

Figure 3.17. The physical layout of the πChip2, together with the placement and microphotographs of the circuits. The dimensions of the IC are 5mm X 10mm. The dimensions of the microphoto insets are also given. The pictures are taken just before the deposition of the Nb groundplane, whose lift-off resist stencil can be seen as large bright rectangular opening covering the circuits.

3.2.3 Measurement results

The samples were produced in two series: the πChip2.1X and the πChip2.2X, where "X" is the number of the sample in a given series. The difference between the two series is

- πChip2.2X samples use commercial base layers CeO_2/YBCO/CeO_2 (50nm/120nm/50nm) on an r-cut sapphire substrate (Al_2O_3) instead of PLD-grown YBCO/STO (120nm/70nm) base layers on an STO substrate found in πChip2.1X samples

- the Nb1 layer on the πChip2.2X samples was structured using reactive plasma etch in SF_6, while for the πChip2.1X series it was structured by lift-off

- for samples from the πChip2.2X series, the mask used to define the YBCO resist stencil is always cleaned before lithography in order to achieve straight (lengthwise) edges for the ramp-type junctions

- all samples from the πChip2.1X series were measured in a flow cryostat system while for the πChip2.2X samples, a bath cryostat was used. Although the former measurement system offers the possibility to sweep the sample temperature for the purposes of fine-tuning the operating point of the RSFQ circuits, the latter system offers better magnetic shielding and higher noise immunity.

The intention of the measures listed above is to improve the general robustness of the manufactured samples by having better control of the most unreliable processing steps as well as eliminate systematic errors originating in the measurement equipment. In the next Chapter, these and other measures are presented in more detail.

In total there are 20 samples of the πChip2 manufactured. During fabrication, all samples were targeted with nominal layer thicknesses (given in Figure 3.3 and Figure 3.5) so that the variations between them are determined by the repeatability of the processing steps themselves.

In Table 3.5 and Table 3.6, a summary of the sample details is given for each πChip2 series separately. A selection of the obtained measurement results, per sample, is presented after each table.

Series	Nr.	Status	Available data	Comment
πChip2.1	1-5	F.D.P.*	/	/
πChip2.1	6	Measured	- Junction parameters vs. temperature see Figure 3.18	- YBCO $T_c \approx 75$K - measured I_C's not consistent across measurement sessions - suppressed DI-SQUID I_C, large series resistance - functional RSFQ tests not attempted
πChip2.1	7	Measured	- Junction parameters vs. temperature see Figure 3.19	- YBCO $T_c \approx 89$K - junction I_C's about 1/3 of nominal values - suppressed DI-SQUID I_C, large series resistance - functional RSFQ tests not attempted
πChip2.1	8	Measured	- Junction parameters vs. temperature see Figure 3.20 - DI-SQUID modulation see Figure 3.20	- YBCO $T_c \approx 89K$ - junction I_C's about 1/4 of nominal values - functional RSFQ tests not attempted
πChip2.1	9	F.D.P.	/	/
πChip2.1	10	Measured	- Junction parameters vs. temperature see Figure 3.21 - DI-SQUID modulation see Figure 3.21	- YBCO $T_c \approx 89$K - test junction I_C's about 3/2 of nominal values - functional RSFQ tests unsuccessful
πChip2.1	11	F.D.P.	/	/
πChip2.1	12	F.D.P.	/	/

Table 3.5. A summary of the measurement results per sample for the πChip2.1X series.
* F.D.P.=Failure During Processing

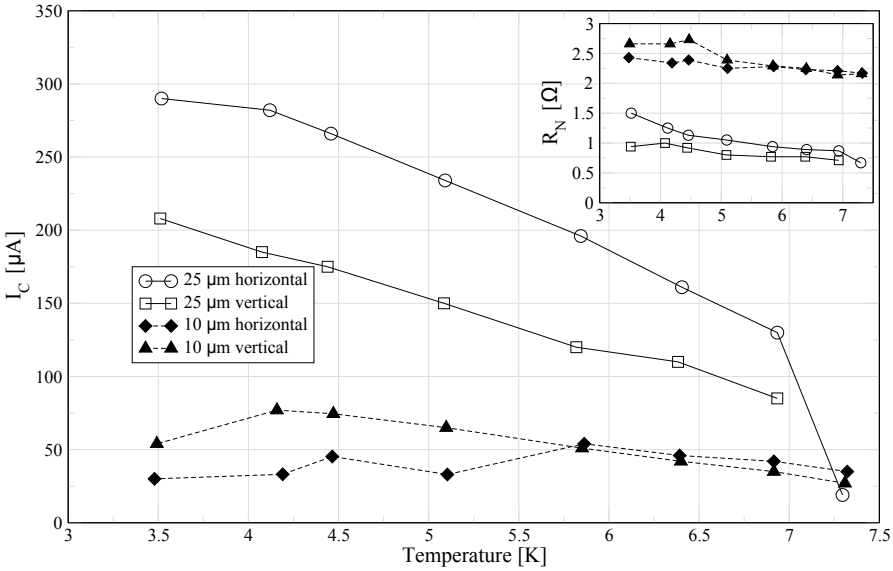

Figure 3.18. Parameters of the test junctions measured on the πChip2.1-6.

In Figure 3.18, the junction parameters are not far from their nominal values of $J_{C,\mathrm{nom}} = 12\frac{\mu\mathrm{A}}{\mu\mathrm{m}}$, $R'_{N,\mathrm{nom}} = 21\Omega\mu\mathrm{m}$ at 4.2K. Also, the differences between the junctions roughly follow their geometrical scaling (ratio 2.5), albeit with a considerable spread in their I_C's. Nevertheless, the results given in Figure 3.18 could not be reproduced in subsequent measurement sessions where the I_C values were found to be about 3 times lower and randomly distributed across the temperature axis. Additionally, only a single I/V curve of a direct-injection SQUID was obtained that had a junction-like shape, showing a highly suppressed I_C with a large resistance in series with the device. A modulation pattern on this device was not observed.

Based on these measurement results, it was found highly unlikely that the RSFQ circuits of the πChip2.1-6 would function correctly. Hence, no functional tests were carried out.

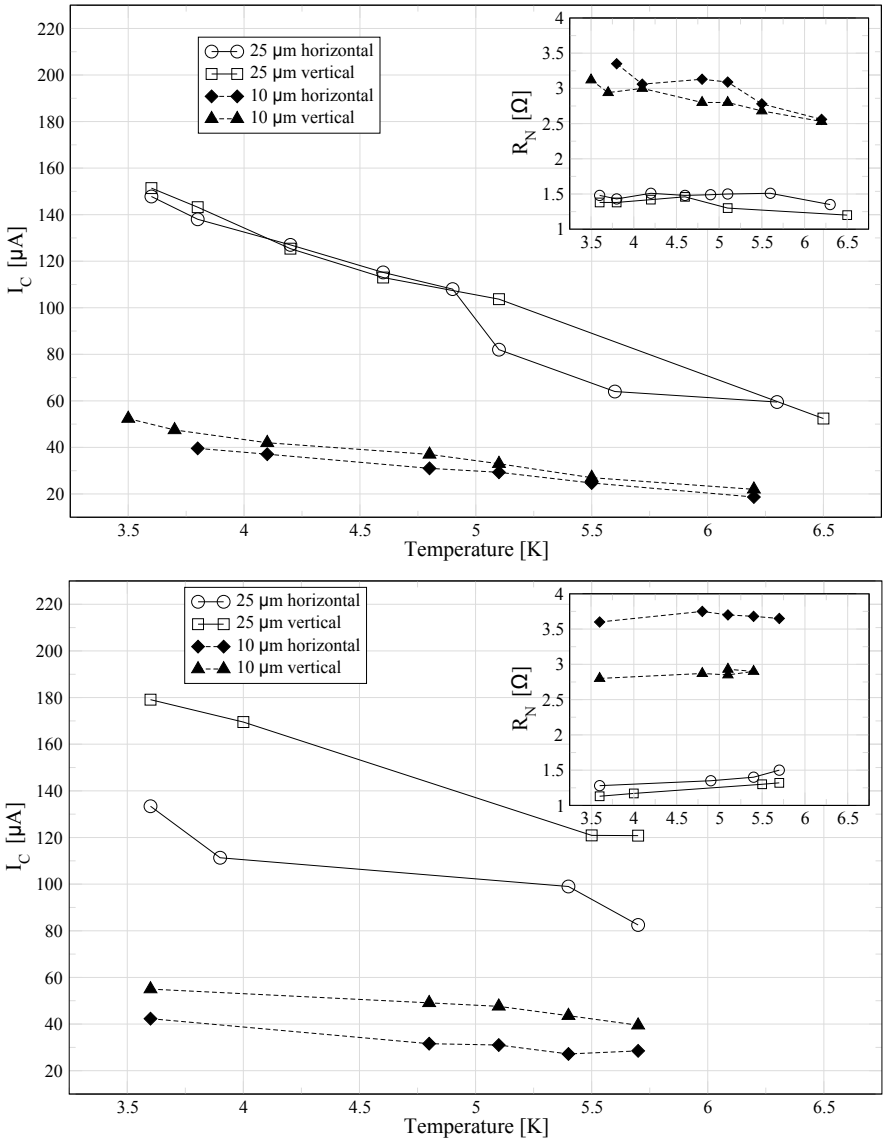

Figure 3.19. Junction parameters of πChip2.1-7 from two different measurement sessions.

Although the inter-session spread between the parameters of the test junctions in Figure 3.19 is relatively small, the rest of the results were poor and prohibited functional RSFQ tests on πChip2.1-7, just like with the πChip2.1-6 sample.

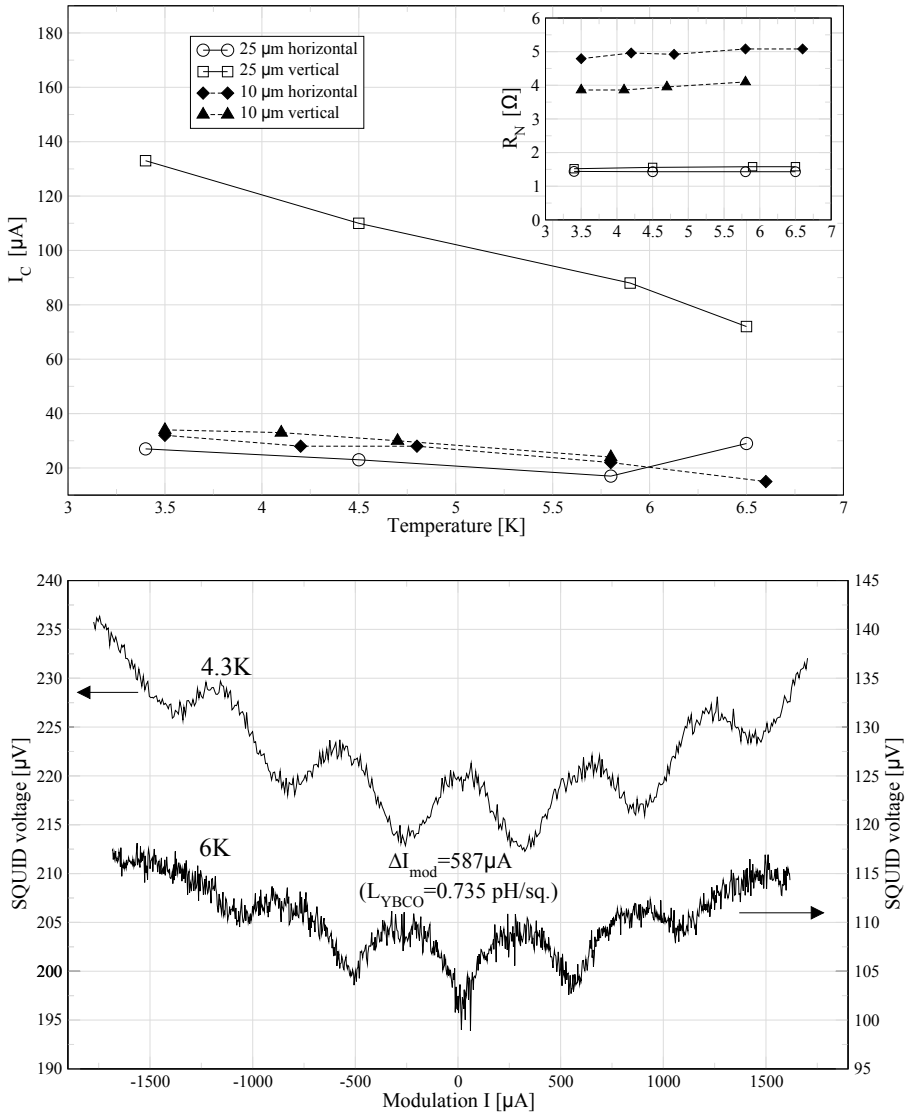

Figure 3.20. πChip2.1-8 parameters of the test junctions (top) and direct-injection SQUID modulation patterns (bottom) showing the YBCO sheet inductance. The 25μm horizontal junction had a suppressed I_C in all sessions, suggesting manufacturing spread. The YBCO segment whose inductance is measured by the DI-SQUID is 4.8 squares large. The larger modulation pattern extending beyond the scale of the plot is a consequence of the $I_C(\Phi)$ modulation of the junctions in the DI-SQUID.

Due to very low I_C's (∼1/4 of the nominal value) and considerable inter-session spread, functional RSFQ tests were also not attempted with sample πChip2.1-8.

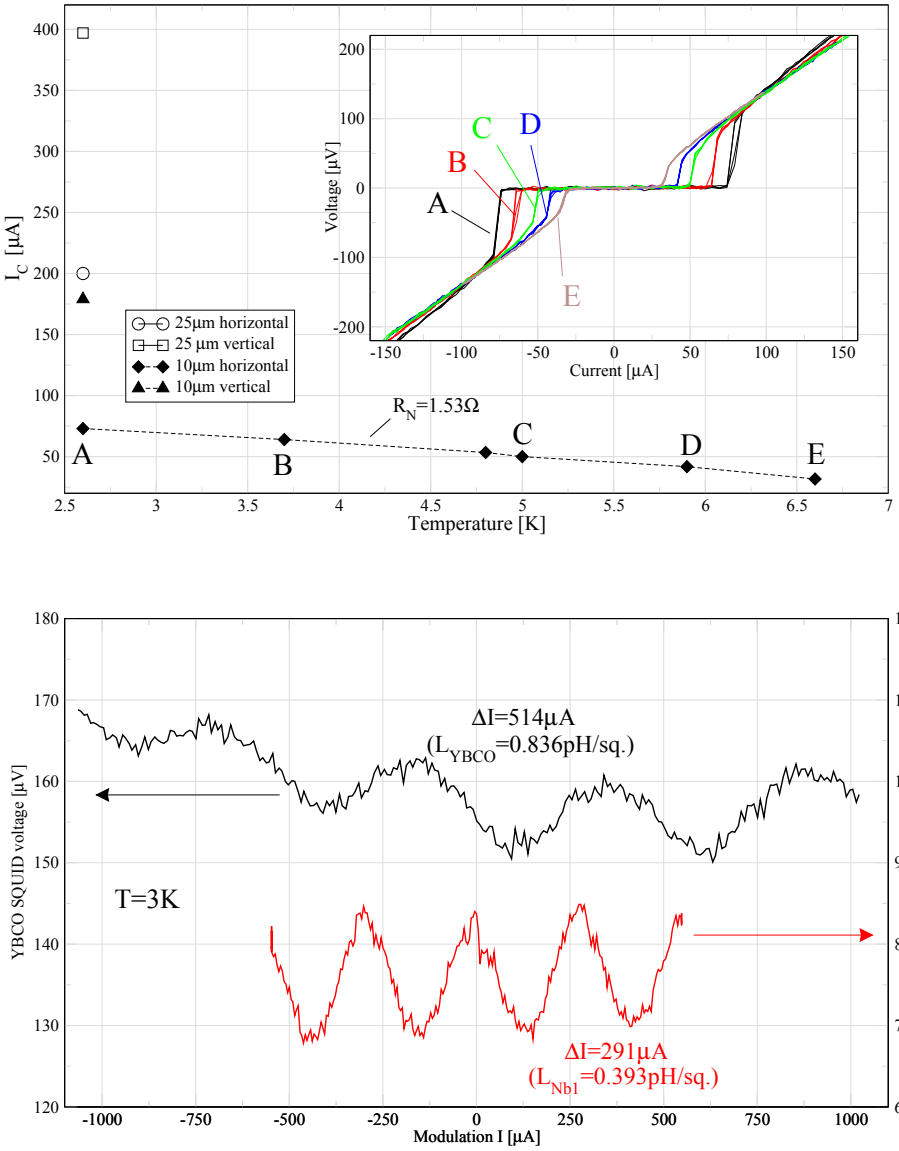

Figure 3.21. Junction parameters with an I/V curve family across T (top) and DI-SQUID modulation patterns for obtaining both the YBCO and the Nb1 sheet inductance (bottom) of πChip2.1-10. For the DI-SQUIDs, the YBCO segment has 4.8 squares while the Nb segment is 18.1 squares large.

Although the junction data vs. temperature is not complete in Figure 3.21, it is reasonable to expect that the trends from the previous samples would repeat here as well. In this sample however, there is a clear difference in the parameters between the "horizontal" and "vertical" junctions, also corroborated by the results from other measurement sessions. This indicates a misalignment of the YBCO structures with its crystal axes, or (less likely) that the YBCO layer is "untwinned".

The nominal value of the critical current density $J_{C,\mathrm{nom}} = 12\frac{\mu\mathrm{A}}{\mu\mathrm{m}}$ falls within the measured range $7.5 - 16\frac{\mu\mathrm{A}}{\mu\mathrm{m}}$ estimated from Figure 3.21. Additionally, the sheet inductances of the superconducting layers are not too far from their nominal values, thus justifying a functional RSFQ test for this sample. Nevertheless, the measurements of the digital RSFQ blocks on πChip2.1-10 were unsuccessful: there was no switching behaviour observed even after a thorough bias and temperature tuning. The input and output waveforms remained of the same frequency and followed an analog modulation pattern, either due to stray magnetic coupling or direct galvanic input/output connection.

For the πChip2.1 series, there were only 4 samples available for measurement while the total number of processed samples was 12. This implies a fabrication failure rate of 66%, with approximately 2 in 3 samples aborted during manufacturing due to process errors. The most common failures are incomplete Nb1 (or Nb2) lift-off and surface contamination preventing the completion of the manufacturing steps. In any case, a physical yield of 33% is not surprising for a complex manufacturing process in a very early experimental phase.

However, the approximately 0% yield in the device parameters for the samples that did not fail during processing presents a larger problem. The measurement results show large deviations in the junction's critical currents from the nominal values and, more importantly, a large spread between samples or even between junctions on the sample. Expectedly, only the sheet inductances exhibit a low sample-to-sample (better known as run-to-run or inter-chip) spread: for instance the two measurements of $L_{\square,\mathrm{YBCO}}$ from πChip2.1-8 and πChip2.1-10 lie very close to each other. Nevertheless, the results from the πChip2.1 series are in general not permitting functional RSFQ testing.

The measurement data additionally suffers from systematic errors originating from the measurement system itself, presumably due to excessive flux trapping, as the inter-session spread in the measurement data indicates.

After making a number of changes in both the processing and the measurement methods, a new sample series was manufactured and measured. The summary of the most relevant data for the πChip2.2 series is given in Table 3.6, after which selected results are given in graphical form. The chip design was modified to include 6 more junctions (10μm length) in order to better capture parameter spread.

All samples have commercial base layers with YBCO $T_c \approx 87$K. All measurements were taken at 4.2K.

Series	Nr.	Status	Available data	Comment
πChip2.2	1-2	Measured	/	- low Nb1&Nb2 $T_c \approx 6$K - junction I/V curves not superconducting
πChip2.2	3	Measured	- Junction parameters see Figure 3.22	- test junction J_C just a few % of nominal
πChip2.2	4	Measured	/	- YBCO interlayer superconducting @60K
πChip2.2	5	Measured	- Junction parameters see Figure 3.23 - DI-SQUID modulation see Figure 3.24 - SFQ switching events see Figure 3.25	- functional RSFQ tests unsuccessful
πChip2.2	6	Measured	/	- junction I/V curves not superconducting
πChip2.2	7	F.D.P.	/	/
πChip2.2	8	Measured	- Junction parameters see Figure 3.26 - DI-SQUID modulation see Figure 3.27 - SFQ switching events see Figure 3.28	- functional RSFQ tests unsuccessful

Table 3.6. A summary of the measurement results per sample for the πChip2.2-X series.
* F.D.P.=Failure During Processing

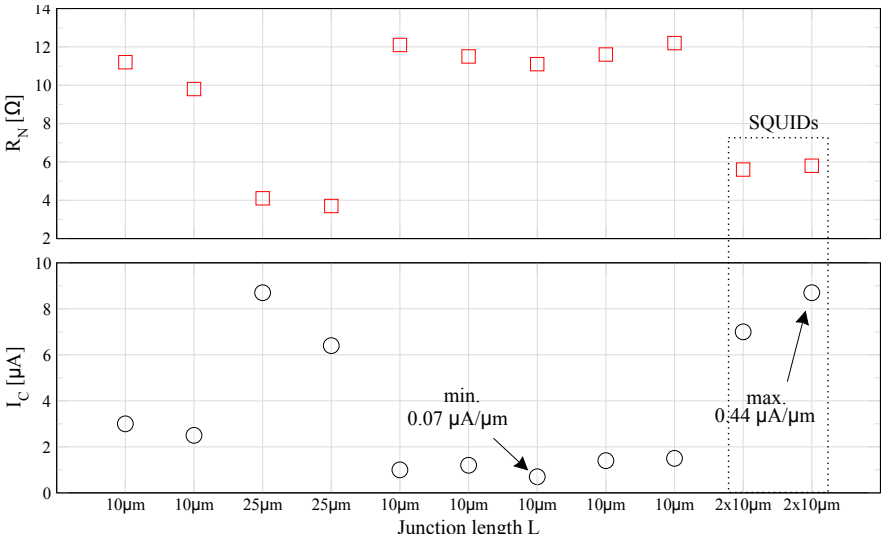

Figure 3.22. Distribution of the measured junction parameters on πChip2.2-3. Note that the measured J_C is only about 2% of the nominal value of $12\frac{\mu A}{\mu m}$.

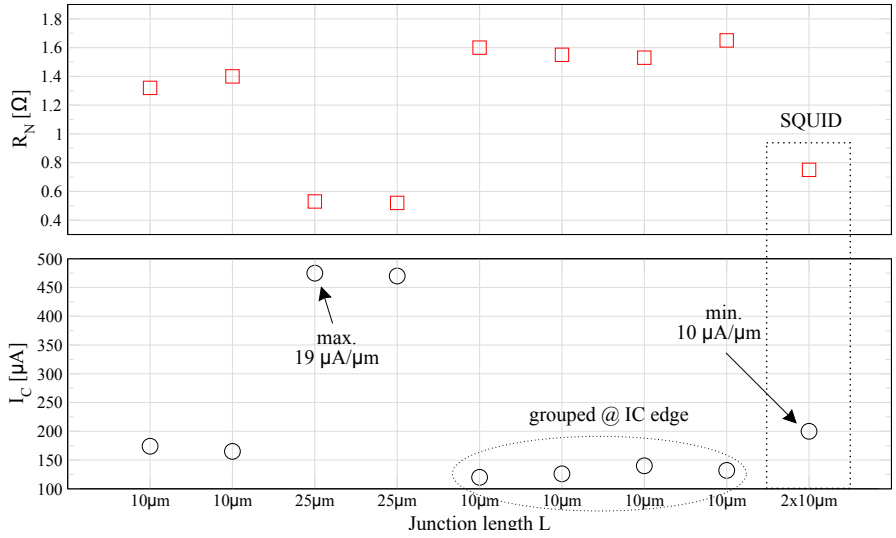

Figure 3.23. Distribution of the measured junction parameters on πChip2.2-5. From the data, the average J_C is $14.5\frac{\mu A}{\mu m}$ while the average $I_C R_N$ is $\sim 220\,\mu V$, both with about 30% spread across the junctions. They are both well in line with their nominal values.

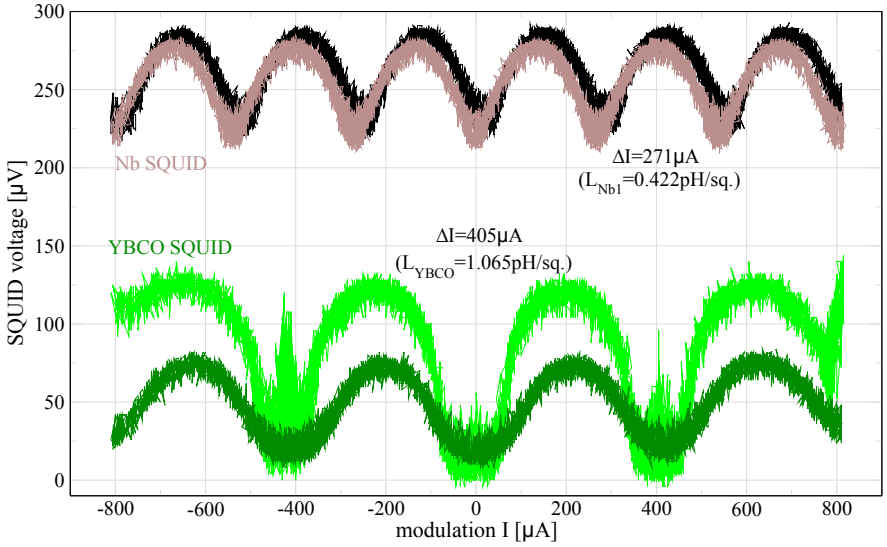

Figure 3.24. Direct-Injection SQUID modulation patterns for determining both the YBCO and Nb1 sheet inductances of πChip2.2-5. There is a warm-up/cool-down cycle through the Nb T_c between the two measurements per SQUID.

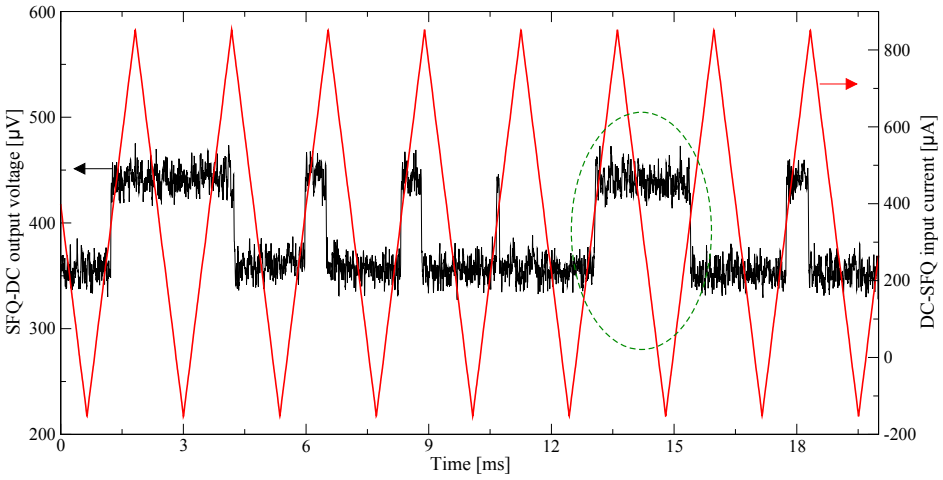

Figure 3.25. Part of the input/output signal traces from a functional test of a DC-JTL-DC circuit on the πChip2.2-5. Switching events that trigger at the correct input signal slope, like for instance the encircled pulse in the plot, are very rarely observed even after extensive bias tuning of the circuit and multiple warm-up/cool-down cycles.

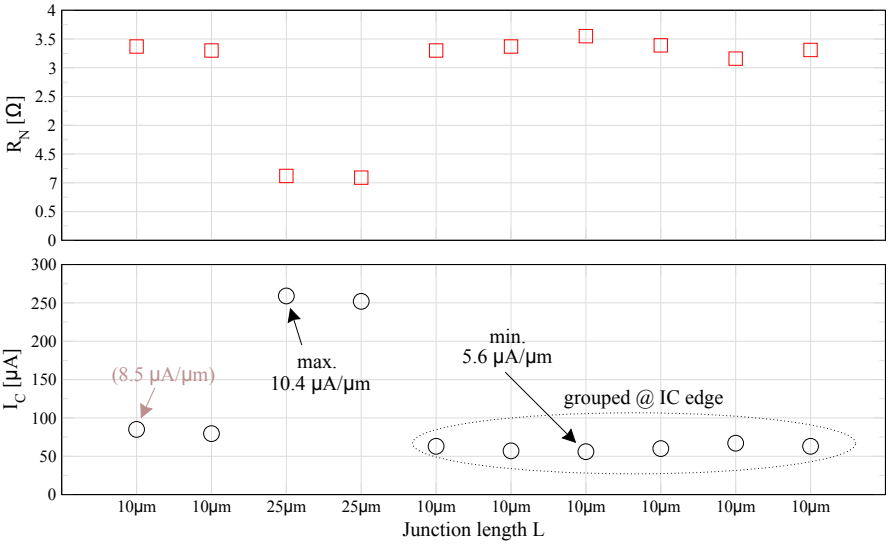

Figure 3.26. Distribution of the junction parameters on the πChip2.2-8. From the measurement data, the $J_C = 8\frac{\mu A}{\mu m} \pm 30\%$ and the $I_C R_N = 234\mu V \pm 20\%$, reasonably in line with their nominal values. If the long junctions are excluded from the distribution, the spread numbers improve considerably. Also, note how the junctions placed at the edge of the IC have systematically lower I_C's by ≈25%, indicating an effect from the thickness profile of (most likely) the Au barrier layer across the surface of the sample. The same effect is also visible in the data from πChip2.2-3 and πChip2.2-5 (Figure 3.22 & 3.23).

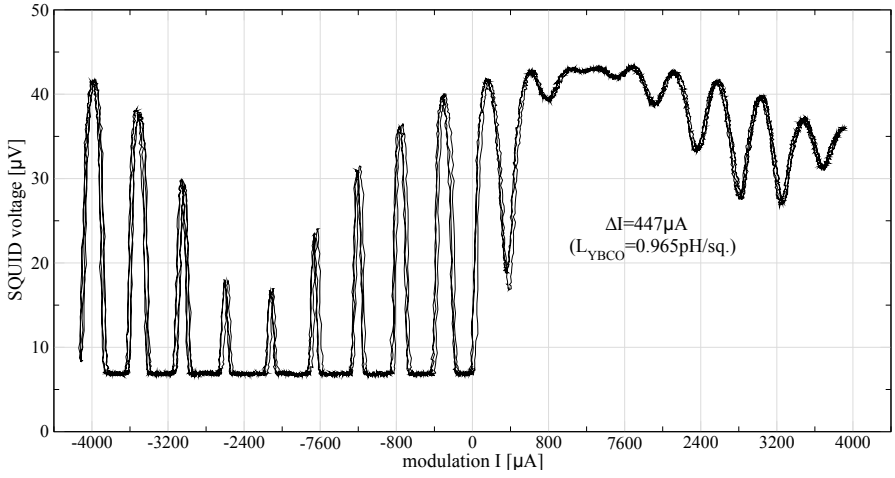

Figure 3.27. DI-SQUID modulation pattern indicating the YBCO sheet inductance on the πChip2.2-8. There is considerable trapped flux or other source of disturbance present.

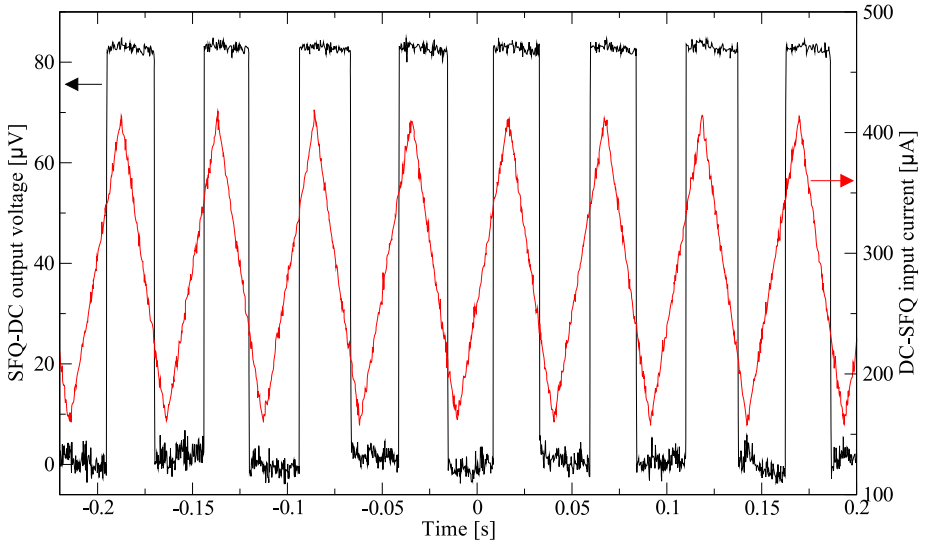

Figure 3.28. Example of typical signal traces showing (incorrect) switching events during a functional test of a DC-JTL-DC circuit on the πChip2.2-8. Namely, to have a correct switching event in the DC-JTL-DC circuit, the state of the output signal should change at each rising edge of the input signal, contrary to what is shown above. None of the functional tests of the RSFQ circuits available for measurement on the πChip2.2-8 let correct switching events be seen, despite tuning of bias currents and many temperature cycles through the T_c of the Nb films.

The measurement results of the second πChip2 series are improved as compared to the first series, mostly due to the better shielding of the sample from noise and stray magnetic fields, as well as the more robust fabrication steps. The physical yield is approximately 7 in 8 (just one sample failed during processing), while the junction parameters of the measured samples fall more closely to the nominal (design) values. Most importantly however, the device parameters stay stable across a number of consecutive samples, a feature necessary for overall reliability of the π-shift technology. In Chapter 4, these improvements are quantified by the results from I_C spread measurements performed on several samples manufactured after the πChip series.

Nevertheless, the improvements did not translate in successful functional RSFQ tests. From the analysis of the data, it is reasonable to expect that, if enough samples are produced, at least one simple functional RSFQ block would be encountered, thus reproducing the experiment reported in [8] and [3]. It is however not

probable that the most important (and novel) RSFQ circuit, the "Pattern Generator" containing 47 Josephson junctions, would be successfully operated without more improvements in the measurement and processing aspects of the technology. Secondly, since the average measured YBCO sheet inductance is systematically less than 50% of its design value (simulations show that the circuits can still operate however), a physical redesign of all RSFQ circuits on the πChip2 using a new nominal value for $L_{\square,\mathrm{YBCO}}$ is highly preferred. Considering the relatively large amount of resources necessary for accomplishing all those tasks, estimated by simply extrapolating the current rate of progress, it was decided that further experiments with π-shift RSFQ circuits are outside the scope of a small application-oriented exploratory effort of the π-shift technology. The rest of this thesis will therefore not focus on complex π-shift (RSFQ) circuits, but instead expand the use of π-loops in other types of superconducting circuits that are both novel and simpler to implement.

After reaching the above conclusions, improvements to all components of experimentation were next considered. These advances should however be small and incremental, their aim at reducing the effort necessary to manufacture and measure general π-shift circuits of low junction-count and not focus exclusively on very complex RSFQ designs. The next Chapter discusses these improvements, their implementation and achieved results. This work allowed simple static π-shift circuits, described in Chapters 5 and 6, to be successfully designed and tested across a number of samples.

Chapter 4

Experimental aspects of the hybrid YBCO-Nb planar technology

The central theme of this chapter is the hybrid YBCO/Nb π-shift fabrication technology with a focus on improvements/upgrades of the standard fabrication techniques presented in Chapter 3, as well as observations on the measurement issues with concrete proposals for the direction of future work in that area. The last part of this Chapter, Section 4.2, presents measurement results from a few samples designed specifically for characterization of the devices manufactured with the π-shift technology.

4.1 YBCO/Nb process & measurement techniques

The extent to which improvements in an experimental fabrication procedure can be realized is constrained by the limits of the processing resources that are, necessarily, optimized for experimental versatility. For instance, in an experimental setting, most of the equipment is built as non-standard for the purposes of experimentation. In order to remove any uncertainty during fabrication on the other hand, one needs dedicated apparatus that is consigned for a specific processing step. In other words, *robustness asks for standardization of the fabrication steps while experimentation needs the opposite*. The overcoming of this contradiction, usually encountered within the frame of a technological exploration, marks the passing of a technological threshold. In general, standardization of the methods employed within a certain technology defines the threshold between exploration and application.

However, much effort is needed to standardize engineering methods. It is necessary to have an empirical in addition to qualitative (scientific) understanding of the sub-processes constituting a certain method. Therefore, empirical models calibrated with measured data are essential for standardization. One needs to gather a lot of sensitivity information from measurements so that it can be predicted how, for instance, will the height profile of an ion-milled ramp surface of a thin film depend on the angle of incidence of the accelerated Ar+ ions. Having such empirical data makes it possible to discover the critical sub-processes within the method that must be tightly controlled and hence standardized. Possessing only qualitative knowledge is not enough for designing robust engineering methods since, as a rule of thumb, complex processes are unpredictable and impractical for theoretical modelling.

Note that identifying critical issues is not always trivial, nor are they often mentioned as such in the literature. In the case of Ar+ ion gun milling for example, it was noticed during experimentation that the resistance of the grounding path of the rotating sample holder had a very large influence on the total etched height. Without a certain number of trial&error empirical data-gathering steps, this property of ion gun milling with rotating substrates will have, most likely, remained hidden and resulted in poor process control.

Accumulating empirical data thus helps in two ways: calibration for process sensitivity models and the identification of non-trivial effects by its trial&error nature.

A second important aspect of the exploration-to-application transition is the incorporation of existing industrial methods with minimal or no modification. Many technologies in fact contain just a few engineering methods specific to it, the rest being mostly generic. The "outsourcing" of many of these steps makes it easier to manage the collection of empirical data about the technology-specific methods,

while at the same time avoiding the common problem of trying to repeat already modelled and optimized ones.

The above issues have been taken into account during the exploration of the π-shift technology. The application threshold has not been reached, although a fair number of sensitive points has been identified. They are all listed in the following subsections.

4.1.1 Base layers

In the standard YBCO/Nb fabrication process, the first process step is the growth of the superconducting YBCO and the isolating STO ($SrTiO_3$) layers on the monocrystalline and polished STO substrate surface by PLD (Pulsed Laser Deposition). This epitaxial growth method is very often used for experiments with thin films of complex-oxide materials, including the family of superconducting cuprates to which YBCO belongs to. However, the deposition of the films with an experimental PLD system has two main drawbacks:

- the deposition is sequential i.e. there can only be one sample produced at the same time
- the need for frequent re-optimization of the grown films due to drift in the process parameters

Combined together, the two points above limit the repeatability of the whole fabrication procedure: the turnaround time between experiments is too large.

A good example of this process issue is the roughness of the top STO layer. For multi-layer planar circuits, it is very important that the surface roughness of the first few layers is as low as possible, since all subsequent layers will inherit and even add to any surface irregularities. Hence, as more and more films are grown on top of each other, they incrementally lose their crystallinity and epitaxial properties.

In Figure 4.1, an AFM image of the typical surface of the YBCO/STO bilayer, grown using the PLD settings from Chapter 3, is shown. Below that, in Figure 4.2, a SEM image of the surface of the same sample is given.

Analysis of the AFM data of the samples with PLD-grown base layers gives an RMS surface roughness of about 5nm, while the number density of the particles seen in the images below averages $0.7\mu m^{-2}$ over a large area. The average particle size is $\sim$100nm in diameter and $\sim$50nm in height.

The plots clearly indicate the porosity of the 70nm thick top STO layer. Although the surface roughness is acceptable, the fact that sharp and >30nm deep recessions exist on the surface is a large problem: the pores in the STO layer can potentially reach the underlying YBCO layer, facilitating undesired contacts with other films that are deposited on top of this STO surface.

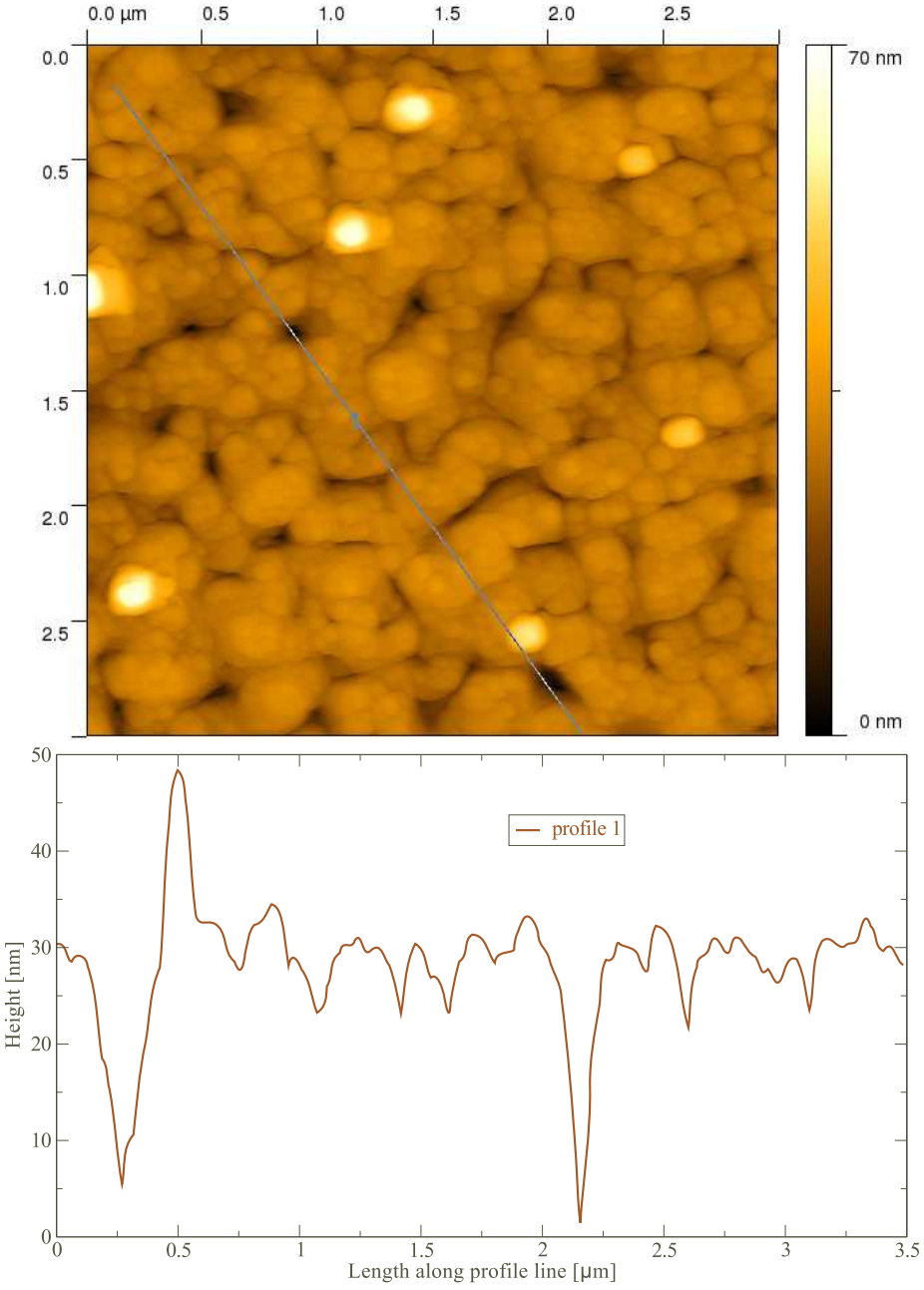

Figure 4.1. An AFM image with a profile line of a YBCO/STO bilayer of 120nm/70nm thickness grown with PLD on an STO substrate at the settings given in Table 3.1 from Chapter 3.

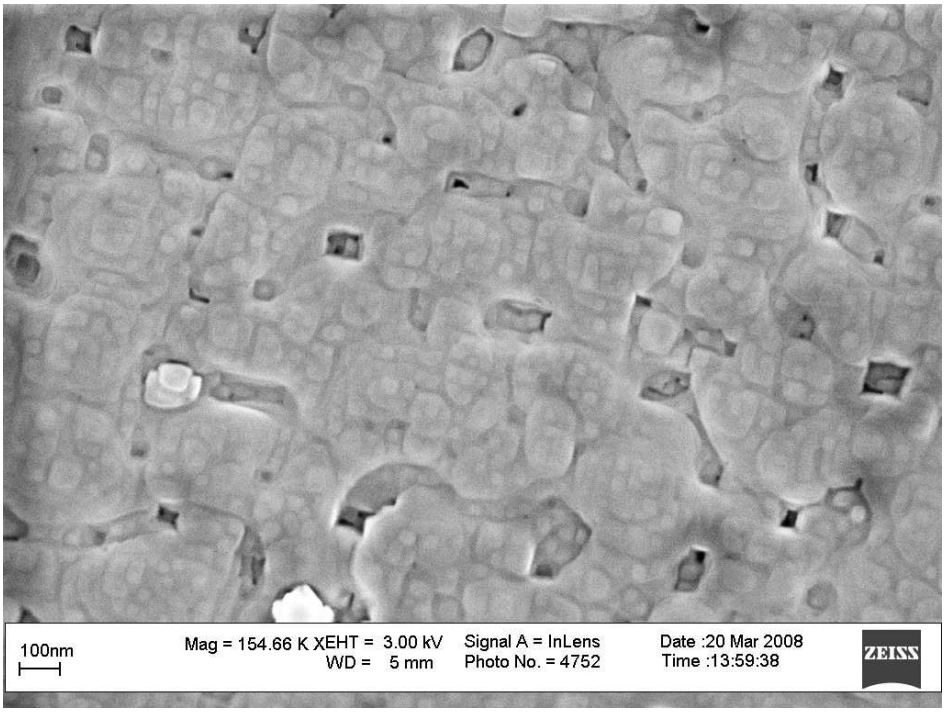

Figure 4.2. A SEM image of the same sample from Figure 4.1. The area shown is about 2.3μm x 1.7μm, comparable in size to the AFM image from Figure 4.1.

On the other hand, the number density of the particles presents a different problem: particles existing exactly in the active ramp-edge Josephson junction area. Considering that the average ramp angle is about 10° and that the YBCO layer is 120nm thick, the planar width of the junction calculates to approximately 120nm $\cdot$ ctan(10°) = 0.68μm. Then, since there is one particle per 1.43μm^2 of surface area ($1.43 = \frac{1}{0.7}$), for each $\frac{1.43}{0.68} \approx 2\mu$m of junction length at least one particle will fall within the junction area. The typical junction with $L = 5\mu$m will then have, on average, between 2 and 3 particles on the ramped junction surface. Even if it is assumed that the presence of particles on the active junction area does not destroy the Josephson effect but only modifies the junction parameters, the random surface distribution of these particles will directly reflect in the spread in the parameters of the junctions on the sample.

A solution to the problem of the rough top layer is to optimize the film growth

by experimenting with the PLD parameters. Again, due to the features of experimental PLD, one can quickly conclude that such optimization is not only costly but it also does not solve the problem with repeatability. The drift in the parameters of the experimental PLD equipment will again, after some time, require re-optimization. This is accentuated by the sequential nature of sample manufacturing with PLD. The only acceptable solution is the standardization of the PLD procedure by acquiring empirical data on the whole PLD process step and then designing a dedicated large-area deposition system where the base layer growth will be performed simultaneously on many samples.

Fortunately, the production of thin epitaxial YBCO films on crystalline substrates with properties suitable for electronic application is already available commercially. As the growth of the base layers is not specific to the π-shift hybrid technology, the step is a good candidate for external procurement.

In Figure 4.3, the AFM image of the commercially available base layers is given. The 120nm thick YBCO film is grown on a r-cut Al_2O_3 substrate with a 50nm CeO_2 buffer layer. A 50nm CeO_2 isolation (capping) layer is then grown on top of the YBCO film.

The RMS roughness of the top CeO_2 surface is about 1.6nm, while the number density of the particles is slightly lower then previously. The particles are however on average just 20nm high, making them less influential to the junction properties than the approximately 2.5x bigger particles on the top surface of the YBCO/STO bilayer previously. At the same time, the top CeO_2 layer is very smooth and even regular orthogonal surface features can be discerned. These crystalline rectangular outgrowths are 5-10nm high and about 10x that size in diameter. Their planar orientation in Figure 4.3 corresponds with the expected crystal orientation of the top CeO_2 film, taking into account the AFM tip scan direction relative to the crystal axis-aligned substrate edges.

From x-ray diffraction measurements, the crystalline structure of the commercial base layers was investigated. All (00l) diffraction peaks were observed with relatively high amplitudes in θ-scans indicating that the films are crystalline and correctly oriented (c-axis normal to the substrate surface). Reciprocal HKL plots on the other hand corresponded with a twinned YBCO film, that is also as desired. The T_c of the film was determined to be in the vicinity of 88K, both from 4-point RT measurements of structured samples (a YBCO bridge) and an inductive non-contact technique used by the film manufacturer itself.

The growth technique used for the YBCO/CeO_2 base layers, thermal co-evaporation, allows the deposition of the base layers to be performed on many samples simultaneously. Such a method of batch fabrication of the base layers would also improve the repeatability of the π-shift process, in addition to the beneficial features described above. Also the total manufacturing time of each π-shift sample is reduced by approximately 15% when the base layers are not grown by PLD.

All samples from the πChip2.2X series were manufactured using these commercially acquired YBCO/CeO_2 films.

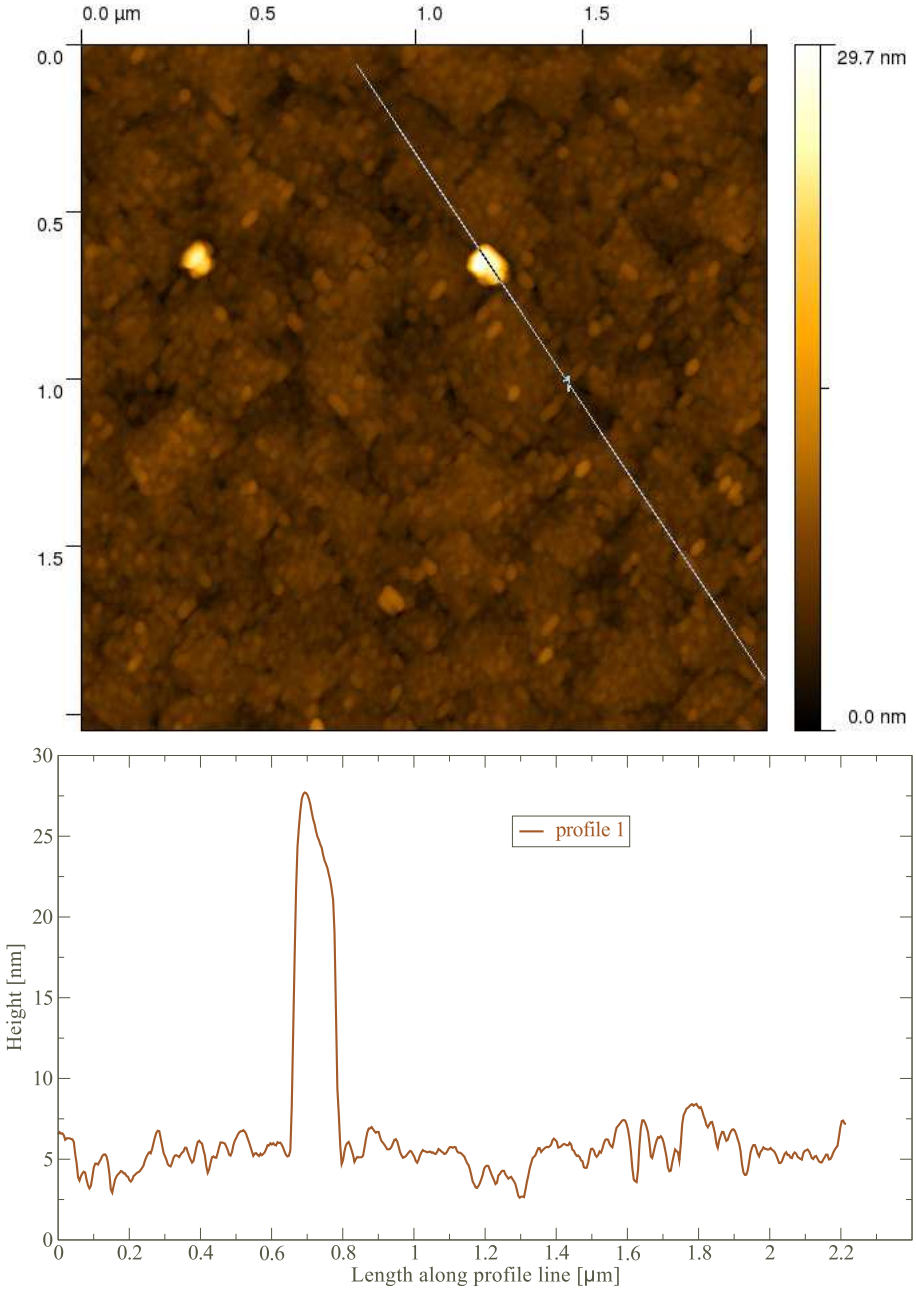

Figure 4.3. AFM image with a profile line of commercially available YBCO/CeO_2 base layers of 120nm/50nm thickness on a sapphire (Al_2O_3) substrate with a 50nm CeO_2 buffer.

4.1.2 Niobium reactive plasma etch (SF_6)

In the standard process described in Chapter 3, the structuring of the niobium films is performed with a lift-off method using a positive photoresist. A drawback of this technique is the frequent appearance of protrusions along the edges of the Nb structures as depicted in Figure 4.4. These defects can reach as far as the photoresist thickness, but are usually less than 1μm high. Since there are always more layers deposited on top of the first Nb film, there is thus a high probability of shorts or other step-coverage problems. In Figure 4.5, a large-area AFM scan of a πChip2.1X sample is given confirming the above issue.

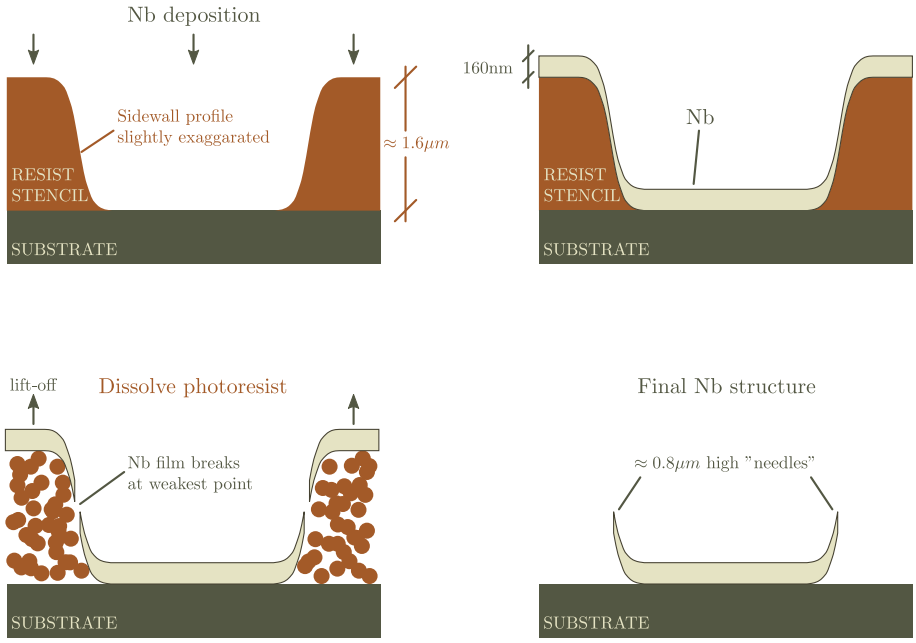

Figure 4.4. The needle-like protrusions at the edges of a thin film, sometimes also called "ears", structured by a lift-off technique are due to the sloping sidewall profile of the photoresist stencil. Only with very sharp, or even better undercut, resist profiles can the protrusions be eliminated everywhere on the sample as the Nb film can then not deposit at the sidewalls.

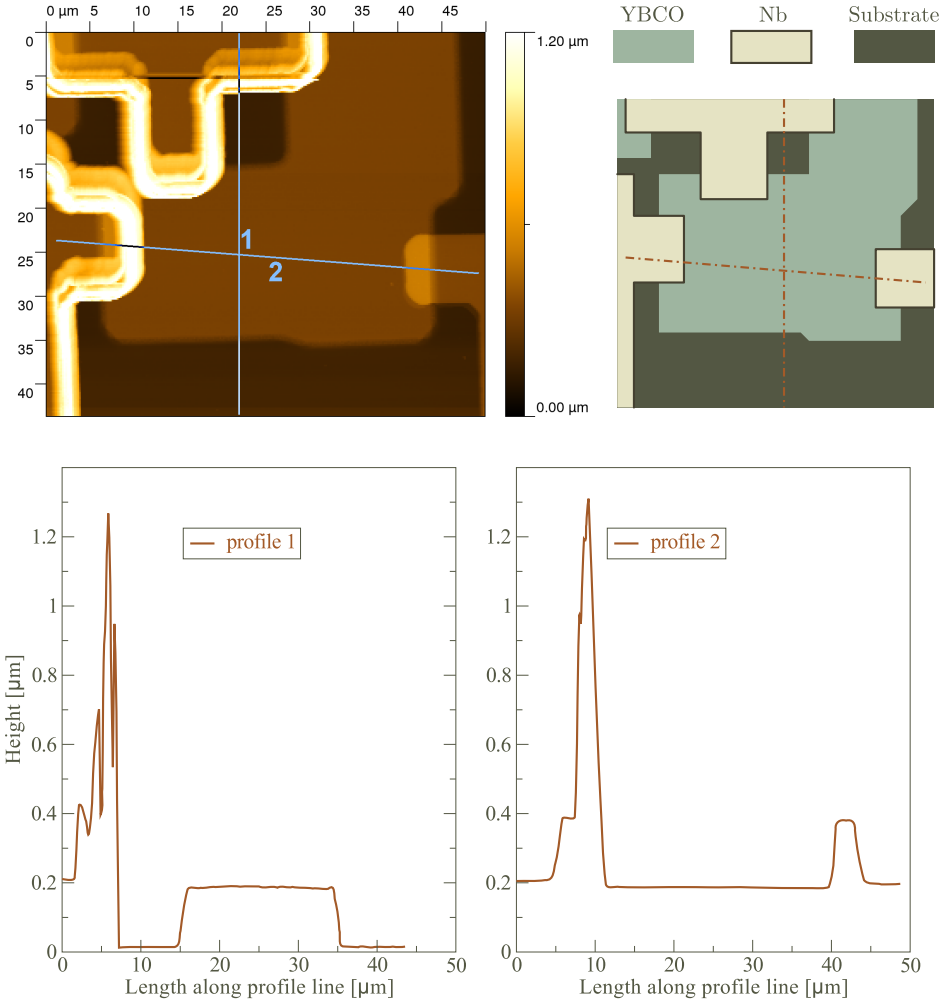

Figure 4.5. A large-area AFM scan of a part of a circuit just after the structuring of the first Niobium layer by lift-off. On the top right a drawing is given of the circuit as designed. Note the very high protrusions found around the edges of the Niobium layer defining the top and left junctions. The junction on the right on the other hand has a well-defined edge indicating that Nb was not deposited on the sidewalls of the photoresist in that area.

Another problem that is very often encountered when performing lift-off arises when the sidewall profiles are not sharp enough for the Nb film to break (and lift off) even at its weakest point. The result is a sample with a Nb film that does not clear the parts covered with the photoresist across a large area of the circuit. This was the most frequent reason for the samples of the πChip2.1X series to fail during manufacturing.

A simple method to acquire undercut (inversely sloped) sidewall profiles of the photoresist is the "image-reversal" technique. The special photoresist then forms in fact a negative stencil, being rendered insoluble in photo-developer by the combination of UV and air exposure. This step is however more lengthy than normal (positive resist) photolithography and requires a baking step at elevated temperatures (120C) for a longer time that may degrade the YBCO layer.

There are a few more practical disadvantages of using any lift-off method for the structuring of the first Niobium layer in the π-shift technology:

- at the moment when the lift-off resist stencil is created, the sample is covered with the Au barrier layer. The sensitive barrier surface is hence exposed to the air and the various chemicals used during lithography.

- the backside of the sample usually has remains of the silver paint used to fix it to the heater holder during PLD (when the YBCO interlayer and Au barrier are deposited). Since the sample's backside must be smooth for the subsequent lithographic step (exposure through a contact mask), it is necessary to mechanically scrape and polish the underside. This increases the chances of damaging or contaminating the fragile Au barrier layer at the top sample surface. If, on the other hand, the lithographic step defining the Nb structures is performed after Nb deposition, then eventual contamination from the polishing of the sample backside will not reach the internal junction area.

- an ultra high vacuum must be reached in the deposition chamber before the Nb layer can be grown. Since this must be achieved with a sample in the chamber that has a considerable area covered by the lift-off resist stencil, film contamination due to the outgassing of the photoresist may occur.

All the above disadvantages are eliminated if the Nb1 layer is first deposited everywhere on the sample immediately after the YBCO interlayer and Au barrier are grown, followed by an Nb etch-step with a suitable photoresist mask (which must thus be inverse w.r.t. lift-off). The typical process used for the structuring of Nb layers in the various thin-film superconducting technologies is an SF_6 reactive plasma etch. This method was also adopted in the π-shift technology, first only for the Nb1 layer in the πChip2.2X series and then for all Nb layers in the subsequent π-shift samples. A summary of the process parameters used in the SF_6 etch step is given in Table 4.1.

Note that the SF_6 plasma does not react with the Au barrier layer beneath the Nb1. The etching is thus automatically stopped exactly at the desired layer in the stack.

Since the SF_6 plasma also etches the photoresist, albeit slowly, the Nb structures are slightly smaller than projected. At the same time however, a gently sloping profile of the edges of the Nb structures is obtained, eliminating step-edge coverage problems for any layers subsequently deposited.

After the Nb1 etch, the remaining resist is dissolved and the SiO_2 isolation layer is grown by RF sputtering. Before the SiO_2 deposition however, the sample is shortly exposed to a low-power RF-sputter etch step in O_2 atmosphere (oxygen ash) to remove any SF_6-hardened photoresist remains. Subsequently, a more powerful RF-sputter etch step in Ar gas is performed to remove the Au barrier and YBCO interlayer on the bare parts of the sample using the just structured Nb1 layer as a hard mask. The SiO_2 deposition then proceeds *in-situ*. The parameters for the O_2 ash and Ar plasma etch are also given in Table 4.1.

	SF_6 reactive plasma etch	O_2 ashing	Ar clean etch
Background P Process P	$<7\cdot10^{-7}$ mbar $5.3\cdot10^{-2}$ mbar SF_6	$<10^{-8}$ mbar $27\cdot10^{-3}$ mbar O_2	*in-situ* $24\cdot10^{-3}$ mbar Ar
RF Power	20W	25W	200W
Voltage	120V	50V	400V
Nb etch rate	≈200nm/10min	/	/
time	>7min	3min	10min

Table 4.1. General parameters of the reactive plasma etch of the Nb layers and the subsequent cleaning steps before the deposition of the SiO_2 isolation layer.

4.1.3 Sputtered *in-situ* Au barrier layer

Although pulsed laser deposition is very useful as a method of epitaxial growth of a wide selection of (complex) materials, some metallic thin films are more easily grown with other techniques. Such is also gold that can be sputter-grown with a DC discharge source in Ar plasma via a simple modification of any existing vacuum system, including a PLD chamber for instance. This was adopted as a growth method of the Au barrier for all π-shift ICs manufactured after the πChip2 series of samples. These circuits are described at the end of this chapter and also in the last chapter of this thesis.

Since Au reflects a great deal of the incoming UV energy (from a KrF excimer source), the laser ablation threshold for gold is necessarily high ($>3.5\frac{\mathrm{J}}{\mathrm{cm}^2}$, see Table 3.1). There are two consequences of using a high energy density at the laser target during ablation:

- taking into account the maximal energy output of a typical excimer laser, it is necessary to use a small spot size in order to reach the required energy density on the Au target

- the high energy density causes large particles to be ejected from the target and deposited as droplets on the substrate

The former results in a small plasma plume diameter that requires a short target to substrate distance, thus increasing the burden on the accuracy of the substrate positioning subsystem. Secondly, the excimer laser source is usually operated at the maximum rated energy output, negatively impacting the pulse-to-pulse and run-to-run variation in output and hence increasing the uncertainty in the thickness of the deposited film.

Additionally, as indicated in subsection 4.1.1, the usage of an experimental PLD apparatus should be avoided when looking for sample-to-sample repeatability. This is further accentuated in the case of the Au deposition by the tight thickness accuracy required of Josephson junction barrier films.

The PLD chamber where the YBCO interlayer is deposited was hence modified by inserting a magnetron-assisted DC sputterhead with an Au target of about 15cm diameter. After the pulsed laser deposition and O_2 annealing of the YBCO interlayer, as described by the standard procedure in Chapter 3, the sample is cooled to 100C and rotated to face the sputterhead. The Au barrier is then deposited *in-situ* after cycling to an Ar atmosphere. The parameters of this step are given in Table 3.3 from Chapter 3.

4.1.4 Ar ion milling of the YBCO ramp surface

This is an important step during the definition of the Josephson junctions in the π-shift technology. The microcrystalline structure of the sloped surface, as well as its angle, substantially influence the properties of the manufactured junctions.

The ramp-etch step with Ar ions has been initially developed for implementation of superconducting circuits in an all-high-T_c film technology. In those early cases the incident Ar beam fell at a fixed in-plane angle w.r.t. the structures on the surface, resulting in a slope as depicted in Figure 3.2 of Chapter 3. However, this method can produce the same ramp angle at only pairs of edges of the aligned YBCO structures at most, see Figure 4.6. At the two edges where the Ar beam throws no shadow and directly etches the resist sidewall, the surface profile will be different when compared to the other two edges where a beam shadow region is formed. Junctions will thus have a different barrier microstructure and exhibit different properties. The circuits built with the π-shift technology typically require junction placement at all four edges of the planar YBCO structures - it is thus necessary to use a ramp etch method where all 4 edge-orientations will be structured in the same way.

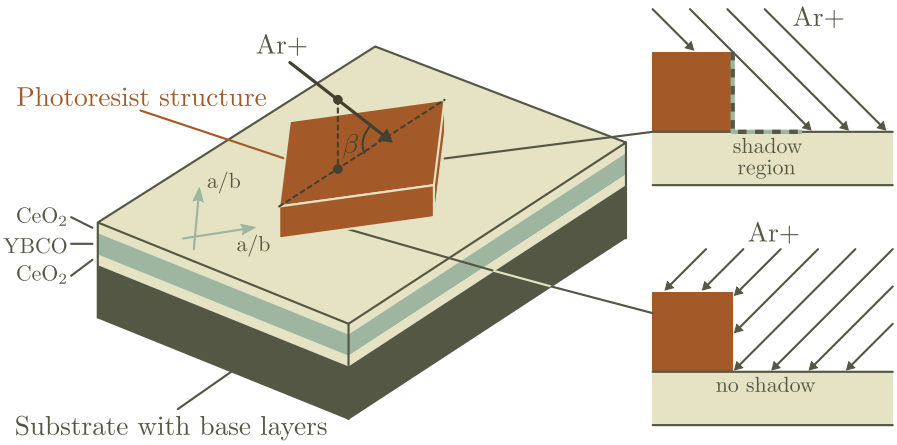

Figure 4.6. Positioning of the substrate for non-rotating ion milling under an angle. The projection of the ion beam on the sample's surface coincides with a diagonal of the rectangular (and YBCO a/b axis aligned) photoresist structures. The two edges sharing the upper right corner will have the same surface profile, which will be different from the one obtained at the two edges sharing the lower left corner.

For the π-shift technology, the substrate holder was made to rotate during the ion-milling with the normal of the sample's surface kept under an angle of 45 degrees with the incoming beam, see Figure 3.2. As a result, the ramped surfaces are all the same at the 4 sides of the rectangular YBCO structures but with an sloped profile that is more complex than the one obtained during a non-rotating ion etch.

If the Ar ions arrive from behind the resist sidewall, throwing a shadow across a region of the substrate surface, the slope of the obtained ramped surface is calculated as

$$\alpha_1 = \arctan\left(\frac{\tan(\gamma)}{1+x(\beta)}\right) \tag{4.1}$$

where γ is the "shadow angle" that the incident Ar beam forms with the resist structure and $x(\beta) = \frac{R_{\mathrm{resist}}(\beta)}{R_{\mathrm{film}}(\beta)}$ is the ratio between the etch rates of the resist and the film on the bare substrate surface (see Figure 4.7). The etch rates depend only on the angle of impact of the Ar ions on the respective surfaces, in this case equal to β for both materials. The shadow angle γ

$$\tan(\gamma) = \frac{\tan(\beta)}{\cos(\delta)}$$

depends on both β and δ, the last the angle that the projection of the Ar ion beam on the surface makes with the normal of the photoresist's sidewall (the "rotation angle"). In Figure 4.7, a graphical representation of the etch process and all angles is given.

Alternatively, if the Ar ions arrive from the other side, striking both the resist sidewall and its top surface, the produced ramp angle is

$$\alpha_2 = \arctan\left(\frac{1}{x(\beta,\delta)}\right) \tag{4.2}$$

which is usually higher than α_1. The photoresist etch rate $R_{\mathrm{resist}}(\rho)$ used to calculate the ratio $x(\beta, \delta) = \frac{R_{\mathrm{resist}}(\rho)}{R_{\mathrm{film}}(\beta)}$ in this case depends on the ion beam impact angle ρ on its sidewall. This angle is, generally, different than β:

$$\cos^2(\rho) = 1 - \cos^2(\beta)\cos^2(\delta)$$

Figure 4.7 illustrates this etch process as well.

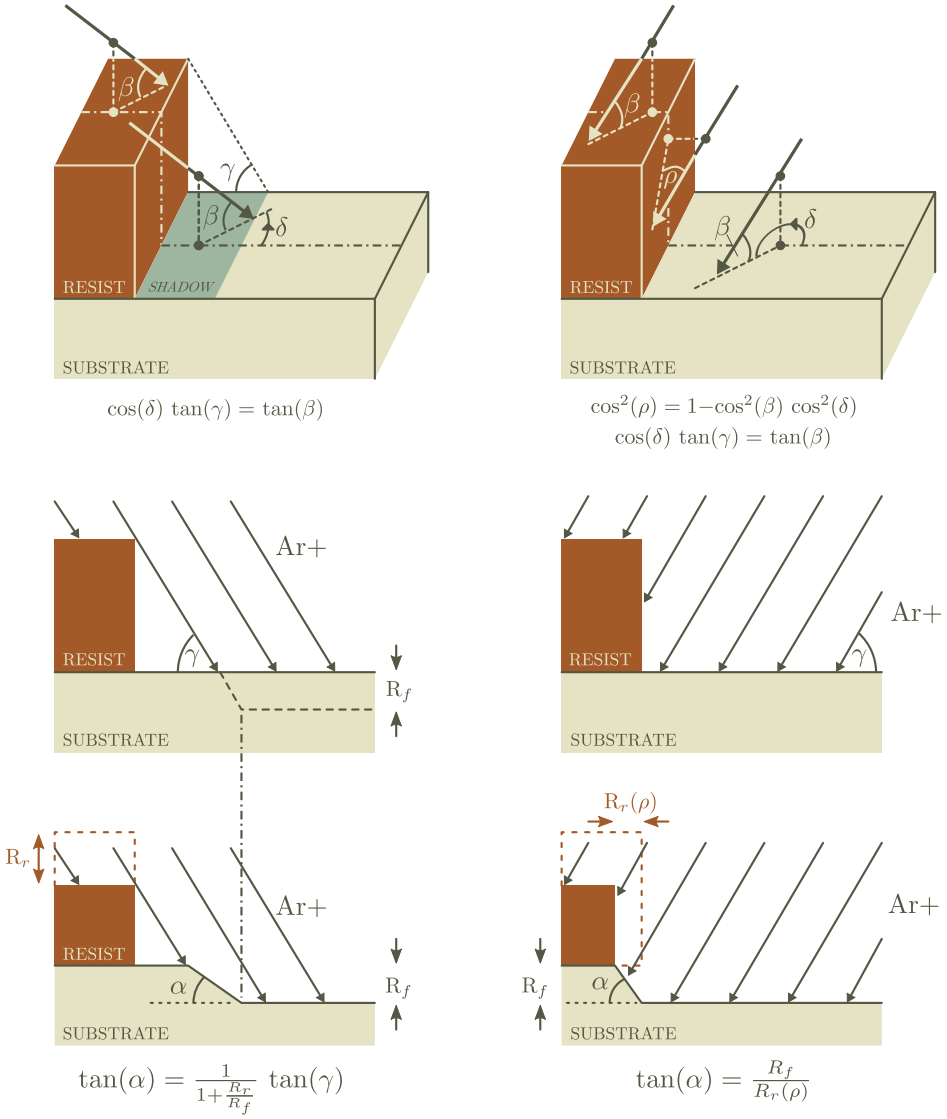

Figure 4.7. Graphic representation of the two types of etch processes taking place for different rotation angles δ. On the left, when $-\frac{\pi}{2} < \delta < \frac{\pi}{2}$, the Ar ion beam throws a shadow across the sample surface whose length varies with the rotation angle δ, while the etch rates of the materials depend solely on the impact angle β. On the right, for $\frac{\pi}{2} < \delta < \frac{3\pi}{2}$, there is no shadow and the slope forms by milling of the resist sidewall, gradually exposing the sample surface underneath. Here, the impact angle on the resist sidewall is ρ, generally different than the impact angle on the photoresist's and substrate's top surface which is β. Hence, the etch rate of the resist sidewall will be different than the etch rate of the resist top surface. The shadow angle γ plays no role in this case.

According to Figure 4.7 and the equations 4.1 - 4.2, there is a combination of the angles β and δ that, given the etch rates of the photoresist and substrate films as a function of the ion beam impact angle, can result in $\alpha_1 = \alpha_2$. Therefore, looking at the case described in Figure 4.6, where $\delta = 45°$, one can find an incidence angle β for which the sloped substrate profile on all the edges of the structure will have the same angle. It then seems not necessary to use rotational etching as a method to equalize the slopes on the four edges. This is however not the case. First, the model from Figure 4.7 does not take into account some finer effects, such as the impact angle of the Ar ions on the sloped substrate surface which is not only other than β but also different in both cases (roughly $\beta - \alpha$ on the left and $\beta + \alpha$ on the right side of Figure 4.7). Hence, the microcrystalline properties of the sloped substrate surfaces will be different. Secondly, the edges where the ion beam throws a shadow will accumulate hardened resputtered material in the shadow region on the substrate surface. This will not happen for the other two edges. As a conclusion, it is safe to state that such a "β-tuned" non-rotating ion mill is not a good method to provide equal-slope ramped surfaces.

A single rotation of the sample under the ion beam can be taken into account as a modulation of the angle δ from 0 to 2π while the incidence angle β is constant. During half of a rotation period, the ramp surface is formed according to the regime of equation 4.1 and in other half according to the process described by equation 4.2, all the while δ is changing. The resulting surface profile is a combination of the two ion mill regimes and can be described with a theoretical model by expanding the concept from Figure 4.7. There are a few difficulties however:

- resist sidewall profiles are not normal to the surface but form a sloping edge that is highly dependent on resist type and lithographic procedure - the sloping resist sidewall profile is unpredictable in practice.
- the model requires a finite-element approach to the space occupied with the resist and the substrate film in addition to a discretisation of the total etch time (not just a single cycle) in small increments.
- when the ramp surface must pass through multiple layers on the substrate, as is the case with the base layers in the π-shift technology, the model becomes even more complex.
- photoresist hardening from redeposition and the behaviour of materials at their interfaces is difficult to take into account

It is therefore not practical to theoretically model the rotating ion mill process, but nevertheless, a qualitative understanding of the mechanism can be made. In Figure 4.8 for instance, it is assumed that the Ar ion beam does not rotate but alternates in direction between the front ($\delta = 0°$) and back ($\delta = 180°$) of the resist sidewall while the impact angle with the surface is kept at $\beta = 45°$. The result is

a double-ramp surface with approximately two slope angles α_1 and α_2 that meet after a certain number of δ alterations. When the substrate surface is continuously rotated, the obtained slope will also have roughly two components but with a gradual change between them. This is also confirmed from AFM images of ramp surfaces, given in Figure 4.9 and Figure 4.10.

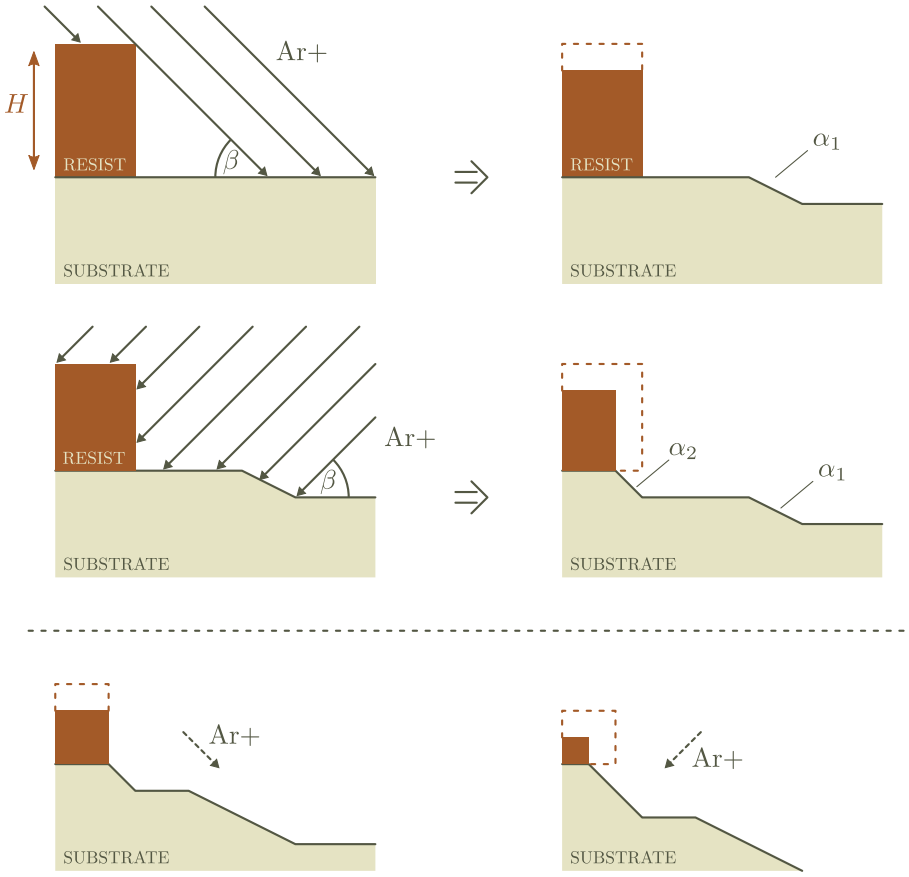

Figure 4.8. A diagram of the etch process for an alternating $\delta = (0°, 180°)$. Note that initially, the two sequentially etched slopes are horizontally separated on the substrate by a length of $H \cdot \mathrm{ctan}\,(\beta)$ with H the (changing) photoresist height. As the resist becomes thinner and the substrate is etched deeper, the two sloped surfaces move towards each other and eventually join at some distance along the substrate surface. The end result, after many $0 \to 180 \to 0 \to 180 \to \ldots$ iterations, is a complex sloped surface with roughly two angles of inclination.

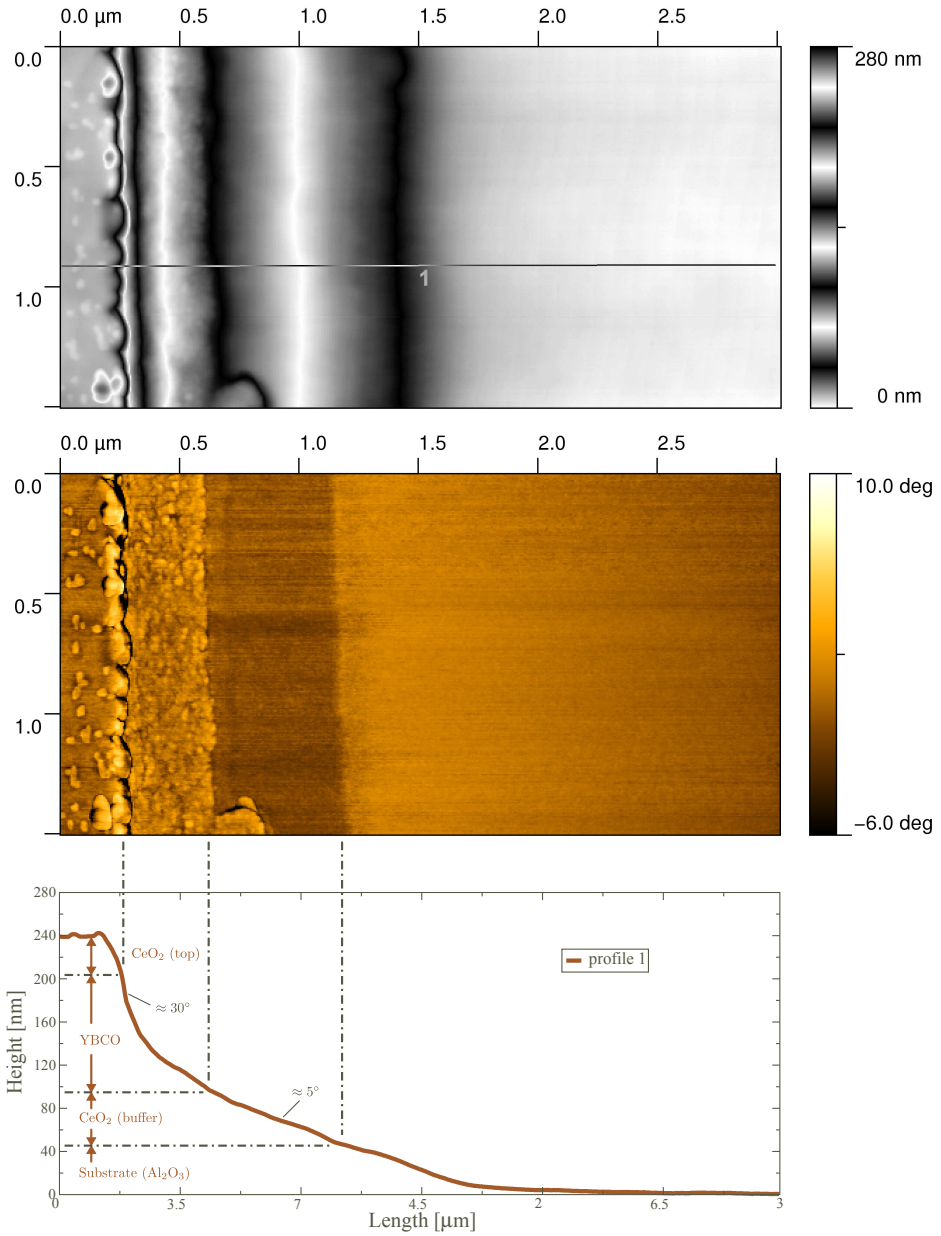

Figure 4.9. AFM image of a slope produced by a rotating ion mill with $\beta = 45°$. At the top the height sensor is plotted (cyclic colour), in the middle is the phase signal of the tapping-mode AFM tip while the plot below is the height profile averaged over the whole width of the scan (1.5 μm). Aligning the different regions visible in the phase image with the height profile, one can determine the composition of the different layers on the slope.

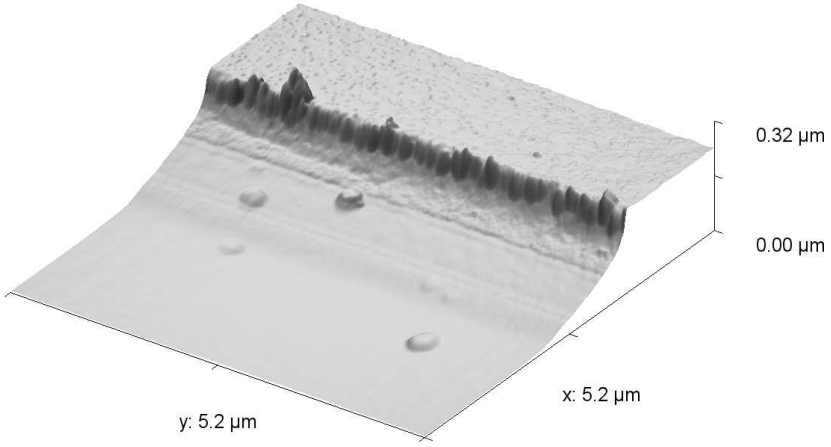

Figure 4.10. A 3D height plot (with shading effect) from an AFM scan of a ramp structured by rotating ion mill with $\beta = 45°$. It shows a larger area centered around the same region as in Figure 4.9 above.

Both AFM images, Figure 4.9 and Figure 4.10, are taken after the 500V/50V Ar ion cleaning step (see Table 3.2 in Chapter 3) and thus before the deposition of the YBCO interlayer and Au barrier. The double sloped surface of the ramp can clearly be seen, as does the different texture of the materials incorporated in the multiple base layers. From Figure 4.9, the point where the two slopes meet, or the "knee" of the height profile, lies within the YBCO layer about half-way along its thickness. The maximum angle of the YBCO ramp is about 30° at the top and slightly above 5° at the bottom part of the slope, while its average angle is 17°. The whole ramp, including the top and bottom CeO_2 layers but excluding the part etched in the Al_2O_3 substrate, has an average slope of $\approx$10°.

Note that if the total etched height changes, for instance due to process drift in the ion milling apparatus that usually results in an uncertain etch rate of the materials, then the position of the "knee" of the double-sloped surface will also change. For a lower total height, the "knee" shifts upwards in position relative to

the YBCO layer and leaves the ramped YBCO surface with a predominantly 5° slope. Conversely, when the total etch height is greater, the "knee" shifts lower and the exposed YBCO surface will have a predominantly 30° angle. Since it is expected that ramp-type junctions formed on a different slope will exhibit different characteristics, the total height etched through the base layers during rotating Ar ion milling is an important parameter during junction fabrication. Although there were no systematic experiments performed on junction J_C vs. total etched height of the ramp, available data from a few samples suggests a positive correlation between them: J_C increases with the total etched height of the ramp. A simple explanation for this trend would be that when the YBCO ramp has a higher average slope, expected when the ramp is predominantly of a 30° angle and thus of a higher total etch height, the thickness of the barrier *in the direction of current transport reduces* although the deposited thickness of the barrier on the flat parts remains equal. The J_C of the junction is then higher.

Controlling the total etched height (with AFM) after the Ar ion milling of the ramp has therefore been added as an essential part of the π-shift process for all post πChip2 samples.

4.1.5 Measurement artifacts

Many of the fabricated πChip circuits, as mentioned previously in Chapter 3, suffer from systematic measurement problems. These are caused by insufficient shielding of environmental noise or, in some cases, by poor protection from overvoltage/overcurrent damage from ESD (electrostatic discharge) during handling and during the measurement itself. It is notable that ESD phenomena in superconducting circuits are poorly understood even though superconducting devices like Josephson junctions consist of thin isolating barriers that may be easily damaged by excessive discharge voltages (at room T).

Magnetic shielding is a common problem that plagues superconducting circuits of all kinds. Even the very weak static magnetic field of the Earth is more than sufficient to disable a superconducting IC by inducing Abrikosov and/or Josephson vortices in the thin films and/or junctions respectively. Alternating magnetic fields (noise) are easily picked up by the superconducting traces while high frequency fields will even create interference with the Josephson oscillations of a junction when it is in a voltage state. Magnetic shields are thus necessary to block DC fields and continuously protect against noise while the circuits operate. Bulk superconducting shields enveloping the superconducting IC, its holder and connectors are mostly used when the IC is operated in a liquid helium bath while high-mu materials and superconducting shielding very local to or on the IC is used in other cases.

The magnetic shielding is however not always effective for sensitive circuits and is usually very difficult to correctly apply in each experimental system. Especially high-T_c superconducting circuits need very elaborate shielding since there is a lack

of suitable materials that have good DC shielding properties at those temperatures.

Along with magnetic shielding, a time consuming procedure, called *magnetic defluxing*, is additionally used to cancel-out the Earth's and other DC magnetic fields. The defluxing method consists of repeated warm-up/cool-down cycling of the circuit around the T_c of the used materials all the while attempting to cancel the environmental magnetic field with a compensation coil. A circuit parameter, usually the I_C of a DC-SQUID (or a similar structure), is measured at the end of each temperature cycle while keeping the current I_{comp} through the compensation coil at a fixed value. After calculating the standard deviation σ of the circuit parameter across a number of temperature cycles (eg. 10), the field of the compensation coil is changed by incrementing I_{comp} with a small value and the statistics of the circuit parameter are again obtained for the same number of temperature cycles. In this way, one obtains the standard deviation of the circuit parameter as a function of the compensation current $\sigma = \sigma(I_{\mathrm{comp}})$. At the end, the compensation current is set at the value that corresponds with a minimum in the $\sigma(I_{\mathrm{comp}})$ plot and the defluxing procedure is completed.

The reasoning behind this method is that when the external fields are cancelled with the field created by I_{comp} flowing through the compensation coil, there will be no flux trapping in the thin films and hence no influence on the circuits parameters - they will be the same after each temperature cycle and there will be zero variation along cycles. If, on the other hand, the environmental magnetic field is not cancelled, then the stochastic nature of the flux trapping mechanism in the superconducting films with each warm-up/cool-down cycle will reflect in variations in the circuit parameters between cycles.

Unfortunately, this method is impractical for the hybrid YBCO/Nb π-shift circuit technology. The problem lies in the fact that the temperature cycling of the samples must pass through the T_c of the YBCO films in order to deflux them. As the operating temperature of the circuits lies below the T_c of the Nb films, every temperature cycle must span at least $T_{c,\mathrm{YBCO}} - T_{c,\mathrm{Nb}} \approx 80K$! In comparison, the defluxing temperature span for an all-Nb circuit is just a few Kelvin (between 10K and 4K for instance) and is usually performed locally by passing a pulse of high current through an on-chip resistor. The time needed for each temperature cycle is then just a couple of seconds. An 80K temperature cycle on the other hand requires, at the very least, about 15 minutes as it must be performed in a controlled way on the whole sample & holder assembly, not just locally (otherwise T gradients and the associated mechanical stresses will be too great). Taking 10 measurements for the statistical data set per compensation current point and 10 compensation current points in total, which is barely enough data to recognise a minimum in the $\sigma(I_{\mathrm{comp}})$ plot, one needs at least $10 \cdot 10 \cdot 15\mathrm{min} = 25\mathrm{h}$ to deflux a YBCO/Nb sample. In reality, the procedure is likely to take about 2 days. Obviously, this is not a viable method.

Nevertheless, a low T-span defluxing procedure was attempted with the πChip2.25 sample in a measurement setup specialized for experiments with low-T_c Nb superconducting circuits and equipped with an automatized defluxing system [46]. A short current pulse through an Au resistor structured on the sample was used to temporarily raise the temperature of the neighbouring RSFQ π-shift circuit structures above the Nb T_c, while the measurement system, synchronised with the pulse, was set to automatically measure and record the I_C at the output of a DC-SFQ-DC after the temperature dropped to the operating value of 4.2K at the end of each cycle (a few seconds after the end of the current pulse). After taking 10 measurements, the current through a compensation coil placed on the backside of the sample holder was changed. The system then plots the statistical variation σ in the I_C data for each compensation current setting I_{comp}. There were no observable features in the σ vs. I_{comp} plot (except noise) even though the critical current of the circuit was visibly modulated by the compensation coil at the working temperature of 4.2K. A reasonable conclusion is that the heating of the circuits with the local resistor does not reach the desired 80K temperature span and hence leaves eventual trapped vortices in the YBCO films unchanged.

To solve the magnetic shielding problems one must, in fact, use solutions specific to high-T_c circuits as standard shielding and defluxing procedures are not effective for YBCO/Nb π-shift circuits. Such an approach was used during experiments with the πChip2.2X and later samples where 3 different shielding canisters (from inner to outer: BSCCO pot, cryoperm pot, Nb foil) were used around the dipping sample assembly in addition to the low-noise enclosure of a bath cryostat. In comparison to the πChip2.1X series, that were measured in a flow cryostat with both poor DC shielding (cryoperm only) and low measurement leads noise immunity, the results obtained from the πChip2.2X series were more stable. Nevertheless, variations in the measured results across sessions were sometimes observed even with the more elaborate shielding setup for complex circuits that are sensitive to environmental noise.

An intrinsic solution to the shielding problem for all superconducting circuits is operation at sub-kelvin temperatures (eg. 600mK), where "perfect" magnetic shields made out of type I superconductors such as Aluminium can be used. The refrigeration equipment already exists for some time, albeit at an increased cost, and is used in qubit experiments with great success. It is the firm belief of the author that adopting the direction of sub-kelvin operation will prove beneficial even with the increased cost of cryogenic refrigeration. The last is already quite high for existing 4.2K circuits and will not materially affect the decisions of an interested investment party as opposed to the case where *both* refrigeration and the inability to demonstrate that shielding problems are sufficiently addressed will be

their main objections. In addition, and also borrowed from flux qubit experiments, one can replace Niobium altogether with Aluminium as a superconducting material used in thin-film circuits.

For the π-shift circuits, if operated at sub-kelvin temperatures with Al canister shielding, the last can be made to reach its T_c before the YBCO does and thus protect the circuit from environmental fields. It will then not be necessary to use defluxing or high-T_c shielding.

4.2 I_C spread estimation

Following the changes to the manufacturing process described in Section 4.1, several samples were manufactured in order to investigate the spread in the junction parameters. For that purpose, series arrays of Josephson junctions with the same dimensions were manufactured and their I/V characteristics were measured. One can then estimate the spread in the I_C of the junctions in the array from the obtained measurement plot. The average R_N of the junctions can be calculated as well.

The physical layout of the arrays is given in Figure 4.11, together with a microphotograph of the manufactured structure on one of the samples.

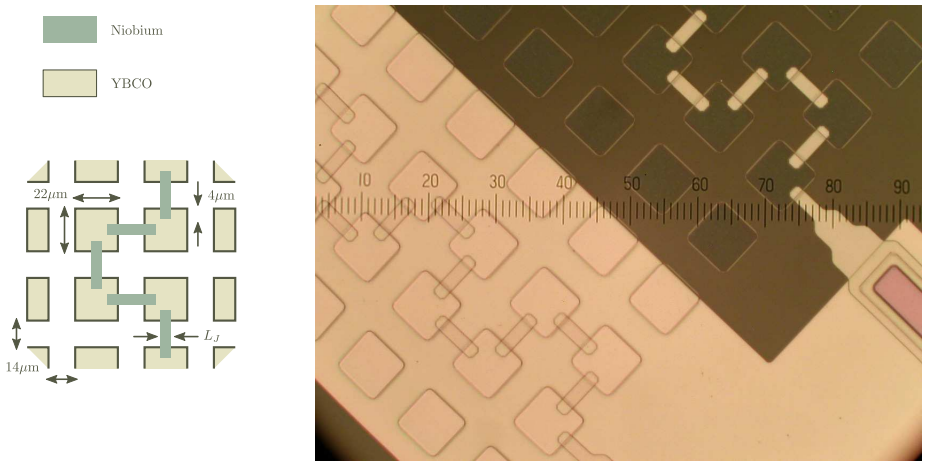

Figure 4.11. A drawing and a microphoto of a standard ramp-type junction array. The latter also includes part of the contact structure and a second, identical, array that is covered by a groundplane layer. Ten units of the ruler on the right measure about 30μm. The junction width $L_J = 6\mu$m for the ladders on the right.

Had all junctions in the array the same I_C, then the I/V characteristic would exhibit a large jump to the voltage state at $I = I_C$ as all junctions switch to their voltage state at the same current. The I/V characteristic of an N-junction array would then be similar to the one of a single junction, except for the scaling of voltage axis by N times (barring any phase-locking effects).

When the junctions in the array have different I_C's, bound in a range, then the I/V characteristic is similar to the plotted data in Figure 4.12. The junctions will sequentially switch to the voltage state as I is incremented higher, creating an intermediate transition region between the superconducting and voltage state. Estimating the width of the transition region on the current axis, the I_C range of the junctions in the array is approximated. Looking at the slope of the characteristic at higher I, typically at $>5\,I_C$, the average normal resistance R_N of all junctions is found.

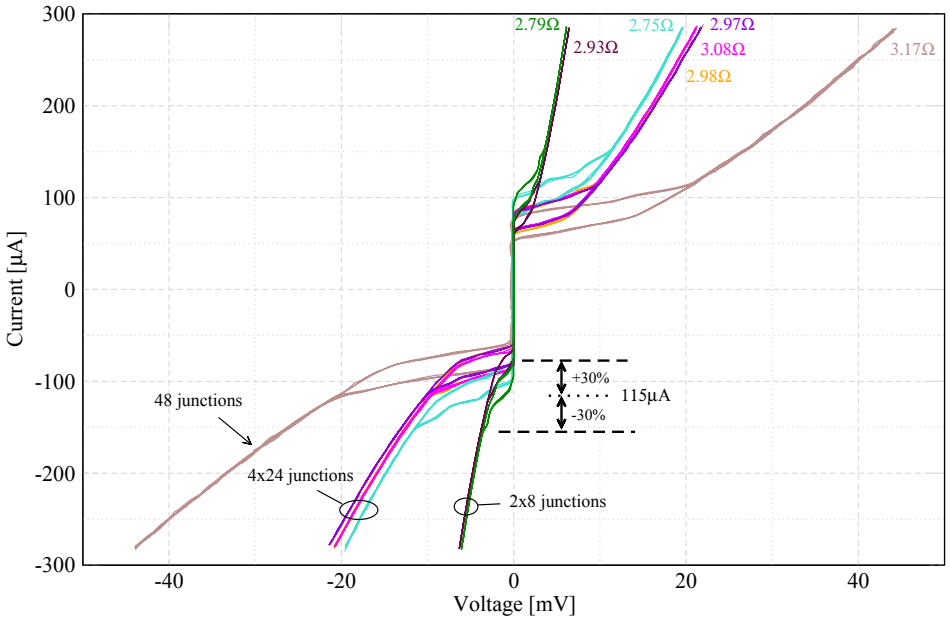

Figure 4.12. The I/V curves of seven arrays, measured separately (4.2K), containing in total $48 + 4 \cdot 24 + 2 \cdot 8 = 160$ YBCO/Nb ramp-type Josephson junctions with $L_J = 10\mu$m. The resistances indicate the average R_N of the junctions for each array separately. They are calculated as the slope of the I/V characteristic at $I \approx 500$uA (plot area not shown).

When the $I_C\,R_N$ product of the junctions is high, one can even observe the individual switching of the junctions in the array on the I/V characteristic. It is then possible to process the measured data and identify the I_C of every junction,

yielding a more reliable estimation of the I_C spread. Unfortunately, the YBCO/Nb ramp-type junctions have a $I_C R_N < 500\mu$V and the individual switching events are typically drowned by measurement noise. The ranges given below are thus not determined by the standard method of individually-resolved switching events but nevertheless, they offer an estimate of the actual I_C spread for the manufacturing process. Note that the spread obtained in this way gives the maximum and minimum limits, as well as a mean value. For a large number of junctions in the array, these limits will approach the $\pm 3\,\sigma$ spread in the I_C of the junctions.

In Table 4.2, a summary is given of the I_C spread data for the various samples.

sample name	ramp height H	barrier thickness d_{Au}	Arrays with GP $I_C\left[\frac{\mu\mathrm{A}}{\mu\mathrm{m}}\right]$	Arrays with GP $R_N\ [\Omega\,\mu\mathrm{m}]$	Arrays no GP $I_C\left[\frac{\mu\mathrm{A}}{\mu\mathrm{m}}\right]$	Arrays no GP $R_N\ [\Omega\,\mu\mathrm{m}]$
SJLπ1	170nm	20nm	/	/	$11.5 \pm 30\%$	30
SJLπ3	220nm	20nm	$19.5 \pm 20\%$	23	/	/
SJLπ4	235nm	25nm	$28 \pm 20\%$	18	/	/
SCAL1.1	230nm	30nm	$18 \pm 20\%$	13	$20 \pm 30\%$	21
SCAL1.2	242nm	40nm	$36 \pm 56\%$	7	$21.5 \pm 30\%$	20
SCAL2.1	215nm	40nm	$9.5 \pm 26\%$	26	$11 \pm 38\%$	26
SCAL2.2	200nm	40nm	/	/	$3.5 \pm 46\%$	76

Table 4.2. Collated measured I_C spread and R_N data per unit junction width, separately for junction arrays with and without a groundplane (GP). Also given are the heights of the YBCO ramp and the thickness of the gold barrier. The former is measured during manufacturing while the latter is the targeted nominal value (calibrated separately). All measurements were performed at 4.2K. The base layers for the samples from the two series originate from different batches, SJLπX samples having a YBCO base layer of a slightly greater T_c. The number of junctions in total per data point is >100.

The measurement data shows a considerable junction spread: in every case the $3\,\sigma > 20\%$. The measurements above also indicate a correlation between the height of the YBCO ramp and the mean value of the junction critical current. Even more interesting is the lack of strong correlation between the barrier thickness and critical current.

However, it must be mentioned that the measurement data presented in Table 4.2 was not obtained as a part of a controlled experiment for finding statistical relations between the process and device parameters. Any observed connection is therefore just an indication of a possible effect, not a proof for one.

Together with the I_C spread data, measurements were performed on direct-injection SQUID circuits with different dimensions of the modulation segments in order to find the electrical parameters of the films, with special attention to the YBCO layer. The measured data was then compared to EM simulations of the same structures, following the method from Section 2.3 in Chapter 2, yielding the best fit for $\lambda_{L,\mathrm{YBCO}} = 200\mathrm{nm}$ at 4.2K. Although higher than expected, the penetration depth is still reasonable for a YBCO film. A penetration depth of between 60nm and 100nm is the best fit for the Nb film, the wide range a consequence of the lower sensitivity of the inductive parameters in a circuit to the $\lambda_{L,\mathrm{Nb}}$.

After the changes described in the first section of this Chapter were introduced, clear improvements in process robustness were observed in some areas. First, the average J_C value of the junctions across many samples was consistent, not varying much between the various samples (contrast to the πChip results from Chapter 3). Further, a good agreement was found between EM simulations and measurements of the electrical characteristics of the superconducting films. Although some improvement has been booked in the magnetic shielding and noise-immunity areas, it is still insufficient and most importantly, it is doubtful whether further reduction is possible. At the end, the junction spread on each sample showed a considerable advance towards lower values, acceptable in some applications but generally too high for complex circuits.

Extrapolating the rate of progress in the experimentation aspects of the YBCO/Nb π-shift technology, it can be expected that the technological threshold can be reached at a moderate cost, provided that the shielding problems are satisfactorily solved. In this direction, one may look for the approach where Nb is replaced by Al and the operation temperature is lowered to a few hundred mK, including Al shielding. Additionally, outsourcing of the interlayer/barrier deposition step, resulting in an ex-situ processing, as well as of the backend (SiO_2 and Nb layers) can reduce sample turnaround time considerably. In that case, only the Ar+ ion gun etch of the barrier ramp surface will remain as a process step specific to this π-shift technology - this is probably the most optimal situation given the more than sufficient stability in the other processing steps when outsourced commercially. Another avenue that can be explored is the use of standard Nb SIS junctions instead of the YBCO/Nb ramp-type contacts, where the last are manufactured with a very high J_C so that they are considered as short-circuits only.

Chapter 5

Static superconducting circuits using inductively modulated π-loops

A consequence of the collective state in which the charge carriers reside in a superconductor, as indicated by the existence of the macroscopic quantum wavefunction $\Psi(\vec{r},\ t)$ throughout the superconducting material, is the disappearance of DC electrical resistance. Some common properties of superconducting digital devices, such as low power dissipation and high operation speed, ultimately originate from such an extremely low-ohmic environment. However, superconducting circuits also show other, more fundamental, phenomena connected to the collective state of the charge condensate. An important one is flux quantization in superconducting loops: the amount of magnetic flux quanta held in a loop acts as a degree of freedom that physically implements the state-space of the computing architecture. The advantages of superconducting circuits based on the flux quantization principle are: an ultra low dissipated energy per bit ratio, processing rates multiple times higher than semiconducting equivalents of same integration density, and relatively simple manufacturing technology.

The most widely known example of such circuits is the SFQ (Single Flux Quantum) [2], [47], [48], logic family. SFQ circuits use picosecond voltage pulses, with a quantized time integral, as signals communicated between logic gates. However, since only unipolar pulses are available, a multi-symbol communication (e.g. binary) necessitates the definition of the symbols to at least include a second, or reference, signal. That signal will need to be compatible with the SFQ circuits and thus also transient (pulsed) in nature. In synchronous machines, this is most efficiently achieved by using the fixed periodic pulse sequence of the clock as a reference in the definition of each communicated symbol. Hence, if a synchronous computing machine is to be implemented in SFQ hardware, it results in a heavily pipelined realization where all elementary gates must be synchronous. A class of event-driven SFQ circuits [49] has been proposed to circumvent this drawback, but it requires asynchronous operation that is not conductive to wide-spread digital design methodologies. Other techniques, for instance the "dual rail" method [50], [51], attach two unipolar pulsed signals to each symbol in a differential way so as to approximate a level-based symbol definition.

As an alternative to SFQ circuits, a few proposals for static implementation of discrete superconducting computing machines appear in the literature. The common idea is not to define each communication symbol with pulses but rather by a corresponding signal level range. This would be similar with standard semiconductor technology, where voltage levels unambiguously define the symbols communicated between interconnected gates. However, in order to keep the advantages of implementing the state-space of a superconducting discrete machine as static flux quanta held in loops, the signal domain must be other than voltage. The reason is the fact that superconducting devices can produce voltage levels only during dynamic (transient) situations when continuous oscillations between states appear.

Static flux-domain circuits usually possess the interesting characteristic of physical and logical reversibility, where information "propagated" through the circuit is minimally affected by energetic exchange with the environment and essentially remains conserved throughout the computational process. Some superconducting qubit devices [9] also operate in the magnetic flux domain, where state operations are performed. As static flux-domain devices, including the ones proposed in this thesis, exist in near-equilibrium during the transitions and are almost completely isolated from the environment, they can be useful in superconducting quantum circuits.

Most notable examples of static level-based superconducting circuits, where the signal domain is magnetic flux, are those based on parametron [52], [53], [54], [55], and complementary SQUID [56] devices.

QFP (Quantum Flux Parametron) circuits [54], [55], are built around a parametric amplifier device, realized as an inductively coupled superconducting loop with Josephson junctions inserted in each arm. The device works with signals in the magnetic flux domain and uses the parametric amplification principle: a periodic "pump" signal mixes the inputs in a nonlinear way that eventually results in a transfer characteristic with signal gain. This principle enables the implementation of basic logic functions, like for instance majority gates. Input/output signal isolation is absent in the basic QFP device and is architecturally implemented by a pipelined 3-phase clocking scheme. A different parametric device, inspired by the earliest [52] [53] flux parametrons, is the n-SQUID [57]. It uses locally generated clock phases and employs a novel galvanic device coupling idea that allows common-mode (or DC) isolation between devices. Although this recent development improves the practicality of parametron circuits, their common limitation to only a multi-phase synchronous realization remains. It is worth noting that also a quantum mode of operation [58] is proposed with parametron devices.

The complementary circuits [56] are closely related to the circuits described in this text and also posses the property of static signal gain. But, it is achieved only in the presence of a (constant) external current source and thus elementary

gates tend to be more complex. Complementary circuits can however be used at interfaces where the reversible nature of the devices proposed below limits operation.

Other practical problems in implementing the two mentioned families of static circuits, like for instance transport of the signal across a long interconnect, restrict their application to moderate complexities [59], [60], [61] only.

The flux-domain circuits based on an inductively coupled π-loop on the other hand, exhibit static signal gain that enables the construction of simple combinational logic blocks. Additionally, the gain and the dynamic range are proportional, within certain parameter limits, to the load inductance thus offering greater flexibility in the signal transport. The main potential of the proposed static π-shift family lies in low complexity combinational circuits that need to work in a domain other than voltage due to dissipation reasons, for instance alongside superconducting qubits.

In this Chapter, a new type of computational application of superconducting circuits will be presented, based on inductively coupled π-loop devices. In the following section, it is shown that a magnetically modulated π-loop, under certain conditions, exhibits gain between the applied and the output flux across a load in a limited region of the input-output characteristic. Afterwards, in Section 5.2, an analysis of the properties of the π-loops when equipped with an inductive modulation terminal and cascaded in larger circuits is given. At the end, Section 5.3 concludes this Chapter with a summary and proposes a majority-based logic cell implemented with inductively-coupled π-loops.

Measurements results of a flux-modulated π-loop are given in the following Chapter.

5.1 A two-port, flux modulated π-loop

The main focus in this section is a device consisting of a superconducting loop interrupted by two Josephson junctions, more commonly known as a SQUID (Superconducting QUantum Interference Device) [62] [16] and widely used in magnetic flux sensors and for storage of the states in superconducting discrete machines. A π-loop [6] [7] is a special kind of SQUID that has a built-in phase offset of π radians between the interferometer arms. A circuit model and a conceptual drawing of a π-loop are given in Figure 5.1. Notably, the asymmetry between the loop's arms must be intrinsic to the physical structure of the device and not externally generated on a symmetric device, for example by an external flux bias. A more detailed discussion about the spatial symmetry of the loop and its properties is given further below (see Fig. 5.5).

Due to the requirement for single-valuedness of the condensate's wavefunction, the π-loop needs to compensate the built-in asymmetry originating from the π-shift located within one of the interferometer arms by self-excitation of a circulating current. Such a current will be established in the structure *without* an external field or any other action: it is enough to just cool the device below the T_C of the superconducting material(s) and the compensation current will appear. This property of spontaneous flux generation is found to be symmetric with respect to the direction of circulation of the generated current. Hence, the π-SQUID is a naturally bistable device [6]: both circulating states are equivalent thermodynamically but symmetrically opposite in circuit terms. The effect has been used to construct superconducting circuits in the logic family RSFQ [8] [3] that are expected, all things equal, to have a remarkable process margin improvement when compared to circuits based on conventional superconducting loops [4].

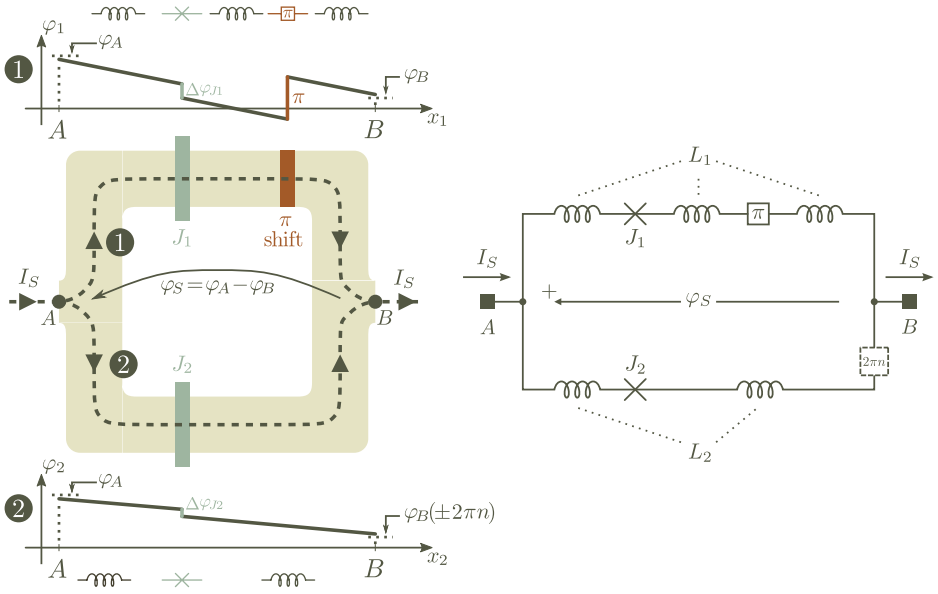

Figure 5.1. Drawing of a π-loop including the Josephson junctions J_1 and J_2, the π-shift element, a sketch of the condensate wavefunction's argument (the phase) in the two arms (left) and a circuit diagram representing the equivalent electrical elements and their connections (right).

The discrete π-shift in the phase of the superconducting condensate's wavefunction is considered as a passive circuit element in equivalent electrical schematics. In its constitutive relation, $\varphi = \pm\pi$, it is not defined whether the π-shift element is an ideal π-phase-drop or π-phase-source: the phase across its terminals is always taken to be$\pm\pi$ regardless of the direction of the current flowing through the element.

According to the present state-of-the-art in superconducting devices, the most widely used ways to implement a π-shift are:

- a 90° turn of the current path in the (001) crystal plane (a-b plane) of a superconductor with a *d-wave* order parameter symmetry (such as $YBa_2Cu_3O_{7-\delta}$) [63]

- using a Josephson junction with a ferromagnetic barrier of a certain thickness that effectively integrates the π-shift element with one of the interferometer junctions [64]

- between symmetric terminals of a superconducting loop in which one flux quantum Φ_0 is "frozen", i.e. a loop in which the condensate's vorticity is excited and held in the metastable +1 or -1 state [65].

- a long (distributed) junction with a current injection-extraction pair placed in one of the electrodes where, under certain conditions, the distributed junction-inductor system can equivalently behave as if a phase shift of tunable amplitude was present at the injection points [66].

In [37], the physics, phenomenology and other, less known ways to implement the π-shift effect are briefly summarized with an extensive bibliography. The measurements presented in this text are based on samples that implement the π-shift using the first method above.

The exact nature of the π-shift implementation is, in first instance, not relevant since all realizations are equivalent between each other in circuit terms, except for [66] that requires distributed network modeling. As the main concern in this text is to illustrate the operation of generic π-shift circuits, no difference is made between the various π-shift implementations unless explicitly stated. We shall thus use the π-shift as a basic circuit element without taking into account eventual parasitics or secondary effects arising from the specific implementation.

Fig. 5.2 compares the dependence of the total critical current of a normal and a π-loop as a function of the magnetic flux externally applied to the loop. The normal loop follows the well-known cosine modulation of its critical current, compared to the sine modulation apparent at the terminals of a π-loop. Observing Fig. 5.2, one may notice the complementarity of the two characteristics: when the normal loop is "on", i.e. the critical current is at a maximum, the π-loop is "off", i.e. its critical current is at a minimum and vice-versa. This complementarity lead to the idea in [56] to construct a "current switch" device, where a bias current's path is guided from one to the other in a pair of these complementary loops that are placed in parallel and sharing the same externally applied magnetic flux as a steering signal.

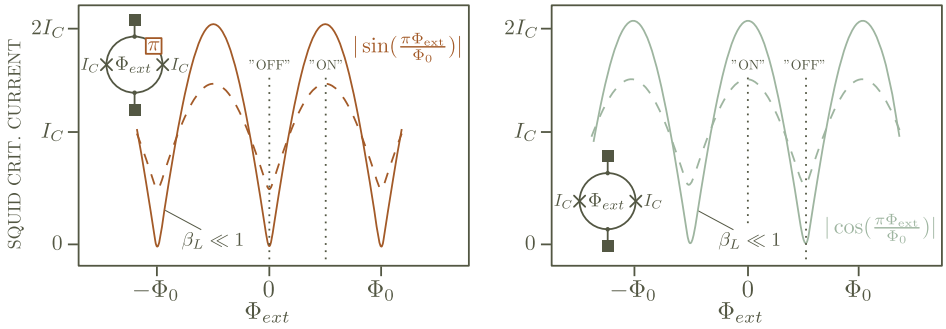

Figure 5.2. A sketch of the dependence of the critical current of a π- and a normal-SQUID as a function of applied magnetic flux Φ_{ext}, where β_L is the loop's normalized inductance. The plots are based on calculations made later in the text.

In the flux (or phase) domain, a (π)-loop can be treated as a two-port device, where a modulation of the characteristics on the output port, situated across the terminals of the loop, can be achieved by altering a quantity at the input port, that quantity given by Φ_{ext}. In order to present the properties of the flux modulated π-loop and establish the importance of its various circuit parameters, it is instructive to first look at the principle of operation and then later introduce the circuit in detail. Therefore, it is first assumed that the loop has a negligible normalized inductance where the calculations are very simplified. Later, the model is expanded to account for the effects of said loop inductance. At the end, inductive coupling between separate loops is included, thus completing the basic device necessary to build a logic circuit. In it worth noting that some structures involving *d-wave* superconductors which satisfy the limit of negligible inductance, for instance $0-\pi$ corner junctions [36], are similar to the circuit from the next section and can thus also exhibit phenomena such as near-equilibrium state evolution under an external field.

5.1.1 Transfer characteristic of an ideal flux-modulated π-loop with negligible normalized loop inductance

Under the condition that the normalized inductance of the (π)-loop is much less than unity:

$$\beta_L = \frac{2\pi L_s I_C}{\Phi_0} \ll 1$$

where I_C is the junction critical current and L_s the total loop inductance, it is useful to treat the loop as a composite controlled junction between the terminals, as depicted on the right in Figure 5.3. The current-phase relationship of the com-

posite junction can in this case be easily calculated from the Kirchhoff's relation at the terminals and the flux quantization principle in the flux-modulated loop:

$$I_s(\varphi_s) = \left[2I_C \cdot \sin\left(\pi \frac{\Phi_{\text{ext}}}{\Phi_0}\right) \right] \cdot \cos\left(\varphi_s\right) \tag{5.1}$$

for a π-loop and

$$I_s(\varphi_s) = \left[2I_C \cdot \cos\left(\pi \frac{\Phi_{\text{ext}}}{\Phi_0}\right) \right] \cdot \sin\left(\varphi_s\right) \tag{5.2}$$

for a normal loop, where it is assumed that the Josephson junctions have equal critical currents. The quantity within the brackets in equations 5.1 and 5.2 gives the critical current of the (π)-loop as a function of the applied flux Φ_{ext}, as previously plotted in Figure 5.2.

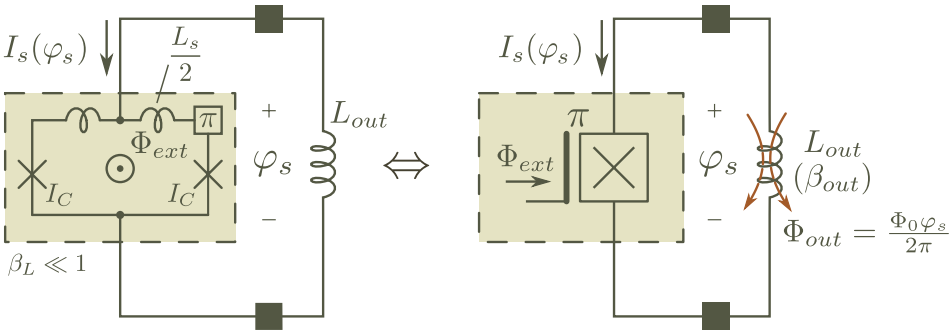

Figure 5.3. A flux-modulated (π)-loop with negligible normalized loop inductance can be viewed as a complex junction with critical current controlled by the external flux, according to equations (5.1) and (5.2). Depicted is also an inductor connected across the "junction", usually referred to as a load inductor, that creates an output flux Φ_{out}.

When loaded with an inductance L_{out}, one can calculate the dependence of the flux Φ_{out}, created within the load inductor L_{out}, on the applied flux Φ_{ext}. Using equations 5.1 and 5.2, as well as the flux quantization relation in the loop made from the load inductor and the composite junction, the transfer function $\Phi_{\text{out}}(\Phi_{\text{ext}})$ can be analytically written in an implicit way:

$$2\pi \frac{\Phi_{\text{out}}}{\Phi_0} = -2\beta_{\text{out}} \cdot \cos\left(2\pi \frac{\Phi_{\text{out}}}{\Phi_0}\right) \cdot \sin\left(\pi \frac{\Phi_{\text{ext}}}{\Phi_0}\right) \tag{5.3}$$

for a π-loop, and

$$2\pi \frac{\Phi_{\text{out}}}{\Phi_0} = -2\beta_{\text{out}} \cdot \sin\left(2\pi \frac{\Phi_{\text{out}}}{\Phi_0}\right) \cdot \cos\left(\pi \frac{\Phi_{\text{ext}}}{\Phi_0}\right) \tag{5.4}$$

for a normal loop, where $\beta_{\text{out}} = \frac{2\pi I_C L_{\text{out}}}{\Phi_0}$ is the normalized output inductance. The implicit equations above are plotted in Figure 5.4.

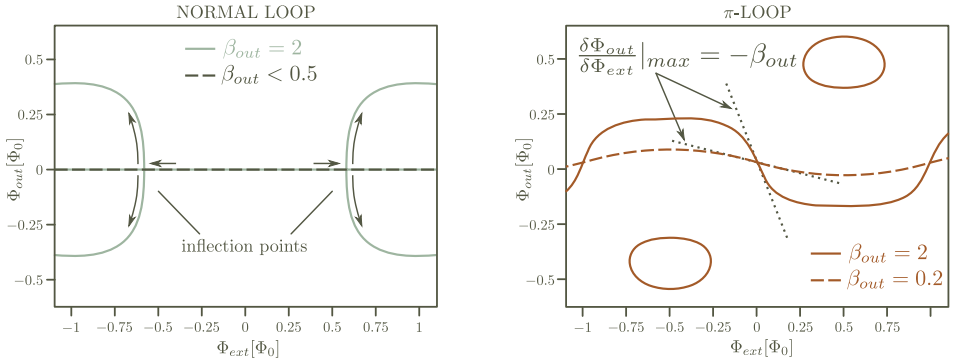

Figure 5.4. Calculated input-output transfer characteristic $\Phi_{\text{out}}(\Phi_{\text{ext}})$ of a normal and a π-loop, with the normalized load inductance β_{out} as a parameter, in the case of negligible loop inductance and equal junctions. The arrows in the plot on the left illustrate the possible trajectories when Φ_{ext} moves through the inflection points.

The normal loop equation 5.4 has a trivial solution $\Phi_{\text{out}} \equiv 0$. The solution can be proved to be the only one when $\beta_{\text{out}} < 0.5$. Hence, for a normal loop loaded with an inductor of normalized inductance $\beta_{\text{out}} < 0.5$, the flux in the load inductor Φ_{out} is zero for any value of the externally applied flux Φ_{ext} in the loop. For larger values of the normalized load inductance β_{out}, two new solutions of non-zero Φ_{out} are possible in equation 5.4. The two solutions are symmetric: Φ_{out} is equal in amplitude but with an opposite direction. These two states appear only when the absolute value of the external flux is greater than the inflection point $\Phi_{\text{ext,ip}}$, given by

$$\Phi_{\text{ext,ip}} = \Phi_0 \cdot (1 - \frac{\arccos(\frac{1}{2\beta_{\text{out}}})}{\pi})$$

Lets analyse a normal loop loaded with an output inductor of normalized inductance $\beta_{\text{out}} > 0.5$. It can be calculated from equation 5.4 and the Gibb's free energy of the circuit that for $|\Phi_{\text{ext}}| < \Phi_{\text{ext,ip}}$, the trivial solution $\Phi_{\text{out}} = 0$ always corresponds to a potential minimum in the potential landscape. As there are no other competing states, the flux through the output inductor will be then be $\Phi_{\text{out}} = 0$. For $|\Phi_{\text{ext}}| > \Phi_{\text{ext,ip}}$ on the other hand, it can be calculated that $\Phi_{\text{out}} = 0$ corresponds to an energetic maximum and is thus unstable. There are however two other states, appearing when $|\Phi_{\text{ext}}| > \Phi_{\text{ext,ip}}$, of the same but opposite Φ_{out}. Free energy calculations show that they correspond to energetic minimums and are thus stable. In that case, the normal loop will find itself in a state of non-zero output flux, corresponding to one of the two symmetric solutions. Since they are energetically equal ($|\Phi_{\text{out}}|$ is the same), the choice between the two states when Φ_{ext} is varied beyond the inflection points depends solely on the *noise* present in the circuit at that moment.

In a QFP, which is essentially the same as the analysed circuit, an input signal acts as "noise". It adds or subtracts a small current between the output terminals and thus sets the preference in which direction (positive or negative Φ_{out}) the output swings after the "pump" signal Φ_{ext} crosses the inflection point. In other words, the polarity of a small input signal determines which one of the trajectories in Figure 5.4 will the circuit trace if Φ_{ext} is varied between, for example, 0 and $+\Phi_0$. This type of parametric amplification is known to produce large gains w.r.t. the polarity of the input signal, but lacks static (analog) gain and signal isolation (the output and input signal are not separable).

In the π-loop on the other hand, there are no such bifurcations and a single continuous curve is traced in the transfer characteristic, passing through the origin of the plot $(\Phi_{\text{out}}, \Phi_{\text{ext}}) = (0, 0)$. It can be calculated from equation 5.3 that the slope (incremental gain) of the $\Phi_{\text{out}}(\Phi_{\text{ext}})$ characteristic reaches its maximum value around the origin, where it is equal to the normalized output load inductance,

$$\left.\frac{\partial \Phi_{\text{out}}}{\partial \Phi_{\text{ext}}}\right|_{\Phi_{\text{ext}}=0} = G_{\max} = -\beta_{\text{out}} \tag{5.5}$$

For values of Φ_{ext} going away from zero, the transfer characteristic "saturates" with the incremental gain gradually decreasing. The gain reduces to zero at $\Phi_{\text{ext}} = \pm\frac{\Phi_0}{2}$ and periodically extends beyond with the opposite sign, so that at $\Phi_{\text{ext}} = \pm\Phi_0$ the gain is again the greatest in amplitude but of opposite sign.

It can thus be concluded that a flux-modulated π-loop with a normalized load inductance $\beta_{\text{out}} > 1$ offers gain in the magnetic flux domain: the output signal Φ_{out} changes faster than the input signal Φ_{ext}. In comparison to the normal loop, where only the polarity of the input and output signal are gain-related, the π-loop offers continuous amplification of the input signal around the origin i.e. the device has analog signal gain. This fact is the principal property of the π-loop that allows it to be used as an active device in the circuits described in this chapter.

The transfer characteristic of the π-loop, given by equation 5.3, allows more solutions for Φ_{out} to exist in the vicinity of $\Phi_{\text{ext}} \approx \pm\frac{2n+1}{2}\Phi_0$, but only when $\beta_{\text{out}} \geqslant 1.486$. These extra states are illustrated by the closed ellipsoids in the right plot of Figure 5.4. The limiting value for β_{out} is a trigonometric constant: it is equal to the inverse of the value of y for which the equation $\frac{\cos(x)}{x} = y$ has more than one solution for x. Writing equation 5.3 as

$$\frac{\cos\left(2\pi\frac{\Phi_{\text{out}}}{\Phi_0}\right)}{2\pi\frac{\Phi_{\text{out}}}{\Phi_0}} = -\frac{1}{2\beta_{\text{out}} \cdot \cos\left(\pi\frac{\Phi_{\text{ext}}}{\Phi_0}\right)}$$

and letting Φ_{ext} take any value, it can be shown that the limit $\beta_{\text{out}} < 1.486$ is a sufficient and necessary condition for the equation above to have only one solution for Φ_{out} across the whole range of externally applied flux Φ_{ext}. This solution $\Phi_{\text{out}}(\Phi_{\text{ext}})$ defines the transfer characteristic passing through the origin and exhibiting the analog signal gain. When $\beta_{\text{out}} \geqslant 1.486$ however, more states are possible as equation 5.3 may have more solutions, each tracing a different transfer characteristic.

Energetically, the additional stable states are separated by an energetic barrier from the "desired" state that belongs to the analog-gain part of the transfer characteristic. Their energy levels are of the order $\frac{\Phi_0 I_C}{\pi}$ higher as well. These isolated states should therefore not interfere with the normal operation of the circuit as long as the Josephson junctions have sufficiently high critical currents, usually more than a few tens of μA at 4K, to prevent thermal excitation to a $\sim\frac{\Phi_0 I_C}{\pi}$ higher level.

As shown later, the π-loop exhibits sufficient gain in the parameter range $\beta_{\text{out}} < 1.486$ where multiple states do not exist, even in the realistic cases of non-zero β_L and unequal junctions. Hence, even lower critical currents can be used if the circuit parameters are chosen carefully.

There is one more important conclusion that can be drawn from the equations 5.3 and 5.4. The discussion is supported by the drawing in Figure 5.5. It is common in the literature on π-shift circuits to cite the equivalence between a π-loop and a normal loop biased at $\Phi_{\text{ext}} = \frac{\Phi_0}{2}$. This reasoning is primarily based on the $I_C(\Phi_{\text{ext}})$ characteristic sketched in Figure 5.2. However, the analysis above suggests that such equivalence does not actually hold in the $(\Phi_{\text{ext}}, I_{\text{out}})$ domain: the two plots in Figure 5.4 are not horizontally-shifted versions of each other nor do the relations 5.3 and 5.4 mutually transform under a $\frac{\Phi_0}{2}$ shift of Φ_{ext}.

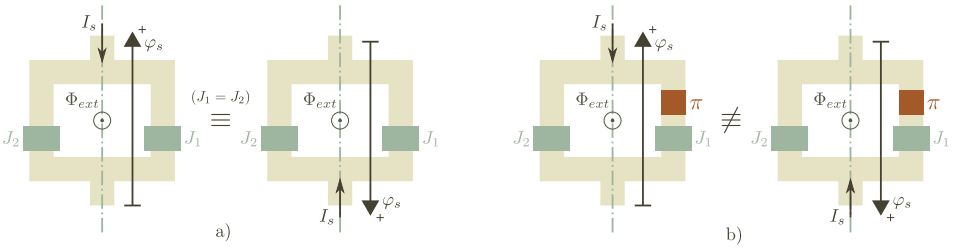

Figure 5.5. The spatial asymmetry in the π-loop b), as opposed to the normal loop a).

The reason is that a π-loop is always asymmetrical, while a normal loop biased by a half-flux quantum stays symmetrical with respect to the current direction

between the terminals. The π-shift element is physically localized in one of the two arms of the loop, allowing one to always make the distinction between a "right" and "left" arm of the loop. This is not the case for a normal loop with physically symmetric arms.

To wit: looking along the axis in parallel to the current I_s of a normal loop, a reversal of the sign of Φ_{ext} can be taken into account by rotating the whole structure along the viewing axis by 180°. The observer will then see exactly the same circuit since there is no distinction between the "left" and "right" arm of the loop. Hence, the I_s will be the same. Further, since the observer still sees into the same terminal of the loop, also the flux angle φ_s across the terminals remains the same. So, it can be written

$$I_{s,N}(\Phi_{\text{ext}}, \varphi_s) = I_{s,N}(-\Phi_{\text{ext}}, \varphi_s) \tag{5.6}$$

for a normal loop. If the observer changes the direction of the viewpoint, reversing both I_s and φ_s, while Φ_{ext} is kept in the same direction, then one more time the same structure is seen. Consequently, for the normal loop it is also valid that:

$$I_{s,N}(\Phi_{\text{ext}}, \varphi_s) = -I_{s,N}(\Phi_{\text{ext}}, -\varphi_s) \tag{5.7}$$

Performing the same exercise for the π-loop, one finds that a reversal of Φ_{ext} can be equivalented by rotating along the viewing axis and, at the same time, reversing the direction of the current I_s. Hence, for the π-loop it is obtained that

$$I_{s,\pi}(\Phi_{\text{ext}}, \varphi_s) = -I_{s,\pi}(-\Phi_{\text{ext}}, \varphi_s) \tag{5.8}$$

It is concluded that the current I_s through the terminals of a normal loop has an even dependence on the external flux Φ_{ext} and an odd dependence on the flux angle φ_s across the terminals, while a π-loop's current is odd in Φ_{ext}.

Lets assume that the hypothesis "a π-loop is equivalent to a normal loop with a flux bias of odd number of half flux-quanta" is true. This claim can be cast in equation form as

$$I_{s,\pi}(\Phi_{\text{ext}}, \varphi_s) = I_{s,N}\left(\Phi_{\text{ext}} + \frac{(2n-1)\,\Phi_0}{2}, \varphi_s\right)$$

Applying equation 5.6 to the right-hand side above and equation 5.8 to the left-hand side, it is obtained

$$I_{s,\pi}(-\Phi_{\text{ext}}, \varphi_s) = -I_{s,N}\left(-\Phi_{\text{ext}} - \frac{(2n-1)\,\Phi_0}{2}, \varphi_s\right) \tag{5.9}$$

but this is in contradiction with the starting hypothesis: adding a bias $-\frac{(2n-1)}{2}\Phi_0$ to the external flux $-\Phi_{\text{ext}}$ of a normal loop is *not* equivalent to a π-loop with external flux $-\Phi_{\text{ext}}$. From the Principle of Contradiction it then follows that the "equivalence" hypothesis is not true. Note that even if the hypothesis stated that the equivalence lies in opposite but equal currents, i.e. starting from 5.9, it would still not have been true (follow the steps backwards for a proof).

An interesting problem now arises: how can the $I_C(\Phi_{\text{ext}})$ plot in Figure 5.2 be true if it was just proved that the "$\frac{\Phi_0}{2}$" equivalence between a normal and a π-loop does not hold? The answer lies in the fact that the critical current of a loop is actually a measure of the absolute value of the maximum current passing through the loop. Then, the intrinsically odd $I_s(\Phi_{\text{ext}})$ dependence of a π-loop transforms to an even $I_C(\Phi_{\text{ext}})$ dependence, changing the symmetry equations in such a way as to yield that $I_{C,\pi}(\Phi_{\text{ext}}) \equiv I_{C,N}\Big(\Phi_{\text{ext}} + \frac{(2n-1)}{2}\Phi_0\Big)$.

Another way of looking at the topic is to note that a flux bias of $\frac{\Phi_0}{2}$ in a normal loop will distribute equally between the two arms, creating a $\frac{\pi}{2}$ flux angle source in series with each arm but of an opposite amplitude. Although the sum of these two sources is $\pm\pi$, just like in the π-loop, the fact that they are equally and oppositely distributed largely preserves the "left-right" spatial symmetries of the normal loop. The π-loop on the other hand does not have any such symmetry due to the physical presence of the "extra π" in just one of the arms. This then reflects in different behaviour of the two loops.

In the next section, an analysis of the properties of a flux-modulated π-loop are presented, where the loop is allowed to have a normalized inductance that is not negligible. The results are then summarized with respect to the two circuit parameters, the normalized loop and load inductance, which determine the exact nature of the transfer characteristic and can be chosen to yield the best properties of the device as an amplifier. At the end, it is suggested that a flux-modulated π-loop exhibits the interesting property of (nonlinear) scalability of the gain and saturation amplitude with loading levels. The former can already be seen in equation 5.5 where the maximum incremental gain is exactly proportional to the normalized load inductance. Although for a loop with non-zero β_L it changes to a more complex dependence, it nevertheless still follows the same general trend. The π-shift amplifier device thus possesses a very important advantage over other circuits that operate in the flux-domain: it is possible to transport a signal over bigger passive interconnect lengths without corresponding reduction of the amplitude available at the receiver. In some cases, it is even expected to see *greater* signal amplitudes when the intervening interconnect between amplifying device and load inductance is *greater*.

5.1.2 Parameter margins and performance of a flux-modulated π-loop with non-zero normalized loop inductance

When the normalized inductance of the π-loop is not negligible, a simple closed-form relation between the input and output flux is not directly obtainable. Instead, two parametric equations can be written for the π-loop:

$$\begin{aligned} -\pi\frac{\Phi_{\text{out}}}{\Phi_0} &= \beta_{\text{out}} \cdot \cos\left(2\pi\frac{\Phi_{\text{out}}}{\Phi_0} \cdot (1+\frac{\beta_L}{4\beta_{\text{out}}})\right) \cdot \sin(t) \\ \pi\frac{\Phi_{\text{ext}}}{\Phi_0} &= t + \frac{\beta_L}{2} \cdot \sin\left(2\pi\frac{\Phi_{\text{out}}}{\Phi_0} \cdot (1+\frac{\beta_L}{4\beta_{\text{out}}})\right) \cdot \cos(t) \end{aligned} \tag{5.10}$$

where the parametric variable t should be eliminated and β_L, β_{out} are defined as previously. Physically, t is equal to the difference of the flux angles across the left and right junction of the loop, including the π-shift: $t = \frac{\varphi_L - \varphi_R \pm \pi}{2}$. The output flux angle $\varphi_s = 2\pi\frac{\Phi_{\text{out}}}{\Phi_0}$ from Figure 5.3 on the other hand, is equal to the arithmetic average of the flux angles of the junctions and multiplied with the ratio $\frac{4\beta_{\text{out}}}{4\beta_{\text{out}}+\beta_L}$.

Relations 5.10 are valid for the reference directions and π-shift position as given in Figure 5.3 (the reference directions of the junction terminals are not relevant). Symmetry of reflection around the axis drawn in Figure 5.5 dictates that in order to write the equivalent of 5.10 for a loop where the π-shift element is located in the opposite arm, it is sufficient to only invert the sign of Φ_{ext}. This is, in effect, equivalent to looking at the planar circuit from the back of the drawing. The sign of t also must be inverted in that case as the junctions trade places, but that is irrelevant to the relation $\Phi_{\text{out}}(\Phi_{\text{ext}})$ as t must be eliminated from 5.10 to obtain that relation. The conclusion is thus that it is enough to place the π-shift element on the other side in order to reflect the transfer characteristic around the y-axis or, which is the same, obtain a circuit with an output that is inverted as a function of the input.

If one wishes to solve for the transient dynamics of the system, then the two variables t and φ_s, being a linear combination of the junction flux angles, must be taken as the state-space coordinates for which to write the differential equations of motion, as the only resistive/capacitive elements in the circuits (that are defined with time-derivative constitutive laws) are located across the two junctions only. Because this thesis is concerned only with the static transfer characteristics of the system, effectively the circuits' DC response, the transient dynamics are not examined unless specifically stated otherwise.

The numerically obtained relation $\Phi_{\text{out}}(\Phi_{\text{ext}})$ by eliminating t from the system 5.10 is given in Figure 5.6 for a few values of the loop's normalized inductance β_L with β_{out} as a parameter.

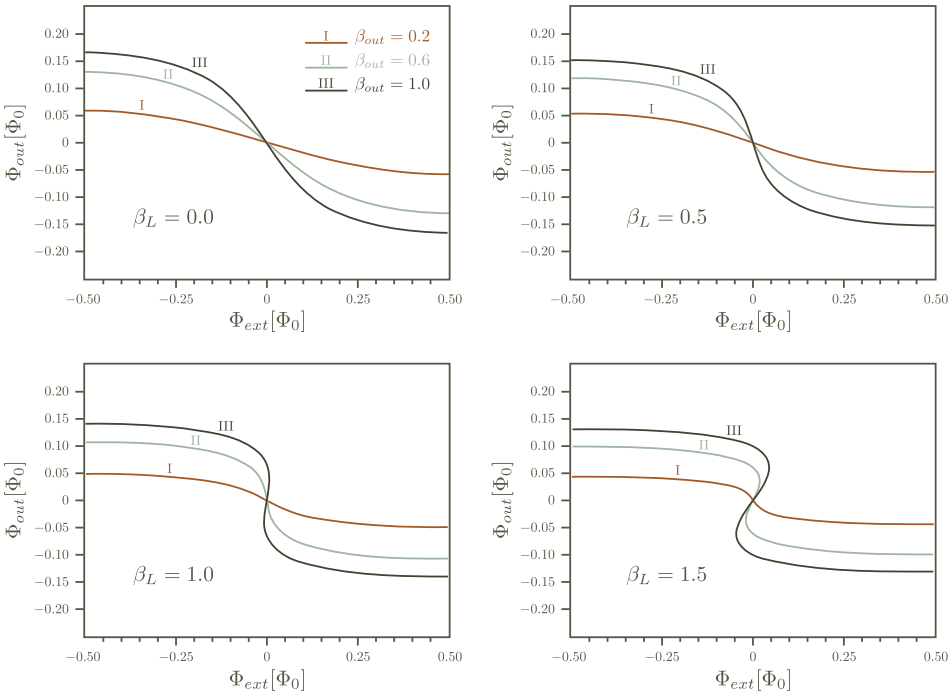

Figure 5.6. Transfer characteristics $\Phi_{\mathrm{out}}(\Phi_{\mathrm{ext}})$ with the normalized load inductance β_{out} as a parameter, for a few values of the normalized loop inductance β_L assumed to be symmetrically distributed between the two interferometer arms and for equal junctions. Any isolated stable states are not shown.

The plots in Figure 5.6 show that for certain values of the circuit parameters, a hysteretic transfer characteristic will be obtained. In these cases, the state trajectory of the circuit will contain a (dissipative) relaxation part, starting at those points of the transfer curves where the incremental gain becomes infinite (the slope is vertical). If one looks at the accompanying potential landscape plots, given in Figure 5.7, it is evident that the mechanism of the transition is similar as in SFQ circuits: the curvature of the potential around a stable state becomes zero in a given direction, subsequently changing sign and causing the circuit to relax towards the next potential minimum. The transient then becomes self-sustained and the circuit follows a trajectory through state-space where internal energy is exchanged with the environment. Due to the short eigen-time constants of the circuit guiding the self-sustained transition and the inevitable presence of resistances across the junctions, this exchange happens in a dissipative way and the transition is irreversible. From an information perspective, the irreversibility can be illustrated in the following way: once the self-sustained transition is over,

the information about whether the circuit made a transition or not (its history) is lost and the same trajectory cant be retraced back without that knowledge.

In the parameter range for which the transfer characteristic is not hysteretic, a second connected potential minimum does not form during the process of state-change. As illustrated in the plots of Figure 5.8, *the circuit rests in a potential minimum during the whole process of state change,* i.e. the state evolves near-adiabatically (completely adiabatic at zero temperature and infinitely slow transition) without any possibility for a irreversible trajectory to be chosen.

One can calculate the condition under which there will be no hysteresis and consequently, reversibility of operation, by simply seeking the parameter range for which the maximum differential gain satisfies:

$$-\infty < \left.\frac{\partial \Phi_{\text{out}}}{\partial \Phi_{\text{ext}}}\right|_{\Phi_{\text{ext}}=0} < 0 \tag{5.11}$$

as the onset of hysteresis is equivalent to a vertical slope of the gain in the origin (the left limit of the condition). Using 5.10, the maximum gain can be calculated as:

$$\left.\frac{\partial \Phi_{\text{out}}}{\partial \Phi_{\text{ext}}}\right|_{\Phi_{\text{out}}=0} = G_{\max} = -\frac{1}{\frac{1}{\beta_{\text{out}}} - \beta_L\left(1+\frac{\beta_L}{4\beta_{\text{out}}}\right)} \tag{5.12}$$

Due to the subtraction operation of two positive values in the denominator of the right-hand side in 5.12, the maximum gain in the case when $\beta_L \neq 0$ can diverge and become infinite. That is exactly the limit of 5.11. Using 5.12, one can re-write 5.11 in terms of the circuit parameters:

$$\beta_{\text{out}} < \frac{4-\beta_L^2}{4\beta_L} \tag{5.13}$$

as a condition for non-hysteretic (near-adiabatic) operation. Note that condition 5.13 is valid regardless of the convention for the directions of the signals w.r.t. the position of the π-shift element.

Since the circuit also needs to show absolute gain larger than unity for it to be useful in any application, a second criterion can be stated as:

$$|G_{\max}| > 1 \tag{5.14}$$

which results in:

$$\beta_{\text{out}} > \frac{4-\beta_L^2}{4(1+\beta_L)} \tag{5.15}$$

that is, again, independent of the direction of the signals and position of the π-shift in the flux-modulated loop.

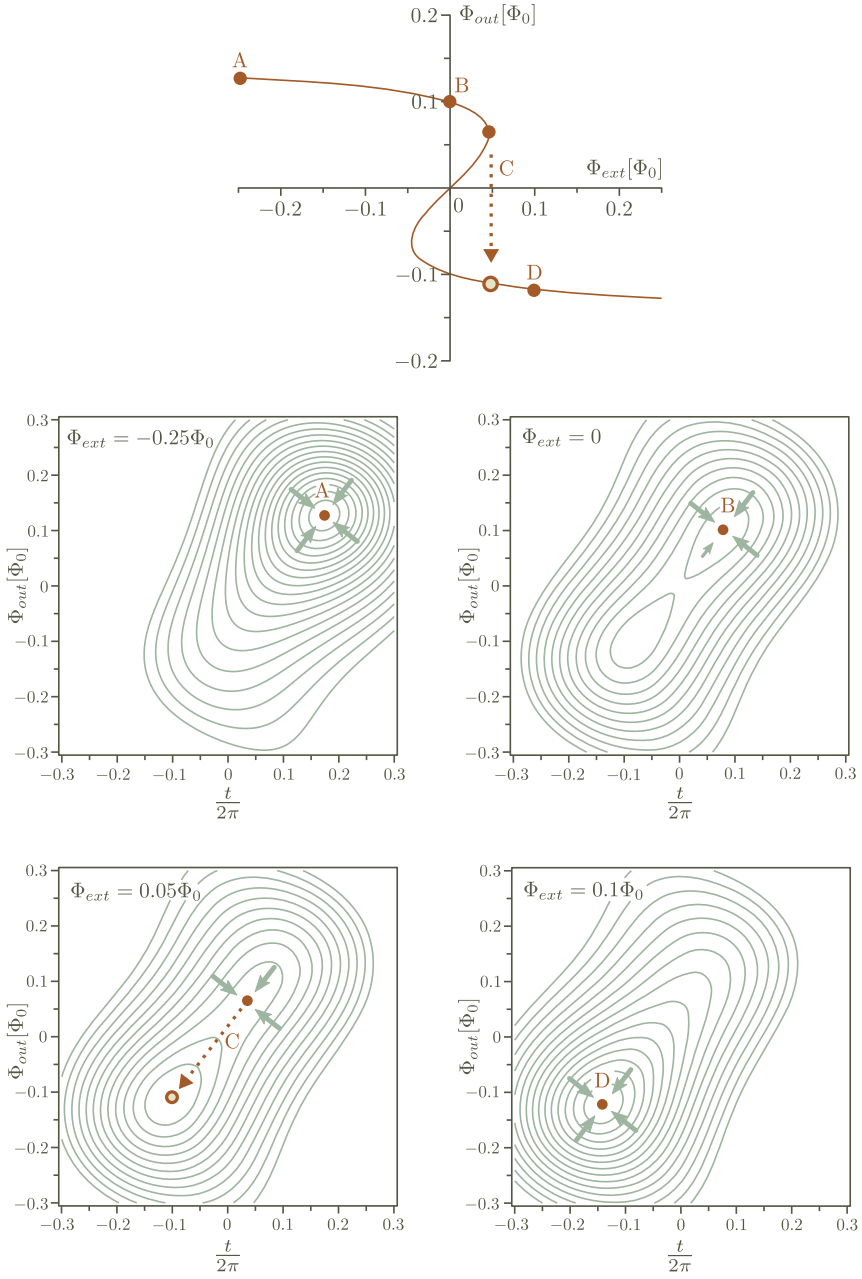

Figure 5.7. Transfer characteristic (top) and contour plots of the circuit's Gibbs Free Energy (bottom) as a function of the two degrees of freedom for a few values of the external flux Φ_{ext}, in the hysteretic case $\beta_L = 1.5$ and $\beta_{\text{out}} = 1.0$. The circuit will commence a self-sustained transition in the part labeled with "C", when the gradient of the local potential, as sketched by the arrows, changes sign along at least one direction.

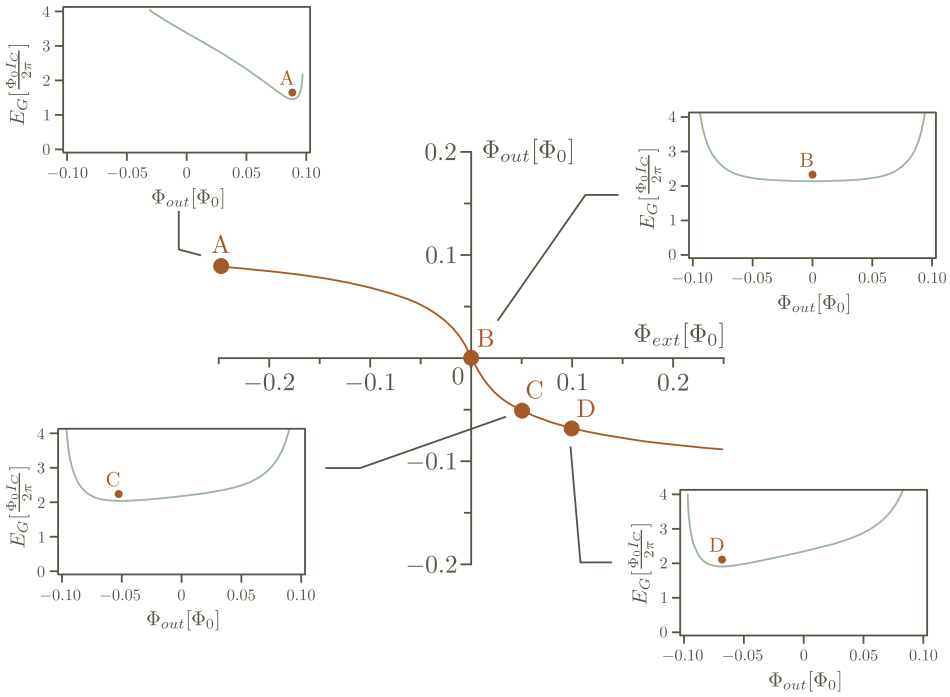

Figure 5.8. The non-hysteretic transfer characteristic obtained for $\beta_L = 1$ and $\beta_{\text{out}} = 0.5$, along with a section of the Gibb's Energy E_G along one of the degrees of freedom where its derivative is zero.

The conditions for near-adiabatic operation (5.13) and gain larger than unity (5.15) are bounding the contour plot of the maximum incremental gain, as calculated from 5.12, in the circuit parameter plane of Figure 5.9. Similar to the $\beta_L \sim 0$ case, one can add the requirement for absence of multiple isolated stable states, which in this case is given by :

$$\frac{\beta_L}{4} + \beta_{\text{out}} < 1.486 \tag{5.16}$$

The relation 5.16 is arrived at by using the same reasoning as before but applied to the top equation of the system 5.10 and letting t take any value.

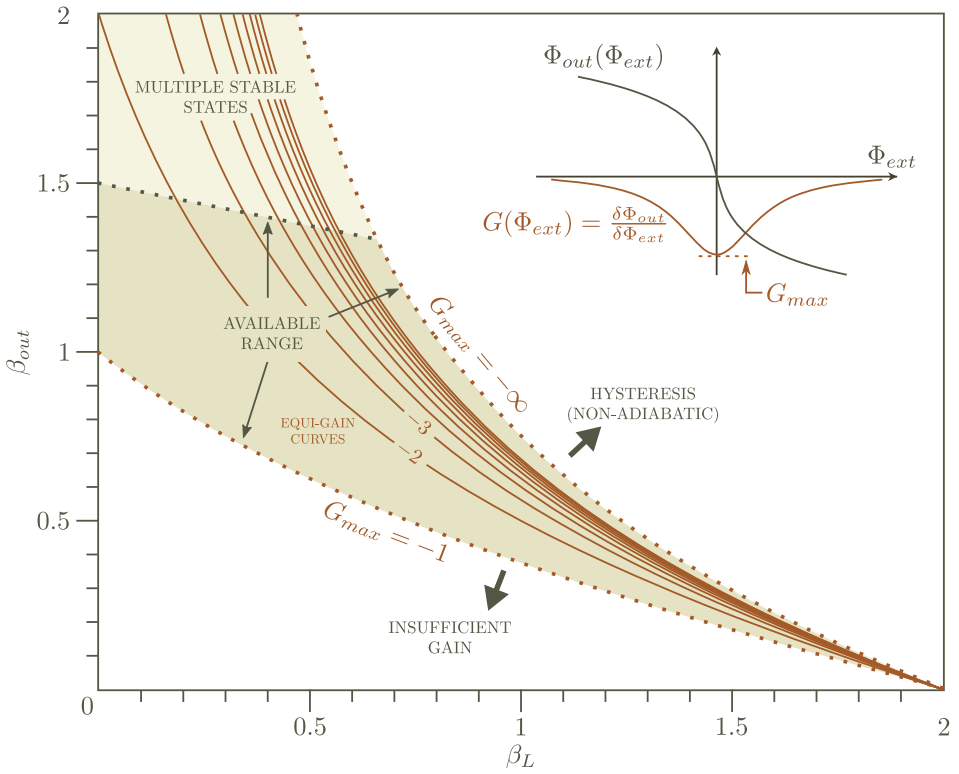

Figure 5.9. A plot of the maximum gain $G_{\max}$ as calculated from equation 5.12 projected on the parameter plane (β_L, β_{out}), yielding equi-gain curves, together with the bounding conditions 5.13, 5.15 and 5.16. The shaded region represents the useful near-adiabatic regime.

As already stated, the requirement 5.16 is not a critical restriction as long as the thermal excitation rate to the isolated stable states is negligible. This will be the case when the energy barrier $\frac{\Phi_0 I_C}{\pi}$ separating the desired and isolated states is much larger than the thermal energy $k_B T$. However, it is evident from Figure 5.9 that such precautions are hardly necessary as there is plenty of choice for the values of the two circuit parameters β_{out} and β_L in the available range bounded by 5.13, 5.15 and 5.16.

Another interesting plot is the dynamic range of the flux amplifier, as plotted in Figure 5.10. Here, the transfer characteristic $\Phi_{\text{out}}(\Phi_{\text{ext}})$ for a set of given parameters β_L and β_{out} was first found. The data were then numerically processed to obtain the dynamic range according to two different criteria: a) as the amplitude at which the output signal equals the input signal (saturation) and b) as the maximum output signal amplitude between the points where the gain $|G(\Phi_{\text{ext}})| = 1$

(small-signal range). While the latter is used to find noise margins in digital circuits, the former measure gives the maximum signal amplitude achievable in a cascade of such amplifiers. For both cases, the values for the dynamic range are similar and essentially limited by the condition 5.16 or, when it is ignored, either the lowest experimentally achievable values for β_L or the greatest values for β_{out} that still allow near-adiabatic operation. Looking at the plots in Figure 5.10, it can be estimated that, in practice, most circuits with flux modulated π-loops will exhibit signals swings of around one hundred $m\Phi_0$.

The circles on the plots in Figure 5.10 attempt to illustrate how the proper values for the circuit parameters β_L and β_{out} are chosen, given the constraints already discussed in the above paragraphs. If it is desirable to have large process margins while the circuit performance just needs to stay within the useful near-adiabatic regime, for instance in large digital circuits, one can choose the center of the "Parameter Margin" circle that maximizes the range of parameter values. The pair $(\beta_L, \beta_{\text{out}}) = (\frac{1}{2}, 1)$ is in this case a good choice for the nominal parameter values as it should allow for approximately 40% process margin on the two circuit parameters (they are correlated to each other during process variation) before exiting the useful near-adiabatic regime.

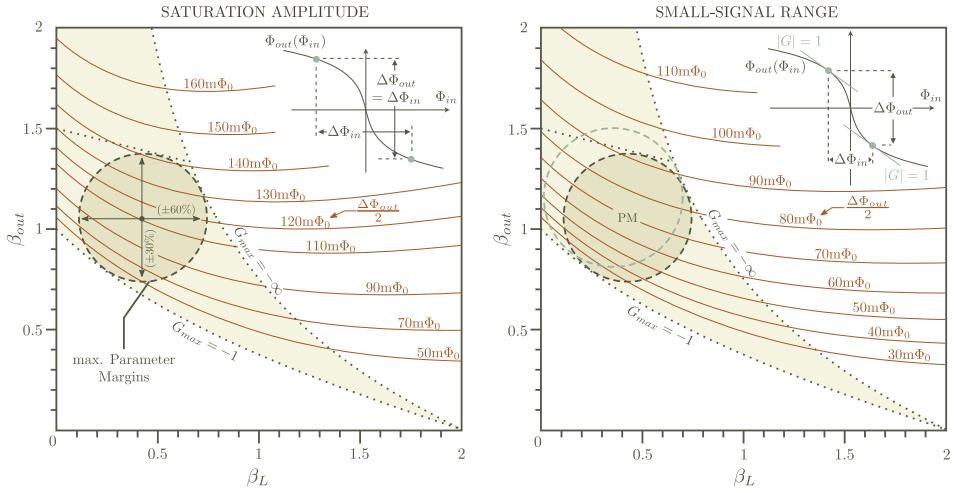

Figure 5.10. Two methods for estimating the dynamic range of a flux-modulated π-loop amplifier as a function of the parameter pair $(\beta_L, \beta_{\text{out}})$, together with suggestions for optimal choices of the latter (see text). The lines are numerically calculated contour plots of the dynamic range(s) as a function of the two process parameters β_L and β_{out}. The limiting conditions 5.13, 5.15 and 5.16 are also plotted in the $(\beta_L, \beta_{\text{out}})$ plane, just like in Figure 5.9.

If the condition 5.16 is dropped from the parameter boundaries, then the circuit parameters can be chosen to have nominal values different than the "Parameter Margin" centering, with a tendency for lower β_L and higher β_{out}. The parameter margins can be slightly improved then, as illustrated on the right plot of Figure 5.10 by the empty circle, and the signal amplitudes will also increase.

The theoretical maximum saturation amplitude that can be achieved is $\pm 250m\Phi_0$, for $\beta_L = 0$ and $\beta_{\text{out}} \to \infty$. The transfer characteristic in the case of large β_{out}, together with the set of isolated solutions that appear in that parameter region, is presented in Figure 5.11.

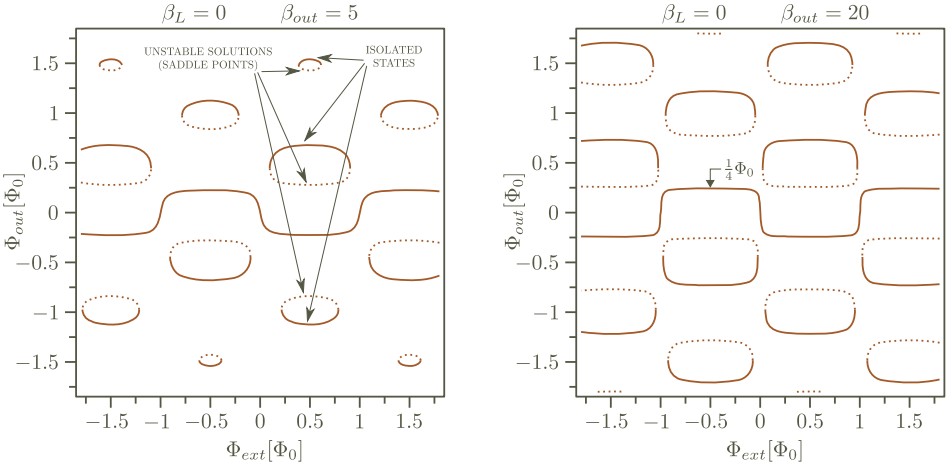

Figure 5.11. The transfer characteristic $\Phi_{\text{out}}(\Phi_{\text{ext}})$ for large load inductance including the isolated states. The maximum output amplitude $\frac{1}{4}\Phi_0$ is asymptotically approached for $\beta_{\text{out}} \to \infty$.

A very important feature of the flux-modulated π-loop can be implied from Figures 5.9-5.11: the larger the normalized output inductance, and hence the larger the load inductance L_{out}, the higher the gain and the dynamic range are in principle. This makes the transport of a flux-domain signal on a load that is adjacent to the π-loop more flexible as the signal amplitude at the far end does not reduce when the total output inductance is higher due to the intervening interconnect. The following subsection deals with this practical advantage of the flux-modulated π-loop.

5.1.3 Transport of a flux domain signal on a passive interconnect using a flux-modulated π-loop

As in any flux-domain circuit, a series parasitic inductance, proportional to the length of the interconnect between the π-shift device and the load, is always present and reduces the signal amplitude at the remote load. This can be taken into account by considering the series combination of the parasitic inductance and load as an inductive divider circuit, as depicted in Figure 5.12.

The actual gain can in this case be written as:

$$\frac{\partial \Phi_{\text{load}}}{\partial \Phi_{\text{ext}}} = \frac{L_{\text{load}}}{L_{\text{load}} + L_{\text{par}}} \cdot \frac{\partial \Phi_{\text{out}}}{\partial \Phi_{\text{ext}}} \tag{5.17}$$

Since the ratio $\frac{L_{\text{load}}}{L_{\text{load}} + L_{\text{par}}}$ is always less or equal to 1, the actual gain is, in the first instance, expected to be lower than the gain in the ideal case when $L_{\text{par}} = 0$. The same should be valid for the dynamic range that is reduced by the same ratio. However, since the intrinsic gain $\frac{\partial \Phi_{\text{out}}}{\partial \Phi_{\text{ext}}}$ and signal amplitudes generally increase with the total load at the output $L_{\text{load}} + L_{\text{par}}$, it is possible that a situation arises where the two effects offset each other.

Taking into account the schematic in Figure 5.12 and equation 5.12, the following relation can be written:

$$\left| \frac{G_{\max}(q)}{G_{\max}(0)} \right| = \frac{1}{1 - \beta_L |G_{\max}(0)| \cdot q} \tag{5.18}$$

where

$$G_{\max}(q) = \left. \frac{\partial \Phi_{\text{load}}}{\partial \Phi_{\text{ext}}} \right|_{\Phi_{\text{ext}}=0}$$

is the actual maximum gain, $q = \frac{L_{\text{par}}}{L_{\text{load}}}$ and $G_{\max}(0)$ is the maximum gain when the parasitic inductance is zero, i.e. when the load inductance is equal to the total output inductance as assumed in the previous subsection. Hence, $G_{\max}(0)$ can be calculated using equation 5.12 by substituting L_{out} with L_{load}.

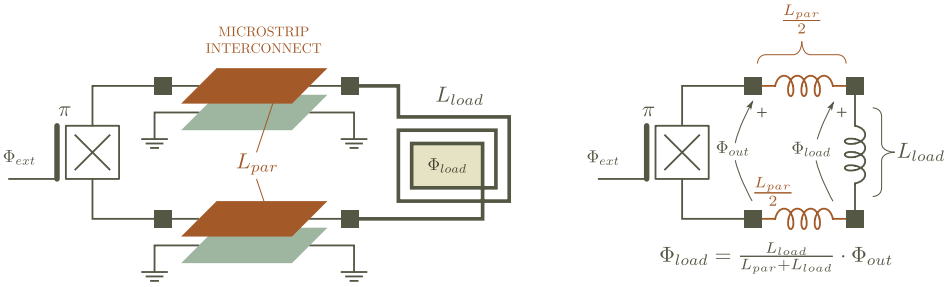

Figure 5.12. A sketch and an equivalent electrical schematic of a π-shift device connected to a remote load L_{load} through a microstrip transmission lines with inductance L_{par}.

In the case $\beta_L = 0$, the right side of equation 5.18 evaluates to 1, which means that the incremental gain is then *insensitive* to the parasitic inductance L_{par}. Such a result is naturally expected since

$$\left. \frac{\partial \Phi_{\text{load}}}{\partial \Phi_{\text{ext}}} \right|_{\Phi_{\text{ext}}=0} = \frac{L_{\text{load}}}{L_{\text{load}} + L_{\text{par}}} \cdot \left. \frac{\partial \Phi_{\text{out}}}{\partial \Phi_{\text{ext}}} \right|_{\Phi_{\text{ext}}=0} = \frac{L_{\text{load}}}{L_{\text{load}} + L_{\text{par}}} \cdot (-\beta_{\text{out}}) = -\beta_{\text{load}}$$

using equation 5.12 in the case of $\beta_L = 0$. Note that the parameter β_{load} is here defined as the normalized inductance of the remote load only, $\beta_{\text{load}} = \frac{2\pi L_{\text{load}} I_C}{\Phi_0}$, while the normalized total load β_{out} also includes the interconnect inductance, $\beta_{\text{out}} = \frac{2\pi(L_{\text{out}} + L_{\text{par}})I_C}{\Phi_o} = (1+q)\beta_{\text{load}}$. It can thus be concluded that in the case of negligible loop inductance, i.e. when $\beta_L = 0$, adding a parasitic inductance at the output has no effect on the total maximum gain.

When the normalized loop inductance β_L is increased, the right side of relation 5.18 becomes *greater* than 1, meaning that adding a parasitic inductance to the output *increases* the total maximum gain. This is true until the adiabatic condition given by equation 5.13, where $\beta_{\text{out}} = \beta_{\text{load}}(1+q)$ should be substituted,

$$\beta_{\text{load}}(1+q) < \frac{4-\beta_L^2}{4\beta_L}$$

becomes invalid. Relation 5.18 then has a discontinuity and the gain reverses sign, indicating the appearance of hysteresis in the transfer characteristic of the circuit and thus the undesired dissipative mode of operation. Hence, if one's goal is to achieve incremental gain greater than one, the parasitic interconnect inductance *does not matter* as long as the near-adiabatic condition

$$q = \frac{L_{\text{par}}}{L_{\text{load}}} < \frac{4-\beta_L^2}{4 \cdot \beta_L \cdot \beta_{\text{load}}} - 1 \tag{5.19}$$

is satisfied and the maximum gain $G_{\max}(0)$ without parasitics is already greater than one.

The saturation amplitude when a parasitic inductance $L_{\text{par}} = q \cdot L_{\text{load}}$ is present, defined as in the previous section (left plot of Figure 5.10), can be determined in a similar way. A simple expression of the type as 5.18 is however not possible. In Figure 5.13, the saturation amplitude

$$\Delta\Phi_{\text{load}}(q) = \frac{1}{1+q} \cdot \Delta\Phi_{\text{out}}(\beta_L, \beta_{\text{out}}) = \frac{1}{1+q} \cdot \Delta\Phi_{\text{out}}(\beta_L, (1+q)\beta_{\text{load}}) \tag{5.20}$$

is numerically calculated and plotted as a function of the ratio $q = \frac{L_{\text{par}}}{L_{\text{load}}}$ with β_{load} as a parameter for different values of the normalized loop inductance β_L. For some choices of the parameters, there is little change of the maximum saturation amplitude $\Delta\Phi_{\text{load}}$ as a function of the parasitic inductance ratio q, usually for small values of β_{load} (for example see the plots in Figure 5.13 for $\beta_{\text{load}} = 0.25$). Although the amplitude is quite small, in the tens of $m\Phi_0$ in those cases, its low sensitivity to changes in the parasitic inductance offers great flexibility in designing the circuit's interconnect lines.

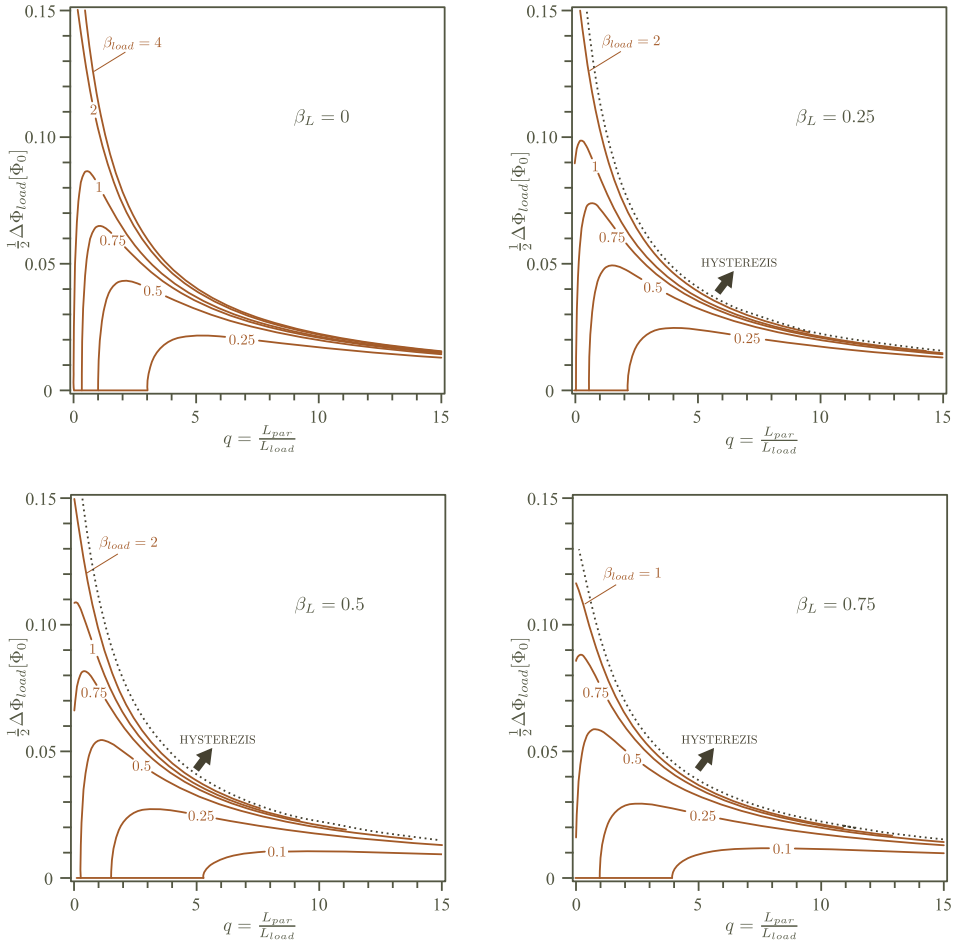

Figure 5.13. The dependence of the saturation amplitude $\frac{1}{2}\Delta\Phi_{\text{load}}$ on the ratio q between the parasitic interconnect and load inductance with the normalized load inductance β_{load} as a parameter. The plot is repeated for few values of the π-loop normalized inductance β_L. The near-adiabatic condition from equation 5.19 is also plotted with a dotted line.

Along with the fact that the incremental gain increases with the parasitic inductance, the implications of the plots in Figure 5.13 establish a convenient property of the π-loop flux-modulated device: the amplitude of a signal transported on the passive interconnect does not greatly depend on the inductance and hence length of those interconnect lines as long as the circuit parameters are properly

chosen (and the near-adiabatic condition (5.19) is satisfied).

For example, lets choose $\beta_L = 0.75$ and $\beta_{\text{load}} = 0.25$. The saturation amplitude of the circuit will then be zero (there is no gain) for all parasitic inductances L_{par} that are equal or smaller than L_{out}. This is seen for q less than approximately unity on the bottom right plot of Figure 5.13. But as soon as the parasitic inductance is increased, the saturation amplitude quickly rises to about $30\text{m}\Phi_0$ and drops again but very slowly. For instance, the saturation amplitude does not reach $20\text{m}\Phi_0$ until $q > 10$, or until ten times the parasitic inductance when the amplitude was $30\text{m}\Phi_0$. There is thus a lot of design room in the interconnect length. A disadvantage is that the signal amplitude at the remote load is rather low.

In the previous three sections, some properties of a flux-modulated π-loop device were presented, along with estimations of the parameter margins in specific applications. A choice of circuit parameters exists depending on the intended application:

- as a building block in a digital device, where the interconnect and other parasitic inductances are low, it is best to achieve the widest parameter margins, i.e. around $(\beta_L, \beta_{\text{out}}) = (\frac{1}{2}, 1)$

- as an analog amplifier with a large parasitic interconnect inductance to the actual load, the most flexible design is to choose a normalized low load inductance.

The coupling between the π-loop devices in a larger circuit was not addressed so far: it was implicitly assumed that the external flux Φ_{ext} was applied by a source "forcing" a magnetic field through the loop. Essentially, all calculations were made in the case when the signal source does not receive back-action from the π-loop. This is a realistic situation if, for instance, a room-temperature electronic current source I_{ext} is fed to a magnet coil used to generate a local magnetic field and hence introduce an external flux $\Phi_{\text{ext}} = M \cdot I_{\text{ext}}$ through the π-loop, where M is the mutual inductance between the magnet coil and the π-loop.

However, if we use π-loop devices to make a bigger circuit, they must be inductively coupled in such a way that the output flux of one device is used as an input to the next device. In this situation, the previous stage "feels" the next stage as reflected through the coupling device, that is usually a superconducting thin-film transformer, and generally a non-linear load inductance arises because of the Josephson junctions in the loop of the next stage. Thus, the calculations of the preceding subsections must be changed to account for a non-linear load. The next subsection analyzes the effects of coupling between π-loop devices and introduces the π-shift static flux-domain logic circuits based on those devices.

5.2 Circuits with inductively coupled π-shift loops

In Figure 5.14, a schematic of a π-loop with an inductive modulation terminal is depicted along with the symbol used elsewhere in this text. The flux coupling between the input coil and the π-loop is realized as a thin-film superconducting transformer normally used in SQUID sensors [67]. The π-loop's critical current is modulated by the coupled flux from the input coil resulting in, as demonstrated previously, a flux gain observed on the load inductor attached between the output π-loop terminals. It is also necessary for the circuit parameters to be chosen correctly in order for the flux gain to be greater than unity. This section investigates the static gain in the flux angle domain, more precisely between the flux angle at the load, φ_s, and the flux angle at the input terminal, φ_{in}. Replacing the magnetic flux with the flux angles provides compatibility with the superconducting network model, where the standard branch and nodal variables are the currents and flux angles respectively.

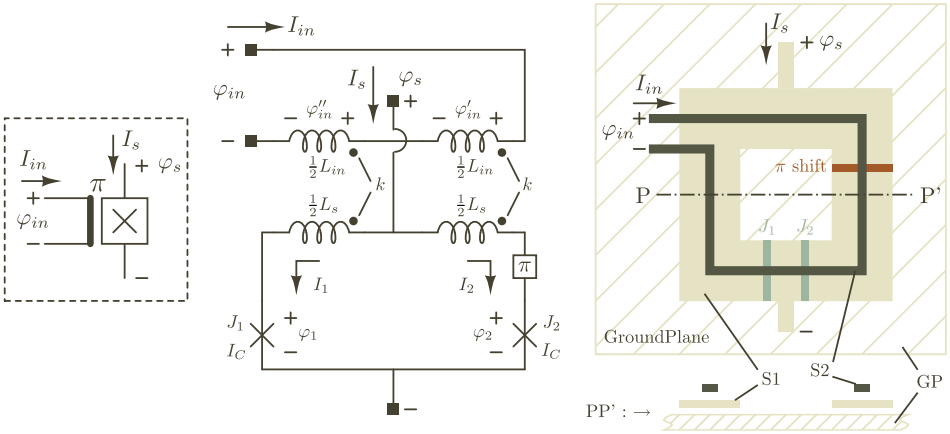

Figure 5.14. From left to right: a circuit symbol, a circuit schematic and a generic realization of the inductively modulated π-loop that is used as a basic building block in the circuits throughout this text. Note that the transformer made by the two thin-film superconducting layers (S1 and S2) can also have more than one turn if desired.

The mutual inductance L_m, per full loop, is given by:

$$L_m = \kappa \cdot \sqrt{L_{\text{in}} L_s}$$

where L_{in} and L_s are the primary and secondary inductances of the thin-film transformer made up respectively by the coupled input (S2) and π-loop (S1) super-

conducting layers. The normalized mutual inductance is defined as

$$\beta_m = \frac{2\pi L_m I_C}{\Phi_0} = \kappa \sqrt{\beta_{\text{in}} \beta_L}$$

where the primary and secondary transformer inductances are also normalized, $\beta_{\text{in}} = \frac{2\pi L_{\text{in}} I_C}{\Phi_0}$ and $\beta_L = \frac{2\pi L_s I_C}{\Phi_0}$. The coupling coefficient κ, in the case of a thin-film transformer as drawn in Figure 5.14, can be approximated by [38]:

$$\kappa^2 = \frac{L_m^2}{L_{\text{in}} L_s} = \frac{d + 2\lambda}{d + 2s + 6\lambda}$$

where d is the distance between the superconducting groundplane GP and the first layer S1, λ is the London penetration depth of the used material and s is the distance between the first S1 and second S2 superconducting layers. Reasonably high values of κ can be readily achieved in thin-film superconducting transformers as proved by the many applications of such devices in SQUID sensors [68]. In this text, often a conservative value of $\kappa = 0.4 - 0.5$ will be used as a technological constant. Note however that, in the later part of this presentation, it will be shown that high coupling coefficients are in fact not beneficial for the static π-shift circuits - a large κ typically narrows the useful parameter range of the devices.

5.2.1 Inductively coupled π-loop with a single linear load

In the first instance, it is worth looking at the circuit when loaded with a linear inductor and then later replace it with a realistic load representing an eventual subsequent stage. It will be further assumed that the circuit's input is connected to a Josephson network of similar characteristics as the circuit itself and considered as a "black box". The situation then becomes as depicted in Figure 5.15.

The Gibb's Free energy E_π of the loaded π-device can be calculated as a function of all circuit parameters (normalized inductances β_L, β_{in}, β_m, β_{out}) and of the three independent state variables t, φ_{in} and φ_s:

$$\frac{E_\pi}{\frac{\Phi_0 I_C}{2\pi}} = \frac{\frac{\beta_L}{2}\varphi_{\text{in}}^2 - 2\beta_m \varphi_{\text{in}} t + 2t^2 \beta_{\text{in}}}{\beta_{\text{in}}\beta_L - \beta_m^2} + \varphi_s^2 \frac{4\beta_{\text{out}} + \beta_L}{8\beta_{\text{out}}^2} - 2 \cdot \sin(t) \cdot \sin\left(\varphi_s \frac{4\beta_{\text{out}} + \beta_L}{4\beta_{\text{out}}}\right) \qquad (5.21)$$

where, as previously, $t = \frac{\varphi_2 - \varphi_1 \pm \pi}{2}$, $\varphi_s = \frac{4\beta_{\text{out}}}{4\beta_{\text{out}} + \beta_L} \cdot \frac{\varphi_2 + \varphi_1 \mp \pi}{2}$ are the average difference and sum of the flux angles across the two junctions φ_1 and φ_2 respectively (including the π-shift), the last scaled by a divider ratio between the loop and load.

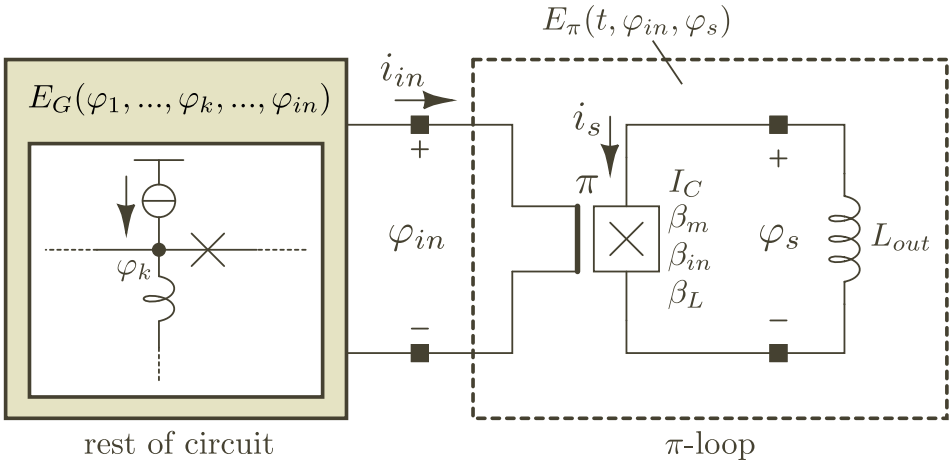

Figure 5.15. A π-loop loaded with an inductor with the input terminals connected to a similar type of circuit represented by the "black box" on the left. The Gibb's free energy of the complete system is the sum of E_G and E_π.

Minimization of the Gibb's energy with respect to the free variables will yield steady-state equations that, in Josephson circuits, are always equal to Kirchhoff's electrical network equations sans contributions from resistive and capacitive elements. If it is assumed that a given circuit will have dynamics slow enough such that the resistive and capacitive elements (present only on the junctions) can be neglected, then the Gibb's energy of that circuit is the only expression necessary to investigate its behavior. Notably, the above assumption also includes that no self-sustained transitions will happen, such as for example in the hysteretic cases from the previous section, since then the dynamics of the system will be determined by intrinsic junction elements and hence be very fast.

Seeking a minimum of equation 5.21 with respect to the variables t and φ_s can be done without knowing anything about the rest of the circuit since E_G is not a function of these two coordinates. The result, given below in equation 5.22, will be a system of network equations very similar to the system 5.10 from the previous section.

Minimization of the Gibbs free energy with respect to the third variable φ_{in} must be done on the sum $E_\pi + E_G$ in order to take into account the contribution of the rest of the circuit as well. If for example, the rest of the circuit is simply a constant current source I_{ext} connected across the terminal φ_{in} with the same direction as i_{in} in Figure 5.15, then its contribution will be simply

$$E_G = -\frac{\Phi_0 I_C}{2\pi} \cdot \varphi_{\text{in}} \cdot I_{\text{ext}}$$

as defined for a current source element in the Josephson network model (Chapter 2). Then the full expression $E_\pi + E_G$ can be minimized w.r.t. φ_{in}. Substituting the result back in $E_\pi + E_G$ and performing the minimization for t and φ_s, the system of relations 5.10 from the previous section will be exactly reproduced, with $\Phi_{\text{ext}} = -L_m I_{\text{ext}}$. This result can be confirmed by inspection of the relevant Figures 5.14, 5.15 and 5.3: a circuit consisting of a current source I_{ext} connected across the input terminals of an inductively-modulated π-loop is equivalent to the flux-modulated π-loop device from the previous sections but with the flux-coupling structure (the transformer) omitted.

In the case presented by Figure 5.15, the rest of the circuit is given as a generic black box in order for the properties of the loaded inductively-modulated π-loop to be examined separately from its electrical environment. Any further analysis therefore results in relations that include φ_{in} as a parameter. This variable will be treated as an input signal for the circuit. The flux angle across the output inductor on the other hand, φ_s, will be treated as the output signal.

It must be mentioned that there is a subtle but important difference between the flux-modulated and the inductively-coupled π-loop. While the former has Φ_{ext} as an input signal, proportional to a current I_{in} in some nearby coil coupled to the π-loop, the latter's input signal is the flux angle φ_{in} across such a coil. Due to the the π-loop/coil coupling however, the relation between I_{in} and φ_{in} is not linear. Consequently, the analysis from the previous sections can not be directly applied to the present circuit. Although the transfer characteristics are similar, the properties of the inductively-coupled loop will be generally more complex as it also includes effects from the coupling between the modulation coil and the π-loop.

The analysis of the inductively coupled loop will proceed in a similar manner as before: calculating the circuit equations and the transfer characteristic, as well as defining the available parameter range in the near-adiabatic regime. To obtain the circuit relations, E_π is minimized for t and φ_s :

$$\begin{cases} \dfrac{\partial E_\pi}{\partial t} = 0 \;\Rightarrow\; \varphi_{\text{in}} = 2t \cdot \dfrac{\beta_{\text{in}}}{\beta_m} - \dfrac{\beta_{\text{in}}\beta_L - \beta_m^2}{\beta_m} \cdot \cos(t) \cdot \sin\left(\varphi_s \dfrac{4\beta_{\text{out}} + \beta_L}{4\beta_{\text{out}}}\right) \\ \dfrac{\partial E_\pi}{\partial \varphi_s} = 0 \;\Rightarrow\; \varphi_s = 2\beta_{\text{out}} \cdot \sin(t) \cdot \cos\left(\varphi_s \dfrac{4\beta_{\text{out}} + \beta_L}{4\beta_{\text{out}}}\right) \end{cases} \tag{5.22}$$

If one solves the system 5.22 by eliminating t and plotting φ_s vs. φ_{in}, the transfer characteristic for the circuit from Figure 5.15 will be obtained. This dependence is very similar to what was previously obtained for the magnetic flux transfer in

a flux-modulated loaded π-loop, Figures 5.4 and 5.6. Depending on the values for the circuit parameters, it can also exhibit incremental and large signal gain around the origin (for $\varphi_s, \varphi_{\text{in}} \cong 0$) as well as hysteretic characteristics. For clarity, a plot of the transfer characteristic will be here omitted.

The incremental gain $G = \frac{\partial \varphi_s}{\partial \varphi_{\text{in}}}$ can be analytically calculated from the system 5.22, yielding a rather complex relation where it is difficult to examine the various parameter influences separately. However, it can be shown that the incremental gain has an extremum when $\varphi_s = 0$, resulting in the compact expression:

$$\left.\frac{\partial \varphi_s}{\partial \varphi_{\text{in}}}\right|_{\varphi_s=0} = G_{\max} = \kappa \cdot \sqrt{\frac{\beta_L}{\beta_{\text{in}}}} \cdot \frac{4\beta_{\text{out}}}{4 - (1-\kappa^2)\beta_L(\beta_L + 4\beta_{\text{out}})} \tag{5.23}$$

Relation 5.23 has a discontinuity that, similar as in the case of a flux-modulated π-loop, gives the condition for a hysteretic transfer characteristic that bounds the near-adiabatic regime of the device:

$$\beta_{\text{out}} < \frac{4 - \beta_L^2(1-\kappa^2)}{4\beta_L(1-\kappa^2)} \tag{5.24}$$

The near-adiabatic condition 5.24 is equal to the one for a flux-modulated π-loop, equation 5.13, when $\kappa = 0$. Of course, in that case there will be no gain as there is no signal coupled to the loop. For non-zero coupling however, the condition 5.24 is generally more relaxed than 5.13, allowing greater parameter margins for β_L and β_{out}. In fact, if the flux coupling is ideal, $\kappa = 1$, the condition 5.24 is satisfied for every value of the pair $(\beta_L, \beta_{\text{out}})$: the circuit will operate in a near-adiabatic regime for any choice of circuit parameters. Note however that a device with $\kappa = 1$ is sensitive to process variations and, as shown later, not the most optimal choice when larger circuits are to be built.

The other side of the useful regime, bounded by having a gain $|G_{\max}| > 1$, results in the following expression:

$$\beta_{\text{out}} > \frac{4 - (1-\kappa^2)\beta_L^2}{4\kappa\sqrt{\frac{\beta_L}{\beta_{\text{in}}}} + 4\beta_L(1-\kappa^2)} \tag{5.25}$$

On the basis of relations 5.24 and 5.25, the plots in Figure 5.16 were obtained. They illustrate the useful near-adiabatic range on the $(\beta_L, \beta_{\text{out}})$ plane with the ratio $\frac{\beta_L}{\beta_{\text{in}}}$ as a parameter, for a few values of the coupling coefficient $0 < \kappa < 1$. Interestingly, the condition that guarantees no isolated stable states, given previously by relation 5.16 for a flux-modulated π-loop, can be shown to be valid in the present case as well. It is also plotted as a boundary in Figure 5.16.

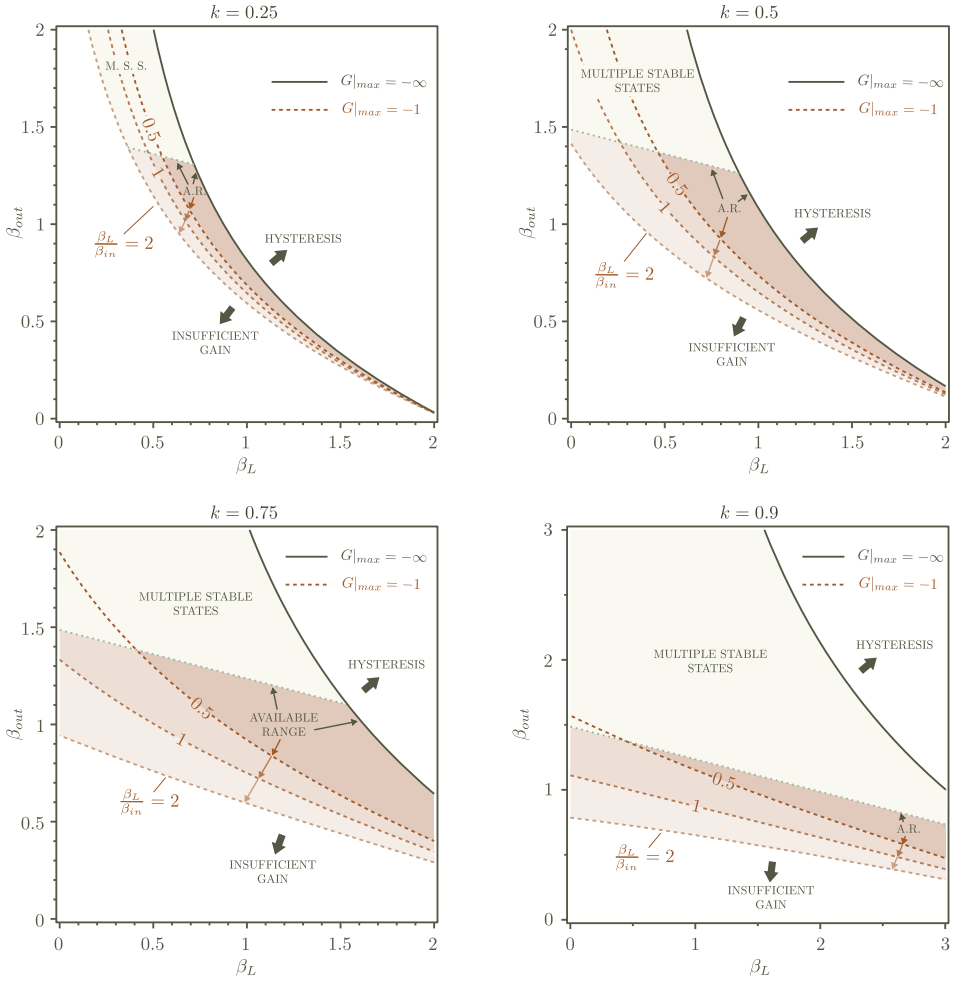

Figure 5.16. Plots of the available near-adiabatic range, bounded by relations 5.24, 5.25 and 5.16, with the ratio between the normalized loop and primary transformer inductance $\frac{\beta_L}{\beta_{in}}$ as a parameter, for a few values of the transformer coupling coefficient κ. The axes scale is different on the plot for $\kappa = 0.9$. Note that while Figure 5.9 from the previous section seems similar, the plot above shows only the available range of the circuit parameters and does not include "equi-gain" lines as Figure 5.9 does (the dotted lines in the plots above correspond to the gain condition 5.25 as it changes with $\frac{\beta_L}{\beta_{in}}$).

For a small value of the coupling coefficient κ, a narrow range of the circuit parameters is found, as illustrated by the plot for $k = 0.25$ in Figure 5.16. A large value of κ on the other hand, does not significantly improve the near-adiabatic

range if the design is bounded by the requirement not to have any isolated stable states during transitions (equation 5.16). If that boundary is not important, for instance when one makes sure that the I_C of the junctions is high enough to prevent thermal activation to the isolated states, then a large κ results in the broadest near-adiabatic range for the circuit parameters.

Compared to similar plots for the flux-modulated loop, for example Figure 5.9 or Figure 5.10, it can be seen that the inductively-coupled loop with a reasonable κ has a slightly narrower parameter range. Although the hysteretic condition is more relaxed for the inductively-coupled loop, the requirement for a greater than unity gain from relation 5.25 severely limits the available range of circuit parameters. This is especially apparent when the ratio $\frac{\beta_L}{\beta_{\rm in}} = \frac{L_s}{L_{\rm in}}$ between the secondary and the primary inductance of the transformer is small. The effect takes place due to the fact that the modulating "action" in the circuit lies in the magnetic flux coupled to the secondary (the π-loop) - this value is smaller, for a fixed $\varphi_{\rm in}$, as $L_{\rm in}$ increases and all else is kept equal. A reduced signal gain is then a natural consequence.

It is important to note that when more inductively coupled π-loops are connected in a cascade, as it would be the case in a large-scale application, the values of $\beta_{\rm out}$ and $\beta_{\rm in}$ will not be independent: the output load of one stage will be approximately equal to the primary transformer inductance (input load) of the next stage, $L_{\rm out} \approx L_{\rm in}$, assuming low interconnect inductance. An interesting observation supported by the plots of Figure 5.16 is that if $\beta_{\rm out}$ and $\beta_{\rm in}$ are thus taken to vary in a highly correlated manner, small changes in the absolute value of these parameters while β_L is kept constant will compensate and the circuit will tend to stay in the near-adiabatic regime.

The property of scaling the maximum gain with output inductance, established for a flux-modulated loop in the previous section, is also present in this circuit. The above is very evident when the case of ideal coupling $\kappa = 1$ is examined. The resulting maximum gain will then be simply reduced to the expression $G_{\rm max} = \beta_{\rm out}\sqrt{\frac{\beta_L}{\beta_{\rm in}}}$. Adding parasitic interconnect inductance to the output load $L_{\rm out}$, while keeping the other parameters constant, results in a larger $G_{\rm max}$. This offsets the static signal losses on the interconnect, expressed as the inductive divider ratio $\frac{L_{\rm load}}{L_{\rm load}+L_{\rm par}}$ multiplying $G_{\rm max}$ in the final gain expression. For smaller coupling, the effect is less significant.

Variations in the π-loop's normalized inductance β_L do not work out in such a compensating fashion however. The plots in Figure 5.16 confirm that decreasing β_L and holding the other parameters constant will shift the operating point to the left while the available range itself will shrink towards the right hand side of the plot through the dependence on the parameter $\frac{\beta_L}{\beta_{\rm in}}$. It is therefore useful to have as large as possible β_L that still satisfies the "upper" bound (no-hysteresis condition) in the plots of Fig. 5.16.

The large number of relevant circuit parameters (4 in total) is prohibitive to attempt a more detailed analysis of the circuit's performance, like for instance the dependence of the saturation amplitudes on the parameters. It is therefore necessary to fix the relationships of the parameters to each other such that some aspect of the circuit is optimized. In the following subsection, it is chosen to analyse the impact of process variations on the maximum incremental gain $G_{\max}$. More importantly, the analysis is done using a model for the load inductances, already briefly mentioned above, that will introduce the concept of cascaded connection of more π-devices in a circuit, necessary in order to perform a certain logical function.

5.2.2 Analysis of a π-device with multiple linear load inductances

An analytical analysis of the maximum gain relation 5.23 with respect to process variations, in a practical output configuration, will be performed next. The purpose is to find the values of the circuit parameters that result in an operating point where the circuit's maximum incremental gain $G_{\max}$ is the least sensitive to process variations. In addition, some aspects of loading the device with several inductors, albeit linear for now, will be introduced and the impact of such 'fanout' will be estimated.

The uncertainty in the process parameters expresses itself, on the lowest circuit-level, as variations in the critical current density of the junctions and as variations in the sheet inductance of the used wiring layers. These are the two basis processing parameters whose statistics give rise to correlated variations of the circuit parameters such as the normalized inductances. For simplicity, it will be assumed that the coupling factor of the transformer, κ, as well as the dimensions of the structures do not vary.

First, the general architecture of a π-device loaded with other, subsequent, stages will be presented. Next, an analysis is performed on the maximum gain and its sensitivity to process variations, the optimisation of which results in practical guidelines for these multi-stage circuits. At the end, the analysis is taken further in order to, besides process robustness, also achieve standardization of the circuits and simplify the design procedure.

In reality, the output load inductances in a cascade connection of π-devices are not ordinary inductive segments: they are the input inductances of other stages which do not have a simple linear $\varphi - I$ relationship. Fortunately, much of the analysis below can be translated to such a case. Section 5.2.3 deals with the issue of realistic output loading in a cascade connection of π-devices.

5.2.2.1 A π-device loaded with multiple stages

The inductively-modulated loop is connected to the load through an interconnect inductance, just as in the case given by Figure 5.12. The ratio between the load and parasitic inductances is again defined as:

$$q = \frac{L_{\text{par}}}{L_{\text{load}}} \tag{5.26}$$

In order for the following analysis to encompass the situation where multiple stages are connected to a single π-device as a load, it is necessary to connect the input inductance of the driving π-device, L_{in}, with the inductance that is presented as a (remote) load, L_{load}. This is expressed as

$$p = \frac{L_{\text{load}}}{L_{\text{in}}} \tag{5.27}$$

where the parameter p can be qualitatively described as the *relative load factor*. The meaning is exemplified as follows:

- $p = 1$ means that the π-device is loaded with a single π-loop stage
- $p = 2$ means that two π-loop stages are placed in series at the output
- $p = \frac{1}{2}$ means that two π-loop stages are placed in parallel at the output

etc. assuming that the subsequent stages are of the same input inductance as the driving π-device $L_{\text{in,subsq}} = L_{\text{in,drive}}$. The situation is more clearly depicted in Figure 5.17.

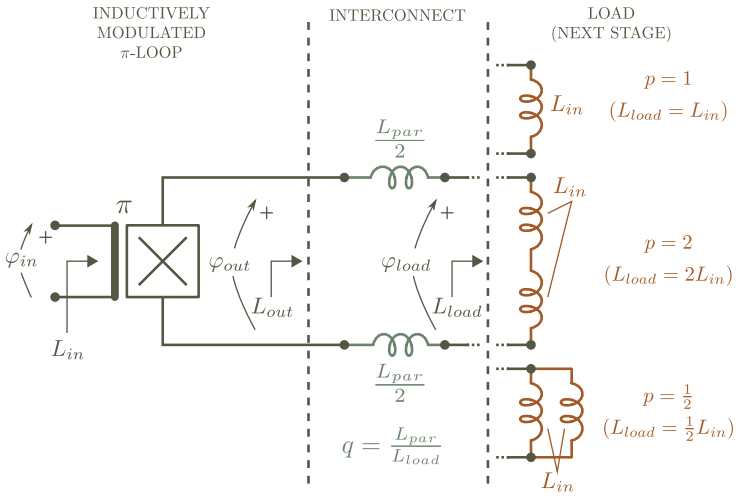

Figure 5.17. A schematic of a loaded π-device including the interconnect inductance and the loading stages. It is assumed that these are identical to the driving stage.

The "relative load factor" p is the net effect arising from the load's configuration (series/parallel) and the values of the inductances. For instance, if the input inductance of two subsequent stages is half of the driving stage's input inductance and they are connected in series, the factor p will still be unity. The same value is achieved if the two stages are placed in parallel but their input inductances are twice the one of the driving π-device.

For complete accuracy, one more parameter needs to be introduced. When the output of the π-device consists of stages connected in series, for example the case denoted with $p = 2$ in Fig. 5.17, the signal delivered to *each* of those stages is a fraction of the output signal φ_{out}, that fraction equal to the number of stages in series. Therefore, in order to accurately capture the complete transfer from the input of the π-device to the input of each of the devices in the subsequent stages, the gain equation needs to be divided by the number of stages in series, s. In the case when the stages are connected in parallel, the value of s is unity regardless of their number.

In the analysis of this section, it is assumed that all load stages, whether placed in parallel or in series, are identical. It should also be mentioned that the back-action from the subsequent stages to the driving π-device is neglected. This effect is however studied in the following section.

5.2.2.2 Optimal process sensitivity of the maximum gain

Under these conditions, the maximum gain is found to be:

$$G_{\max,l} = \left| \frac{\partial \varphi_{\mathrm{load},s}}{\partial \varphi_{\mathrm{in}}} \right|_{\max} = 4\kappa \cdot p \cdot \frac{\sqrt{\beta_L \beta_{\mathrm{in}}}}{4 - (1-\kappa^2)\beta_L(\beta_L + 4(1+q)p\beta_{\mathrm{in}})} \cdot \frac{1}{s} \tag{5.28}$$

where $\varphi_{\mathrm{load},s} = \frac{1}{s}\varphi_{\mathrm{load}}$ is the signal delivered to each subsequent stage and s is defined as described above. Under the influence of process variations, expressed as changes in the sheet inductance of the superconducting films and in the critical current density of the junctions, the normalized inductances β_L and β_{in} will vary while q, p, κ and s stay constant. The case when the circuit parameters can also exhibit a variation between the elements individually will lead to circuit asymmetry. The effect of asymmetry is considered in one of the next sections. At this moment, it will be assumed that the parameter variations are global for the circuit, affecting all elements equally.

The normalized inductances have the following sensitivities to the process parameters:

$$\frac{\mathrm{d}\beta_L}{\beta_L} = \frac{\mathrm{d}\beta_{\mathrm{in}}}{\beta_{\mathrm{in}}} = \frac{\mathrm{d}L_\square}{L_\square} + \frac{\mathrm{d}J_C}{J_C} \tag{5.29}$$

where $L_\square$ is the sheet inductance of the used materials and J_C is the critical current density. The sensitivity of the maximum gain at the load is now written as:

$$\begin{aligned}\frac{\mathrm{d}G_{\max,l}}{G_{\max}} = &\left(\frac{\beta_L}{G_{\max,l}}\cdot\frac{\partial G_{\max,l}}{\partial\beta_L}+\frac{\beta_{\mathrm{in}}}{G_{\max,l}}\cdot\frac{\partial G_{\max,l}}{\partial\beta_{\mathrm{in}}}\right)\cdot\left(\frac{\mathrm{d}L_\square}{L_\square}+\frac{\mathrm{d}J_C}{J_C}\right)= \\ &= G_{\max,\mathrm{sens}}\cdot\left(\frac{\mathrm{d}L_\square}{L_\square}+\frac{\mathrm{d}J_C}{J_C}\right)\end{aligned} \tag{5.30}$$

The purpose of this section is to find the range of the circuit parameters for which the relative process sensitivity of the maximum incremental gain, $G_{\max,\mathrm{sens}}$, is as low as practicality allows.

An expression for $G_{\max,\mathrm{sens}}$ can be calculated from 5.30:

$$G_{\max,\mathrm{sens}} = \frac{4+(1-\kappa^2)\,\beta_L\,(\beta_L+4\,(1+q)\,p\,\beta_{\mathrm{in}})}{4-(1-\kappa^2)\,\beta_L\,(\beta_L+4\,(1+q)\,p\,\beta_{\mathrm{in}})} \tag{5.31}$$

Not surprisingly, the process sensitivity of the gain approaches infinity as the gain itself approaches the same value. That happens in the case when the values of the parameters fall close to the near-adiabatic condition 5.24 since the denominator (which causes the divergence to $\propto$) is the same for both the gain and its relative process sensitivity.

A better measure will then be to find the parameter range where the relative sensitivity $G_{\max,\mathrm{sens}}$ is lowest while the absolute value of the gain $G_{\max,l}$ is the highest. This "gain figure of merit" can be constructed as:

$$\mathrm{FM}_G = \left|\frac{G_{\max,l}}{G_{\max,\mathrm{sens}}}\right| = \frac{4\,\kappa\,p\,\sqrt{\beta_{\mathrm{in}}\,\beta_L}}{4+(1-\kappa^2)\,\beta_L\,(\beta_L+4\,(1+q)\,p\,\beta_{\mathrm{in}})}\cdot\frac{1}{s} \tag{5.32}$$

and should be maximized as a function of the circuit parameters. It is immediately evident that the best figure of merit is achieved when both s and q are small. The lowest value for s is unity, when there are no stages in series at the output, while the lowest value for q is zero, when there are no parasitic inductances at the output. Further, keeping everything the same and varying κ from 0 to 1, it is obtained that FM_G is the highest for the best possible coupling, $\kappa\approx 1$. Similarly, the higher the relative load factor p, the better the figure of merit is.

Note that there is an optimum of FM_G with respect to the output configuration since the number of stages s and the loading factor p are not independent. This optimum will be found towards the end of the section.

As far as the normalized inductances β_L and β_{in} are concerned, during the optimization of 5.32 their available range should be taken into account. The most important bound of the available range, the hysteretic condition, for the present case calculates to

$$\beta_{\mathrm{in}} < \frac{4-(1-\kappa^2)\,\beta_L^2}{4\,p\,(1+q)\,(1-\kappa^2)\,\beta_L} \tag{5.33}$$

When the figure of merit 5.32 is optimized as a function of β_{in}, a maximum is found. However, it can be proved that this maximum always lies outside the boundary of the hysteretic condition 5.33.

The figure of merit 5.32 has also maximum as a function of β_L. The relation between β_L and β_{in} along that maximum calculates to:

$$\beta_{\text{in,opt}} = \frac{4-(1-\kappa^2)\,\beta_L^2}{4\,p\,(1+q)\,(1-\kappa^2)\,\beta_L} - \frac{\beta_L}{2\,p\,(1+q)} \tag{5.34}$$

which obviously lies within the boundary defined by the hysteretic condition 5.33. Note that $\beta_{\text{in,opt}}$ should be positive for a realistic circuit. In 5.34 this requires

$$\beta_L < \frac{2}{\sqrt{3\,(1-\kappa^2)}} \tag{5.35}$$

and hence sets an upper limit of β_L for any π-device that is optimized for the figure of merit.

If β_L is known, then the normalized input inductance should be chosen according to 5.34 in order to have the best gain figure of merit. In Figure 5.18, the expression for $\beta_{\text{in,opt}}$ is plotted as a function of β_L for different κ.

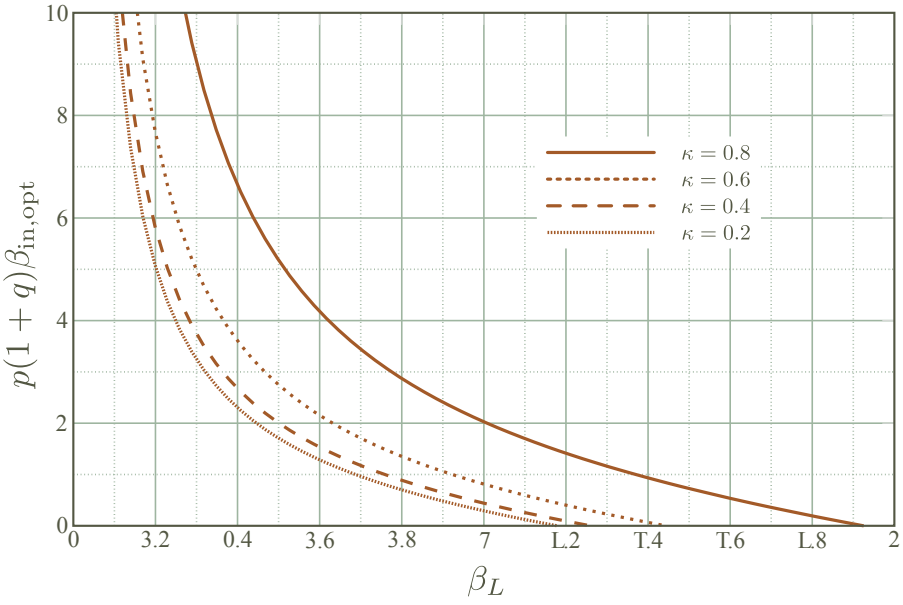

Figure 5.18. The optimal normalized output inductance, multiplied by the relative loading factor p and the parasitic inductance ratio $1+q$, as a function of the normalized loop inductance β_L with the coupling factor κ as a parameter.

Let's now find whether the optimal β_{in} choice from 5.34 violates the second boundary of the available range, the gain condition given by

$$|G_{\max,l}| = 4\kappa \cdot p \cdot \frac{\sqrt{\beta_L \beta_{\text{in}}}}{4-(1-\kappa^2)\beta_L(\beta_L+4(1+q)p\beta_{\text{in}})} \cdot \frac{1}{s} > 1 \tag{5.36}$$

Replacing 5.34 in the relation above, it is obtained that $\beta_L < \beta_{L,\max}$ where

$$\beta_{L,\max}^2 = \frac{3\kappa^2\, p}{2\, s^2\,(1+q)\,(1-\kappa^2)^2} \cdot \left(\sqrt{1+\frac{16\,(1-\kappa^2)\,(1+q)\,s^2}{9\,\kappa^2\, p}} - 1 \right) \tag{5.37}$$

Hence, as long as the normalized loop inductance is chosen such that it is less than $\beta_{L,\max}$ from 5.37 for a given set of parameters κ, q, p and s, then setting β_{in} at the optimum value of 5.34 violates neither the hysteretic 5.33 nor gain condition 5.36.

If the optimal value of the input inductance $\beta_{\text{in,opt}}$ is now replaced in the expression for the figure of merit, then it is obtained that FM_G is the highest for the lowest β_L, regardless of the values of the other parameters. The monotonicity is, of course, expected since FM_G was already optimized w.r.t. β_L, the result being 5.34. One should therefore always choose the normalized loop inductance to be as low as possible.

5.2.2.3 Output load configuration

In practice, a circuit designer is always given only the number of subsequent stages N and is usually constrained by the maximum coupling factor κ and the lowest parasitic inductance in the interconnect L_{par} that is achievable with the given technology. There is often a minimal normalized loop inductance β_L given as well, determined by the minimum feature sizes that can be defined in the physical layout of the circuit (constraining both L_s and I_C). Although there is still freedom to choose the β_L of the devices, lets assume for the moment that a value has already been given. This value will be calculated later towards the end of the section from other considerations.

In this case, assuming that β_L, κ and L_{par} are determined by the available technology, the designer's choice lies in the selection of the input inductance of the π-device $L_{\text{in,drive}}$, the relative loading factor p and the connection type: in parallel or in series. The normalized input inductance of the subsequent stages $L_{\text{in,subsq}}$ can then be calculated, completing the circuit design as all parameters will then be known. Lets outline the design procedure for this task. It is taken that $N=2$, i.e. the output of the π-device should feed to two subsequent stages.

First, from the plot in Figure 5.18, the value of $B_{\text{in}} = p\,(1+q)\,\beta_{\text{in}}$ is found for the given κ and β_L. Indeed, β_L should be less than its maximum value from 5.37,

but as s and p are unknown at this time, one can only check this boundary later. The figure of merit FM_G can be re-written as a function of B_{in}:

$$\mathrm{FM}_G = \frac{2\,\kappa\,\sqrt{B_{\mathrm{in}}\cdot\beta_L}}{(4+(1-\kappa^2)\,\beta_L^2)}\cdot\frac{\sqrt{p}}{s\cdot\sqrt{1+q}} = C_{\mathrm{FM}}\cdot\frac{\sqrt{p}}{s\cdot\sqrt{1+q}}$$

where C_{FM} is already known from the given parameters. Lets first put the two stages in parallel, $s=1$. To obtain the highest p, and hence the highest FM_G, the input inductances of the two loading stages $L_{\mathrm{in,subsq}}$ must be high. Lets suppose that it is chosen that they are twice the input inductance of the driving stage, $L_{\mathrm{in,subsq}} = 2\cdot L_{\mathrm{in}}$. Then, for $N=2$, it is obtained

$$p_{\mathrm{par}} = \frac{\frac{L_{\mathrm{in,subsq}}}{N}}{L_{\mathrm{in}}} = 1 \quad , \quad q_{\mathrm{par}} = \frac{L_{\mathrm{par}}}{\frac{L_{\mathrm{in,subsq}}}{N}} = N\cdot\frac{L_{\mathrm{par}}}{L_{\mathrm{in,subsq}}} = \frac{L_{\mathrm{par}}}{L_{\mathrm{in}}}$$

and the figure of merit is

$$\mathrm{FM}_{G,\mathrm{par}} = \frac{C_{\mathrm{FM}}}{\sqrt{1+q_{\mathrm{par}}}}$$

If the two stages were placed in series, $s=N=2$, then it follows

$$p_{\mathrm{ser}} = \frac{N\cdot L_{\mathrm{in,subsq}}}{L_{\mathrm{in}}} = 4 \quad , \quad q_{\mathrm{ser}} = \frac{N\cdot L_{\mathrm{par}}}{N\cdot L_{\mathrm{in,subsq}}} = \frac{1}{2}\cdot\frac{L_{\mathrm{par}}}{L_{\mathrm{in}}} = \frac{1}{2}\cdot q_{\mathrm{par}}$$

since adding stages in series results in proportionally increasing the parasitic inductance at the output due to the new wiring between the devices. The figure of merit is now

$$\mathrm{FM}_{G,\mathrm{ser}} = \frac{C_{\mathrm{FM}}}{\sqrt{1+\frac{q_{\mathrm{par}}}{2}}} = \frac{\sqrt{1+q_{\mathrm{par}}}}{\sqrt{1+\frac{q_{\mathrm{par}}}{2}}}\cdot\mathrm{FM}_{G,\mathrm{par}} > \mathrm{FM}_{G,\mathrm{par}}$$

Were the input inductances of the subsequent stages three times the input inductance of the driving stage, then in the case of their parallel combination the figure of merit is $\mathrm{FM}_{G,\mathrm{par}} = C_{\mathrm{FM}}\cdot\sqrt{\frac{1.5}{1+\frac{2}{3}\cdot\frac{L_{\mathrm{par}}}{L_{\mathrm{in}}}}}$ while in case of a series connection $\mathrm{FM}_{G,\mathrm{ser}} = C_{\mathrm{FM}}\cdot\sqrt{\frac{1.5}{1+\frac{1}{3}\cdot\frac{L_{\mathrm{par}}}{L_{\mathrm{in}}}}}$.

This continues for any ratio a between the input inductances of the subsequent and the driving stage

$$a = \frac{L_{\mathrm{in,subsq}}}{L_{\mathrm{in,drive}}}$$

as

$$\mathrm{FM}_{G,\mathrm{series}} = \sqrt{\frac{a + N \cdot \frac{L_{\mathrm{par}}}{L_{\mathrm{in,drive}}}}{a + \frac{L_{\mathrm{par}}}{L_{\mathrm{in,drive}}}}} \cdot \mathrm{FM}_{G,\mathrm{parallel}} = C_{\mathrm{FM}} \cdot \frac{a}{\sqrt{N \cdot \left(a + N \cdot \frac{L_{\mathrm{par}}}{L_{\mathrm{in,drive}}}\right)}}$$

where $\frac{L_{\mathrm{par}}}{L_{\mathrm{in,drive}}}$ is a given constant. So, all things equal, the figure of merit in the case of a series connection is always greater or equal to the figure of merit in case of a parallel connection.

Note that the gain itself, equation 5.28, also has the same property

$$G_{\max,l} = \frac{2\,\kappa\,\sqrt{B_{\mathrm{in}} \cdot \beta_L}}{(1-\kappa^2)\,\beta_L^2} \cdot \frac{\sqrt{p}}{s \cdot \sqrt{1+q}} = C_G \frac{\sqrt{p}}{s \cdot \sqrt{1+q}} \tag{5.38}$$

where the coefficient

$$C_G = \frac{2\,\kappa\,\sqrt{B_{\mathrm{in}} \cdot \beta_L}}{(1-\kappa^2)\,\beta_L^2} \tag{5.39}$$

is, again, a known constant for the task at hand. Hence, a series combination at the output has a higher gain as well.

It can be thus concluded that as long as $\beta_{\mathrm{in}} = \beta_{\mathrm{in,opt}}$ is chosen and the scaling ratio a between the stages is kept the same, both the gain and the gain figure of merit are higher for a series than for a parallel combination of N stages at the output.

Moreover, not only is the series output configuration superior with respect to both process robustness and gain, it is also more practical: a parallel combination will result in an all-inductive loop in the circuit, making it possible to trap flux quanta that will interfere with the operation of the circuit. A series combination on the other hand produces no such effect. Therefore, a most suitable choice would be a series combination of subsequent stages when a fanout N must be achieved.

The only choice that the designer has left at this point is that of the ratio a between the input inductances of the subsequent and the driving stage as well as the choice of β_L. As can be seen from the equations above, given that $N = 2$, choosing $a = 2$ yields both the same figure of merit and the same gain as if a single subsequent stage of $L_{\mathrm{in,subsq}} = L_{\mathrm{in,drive}}$ was used as a load at the output ($N = 1$, $a = 1$). This is quite suitable for design standardization, especially when there are more such circuits to be designed and connected: adding stages at the output requires to proportionally increase the input inductances of those stages if the gain is to remain equal.

It was shown in this section that when a π-device is loaded with multiple stages at its output, there exists an optimal relationship between its normalized input and normalized loop inductances resulting in the highest gain and simultaneously the lowest process sensitivity of the same. This relationship is given by equation 5.34 and depends on the choice of the ratio between the input inductances of the subsequent and driving stages, as well as on the parasitic inductance, the coupling factor and the number of stages in series.

Further, it was determined that when the optimal parameter choice 5.34 is made, connecting the output stages in series or in parallel makes a difference in circuit performance. It was shown that a series combination yields both a higher gain and a lower process sensitivity, in addition to some other practical advantages. Another conclusion from the analysis given in this section states that when a circuit designer must add stages at the output, preserving the same gain can be achieved by increasing the input inductances of those stages proportionally with their number.

5.2.3 π-devices with nonlinear load inductances

The analysis in the previous section was given under the assumption that the input inductance of a general π-device is constant across the range of the input signal. The assumption leads to a relationship between the flux angle φ_{in} and current I_{in} at the input of the device

$$\varphi_{\text{in}} = \frac{2\pi}{\Phi_0} L_{\text{in}} \cdot I_{\text{in}}$$

where L_{in}, the input inductance, is a constant. However, the input inductance of the device is not only different than L_{in}, but it is also non-linear - it depends on the current I_{in}. To see why, lets view the π-device as a transformer where L_{in} is the primary while L_s in series with the junctions (and π-shift) is the secondary coil. Then, the coupling between them makes the elements of the secondary coil to be "felt" between the primary terminals in addition to the primary inductance. One can also treat this effect as a reflection of the circuit attached at the secondary onto the primary through the coupling action of the transformer. Since the junctions are non-linear elements, the input inductance "seen" at the primary is also non-linear. This manifests, equivalently, as a current-dependent inductance $L_{\text{in}} = L_{\text{in}}(I_{\text{in}})$.

The value of $L_{\text{in}}(0)$ is of the highest importance in the analysis of the loaded π-devices. The reason is that the maximum gain $G_{\max}$ is achieved at the origin of the transfer characteristic, when both the input and output current, as well as the corresponding flux angles, are equal to zero.

In the analysis that follows, to avoid confusion, the inductance of the primary coil of the transformer in the π-device will still be marked as L_{in}. Similarly, the normalized input inductance of the circuit will remain defined w.r.t. L_{in} in order to keep the conventions from the beginning of this Chapter: $\beta_{\text{in}} = \frac{2\pi\, L_{\text{in}}\, I_C}{\Phi_0}$.

Since only the incremental gain $\frac{\partial \varphi_{\text{out}}}{\partial \varphi_{\text{in}}}$ at zero input signal will be analysed, all elements are linearized around the origin. This means that the constitutive laws of the elements $\varphi = \varphi(I)$ will be replaced by their derivative version

$$\left.\frac{\partial \varphi}{\partial I}\right|_{\varphi_{\text{in}}=0} = \frac{2\pi}{\Phi_0} \cdot L_0$$

around the point of operation of the element. This operating point is, in this case, at zero input signal. The value of L_0 for each element is the *incremental* inductance: it equals the derivative of the $\varphi = \varphi(I)$ constitutive law evaluated at the operating point when the input and output signal to the circuit are zero. The replacement of the elements with their incremental inductance will result in the "small-signal" network schematic of the π-device shown on the right in Figure 5.19. All elements are now linear but the branch and node variables are the *increments* of the currents and flux angles of the original schematic around an operating point (zero input and output signal).

The π-device will be loaded with an incremental inductance $L_{\text{out}0}$ since any subsequent stages connected at the output can also have non-linear input inductances.

For the linear inductors, the element values remain the same ($L_0 = L$). For the junctions however, from the constitutive law $I_J = I_C \cdot \sin(\varphi)$, the incremental inductance is equal to their Josephson inductance L_J:

$$L_0 = \frac{\Phi_0}{2\pi} \cdot \left.\frac{\partial \varphi_J}{\partial I_J}\right|_{\varphi_{\text{in}}=0} = \left.\frac{\Phi_0}{2\pi\, I_C \cos(\varphi_J)}\right|_{\varphi_{\text{in}}=0}$$

calculated at the operating point φ_J for which the input and output signals $\varphi_{\text{in}} = \varphi_{\text{out}} = 0$. The π-shift element is removed since its incremental inductance is zero.

From the initial analysis of the inductively-modulated π-device, for example the network equations 5.22, it can be seen that

$$\varphi_{\text{in}} = \varphi_{\text{out}} = 0 \;\Rightarrow \begin{cases} \varphi_{J2} - \varphi_{J1} \pm \pi = 0 \\ \varphi_{J2} + \varphi_{J1} \mp \pi = 0 \end{cases}$$

and hence the flux angles of the two junctions are $\varphi_{J2}=0, \varphi_{J1}=\pm\pi$ when the input and output signals are zero. The Josephson inductances of the junctions are then

$$L_{J1}=-L_{J2}=\frac{\Phi_0}{2\pi I_C}$$

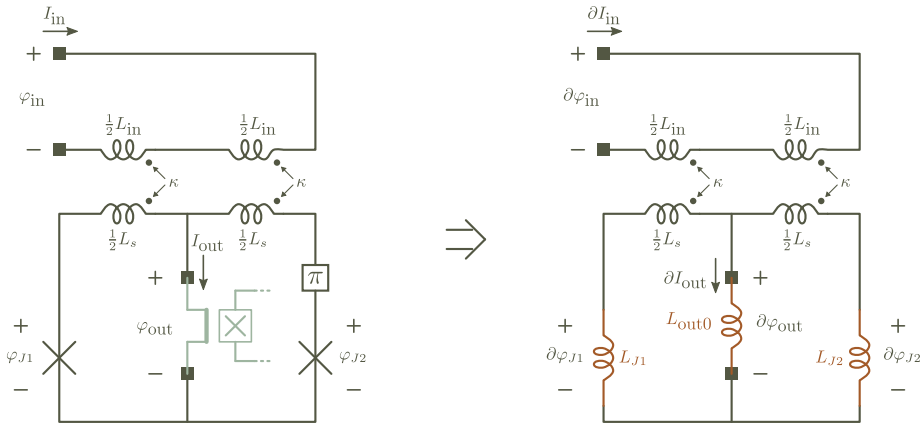

Figure 5.19. The original schematic of a (loaded) π-device is shown on the left. The "small signal" schematic on the right is obtained by linearisation of the constitutive laws of all elements around their operating points.

The network equations for the schematic on the right in Figure 5.19 can now be found by a simple network analysis:

$$\partial\varphi_{\text{out}}=\partial\varphi_{J1}\left(1+\frac{L_s}{2\,L_{J1}}\right)+\partial I_{\text{in}}\cdot\frac{2\pi}{\Phi_0}M$$

$$\partial\varphi_{\text{out}}=\partial\varphi_{J2}\left(1+\frac{L_s}{2\,L_{J2}}\right)-\partial I_{\text{in}}\cdot\frac{2\pi}{\Phi_0}M$$

$$\frac{\partial\varphi_{J1}}{L_{J1}}+\frac{\partial\varphi_{J2}}{L_{J2}}+\frac{\partial\varphi_{\text{out}}}{L_{\text{out0}}}=0$$

$$\partial\varphi_{\text{in}}=\partial I_{\text{in}}\cdot\frac{2\pi\,L_{\text{in}}}{\Phi_0}+M\left(\frac{\partial\varphi_{J1}}{L_{J1}}-\frac{\partial\varphi_{J2}}{L_{J2}}\right)$$

where $M = \frac{\kappa}{2} \cdot \sqrt{L_{\rm in} \cdot L_s}$. Eliminating $\partial\varphi_{J1}$, $\partial\varphi_{J2}$ and $\partial I_{\rm in}$ from the system above and using $L_{J1} = -L_{J2} = L_J$, the gain can be obtained

$$\frac{\partial\varphi_{\rm out}}{\partial\varphi_{\rm in}} = \frac{-2\,M\,L_J\,L_{\rm out0}}{L_{\rm in}\,L_{\rm out0}\,L_s + \frac{L_{\rm in}\,L_s^2}{4} - L_{\rm in}\,L_J^2 - 4\,M^2\,L_{\rm out0} - M^2\,L_s}$$

that, when replacing $L_J = \frac{\Phi_0}{2\pi I_C}$ and $M^2 = \frac{1}{4}\kappa^2\,L_{\rm in}\,L_s$, reduces to the already known expression

$$G_{\rm max} = \frac{\partial\varphi_{\rm out}}{\partial\varphi_{\rm in}} = \sqrt{\frac{\beta_L}{\beta_{\rm in}}} \cdot \frac{4\,\kappa \cdot \beta_{\rm out0}}{4 - (1-\kappa^2)\,\beta_L\,(\beta_L + 4\,\beta_{\rm out0})} \tag{5.40}$$

The difference is that in place of the linear output inductance $L_{\rm out}$, the incremental output inductance $L_{\rm out0}$ of the load around zero signal is used

$$\beta_{\rm out0} = \frac{2\pi\,L_{\rm out0}\,I_C}{\Phi_0}$$

When the load inductance is indeed just an inductor, then $L_{\rm out0} = L_{\rm out}$, as was assumed in all analyses thus far. But when at the output of the π-device the input terminals of another such device are connected, then $L_{\rm out0} = L_{\rm in0,subsq}$ where $L_{\rm in0,subsq}$ is the incremental input inductance of the subsequent device.

The incremental input inductance of a general π-device can be calculated from the system of network equations above when $\partial\varphi_{J1}$, $\partial\varphi_{J2}$ and $\partial\varphi_{\rm out}$ are eliminated:

$$L_{\rm in0} = \frac{\Phi_0}{2\pi} \cdot \frac{\partial\varphi_{\rm in}}{\partial I_{\rm in}} = L_{\rm in} \cdot \frac{4 - (1-\kappa^2)\,\beta_L\,(\beta_L + 4\,\beta_{\rm out0})}{4 - \beta_L\,(\beta_L + 4\,\beta_{\rm out0})} \tag{5.41}$$

The incremental input inductance $L_{\rm in0}$ depends linearly on the inductance of the primary of the π-loop transformer $L_{\rm in}$. Further, for positive β_L and $\beta_{\rm out0}$, it is obtained that $L_{\rm in0} \geqslant L_{\rm in}$, with the equality valid when there is no coupling $\kappa^2 = 0$.

Note that when the incremental input inductance is zero,

$$4 - (1-\kappa^2)\,\beta_L\,(\beta_L + 4\,\beta_{\rm out0}) = 0$$

the gain of the circuit is infinite. The relation above is nothing else than the boundary of the available range defined by the hysteretic condition found previously for a linear load

$$0 < \beta_{\rm out0} < \frac{4 - \beta_L^2\,(1-\kappa^2)}{4\,(1-\kappa^2)\,\beta_L} \tag{5.42}$$

except that in this case it applies to the normalized incremental load β_{out0} at the output of a general π-device. Note that since L_{out0} is an incremental inductance, it is possible for it to be negative. The same applies to L_{in0} as well. The case when $\beta_{\text{out0}} < 0$ will be considered further below.

In order for the hysteretic condition 5.42 to be satisfied for a cascade connection of stages, one needs to calculate the incremental input inductance of the subsequent stage $L_{\text{in0,subsq}}$ by using 5.41. Then, the condition 5.42 can be tested with $L_{\text{out0}} = L_{\text{in0,subsq}}$. The problem is that $L_{\text{in0,subsq}}$ can not be calculated without knowing the incremental load inductance of the subsequent stage itself. In fact, given a cascade connection of many π-devices, it is necessary to start from the end (the output) and work backwards, calculating L_{in0} for every stage and testing the hysteretic condition for the preceding stage.

This method is not practical in a large circuit. It would be very convenient if a general rule was available that makes it possible to place the π-devices in the near-adiabatic range without knowing many details about the circuits connected at its output.

To find such a design rule, lets analyse the circuit when a driving π-device is connected to the input terminals of N subsequent stages, just like in Figure 5.17 from the previous section. In this case however, in order to keep the analysis the same, the definitions of both the parasitic inductance and the relative loading factor will be slightly different:

$$L_{\text{out0}} = L_{\text{par}} + L_{\text{load0}} = (1+q) \cdot L_{\text{load0}} = (1+q) \cdot p \cdot L_{\text{in}} \tag{5.43}$$

The parasitic inductance factor q will be equal to the ratio of the (linear) parasitic inductance L_{par} and the *incremental* load inductance L_{load0}:

$$q = \frac{L_{\text{par}}}{L_{\text{load0}}} \tag{5.44}$$

The incremental load inductance, equal to the net load of all N stages connected at the output (whether in series or in parallel) is related to L_{in}, the inductance of the primary of the driving π-stage, through the relative loading factor

$$p = \frac{L_{\text{load0}}}{L_{\text{in}}} \tag{5.45}$$

In this situation, the analysis from the previous section stays valid since the expression for the gain will be exactly the same. So, choosing the normalized inductance of the primary according to the optimal value 5.34

$$\beta_{\text{in}} = \frac{4 - 3(1-\kappa^2)\,\beta_L^2}{4\,p\,(1+q)(1-\kappa^2)\,\beta_L} \tag{5.46}$$

gives the best figure of merit for the driving device. Replacing 5.43 in 5.46 and then taking the result to the expression for the incremental input inductance 5.41, it is obtained

$$L_{\text{in0}} = \frac{(1-\kappa^2)^2 \cdot \beta_L^2}{(1-\kappa^2)\,\beta_L^2 - 2\kappa^2} \cdot L_{\text{in}} = B(\kappa, \beta_L) \cdot L_{\text{in}} \tag{5.47}$$

Thus, designing the π-device with an optimum figure of merit will result in the incremental input inductance being proportional to L_{in}, with a coefficient of proportionality

$$B(\kappa, \beta_L) = \frac{(1-\kappa^2)^2 \cdot \beta_L^2}{(1-\kappa^2)\,\beta_L^2 - 2\kappa^2} \tag{5.48}$$

that is a function only of the coupling factor κ and of the normalized loop inductance β_L.

Since using the optimal β_{in} from 5.46 never leads to a breach of the hysteretic condition, the stage will, regardless of the loading factor p, always stay in the near-adiabatic range. Of course, calculating β_{in} necessitates the knowledge of p and q. However, these can now be easily computed from the $L_{\text{in,subsq}}$ and B_{subsq} of the subsequent stages if they are optimized for the figure of merit as well.

It was mentioned before that the normalized loop inductance of a π-device must satisfy

$$\beta_L < \frac{2}{\sqrt{3\,(1-k^2)}} \tag{5.49}$$

in order for the optimal condition 5.46 to result in a realisable (positive) β_{in}. This is true as long as the incremental output load β_{out0} is positive: for a negative incremental load inductance, the opposite must hold $\beta_L > \frac{2}{\sqrt{3\,(1-k^2)}}$. However, it can be easily shown that when $\beta_{\text{out0}} < 0$, satisfying the above always results in a hysteretic transfer characteristic. In other words, if a π-device is presented with a negative incremental load inductance at its output terminals, it is not possible to simultaneously optimize its figure of merit and have a non-hysteretic transfer characteristic. Hence, the incremental output load should be kept positive if one wishes to build the best circuits. This translates to requiring the incremental input inductances of the subsequent stages to be positive (unless the parasitic inductance factor $|q| > 1$ which is rarely the case for $N > 1$).

The incremental input inductance of a general π-device is positive when the coefficient $B(\kappa, \beta_{L,\text{subsq}}) > 0$. From equation 5.47, it is then obtained

$$\beta_L > \frac{\sqrt{2} \cdot \kappa}{\sqrt{1-\kappa^2}} \tag{5.50}$$

thus limiting the minimum value of the normalized loop inductance. Conditions 5.49 and 5.50 now together give a range for the β_L of an optimized π-device, as plotted in Figure 5.20.

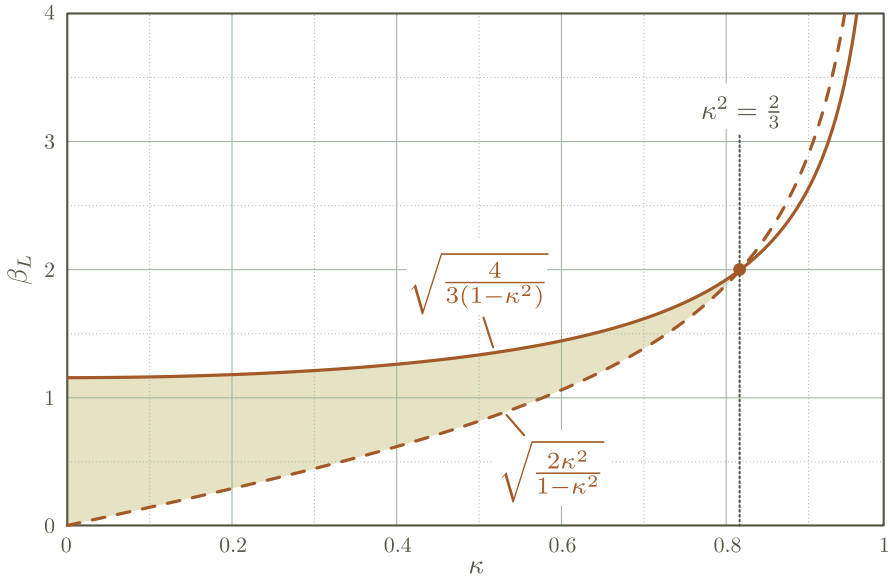

Figure 5.20. The two conditions bounding the choice of normalized loop inductance for a general π-device. When β_L is within the shaded region, the π-device can be optimized with respect to the process variations of the gain without resulting in a negative incremental input inductance.

When $\kappa^2 > \frac{2}{3}$, the conditions 5.49 and 5.50 become impossible to satisfy simultaneously. Fortunately, values of $\kappa > \sqrt{\frac{2}{3}} = 0.82$ for a thin-film superconducting transformer are rarely obtained, requiring films of very high quality (low λ_L) and a device of large dimensions (small edge effects). In practice, the coupling coefficient is in the range of $0.4 - 0.6$ so that, depending on the exact value of κ, the values of β_L should be somewhere between 0.6 and 1.4.

Note that the allowed relative range of β_L given above

$$\frac{\Delta\beta_L}{\beta_L} = \frac{\beta_{L,\max} - \beta_{L,\min}}{\frac{\beta_{L,\max} + \beta_{L,\min}}{2}} = 2 \cdot \frac{\frac{2}{\sqrt{3\,(1-k^2)}} - \frac{\sqrt{2}\kappa}{\sqrt{1-\kappa^2}}}{\frac{2}{\sqrt{3\,(1-k^2)}} + \frac{\sqrt{2}\kappa}{\sqrt{1-\kappa^2}}} = 2 \cdot \frac{1 - \kappa\sqrt{\frac{3}{2}}}{1 + \kappa\sqrt{\frac{3}{2}}}$$

must be greater than twice the total process sensitivity in the normalized inductance $\frac{\mathrm{d}\beta}{\beta} = \frac{\mathrm{d}J_C}{J_C} + \frac{\mathrm{d}L_\square}{L_\square}$ in order for a π-device implemented in the given technology to never leave the requirements from 5.49 and 5.50 under a process variation. The maximum process sensitivities in the implementation technology then limit the coupling coefficient. Taking a value for the critical current variation of 30% and a value for the inductance variation of 5%, which is a large variation in practice, then the coupling factor must be less than $\sqrt{\frac{2}{3}} \cdot \frac{1-0.35}{1+0.35} \approx 0.4$. The higher the process variations are, the lower the coupling factor should be.

It should be mentioned that π-device circuits can also be built with a coupling factor higher than these estimations. The limits given in 5.49 and 5.50 apply only when the circuits are designed for an optimal figure of merit. One can also make the π-devices follow other "good design" practices, resulting in a different set of technological limits. What the limits 5.49, 5.50 and the plot in Figure 5.20 actually indicate is that when the technology to build π-devices offers higher coupling factors, the best choice for a circuit designer is to optimize performance features other than the maximum gain. For example one can look at the signal amplitudes or energy dissipation.

In any case, the most important limit is the hysteretic condition which, if violated, results in circuits where self-sustained transitions will exist. Such devices have a mode of operation that is little, if at all, different from existing superconducting digital architectures (ex. RSFQ). Moreover, the analog gain feature will be lost and thus a great advantage of static signal processing will not be available anymore. Therefore, the development of any circuit design practice where modulated π-loops are used should first take care that the hysteretic condition is satisfied.

5.2.4 Circuit design example

Armed with the knowledge of the previous few sections, a circuit designer can now make informed choices about the best circuit parameters given a design task and a few technological constraints. Lets illustrate this design flow on a practical example.

A π-shift technology is given where the coupling factor is $\kappa = 0.4$ and the parasitic inductance at the input of any cell is about 1/4 of the primary inductance of the preceding stage. It is also given that the transformer of all π-devices can be made of a just a single turn. This indirectly implies that the ratio $\frac{L_s}{L_{\mathrm{in}}}$ of all devices must be kept close to unity. Further, the lowest I_C of a junction that can be reliably manufactured with the technology is $\sim 10\mu$A.

Given the above constraints, design a two-stage circuit with the following requirements:

- the second stage comprises of $N = 2$ identical devices (in series)

- each output of the devices in the second stage is loaded with a linear inductor of inductance L_{out}
- all devices should be optimized with respect to their figure of merit
- the first stage must have a positive incremental inductance

Suggest a couple of values for the key circuit parameters and calculate the total maximum gain.

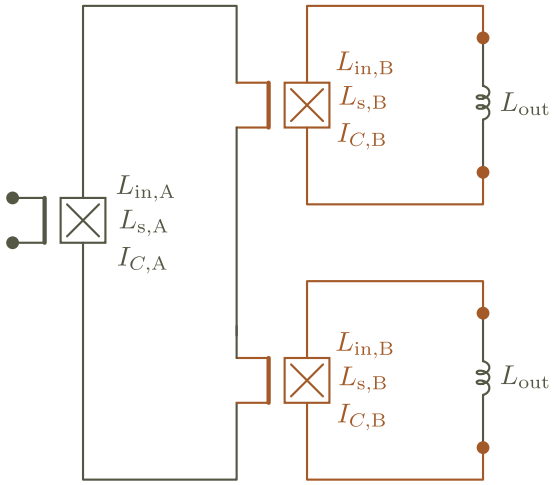

Figure 5.21. A 2-stage circuit of fanout $N=2$ loaded with a linear inductance L_{out}

The circuits parameters of the first stage are marked with $I_{C,A}$, $L_{\text{in},A}$ and $L_{s,A}$ while the circuit parameters of the second stage will be given through the ratios $a=\frac{L_{\text{in},B}}{L_{\text{in},A}}=\frac{L_{s,B}}{L_{s,A}}$ and $a_C=\frac{I_{C,B}}{I_{C,A}}$. It is hence taken into account that the devices in the second stage are geometrically scaled versions of the driving device so that the physical design of the structures would be simpler. Note that such scaling fixes the relationships between the normalized inductances as

$$\begin{aligned}\beta_{\text{in},B}&=a\cdot a_C\cdot\beta_{\text{in},A}\\ \beta_{L,B}&=a\cdot a_C\cdot\beta_{L,A}\end{aligned}\tag{5.51}$$

The relative loading factor for the first stage is

$$p_A=\frac{N\cdot L_{\text{in0},B}}{L_{\text{in},A}}=\frac{N\cdot B(\beta_{L,B},\kappa)\cdot L_{\text{in},B}}{L_{\text{in},A}}=N\cdot a\cdot B(a\cdot a_C\cdot\beta_{L,A},\kappa)$$

while the parasitic inductance factor is

$$q_A=\frac{N\cdot L_{\text{par},A}}{N\cdot L_{\text{in0},B}}=\frac{N\cdot\frac{1}{4}L_{\text{in},A}}{N\cdot L_{\text{in0},B}}=\frac{N}{4\cdot N\cdot a\cdot B(a_C\cdot a\cdot\beta_{L,A},\kappa)}=\frac{N}{4\,p_A}$$

For the second stage we shall assume that the parasitic inductance in series with each of the load inductors L_{out} is zero, $q_B = 0$. On the other hand, the relative loading factor p_B is

$$p_B = \frac{L_{\text{out}}}{L_{\text{in},B}} = \frac{1}{a} \cdot \frac{L_{\text{out}}}{L_{\text{in},A}}$$

Further, both stages must be optimized with respect to the figure of merit

$$\begin{aligned} p_A \cdot (1+q_A)\beta_{\text{in},A} &= \frac{4-3\,(1-\kappa^2)\,\beta_{L,A}^2}{4\,(1-\kappa^2)\,\beta_{L,A}} \\ p_B \cdot (1+q_B)\beta_{\text{in},B} &= \frac{4-3\,(1-\kappa^2)\,\beta_{L,B}^2}{4\,(1-\kappa^2)\,\beta_{L,B}} \end{aligned} \tag{5.52}$$

The most strict technological limitation in this case is the requirement that the primary and secondary inductances of both types of π-devices must be equal $L_{\text{in},A} \approx L_{s,A}$ and $L_{\text{in},B} \approx L_{s,B}$. This means that the normalized inductances are equal as well: $\beta_{L,A} = \beta_{\text{in},A}$ and $\beta_{L,B} = \beta_{\text{in},B}$. Introducing the above restrictions in the system 5.52, one obtains

$$\begin{aligned} N \cdot \left(a \cdot B(a \cdot a_C \cdot \beta_{L,A}, \kappa) + \frac{1}{4} \right) &= \frac{4-3\,(1-\kappa^2)\,\beta_{L,A}^2}{4\,(1-\kappa^2)\,\beta_{L,A}^2} \\ \beta_{\text{out}} &= \frac{4-3\,(1-\kappa^2)\,\beta_{L,B}^2}{4\,(1-\kappa^2)\,\beta_{L,B}} \end{aligned} \tag{5.53}$$

where $\beta_{\text{out}} = \frac{2\pi\, L_{\text{out}}\, I_{C,B}}{\Phi_0}$. Since κ and N are known, the first relation of 5.53 is a function of only a, a_C and $\beta_{L,A}$: knowing any two of them, the third parameter can be found. Then, all circuit parameters can be calculated from the remaining relations.

The normalized loop inductances $\beta_{L,A}$ and $\beta_{L,B}$ must have a value that falls within the range of the plot from Figure 5.20. For $\kappa = 0.4$, the range for both is

$$0.62 < \beta_{L,A\,B} < 1.26$$

Given a $\beta_{L,A}$, the above simultaneously limits $a \cdot a_C = \frac{\beta_{L,B}}{\beta_{L,A}}$ to an available range of

$$\frac{0.62}{\beta_{L,A}} < a \cdot a_C < \frac{1.26}{\beta_{L,A}} \tag{5.54}$$

since also $\beta_{L,B}$ falls within the same range.

The first equation from the system 5.53 can be re-written as

$$a = \frac{\left(\frac{4}{(1-\kappa^2)\cdot\beta_{L,A}^2} - 3 - N \right) \cdot \left(1 - \frac{2\,\kappa^2}{\beta_{L,A}^2 \cdot (a \cdot a_C)^2 \cdot (1-\kappa^2)} \right)}{4\,N\,(1-\kappa^2)} \tag{5.55}$$

after replacing the expression for the coefficient $B(\beta_{L,A}, \kappa)$ given in relation 5.48 from the previous section. Requiring that $a > 0$ in the expression 5.55, another restriction is obtained: $\beta_{L,A} < 0.98$ for $N = 2$ and $\kappa = 0.4$ and for any value of $a \cdot a_C$ within its available range 5.54.

Lets plot the value of a, as calculated from 5.55, as a function of $a \cdot a_C$ for a few values of $0.62 < \beta_{L,A} < 0.98$. The available range of $a \cdot a_C$ from 5.54 should then be taken into account for each value of $\beta_{L,A}$. The result is given in Figure 5.22.

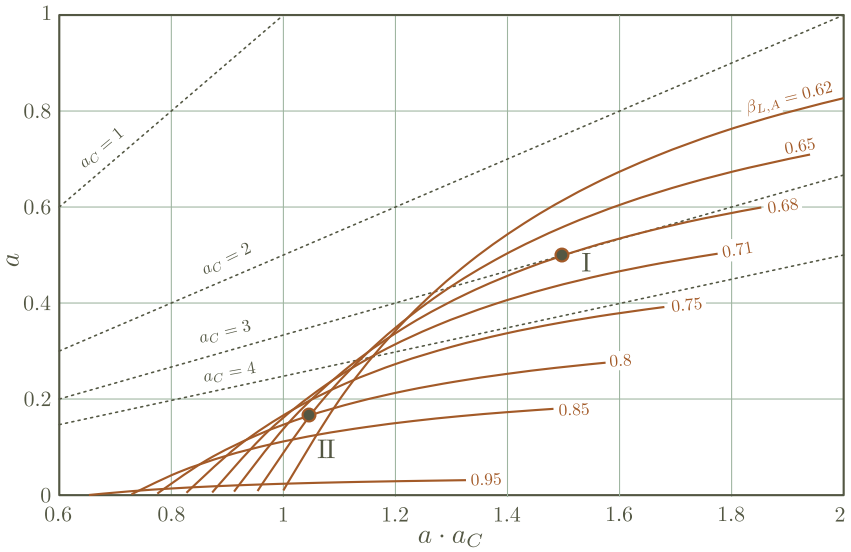

Figure 5.22. A graphical solution to the equation 5.55. The values of the parameters at the marked spot I are $\beta_{L,A} = 0.68$, $a = \frac{1}{2}$ and $a_C = 3$ while at the spot II $a \approx \frac{1}{5.5}$, $a_C \approx 5.8$ and $\beta_{L,A}$ in the vicinity of 0.8.

The plot allows one to make a good decision about the parameter choice. So, for example, values of a far away from unity require a high degree of geometrical scaling between the physical structure of the devices. In practice, scaling beyond a ratio of three is difficult to achieve. The scaling of the critical currents is less challenging and in practice ratios of up to five times are achievable.

From the plot, a good choice of parameters with low geometric scaling is then $a = \frac{1}{2}$, $a_C = 3$ and $\beta_{L,A} = 0.68$, the spot marked with "I". One can also set $\beta_{L,A}$ in the area of the highest line density in the plot so that the process variations of $\beta_{L,A}$ do not require drastically different a and $a \cdot a_C$. This choice however necessitates higher geometric scaling: for example the spot marked with "II" in the plot where $a \approx 0.18(\frac{1}{5.5})$, $a_C \approx 5.8$ and $\beta_{L,A}$ is in the vicinity of 0.8.

Once a choice is made for $\beta_{L,A}$, a and a_C, all other parameters can be calculated. Since in any case the critical current ratio $a_C > 1$, it is also chosen that the I_C of the junctions in the first stage will be the lowest possible, $I_{C,A} = 10\mu\text{A}$. In Table 5.1, the values of all circuit elements are given for the two design points from the plot in Figure 5.22.

Design point	$L_{s,A} = L_{\text{in},A}$	$L_{s,B} = L_{\text{in},B}$	L_{out}	$I_{C,A}$	$I_{C,B}$	$G_{\text{tot}} = \lvert G_A \cdot G_B \rvert$
I	22.5pH	11.2pH	4.4pH	10μA	30μA	≈0.17
II	26.5pH	4.8pH	3.3pH	10μA	58μA	≈0.227

Table 5.1. Values of the circuit elements for an optimal 2-stage design with $N = 2$.

In Figure 5.23, the results from a circuit simulation using the element values of the design point "I" are given.

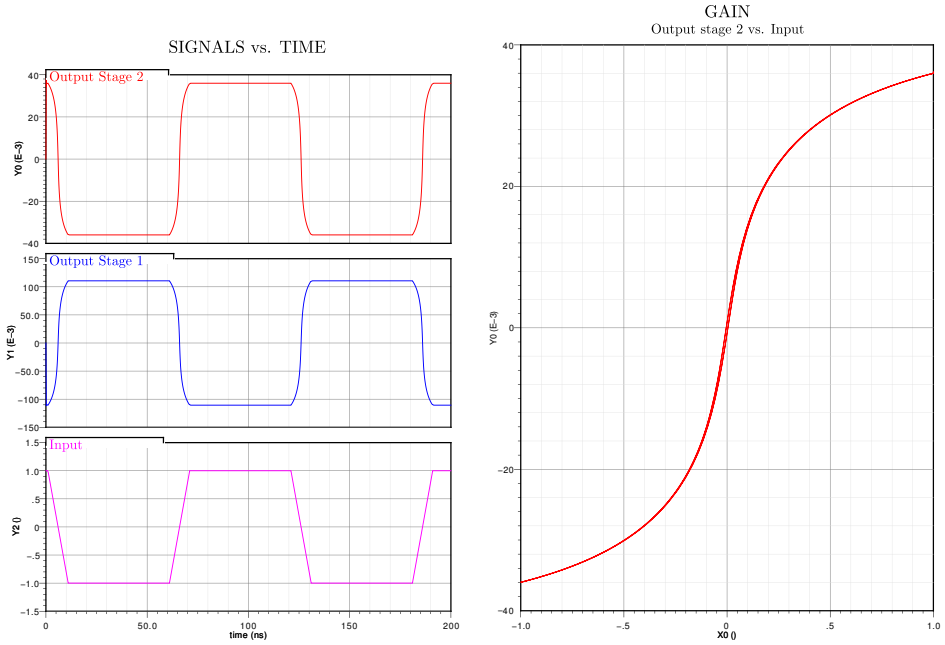

Figure 5.23. Simulation results of the circuit from Figure 5.21 with the element values of the design point "I". The flux angles are given in units of π.

Note how the total gain is quite small for both of the chosen designs. This stems from the technological limitation $\beta_L \approx \beta_{\text{in}}$ that was used. In general, the

maximum gain of a π-device

$$G_{\max} = \sqrt{\frac{L_s}{L_{\text{in}}}} \cdot \frac{4\,\kappa\,\beta_{\text{out0}}}{4-(1-\kappa^2)\,\beta_L\,(\beta_L+4\,\beta_{\text{out0}})} \cdot \frac{1}{1+q}$$

when optimized with respect to the figure of merit

$$\beta_{\text{out0}} = p(1+q)\cdot\beta_{\text{in}} = \frac{4-3(1-\kappa^2)\,\beta_L^2}{4\,(1-\kappa^2)\,\beta_L}$$

calculates to

$$G_{\max} = \frac{1}{1+q} \cdot \sqrt{\frac{L_s}{L_{\text{in}}}} \cdot \frac{1}{2}\,\kappa \cdot \frac{4-3\,(1-\kappa^2)\beta_L^2}{(1-\kappa^2)^2\cdot\beta_L^3}$$

and is hence directly proportional to the geometric transformer ratio $r_g = \sqrt{\frac{L_s}{L_{\text{in}}}}$. In Figure 5.24, the maximum gain of an optimized π-device normalized with r_g and $\frac{1}{1+q}$ is plotted as a function of β_L for a few choices of the coupling coefficient κ. Indeed, the range of β_L for which the incremental input inductance is positive, relation 5.50, is taken into account as well.

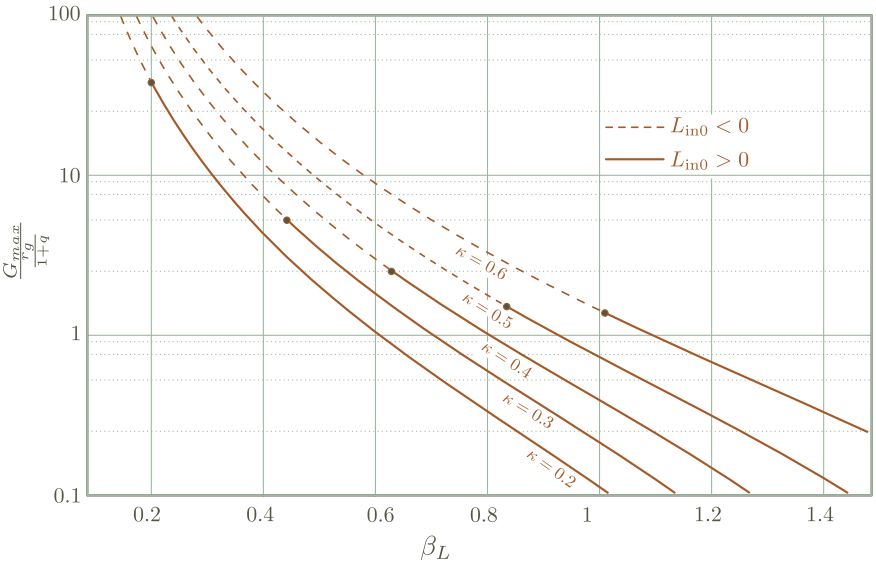

Figure 5.24. The maximum gain of an optimized π-device, normalized with the geometric transformer ratio $r_g = \sqrt{\frac{L_s}{L_{\text{in}}}}$ and the parasitic inductance factor $1+q$, as a function of the normalized loop inductance β_L for a few values of the coupling coefficient κ. The limit for a positive incremental input inductance, expression 5.50, is also indicated on the plot. Note that when there are N devices in series at the output, the gain *per device* is N times lower than the above.

There are a few observations that can be made from the plot. First, although the gain strongly increases with the coupling coefficient at a constant β_L, the incremental input inductance quickly becomes negative. This will lead to a hysteretic transfer characteristic for the previous stage if also optimized, as already mentioned. Secondly, at a constant κ, a lower β_L results in a higher gain, this proportionality almost logarithmic in nature.

One can also observe that if a π-device has a transformer with very strong coupling, i.e. >0.6, achieving a gain higher than unity and simultaneously keeping $L_{\mathrm{in}0} > 0$ will be impossible. It is therefore very important not to use a high κ as a means to achieve high signal gains but rather use high geometric transformer ratios and low parasitics at the output. As a matter of fact, the common goal of thin-film transformer design where κ is sought to be maximised does not apply for the static π-shift circuits of optimal figure of merit. Instead of high coupling coefficients, one should focus on obtaining high ratios between the secondary and primary coils $\frac{L_s}{L_{\mathrm{in}}}$ with the challenge of low absolute secondary (the π-loop) inductance L_s. This design goal allows the circuits to have a higher signal gain when optimized with respect to process variations.

In the example analysed in this section, the restriction $L_s \approx L_{\mathrm{in}}$ is therefore very limiting in the maximum gain of the whole circuit. This is especially true for the second stage that has a generally higher β_L and thus lower gain: one typically has no room to choose $a \cdot a_C = \frac{\beta_{L,B}}{\beta_{L,A}} < 1$ in the plot of Figure 5.22. Relaxing the limitation of the transformer $\frac{L_s}{L_{\mathrm{in}}} = r_g^2 \approx 1$ to higher values will not only give higher gain due to the proportionality $G_{\max} \sim r_g$, but also broaden the lower limits for the choice of scaling $a \cdot a_C$ between the stages (the lines in Figure 5.22 will be "stretched" higher when $\frac{L_s}{L_{\mathrm{in}}} > 1$). The normalized inductance of the second stage can then be chosen to be lower and the total gain increased.

Another way to achieve a total gain greater than unity is to add one more device before the first stage with a high gain to compensate the rest. It is actually preferable to have this pre-amplifier stage optimized with respect to the process variations of the gain rather than the subsequent 'fanout' structure. This may relax the choice for the circuit parameters and the element values when implemented.

5.2.5 Junction asymmetry

The analysis of the π-devices in the preceding sections was performed by assuming that the arms of the π-loop were symmetric. i.e. that the loop inductance was equally split in the left and right arm, as well as that the two junctions have the same critical current.

In this section the effects of loop asymmetry will be considered. Typically, a greater relative variation is expected to be present between the I_C of the two junctions than between the inductance of the two arms. This is a consequence of the high sensitivity of the junction's I_C to microscopic irregularities in their barriers as opposed to the inductances of the segments that are, in fact, space-averaged functions of the circuit geometry. Therefore, assuming that the typical inductance asymmetry is too small to exert substantial influence on the circuit properties, only the asymmetry in the critical currents of the Josephson junctions will be investigated.

The circuit schematic of a π-device with junction asymmetry is given in Figure 5.25, together with its small-signal variant.

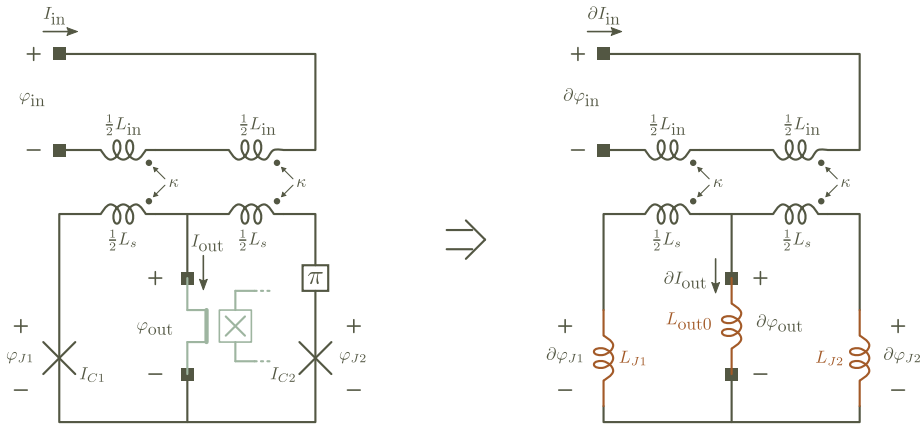

Figure 5.25. The circuit schematic of a π-device with junction asymmetry and the corresponding small signal network.

The difference with the circuits from the previous sections lies only in the inequality of the junction critical currents:

$$I_{C1} = (1+\alpha)\, I_C$$
$$I_{C2} = (1-\alpha)\, I_C$$

while all the rest of the parameters are defined in the same way. The parameter $-1 < \alpha < 1$ is the asymmetry coefficient of the Josephson junctions for the π-device. Note that the normalized inductances use the average current $I_C = \frac{I_{C1}+I_{C2}}{2}$ in

their definition. Also, the Josephson inductances of the two junctions are now

$$L_{J1}(\varphi_1) = \frac{1}{1+\alpha} \cdot \frac{\Phi_0}{2\pi\, I_C \cos(\varphi_1)}$$

$$L_{J2}(\varphi_2) = \frac{1}{1-\alpha} \cdot \frac{\Phi_0}{2\pi\, I_C \cos(\varphi_2)}$$

The circuit equations will be modified to also include the asymmetry coefficient α:

$$\begin{cases} \varphi_{\text{in}} = 2t \cdot \dfrac{\beta_{\text{in}}}{\beta_m} - \dfrac{\beta_{\text{in}}\beta_L - \beta_m^2}{\beta_m} \cdot (\cos(t) \cdot \sin(r) + \alpha \cdot \sin(t) \cdot \cos(r)) \\ \dfrac{4\beta_{\text{out0}}}{4\,\beta_{\text{out0}} + \beta_L} \cdot r = 2\beta_{\text{out0}} \cdot (\sin(t) \cdot \cos(r) + \alpha \cdot \cos(t) \cdot \sin(r)) \end{cases} \tag{5.56}$$

where the help variables are defined as

$$t = \frac{\varphi_2 \pm \pi - \varphi_1}{2} \quad , \quad r = \frac{\varphi_2 \pm \pi + \varphi_1}{2} = \varphi_{\text{out}}\, \frac{4\beta_{\text{out0}} + \beta_L}{4\beta_{\text{out0}}}$$

and φ_2, φ_1 are the flux angles across the junctions, as drawn in Figure 5.25. The network equations for the small-signal schematic will remain the same as before, taking into account that L_{J1} and L_{J2} are defined as above.

The signal gain and the incremental input inductance should be evaluated at the origin of the transfer characteristic $\varphi_{\text{out}} = \varphi_{\text{in}} = 0$. From the system 5.56, it is seen that when both the output and input flux angles are zero, it also follows that $t = r = 0$. The values of the junction flux angles are then just like before: $\varphi_1 = 0$ and $\varphi_2 = \mp\pi$. The Josephson inductances on the other hand

$$L_{J1}(0) = \frac{1}{1+\alpha} \cdot \frac{\Phi_0}{2\pi\, I_C} = \frac{1}{1+\alpha} \cdot L_J$$

$$L_{J2}(\mp\pi) = -\frac{1}{1-\alpha} \cdot \frac{\Phi_0}{2\pi\, I_C} = -\frac{1}{1-\alpha} \cdot L_J$$

Using the above values for the Josephson inductances and the small-signal circuit equations, the maximum gain can be found

$$G_{\max} = \sqrt{\frac{L_s}{L_{\text{in}}}} \cdot \frac{4\,\kappa\,\beta_{\text{out0}}}{4 - \beta_L(\beta_L + 4\beta_{\text{out0}})(1-\kappa^2)\,(1-\alpha^2) + 2\,\alpha(\beta_L(2-\kappa^2) + 4\beta_{\text{out0}})}$$

while the incremental input inductance will be

$$L_{\text{in}0} = L_{\text{in}} \cdot \frac{4 - \beta_L(\beta_L + 4\beta_{\text{out}0})(1-\kappa^2)\,(1-\alpha^2) + 2\,\alpha(\beta_L(2-\kappa^2) + 4\beta_{\text{out}0})}{4 - \beta_L(\beta_L + 4\beta_{\text{out}0})\,(1-\alpha^2) + 2\,\alpha(2\beta_L + 4\beta_{\text{out}0})}$$

Note that, for each π-device, α is not known beforehand: it is a random variable for which only its maximum absolute value $|\alpha| < \alpha_{\max}$ is given as a technological parameter. Hence, a circuit designer can not optimize the π-device for a given α - it is always different. It is therefore practical to optimize the device for $\alpha = 0$ and then find the limits of the circuit parameters such that they do not violate the good design practices from the previous sections by taking into account that the junction asymmetry parameter may have values $-\alpha_{\max} < \alpha < \alpha_{\max}$.

Replacing the $\beta_L, \beta_{\text{out}0}$ relation for an optimized π-device found in the previous sections,

$$p(1+q) \cdot \beta_{\text{in}} = \beta_{\text{out}0} = \frac{4 - 3(1-\kappa^2)\,\beta_L^2}{4\,(1-\kappa^2)\,\beta_L} \tag{5.57}$$

in the expressions for the gain and incremental input inductance above, it is found

$$G_{\max} = \frac{\kappa}{2}\sqrt{\frac{L_{\text{in}}}{L_s}} \cdot \frac{4 - 3(1-\kappa^2)\beta_L}{(1-\kappa^2)\,\beta_L\,(2\alpha^2 + \beta_L^2\,(1-\kappa^2)(1-\alpha^2) - \alpha(1+\kappa^2)\,\beta_L) + 4\alpha}$$

for the maximum gain and

$$L_{\text{in}0} = L_{\text{in}} \cdot \frac{(1-\kappa^2)^2\,(1-\alpha^2)\beta_L^2 + \alpha\,(1-\kappa^2)\,(2\alpha - (1+\kappa^2)\beta_L) + \frac{4\alpha}{\beta_L}}{(1-\kappa^2)\,(1-\alpha^2)\beta_L^2 - 2\kappa^2 + \alpha\,(2\alpha - (1-\kappa^2)\beta_L) + \frac{4\alpha}{\beta_L}}$$

for the incremental input inductance. Finding the limits of the parameters such that they satisfy the hysteretic condition $0 < G_{\max} < \infty$ and at the same time yield a positive incremental input inductance $L_{\text{in}0} > 0$ is cumbersome to be done analytically. It can however be proved that when α, κ and β_L have values that result in a positive $L_{\text{in}0}$, the hysteretic condition is always satisfied as well. Hence, only the limit of $L_{\text{in}0} > 0$ will be used to bound the parameter range. The other boundary will be the same as when $\alpha = 0$, namely that the optimal relation 5.57 yields physically realizable inductances, i.e. $4 - 3(1-\kappa^2)\,\beta_L^2 > 0$.

In Figure 5.26, both boundaries are plotted on the (β_L, κ) space for a few values of the asymmetry coefficient α (compare to Figure 5.20).

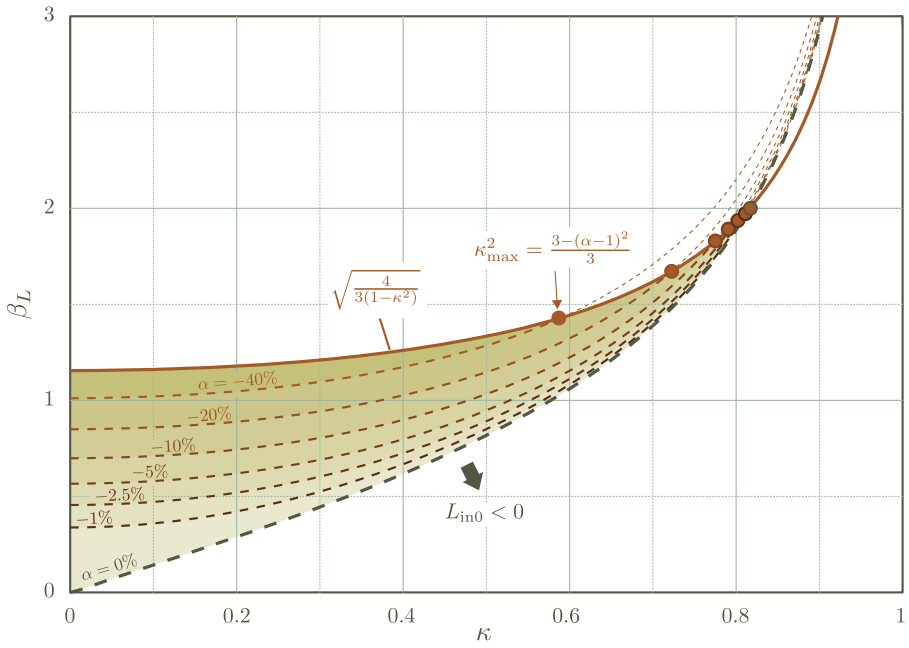

Figure 5.26. The available parameter range for an optimized π-device with junction asymmetry α. The gradual shading illustrates the contraction of the available range as $|\alpha|$ increases. When $\kappa^2 > \frac{3-(\alpha-1)^2}{3}$, it is not possible to physically realize an optimal π-device with a positive incremental inductance.

It can be shown that when $\alpha > 0$, the parameter range does not contract i.e. the limits from the previous sections (when $\alpha = 0$) apply in that case. Hence, in the plot of Figure 5.26, only $\alpha < 0$ is considered as that is the only case when the parameter range is adversely affected. Note that it should not be surprising that the performance of the circuit differs for $\alpha > 0$ and $\alpha < 0$. The phenomenon is simply contributing to the already present asymmetry in a π-loop. In other words, there is a distinction between a "left" and a "right" junction in the π-loop determined by the position of the π-shift element in one of the loop's arms. Plots of the transfer characteristic for asymmetry factors of opposite sign are given in Chapter 6, for example Figure 6.11.

It is seen that for large asymmetry, the parameter range becomes very small. At $|\alpha| > 0.4$, there is basically no room left in β_L, κ space to implement an optimized π-device.

The influence of the junction asymmetry on the maximum gain of an optimized π-device is illustrated in Figure 5.27.

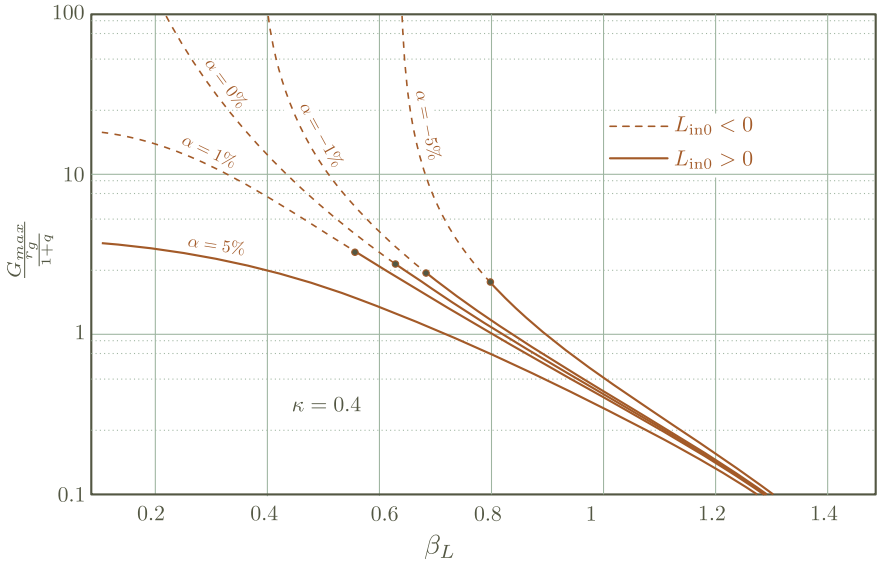

Figure 5.27. The gain of an optimal device as a function of the normalized loop inductance for a coupling coefficient $k = 0.4$ and a few values of the asymmetry parameter α. The points where the incremental inductance changes sign are also given.

Nevertheless, junction asymmetry in a π-device does not result in an asymmetric transfer characteristic. Lets look at the value of the output signal for equal but opposite values of the input signal. This is achieved by inverting the sign of φ_{in} in the system of network equations 5.56 and finding whether the output, proportional to the help variable r, also changes sign. A quick inspection of the equations indeed confirms that they are invariable under a sign change of r and φ_{in} (also t must change sign). Hence, even when there is asymmetry in the junctions, the transfer characteristic remains odd-symmetric around the origin.

5.3 Discussion and conclusions

In this Section, the features of the inductively modulated π-devices are briefly summarized and a static logic cell based on majority logic is proposed, together with circuit simulation results of the same. Comments on the practicality of the static π-shift circuits are also given.

It was shown in the first Section of this Chapter that when an external magnetic flux Φ_{ext} is applied in a π-loop, and an inductor L_{out} is connected across the terminals of said loop, Figure 5.3, there exists a range of circuit parameters for which a signal gain $\frac{\partial \Phi_{\text{out}}}{\partial \Phi_{\text{ext}}}$ larger than unity is observed. The transfer characteristic $\Phi_{\text{out}}(\Phi_{\text{ext}})$ strongly resembles the one of a conventional amplification device, with the exception of the $\frac{\Phi_0}{2}$ periodicity in the input signal: the output signal saturates at large inputs and the characteristic passes through the origin where the gain is maximal. In the plot of Figure 5.6, reproduced below, the transfer characteristics are given for a few choices of the normalized loop and output inductances, β_L and β_{load} respectively, of the π-loop.

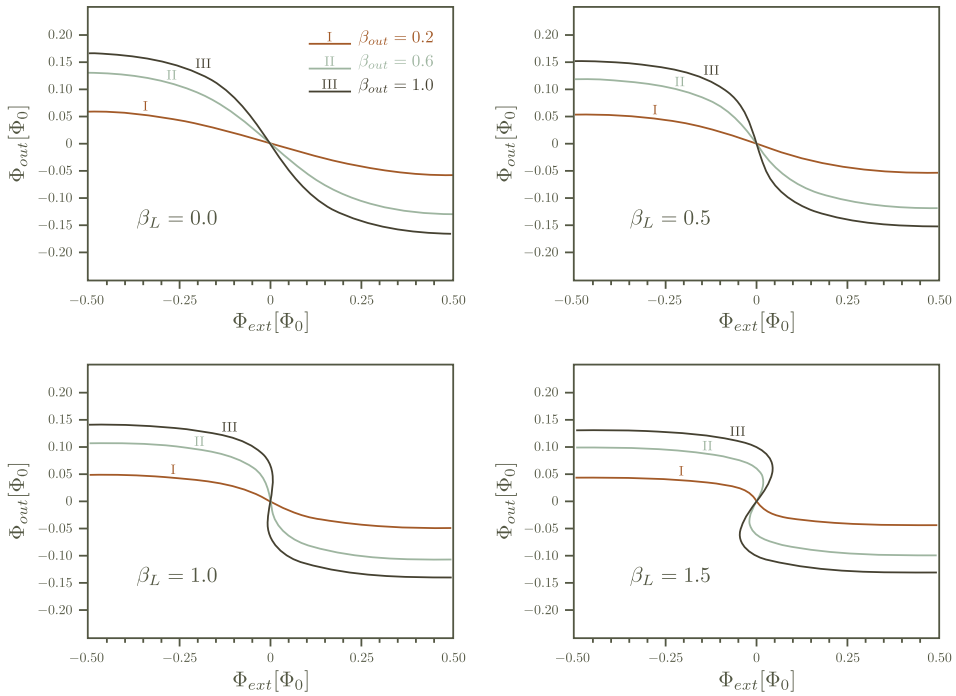

Figure 5.28. Transfer characteristic $\Phi_{\text{out}}(\Phi_{\text{ext}})$ of a flux-modulated π-loop with an inductor L_{out} connected across the loop terminals. The parameters β_L and β_{out} are the normalized loop and normalized output inductances.

Further, an analysis of the potential landscape of the circuit shows that when the transfer characteristic does not exhibit a hysteresis, the circuit always remains in a potential minimum during state evolution, see Figure 5.8. Hence, in the modulated π-loop without hysteresis, the trajectory that the circuit takes in potential

space is one of movement in the *position* of a single stable state and not of a transition *between* multiple stable states through a potential barrier. Secondly, while in the modulated π-loop the state changes at the same speed as the input signal, the state transition in other types of digital circuits, for example RSFQ, evolves according to intrinsic timing constants once the potential barrier is crossed.

A consequence of the above feature is that there is little dissipation in the static π-loop circuit during state transitions since the $\frac{1}{2}\cdot\frac{V_J^2}{R_N}$ developed at the resistances of the Josephson junctions is typically small. Namely, from $V_J = \frac{\Phi_0}{2\pi}\cdot\frac{\partial\varphi_J}{\partial t}$ where φ_J is the flux angle across a junction, when the state of the circuit changes slowly, $\frac{\partial\varphi_J}{\partial t}\approx 0$, it follows that there will be (ideally) zero dissipation. If it is assumed that the signals in the static circuit are driven at the rate of $f=\frac{1}{T}$ between $+\pi$ and $-\pi$ for every state change (every processed bit), $\frac{\partial\varphi_J}{\partial t}\approx 2\pi f$, the energy per bit will be

$$\Delta E_J = \int_{-T/2}^{T/2}\frac{1}{2}\cdot\frac{V_J^2}{R_N}\cdot \mathrm{d}t \approx \frac{1}{2\,R_N}\cdot\Phi_0^2\cdot f^2\cdot\left(\frac{T}{2}-\frac{-T}{2}\right)=\frac{\Phi_0^2}{2R_N}\cdot f$$

Using $f = 30\mathrm{GHz}$ and $R_N = 2\Omega$, the dissipated energy per bit in a static circuit will be in the order of 10^{-20}J, ten times less than the dissipated energy per bit in a typical RSFQ circuit $\Delta E_J \approx \Phi_0 \cdot I_C \approx 10^{-19}$J. At $f \approx 0$, the dissipated energy per bit in a static π-device will be approximately zero. Moreover, as already shown before, the maximum amplitudes in the static circuits are far less than 2π: typically, the signals swing just a few hundred mπ in each direction. This reduces the dissipated energy by a factor of ∼10.

Note that the normal junction resistance R_N in the static circuits is not limited by the requirement of non-hysteretic junctions, as is the case in RSFQ circuits. As a matter of fact, the static circuits can work without resistive shunts for the junctions: R_N is then the "native" barrier resistance of the junction that can be in the 100s of Ω's, further reducing the dissipated energy per bit by a couple of orders of magnitude.

The parameter range for which the transfer characteristic of a flux-modulated loop is non-hysteretic is given by the condition

$$\beta_{\mathrm{out}} < \frac{4-\beta_L^2}{4\,\beta_L}$$

When the normalized inductance of the π-loop β_L and of the output inductor β_{out} satisfy this condition, the process of state change takes place in the near-adiabatic manner that was briefly described above. Hence, the hysteretic limit can be said to be the boundary of the 'near-adiabatic range' for the flux-modulated π-loop.

A second benefit of the flux-modulated π-loop lies in the roughly proportional gain and output load: when the output inductance is increased, for instance by adding parasitic interconnect segments, the gain also increases. This partly compensates for the signal loss on the interconnect. From Figure 5.13, where the saturation amplitude at the remote load was calculated as a function of the relative parasitic inductance q at the output, it follows that for some choices of the circuit parameters the output amplitude is almost insensitive to q. Such a property is very convenient in practice if, for example, a signal needs to be transported on a long interconnect or if the interconnect sub-circuit is not well defined beforehand.

In order to build circuits of interconnected π-loops, it is necessary for them to have input and output terminals that are compatible, i.e. the device should posses 'back-to-front connectivity'. A flux-modulated π-loop does not satisfy this requirement: the input signal Φ_{ext} originates from a magnetic field created by a remote current source and is hence an "ideal" flux drive, while the output signal Φ_{out} does not have a property of an ideal flux source (it depends on the load inductance L_{out}). To create terminal compatibility, a thin-film segment inductively coupled to the π-loop was added, Figure 5.14, in effect creating a thin-film transformer structure between the π-loop and the segment. Declaring the flux angle across the free transformer terminals as the input signal φ_{in} and the flux angle across the output terminals of the π-loop as the output signal φ_{out}, the new device is seen to posses the input/output signal compatibility necessary for building larger circuits. The output terminals of the preceding device can be connected across the input terminals of the following device, allowing the creation of cascaded connections and the duplication of signals (output fanout). These two features are essential for creating practical digital circuits.

This new inductively-coupled device also has a transfer curve $\varphi_{\text{out}}(\varphi_{\text{in}})$ that exhibits signal gain, saturation and passes through the origin $(\varphi_{\text{in}}, \varphi_{\text{out}}) = (0, 0)$. Just as was the case for the flux-modulated π-loop, the state changes occur without self-sustained transitions when the transfer characteristic is not hysteretic. The condition limiting this 'near-adiabatic' regime for the inductively-coupled π-loop is given by a similar expression

$$\beta_{\text{out}} < \frac{\frac{4}{1-\kappa^2} - \beta_L^2}{4\beta_L} \tag{5.58}$$

where $0 < \kappa < 1$ is the coupling coefficient of the thin-film transformer. Marking the inductance of the transformer secondary (i.e. the π-loop inductance) with L_s and of the transformer primary with L_{in}, the maximum gain $\frac{\partial \varphi_{\text{out}}}{\partial \varphi_{\text{in}}}$ is scaled by a factor $\kappa \cdot \sqrt{\frac{\beta_L}{\beta_{\text{in}}}} = \kappa \cdot \sqrt{\frac{L_s}{L_{\text{in}}}}$ in comparison to the signal gain of flux-modulated π-loop.

Note that, all things equal, the hysteretic limit above is less constrictive than the same condition for a flux-modulated loop. Nevertheless, the maximum gain of the inductively-coupled π-loop is typically lower since, in practice, digital devices are limited in size: small thin-film transformers usually have a coupling factor $\kappa \leqslant 0.5$ and inductive geometric ratios close to unity $\frac{L_s}{L_{\text{in}}} \approx 1$.

The property of proportionality between the signal gain and the output load inductance, partially compensating for signal loss on the inter-device connections, is also present in this case. It allows a circuit of cascaded devices to be realized without unrealistic constraints on the circuit elements.

The number of parameters (4) in the inductively-modulated π-loop is too great for a clear performance analysis, hence making it difficult to find practical circuit design guidelines. This task is even more cumbersome when π-devices are connected in larger circuits. It is therefore best to first fix the relationship between some of the parameters in a way that, generally, yields the best performance per device. Then, global rules can be derived that, when followed during the design of bigger circuits, result in a near-adiabatic operation.

A figure of merit of each device can be defined as

$$\text{FM}_G = \left| \frac{G_{\max}}{G_{\max,\text{sens}}} \right|$$

where $G_{\max}$ is the maximum signal gain while $G_{\max,\text{sens}}$ is the sensitivity of the maximum gain to process variations in the nominal values of the circuit elements. Looking for a maximum in the figure of merit will thus result in the highest gain and the lowest gain sensitivity. The maximum is found when the normalized inductance parameters follow the optimal relationship

$$p\,(1+q)\,\beta_{\text{in}} = \beta_{\text{out}} = \frac{4 - 3\,(1-\kappa^2)\,\beta_L^2}{(1-\kappa^2)\,\beta_L} \tag{5.59}$$

where $p = \frac{L_{\text{load}}}{L_{\text{in}}}$ is the relative loading factor and $q = \frac{L_{\text{par}}}{L_{\text{load}}}$ is the parasitic inductance factor of the π-device. The load inductance L_{load} is the total inductance presented at the output of the π-device, except for the interconnect and various other parasitic inductances L_{par}, while L_{in} is the inductance of the transformer primary in the π-device. Using the definitions of p and q, the total output load of the π-device is then $L_{\text{out}} = L_{\text{par}} + L_{\text{load}} = p(1+q)\,L_{\text{in}}$.

Note that $4 > 3(1-\kappa^2)\,\beta_L^2$ in order for the optimal relationship to be physically realizable (positive L_{in}). This sets a maximum $\frac{2}{\sqrt{3(1-\kappa^2)}}$ for the normalized loop inductance of an optimal π-device. Another important observation is that when the parameters of a π-device satisfy the optimal relation 5.59, the hysteretic condition 5.58 is automatically satisfied.

In a multi-stage circuit, the inductance L_{load} has a value that is determined by the input inductances of the subsequent stages and by their configuration: in parallel or in series. It was shown that, all things equal, a series combination of N subsequent stages yields both a higher value for the figure of merit FM_G and a higher gain than a parallel combination. Also, the parallel combination of stages creates all-inductive loops where flux trapping may occur, disturbing the correct operation mode of the circuit. Consequently, it is a good design practice to connect the subsequent stages in series rather than in parallel.

The above analysis was performed by assuming that the output load of a π-device in a multi-stage circuit has a purely inductive characteristic. However, the input inductances of the devices in the load do not posses the properties of a linear circuit element. This is due to the fact that the (φ, I) relationship of the Josephson junctions in the π-loop is not linear, reflecting as such through the transformer at the input terminals of the π-device. In order to find L_{load}, and hence the relative loading and parasitic factors p and q in a multi-stage circuit, one must then take into account the nonlinear input inductances of the subsequent stages.

Using the *incremental* inductance between the input terminals $L_{\text{in}0} = \frac{\Phi_0}{2\pi} \cdot \frac{\partial \varphi_{\text{in}}}{\partial i_{\text{in}}}$ evaluated at the origin of the transfer characteristic $\varphi_{\text{in}} = \varphi_{\text{out}} = 0$ as the input inductance of each subsequent stage, the incremental load inductance $L_{\text{load}0}$ can be found. Defining p and q with $L_{\text{load}0}$, the analysis stays the same as if the elements of the load were linear inductances. Hence, the optimal relation 5.59 between β_{in}, κ and β_L in a π-device is still valid, except that the relative load and parasitic factor are now defined through the incremental load inductance $L_{\text{load}0}$ that, on its turn, is found from the incremental input inductances $L_{\text{in}0}$ of each subsequent stage.

When a π-device is optimized with respect to its figure of merit, the incremental input inductance can be found by circuit analysis to be

$$L_{\text{in}0} = \frac{(1-\kappa^2)^2 \cdot \beta_L^2}{(1-\kappa^2)\,\beta_L^2 - 2\kappa^2} \cdot L_{\text{in}}$$

The relation above yields a positive $L_{\text{in}0}$ when $(1-\kappa^2)\beta_L^2 - 2\kappa^2 > 0$. Hence, the loop inductance of an optimized π-device must be higher than the minimal value of $\frac{\kappa\sqrt{2}}{\sqrt{1-\kappa^2}}$ in order for the incremental input inductance to be positive. It can be shown that a π-device of $L_{\text{in}0} < 0$ can not be used as a loading stage since it will automatically result in a hysteretic transfer characteristic of any preceding stage that is optimized. Hence, when building multi-stage circuits, it is a good design practice to always choose for devices with positive incremental inductances if one wishes for all devices to be optimized w.r.t. their figure of merit.

The loop inductance of π-device is hence limited from both sides

$$\frac{\kappa\sqrt{2}}{\sqrt{1-\kappa^2}} < \beta_L < \frac{2}{\sqrt{3(1-\kappa^2)}} \tag{5.60}$$

if one wishes to both optimize the figure of merit of the devices and build larger multi-stage circuits that operate in the near-adiabatic regime. The range of β_L given above narrows to zero for $\kappa > \sqrt{\frac{2}{3}}$, Figure 5.20, effectively setting a maximum limit for the coupling factor in any static π-loop circuit. Fortunately, typical values of κ for small thin-film transformers are below this limit.

When asymmetry in the Josephson junctions is present, the available range for β_L from 5.60 is substantially reduced. The plot in Figure 5.26, reproduced below, gives the range of β_L as a function of the coupling coefficient κ and the asymmetry factor $\alpha = \frac{\Delta I_C}{\frac{1}{2}\Sigma I_C}$ in the junctions.

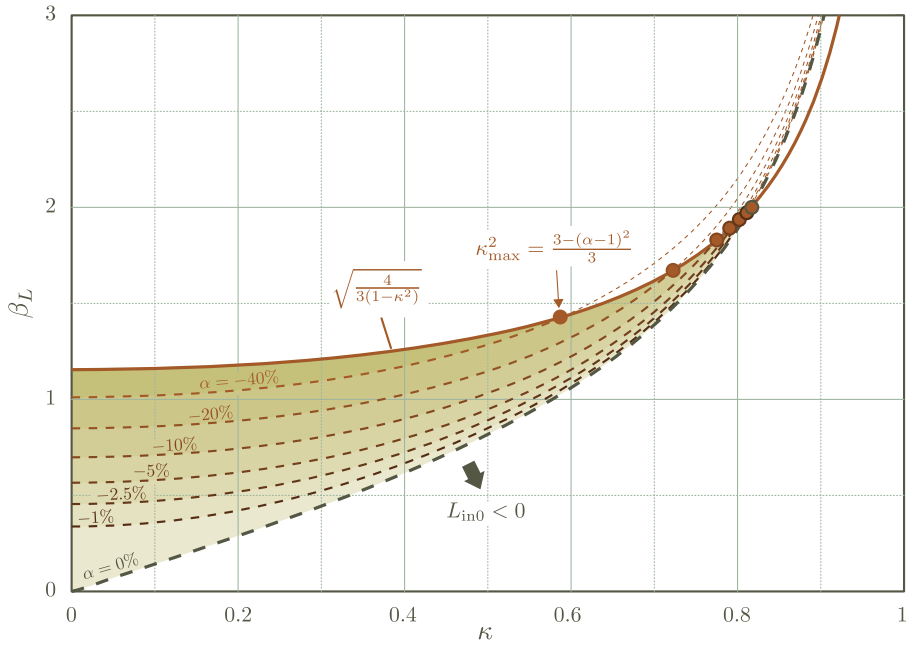

Figure 5.29. The range of β_L for which the devices in a larger static π-loop circuit can be optimized and at the same time function in the near-adiabatic range. The coupling coefficient κ and especially the junction asymmetry α appear as factors limiting the available range of β_L (a positive α broadens the range).

On the basis of the above plot, it can be concluded that it is impractical to implement static π-loop circuits in a technology that has a junction spread higher than 20%. Also, since the plot indicates the available values of the normalized loop inductances to typically lie below or around unity, the $L \cdot I_C$ product of segment-junction structures that can be reliably implemented in a given π-shift technology should be less than $\frac{\Phi_0}{2\pi} \approx 330\,\mathrm{pH} \cdot \mu\mathrm{A}$, a low but still reasonable number.

As far as the thin-film transformer is concerned, a coupling coefficient greater than 0.5 should not be used as the available range of the circuit parameters is then severely reduced, especially when the asymmetry in the circuit is high. To increase the signal gain, proportional to $\kappa \cdot \sqrt{\frac{L_s}{L_{\mathrm{in}}}}$, it is then better to design transformers with high secondary-to-primary inductance ratio $\sqrt{\frac{L_s}{L_{\mathrm{in}}}}$ rather than with a high κ.

The signal amplification property found in the transfer characteristic of the modulated π-devices makes it possible to build basic analog circuits, like amplifiers and fanout (signal duplication) structures. A single modulated π-loop with a gain higher than unity can be considered as a logic inverter, defining the binary symbol alphabet to map onto the polarity of the flux angles in the circuit, for example $(0, 1) \rightarrow (\varphi < 0, \varphi > 0)$. Digital combinational circuits other than an inverter can also be built, but their complexity exceeds the scope of this thesis. Nevertheless, an example of a simple digital cell is given below, along with a few details and comments for the direction of further work in this area.

A basic digital circuit performing the logic function of a 3-input/1-output majority gate, its truth table given in Table 5.2, is demonstrated in Figure 5.30. The values of the circuits parameters are given, as well as circuit simulation results.

A	B	C	$\mathrm{Maj}\{A, B, C\}$
0	0	0	0
0	0	1	0
0	1	0	0
0	1	1	1
1	0	0	0
1	0	1	1
1	1	0	1
1	1	1	1

Table 5.2. The truth table of a 3-input/1-output majority gate

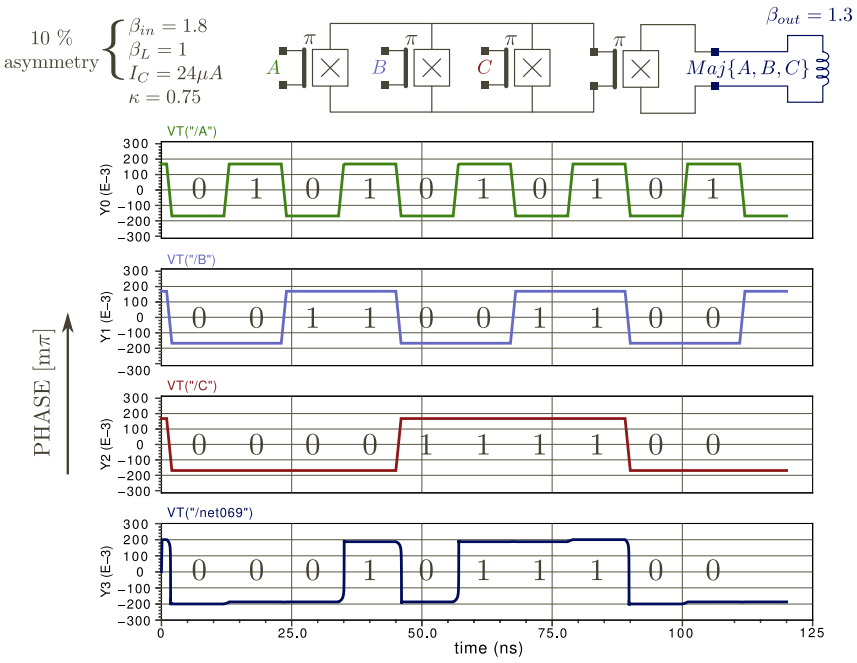

Figure 5.30. The schematic of a 3-input/1-output majority gate implemented with modulated π-devices. The result of a circuit simulation of the cell is given as well. One may notice that output signal is level-triggered and exhibits a self-sustained transition features: the circuit hence does not operate in the near-adiabatic regime.

The main issue with such type of combinational logic cells lies in the possibly related phenomena of back-action and thermodynamic reversibility. The former is the effect where the output signal appears at the device's input (inverse signal propagation), while the latter stems from the energy-conserving nature of the state transitions in the circuits.

Back-action is apparent when the outputs of a few cells are connected together, for example like in Figure 5.30. The output signal, which depends on the values of all input signals, then partly appears at the input terminals of each of the π-devices through back-action. The result is that the rest of the circuit connected at a given input terminal will be affected by the values of the signals at the other input terminals. This inverse route of signal propagation may create parasitic signal processing mechanisms disturbing the desired operation of the whole digital block.

Logic reversibility of a digital cell implies that one can always find the state of all input signals from the state of all output signals. In other words, the logic function mapping the inputs onto the outputs is bijective: when the inputs and outputs reverse their role, a valid logic function is again obtained. For example, the 3-input/1-output majority gate from Figure 5.30 is not reversible: the two possible output states 0 and 1 map to eight different input states and hence the reverse operation is not a proper logic function since it will be multiply-defined. A logically reversible function has the property that information is never lost as it passes the cell.

Logical reversibility is connected to thermodynamic reversibility [69] [70] [71]: assuming that all information is physical, it is not difficult to imagine a link between the conservation of information and the conservation of energy in a circuit. It is theorized, for example in [71], that in a circuit implementing a logically irreversible function, where some of the information contained in the input state vector is lost, the physical phenomenon underlying the signal processing must be accompanied with a thermodynamically irreversible process as well. In other words, logical irreversibility implies thermodynamic irreversibility. In the example of Figure 5.30 however, the logically irreversible function $y = \mathrm{Maj}(x_1, x_2, x_3)$ is implemented with a thermodynamically reversible process, assuming the π-devices operate in the near-adiabatic range. To solve this contradiction, if indeed the claim of [71] is true, it will be impossible to either implement the majority function properly or to place the devices in the near-adiabatic range. It is thus not strange that a mechanism, back-action, appears that introduces parasitic modes of operation or, as is the case in Figure 5.30, that the devices are not operating in their near-adiabatic range

In order to build static π-shift logic cells in the near-adiabatic regime, it is thus necessary to use only reversible logic functions. An important area of further work with the static π-loop devices should be in the direction of finding circuits that implement such reversible logic functions. For example, it has been shown that majority-based logic cells are not only universal, meaning that one can synthesise all logic functions with only the majority function as a basic building block, but that there exists a class that is reversible too [72]. Finding structures that implement such functions with modulated π-devices is thus a good starting point.

Chapter 6

Experiments with flux-modulated π-loop circuits

In this Chapter, the results of a test circuit, designed for the purpose of verifying the $\Phi_{\text{out}}(\Phi_{\text{ext}})$ transfer characteristic of a flux-modulated π-loop, will be presented. The following section defines the test structure chosen for the above purpose, while the measurement results are given in the second section.

The method chosen to verify the phenomenon of flux gain in a modulated π-loop is based on a comparison between simulation and measurement of the same test structure. Some unique features of the transfer characteristic of a modulated π-loop are optimized by simulation and a circuit structure is then physically drawn with the chosen parameters. The same features are subsequently sought for in the measurement data of the implemented circuit.

The process technology used to build the test structure is the hybrid YBCO/Nb technology from Chapter 3, together with the modifications described in Chapter 4. However, the process stack of the technology, given in Figure 3.5, is extended with one more SiO_2/Nb bilayer at the top. The top-most Nb superconducting film is now used as a groundplane, while the two Nb and one YBCO levels below the groundplane are used as interconnect (see also Figure 2.41) . The layer thicknesses are identical with the ones previously given in Table 2.1 from the circuit design example in Chapter 2. For completeness, the superconducting layer parameters are reproduced below together with the thicknesses of the SiO_2 isolation layers between them.

	YBCO	CeO_2	Nb1	SiO_2 #1	Nb2	SiO_2 #2	Nb GP
d [nm]	110	50	160	170	250	300	300
λ_L [nm]	200	/	100	/	100	/	100
L_S [pH]	0.502	/	0.136	/	0.127	/	0.126

Table 6.1. The parameters of the thin film layers used in the implementation of the modulated π-loop test circuits. Also L_S, the surface inductance used in the 2D single-sheet model of the conducting layers, is given.

The other process parameters, such as the thickness of the Au barrier layer and the height of the ramp profile in the YBCO/Nb junctions, were varied. These can be found in Table 4.2 at the end of Chapter 4 for the few manufactured samples under the label "SCALx.x".

The same table shows that the spread in the critical currents of the junctions for the YBCO/Nb manufacturing process is still about 30%. Consulting with Figure 5.26, it is clear that the junction asymmetry would be too great for experiments with any digital static π-shift circuits. The measurements presented below are thus focused only on the transfer characteristic of single π-devices.

6.1 Description of the test structures

The most intuitive manner to obtain the $\Phi_{\text{out}}(\Phi_{\text{ext}})$ characteristic of a flux-modulated π-loop, this curve shown in Figure 5.6 of the previous Chapter, is to simply measure the magnetic flux created on the output inductor as a function of a magnetic flux externally applied in the π-loop. The structure would then consist of a π-loop, an inductive segment connected across its terminals as a load and a second inductive segment magnetically coupled to the π-loop where the input terminal will be located. The last can be implemented as a thin-film transformer - the structure is then exactly the same as the inductively-modulated π-devices from Section 5.2 in the previous Chapter. Sending a current I_{in} through the input terminal will create Φ_{ext} while measuring the magnetic flux created at the load segment will give Φ_{out}.

There are two main challenges that should be addressed with the above method:

- Both L_{out}, the inductance of the load segment, and Φ_{out}, the output signal amplitude, are too low for traditional magnetic sensors
- Since the circuit operates in the (φ, I) domain and magnetic sensors typically require voltage bias, the chance of back-action due to reverse energy transfer during measurements is large

The fact that L_{out} and Φ_{out} are low requires both small and sensitive sensors, while the large chance of back-action requires sensors that exchange little energy with the measured device.

Note that obtaining the $\Phi_{\text{out}}(\Phi_{\text{ext}})$ characteristic of a π-device is similar to the measurement of the phase-current relationship in Josephson junctions. Defining M as the mutual coupling inductance of the π-device's transformer, it follows from $\Phi_{\text{ext}} = M\, I_{\text{in}}$ and $\Phi_{\text{out}} = \frac{\Phi_0}{2\pi} \cdot \varphi_{\text{out}}$ that one would actually need to measure the $\varphi_{\text{out}}(I_{\text{in}})$ of the modulated π-device in order to directly find $\Phi_{\text{out}}(\Phi_{\text{ext}})$. Nevertheless, a $\varphi - I$ measurement requires a specialized setup that is also customized for use with π-loops and high-T_c circuits. In favour of simplicity, such a direct measurement method was not used.

In order to address the above issues, the measurement circuit was chosen to locally integrate the sensor and the modulated π-loop in a composite structure on the same sample. The output inductor L_{out} of the π-device is tightly coupled to a DC-SQUID loop, the magnetic flux Φ_{out} created by it modulating the critical current of the SQUID loop with a $\sim\cos\left(\pi\,\frac{\Phi_{\text{out}}}{\Phi_0}\right)$ dependence, see for instance Figure 5.2. Hence, measuring the I_C of the SQUID indirectly gives the value of $|\Phi_{\text{out}}|$. Repeating the I_C measurement for a number of values of Φ_{ext}, which is proportional to the input current I_{in} at the modulation terminals of the π-device, an $I_C(I_{\text{in}})$ curve is obtained. This characteristic will posses features unique to the $\Phi_{\text{out}}(\Phi_{\text{ext}})$ transfer, such as sharp peaks at $\Phi_{\text{ext}} = \Phi_{\text{out}} = 0$ and gradually forming valleys at $\Phi_{\text{ext}} = \pm\frac{\Phi_0}{2}$ (when Φ_{out} is maximum and thus the SQUID I_C is at minimum). Comparing these features in the measured characteristic with simulation results, one can indirectly confirm the general shape of the $\Phi_{\text{out}}(\Phi_{\text{ext}})$ curve. A diagram of this measurement structure is given in Figure 6.1.

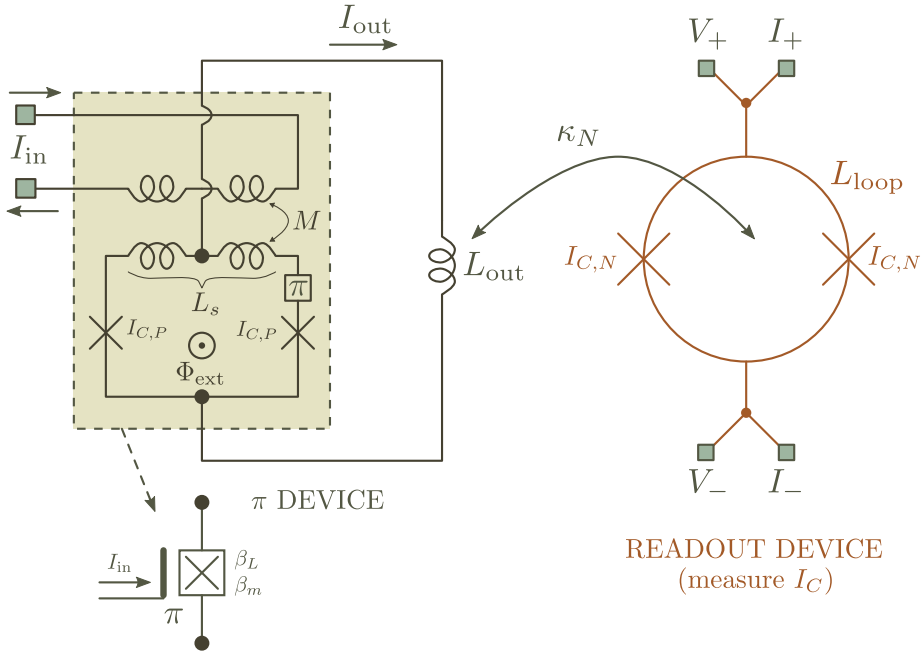

Figure 6.1. A schematic of the structure used to experimentally verify the π-loop transfer characteristic. Note that the symbol of the π-device, also shown above, will be used in all subsequent drawings instead of the full device schematic.

The readout device consists of a normal loop (a DC-SQUID) of inductance L_{loop}, and two junctions of critical current $I_{C,N}$. The $V_{\pm}$ and $I_{\pm}$ terminals are used to perform a 4-point measurement of the critical current of the SQUID loop. The π-device on the other hand, consists of an inductively-coupled π-loop where the mutual inductance of the transformer is M, the loop inductance is L_s and the critical current of the junctions is $I_{C,P}$. Hence, the normalized mutual coupling inductance of the π-device's transformer is $\beta_m = \frac{2\pi M I_{C,P}}{\Phi_0}$ and the normalized loop inductance is $\beta_L = \frac{2\pi L_s I_{C,P}}{\Phi_0}$. The input inductance, or the inductance of the transformer primary in the π-loop, as well as its coupling coefficient are not important for the experiment. At the end, a load inductance L_{out} is connected across the terminals of the π-loop and coupled to the SQUID loop with a coupling coefficient κ_N.

The input current I_{in} is externally supplied and creates an applied flux of $\Phi_{\text{ext}} = M I_{\text{in}}$ in the π-loop. The output flux $\Phi_{\text{out}} = L_{\text{out}} \cdot I_{\text{out}}$ is then related to the input current I_{in} through the $\Phi_{\text{out}}(\Phi_{\text{ext}})$ transfer characteristic of the π device. The critical current of the readout SQUID is modulated via the coupling with L_{out} as

$$\sim \left| \cos\left(\pi \cdot \frac{\kappa_N \sqrt{L_{\text{out}} \cdot L_{\text{loop}}}}{\Phi_0} \cdot I_{\text{out}} \right) \right| \tag{6.1}$$

if L_{loop} is taken to be small. When $I_{\text{in}} = \frac{n \cdot \Phi_0}{M}$, the applied flux Φ_{ext} is an integer (n) amount of flux quanta and, as seen in the general transfer characteristic of the flux-modulated loop (ex. Figure 5.4), the output flux will be always $\Phi_{\text{out}} = 0$. Hence, also $I_{\text{out}} = 0$ and the critical current of the SQUID is then at a maximum. As I_{in} is changed, Φ_{ext} moves towards a value of a half integer flux quantum. The transfer characteristic then indicates that $|\Phi_{\text{out}}|$ increases until it reaches its amplitude $|\Phi_{\text{out}}|_{\max}$ when the applied flux Φ_{ext} is exactly a half-integer flux quantum, at which point the input current is $I_{\text{in}} = \frac{1}{M} \frac{2n+1}{2} \Phi_0$. Then, the output current of the π-device is also at a maximum $|I_{\text{out}}|_{\max}$ and the critical current of the SQUID is at its lowest value. Further changes in I_{in} result in a periodic extension of the $I_C(I_{\text{in}})$ curve.

Note that the maximum output flux $|\Phi_{\text{out}}|_{\max}$ in a π-device is always less than $\frac{1}{4}\Phi_0$ (Figure 5.11). Hence, the maximum flux coupled to the readout SQUID will be always less than a quarter Φ_0 (unless L_{loop} is made of multiple turns - this is not the case here). The argument of the cosine in the modulation pattern of the readout SQUID will thus never go beyond $\pm\frac{\pi}{4}$, even with $\kappa_N = 1$. The maximum modulation depth is then $\frac{\cos(0) - \cos(\pi/4)}{\cos(0)} \approx 30\%$. In practice, where $|\Phi_{\text{out}}|_{\max}$ is about a hundred mΦ_0, the modulation depth is just a few percent. The readout mechanism explained above is also graphically illustrated in Figure 6.2.

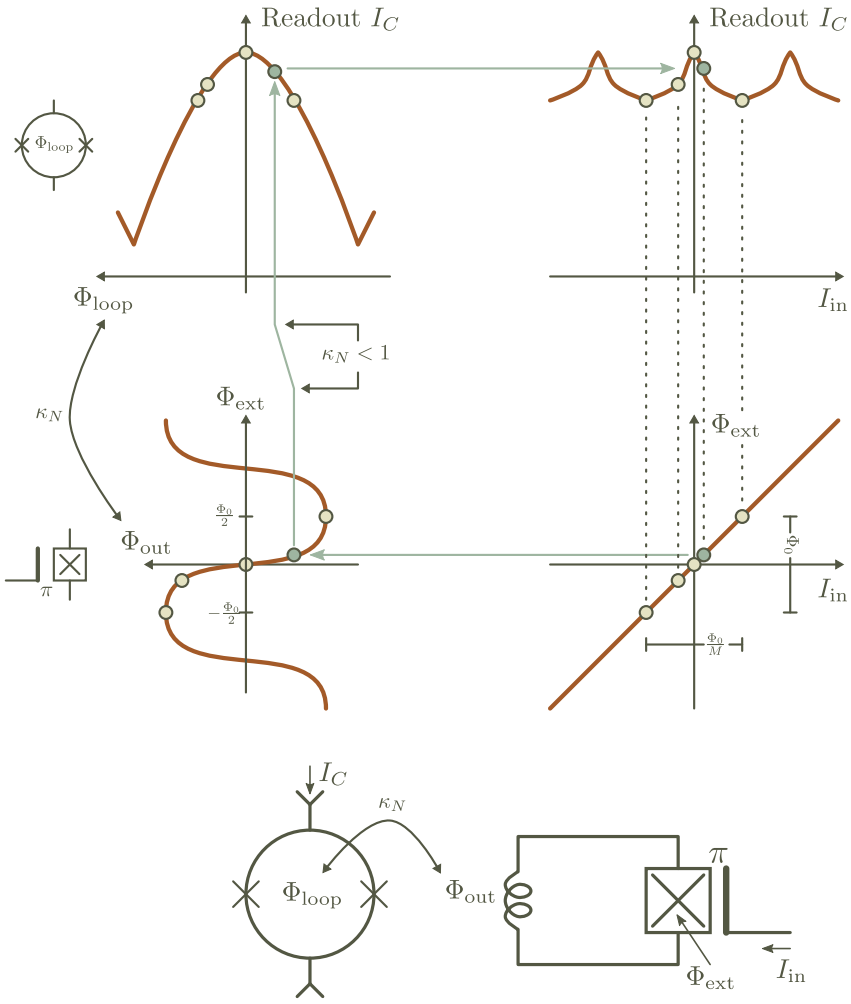

Figure 6.2. A sketch of the transfer curve $I_C(I_{\text{in}})$ for the test structure from Figure 6.1.

Note that the distinct peaks in the $I_C(I_{\text{in}})$ curve from Figure 6.2 correspond to the sharpest region of the $\Phi_{\text{out}}(\Phi_{\text{ext}})$ characteristic where the actual flux gain takes place. The valleys on the other hand correspond to the saturation region of the π-device's transfer characteristic. Hence, the shape of the $I_C(I_{\text{in}})$ curve is a signature of the flux gain mechanism in the π-device. Were one to place a normal loop instead of the π-loop in the test structure, the shape of the $I_C(I_{\text{in}})$ curve would be different as the $\Phi_{\text{out}}(\Phi_{\text{ext}})$ transfer characteristic of a modulated normal loop is different as well (see Figure 5.4).

A second observation is connected to the type of transfer characteristic of the π-device. In Figure 6.2, it is assumed that the $\Phi_{\text{out}}(\Phi_{\text{ext}})$ characteristic is non-hysteretic. If however there is a hysteresis in $\Phi_{\text{out}}(\Phi_{\text{ext}})$, the peaks in the $I_C(I_{\text{in}})$ curve will be reduced as the output flux will never pass through the origin of the flux transfer characteristic. The modulation depth will be then reduced, adversely impacting the sensitivity of the measurement. It is hence important to design the π-device with a non-hysteretic transfer characteristic, i.e. the π-device should be in the near-adiabatic regime.

At the end, the value of M can be directly obtained by measuring the period in the $I_C(I_{\text{in}})$ curve. Additionally, if the measurement noise and other parasitic effects are kept low, one can estimate the maximum gain of the device by looking at the "sharpness" of the peaks.

Based on the above discussion, the measurement procedure would then be as follows: a) measure the I_C of the DC-SQUID as a function of the current I_{in} applied in the π-device; b) in the measured $I_C(I_{\text{in}})$ characteristic look for a peak/valley structure and compare to a circuit simulation of the two coupled devices; c) a reasonable match in the shapes of the two curves would indicate a correctly operating circuit; d) calculate M from the period in the measured data and re-simulate by scaling all inductances proportionally; e) use the refined simulation to quantitatively validate the π-device theory (if the data are sufficiently free of noise and other effects).

Additionally, one can perform the same measurement on a copy of the same structure except for the absence of the π-shift element. Observing a distinct difference in the shape of the $I_C(I_{\text{in}})$ curves between the two types of devices would then confirm that the π-loop and normal loop have a different behaviour in the (φ, I) domain (i.e. that a π-loop is *not* just a normal loop with a flux bias of $\frac{\Phi_0}{2}$).

6.1.1 Device parameters

In order to maximise the sensitivity of the measurement, it is necessary to have the highest modulation depth in the $I_C(I_{\text{in}})$ curve. First, lets focus on the π-device parameters and load inductor L_{out}, while the loop inductance L_{loop} of the DC-SQUID will be discussed later.

It is here important to mention that the choice of parameters for the test structure will not follow the optimization path outlined in Section 5.2 - instead of targeting the lowest process sensitivity, the test structure will be designed for the largest signal amplitudes. The device analysis presented before, in Section 5.2, is thus not applicable in this case. A new set of circuit design guidelines needs to be developed.

Assuming that L_{loop} and κ_N are given, the parameters of the π-device and L_{out} should be chosen such that the amplitude $|\Phi_{\text{out}}|_{\max}$ of the output flux, achieved at $\Phi_{\text{ext}} = \pm\frac{(2n+1)\Phi_0}{2}$, is the highest. From the circuit equations of a flux-modulated

loop, see for example the system 5.10 from Chapter 5, it is found that

$$\pi\,|\Phi_{\text{out}}|_{\max} = \beta_{\text{out}} \cdot \cos\left(2\pi\,\frac{|\Phi_{\text{out}}|_{\max}}{\Phi_0}\left(1+\frac{\beta_L}{4\,\beta_{\text{out}}}\right)\right) \tag{6.2}$$

where the normalized inductances are defined in the standard way as $\beta_L = \frac{2\pi\,L_s\,I_{C,P}}{\Phi_0}$ and $\beta_{\text{out}} = \frac{2\pi\,L_{\text{out}}\,I_{C,P}}{\Phi_0}$. When β_L and β_{out} are given, the equation above can be implicitly solved to yield the amplitude of the output flux $|\Phi_{\text{out}}|_{\max}$. In the plot of Figure 6.3, equi-amplitude lines for the output flux are calculated according to 6.2 on the $(\beta_L, \beta_{\text{out}})$ plane.

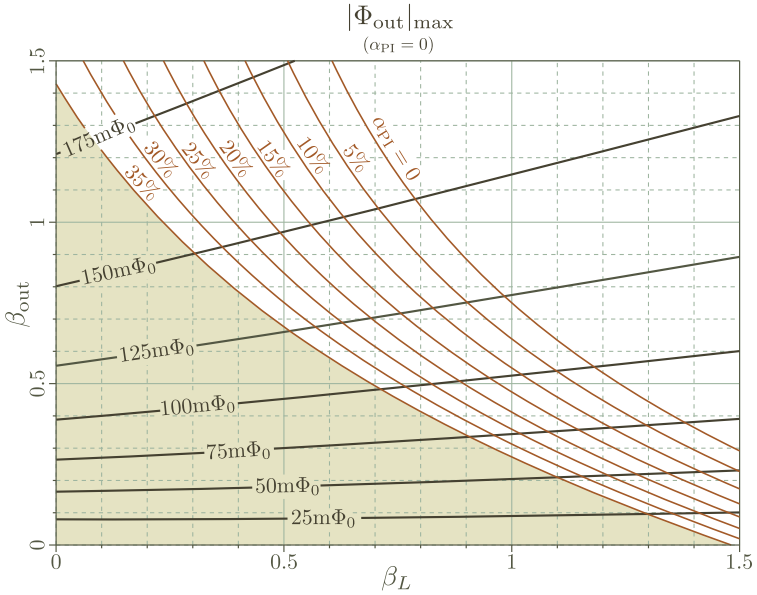

Figure 6.3. Equi-amplitude curves (contour lines of $|\Phi_{\text{out}}|_{\max}$) of a flux-modulated π-loop as a function of the normalized loop and output inductances calculated for zero junction asymmetry. The hysteretic condition 6.3 is also plotted for different asymmetry factors α_{PI} of the junctions in the π-loop. The shaded region satisfies the hysteretic condition.

From the plot, it can be concluded that the output amplitude increases with increasing β_{out} and decreasing β_L. One should therefore choose a large output inductance L_{out} and small π-loop inductance L_s in order to have a high output flux amplitude.

There are however limits to the choice of the normalized inductances. At the low end, β_L is limited by the minimum device size for the given processing technology while, in general, the high end (β_{out}) is limited by the condition for a

non-hysteretic transfer characteristic. In a flux-modulated loop, the hysteretic condition was given by relation 5.13 from Section 5.1.2:

$$\beta_{\text{out}} < \frac{4 - \beta_L^2}{4\,\beta_L}$$

However, the limit above does not take into account any asymmetry in the critical currents of the junctions in the π-loop. Let's define the asymmetry coefficient in the standard way as $\alpha_{\text{PI}} = 2\,\frac{\Delta I_{C,P}}{\Sigma I_{C,P}}$. In accordance with the procedure outlined in Section 5.2.5, a small-signal schematic of the π-device can be used to obtain the incremental gain $G = \left|\frac{\partial \Phi_{\text{out}}}{\partial \Phi_{\text{ext}}}\right|$ as a function of the circuit parameters and the asymmetry factor α_{PI}. Then, looking for the incremental gain at the origin to be less than ∞, a new hysteretic condition is found

$$\beta_{\text{out}} < \frac{1}{4} \cdot \frac{(2 - \beta_L(1+\alpha_{\text{PI}})) \cdot (2 + \beta_L(1-\alpha_{\text{PI}}))}{\beta_L + \alpha_{\text{PI}}\,(2 - \alpha_{\text{PI}}\,\beta_L)} \tag{6.3}$$

The inequality 6.3 is overlaid on the plot of the equi-amplitude curves in Figure 6.3. It is seen that, given a normalized loop inductance β_L, high junction asymmetry impacts the region of large β_{out}, restricting the choice of output inductances to small values and hence smaller output amplitudes as well.

The equi-amplitude curves implicitly found from 6.2 are valid only for $\alpha_{\text{PI}} = 0$. When there is junction asymmetry, the maximum amplitude satisfies a different (more complex) relation. Nevertheless, although the exact values are different, the overall trend of $|\Phi_{\text{out}}|_{\max}$ shown in Figure 6.3 stays valid.

As a conclusion, it can be stated that in order to maximize the amplitude of the output flux, the design should use the smallest π-loop that can be reliably manufactured while the output inductor should be chosen as close to the limit 6.3 as possible. In practice, as shown towards the end of this section, the lower limit for the normalized loop inductance in the YBCO/Nb process technology is about 0.5.

Note that just like in the case of a cascade of π-devices, a situation that was analysed in Section 5.2.3, the output inductance that the flux-modulated π-loop "sees" as a load is both non-linear and dependent on the parameters of the following device in the chain, i.e. the DC-SQUID. Hence, β_{out} from relations 6.2 and 6.3 is not the same parameter: the former is defined by the large-signal inductance $L_{\text{out}} = \frac{\Phi_{\text{out}}}{I_{\text{out}}}$ evaluated at the maximum Φ_{out} in the transfer characteristic while the latter is the small-signal incremental inductance $L_{\text{out0}} = \frac{\partial \Phi_{\text{out}}}{\partial I_{\text{out}}}$ evaluated at zero Φ_{out}. For the sake of simplicity, this further analytical refinement of the conditions in 6.2 and 6.3 will be omitted in favour of empirical optimization by circuit simulation, as presented shortly below. The plot in Figure 6.3 should then be used as a visual guideline only.

Having analysed the approximate limits of the normalized inductance of the π-loop and load inductor, lets focus on the loop inductance L_{loop} of the DC-SQUID. As seen in equation 6.1, the argument of the cosine-shaped modulation is proportional to $\sqrt{L_{\mathrm{loop}}}$ and one would then like an as high L_{loop} as possible. The DC-SQUID modulation pattern from equation 6.1 is however only valid at small values of L_{loop}. As shown in Appendix A, the modulation pattern of a DC-SQUID is more complex at finite loop inductances. In any case, it is necessary for the normalized loop inductance of the DC-SQUID to be less than 2 so that SFQ states do not appear (see Section 2.2.6.2).

Since it is difficult to exactly quantify the impact of L_{loop} on the I_C modulation depth and hence choose an optimal value, a set of circuit simulations were performed with different values of the ratio $\frac{L_{\mathrm{loop}}}{L_{\mathrm{out}}}$, coupling coefficient κ_N and normalized π-loop inductance β_L. The simulation results, shown in Figure 6.4, plot the modulation depth in the critical current of the SQUID as a function of the various circuit parameters.

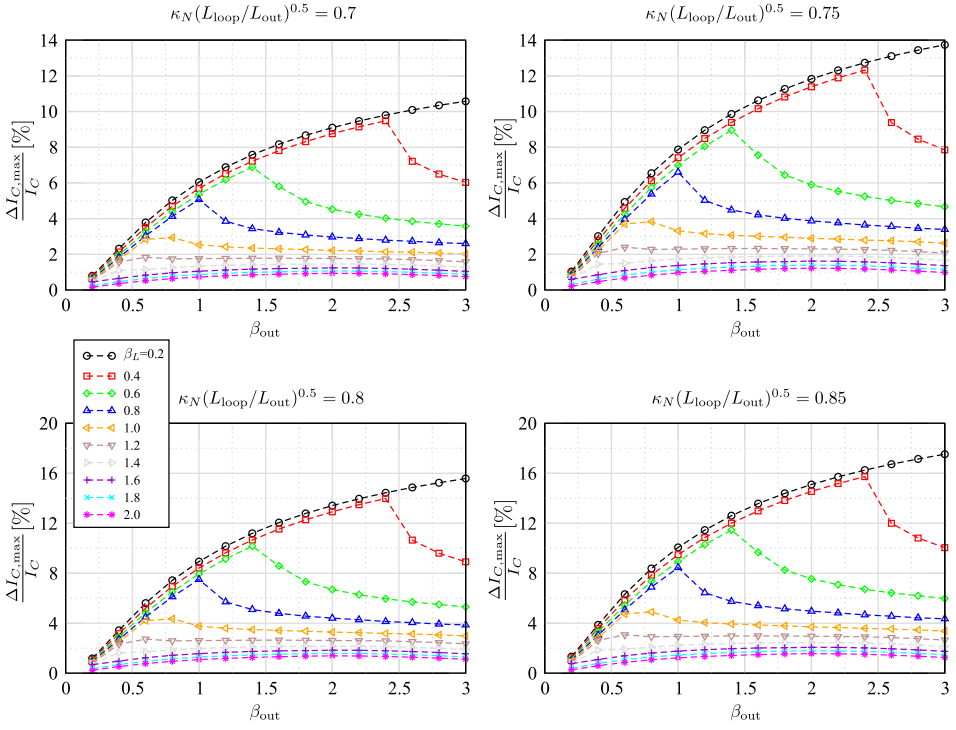

Figure 6.4. The modulation depth of the critical current of the DC-SQUID as a function of the various circuit parameters. The data is obtained by a circuit simulation of the complete structure from Figure 6.1. The junction asymmetry is zero in both the π-loop and DC-SQUID.

The distinct "peaks" in the simulation data from Figure 6.4 correspond to the border of non-hysteretic operation in the π-device. As previously mentioned, the modulation depth is reduced when a hysteresis is present in the transfer curve - the output flux never attains a value of zero (except for a very short time during the state-change transient) and the critical current of the coupled DC-SQUID never reaches its maximum value. This reduction is directly visible in the plots of Figure 6.4 as a sharp downturn in the trend. It important to mention that the plots are made with zero junction asymmetry: in reality when $\alpha_{\mathrm{PI}} \neq 0$ the peaks in the data will move to the "left" towards lower β_{out}, as given by the hysteretic condition plotted in Figure 6.3.

The plots in Figure 6.4 confirm the previous conclusion with regard to β_L and β_{out} but also add an additional guideline: target a large coupling factor κ_{N} and a large ratio $\frac{L_{\mathrm{loop}}}{L_{\mathrm{out}}}$. Since the devices are small, there is very little space to design multiple-turn coupled loop segments that are necessary to achieve both a high coupling coefficient κ_N and a large geometric ratio $\frac{L_{\mathrm{loop}}}{L_{\mathrm{out}}}$. In practice, the product $\kappa_N \sqrt{\frac{L_{\mathrm{loop}}}{L_{\mathrm{out}}}}$ ranges between 0.7 and 0.85 for small ($\sim 30 \times 30 \mu$m) thin-film structures made with the YBCO/Nb process technology.

The smallest Josephson junction that can be reliably manufactured in the standard photolithographic process is limited by the minimum lithographic size of circuit structures to about 2-3μm. Together with a nominal J_C of $12\frac{\mu\mathrm{A}}{\mu\mathrm{m}}$, the lowest I_C of a reliable junction is thus $\sim 30\mu$A. The two junctions, approximately 3μm in length, should be positioned at a 90° angle and then joined with YBCO and Nb segments on each side together to form the π-loop (see also Figure 3.4 from Chapter 3). Taking that the smallest lateral spacing (clearance) between the junctions is also 3μm, the minimum inner diameter of the π-loop, if circular in shape, can not be made smaller than $2 \times 3\mu\mathrm{m}{=}6\mu\mathrm{m}$. The width of the loop, if again guided by the lowest lithographic linewidth resolution, can then not be larger than $3 \times 3\mu\mathrm{m}{=}9\mu\mathrm{m}$ (junction + 2 times side clearance). The smallest average π-loop diameter is then $6 + 9 = 15\mu$m. Hence, the number of squares for this minimal-size circular loop of average diameter 15μm and width of 9μm would be $\frac{\pi \cdot 15}{9} = 5.2$ squares.

Note that making a wider loop also proportionally increases the average diameter so that the number of squares does not reduce very much. Secondly, as shown in [38], the self-inductance of the loop essentially stays constant after a certain width (∼a few times the inner diameter) as the current mostly flows along the inner loop perimeter - increasing the segment width does not change the loop inductance. Consequently, the value of 5.2 is taken as a good approximation of the lower limit for the effective number of squares in a loop manufactured in the YBCO/Nb technology at hand.

Assuming that $\frac{1}{3}$ of the loop's volume consists of YBCO and $\frac{2}{3}$ of Nb, as well as taking the sheet inductances of the two films from Chapter 3 as $\approx 2\frac{\mathrm{pH}}{\mathrm{sq.}}$ and $\approx 0.5\,\frac{\mathrm{pH}}{\mathrm{sq.}}$, the self-inductance of the minimal π-loop would then be

$$\left(\frac{1}{3}\cdot 2\frac{\mathrm{pH}}{\mathrm{sq.}} + \frac{2}{3}\cdot 0.5\frac{\mathrm{pH}}{\mathrm{sq.}}\right) \times 5.2\,\mathrm{sq.} = 5.2\mathrm{pH}$$

Using $I_{C,P} = 30\mu\mathrm{m}$ and $L_s = 5.2\mathrm{pH}$, the normalized inductance of the π-loop then calculates to about $\beta_L = 0.47$. That is thus the minimum β_L that can be reliably manufactured with the given process technology.

Taking a β_L of 0.5 and an α_{PI} that can theoretically reach 35%, as shown in the I_C spread measurements from Table 4.2, the hysteretic condition 6.3 limits the upper value of β_{out} to about 0.65 (see also Figure 6.3). From the data in Figure 6.4, the maximum modulation depth in the critical current of the DC-SQUID that one may expect during the measurement would then range between 3% and 5%, depending on the exact values of κ_N and the ratio $\frac{L_{\mathrm{loop}}}{L_{\mathrm{out}}}$. Adding other effects, such as measurement noise, flux trapping and parasitic modulation phenomena (ex. suppression of the junction's I_C), the I_C modulation depth may become lower than the detection limits of the measurement.

Note that the expected maximum junction asymmetry puts a very heavy toll on the design decisions for the test structure. If one were allowed to theoretically enter the hysteretic regime or, equivalently, assume that the asymmetry between the two π-loop junctions is likely to be lower than the collective I_C spread, it follows from the plots above that the design constraints can be relaxed and a higher modulation depth achieved. So, for instance if the parameters are chosen to be $\beta_L = 0.7$ and $\beta_{\mathrm{out}} = 0.85$, the modulation depth will range between 5% and 8% - on average a half more than before. This test structure would however be more sensitive to junction asymmetry, the hysteretic condition violated already at $\alpha_{\mathrm{PI}} > 10\%$.

As α_{PI} is not known beforehand, it is best to design two structures: one for a "worst-case" and one for a "best-case" junction asymmetry. If the junction spread on the manufactured sample is low, the "best-case" structure will offer a good modulation depth while at high junction asymmetry the "worst-case" structure will perform better. The parameters for the two structures are taken from the two examples above: $\beta_L = 0.5/0.7$ and $\beta_{\mathrm{out}} = 0.6/0.85$ for the worst/best case. Additionally, copies of the two structures lacking the π-shift element were manufactured as control circuits.

6.1.2 Physical design of the test structures

The device analysis from the previous section resulted in few design guidelines for the test structures. These will be briefly summarized before the physical design of the test circuits is presented further below.

It was determined that in order to optimize the modulation depth in the I_C of the SQUID sensor and simultaneously take into account the possibility of high junction asymmetry, two structures should be designed. One is the "worst-case" structure with $\beta_L = 0.5$ and $\beta_{\text{out}} = 0.6$ while the other "best-case" structure targets a π-loop of $\beta_L = 0.7$ with an output inductor of normalized inductance $\beta_{\text{out}} = 0.85$. Two more circuits of identical parameters but lacking the π-shift elements need to be also present on the same sample. The length of the Josephson junctions should be on the lowest lithographical limit, yielding an $I_C = 30\mu$m. Further,

- the coupling coefficient κ_N between the output inductor and DC-SQUID loop should be as high as possible
- the loop inductance L_{loop} of the DC-SQUID should be as high as practically possible

Additionally, any parasitic inductance in series with L_{out} should be kept at minimum as it does not take part in the magnetic coupling with the DC-SQUID.

At the end, a good practical guideline is to have as large as possible mutual inductance M between the input segment and the π-loop so that one does not need large amplitudes of I_{in} to produce $\Phi_{\text{ext}} = M \cdot I_{\text{in}}$ during the measurement - large I_{in} may create parasitic modulation through secondary coupling mechanisms and contribute to flux trapping locally on the sample. Hence, also the coupling factor between the input modulation segment and the π-loop needs to be kept as high as possible.

The four circuits designed according to the above guidelines and parameter targets have a designation as follows:

1. **π-small**: $\beta_L = 0.5$; $\beta_{\text{out}} = 0.6$; with π-shift
2. **π-big**: $\beta_L = 0.7$; $\beta_{\text{out}} = 0.85$; with π-shift
3. **n-small**: $\beta_L = 0.5$; $\beta_{\text{out}} = 0.6$; without π-shift
4. **n-big:** $\beta_L = 0.7$; $\beta_{\text{out}} = 0.85$; without π-shift

The circuit schematic of the four test structures is the same, except for the π-shift element. In Figure 6.5, the collective schematic is drawn while in the subsequent Figures 6.7 - 6.10 the physical design of the 4 structures is shown, together with a microphotographs of each as manufactured. Table 6.2 gives the element values of the structures as calculated from an EM inductance analysis of the physical structures from Figures 6.7 - 6.10 (see Section 2.3.3 in Chapter 2 for an example of the inductance analysis process).

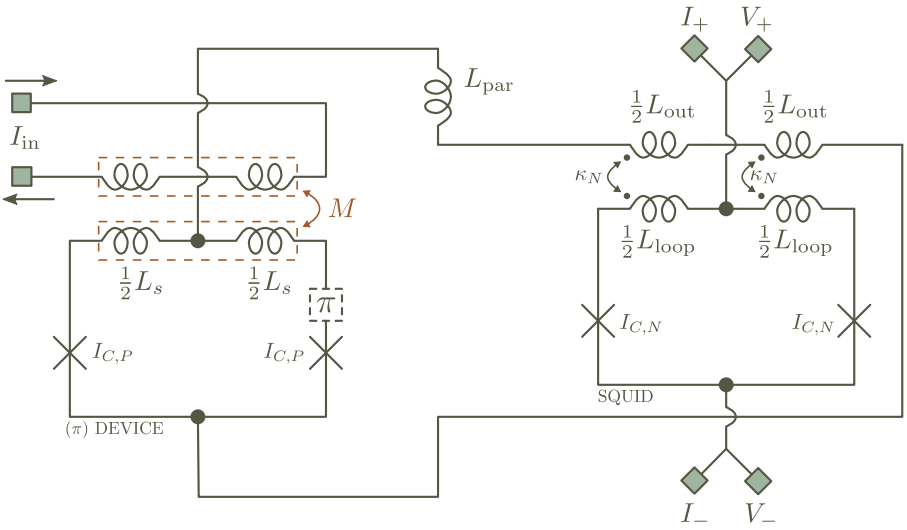

Figure 6.5. The full circuit schematic of the test structures.

	M	L_s	L_{par}	L_{out}	L_{loop}	κ_N	$I_{C,P}$	$I_{C,N}$
π-small	2.21pH	5.33pH	1pH	6.5pH	12.35pH	0.588	30μA	30μA
π-big	3.69pH	7.83pH	1pH	9.42pH	16.13pH	0.613	30μA	30μA
n-small	2.15pH	5.91pH	0.94pH	6.95pH	12.35pH	0.588	30μA	30μA
n-big	3.3pH	7.44pH	1pH	9.42pH	16.13pH	0.613	30μA	30μA

Table 6.2. Element values calculated by inductance extraction of the respective physical designs from Figures 6.7-6.10. Used is a single 2D-sheet model of the superconducting films (Section 2.3) while the EM analysis was performed with Sonnet *em* [42]. The superconducting film properties as well as the layer thicknesses are given in Table 6.1.

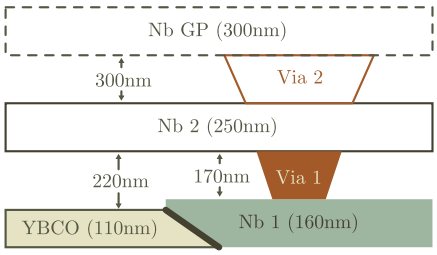

Figure 6.6. Process stack of the implementation technology

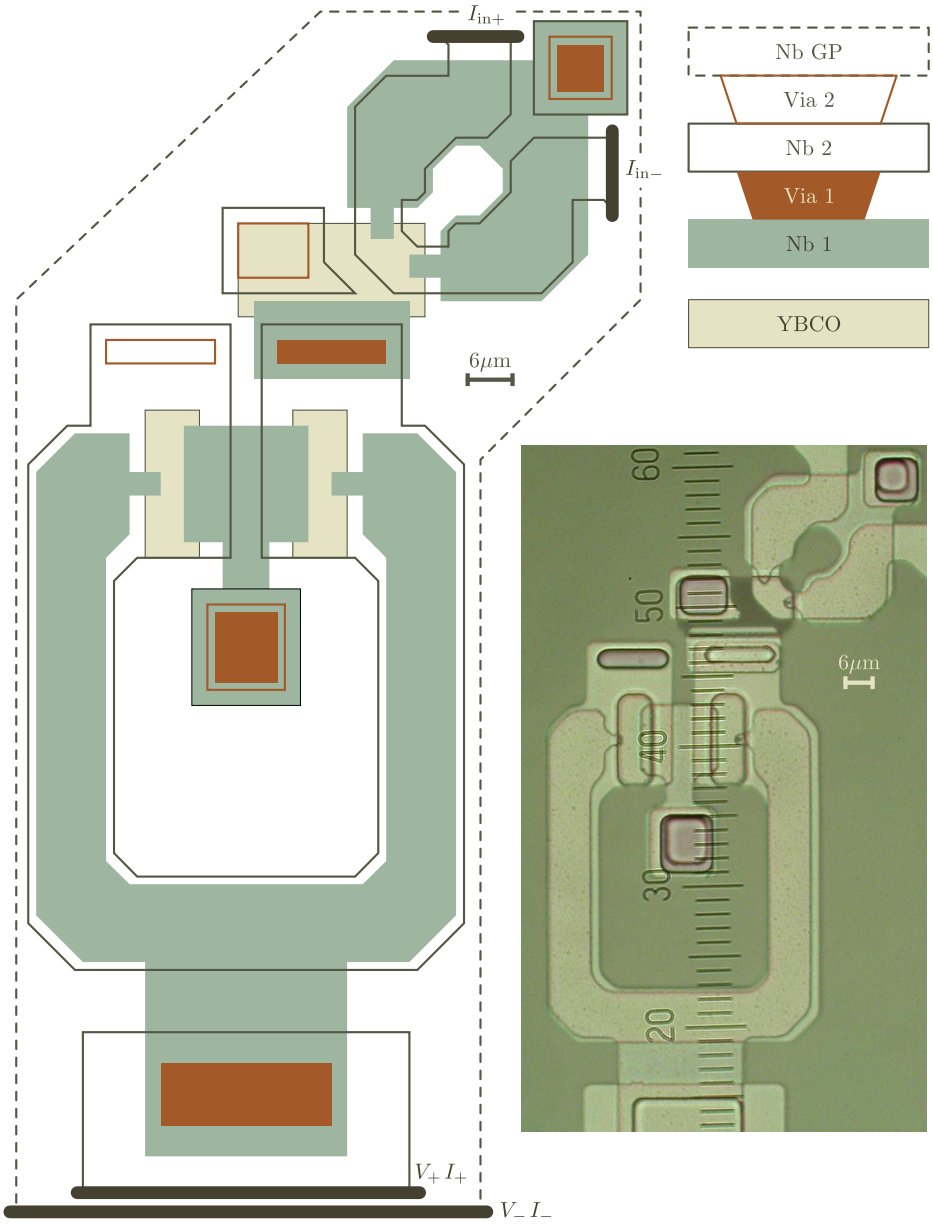

Figure 6.7. The physical layout and microphotograph of the **π-small** structure

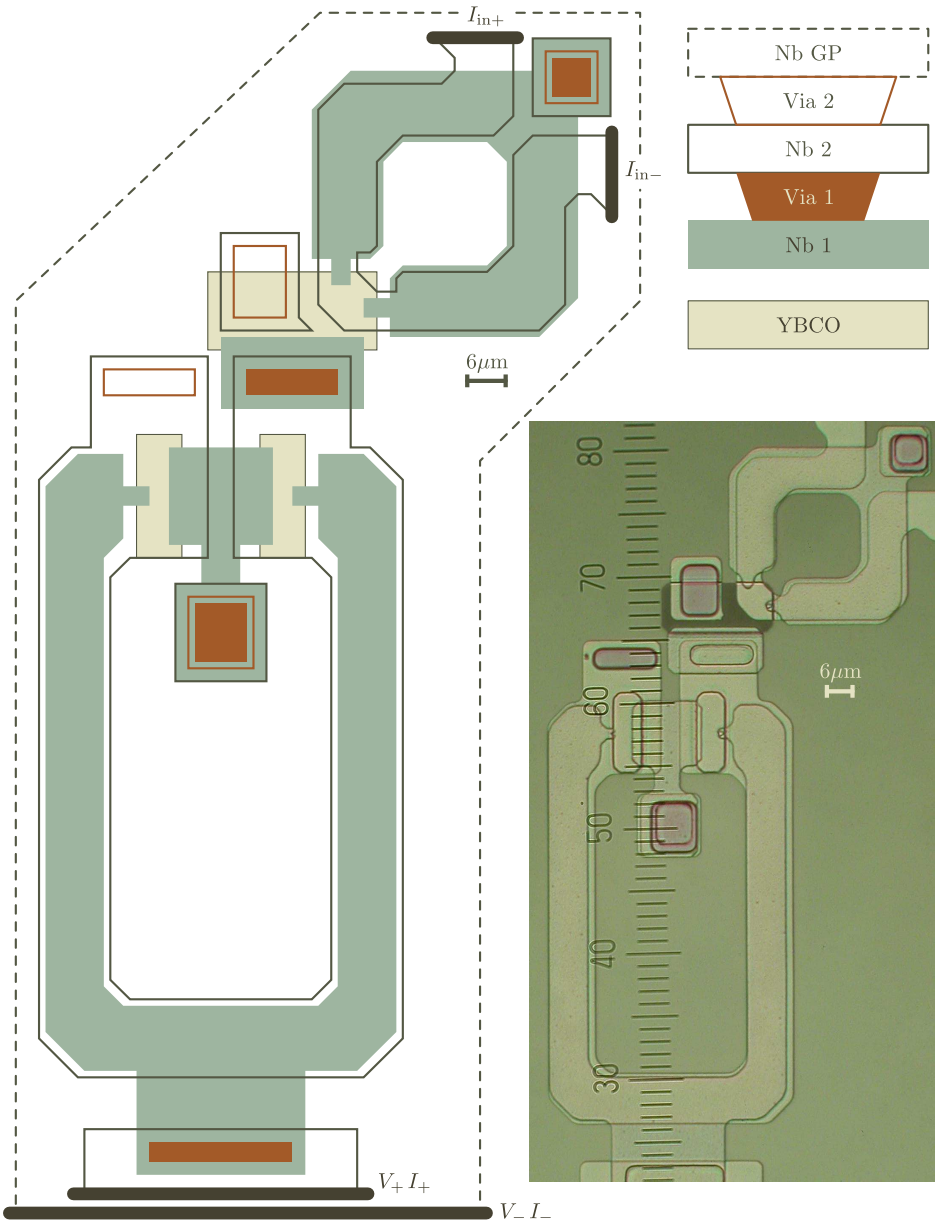

Figure 6.8. The physical layout and microphotograph of the **π-big** structure

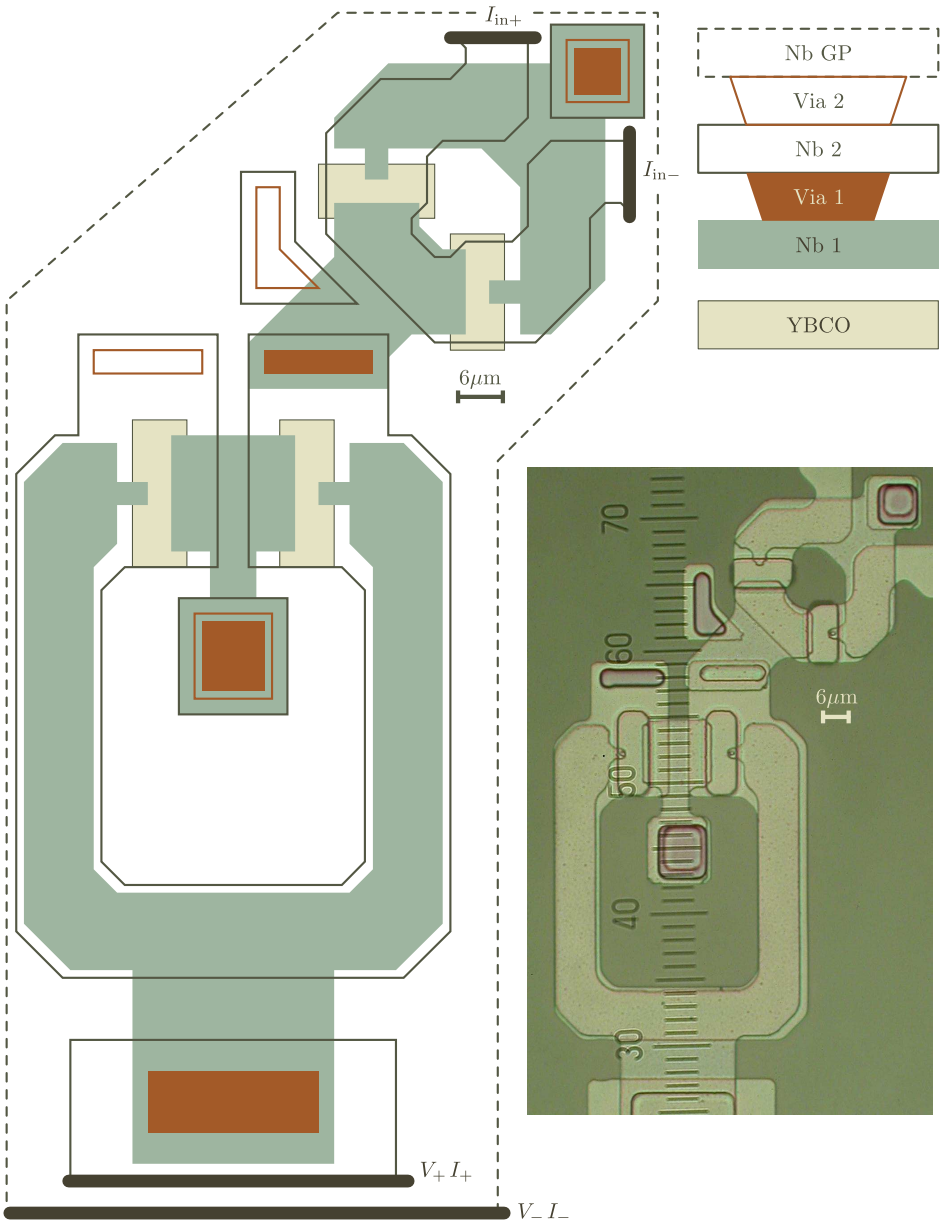

Figure 6.9. The physical layout and microphotograph of the **n-small** structure

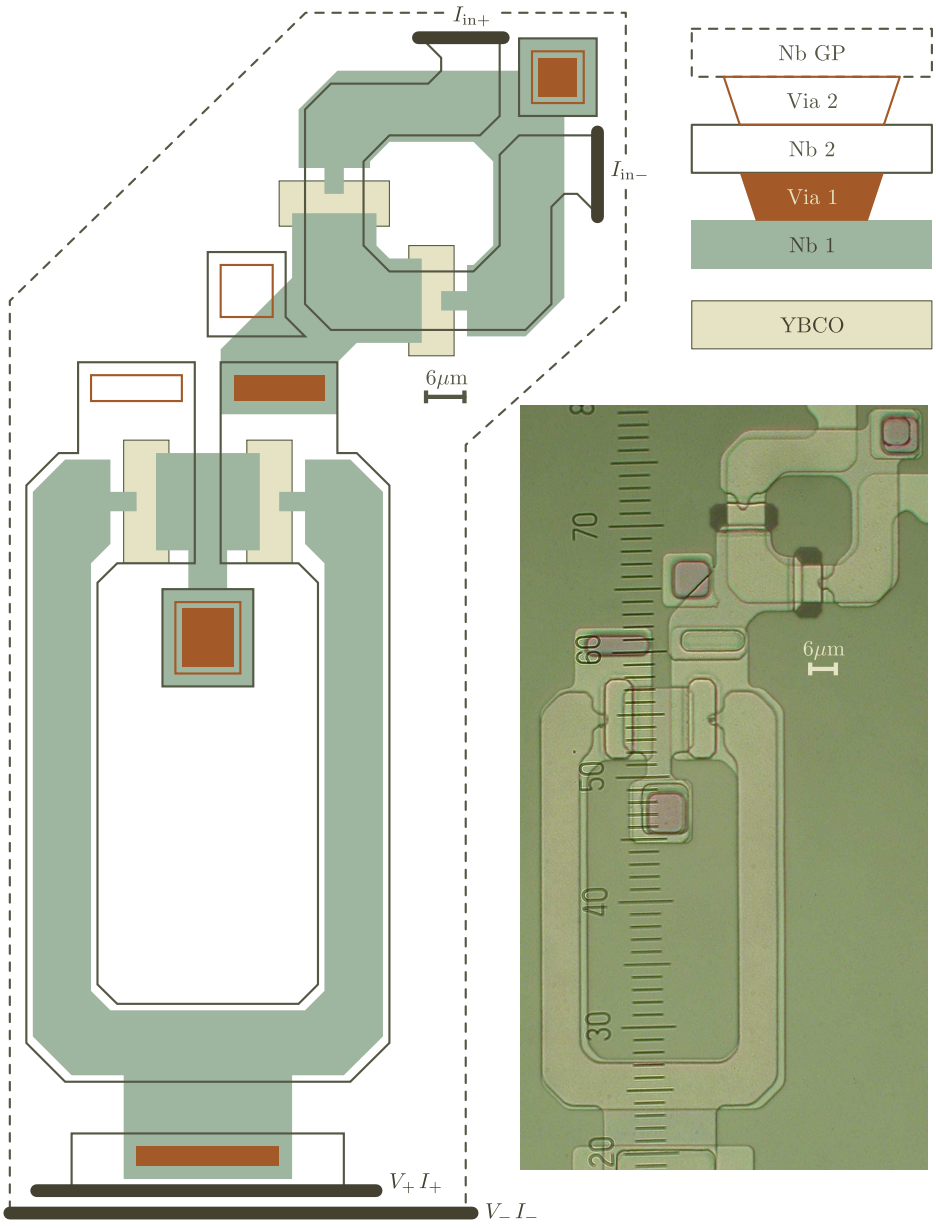

Figure 6.10. The physical layout and microphotograph of the **n-big** structure

6.1.3 Circuit simulation & asymmetry effects

The asymmetry α_{PI} in the Josephson junctions of the π-loop was previously shown to result in a reduction of the non-hysteretic parameter range, for instance see equation 6.3 and Figure 6.3. Nevertheless, asymmetry in the critical currents of the junctions also changes the shape of the $\Phi_{\mathrm{out}}(\Phi_{\mathrm{ext}})$ transfer curve, influencing the maximum amplitude $|\Phi_{\mathrm{out}}|_{\mathrm{max}}$ and the input flux at which that maximum amplitude is obtained. In Figure 6.11, simulation data showing the transfer characteristic and output DC-SQUID modulation pattern of the **π-small** test structure are given, for a few values of the asymmetry factor α_{PI}.

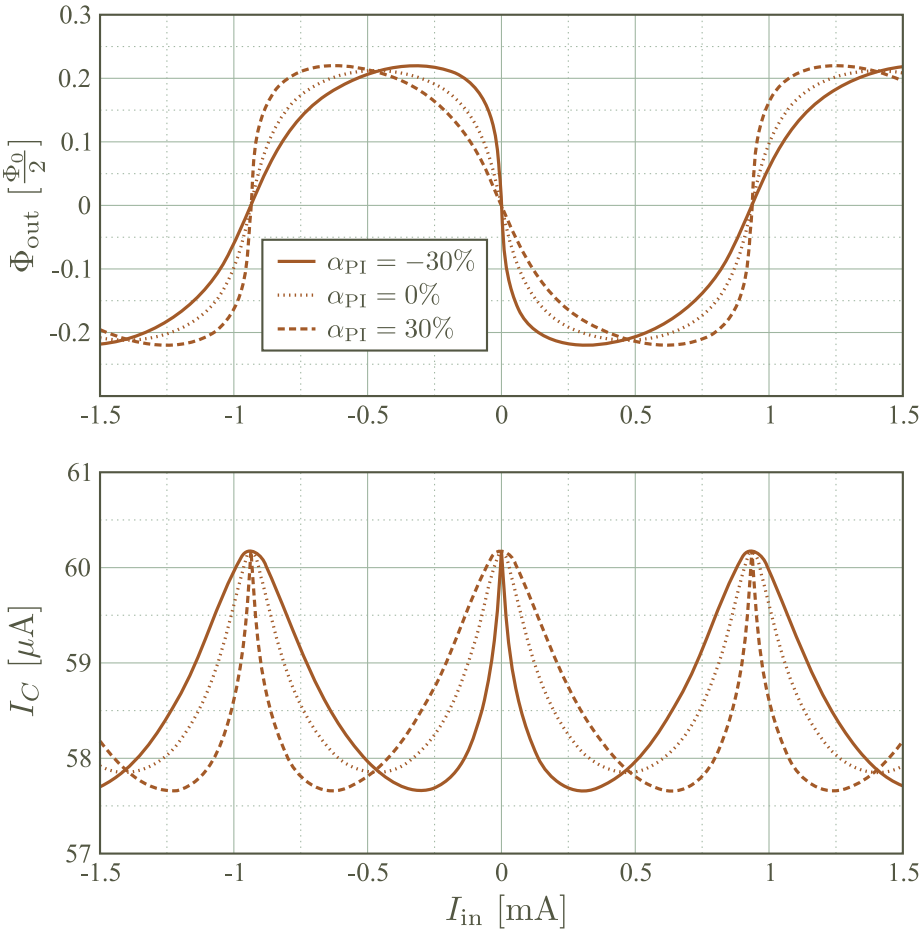

Figure 6.11. The transfer characteristic and output SQUID I_C modulation pattern of the **π-small** structure for a few asymmetry factors α_{PI}. The input flux Φ_{ext} can be calculated from the input current as $\Phi_{\mathrm{ext}} = M \cdot I_{\mathrm{in}}$, where $M = 2.21\mathrm{pH}$ (see Table 6.2).

The most notable impact of asymmetry in the π-loop junctions is thus the alternating sharp-smooth peak periodicity in the I_C modulation pattern. The reason is the alternating increase/decrease in the gain as the transfer characteristic passes through $\Phi_{\text{out}} = 0$ at each Φ_0-cycle in the input flux Φ_{ext}. Secondly, the position of the valleys (the minimum in the I_C) changes with α_{PI} since the position of the maximum in the output flux deviates from $\Phi_{\text{ext}} = \frac{2n+1}{2}\Phi_0$. Also the depth of the valleys changes with α_{PI} as the value of the maximum output flux itself is different. However, the zero-crossings in the transfer curve and hence peak positions in the I_C modulation pattern remain at $\Phi_{\text{ext}} = n\,\Phi_0$ for any α_{PI}.

A second effect that must be accounted for takes place when there is an asymmetry α_N in the junctions of the output DC-SQUID. Calculations show that a non-zero α_N has little influence on the transfer characteristic of the π-loop, but only when the externally applied current through the DC-SQUID is zero. When there is a current applied through the $I_\pm$ terminals of the output device, which is necessary during the measurement to obtain its I_C, junction asymmetry causes this current to split unequally between the two arms of the output loop. As a consequence, a circulating current is effectively present in the output loop, creating a net magnetic flux on L_{loop} that then couples back to the π-loop through the output inductor L_{out}. Hence, when $\alpha_N \neq 0$, there is a back-action effect when a current through the DC-SQUID terminals is applied. Since the junctions are non-linear elements, the back-coupled flux depends on the measurement current, achieving a maximum as $I_\pm$ approaches the SQUID I_C. Moreover, the sign of the back-coupled flux also depends on the direction of the external current.

It can be thus concluded that when asymmetry is present in the junctions of the output loop, there is an effective magnetic flux coupled back to the π-loop as the measurement current $I_\pm$ across the DC-SQUID terminals is ramped towards its I_C. In the first approximation, one may take into account this back-coupled flux as an $I_\pm$-dependent bias added to Φ_{out} in the π-loop transfer characteristic. Equivalently, one may also imagine that regular cosine-shaped $I_C(\Phi)$ modulation pattern of the DC-SQUID shifts to the left or right on the Φ axis, depending whether the measurement current $I_\pm$ is positive or negative (use Figure 6.2 as a reference).

Hence, the modulation pattern will be affected such that the peaks will not longer be found at $\Phi_{\text{ext}} = n \cdot \Phi_0$ as the output flux is not zero at those positions but equal to the back-coupled flux bias. However, the more remarkable change in the modulation pattern as compared to the one for $\alpha_N = 0$ will be found in the depth of the valleys: they will be not equal on each side of a peak as the constant bias makes the signal swing in Φ_{out} not centered around $\Phi_{\text{out}} = 0$.

Another interesting change vs. the situation $\alpha_N = 0$ is that the I_{C+} and I_{C-} of the DC-SQUID will be different as the sign of the back-coupled flux inverts when the measurement current through the output terminals $I_\pm$ changes direction.

Figure 6.12 presents I_C modulation patterns for an asymmetry factor $\alpha_N = 0.3$

of the junctions in the output circuit. The pattern for $\alpha_N = -0.3$ is obtained by reflecting the curves from Figure 6.12 along the I_C axis. For lower $|\alpha_N|$, the difference in the depth of the valleys at each side of a peak becomes lower and the pattern converges towards Figure 6.11.

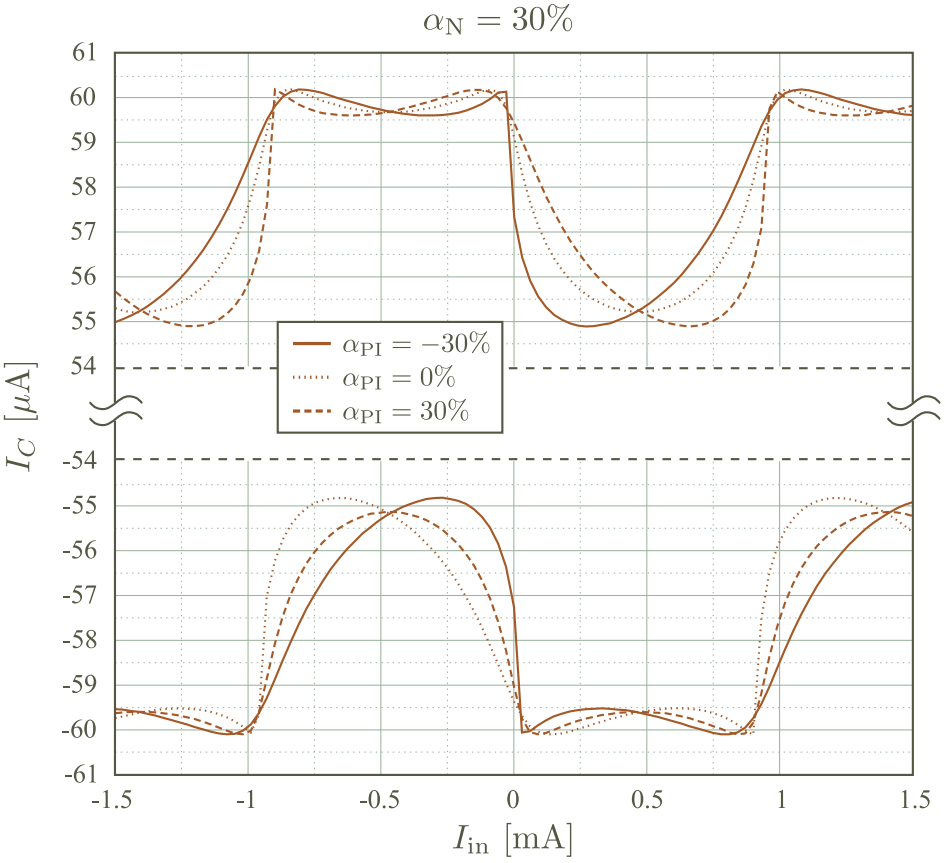

Figure 6.12. Output SQUID I_C modulation pattern of the **π-small** structure for a few π-loop asymmetry factors α_{PI} and for 30% asymmetry in the junctions of the output loop. Same as before, $\Phi_{ext} = M \cdot I_{in}$ where $M = 2.21$pH. Note that the pattern above is symmetric across the origin of the data.

One can see both signatures of asymmetry in the plot above: π-loop asymmetry results in alternating sharp/smooth peaks and valley positions that are not halfway between the peaks while an output loop asymmetry results in depth differences of the valleys as well as in peak positions deviating away from $I_{in} = \frac{n \cdot \Phi_o}{M}$ ($\Phi_{ext} = n\,\Phi_0$).

A third effect that one must take into account during the analysis of the mea-

sured data is the difference in inductance between the left and right arm in both of the superconducting loops of the test structure. This type of loop asymmetry is usually not influencing the operation of the static π-shift circuits but, as shown below, it has an impact in this particular test circuit.

Calculations show that a small difference in self-inductance between the left and right arms in an inductively-modulated (π)-loop does not in itself produce a large effect on the shape of the transfer characteristic. Nevertheless, the associated difference in mutual inductances and hence difference in the external flux coupled to each of the arms does impact the circuit's operation at high input signals. The mechanism responsible for this effect is explained in the drawing of Figure 6.13 below.

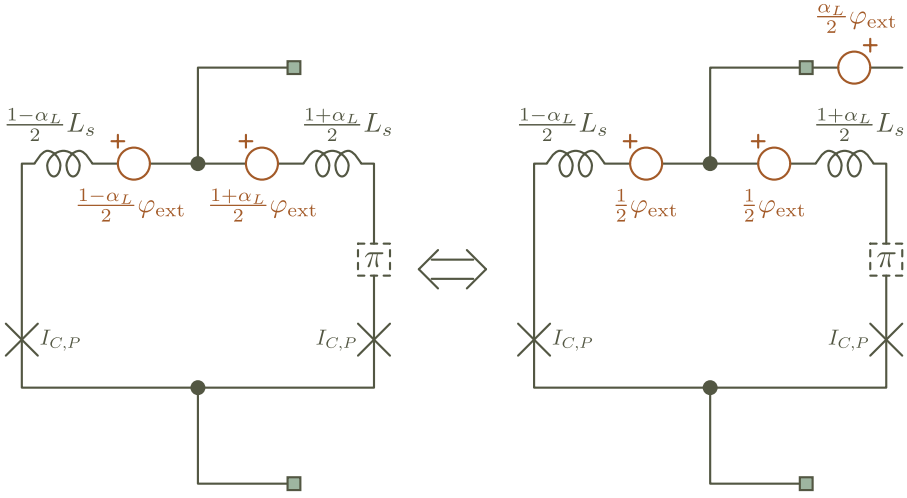

Figure 6.13. A schematic drawing of a modulated (π)-loop with asymmetry α_L between the left and right inductive arms, proportionally resulting in an asymmetry between the externally-coupled flux angle sources in each arm. Shifting the α_L-dependent part of one of the flux angle sources through their common node results in the equivalent schematic shown on the right. There, $\varphi_{\text{ext}} = \frac{2\pi}{\Phi_0}\Phi_{\text{ext}}$ is symmetrically distributed between the arms but an extra flux angle source $\frac{\alpha_L}{2}\varphi_{\text{ext}}$ must be placed in series with the output.

As the Figure above shows, if there is inductance asymmetry α_L between the loop's arms, one may keep the externally applied flux distributed evenly between the arms but must add an extra source $\frac{\alpha_L}{2} \cdot \frac{2\pi}{\Phi_0}\Phi_{\text{ext}}$ in series with the output.

Note that α_L is typically just a couple of percent in practice and, since the signal amplitudes in the static circuits are never greater than approximately $100\text{m}\Phi_0$, the series flux source at the output is never greater than about $1\text{m}\Phi_0$ (or $2\pi \cdot 10^{-3}$ in flux-angle units). One can safely ignore an effect of this amplitude. The remaining asymmetry lies only in the self-inductance of the loop's arms but it does not produce a large effect in the transfer characteristic. However,

the flux externally coupled to the π-loop in the test circuits is typically swept across several Φ_0: the asymmetry component $\frac{\alpha_L}{2} \cdot \frac{2\pi}{\Phi_0} \Phi_{\text{ext}}$ can then be significant.

Hence, in the case of our test structure, inductance asymmetry $\alpha_{L,\text{PI}}$ in the π-loop results in a component added to Φ_{out} that is proportional to the input flux Φ_{ext} and thus input current I_{in}. Equivalently, the transfer characteristic $\Phi_{\text{out}}(\Phi_{\text{ext}})$ is "tilted", as the simulation data in Figure 6.14 below shows.

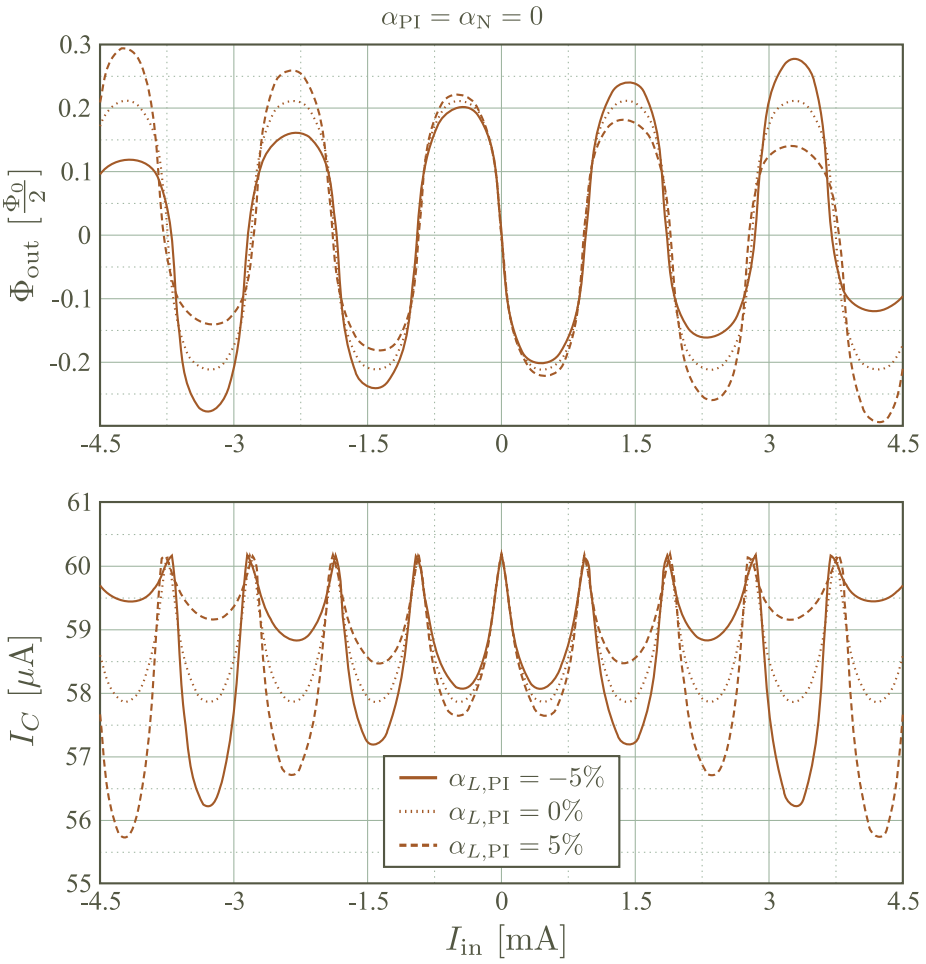

Figure 6.14. Transfer characteristic and SQUID I_C modulation pattern of the **π-small** test structure, for different inductive asymmetry factors $\alpha_{L,\text{PI}}$ in the π-loop. The junctions for both loops in the test structure are taken to be equal, $\alpha_{\text{PI}} = \alpha_N = 0$.

As a result of the linear background in the flux transfer characteristic of the π-loop, on its turn caused by inductive asymmetry $\alpha_{L,\text{PI}}$ in the loop, the I_C

modulation pattern of the output SQUID shows: a) the depth of the valleys is dependent on I_{in} and b) a difference in the depth of the valleys on each side of a peak.

The last distortion b) is very similar to the one caused by asymmetry in the junctions of the output SQUID, see Figure 6.12. The difference is that α_L-caused distortion is dependent on I_{in} and *does not change* when the measurement current is inverted. In other words, were one to measure the I_C of the output SQUID with an opposite measurement current $I_{\pm}$, the pattern as a function of I_{in} will be exactly the same as Figure 6.14 but only inverted, i.e. only x-axis reflection. This is a major difference with the effect of asymmetry in the output SQUID junctions where an inversion in the measurement current produces a pattern that is reflected through the origin. This is useful in order to estimate the strength of both effects during the analysis of measured data.

Note that inductance asymmetry $\alpha_{L,N}$ between the arms of the output SQUID produces almost exactly the same effect as junction asymmetry in the same device (through flux back-action). Hence, when $\alpha_{L,N} \neq 0$, the I_C modulation pattern will be very similar to 6.12.

Below, the impact all the effects on the output I_C modulation data is summarized:

- α_{PI}: asymmetry in the junctions of the π-loop
  - alternating sharp/smooth peak periodicity
  - valley position is not half-way between two peaks

- α_N: asymmetry in the junctions of the output SQUID
  - peak position is not at external flux of integer multiples of Φ_0
  - unequal valley depth on each side of a peak
  - inversion of the measurement current reflects the $I_C(I_{\text{in}})$ modulation pattern across the origin and not across the $x-$axis

- $\alpha_{L,\text{PI}}$: asymmetry in the inductance between the π-loop left/right arms
  - unequal valley depth on each side of a peak
  - the pattern has an approximately linear I_{in} component

- $\alpha_{L,N}$: asymmetry in the inductance between the output loop arms
  - approximately the same impact as α_N above

All of the above effects influence the measured data in a different measure. By a quantitative analysis of the $I_C(I_{\text{in}})$ data, one can perform a fit to theory (simulation) and indirectly validate the flux-transfer properties of a modulated π-loop. Nevertheless, using the above points, one can also make a qualitative estimation of the strength of each effect in the measured data and try to extract

only the signature of an amplifier-like $\Phi_{\text{out}}(\Phi_{\text{ext}})$: periodic sharp peaks and shallow valleys in the I_C modulation pattern.

For reference purposes, the transfer characteristic and I_C modulation pattern of the **n-small** test structure is given below for a few values of the junction asymmetry factor of the modulated normal loop α_{nPI}. A signature of the transfer characteristic of a modulated *normal* loop is the low slope $\frac{\partial \Phi_{\text{out}}}{\partial \Phi_{\text{ext}}}$ at the zero-crossings of Φ_{out} and the relatively high slope at large $|\Phi_{\text{out}}|$. This results in a distinct I_C modulation pattern containing a two-level structure. The other two asymmetry effects have similar impact as for a modulated π-loop.

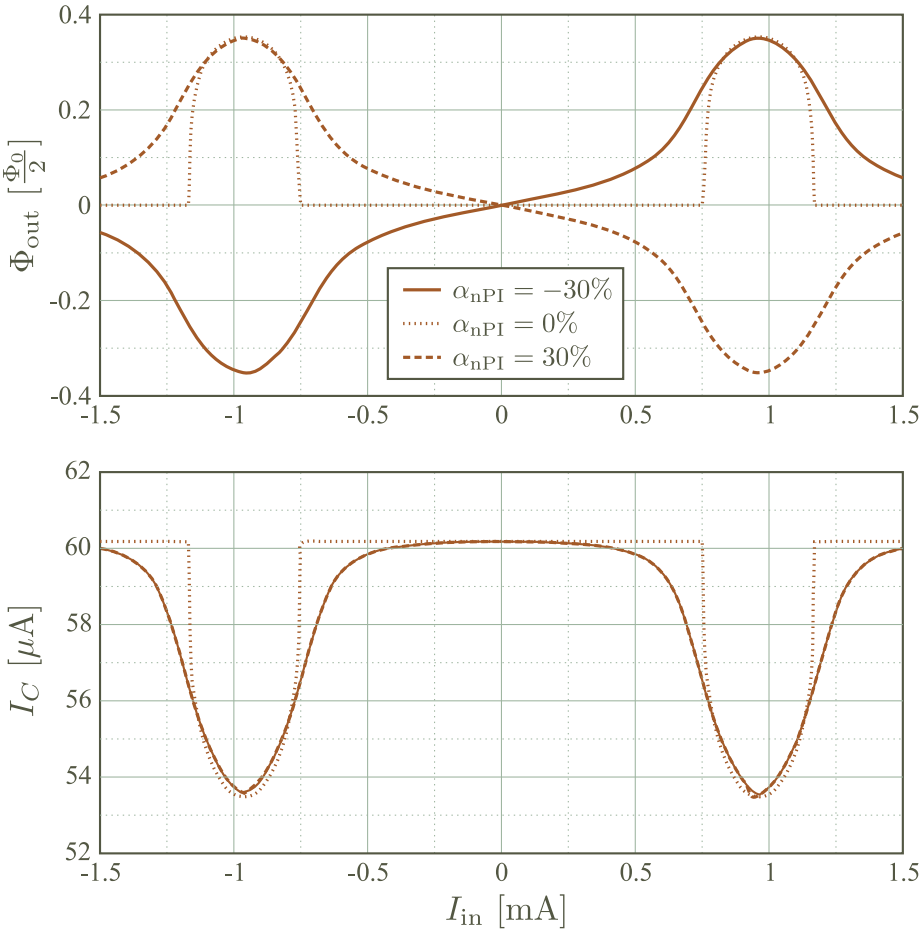

Figure 6.15. Transfer characteristic and I_C modulation pattern of the **n-small** test structure for a few values of the junction asymmetry factor α_{nPI} in the modulated loop.

6.2 Measurement data

This section presents the analysis of the data obtained from the measurement of several manufactured samples containing the circuits described from the previous sections.

A brief description of the measurement method is first given, together with a diagram of the measurement setup. Next, selected measurement data is presented for each of the test circuits.

6.2.1 Measurement system

A diagram of the measurement system is given in Figure 6.16. The signal sources are obtained from Digital-to-Analog-Converter (DAC) instruments while the signal readout is performed with instruments based on high precision ADCs. The analog amplifier has ultra-low noise ($\sim 6\frac{\mathrm{nV}}{\sqrt{\mathrm{Hz}}}$ noise floor) and is battery powered. It is the only component that is not centrally controlled by the measurement application software.

The goal of the measurement method is to find the critical current of the output DC-SQUID as a function of the applied current I_{in}. The measurement procedure will then need to be iterative: sweep the input current I_{in} between two values (of opposite sign) by small increments and measure I_C at each iteration.

The measurement of the critical current of the output SQUID is performed by detecting the onset of its voltage state as the measurement current $I_{\pm}$ is changed between zero and a value beyond the estimated SQUID maximum I_C (i.e. $2 \cdot I_{C,N}$). When the voltage $V_{\pm}$ across the SQUID terminals rises above a small threshold value, usually 30μV, a trigger is generated in the measurement software to save the momentary value of the measurement current $I_{\pm}$ and terminate the present step. A data point for I_C has then been obtained.

Next, $I_{\pm}$ is set to zero for a small period of time while the system measures the average voltage across the SQUID terminals. This average value is then added to the nominal detection threshold for the next I_C measurement step. The goal of this "auto-zero" technique is to eliminate drift and low-frequency ($\frac{1}{f}$) noise from the measurement results.

Again, $I_{\pm}$ is incremented from zero towards a value beyond the projected maximum I_C. When $V_{\pm}$ becomes greater than the (modified) threshold, the momentary value of $I_{\pm}$ is saved and a new data point for I_C is added. After a new "auto-zero" period, the I_C measurement is performed again. The above process is repeated until approximately 100 data points are gathered. One can now calculate the average I_C, as well as a max/min and standard deviation values at the given input current I_{in}.

After incrementing I_{in} to a new value, the above procedure is again iterated and a new set of I_C statistics is measured.

At the end, the measurement data for $I_{C,\text{mean}}(I_{\text{in}})$, $I_{C,\text{max}}(I_{\text{in}})$, $I_{C,\text{min}}(I_{\text{in}})$ and $I_{C,\sigma}(I_{\text{in}})$ are obtained per test structure on each manufactured sample.

The measurement is performed in a bath cryostat at 4.2K with both a high-T_c and low-T_c shields enveloping the sample assembly.

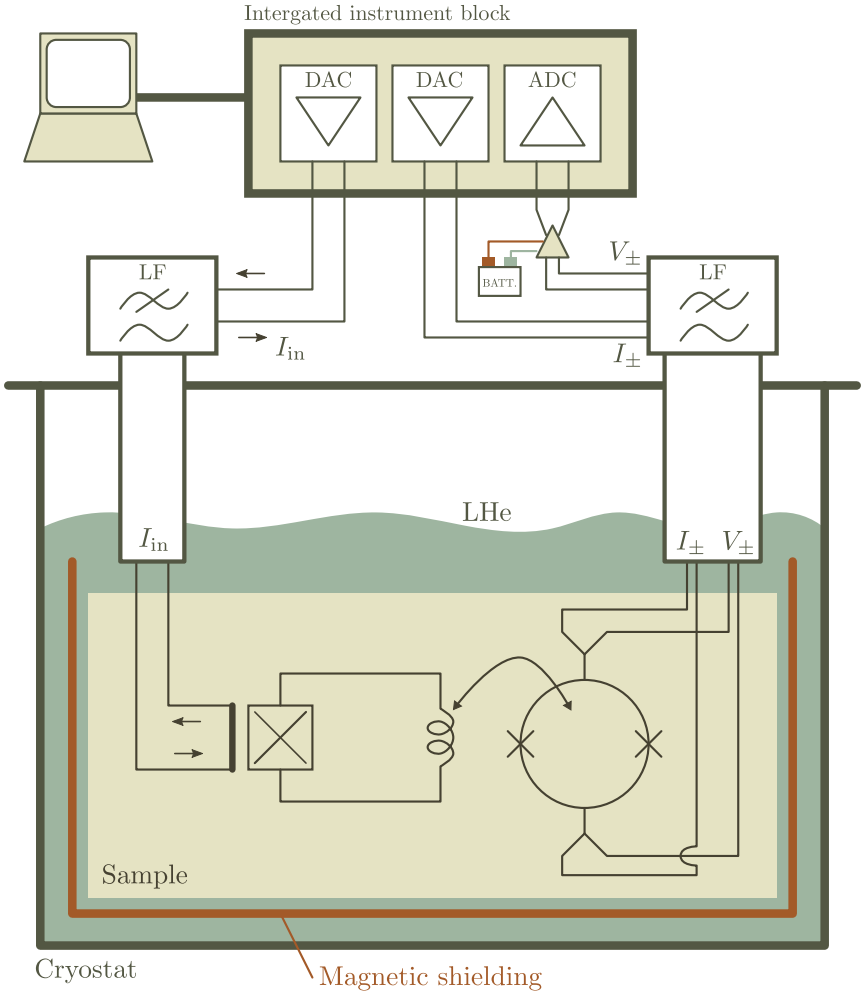

Figure 6.16. A diagram of the measurement system together with the bath cryostat.

6.2.2 Data selection and comparison with simulation

Not all of the data sets could be used for analysis as some of the circuits had manufacturing faults while many suffered from flux-capturing and other parasitic phenomena such as direct (galvanic) I_C modulation through short-circuit defects. Almost all of the $I_C(I_{\text{in}})$ curves contained evidence for substantial offset in the I_{in} coordinate, indicating flux-bias effects from locally captured fluxons or direct magnetic coupling between the input current leads and the output SQUID loop.

The data sets where the period ΔI_{in} in the $I_C(I_{\text{in}})$ modulation pattern was far from $\frac{2\,\Phi_0}{M}$, with M the mutual input coupling obtained by EM analysis of the structure under test (see Table 6.2), were discarded. Sets where the output SQUID I_C swings around a value far outside the one projected (nominal 60μA) from I_C-spread measurements of the same sample were also not analysed. Additionally, the data where the general shape of the modulation pattern could not be approached by introducing the expected circuit non-idealities (asymmetry in the junctions and loop inductances) were excluded as well. Nevertheless, these sets can be of use if the simulation models are further refined.

6.2.2.1 Data sets *π-small*

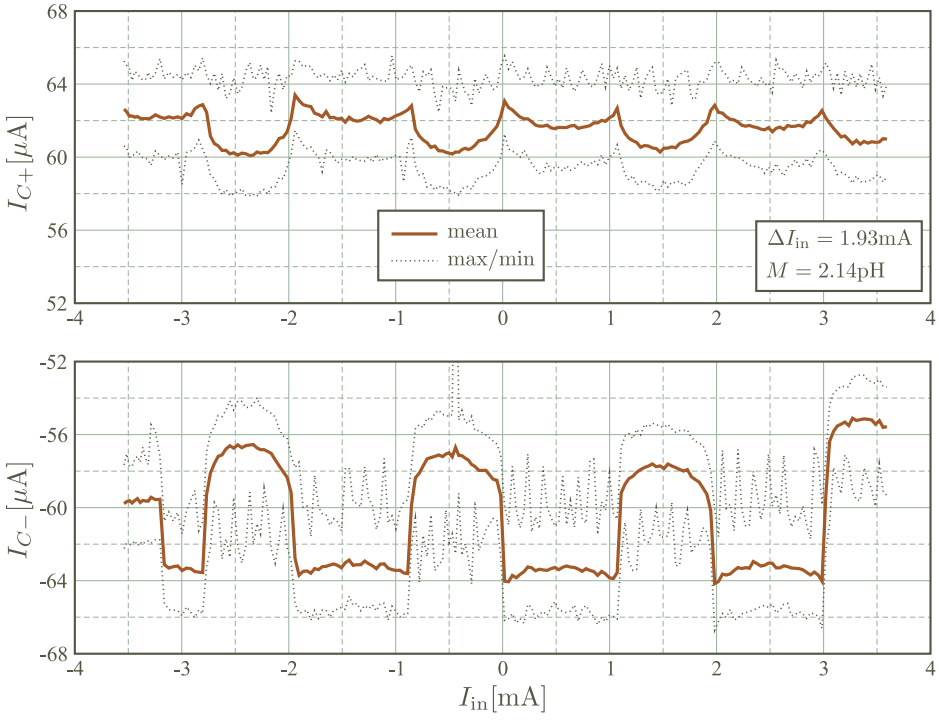

Figure 6.17. Output SQUID I_C modulation pattern for the **π-small** circuit obtained from the sample SCAL1.1.

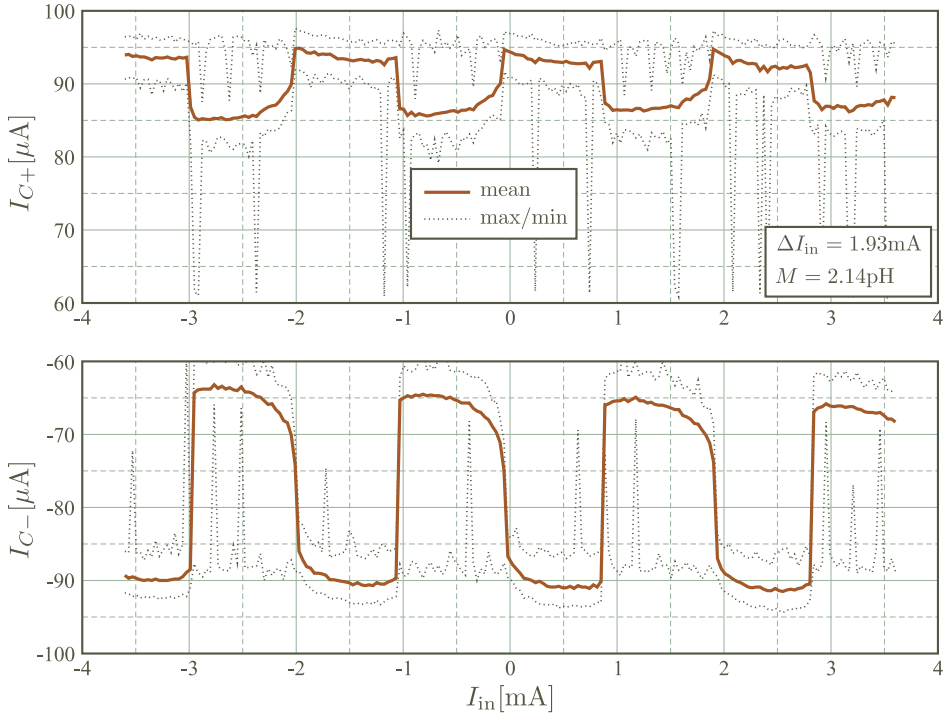

Figure 6.18. Output SQUID I_C modulation pattern for the **π-small** circuit obtained from the sample SCAL1.2.

The modulation patterns from Figures 6.17 & 6.18 exhibit the typical signatures of an amplifier-like $\Phi_{out}(\Phi_{ext})$ characteristic - (sharp) peaks and valleys - along with a few of the expected asymmetry effects as well as some features that were not previously modelled. First, the general properties of the two data sets are discussed and later the shape of the modulation patterns is analysed.

It is seen that the output SQUID I_C from the test circuit of the sample SCAL1.1 (Figure 6.17) is very close to the nominal value of 60μA. This match is also supported by the separate I_C spread measurements performed on junction arrays at the same sample (see Table 4.2), where the measured average J_C

of $18\frac{\mu A}{\mu m}$ is close to the nominal value of $12\frac{\mu A}{\mu m}$. Another important match with nominal values is the mutual inductance: the modulation period ΔI_{in} indicates that $M = \frac{2\,\Phi_0}{\Delta I_{in}} = 2.14$pH while the value from EM analysis $M = 2.21$pH (Table 6.2).

The plot in Figure 6.18 on the other hand, corresponding to a test circuit from the different sample SCAL1.2, shows an I_C of the output SQUID that is larger that the nominal value. Such a deviation is expected if one also takes into account I_C spread measurements on the sample: the average measured J_C is $36\frac{\mu A}{\mu m}$, much higher than the nominal $12\frac{\mu A}{\mu m}$. Interestingly, the measured M is exactly the same with the one for the sample SCAL1.1: as the thin films of the two samples were grown in parallel during the manufacturing, one would expect that their electrical properties are the same as well.

In Figure 6.17, one can conclude that there is little junction asymmetry α_{PI} in the π-loop since all peaks are equally sharp and, more notably, the position of each valley is almost equidistant to the two neighbouring peaks. Similarly, it can be concluded that there is also little inductance asymmetry $\alpha_{L,PI}$ in the π-loop as the modulation depth hardly changes with I_{in}. The difference in valley depth on each side of a peak can however not be explained with asymmetry in the output SQUID circuit (both junction α_N and loop $\alpha_{L,N}$): the patterns for positive and negative measurement current from the plot in Figure 6.17 do not reflect around the origin but along the x-axis. Additionally, the difference in modulation depth between the I_{C+} and I_{C-} patterns does not follow from any of the mechanisms proposed earlier.

The above effect can however be partly explained by the presence of a DC magnetic field on the sample, effectively adding a flux angle source in series with each inductive segment in the circuit. The extra flux source $\varphi_{DC,out}$ in series with the π-loop output inductor L_{out} will have the most influence on the circuit as the signal amplitude is the lowest there. At the same time, the DC field creates an offset in the input current I_{in}, adding to Φ_{ext} in the input loop.

This constant magnetic field background is probably a consequence of insufficient shielding of the sample or from trapped flux in the superconducting materials on and in the vicinity of the sample.

In Figure 6.19, a simulated modulation pattern is shown of the circuit including an extra flux angle source of $70\text{m}\pi$ in series with L_{out} (corresponding to a DC flux bias of about $35\text{m}\Phi_0$). The input current swing is not centered on zero in order to account for any offset in I_{in}. This pattern approximates the measured data from Figure 6.17.

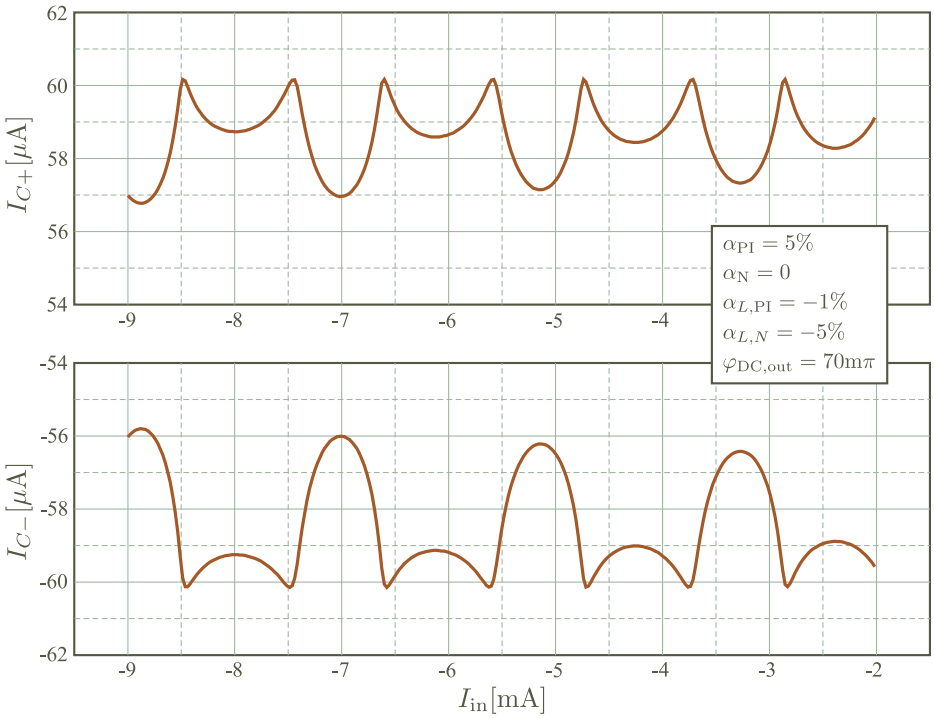

Figure 6.19. A simulated modulation pattern that approximates some features of the the measured data presented in Figure 6.17.

The measured data from Figure 6.18 is more difficult to compare with simulation since the parasitic effect of a constant background field seems to be very prominent and hence difficult to model (every inductive segment needs a series flux angle source). Further, the asymmetry in the junctions of the π-loop is seen to be quite large. Since the I_C is estimated about 50% higher than the nominal, making the normalized inductances proportionally higher as well, one may conclude that the π-device operates in the hysteretic regime (see Figure 6.3). Nevertheless, although the data set from Figure 6.18 does not lend itself to a more quantitative fit, the upper (I_{C+}) pattern still offers evidence of a flux transfer characteristic with the desired properties.

6.2.2.2 Data sets *π-big*

In Figures 6.20 and 6.21, two data sets of the **π-big** test circuit measured on two separate samples are presented. These are selected from a larger collection of data sets showing eligible modulation patterns by looking for the ones that are least impacted by parasitic effects such as a background DC magnetic field.

The quantities measured on the two samples are closely matched with the nominal values, except for the critical current of the output SQUID in SCAL1.1 (Figure 6.20). The mutual coupling inductance at the input of both circuits is just a few percent off the nominal $M = 3.69\text{pH}$, again confirming the results of the EM inductance extraction. The I_C of the output SQUID in the test circuit on the sample SCAL1.2 is almost an exact match with the nominal value of $60\mu\text{A}$, while the same value in the test circuit of SCAL1.1 is about half of nominal.

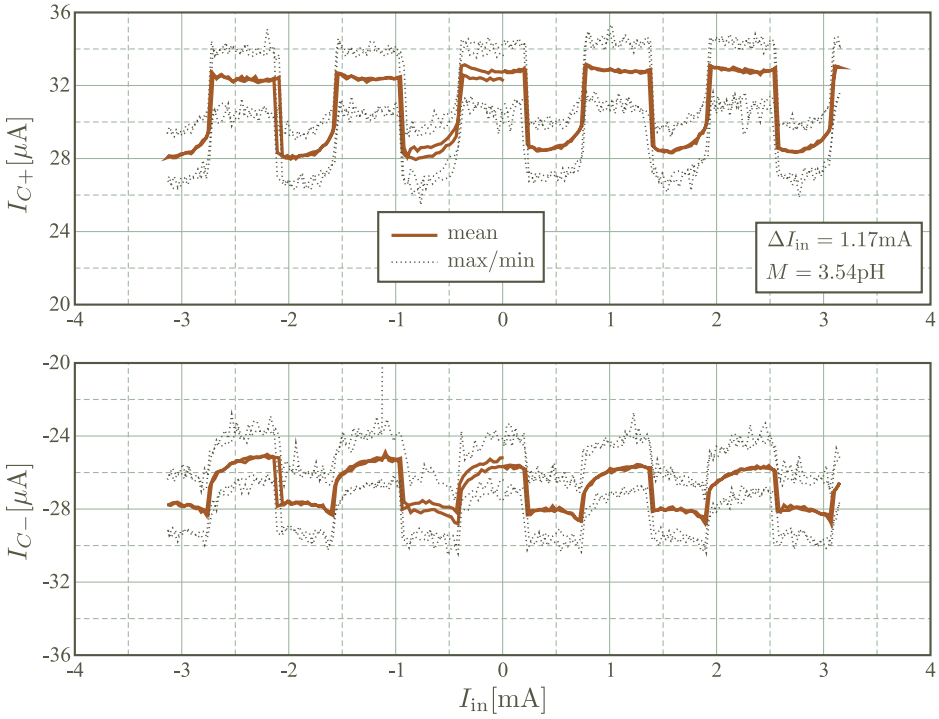

Figure 6.20. Output SQUID I_C modulation pattern for the **π-big** circuit obtained from the sample SCAL1.1.

Both patterns are similar, showing a rather large asymmetry in the output loop junctions, α_N, and in the input π-loop junctions, α_{PI}. Additionally, there is a difference in the modulation depth of the patterns for a positive and for a negative measurement current. Just as before, this indicates a constant DC field that is inducing a flux source in series with each inductive segment.

The effect of asymmetry in the inductances of the π-loop is more prominent for the pattern in Figure 6.21 (sample SCAL1.2) since the modulation depth is more sensitive to the amplitude of I_{in}. The pattern in Figure 6.20 (SCAL1.1) on the other hand offers a less clear structure of peaks and valleys characteristic for a modulated π-loop. It is therefore more difficult to attempt a simulation that fits the pattern in Figure 6.20. Hence, only the pattern shown in Figure 6.21 an approximate fit was produced. The result is given in Figure 6.22.

Although not particularly successful, the simulation results of the test circuit shown in Figure 6.22 can be still further refined towards a better match with the measured pattern. Nevertheless, this process is highly complex as there are five fitting parameters while it is doubtful whether also a highly quantitative likeness between the measured data and the simulation can be achieved with the abundance of parasitic phenomena present on the tested samples.

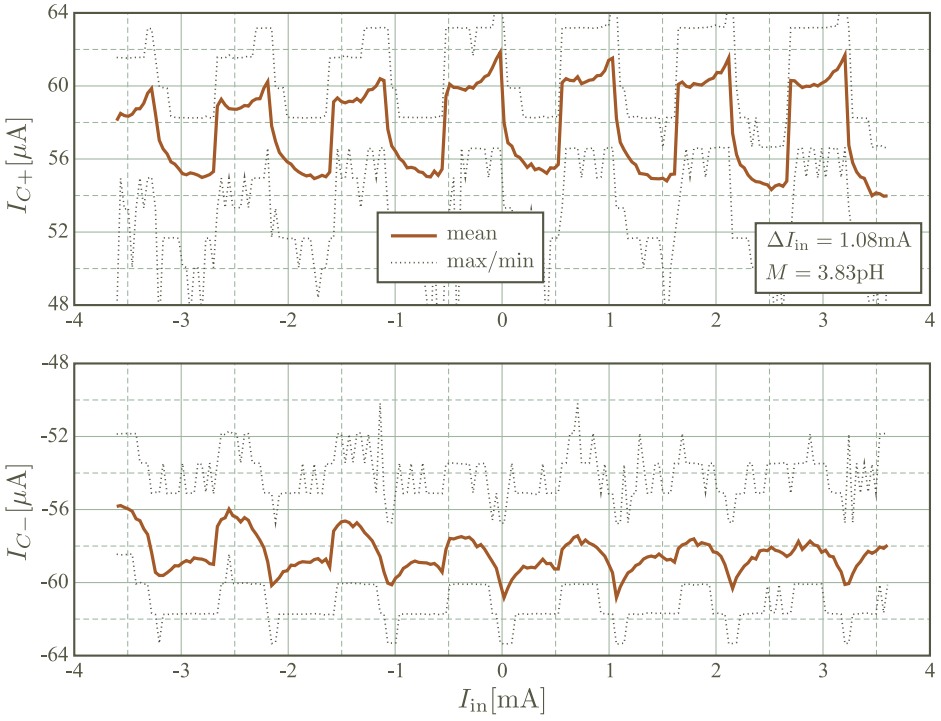

Figure 6.21. Output SQUID I_C modulation pattern for the **π-big** circuit obtained from the sample SCAL1.2.

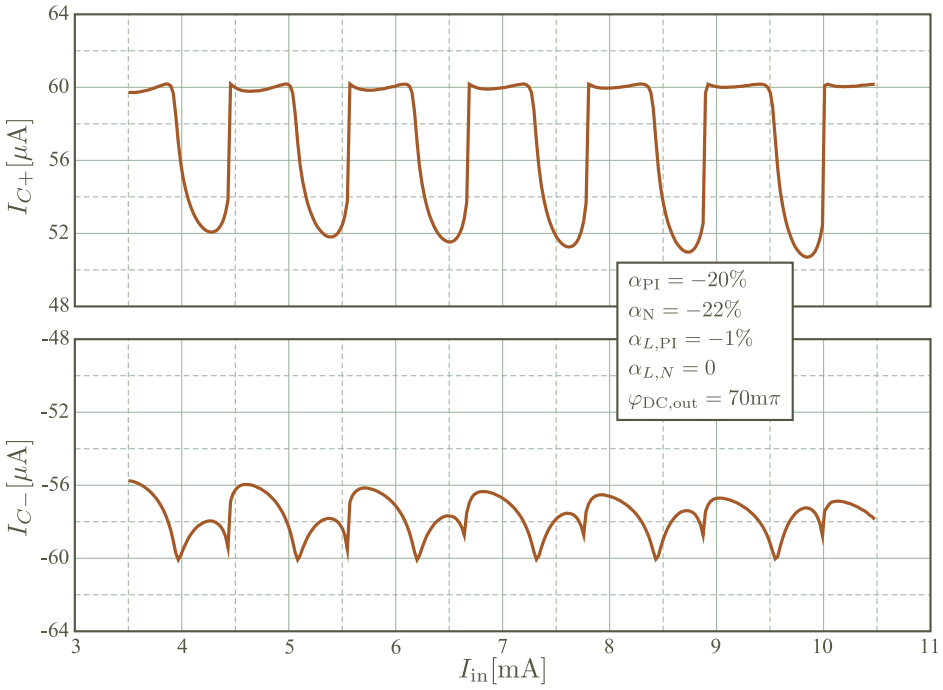

Figure 6.22. A simulated modulation pattern that approximates the measured modulation pattern from Figure 6.21.

6.2.2.3 Data sets of tests circuits with normal loops

In the following few Figures, modulation patterns obtained from the test circuits with modulated normal loops are presented. The data sets generally follow the shape of the expected modulation patterns, as for instance given in Figure 6.15.

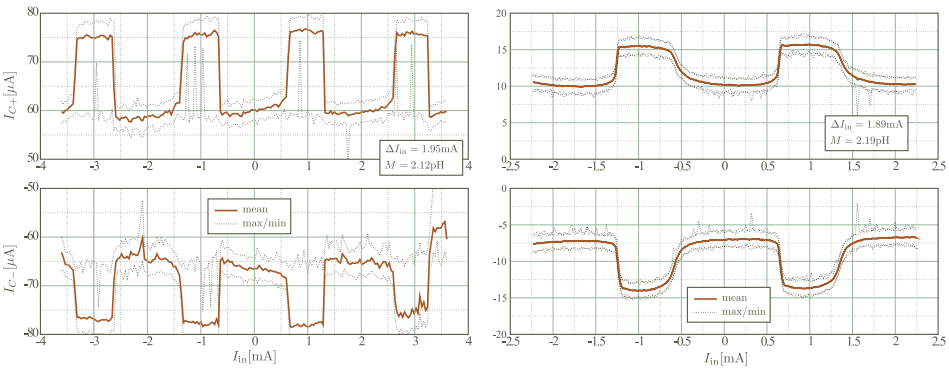

Figure 6.23. Output SQUID I_C modulation pattern for the **n-small** circuit from samples SCAL1.1 (left) and SCAL2.1 (right).

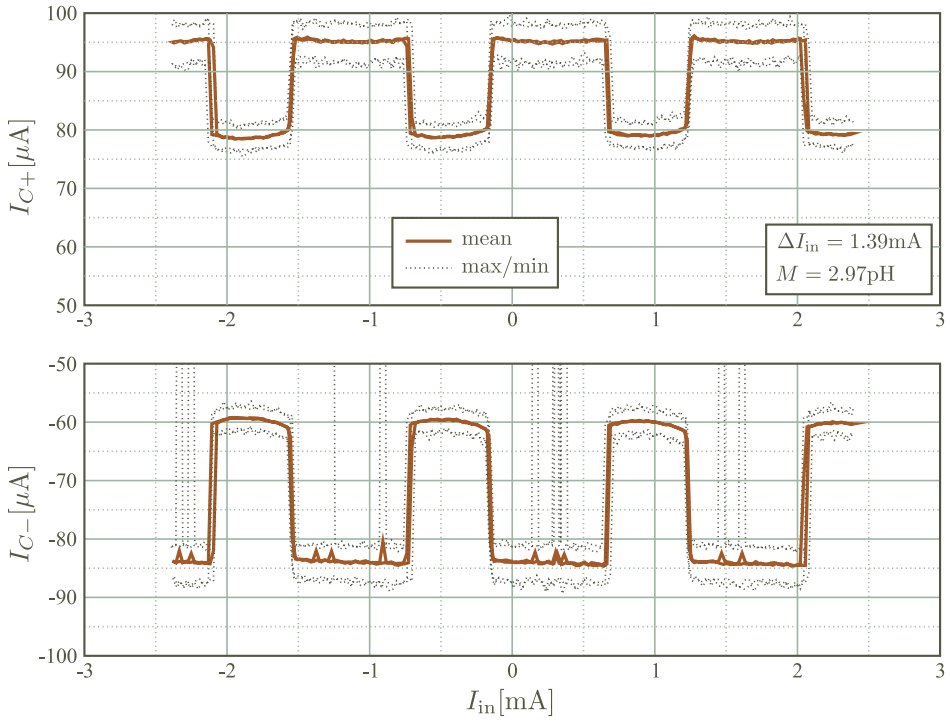

Figure 6.24. Output SQUID I_C modulation pattern for the **n-big** circuit from sample SCAL1.2.

Note that none of the selected plots above show a peak-valley structure in the modulation pattern - the signature of a smooth amplifier-like transfer curve - but rather an "on"/"off" behaviour that is consistent with a $\Phi_{\rm out}(\Phi_{\rm ext})$ transfer curve that swings between two approximately constant $\Phi_{\rm out}$ levels as a function of $\Phi_{\rm ext}$.

6.2.3 Measurement summary

The obtained modulation data from the circuits is, generally, in agreement with the patterns expected from circuit simulation, if also circuit asymmetry is taken into account. The measured curves can be further approached by simulation if the device models are refined to include some additional effects, like for instance a magnetic background field.

A highly quantitative fit of simulation to data is difficult due to the presence of various parasitic phenomena necessitating complex device models, resulting in too many fitting parameters. One needs to reduce both manufacturing errors and process variation in order to build such models reliably. The above is valid for any superconducting device in the YBCO/Nb process technology, including RSFQ circuits as well.

The most striking match between modelling and experiment lies in the accuracy of the EM inductance extraction method introduced in Chapter 2, Section 2.3. Comparing the marked values in the above data sets with Table 6.2, it seen that even though the critical currents of the devices vary considerably on- as well as between samples, the mutual inductance directly obtained from the modulation period is very consistent with the EM model of the superconducting films. This fact is further confirmed by conventional SQUID modulation measurements, for instance the plot in Figure 6.25 below, where the measured parameters are also very close to the ones obtained by EM simulation.

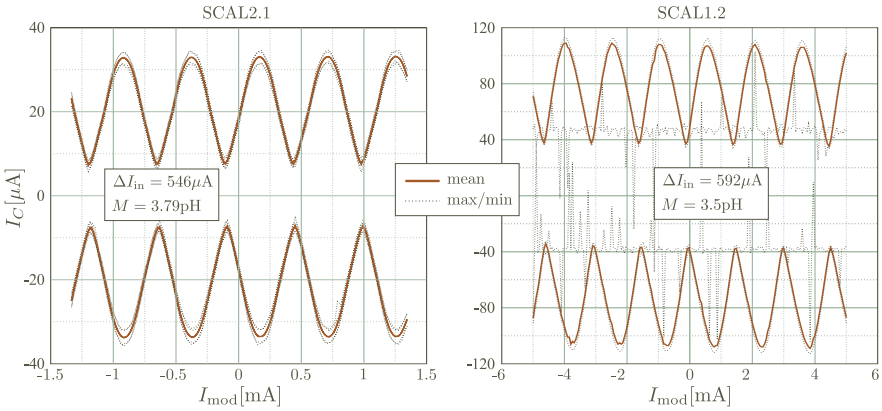

Figure 6.25. The I_C of an inductively-modulated coupled π-loop of dimensions identical to the one used in the **π-big** test circuits .

At the end, the following conclusions can be made from the analysis of the measurement data:

- a flux-modulated π-loop exhibits an amplifier-like transfer characteristic $\Phi_{out}(\Phi_{ext})$
- a flux-modulated normal loop has a transfer characteristic that is different in shape - it is thus not just a translation along the Φ_{ext} axis
- EM simulation using a 2D surface-inductance model for thin-film circuits is accurate even when used for structures comprising of both high-T_c and low-T_c materials

Bibliography

[1] J. R. Kirtley, C. C. Tsuei, A. Ariando, C. J. M. Verwijs, S. Harkema, and H. Hilgenkamp, "Angle-resolved phase-sensitive determination of the in-plane gap symmetry in $YBa_2Cu_3O_{7-\delta}$," *Nature Physics*, vol. 2, no. 3, pp. 190–194, 2006.

[2] P. Bunyk, K. Likharev, and D. Zinoviev, "RSFQ Technology: Physics and Devices," *International Journal of High Speed Electronics and Systems*, vol. 11, no. 1, pp. 257–305, 2001.

[3] T. Ortlepp, Ariando, O. Mielke, C. J. M. Verwijs, K. F. K. Foo, A. Andreski, H. Rogalla, F. H. Uhlmann, and H. Hilgenkamp, "RSFQ circuitry using intrinsic pi-phase shifts," *IEEE Transactions on Applied Superconductivity*, vol. 17, no. 2, Part 1, pp. 659–663, 2007.

[4] O. Mielke, T. Ortlepp, B. Dimov, and F. H. Uhlmann, "Phase engineering techniques in superconducting quantum electronics," *Journal of Physics: Conference Series*, vol. 97, no. 1, 2008.

[5] H.-J. Smilde, *Josephson Contacts Between High-T_c And Low-T_c Superconductors*. PhD thesis, University of Twente, 2001.

[6] H. J. H. Smilde, Ariando, H. Rogalla, and H. Hilgenkamp, "Bistable superconducting quantum interference device with built-in switchable $\pi/2$ phase shift," *Applied Physics Letters*, vol. 85, no. 18, pp. 4091–4093, 2004.

[7] H. J. H. Smilde, Ariando, D. H. A. Blank, H. Hilgenkamp, and H. Rogalla, "π-SQUIDs based on Josephson contacts between high-Tc and low-Tc superconductors," *Physical Review B*, vol. 70, no. 2, 2004.

[8] T. Ortlepp, Ariando, O. Mielke, C. J. M. Verwijs, K. F. K. Foo, H. Rogalla, F. Uhlmann, and H. Hilgenkamp, "Flip-flopping fractional flux quanta," *Science*, vol. 312, no. 5779, pp. 1495–1497, 2006.

[9] J. E. Mooij, T. P. Orlando, L. Levitov, L. Tian, C. H. van der Wal, and S. Lloyd, "Josephson Persistent-Current Qubit," *Science*, vol. 285, no. 5430, pp. 1036–1039, 1999.

[10] L. B. Ioffe, V. B. Geshkenbeln, M. V. Felgel'man, A. L. Fauchére, and G. Blatter, "Environmentally decoupled sds-wave josephson junctions for quantum computing," *Nature*, vol. 398, no. 6729, pp. 679–681, 1999.

[11] K. K. Likharev, *Dynamics of Josephson Junctions and Circuits*. New York: Gordon and Breach, 1986.

[12] A. Barone and G. Paternò, *Physics and applications of the Josephson effect*. New York: Wiley, 1982.

[13] T. van Duzer and C. W. Turner, *Principles of Superconducting Devices and Circuits*. Prentice Hall, 2 ed., 1991.

[14] T. P. Orlando and K. A. Delin, *Foundations of Applied Superconductivity*. New York: Addison-Wesley, 1991.

[15] A. M. Kadin, *Introduction to Superconducting Circuits*. New York: Wiley, 1999.

[16] J. Clarke and A. I. Braginski, *Fundamentals and Technology of SQUIDs and SQUID Systems*, vol. 1 of *The SQUID Handbook*. New York: Wiley, 2004.

[17] W. Hioe and G. Eiichi, *Quantum flux parametron: a single quantum flux superconducting logic device*. Singapore: World Scientific, 1991.

[18] Y. Harada, W. Hioe, and E. Goto, "Flux-Transfer Devices," *Proceedings of the IEEE*, vol. 77, pp. 1280–1286, Aug 1989.

[19] S.-A. Zhou, *Electrodynamics of Solids and Microwave Superconductivity*. Wiley Series in Microwave and Optical Engineering, New York: Wiley-Interscience, 1999.

[20] J. R. Kirtley, C. C. Tsuei, Ariando, H. J. H. Smilde, and H. Hilgenkamp, "Antiferromagnetic ordering in arrays of superconducting π -rings," *Physical Review B*, vol. 72, p. 214521, Dec 2005.

[21] Ariando, *Josephson Junction Arrays with d-wave-induced π-phase-shifts*. PhD thesis, University of Twente, 2005.

[22] D. R. Moorcroft, "Faraday's law—demonstration of a teaser," *American Journal of Physics*, vol. 37, no. 2, pp. 221–221, 1969.

[23] W. Klein, "Experimental "paradox" in electrodynamics," *American Journal of Physics*, vol. 49, no. 6, pp. 603–604, 1981.

[24] F. Reif, "Generalized ohm's law, potential difference, and voltage measurements," *American Journal of Physics*, vol. 50, no. 11, pp. 1048–1049, 1982.

[25] R. H. Romer, "What do "voltmeters" measure?: Faraday's law in a multiply connected region," *American Journal of Physics*, vol. 50, no. 12, pp. 1089–1093, 1982.

[26] S. Ramo, J. R. Whinnery, and T. Van Duzer, *Fields and Waves in Communication Electronics*. New York: Wiley, 3 ed., 1994.

[27] E. B. Rosa, "The self and mutual inductance of linear conductors," *Bulletin of the National Bureau of Standards*, vol. 4, no. 2, pp. 301–344, 1908.

[28] F. W. Grover, *Inductance Calculations: Working Formulas and Tables*. New York: Dover Publications, 1964.

[29] A. Ruehli, "Inductance calculations in a complex integrated circuit environment," *IBM Journal of Resesearch and Development*, vol. 16, pp. 470–481, September 1972.

[30] A. Ruehli, "Equivalent circuit models for three-dimensional multiconductor systems," *IEEE Transactions on Microwave Theory and Techniques*, vol. 22, pp. 216 – 221, Mar. 1974.

[31] H. Kleinert, *Multivalued fields in condensed matter, electromagnetism, and gravitation*. Singapore: World Scientific, 2008.

[32] B. D. Josephson, "Possible new effects in superconductive tunnelling," *Physics Letters*, vol. 1, no. 7, pp. 251 – 253, 1962.

[33] T. Ortlepp and F. Uhlmann, "Technology related timing jitter in superconducting electronics," *IEEE Transactions on Applied Superconductivity*, vol. 17, no. 2, pp. 534 –537, 2007.

[34] W. Chen, A. Rylyakov, V. Patel, J. Lukens, and K. Likharev, "Rapid single flux quantum T-flip flop operating up to 770 GHz," *IEEE Transactions on Applied Superconductivity*, vol. 9, pp. 3212 –3215, June 1999.

[35] A. Fujimaki, M. Tanaka, T. Yamada, Y. Yamanashi, H. Park, and N. Yoshikawa, "Bit-Serial Single Flux Quantum Microprocessor CORE," *IEICE Transactions on Electronics*, vol. 91, no. 3, pp. 342–349, 2008.

[36] C. Verwijs, *Fractional Flux Quanta in High-T_c/Low-T_c Superconducting Structures*. PhD thesis, University of Twente, 2009.

[37] H. Hilgenkamp, "Pi-phase shift Josephson Structures," *Superconductor Science & Technology*, vol. 21, no. 3, 2008.

[38] J. M. Jaycox and M. B. Ketchen, "Planar coupling scheme for ultra low noise dc squids.," *IEEE Transactions on Magnetics*, vol. MAG-17, no. 1, pp. 400–403, 1980.

[39] A. Kerr, "Surface Impedance of Superconductors and Normal Conductors in EM Simulators," MMA Memo 245, National Radio Astronomy Observatory, 1999.

[40] M. Kamon, M. Tsuk, and J. White, "FastHenry - A Multipole-Accelerated 3-D Inductance Extraction Program," *IEEE Transactions on Microwave Theory and Techniques*, vol. 42, no. 9, Part 2, pp. 1750–1758, 1994.

[41] W. Chang, "Inductance of a Superconducting Strip Transmission-Line," *Journal of Applied Physics*, vol. 50, no. 12, pp. 8129–8134, 1979.

[42] Sonnet Software Inc., "Sonnet em." version 12.52, 2009.

[43] M. Hidaka, S. Nagasawa, K. Hinode, and T. Satoh, "Improvements in fabrication process for Nb-based single flux quantum circuits in Japan," *IEICE Transactions on Electronics*, vol. 91, no. 3, pp. 318–324, 2008.

[44] G. Kerber, A. Kleinsasser, and B. Bumble, "Fabrication of submicrometer high current density Nb/Al-AlN$_x$/ Nb junctions," *IEEE Transactions on Applied Superconductivity*, vol. 19, no. 3, pp. 159–166, 2009.

[45] D. Blank and H. Rogalla, "The effect of ion milling on the morphology of ramp-type josephson junctions," *Journal of Materials Research*, vol. 12, no. 11, pp. 2952–2957, 1997.

[46] B. Ebert, T. Ortlepp, and F. H. Uhlmann, "Experimental study of the effect of flux trapping on the operation of rsfq circuits," *IEEE Transactions on Applied Superconductivity*, vol. 19, no. 3, pp. 607–610, 2009. Cited By (since 1996): 2.

[47] K. Nakajima, H. Mizusawa, H. Sugahara, and Y. Sawada, "Phase mode Josephson computer system," *IEEE Transactions on Applied Superconductivity*, vol. 1, no. 1, pp. 29–36, 1991.

[48] O. A. Mukhanov, V. K. Semenov, W. Li, T. V. Filippov, D. Gupta, A. M. Kadin, D. K. Brock, A. F. Kirichenko, Y. A. Polyakov, and I. V. Vernik, "A superconductor high-resolution ADC," *IEEE Transactions on Applied Superconductivity*, vol. 11, no. 1, pp. 601–606, 2001.

[49] P. Patra, S. Polonsky, and D. S. Fussell, "Delay insensitive logic for RSFQ superconductor technology," *Proceedings of the 3rd International Symposium on Advanced Research in Asynchronous Circuits and Systems*, pp. 42–53, 1997.

[50] M. Maezawa, M. Kurosawa, I. Aoyagi, H. Nakagawa, Y. Kameda, and T. Nanya, "Rapid single-flux-quantum dual-rail logic for asynchronous circuits," *IEEE Transactions on Applied Superconductivity*, vol. 7, no. 2, pp. 2705–2708, 1997.

[51] Z. J. Deng, S. R. Yoshikawa, N. Whiteley, and T. Van Duzer, "Data-driven self-timed RSFQ digital integrated circuit and system," *IEEE Transactions on Applied Superconductivity*, vol. 7, no. 2, pp. 3634–3637, 1997.

[52] K. Likharev, "Dynamics of some single flux quantum devices: I. Parametric quantron," *IEEE Transactions on Magnetics*, vol. 13, no. 1, pp. 242–244, 1977.

[53] K. K. Likharev, S. V. Rylov, and V. K. Semenov, "Reversible conveyer computation in array of parametric quantrons," *IEEE Transactions on Magnetics*, vol. 21, no. 2, pp. 947–950, 1985.

[54] K. Loe and E. Goto, "Analysis of flux input and output Josephson pair device," *IEEE Transactions on Magnetics*, vol. 21, no. 2, pp. 884–887, 1985.

[55] Y. Harada, H. Nakane, N. Miyamoto, U. Kawabe, E. Goto, and T. Soma, "Basic operations of the quantum flux parametron," *IEEE Transactions on Magnetics*, vol. 23, no. 5, pp. 3801–3807, 1987.

[56] E. Terzioglu and M. R. Beasley, "Complementary Josephson junction devices and circuits: a possible new approach to superconducting electronics," *IEEE Transactions on Applied Superconductivity*, vol. 8, no. 2, pp. 48–53, 1998.

[57] V. K. Semenov, G. V. Danilov, and D. V. Averin, "Negative-inductance SQUID as the basic element of reversible Josephson-junction circuits," *IEEE Transactions on Applied Superconductivity*, vol. 13, no. 2, pp. 938–943, 2003.

[58] V. K. Semenov, G. V. Danilov, and D. V. Averin, "Classical and quantum operation modes of the reversible josephson-junction logic circuits," *IEEE Transactions on Applied Superconductivity*, vol. 17, no. 2, pp. 455–461, 2007.

[59] Y. Tarutani, H. Hasegawa, T. Fukazawa, A. Tsukamoto, and K. Takagi, "Investigation of signal isolation and transient characteristics in quantum-flux-parametron (QFP) circuits," *Applied Superconductivity, IEEE Transactions on*, vol. 9, no. 2, pp. 4353–4356, 1999.

[60] M. Hosoya, W. Hioe, J. Casas, R. Kamikawai, Y. Harada, Y. Wada, H. Nakane, R. Suda, and E. Goto, "Quantum flux parametron: a single quantum flux device for Josephson supercomputer," *IEEE Transactions on Applied Superconductivity*, vol. 1, no. 2, pp. 77–89, 1991.

[61] J. Fleischman and T. Van Duzer, "Computer architecture issues in superconductive microprocessors," *Applied Superconductivity, IEEE Transactions on*, vol. 3, no. 1, pp. 2716–2719, 1993.

[62] C. D. Tesche and J. Clarke, "DC SQUID - Noise and optimization," *Journal of Low Temperature Physics*, vol. 29, no. 3-4, pp. 301–331, 1977.

[63] C. C. Tsuei and J. R. Kirtley, "Pairing symmetry in cuprate superconductors," *Reviews of Modern Physics*, vol. 72, no. 4, pp. 969–1016, 2000.

[64] V. V. Ryazanov, V. A. Oboznov, A. Y. Rusanov, A. V. Veretennikov, A. A. Golubov, and J. Aarts, "Coupling of two superconductors through a ferromagnet: Evidence for a π junction," *Physical Review Letters*, vol. 86, no. 11, pp. 2427–2430, 2001.

[65] J. B. Majer, J. R. Butcher, and J. E. Mooij, "Simple phase bias for superconducting circuits," *Applied Physics Letters*, vol. 80, no. 19, pp. 3638–3640, 2002.

[66] E. Goldobin, A. Sterck, T. Gaber, D. Koelle, and R. Kleiner, "Dynamics of semifluxons in Nb long Josephson 0-π junctions," *Physical Review Letters*, vol. 92, no. 5, 2004.

[67] M. B. Ketchen, "Dc squids 1980 - the state of the art.," *IEEE Transactions on Magnetics*, vol. MAG-17, no. 1, pp. 387–394, 1980.

[68] R. L. Fagaly, "Superconducting quantum interference device instruments and applications," *Review of Scientific Instruments*, vol. 77, no. 10, p. 101101, 2006.

[69] R. Landauer, "Irreversibility and heat generation in the computing process," *IBM Journal of Research and Development*, vol. 5, pp. 183 –191, july 1961.

[70] C. H. Bennett, "Logical Reversibility of Computation," *IBM Journal of Research and Development*, vol. 17, pp. 525 –532, nov. 1973.

[71] J. Ladyman, S. Presnell, A. Short, and B. Groisman, "The connection between logical and thermodynamic irreversibility," *Studies In History and Philosophy of Science Part B: Studies In History and Philosophy of Modern Physics*, vol. 38, no. 1, pp. 58 – 79, 2007.

[72] G. Yang, W. N. Hung, X. Song, and M. Perkowski, "Majority-based reversible logic gates," *Theoretical Computer Science*, vol. 334, no. 1-3, pp. 259 – 274, 2005.

Appendix A

The I_C of a direct-injection SQUID as a function of the modulation current

The circuit schematic is given in Figure A.1, together with the nodal and flow variables used in the calculation.

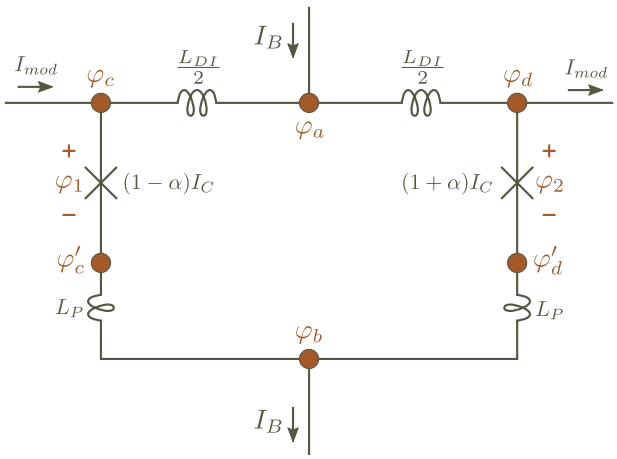

Figure A.1. The circuit schematic of a direct-injection SQUID. The modulation and bias current sources are omitted for clarity but are accounted for in the calculations below. It is assumed that the only circuit asymmetry is in the junction I_C's (which dominates in practical SQUID implementations).

The total Gibb's free energy of the circuit can be constructed from the potential energy definitions of the individual elements (Chapter 2):

$$\frac{E_G}{\frac{\Phi_0 I_C}{2\pi}} = \frac{(\varphi_c-\varphi_a)^2}{\beta_{\mathrm{DI}}} + \frac{(\varphi_a-\varphi_d)^2}{\beta_{\mathrm{DI}}} - (1-\alpha)\cdot\cos(\varphi_1) - (1+\alpha)\cdot\cos(\varphi_2) + \\ + \frac{(\varphi_c-\varphi_1-\varphi_b)^2}{2\beta_{\mathrm{P}}} + \frac{(\varphi_d-\varphi_2-\varphi_b)^2}{2\beta_{\mathrm{P}}} - (\varphi_a-\varphi_b)\cdot i_B - (\varphi_c-\varphi_d)\cdot i_{\mathrm{mod}} \tag{A.1}$$

where it was used

$$\beta_{\mathrm{DI}} = \frac{2\pi \cdot L_{\mathrm{DI}} \cdot I_C}{\Phi_0}$$

$$\beta_{\mathrm{P}} = \frac{2\pi \cdot L_{\mathrm{P}} \cdot I_C}{\Phi_0}$$

$$I_{C1} = (1-\alpha) \cdot I_C$$

$$I_{C2} = (1+\alpha) \cdot I_C$$

$$i_B = \frac{I_B}{I_C}$$

$$i_{\mathrm{mod}} = \frac{I_{\mathrm{mod}}}{I_C}$$

Note that the asymmetry coefficient, as defined above, is always $-1 < \alpha < 1$. The nodal variable substitutions $\varphi_1 = \varphi_c - \varphi_c'$ and $\varphi_2 = \varphi_d - \varphi_d'$ were also performed in order to include the flux angles of the junctions explicitly in the expression for the Gibb's energy A.1.

One can eliminate the nodes φ_a and φ_b by optimizing the Gibb's free energy, i.e. respectively solving for $\frac{\partial E_G}{\partial \varphi_a} = 0$ and $\frac{\partial E_G}{\partial \varphi_b} = 0$:

$$\frac{\partial E_G}{\partial \varphi_a} = 0 \;\Rightarrow\; \varphi_a = \frac{1}{2} \cdot \left(\frac{\beta_{\mathrm{DI}}}{2} \cdot i_B + \varphi_d + \varphi_c \right)$$

$$\frac{\partial E_G}{\partial \varphi_b} = 0 \;\Rightarrow\; \varphi_b = \frac{1}{2} \cdot (-\beta_{\mathrm{P}} \cdot i_B + \varphi_d + \varphi_c - \varphi_2 - \varphi_1)$$

which, after substitution in A.1 yields:

$$\frac{E_G}{\frac{\Phi_0 \cdot I_C}{2\pi}} = \frac{\varphi_{\mathrm{cd}}^2}{2\,\beta_{\mathrm{DI}}} - (1-\alpha) \cdot \cos(\varphi_1) - (1+\alpha) \cdot \cos(\varphi_2) +$$

$$+ \frac{1}{2} \frac{(\varphi_{\mathrm{cd}} + \varphi_2 - \varphi_1)^2}{2\,\beta_{\mathrm{P}}} - \frac{1}{2}\, i_B\, (\varphi_1 + \varphi_2) - \varphi_{\mathrm{cd}} \cdot i_{\mathrm{mod}} - \frac{1}{8}\, (2\,\beta_{\mathrm{P}} + \beta_{\mathrm{DI}}) \cdot i_B^2$$

where $\varphi_{\mathrm{cd}} = \varphi_c - \varphi_d$. Again, the variable φ_{cd} can be eliminated by looking for $\frac{\partial E_G}{\partial \varphi_{\mathrm{cd}}} = 0$, which gives

$$\varphi_{\mathrm{cd}} = i_{\mathrm{mod}} \cdot \beta_{II} - (\varphi_2 - \varphi_1) \cdot \frac{\beta_{II}}{2\,\beta_{\mathrm{P}}}$$

where the symbol β_{II} was used to denote the parallel combination of the normalized inductances of the inductors L_{DI} and $2\,L_{\mathrm{P}}$:

$$\beta_{II} = \frac{2\,\beta_{\mathrm{P}} \cdot \beta_{\mathrm{DI}}}{2\,\beta_{\mathrm{P}} + \beta_{\mathrm{DI}}}$$

Substituting back φ_{cd} in the last expression for the Gibbs free energy and rearranging, the 2D potential landscape is finally obtained:

$$\begin{aligned} \frac{E_G(\varphi_1, \varphi_2)}{\frac{\Phi_0 \cdot I_C}{2\pi}} &= -\frac{i_{\mathrm{mod}}^2}{2} \cdot \beta_{II} - \frac{i_B^2}{8} \cdot (2\,\beta_{\mathrm{P}} + \beta_{\mathrm{DI}}) + \\ &+ \frac{(\varphi_2 - \varphi_1)^2}{2(\beta_{\mathrm{DI}} + 2\,\beta_{\mathrm{P}})} - \frac{i_B\,(\varphi_1 + \varphi_2)}{2} + i_{\mathrm{mod}}\,(\varphi_2 - \varphi_1) \cdot \frac{\beta_{II}}{2\,\beta_{\mathrm{P}}} - \\ &- (1-\alpha) \cdot \cos(\varphi_1) - (1+\alpha) \cdot \cos(\varphi_2) \end{aligned} \tag{A.2}$$

where all terms as a function of the junction flux angles are separated in each line. The terms in the first line are constant as a function of the flux angles, the second contains the polynomial while the third line the periodic component of the potential landscape. The modulation and bias currents i_{mod} and i_B change the potential landscape, influencing the positions and the curvature of the energetic minima in which the circuit resides during a stable (non-oscillatory) state. For certain values of the two currents, there will be no potential minima and the circuit will start to oscillate which marks the onset of the voltage state.

Looking for the potential minima w.r.t. each of the flux angles, the network equations emerge:

$$\begin{aligned} \frac{\partial E_G(\varphi_1, \varphi_2)}{\partial \varphi_1} = 0 \;\Rightarrow\; -\frac{\varphi_2 - \varphi_1}{\beta_{\mathrm{DI}} + 2\,\beta_{\mathrm{P}}} + (1-\alpha) \cdot \sin(\varphi_1) = \frac{i_B}{2} + \frac{\beta_{II}}{2\,\beta_{\mathrm{P}}}\, i_{\mathrm{mod}} \\ \frac{\partial E_G(\varphi_1, \varphi_2)}{\partial \varphi_2} = 0 \;\Rightarrow\; \frac{\varphi_2 - \varphi_1}{\beta_{\mathrm{DI}} + 2\,\beta_{\mathrm{P}}} + (1+\alpha) \cdot \sin(\varphi_2) = \frac{i_B}{2} - \frac{\beta_{II}}{2\,\beta_{\mathrm{P}}}\, i_{\mathrm{mod}} \end{aligned} \tag{A.3}$$

that could have also been obtained by simple circuit inspection and without the use of the Gibb's energy method. Nevertheless, it is here necessary to consult the potential landscape in order to find the point at which the circuit will go to the voltage state, i.e. the point where the static state A.3 is no longer stable. This is equivalent to looking for the border case of the potential minimum condition (a second partial derivative test for an extremum of a 2D function):

$$D = \frac{\partial^2 E_G}{\partial \varphi_1^2} \cdot \frac{\partial^2 E_G}{\partial \varphi_2^2} - \left(\frac{\partial^2 E_G}{\partial \varphi_1 \, \partial \varphi_2} \right)^2 = 0$$

From the expression A.2, the condition above is equivalent to

$$-\cos(\varphi_{1m}) \cos(\varphi_{2m}) = \frac{(1-\alpha) \cdot \cos(\varphi_{1m}) + (1+\alpha) \cdot \cos(\varphi_{2m})}{(\beta_{\mathrm{DI}} + 2\,\beta_{\mathrm{P}})\,(1-\alpha^2)}$$

where $\varphi_{1,m}$ and $\varphi_{2,m}$ denote the flux angles of the junctions that correspond to the onset of instability and the transition to the voltage state. The bias current for which the circuit goes to the voltage state is denoted as $i_{B,V}$ and is equal to the SQUID critical current one would measure externally. It is a function of the circuit parameters $\alpha, \beta_{\mathrm{P}}, \beta_{\mathrm{DI}}$ and the modulation current i_{mod}.

To find the threshold curve $i_{B,V}(i_{\mathrm{mod}}, \beta_{\mathrm{DI}}, \beta_{\mathrm{P}}, \alpha)$, one must solve the system consisting of the last equation and A.3 (the system A.3 is re-arranged):

$$\begin{cases} i_{B,V} = (1-\alpha) \cdot \sin(\varphi_{1m}) + (1+\alpha) \cdot \sin(\varphi_{2m}) \\ 2\left(\dfrac{\varphi_{2m} - \varphi_{1m}}{\beta_{\mathrm{DI}} + 2\,\beta_{\mathrm{P}}} + \dfrac{\beta_{II}}{2\,\beta_{\mathrm{P}}}\, i_{\mathrm{mod}} \right) = (1-\alpha) \cdot \sin(\varphi_{1m}) - (1+\alpha) \cdot \sin(\varphi_{2m}) \\ -\cos(\varphi_{1m}) \cos(\varphi_{2m}) = \dfrac{(1-\alpha) \cdot \cos(\varphi_{1m}) + (1+\alpha) \cdot \cos(\varphi_{2m})}{(\beta_{\mathrm{DI}} + 2\,\beta_{\mathrm{P}})\,(1-\alpha^2)} \end{cases} \tag{A.4}$$

and eliminate the flux angles of the junctions from the system. Usually, two of the equations can be combined to at least eliminate one of the flux angles (or a linear combination of them). Treating the remaining variable as a parameter, an implicit plot of $i_{B,V}$ can be then created. A closed-form expression for $i_{B,V}$ as a function of i_{mod}, β_{DI}, β_{P} and α is difficult to obtain from A.4, leaving the above graphical method as most practical.

There are however a few general characteristics of the threshold curve that can be extracted from A.4 in an analytical way.

First, for $\alpha = 0$ (no asymmetry), it is not difficult to prove that the threshold curve has *both* an odd and an even symmetry along the i_{mod} axis:

$$\begin{cases} i_{B,V}(i_{\mathrm{mod}}) = -i_{B,V}(-i_{\mathrm{mod}}) \\ i_{B,V}(i_{\mathrm{mod}}) = i_{B,V}(-i_{\mathrm{mod}}) \end{cases}$$

(for the first invert the signs of the flux angles and for the second trade their places in A.4). The only way this is possible is for the threshold curve to be constituted of two component curves: one for positive and one for negative values of $i_{B,V}$. The two components are mirror images reflected along the i_{mod} axis when $\alpha = 0$. Looking at the geometric symmetry of the circuit, this result is easily checked as true.

When $\alpha \neq 0$, only the odd symmetry holds. However, $i_{B,V} \neq 0$ for any i_{mod} in the case $\alpha \neq 0$ ($i_{B.V}$ never reaches zero, see the peak-trough discussion further below), meaning that the threshold curve never crosses the i_{mod} axis. This conclusion combined with the odd symmetry again implies that the threshold curve must have two separate components, one for $i_{B,V} > 0$ and one for $i_{B,V} < 0$.

It is reasonable to expect that the dependence of the critical SQUID bias current $i_{B,V}$ on the modulation current i_{mod} will be periodic. This means that there must be peaks and troughs in the threshold curve and hence, maximums and minimums could be sought for $i_{B,V}(i_{\mathrm{mod}})$ implicitly from the relations A.4.

Looking for the distance between the points where a consecutive maximum (or minimum) occurs, one can find the period Δi_{mod} in the $i_{B,V}(i_{\mathrm{mod}})$ dependence. Also, looking at the difference between the levels of a neighbouring maximum and minimum, the modulation depth is obtained.

These extremum points are found for $\frac{\partial i_{B,V}}{\partial i_{\mathrm{mod}}} = 0$. Differentiating the first equation in A.4 w.r.t. the modulation current i_{mod}, it is obtained:

$$\frac{\partial i_{B,V}}{\partial i_{\mathrm{mod}}} = \frac{\partial \varphi_{1m}}{\partial i_{\mathrm{mod}}} (1-\alpha) \cdot \cos(\varphi_{1m}) + \frac{\partial \varphi_{2m}}{\partial i_{\mathrm{mod}}} (1+\alpha) \cdot \cos(\varphi_{2m}) \tag{A.5}$$

Next, equating the right-hand side of A.5 to zero and combining with the third relation of the set A.4:

$$\frac{(1+\alpha)\cos(\varphi_{2m})}{\beta_{\mathrm{DI}} + 2\,\beta_{\mathrm{P}}} \cdot \frac{\partial(\varphi_{2m} - \varphi_{1m})}{\partial i_{\mathrm{mod}}} = \frac{\partial \varphi_{1m}}{\partial i_{\mathrm{mod}}} (1-\alpha^2) \cos(\varphi_{1m}) \cos(\varphi_{2m}) \tag{A.6}$$

The derivative of the second relation from A.4 w.r.t. i_{mod} is:

$$\frac{\frac{\partial(\varphi_{2m} - \varphi_{1m})}{\partial i_{\mathrm{mod}}} + \beta_{\mathrm{DI}}}{\beta_{\mathrm{DI}} + 2\,\beta_{\mathrm{P}}} = \frac{\partial \varphi_{1m}}{\partial i_{\mathrm{mod}}} \frac{(1-\alpha)}{2} \cdot \cos(\varphi_{1m}) - \frac{\partial \varphi_{2m}}{\partial i_{\mathrm{mod}}} \frac{(1+\alpha)}{2} \cdot \cos(\varphi_{2m}) \tag{A.7}$$

and combining it with A.6 yields:

$$(1+\alpha)\cos(\varphi_{2m})\left(\frac{2\,\beta_{\mathrm{DI}}}{\beta_{\mathrm{DI}}+2\,\beta_{\mathrm{P}}}+\frac{\partial\varphi_{1m}}{\partial i_{\mathrm{mod}}}(1-\alpha)\cdot\cos(\varphi_{1m})+\frac{\partial\varphi_{2m}}{\partial i_{\mathrm{mod}}}(1+\alpha)\cdot\cos(\varphi_{2m})\right)=0$$

where the right-hand side of A.5 can be recognised as a part of the term within the large brackets. Since A.5 was equated to zero in order to find the extremum points, one finally arrives at:

$$(1+\alpha)\frac{2\,\beta_{\mathrm{DI}}}{\beta_{\mathrm{DI}}+2\,\beta_{\mathrm{P}}}\cos(\varphi_{2m})=0$$

that is true only if $\cos(\varphi_{2m})=0$. From the last relation of A.4, it follows that when $\cos(\varphi_{2m})=0$ also $\cos(\varphi_{1m})=0$. In conclusion, the extremums of the threshold curve $i_{B,V}(i_{\mathrm{mod}})$ occur when the cosine of both flux angles is zero.

Hence, the values of the flux angles at the peaks or troughs of $i_{B,V}$ as a function of the modulation current i_{mod} can be chosen from the following pairs (written modulo 2π):

$$\begin{cases}
\mathrm{A} & \varphi_1=\dfrac{\pi}{2},\varphi_2=\dfrac{\pi}{2} & i_{B,V}=2 & i_{\mathrm{mod}}=-\alpha\left(1+\dfrac{2\,\beta_{\mathrm{P}}}{\beta_{\mathrm{DI}}}\right)\\[2ex]
\mathrm{B} & \varphi_1=\dfrac{\pi}{2},\varphi_2=-\dfrac{\pi}{2} & i_{B,V}=-2\,\alpha & i_{\mathrm{mod}}=1+\dfrac{2\,\beta_{\mathrm{P}}}{\beta_{\mathrm{DI}}}+\dfrac{\pi}{\beta_{\mathrm{DI}}}\\[2ex]
\mathrm{C} & \varphi_1=-\dfrac{\pi}{2},\varphi_2=\dfrac{\pi}{2} & i_{B,V}=2\,\alpha & i_{\mathrm{mod}}=-1-\dfrac{2\,\beta_{\mathrm{P}}}{\beta_{\mathrm{DI}}}-\dfrac{\pi}{\beta_{\mathrm{DI}}}\\[2ex]
\mathrm{D} & \varphi_1=-\dfrac{\pi}{2},\varphi_2=-\dfrac{\pi}{2} & i_{B,V}=-2 & i_{\mathrm{mod}}=\alpha\left(1+\dfrac{2\,\beta_{\mathrm{P}}}{\beta_{\mathrm{DI}}}\right)
\end{cases} \tag{A.8}$$

For $\alpha>0$, the cases A and C belong to the positive component of the threshold curve ($i_{B,V}>0$) while the cases B and D belong to the negative part of the curve. For $\alpha<0$, the cases B and C switch places.

The sign of the second derivative $\frac{\partial^2 i_{B,V}}{\partial i_{\mathrm{mod}}^2}$ evaluated at $\frac{\partial i_{B,V}}{\partial i_{\mathrm{mod}}}=0$ will indicate which pair is a peak and which is a trough:

$$\left.\frac{\partial^2 i_{B,V}}{\partial i_{\mathrm{mod}}^2}\right|_{\frac{\partial i_{B,V}}{\partial i_{\mathrm{mod}}}=0}=-\left(\frac{\partial\varphi_{1m}}{\partial i_{\mathrm{mod}}}\right)^2(1-\alpha)\cdot\sin(\varphi_{1m})-\left(\frac{\partial\varphi_{2m}}{\partial i_{\mathrm{mod}}}\right)^2(1+\alpha)\cdot\sin(\varphi_{2m})$$

Obviously, the case A from A.8 corresponds to a peak while the case D to a trough, regardless of the value of α. Note that since D belongs to the negative part of the curve, where $i_{B,V}<0$, a trough actually indicates a maximum in the absolute value of $i_{B,V}$.

Differentiating the third equation from the set A.4 with respect to i_{mod} and evaluating at the points A.8, the following can be written for the partial derivatives of the flux angles:

$$\frac{\partial\varphi_{1m}}{\partial i_{\mathrm{mod}}}=\frac{1+\alpha}{1-\alpha}\cdot\frac{\partial\varphi_{1m}}{\partial i_{\mathrm{mod}}}\quad\text{when}\quad\frac{\partial i_{B,\max}}{\partial i_{\mathrm{mod}}}=0$$

which, when replaced in the expression for $\frac{\partial^2 i_{B,\max}}{\partial i_{\mathrm{mod}}^2}$, yields:

$$\left.\frac{\partial^2 i_{B,\max}}{\partial i_{\mathrm{mod}}^2}\right|_{\frac{\partial i_{B,\max}}{\partial i_{\mathrm{mod}}}=0}=-\left(\frac{\partial\varphi_{2m}}{\partial i_{\mathrm{mod}}}\right)^2(1+\alpha)\left(\frac{1+\alpha}{1-\alpha}\sin(\varphi_{1m})+\sin(\varphi_{2m})\right)$$

The pairs B and C from A.8 can now be used to find the sign of the above simple relation. For $\alpha>0$, the case C from A.8 corresponds to a trough while case B corresponds to a peak. For $\alpha<0$, the reverse is valid: case C is a peak while B is a trough. Since the two pairs also switch the component of the curve they belong to when the sign of α is inverted, it can be concluded that they are both troughs (minimums) when one looks at the absolute value of $i_{B,V}$.

Another conclusion from the above discussion is that the threshold curve never reaches zero for $\alpha\neq 0$.

The value of $|i_{B,V}|$ at a peak is determined by any of the cases A and D, while at a trough for by any of the cases B and C. This results in a modulation depth

$$\frac{|I_{B,\mathrm{Vpeak}}|-|I_{B,\mathrm{Vtrough}}|}{2I_C}=\frac{I_C\left(|i_{B,\mathrm{Vpeak}}|-|i_{B,\mathrm{Vtrough}}|\right)}{2\,I_C}=\frac{2-2\,|\alpha|}{2}=1-|\alpha|$$

where the normalization is performed with $2\,I_C$ instead of I_C as is usual in SQUID electronic circuits.

The four values from A.8 represent just one period of the threshold curve. Adding $2\pi\,n$ to any of the flux angles leaves $i_{B,V}$ the same while the modulation current changes by (term within the brackets of the second relation of A.4 remains the same):

$$\Delta I_{\mathrm{mod}}=I_C\,\Delta i_{\mathrm{mod}}=I_C\,\frac{2\pi\,n}{\beta_{\mathrm{DI}}}=\frac{n\cdot\Phi_0}{L_{\mathrm{DI}}}$$

The period in the threshold curve is then calculated to be $\frac{\Phi_0}{L_{\mathrm{DI}}}$.

Measuring the modulation period of a direct-injection SQUID, fabricated with thin-film technology, is very often used as a method to experimentally obtain the partial inductance of the segment between the two junctions. This value can then be connected to the material and geometric properties of the superconducting layers, for instance London penetration depths, thicknesses etc.

In Figure A.2 a plot is given of the generalized threshold curve of a direct-injection SQUID, using the values from A.8 to determine the important points while the shape of the curve is chosen to roughly correspond with measurements.

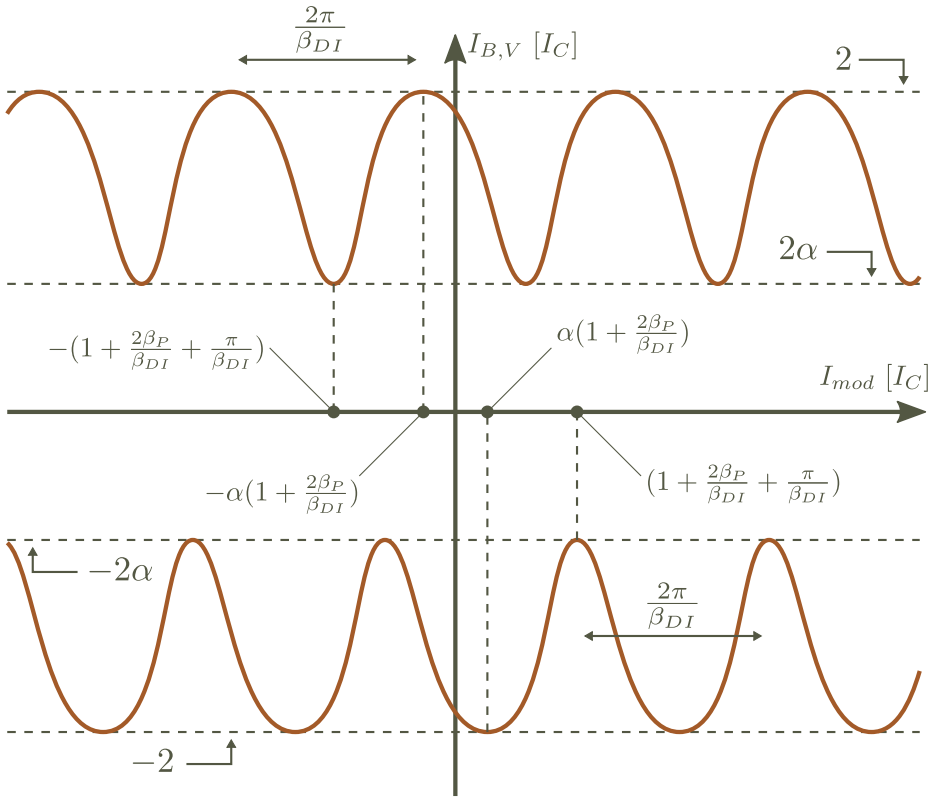

Figure A.2. A generalized plot of the threshold curve of a direct-injection SQUID together with indications of the most important points.

Appendix B

Accuracy analysis of the surface inductance approximation in a single 2D sheet model

In subsection 2.3.1 of Chapter 2, it was derived that a planar thin film segment of thickness d and London penetration depth λ_L can be replaced by a 2D sheet of the same planar dimensions and of a surface inductance given by

$$L_S = \lambda_L \cdot \mu \cdot \coth\left(\frac{d}{\lambda_L}\right) \cdot \frac{B_1^2 + B_2^2 - 2 \cdot B_1 B_2 \cdot \frac{1}{\cosh\left(\frac{d}{\lambda_L}\right)}}{(B_2 - B_1)^2} \tag{B.1}$$

where B_1 and B_2 are the magnetic field at the top and bottom surface of the thin-film. The expression in B.1 is based on the assumption that the magnetic field is homogeneous in the dielectric outside the segment and depends only on the z coordinate inside the film. The drawing in Figure B.1 explains the equivalence graphically.

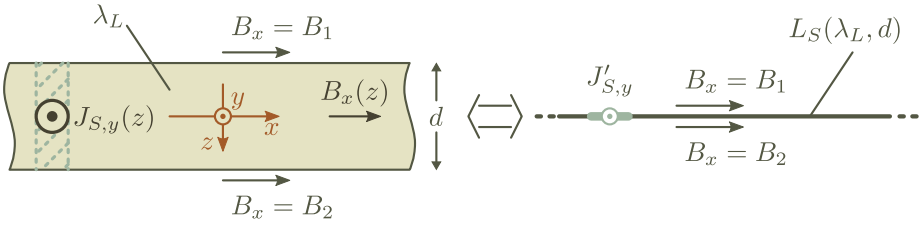

Figure B.1. The various quantities and the coordinate system used in the thin film - 2D sheet equivalence.

The relation B.1 was then approximated by removing the term containing B_1 and B_2:

$$\mathrm{Err}\left(B_1, B_2, \frac{d}{\lambda_L}\right) = \frac{B_1^2 + B_2^2 - 2 \cdot B_1 B_2 \cdot \frac{1}{\cosh\left(\frac{d}{\lambda_L}\right)}}{(B_2 - B_1)^2} \approx 1 \tag{B.2}$$

which yields a simple expression for the surface inductance

$$L_S = \lambda_L \cdot \mu \cdot \coth\left(\frac{d}{\lambda_L}\right) \tag{B.3}$$

The goal of this section is to evaluate the error made by the approximation:

$$\mathrm{Err}\left(B_1, B_2, \frac{d}{\lambda_L}\right) \approx 1 \tag{B.4}$$

Rewriting the above term as:

$$\mathrm{Err}\left(B_1, B_2, \frac{d}{\lambda_L}\right) = \frac{B_1^2 + B_2^2 - 2 \cdot B_1 B_2 \cdot \frac{1}{\cosh\left(\frac{d}{\lambda_L}\right)}}{(B_2 - B_1)^2} = \frac{1 + q^2 - \frac{2\,q}{\cosh\left(\frac{d}{\lambda_L}\right)}}{(1-q)^2}$$

where $q = \frac{B_2}{B_1}$, its value can be calculated as a function of the ratio q while the argument of the hyperbolic cosine, the ratio between the film's thickness and its penetration depth $\frac{d}{\lambda_L}$, can be used as a parameter. The result is plotted in Figure B.2. Note that the correction term is, as expected, invariant when the top and bottom surfaces are exchanged (a z-axis reversal in fact): replacing the ratio q with $\frac{1}{q}$, i.e. effectively trading the places of B_1 and B_2, yields the same value of the correction term (and L_S).

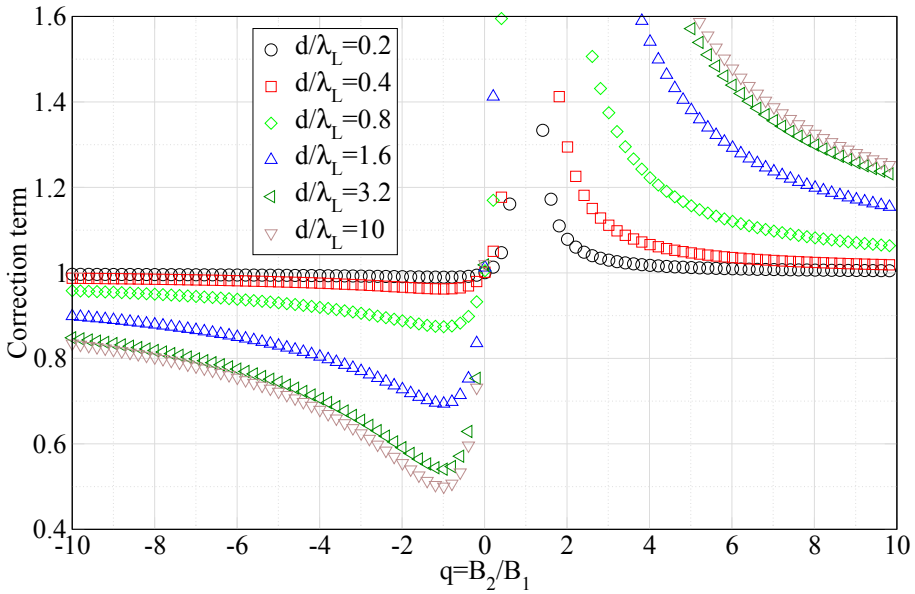

Figure B.2. The correction factor multiplying $\lambda_L \cdot \mu \cdot \cosh\left(\frac{d}{\lambda_L}\right)$ in the expression for L_S as a function of the ratio $q = \frac{B_2}{B_1}$ between the magnetic fields at either surface of the structure with a parameter indicating the thickness d of the superconducting film, replaced by a 2D sheet of surface inductance L_S, expressed in units of the penetration depth λ_L.

There are a number of features that can be observed from the plot. First, the accuracy of the approximation B.4 is very low when the fields at the top and bottom surface are about equal (when $q \approx 1$). In fact, the whole model is wrong at $B_2 = B_1$ as the 2D sheet then carries no current and contains no energy ($J'_{S,y} = 0$) while there is both current and field inside the superconducting film (replace $B_2 = B_1$ in equation 2.77 from subsection 2.3.1 in Chapter 2). Although the net current in the thin film will then be zero, there is still stored energy which is not taken into account by the 2D sheet approximation.

The situation where $B_2 \approx B_1$ is encountered when either: a) the film is placed in a constant magnetic field, excited from both sides or b) when the thickness of the film is so low that the field penetrating it does not change substantially between the two sides. Fortunately, the case under b) is equivalent to thicknesses $\frac{d}{\lambda_L} \ll 1$ when there is a wide range of $q = \frac{B_2}{B_1}$ for which the correction term is ≈ 1: the approximate expression for L_S can then be considered accurate except in a tight range around $B_1 = B_2$. The case under a), when the film is excited from both sides, is however not modelled well by the 2D sheet. One then needs a model with two conducting sheets, one for each of the top and bottom surfaces of the film.

The second observation is connected to the situation when the fields are equal but opposite, i.e. when $q = -1$. This corresponds to the field created by a superconducting segment that is residing in free space, far from other conducting structures. Replacing $B_2 = -B_1$ in equation B.1 and re-arranging, it is obtained that the surface inductance of the 2D sheet is then exactly $L_S = \frac{\lambda_L \cdot \mu}{2} \cdot \coth\left(\frac{1}{2} \cdot \frac{d}{\lambda_L}\right)$. The error made by using the approximate value $\lambda_L \cdot \mu \cdot \coth\left(\frac{d}{\lambda_L}\right)$ is:

$$\text{error} = \frac{\lambda_L \cdot \mu \cdot \coth\left(\frac{d}{\lambda_L}\right) - \frac{\lambda_L \cdot \mu}{2} \cdot \coth\left(\frac{1}{2} \cdot \frac{d}{\lambda_L}\right)}{\frac{\lambda_L \cdot \mu}{2} \cdot \coth\left(\frac{1}{2} \cdot \frac{d}{\lambda_L}\right)} = \frac{\cosh\left(\frac{d}{\lambda_L}\right) - 1}{\cosh\left(\frac{d}{\lambda_L}\right) + 1}$$

which is tabulated in Table B.1.

$\frac{d}{\lambda_L}$	0.2	0.4	0.6	0.8	1	1.2	2	4	10	∞
error [%]	1	3.89	8.49	14.5	21.3	28.8	58	92.9	99.9	100

Table B.1. The error in the surface inductance of a 2D sheet modeling an isolated superconducting film of thickness d and penetration depth λ_L.

The error in the approximation increases with d for ultra-thin films but quickly saturates at 100% for larger thicknesses. From Table B.1, it can be concluded that a 2D sheet having a surface inductance $L_S = \mu \cdot \lambda_L \cdot \coth\left(\frac{d}{\lambda_L}\right)$ overestimates the

internal inductance of a isolated superconducting film by a maximum of twice, achieved only if the film is very thick. In practice however, the superconducting films are of thicknesses comparable to their penetration depth: the accuracy in the approximation of the surface inductance for an isolated segment is acceptable considering the simplicity of the 2D sheet geometry.

Another situation arises when the superconducting film is serving as a shield: an external field is applied (from one side) and the film responds with shielding currents. This is the typical situation for a groundplane in a thin-film circuit. In this case, assuming that the return of the shielding current flows far away from the area under investigation (groundplane is short-circuited), the field exponentially decreases along the film thickness

$$B_2 = B_1 \cdot e^{\pm \frac{d}{\lambda_L}}$$

where the sign in the exponent depends on the side at which the field is incident. Using these values for the field at the surface of the segment in equation B.1, the surface inductance calculates to one half the value that was previously found for an isolated film carrying a current: $L_S = \lambda_L \cdot \mu \cdot \coth\left(\frac{1}{2} \cdot \frac{d}{\lambda_L}\right)$. The relative error is then

$$\frac{\lambda_L \cdot \mu \cdot \coth\left(\frac{d}{\lambda_L}\right) - \lambda_L \cdot \mu \cdot \coth\left(\frac{1}{2} \cdot \frac{d}{\lambda_L}\right)}{\lambda_L \cdot \mu \cdot \coth\left(\frac{1}{2} \cdot \frac{d}{\lambda_L}\right)} = -\frac{1}{1 + \cosh\left(\frac{d}{\lambda_L}\right)}$$

and is tabulated below.

$\frac{d}{\lambda_L}$	0.2	0.4	0.6	0.8	1	1.2	2	4	10	∞
error [%]	-49.5	-48	-45.8	-42.8	-39.3	-35.6	-21	-3.53	-0.01m	0

Table B.2. The error in the surface inductance of a 2D sheet modeling a short-circuited groundplane of thickness d and penetration depth λ_L.

From Table B.2 it follows that the approximation in equation B.1 underestimates the surface inductance of a shorted groundplane by never more than one half of the correct value; even then only for very thin groundplanes is this maximum error approached. Groundplanes in thin-film circuits are usually the thickest superconducting films. It is common to use a film thickness of at least 200nm for the groundplane that, together with a λ_L of less than 100nm for Nb (the metal used as a groundplane), gives an error in the surface inductance that will be always less than $\sim$20% of the correct value. Moreover, the error quickly decreases to zero

for thicker films: at 400nm Nb groundplane thickness for example, the error in its surface inductance is just a few percent. Again, it can be concluded that the approximation of the sheet inductance from B.1 is acceptable for a groundplane as well. The error is however more substantial when the groundplane carries the return of the shielding current as well. The analysis of this case is given further below, towards the end of the section.

Another feature of the correction plot in Figure B.2 is that, in general, the approximation for L_S works better when the fields are opposite and different in value. For instance, when $q<0$, i.e. when the fields on either side of the film are opposite in direction, the maximal error that can be made in the surface inductance is 100% (when q is exactly -1, see Table B.1). Most generally, when $q\approx 0$ and when $q\approx\pm\infty$ (those are really the same as the correction term is invariant for $q\to\frac{1}{q}$), corresponding to situations where B_1 and B_2 are vastly different, the expression for $L_S=\mu\cdot\lambda_L\cdot\coth\left(\frac{d}{\lambda_L}\right)$ is most accurate. These values of q correspond to situations where, for example, the superconducting film is placed in a magnetic field that is sourced from one side only and does not penetrate much on the other side. Another example is when a current-carrying superconducting film is strongly coupled to other structures from one side only, making the fields at the opposing surfaces of the film different both in direction and magnitude.

In reality, the superconducting segments in a thin-film planar circuit are usually coupled at just one side to the groundplane. Sometimes also other segments may be present at the other side, for instance in thin-film transformers. In all these situations, the ratio q usually does not deviate strongly from 0. Consider for instance a superconducting segment of thickness d_F carrying a (planar uniform) current per unit width $J'_{S,F}$ ($J'_{S,F}=\int J_{S,y}\cdot\mathrm{d}z$) placed a distance h below a groundplane of thickness d_G, where the penetration depth λ_L for both is the same, see Figures B.3 and B.4. The groundplane conducts a current $J'_{S,G}$ per unit width. In the most common cases, the magnetic field will be strongly concentrated in the area between the plates while at the far side of the segment the field will be reduced when compared to the situation without a groundplane. As mentioned above, the enlarged difference in the field between each side of the segment increases the accuracy of the surface inductance approximation given by relation B.3 above.

In fact, the field and currents in the system can be exactly solved with the assumption of homogeneity in the planar directions (no x, y dependence). The principle of superposition will be used to solve the current and field distributions in the system. First, it will be taken that the current per unit width in the groundplane $J'_{S,G}=0$ followed by the case when the current per unit width in the segment $J'_{S,F}=0$. Adding the fields and current distributions from the two cases will then yield the final solution.

When $J'_{S,G} = 0$, the integral form of Ampere's law applied to a small rectangular contour lying in the x, z plane circling the whole groundplane yields $B_{1,G} = B_{2,G} = B_I$ where $B_{1,G}$ and $B_{2,G}$ denote the magnetic field at respectively the top and bottom surface of the groundplane. Then, from the general solution of the Helmholtz equation for the magnetic field inside the groundplane, given by equation 2.77 in subsection 2.3.1, it is obtained

$$B_{x,G}(z) = B_I \cdot \frac{\cosh\left(\frac{z}{\lambda_L}\right)}{\cosh\left(\frac{d_G}{2 \cdot \lambda_L}\right)}$$

while for the current distribution, the differential form of Ampere's law is used to find

$$J_{S,y,G}(z) = \frac{1}{\mu} \cdot \frac{\partial B_{x,G}(z)}{\partial z} = \frac{B_I}{\mu \cdot \lambda_L} \cdot \frac{\sinh\left(\frac{z}{\lambda_L}\right)}{\cosh\left(\frac{d_G}{2 \cdot \lambda_L}\right)}$$

In the superconducting segment, the current and field distribution will be equal to the one found for an isolated case (*sans* a groundplane) since there is no net current through the groundplane and its fields do not interfere with the segment: $B_{1,F} = -B_{2,F}$ with $B_{1,F}$ and $B_{2,F}$ the magnetic field at respectively the top and bottom surface of the segment. It is also such that the field is homogeneous between the plates: $B_{1,F} = B_{2,G} = B_I$. Hence, using $B_{1,F} = -B_{2,F} = B_I$ and substituting in the generic solution for the magnetic field inside a planar thin film:

$$B_{x,F}(z) = -B_I \cdot \frac{\sinh\left(\frac{z - \left(h + \frac{d_F}{2} + \frac{d_G}{2}\right)}{\lambda_L}\right)}{\sinh\left(\frac{d_F}{2 \cdot \lambda_L}\right)}$$

The current density in the segment then calculates to

$$J_{S,y,F}(z) = \frac{1}{\mu} \cdot \frac{\partial B_{x,F}(z)}{\partial z} = -\frac{B_I}{\mu \cdot \lambda_L} \cdot \frac{\cosh\left(\frac{z - \left(h + \frac{d_F}{2} + \frac{d_G}{2}\right)}{\lambda_L}\right)}{\sinh\left(\frac{d_F}{2 \cdot \lambda_L}\right)}$$

Note that if the current per unit width in the segment is $J'_{S,F}$, then the integral form of the Ampere law on a contour around the segment gives

$$B_I = -2 \cdot \mu \cdot J'_{S,F} \tag{B.5}$$

Lets now set the current in the segment, $J'_{S,F}$, to zero while allowing the groundplane to conduct $J'_{S,G}$ per unit width. Repeating the same procedure, it is obtained

$$B_{x,F}(z) = B_{II} \cdot \frac{\cosh\left(\frac{z - \left(h + \frac{d_F}{2} + \frac{d_G}{2}\right)}{\lambda_L}\right)}{\cosh\left(\frac{d_F}{2 \cdot \lambda_L}\right)}$$

$$J_{S,y,F}(z) = \frac{B_{II}}{\mu \cdot \lambda_L} \cdot \frac{\sinh\left(\frac{z - \left(h + \frac{d_F}{2} + \frac{d_G}{2}\right)}{\lambda_L}\right)}{\cosh\left(\frac{d_F}{2 \cdot \lambda_L}\right)}$$

$$B_{x,G}(z) = B_{II} \cdot \frac{\sinh\left(\frac{z}{\lambda_L}\right)}{\sinh\left(\frac{d_G}{2 \cdot \lambda_L}\right)}$$

$$J_{S,y,G}(z) = \frac{B_{II}}{\mu \cdot \lambda_L} \cdot \frac{\cosh\left(\frac{z}{\lambda_L}\right)}{\sinh\left(\frac{d_G}{2 \cdot \lambda_L}\right)}$$

In this case, the field between the plates is obtained again from the integral form of Ampere's law applied to a contour encircling the groundplane

$$B_{II} = 2 \cdot \mu \cdot J'_{S,G} \tag{B.6}$$

Finally, the total fields inside the superconducting films can be found by adding the two cases together

$$B_{x,F}(z) = B_{II} \cdot \frac{\cosh\left(\frac{z - \left(h + \frac{d_F}{2} + \frac{d_G}{2}\right)}{\lambda_L}\right)}{\cosh\left(\frac{d_F}{2 \cdot \lambda_L}\right)} - B_I \cdot \frac{\sinh\left(\frac{z - \left(h + \frac{d_F}{2} + \frac{d_G}{2}\right)}{\lambda_L}\right)}{\sinh\left(\frac{d_F}{2 \cdot \lambda_L}\right)}$$

$$B_{x,G}(z) = B_{II} \cdot \frac{\sinh\left(\frac{z}{\lambda_L}\right)}{\sinh\left(\frac{d_G}{2 \cdot \lambda_L}\right)} + B_I \cdot \frac{\cosh\left(\frac{z}{\lambda_L}\right)}{\cosh\left(\frac{d_G}{2 \cdot \lambda_L}\right)}$$

where B_I and B_{II} are given by B.5 and B.6 respectively. Figures B.3 & B.4 depict the currents and field distributions for a number of simple configurations.

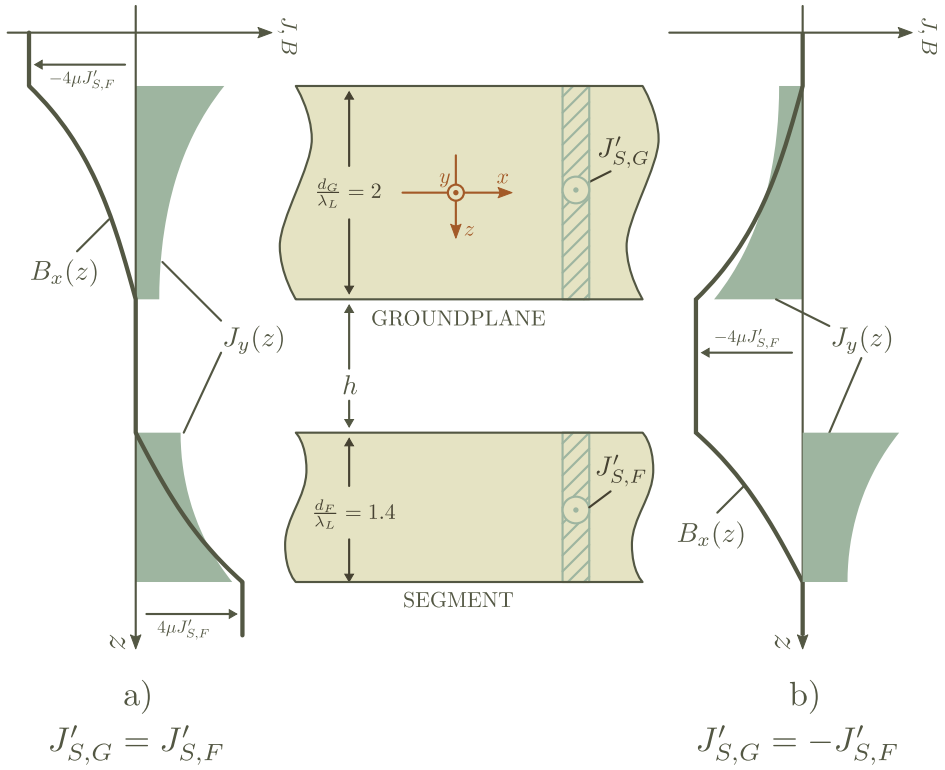

Figure B.3. The magnetic field and the current distribution in a system consisting of a superconducting planar segment placed below a groundplane. The two cases are readily encountered when the system is used as a transmission line (waveguide). The case under a) depicts the "even mode" while the case under b) the "odd mode" wave propagation. For a two-conductor transmission line only the latter mode occurs while the former may arise when there are more conductors in the vicinity that are part of the same transmission line. Note that the current symmetry assumed in the drawings necessitates that both the groundplane and the segment be connected to the same source or be part of the same circuit loop.

Looking at the configurations from Figure B.3, the ratio q between the fields at the top and bottom surfaces of the two thin films is either 0 or $\pm\infty$, which makes the correction term from equation B.2 always equal to 1. Hence, the surface inductance given by the relation B.3 is, for the situation shown in the above figure, an exact expression. It should be noted that, in practice, although for a transmission line the total currents $I_{S,G} = \pm I_{S,F}$, the surface current density will not be strictly symmetrical, $J'_{S,G} \neq \pm J'_{S,F}$, since the groundplane is usually much wider than the segment. Small errors in L_S will thus still be present.

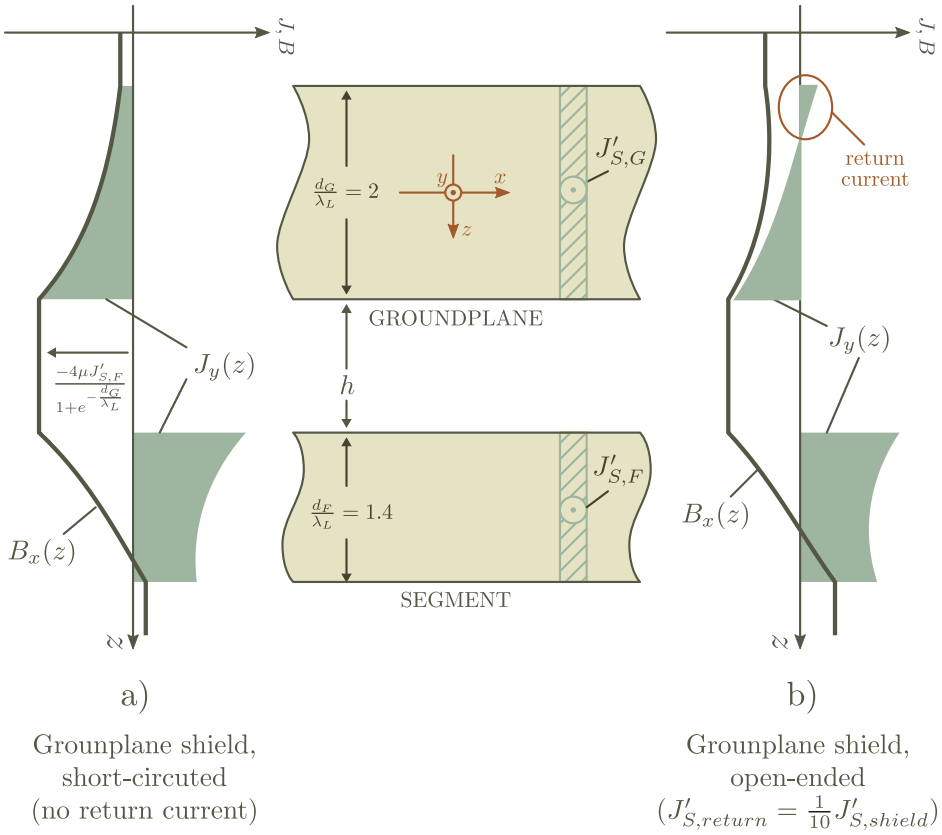

Figure B.4. Another type of solution for the system consisting of a superconducting segment and a groundplane. In this situation, the groundplane is used as a shielding structure and is not connected to the circuit of which the segment is a part of (it is "floating").

In the case under a) from Figure B.4, the groundplane's terminals at each end (length-wise) are assumed to be shorted and thus the return of the shielding current is carried far away from the depicted structure. A more realistic case is given under b), where the groundplane itself is used to carry the return current (also called a "sandbelt" current) at its top surface. If the groundplane is much wider than the segment, the return current will spread across the top surface and be much smaller than the shielding current that is concentrated in the area immediately above the segment. It is taken under b) that approximately 1/10 of the shielding current returns through the top surface per unit width.

In practice, the current and field distributions for the segment-groundplane geometry may be a linear combination (superposition) of any of the cases shown in the two figures above. In an RSFQ circuit for instance, the groundplane is a part of the circuit and Figure B.3 should be, in principle, the most applicable. However, the current flow symmetry assumed in Figure B.3 is generally satisfied just for some segments while for other segments the groundplane has primarily just a shielding role. Hence, there will be some segments where the situations from Figure B.4 will be more applicable. Generally, one cant determine the correct choice of symmetry in any given circuit beforehand - this is indeed the reason why the expression for the surface inductance should be independent on the field configuration.

It is of interest to calculate the magnetic fields at the surface of the two superconducting films from the drawings in Figures B.3 & B.4:

$$B_{1,G} = B_{x,G}\left(z = -\frac{d_G}{2}\right) = -B_{II} + B_I$$
$$B_{2,G} = B_{x,G}\left(z = \frac{d_G}{2}\right) = B_{II} + B_I$$
$$B_{1,F} = B_{x,F}\left(z = \frac{d_G}{2} + h\right) = B_{II} + B_I = B_{2,G}$$
$$B_{2,F} = B_{x,F}\left(z = \frac{d_G}{2} + h + d_F\right) = B_{II} - B_I = -B_{1,G}$$

Lets focus on the situation depicted by Figure B.4 where the groundplane thin film is either not connected or, at most, attached at just a single point to the circuit to which the segment belongs to. In this case, the groundplane, as a whole, cant carry any net current.

If the shielding component $J'_{S,G}$ closes somewhere at the far ends at the structure's length and thus away from the area analysed in the drawing, as shown in Figure B.4 under a), then the magnetic field across the groundplane will exponentially decrease:

$$B_{1,G} = B_{2,G} \cdot e^{-\frac{d_G}{\lambda_L}}$$

whereby the error made by representing the groundplane by a 2D sheet of surface inductance $L_{S,G} = \mu \cdot \lambda_L \cdot \coth\left(\frac{d_G}{\lambda_L}\right)$ was already calculated and given in Table B.2. The maximum error in the surface inductance of the groundplane for a reasonable assumption of $\frac{d_G}{\lambda_L} > 2$ was then less than about 20%.

For the segment,

$$q_F = \frac{B_{2,F}}{B_{1,F}} = -\frac{B_{1,G}}{B_{2,G}} = -e^{-\frac{d_G}{\lambda_L}}$$

which, for a realistic value of $\frac{d_G}{\lambda_L} > 2$, gives $-0.13 < q_F < 0$. From the plot in Figure B.2, the correction term $\mathrm{Err}\left(B_{1,F}, B_{2,F}, \frac{d_F}{\lambda_{L,F}}\right)$ is then never lower than $\sim$0.8: the maximum error that can be made in the surface inductance of the segment is less than $\frac{1-0.8}{0.8} = 25\%$ and even then only for very thick films. Hence, the error in both the segment and groundplane surface inductances is below the 20% to 25% range in this case.

In the more realistic case, where the return of the shielding current closes within the depicted structure, as shown in Figure B.4 under b), the errors will be greater as can be seen from the ratio of the fields on the top and bottom of the two films. In fact, an analytical solution can be found for the fields assuming that the ratio of the shielding and the return current flowing in the groundplane is known

$$r = \frac{J'_{G,\mathrm{shield}}}{J'_{G,\mathrm{return}}}$$

The shielding $J'_{G,\mathrm{shield}}$ and return $J'_{G,\mathrm{return}}$ currents are calculated as contributions of opposite sign to the the total surface current in the groundplane $J'_{S,G} = J'_{G,\mathrm{return}} + J'_{G,\mathrm{shield}}$:

$$J_{S,y,G}(z_0) = 0$$

$$J'_{G,\mathrm{return}} = \int_{-d_G/2}^{z_0} J_{S,y,G}(z) \cdot \mathrm{d}z$$

$$J'_{G,\mathrm{shield}} = \int_{z_0}^{d_G/2} J_{S,y,G}(z) \cdot \mathrm{d}z$$

From the definitions of the shielding and return current, it follows that their ratio r is always negative. In this analysis, we are interested in the cases where the return current is smaller than the shielding current. This corresponds to values of the ratio $r < -1$.

Note that for the analysis to make sense, it is necessary that z_0, the position along the groundplane thickness where the current distribution changes sign, should fall inside the film:

$$-\frac{d_G}{2} < z_0 < \frac{d_G}{2} \tag{B.7}$$

After some calculations, the fields inside the segment and the groundplane can be rewritten in such a was as to contain a dependence on the ratio r:

$$B_{x,F}(z) = \mu\,\lambda_L \cdot C \cdot \left[\frac{\sinh\left(\frac{d_G}{2\,\lambda_L}\right)}{\cosh\left(\frac{d_F}{2\,\lambda_L}\right)} \cosh\left(\frac{z_F}{\lambda_L}\right) - c_P \cdot \frac{\cosh\left(\frac{d_G}{2\,\lambda_L}\right)}{\sinh\left(\frac{d_F}{2\,\lambda_L}\right)} \sinh\left(\frac{z_F}{\lambda_L}\right) \right]$$

$$B_{x,G}(z) = \mu\,\lambda_L \cdot C \cdot \left[\sinh\left(\frac{z}{\lambda_L}\right) + c_P \cdot \cosh\left(\frac{z}{\lambda_L}\right) \right]$$

where the various parameters are

$$C = \frac{J'_{S,G}}{2\,\lambda_L \cdot \sinh\left(\frac{d_G}{2\,\lambda_L}\right)}$$

$$c_P = \frac{(r-1)\cosh\left(\frac{d_G}{2\,\lambda_L}\right) - 2\cdot\sqrt{-r}}{(r+1)\cdot\sinh\left(\frac{d_G}{2\,\lambda_L}\right)}$$

$$z_F = z - \left(h + \frac{d_F}{2} + \frac{d_G}{2}\right)$$

while the condition given by equation B.7 can be shown to hold for any choice of $\frac{d_G}{\lambda_L}$ and r.

The ratio between the fields at the surfaces of the groundplane and of the segment are now respectively:

$$q_G = \frac{B_{x,G}\left(z = \frac{d_G}{2}\right)}{B_{x,G}\left(z = -\frac{d_G}{2}\right)} = \frac{c_P + \tanh\left(\frac{d_G}{2\,\lambda_L}\right)}{c_P - \tanh\left(\frac{d_G}{2\,\lambda_L}\right)}$$

and

$$q_F = \frac{B_{x,F}\left(z_F = \frac{d_F}{2}\right)}{B_{x,F}\left(z_F = -\frac{d_F}{2}\right)} = \frac{\tanh\left(\frac{d_G}{2\,\lambda_L}\right) - c_P}{\tanh\left(\frac{d_G}{2\,\lambda_L}\right) + c_P}$$

In Figure B.5, q_F and q_G are plotted as a function of the ratio r between the shielding and return current with the thickness of the groundplane d_G expressed in λ_L as a parameter.

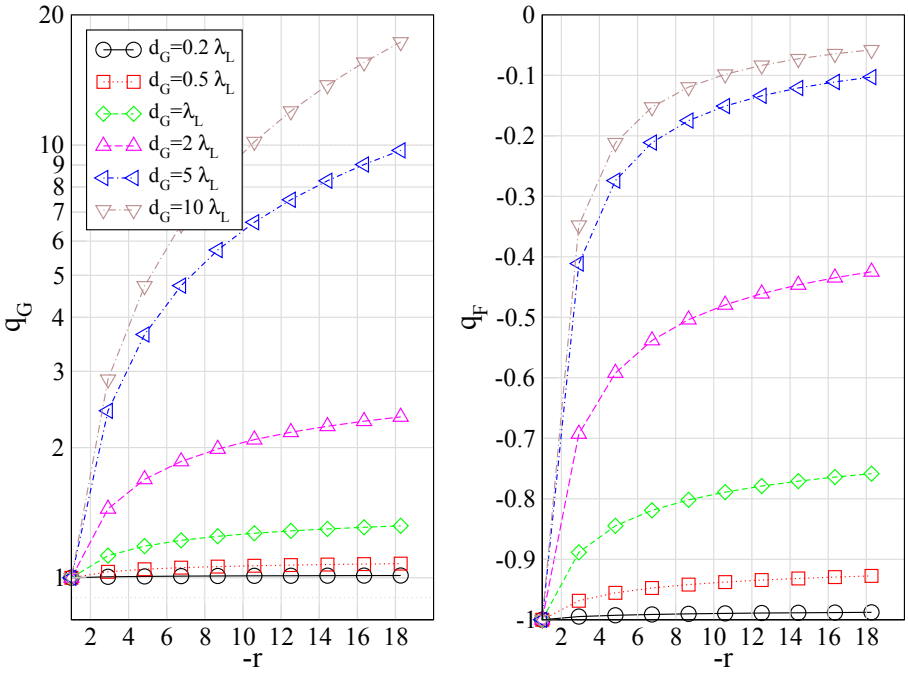

Figure B.5. The ratio between the fields at the top and bottom surfaces for the groundplane (q_G) and the segment (q_F) as a function of the ratio between the shielding and return current $-r = -\frac{J'_{G,\text{shield}}}{J'_{G,\text{return}}}$ with the thickness of the groundplane d_G in units of the penetration depth λ_L as a parameter. The plot pertains to a situation where the groundplane is not a part of the segment's circuit or is connected at a single point to it at most (Figure B.4). Note the logarithmic scale on the left plot.

Combining the figure above with the plot in Figure B.2, where the correction term is plotted as a function of the top/bottom surface field ratio, the accuracy of the approximation from relation B.3 is seen to be very low for groundplanes that are either thin or carry a substantial shielding return current at the top surface (when $q_G \approx 1$). For the segment on the other hand, since q_F is always negative, the surface inductance approximation from relation B.3 is (again) at most twice the correct value. Notably, the error for the segment does not depend on its thickness.

Hence, it is important to be able to estimate the ratio r for a given geometry. Usually, the shielding current in the bottom surface of the groundplane is concentrated (width-wise) in the area in proximity of the segment. The shielding current is thus constrained to flow in an area approximately equal to the width of the

segment. The return current on the other hand can flow across the entire width of the groundplane at its top surface. Since the total shielding current must be equal to the return current (remember that the groundplane is "floating" in this analysis), the ratio between the width of the groundplane and the width of the segment approximates the ratio r used in the plots above.

The conclusion from the analysis is that for the case where a groundplane is not a part of the circuit and is either very thin or not much wider than the segment it shields (or both), the surface inductance approximation given in relation B.3 is not accurate. One then must use two 2D sheets to accurately represent the groundplane, one sheet for each surface. Note that, in this situation, the groundplane is in fact not a very good shield at all: it allows the field of the segment's current to penetrate on the other side ($q_G \approx 1$) and vice-versa, allows a great portion of any external field to reach the segment.

A useful practical result connected to the above observation is that in remote areas of the circuit, where the groundplane is locally not connected to the circuit it shields, one should use wide and thick films for the groundplane. In general however, it is better to avoid circuit structures where the groundplane *locally* lacks a return path for the shielding current.

For the example from Figure B.4 b), where $\frac{d_G}{\lambda_L} = 2$ and $r = -10$, it is obtained that $q_G \approx 2$ and $q_F \approx -0.5$. The error term given by B.2 and plotted in Figure B.2 then calculates to ≈ 3 and ≈ 0.67 for the groundplane and for the segment respectively. It is seen that while the error in the surface inductance for the segment will then be $\approx \frac{1-0.67}{0.67} = 49\%$, the error for the groundplane is higher at $\approx \frac{1-3}{3} = -66.6\%$. In other words, the approximation overestimates the surface inductance of the segment by about twice while it underestimates the surface inductance of the groundplane by about a third. These errors are quite substantial but quickly decrease for thicker and/or wider groundplanes.

The analysis of the approximation of the surface inductance of a thin film has shown that, except in some special cases, one can expect systematic errors of not more than about $\pm 20\%$ and typically of 10% or less. Although this value seems high, the *total* inductance of any structure represented with a 2D sheet is larger than just the surface inductance of the sheet: one must also add the external inductance that measures the energy stored in the field outside the film. Errors made in the surface inductance thus reflect only partially in the total inductance of a given thin-film segment. For example, the YBCO thin films in the π-shift technology have a surface inductance L_S of about 0.5pH per square (per square = per unit width and height) while the sheet (total) inductance is about twice that value. A 20% error in L_S then yields a 10% error in the sheet inductance. In practice, the errors are even lower.

Summary

The topics presented in this thesis can be divided in three, roughly independent, parts: the Superconducting Network model (Chapter 2), π-shift RSFQ circuits together with experimental aspects of YBCO/Nb ramp-type Josephson devices (Chapters 3-4) and static π-shift circuits (Chapter 5-6). A short summary containing the main points of the above three parts is presented below.

A network model for an electromagnetic system is an abstraction of the physical processes taking place within it. Such models are built with the purpose to capture electromagnetic phenomena in the system, mainly the dynamics of electrical currents as they flow between its parts. A crucial task when building a network model is the segmentation of the system in a node-branch architecture (a schematic) where separate devices, as well as the connections between them, can be identified. The model building then proceeds with assigning nodal and flow variables, classically voltages V and currents I respectively, to the schematic. At the end, all devices are described by constitutive laws connecting the nodal and flow variables. These laws reflect the physics local to the concerned devices. Finally, the two Kirchhoff laws are combined with the constitutive relations of the devices in the schematic, resulting in a system of (coupled) differential equations where the flow and nodal variables can be solved for using numerical techniques.

An important property of electrical network models is that the thermodynamics of the modeled system are also accurately captured. The energy balance both between the devices and with their environment is automatically satisfied by solving the network equations.

Applying the classical (V, I) electrical network model to circuits containing superconducting elements, especially closed loops, necessitates keeping track of the initial conditions in the circuit that may, theoretically, originate infinitely far in the past. As a result, even when the system is in a steady-state where both the circuit variables and excitations (sources) do not change in time, one must consider the system's history while solving the network equations. Additionally, the phenomenon of flux quantization in superconducting loops is difficult to model

in (V, I) variable space. It is hence desirable to find a suitable network model for superconducting devices that eliminates the above problems.

During the analysis of superconducting circuits, one can not escape confronting a common, yet not well elucidated in literature, general property of electromagnetic networks: the presence of (partial) inductor elements in a circuit transforms the nodal variables from voltages V to scalar potentials ϕ. In fact, a strict application of electromagnetic laws to networks requires to always assign a scalar potential to the nodes in the network. Otherwise, the I Kirchhoff law - that the sum of the nodal variables around a loop in the network is zero - will not apply. Only when magnetic induction $\int \frac{\partial \boldsymbol{A}}{\partial t} \mathrm{d}\boldsymbol{l}$ is neglected are the nodal variables voltages, as that is precisely the difference between the two quantities. Hence, if one needs to model changing magnetic fields, the nodal variables in the network must be the scalar potentials. Further, to preserve gauge invariance of the network equations and give physical meaning to the nodal variables, one must write the scalar potentials in the circuit gauge i.e. use the Coulomb potentials U as proposed in the analysis of Section 2.2.3. Since magnetic field modeling is very important for superconducting circuits, a precise definition of the nodal variable in a superconducting network, as given above, is essential.

The presentation in Chapter 2 then continues with proposing a Josephson Network Model that is directly derived from the classical schematic of the system but where the nodal variable U is replaced with the flux angle φ. The time derivative of this new variable has to be proportional to the Coulomb potential at the same node, $U = \frac{\Phi_0}{2\pi} \frac{\mathrm{d}\varphi}{\mathrm{d}t}$, in order for the model to accurately represent the thermodynamics of the system. Using this variable change, all network equations can be rewritten in (φ, I) space.

The benefit of the model is twofold: a) all phenomena unique to superconductors (eg. flux quantization) can be included in the system in a more "natural" way and b) the flux angle φ has a physical interpretation as the current-weighted and cross-sectionally averaged phase of the superconducting wavefunction at the interface surfaces of a given superconducting segment. Additionally, as Section 2.2.6 shows, the Josephson Network Model provides a method of superconducting circuit analysis in potential space since the free energy of the system can be found from its schematic following just a few simple rules. This type of analysis is very beneficial, especially for smaller circuits, as it provides potential landscapes where one can graphically observe the system's stable states as potential minima. Eventually, also the dynamic trajectory through minimal-barrier paths between the states can be envisioned in case the circuit is excited with transient signals.

After the definition of the circuit elements typically found in superconducting networks, the potential landscapes of superconducting storage loops, the basic building blocks of RSFQ digital circuits, can be drawn and investigated. This qualitative analysis, found in Section 2.2.6.3, indicates that the usage of a π-

shift element in a binary RSFQ storage loop improves the symmetry between the two flux states of the loop and, generally, increases overall circuit robustness. Moreover, since the π-shift element eliminates the need for a bias current source in the loop, both power dissipation and noise sensitivity are decreased.

The close relation between the (V, I) and (φ, I) network descriptions of the superconducting system allows for the use of conventional circuit tools, for instance circuit simulators and electromagnetic (EM) element analysis. Such practical superconducting network modeling methods are included at the end of Chapter 2.

Chapter 3 presents the attempts for experimental verification of the hypothesis that RSFQ circuits benefit from a π-shift element. These experiments are a natural continuation of the initial successful functional tests of a basic π-shift RSFQ circuit and are designed to investigate circuit robustness at high speeds through the measurement of the bit-error-rate (BER) of a complex pattern-generator block. The manufacturing technology is a high-T_c/low-T_c hybrid thin-film process, where the Josephson junction elements are implemented as ramp-type contacts between the high-T_c superconductor YBCO and the low-T_c superconductor niobium through a thin gold barrier. A π-shift element is obtained by a 90° turn of the current path in a rectangular "L-shaped" YBCO segment, edge-aligned with the principal (a/b) axes of the deposited thin film. Since YBCO is a superconductor with an unconventional *d-wave* order parameter symmetry, a 90 degree turn within its a/b crystal plane results in a $\pm\pi$ added to the phase of the condensate, hence implementing an intrinsic π-shift element appearing in series with the (partial) inductance of the L-shaped segment. Both the details of the manufacturing process and of the RSFQ circuit blocks are documented in Chapter 3 with the purpose of preserving the engineering information for eventual future reference.

Results from the measurements on these π-shift devices, given in Section 3.2.3, were insufficient to confirm the hypothesized benefits of π-shift RSFQ circuits. Of the 20 manufactured samples across two IC series, nearly half failed during manufacturing (this physical yield improving considerably towards the end) while none of the rest provided a functioning digital device. Large spreads were observed in the parameters of the circuit elements, both on the same sample as well as between samples and, most obstructively, between different measurement sessions of the same sample. In addition, the superconducting properties of the YBCO thin film were determined to be different that the ones assumed during the physical design of the circuits structures, as indicated by the sheet inductance $L_\square$ parameter that was measured to be 50% smaller than its nominal value. This discrepancy can be attributed to a combination of two factors: errors in the early measurements of $L_\square$ that led to the initial nominal value and the poorly calibrated EM modelling tools for the YBCO film at that time. However, the highest factor of disturbance during the measurements originated from inadequate magnetic shielding, more precisely the inapplicability of standard defluxing procedures for hybrid YBCO/Nb circuits.

Projecting the rate of progress with these experiments, taking into account the available resources, it was concluded that the effort necessary to successfully perform a BER test on the 47-junction pattern generator circuit lies beyond the scope of a small-scale research effort. Although it is likely that functional basic π-shift devices of the RSFQ type can be (again) successfully manufactured and measured, albeit after a physical re-design of the circuits to account for the lower nominal $L_{\square\,\mathrm{YBCO}}$, the initial goal of confirming robustness vs. conventional RSFQ is, from a present experimental aspect, prohibitively difficult. It was therefore decided that within this research project, absent significant experimental breakthroughs, the work on π-shift superconducting devices in the YBCO/Nb technology should focus more on small and simple structures rather than on complex RSFQ circuitry.

To combat the described experimental issues, at least to a certain extent, efforts were made to increase the physical yield by improving the least reliable manufacturing steps, as well as reduce the spread in the device parameters by identifying critical (sub)processes during the manufacturing. Chapter 4 lists these measures which, as Section 4.2 indicates, resulted in both a high physical yield and an improved sample-to-sample variability of the parameters. The intra-sample spread of the critical currents has been quantified with measurements on junction arrays, indicating a $\pm 3\sigma$ deviation of about $\pm 30\%$ on average. Circuit simulations show that this value is, unfortunately, still not sufficiently low for reliably implementing large circuits.

Together with the earlier results on π-shift RSFQ circuits, the conclusion was made that: a) the present state of the YBCO/Nb technology is insufficiently developed for experimenting with complex designs; b) the easiest direction of improvement is to simply use the YBCO segments for π-shift purposes only and manufacture the Josephson junctions as metal-metal (Nb) contacts. Additionally, it is worth investigating the replacement of Nb with the chemically more stable Al as the low-T_c component in the process even though the refrigeration costs would be higher (the T_c of aluminium is about 1.2K). The reason is that this measure would also significantly improve the noise immunity and vortex-trapping properties of the circuits by admitting the use of better magnetic shielding materials, like for instance Al, in the measurement system.

The last part of this thesis describes novel π-shift devices in Chapter 5 and the measurements of their characteristics in Chapter 6. The structures are physically equivalent to magnetically modulated π-SQUIDs, except that they operate in the static flux domain i.e. they never enter the voltage state. The main feature of the modulated π-loop devices is that, depending on the parameters of the circuit, they can exhibit gain between the flux developed at a load inductor connected across the terminals of said loop and the flux externally applied to the loop. It is important to note that although a simple superconducting transformer with a load inductor

can also show flux gain between its input and output terminals, the range of the structure's circuit parameters (inductances, number of turns) for which that is the case are prohibiting the device to be small and compact. A modulated π-shift loop on the other hand achieves signal gain with a smaller overall size and lower physical complexity. Moreover, it also has a non-linear input/output transfer characteristic that allows signal operations other that simple gain to be implemented.

In a certain range of circuit parameters, a modulated π-loop may also show a hysteretic transfer characteristic, the device then experiencing a transition between two stable states as the input signal passes a threshold value. This situation resembles RSFQ circuits where similar state transitions implement a logic operation, except that here the state change per bit is not marked by the passing of a single but of a fractional flux quantum. This avenue of circuit-architectural research has not been done in this thesis but is nevertheless interesting for eventual further work.

In the case of a non-hysteretic π-device, when the input/output transfer characteristic is a single-valued continuous curve, the circuit never enters a state transition of the self-sustained type. There is only a single stable state in the potential landscape, the input signal influencing the position of this minimum and hence the output signal. When both input and output flux pass through the origin, the incremental gain $\frac{\partial \Phi_{\mathrm{out}}}{\partial \Phi_{\mathrm{in}}}$ is the highest. The curve then saturates with the incremental gain decreasing towards zero when the flux applied to the loop approaches an odd number of half-flux quanta. The transfer characteristic extends periodically as an odd function of the applied flux Φ_{in} thereafter.

The power dissipation of the circuit with non-hysteretic transfer is directly proportional to the speed of the signal change $\frac{\partial \Phi_{\mathrm{in}}}{\partial t}$ and inversely proportional to the resistance of the loop's junctions $\frac{1}{R_N}$. Typically, the dissipated energy per bit in a modulated π-device is about 10 times lower than in a comparable RSFQ cell. This factor becomes even greater if one uses unshunted junctions with high intrinsic normal resistances R_N. Important from this aspect is the fact that the power dissipation of the π-device approaches zero as the signal speed also approaches zero - one can thus set the device to operate below the limit of thermodynamic reversibility. One can find a discussion on the thermodynamic and logical reversibility of π-devices in Section 5.3.

For the creation of logic circuits, of most interest is the cascaded connection of inductively-modulated π-loop devices where the output of one cell is fed to the input of the next one. Also included is the case where the load of a π-device is not a single but a combination, either parallel or series, of more subsequent π-devices. It is shown that there exists a range of circuit variables (inductances and junction I_C's) for which these cascades will result in a non-hysteretic transfer curve and hence operation in the ultra-low dissipation regime.

Efforts on the experimental verification of the transfer characteristic of a π-device are presented in Chapter 6. Due to the fact that the circuits operate in the (Φ, I) domain, a direct measurement of a $\Phi_{\rm out}(\Phi_{\rm in})$ curve of a modulated π-loop is very difficult - it is in essence necessary to employ the same type of measurement used to find the current-phase dependence of various junction devices. These methods are usually specific to a device and require adaptation to an (existing) measurement system. In order to avoid excessive complication, also strongly advised from earlier experiments with the YBCO/Nb technology, the transfer characteristic of a flux-modulated π-loop was measured indirectly through the modulation effect of the device's output flux on a tightly-coupled normal SQUID loop. Investigating the critical current of the SQUID as a function of the magnetic flux externally applied to the preceding π-device, one can indirectly confirm the general shape of the latter's $\Phi_{\rm out}(\Phi_{\rm in})$ curve and look for the features typical to a π-loop transfer characteristic.

Several devices were designed and optimized to return the highest SQUID modulation depth so that the measurement accuracy is maximised. The experimental data confirm the main characteristics of the π-devices as theorized in Chapter 5, namely that there is a sharp $\Phi_{\rm out}(\Phi_{\rm in})$ dependence around the origin and a saturation of the transfer curve away from it. On the other hand, the modulation period in the obtained curves, directly proportional to the mutual coupling inductance between the π-device's input segment and loop, exhibited a very good agreement with EM modeling of the multi-layer structure. Taken together, the experiments can be said to confirm the accuracy of the EM simulation methods from Chapter 2, as well the network analysis specific to a modulated π-loop circuits from Chapter 5.

Samenvatting

De onderwerpen die in dit proefschrift zijn behandeld kunnen worden onderverdeeld in drie thema's, namelijk: het supergeleidende netwerk model (hoofdstuk 2), π-shift RSFQ circuits en de daarbij behorende experimentele aspecten van YBCO/Nb ramp-type Josephson schakelingen (hoofdstukken 3-4) en statische π-shift circuits (hoofdstukken 5-6). Een korte samenvatting met daarin de belangrijkste punten uit de drie bovengenoemde onderdelen wordt hieronder weergegeven.

Een netwerkmodel voor een elektromagnetisch systeem is een abstractie van de fysische processen die daarbinnen plaatsvinden. Dergelijke modellen beschrijven de elektromagnetische verschijnselen in het systeem, met name de dynamiek van elektrische stromen die tussen de verschillende delen van het system lopen. Een cruciale opgave bij het bouwen van een netwerkmodel is de segmentatie van het systeem in een knoop-tak architectuur (een schema) waarbij afzonderlijke elementen, evenals de verbindingen tussen hen, kunnen worden geïdentificeerd. De opbouw van het model gaat dan verder met het toewijzen van nodale (knoop) en stromingsvariabelen, respectievelijk spanningen V en elektrische stromen I, op het schema. De relatie tussen de variabelen wordt voor elk element gegeven door zijn consitutieve wet. Deze wetten weerspiegelen de natuurkundige verschijnselen die lokaal binnen de betrokken elementen plaatsvinden. De twee wetten van Kirchhoff worden uiteindelijk gecombineerd met de constitutieve relaties van de elementen in het schema, wat resulteert in een systeem van (gekoppelde) differentiaalvergelijkingen waarbij de nodale en stromingsvariabelen kunnen worden opgelost door het gebruik van numerieke technieken.

Een belangrijke eigenschap van elektrische netwerken is dat de thermodynamica van de gemodelleerde systeem ook nauwkeurig wordt vastgelegd. Aan de energiebalans, zowel tussen de elementen als met hun omgeving, wordt automatisch voldaan door het oplossen van de netwerkvergelijkingen.

Het toepassen van het klassieke (V, I) elektrisch netwerkmodel op circuits met supergeleidende elementen, in het bijzonder gesloten lussen, vereist het bijhouden van de initiële condities in het circuit die, in theorie, oneindig ver in het verleden kunnen zijn ontstaan. Als gevolg daarvan, ook als het systeem zich in een steady-state bevindt waar zowel de circuitvariabelen als de excitaties (bronnen) niet veranderen in de tijd, moet men rekening houden met de systeemgeschiedenis tijdens het oplossen van de netwerkvergelijkingen. Bovendien, is het moeilijk om

het fenomeen van fluxkwantisatie in het (V, I) domein op te nemen. Het is daarom wenselijk een geschikt netwerkmodel voor supergeleidende schakelingen te vinden die de bovenstaande problemen elimineert.

Tijdens de analyse van supergeleidende circuits, komt een in de literatuur niet goed opgehelderd algemene eigenschap van elektromagnetische netwerken van pas: de aanwezigheid van (partiële) inductorelementen in een circuit transformeert de nodale variabelen van spanningen V naar scalaire potentialen ϕ. In feite vereist een strikte toepassing van elektromagnetische wetten op netwerken om altijd scalaire potentialen toe te wijzen aan de knooppunten in een netwerk. Als dat niet het geval is, wordt de eerste Wet van Kirchhoff - dat de som van de nodale variabelen rond een lus in het netwerk nul is - niet meer geldig. Alleen als de magnetische inductie $\int \frac{\partial \boldsymbol{A}}{\partial t} \mathrm{d}\boldsymbol{l}$ wordt verwaarloosd kunnen de nodale variabelen de spanningen V zijn, want dat is precies het verschil tussen de twee grootheden. Om wisselende magneetvelden te kunnen modelleren, moeten de nodale variabelen in het netwerk de scalaire potentialen zijn. Verder, zoals voorgesteld in sectie 2.2.3, om fysische betekenis aan de nodale variabelen te geven is het noodzakelijk om het zgn. "circuit ijk" (circuit gauge) te gebruiken. Dan zijn de nodale variabelen gelijk aan de Coulomb potentialen U in het systeem.

Omdat het modelleren van het magnetische veld erg belangrijk is voor supergeleidende circuits, is een nauwkeurige definitie van de nodale variabele in een supergeleidend netwerk, zoals hierboven gegeven, van essentieel belang.

De presentatie in hoofdstuk 2 gaat verder met het voorstellen van het Josephson Netwerkmodel dat direct wordt afgeleid uit het conventionele schema van het systeem, maar waar de nodale variabele U door de fluxhoek φ vervangen wordt. De tijdsafgeleide van deze nieuwe variabele moet evenredig zijn met de Coulomb potentiaal op hetzelfde knooppunt, $U = \frac{\Phi_0}{2\pi} \frac{\partial \varphi}{\partial t}$, om de thermodynamica van het systeem nauwkeurig te kunnen beschrijven. Met behulp van deze substitutie van variabelen kunnen alle netwerkvergelijkingen herschreven worden in het (φ, I) domein.

Het voordeel van het model is tweeledig: a) alle verschijnselen die uniek zijn voor supergeleiders (bijv. fluxkwantisatie) kunnen worden opgenomen in het systeem op een natuurlijker manier en b) de fluxhoek φ heeft een fysische interpretatie als de stroomgewogene en doorsneegemiddelde fase van de supergeleidende golffunctie op de grensvlakken van een gegeven supergeleidend segment. Bovendien, zoals sectie 2.2.6 laat zien, biedt het Josephson Netwerkmodel een eenvoudige methode voor de analyse van supergeleidende schakelingen in de potentiaalruimte waar de vrije energie van het systeem gevonden wordt door het toepassen van slechts een paar eenvoudige regels. Dit type analyse is zeer gunstig, vooral voor kleinere circuits, omdat door deze potentiaallandschappen te observeren men grafisch de stabiele toestanden van het systeem als potentiale minima kan identificeren. Uiteindelijk kunnen voor aangedreven circuits ook de dynamische trajecten worden waargenomen als minimal-barrière paden tussen de toestanden.

De potentiaallandschappen van supergeleidende opslaglussen, de elementaire bouwstenen van RSFQ digitale schakelingen, worden vervolgens berekend en onderzocht. Deze kwalitatieve analyse, gevonden in sectie 2.2.6.3, geeft aan dat het gebruik van een π-shift element in een binair RSFQ opslaglus de symmetrie van de twee fluxtoestanden van de lus verbetert en de robuustheid van de circuit verhoogt. Aangezien het π-shift element de noodzaak voor een bias stroombron in de lus elimineert, zullen zowel het energieverlies als ook de ruisgevoeligheid van het circuit lager uitvallen in vergelijking met conventionele RSFQ cellen.

De relatie tussen de (U, I) en (φ, I) netwerkbeschrijvingen van een supergeleidend systeem maakt het gebruik van conventionele circuit tools mogelijk, bijvoorbeeld circuitsimulatoren of elektromagnetische (EM) elementanalyse. Dergelijke praktische methoden van supergeleidende netwerkmodellering zijn aan het eind van hoofdstuk 2 opgenomen.

Hoofdstuk 3 presenteert de pogingen tot experimentele verificatie van de hypothese dat RSFQ circuits profiteren van een π-shift element. Deze experimenten zetten de eerste succesvolle functionele tests van een basis π-shift RSFQ circuit voort en zijn ontworpen om circuitrobuustheid te onderzoeken bij hoge snelheden door de meting van de bit-error-rate (BER) van een complexe patroon-generator schakeling. De productietechnologie is een high-T_c/low-T_c hybride dunne-film-proces, waarbij de Josephson junctie elementen als ramp-type contacten tussen de hoge T_c supergeleider YBCO en de lage T_c supergeleider niobium worden geïmplementeerd. Het π-shift element wordt verkregen door een 90° draai in het stroompad binnen een YBCO segment te maken, de randen van de laatste uitgelijnd met de principale (a/b) assen van de afgezette dunne film. Omdat YBCO een supergeleider met een onconventionele d-wave orderparametersymmetrie is, resulteert een 90 graden draai binnen het a/b kristalvlak in de toegevoeging van $\pm\pi$ aan de fase van het condensaat, waardoor een intrinsieke π-shift element in serie met de (partiële) inductie van het YBCO segment wordt geimplementeerd. De details van zowel het productieproces als van de RSFQ circuitblokken zijn in hoofdstuk 3 gedocumenteerd met als doel het behoud van de technische informatie voor toekomstige referentie.

Resultaten van de metingen van deze π-shift schakelingen, die in sectie 3.2.3 te vinden zijn, zijn onvoldoende om de verwachte voordelen van een π-shift RSFQ circuit te kunnen bevestigen. Van de 20 samples vervaardigd over twee IC-series, mislukte bijna de helft tijdens de productie (deze fysieke opbrengst werd aanzienlijk verbeterd aan het einde van de reeks), terwijl geen enkele een functionerende digitale schakeling bevatte. Grote variaties werden in de parameters van de elementen waargenomen, zowel op hetzelfde sample alsmede tussen hen en, het meest verhinderend, ook tussen de verschillende meet-sessies voor dezelfde sample. Daarnaast bleken de supergeleidende eigenschappen van de YBCO dunne film anders te

zijn dan aangenomen tijdens het ontwerpen van de schakelingen, zoals aangegeven door de blad-inductie parameter $L_\square$ die maar de helft van zijn nominale waarde tijdens de metingen haalde. Deze discrepantie kan worden toegeschreven aan een combinatie van twee factoren: fouten in de eerdere metingen van $L_\square$ die leidden tot de oorspronkelijke nominale waarde en het gebrek aan goed gekalibreerde EM modellen voor de YBCO film op dat moment. De grootste factor van verstoring tijdens de metingen ontstond echter door onvoldoende magnetische afscherming, met name de niet-toepasselijkheid van standaard defluxing procedures voor deze hybride YBCO/Nb circuits.

Door het projecteren van de voortgang van deze experimenten, waarbij rekening werd gehouden met de beschikbare middelen, werd geconcludeerd dat de inspanning die nodig is om een BER-test succesvol uit te voeren buiten het kader van een kleinschalig onderzoeksproject ligt. Hoewel het waarschijnlijk is dat eenvoudige π-shift schakelingen van het RSFQ type (weer) met succes geproduceerd en gemeten kunnen worden, zij het na een fysieke re-design van de circuits om rekening te houden met de lagere nominale $L_\square$, het aanvankelijke doel om de robuustheid van π-shift versus conventionele RSFQ te bevestigen is, met de huidige experimentele stand van zaken, buitengewoon moeilijk te bereiken. Daarom is er besloten dat binnen dit onderzoeksproject, afwezig belangrijke experimentele doorbraken, het werk aan π-shift supergeleidende schakelingen in de YBCO/Nb technologie zich meer op kleine en eenvoudige structuren in plaats van complexe RSFQ circuits moest gaan richten.

Ter bestrijding van de beschreven experimentele problemen werden pogingen gedaan om de fysieke opbrengst te verhogen door het verbeteren van de minst betrouwbare productie stappen en de spreiding in de parameters van de elementen tegen te gaan door het identificeren van kritische stappen tijdens het bewerkingsproces. Hoofdstuk 4 geeft een overzicht van deze maatregelen die, zoals sectie 4.2 aangeeft, resulteerden in zowel een hoge fysieke opbrengst als in een kleinere spreiding van de parameters tussen verschillende samples. Daarnaast, werd de spreiding van de kritische stroom van de Josephson juncties op dezelfde sample gekwantificeerd door metingen op junctie-reeksen: de resultaten wijzen op een $\pm 3\sigma$ afwijking van ongeveer $\pm 30\%$. Circuit simulaties tonen aan dat deze waarde helaas nog steeds niet laag genoeg is om complexe circuits te kunnen maken.

De meetresultaten van π-shift RSFQ circuits laten zien dat: a) de huidige stand van de YBCO/Nb technologie onvoldoende ontwikkeld is om te experimenteren met complexe ontwerpen en b) de gemakkelijkste richting van verbetering is om de YBCO segmenten alleen te gebruiken voor π-shift doeleinden en de Josephson juncties als metaal-metaal (Nb) contacten te fabriceren. Daarnaast is het de moeite waard de vervanging van Nb met het chemisch stabieler aluminium (Al) te onderzoeken, alhoewel de koeling kosten dan hoger uit zullen vallen (de T_c van Al is ongeveer 1.2 K). De reden hiervoor is dat deze maatregel ook zou leiden tot het

aanzienlijk verbeteren van de ruisimmuniteit van de circuits door de toelating van het gebruik van betere magnetische afscherming materialen, zoals bijvoorbeeld Al, in het meetsysteem.

Het laatste gedeelte van dit proefschrift beschrijft een nieuwe type π-shift schakeling in hoofdstuk 5, terwijl de metingen van hun eigenschappen in hoofdstuk 6 verschijnen. De structuren zijn fysisch overeenkomstig met magnetisch gemoduleerde π-SQUIDs, behalve dat ze voortdurend actief in het statische fluxdomein zijn en waar ze zodoende nooit in de spanningstoestand kunnen komen. Het belangrijkste kenmerk van deze gemoduleerde π-lussen is dat, afhankelijk van de parameters van het circuit, ze versterking tonen tussen de magnetische flux die zich ontwikkelt op de belastingsinductor verbonden aan de aansluitingen van de lus en de flux die extern aan de lus aangeboden wordt. Het is belangrijk op te merken dat hoewel een eenvoudige supergeleidende transformator met een belastingsinductor ook fluxversterking tussen de input en output terminals kan vertonen, de waarden van de circuit parameters (inductie-elementen, het aantal windingen) waarvoor dat het geval is het moeilijk maken om de schakeling klein en compact te houden. Aan de andere kant vertoont een gemoduleerd π-shift lus signaalversterking met een kleinere totale omvang en een lagere fysieke complexiteit. Bovendien, blijkt de π-lus een sterk nonlineaire input/output overdrachtskarakteristiek te hebben die het mogelijk maakt om ook andere signaalbewerkingsoperaties uit te voeren.

Waneer de waarden van de circuitparameters binnen een bepaald bereik vallen, toont de gemoduleerde π-lus een hysteretische overdrachtskarakteristiek waarbij er een overgang tussen twee stabiele toestanden plaatsvindt op het moment dat het ingangssignaal een drempel passeert. Deze situatie lijkt op RSFQ circuits die vergelijkbare toestandsovergangen gebruiken om een logische operatie te implementeren, behalve dat hier de statuswijziging per bit niet gekenmerkt wordt door het passeren van een enkele, maar van een fractioneel fluxquantum. Deze richting van circuit-architecturaal onderzoek wordt niet vervolgd in dit proefschrift, maar is niettemin interessant voor eventuele verdere werkzaamheden.

In het geval van een niet-hysteretische schakeling, gekenmerkt door een enkelwaardig continue input/output overdrachtskarakteristiek, zou het circuit nooit een toestandswissel van het "self-sustained" type ervaren. Er is maar een stabiele toestand in het potentiaallandschap - het ingangssignaal beïnvloedt de positie van dit minimum en daarmee de waarde van het uitgangssignaal. Wanneer beide signalen door de oorsprong heengaan, $\Phi_{\mathrm{out}} = \Phi_{\mathrm{in}} = 0$, wordt de incrementele versterking $\frac{\partial \Phi_{\mathrm{out}}}{\partial \Phi_{\mathrm{in}}}$ het hoogst. Daarbuiten verzadigt de overdrachtscurve zodanig dat de incrementele versterking naar nul afneemt wanneer de toegepaste flux in de lus Φ_{in} een oneven aantal half-flux kwanta benadert. De overdrachtskarakteristiek strekt zich als een periodieke oneven functie van de toegepaste flux daarna.

De dissipatie van het circuit met een niet-hysteretische overdrachts karakteristiek is direct evenredig met de snelheid van het wijzigen van het signaal ($\frac{\partial \Phi}{\partial t}$) en omgekeerd evenredig met de weerstand van de juncties in de lus ($\frac{1}{R_N}$). Typisch is de gedissipeerde energie per bit in een gemoduleerde π-schakeling ongeveer tien keer lager dan in een vergelijkbare RSFQ cel. Deze factor wordt nog groter als men gebruik maakt van zgn. "unshunted" juncties met een hoge intrinsieke normale weerstand R_N. Belangrijk vanuit dit oogpunt is het feit dat het vermogensverlies van de π-schakeling nul nadert als de signaalsnelheid ook naar nul gaat - men kan dus de schakeling onder de limiet van thermodynamische omkeerbaarheid bedrijven. Een discussie over de thermodynamische en logische omkeerbaarheid van π-schakelingen wordt in Sectie 5.3 gegeven.

Wat betreft het maken van conventionele digitale circuits, is het meest interessante onderwerp het verbinden van inductief-gemoduleerde π-lus schakelingen in een cascade waar de uitgang van de ene cel op de ingang van het volgende aansluit. Het geval waneer de belasting van een π-schakeling uit een combinatie, parallel dan wel serie, van meerdere π-schakelingen bestaat wordt ook beschouwt. Het wordt aangetoond dat wanneer de circuit parameters binnen een bepaald bereik vallen, deze cascades een gezamenlijk niet-hysteresische overdrachtscurve krijgen waarmee de werking in het ultra-lage dissipatieregime mogelijk is.

De experimentele verificatie van de overdrachtskarakteristiek van een π-schakeling wordt gepresenteerd in hoofdstuk 6. Als gevolg van het feit dat de circuits actief zijn in het statische flux domein, is een directe meting van een $\Phi_{\rm out}(\Phi_{\rm in})$ curve van een gemoduleerde π-lus zeer moeilijk uit te voeren - het is in wezen dezelfde type meting die gebruikt wordt voor het vinden van de stroom-fase afhankelijkheid van Josephson juncties. Deze methoden zijn meestal afgestemd op een specifieke schakeling waardoor (bestaande) stroom-fase meetsysteemen aangepast zullen moeten worden. Om te veel complicaties te vermijden, wat ook door eerdere experimenten met de YBCO/Nb-technologie sterk gesuggereerd wordt, werd de overdrachts karakteristiek van een flux-gemoduleerde π-lus indirect gemeten via het modulatie-effect dat de output flux van de π-lus op een sterk gekoppeld normale SQUID heeft. Het onderzoeken van de kritische stroom van de SQUID als functie van de magnetische flux die extern wordt aangeboden op de voorgaande π-lus kan indirect de algemene vorm van de $\Phi_{\rm out}(\Phi_{\rm in})$ curve bevestigen door het zoeken naar bepaalde kenmerken die typisch zijn voor een π-lus overdrachts karakteristiek.

Meerdere schakelingen werden ontworpen en geoptimaliseerd om de hoogste SQUID modulatiediepte te krijgen en daardoor de meetnauwkeurigheid te maximiseren. De experimentele gegevens bevestigen de belangrijkste kenmerken van de statische π-schakelingen volgens de theorie van hoofdstuk 5, namelijk dat er een scherpe $\Phi_{\rm out}(\Phi_{\rm in})$ afhankelijkheid rond de oorsprong is en een verzadiging van de overdrachtcurve daarbuiten. Aan de andere kant vertoont de modulatieperiode in de meetdata, direct evenredig met de onderlinge koppeling tussen de inductie

van de ingangssegment en de lus in de π-schakeling, een zeer goede overeenkomst met de EM-modellering van de multi-laags structuur. Samengevat bevestigen de experimenten de nauwkeurigheid van de EM simulatie-methoden uit hoofdstuk 2, evenals de netwerkanalyse van de gemoduleerde π-lussen uit hoofdstuk 5.

Dankwoord

Het is een mooie traditie het proefschrift af te sluiten met een stukje die niet aleen de namen van de betrokkene mensen optelt, maar ook aan de vele jaren (hoeveel zal ik niet zeggen) samenwerking met hen terugkijkt. Inderdaad, een proefschrift is het product van interactie tussen mensen en, als men het voorzichting leest, komt ook de aard van deze wisselwerking er tevoorschijn. Het is daarom met grote genoegen dat ik dit proefschrift met een kleine wordje van dank aan mijn collegas en vrienden kan eindigen.

De mensen met wie ik meest nauw samen heb gewerkt - Hans, Kees, Ariando, Frank, Dick en Alexander - wil ik allemaal bedanken voor het vermakelijken van mijn opdracht door, simpel gezegd, zonder enige teken van terughoudenheid hun kennis met mij te delen. Komend vanuit een andere vak, het was voor mij heel belangrijk dat ik goed werd begeleid door het nieuwe terrein.

Hans, ik wil je bedanken voor het kans om mijn promotieonderzoek te beginnen en de steun die ik daarna altijd kreeg, door dik en dun, mijn werk op de jusite spoor te houden. Het spontaniteit waarmee je leiding geeft komt echter niet vaak voor. Ik had me geen betere promotor kunnen wensen.

Kees en Ariando, bedankt voor julie geduld in het lab tijdens mijn eerste jaar toen ik nog geen bal van dunne-film processwerk snapte. Heel veel van mijn routine in het laboratorium heb ik van julie twee geleerd. Alexander, bedankt voor je “open door policy” (waar ik vaak beroep op deed) en de besmettelijke enthusiasme waarmee je ontwerpen van alle soorten benadert.

Het was zeer belangrijk voor me dat ik altijd op iemand kan rekenen als er iets in het lab misging of als ik plotselijk weer een ideë had gekregen die ik met een “reality check” moest toetsen. Frank en Dick, bedankt daarvoor!

Ans en Inke wil ik bedanken voor zowel hun inzet als voor hun stijlvolle manieren. Het was een plezier met julie samen te werken.

I would also like to thank Thomas Ortlepp and Olaf Mielke for sharing their knowledge on RSFQ circuits and providing the physical designs for some of the circuits found in this thesis. Olaf, thanks for your patience in the measurement lab!

Alle andere mensen die in welke dan ook manier bijdroegen: Sybolt, Harry, Jan, Peter L., Mark S. en degene die ik vast vergreten heb - hartelijk dank voor julie ondersteuning!

Ik had de unieke kans om twee generaties AIO-collegas mee te kunnen maken. Aan de “oudere” groep - Kees, Maarten, Martin, Jeroen, Kris, Johannes, Aico, Reinder - ben ik dankbaar voor vele leuke herinneringen, zoals de memorabele gebeurtenissen op zekere conferenties of de tocht door het westen van de VS. Alhoewel de generatiekloof met de “jongere” groep - Joost, Cor, Menno, Marcel, Sebastian, Sander, Peter - vrij groot was, heb ik toch van onze uitjes erg kunnen genieten. Daar was het voor mij prettig dat ik de nederlandse cultuur van dichtbij mee kon maken. Een goede voorbeeld daarvan is toen ons zeilbootje door “piraten” werd aangevallen: ik leerde “Nederlanders op het water niet te vertouwen”. Alle grappen opzij, ik ben erg dankbaar voor alle mooie ervaringen jongens!

Joost, Cor en Bas: bedankt voor het zorgvuldig lezen en corregeren van de (veel) taalfouten in de Samenvatting.

Iedereen moet ik ook bedanken voor in het nederlands tegen mij praten toen ik in Eschede aankwam - zo heb ik uiteraad de taal kunnen leren (al gaat het met schrijven wat trager).

To my friends - Sofka, Vojkan, Maksa, Sanja, Oktay, Banu - I am indebted for their hospitality and the many good memories that we shared during all the years we lived in Enschede. I am very grateful to my parents for pointing me to the right direction all those years ago when I chose to leave my original country - this is the result of that journey!

Er is éen iemand die wezenlijk verantwordelijk is voor het mogelijk maken van het levensreis die in deze promotie eindigt: mijn lieve Jasminka. Bedankt voor je monumentale geduld met mijn capriolen en de onvoorwaardelijke liefde die je me al zo veel jaren geeft.

Je hebt het gelijk: ik kon ook zonder jou promoveren. Maar wat voor zin heeft het om door het leven te gaan als PhD met veel kennis en maar weining verstand?